frontiers | Research Topics

Solar wind - magnetosphere interaction

Edited by
Simon Wing, Lauri Holappa, Joseph E. Borovsky and Olga V. Khabarova

Published in
Frontiers in Astronomy and Space Sciences
Frontiers in Physics

ISSN 1664-8714
ISBN 978-2-8325-2817-4
DOI 10.3389/978-2-8325-2817-4

About Frontiers

Frontiers is more than just an open access publisher of scholarly articles: it is a pioneering approach to the world of academia, radically improving the way scholarly research is managed. The grand vision of Frontiers is a world where all people have an equal opportunity to seek, share and generate knowledge. Frontiers provides immediate and permanent online open access to all its publications, but this alone is not enough to realize our grand goals.

Frontiers journal series

The Frontiers journal series is a multi-tier and interdisciplinary set of open-access, online journals, promising a paradigm shift from the current review, selection and dissemination processes in academic publishing. All Frontiers journals are driven by researchers for researchers; therefore, they constitute a service to the scholarly community. At the same time, the *Frontiers journal series* operates on a revolutionary invention, the tiered publishing system, initially addressing specific communities of scholars, and gradually climbing up to broader public understanding, thus serving the interests of the lay society, too.

Dedication to quality

Each Frontiers article is a landmark of the highest quality, thanks to genuinely collaborative interactions between authors and review editors, who include some of the world's best academicians. Research must be certified by peers before entering a stream of knowledge that may eventually reach the public - and shape society; therefore, Frontiers only applies the most rigorous and unbiased reviews. Frontiers revolutionizes research publishing by freely delivering the most outstanding research, evaluated with no bias from both the academic and social point of view. By applying the most advanced information technologies, Frontiers is catapulting scholarly publishing into a new generation.

What are Frontiers Research Topics?

Frontiers Research Topics are very popular trademarks of the *Frontiers journals series*: they are collections of at least ten articles, all centered on a particular subject. With their unique mix of varied contributions from Original Research to Review Articles, Frontiers Research Topics unify the most influential researchers, the latest key findings and historical advances in a hot research area.

Find out more on how to host your own Frontiers Research Topic or contribute to one as an author by contacting the Frontiers editorial office: frontiersin.org/about/contact

Solar wind - magnetosphere interaction

Topic editors

Simon Wing — Johns Hopkins University, United States
Lauri Holappa — University of Oulu, Finland
Joseph E. Borovsky — Space Science Institute (SSI), United States
Olga V. Khabarova — Tel Aviv University, Israel

Citation

Wing, S., Holappa, L., Borovsky, J. E., Khabarova, O. V., eds. (2023). *Solar wind - magnetosphere interaction*. Lausanne: Frontiers Media SA.
doi: 10.3389/978-2-8325-2817-4

Table of contents

frontiers | Frontiers in Astronomy and Space Sciences

TYPE Editorial
PUBLISHED 06 March 2023
DOI 10.3389/fspas.2023.1158971

OPEN ACCESS

EDITED AND REVIEWED BY
Julio Navarro,
University of Victoria, Canada

*CORRESPONDENCE
Simon Wing,
simon.wing@jhuapl.edu

SPECIALTY SECTION
This article was submitted to Space Physics, a section of the journal Frontiers in Astronomy and Space Sciences

RECEIVED 04 February 2023
ACCEPTED 13 February 2023
PUBLISHED 06 March 2023

CITATION
Wing S, Borovsky JE, Holappa L and Khabarova O (2023), Editorial: Solar wind–Magnetosphere interactions. *Front. Astron. Space Sci.* 10:1158971. doi: 10.3389/fspas.2023.1158971

Editorial: Solar wind–Magnetosphere interactions

Simon Wing[1]*, Joseph E. Borovsky[2], Lauri Holappa[3] and Olga Khabarova[4]

[1]Applied Physics Lab, The Johns Hopkins University, Laurel, MD, United States, [2]Space Science Institute, Boulder, CO, United States, [3]Space Physics and Astronomy Research Unit, University of Oulu, Oulu, Finland, [4]Raymond and Beverly Sackler Faculty of Exact Sciences, Tel Aviv University, Tel Aviv, Israel

KEYWORDS

solar wind-magnetosphere interaction, solar wind, magnetosphere, ionosphere, radiation belt, geomagnetic activity, storm, substorm

Editorial on the Research Topic
Solar wind–Magnetosphere interactions

The Earth's magnetic field shields the planet and its atmosphere from the solar wind. However, this magnetic shielding is not perfect. A fraction of the mass, energy, and momentum from the solar wind can transfer to the magnetosphere and ionosphere through processes that are often referred to as solar wind-magnetosphere interactions (see, for example, reviews in Akasofu, (1981); Rostoker et al. (1988); Gonzalez et al. (1999); Jordanova, (2003); Watermann et al. (2009); Wing et al. (2014); Johnson et al. (2014); Kilpua et al. (2017); Borovsky (2020); Zhang et al. (2022)). The solar-wind-magnetosphere interactions form a basic foundation for the studies of space physics, magnetospheric physics, ionospheric physics, and space weather.

The goals of this Frontiers Research Topic on Solar Wind–Magnetosphere Interactions are 1) to publish research at the forefront of this important topic, 2) to assess the state of knowledge, 3) to point out new directions in research, 4) to apply new mathematical and data-analysis techniques, and 5) to discuss needs for the future.

Seventeen papers on solar wind–magnetosphere interactions are contained in this electronic book. Synopses of the seventeen papers are as follows, ordered by papers that focus on 1) the Sun 2) solar wind, 3) magnetosphere, and 4) ionosphere.

Chapman builds on her previous work that shows that they can map sunspot record, which has irregular cycle duration, onto a regular "clock" where each cycle has the same duration in Hilbert analytic phase. The quiet interval of the solar cycle is located at a fixed phase interval of this solar cycle clock. In the present work, she shows that such mapping can be done without using the Hilbert transform. There is a clear geomagnetically active-quiet switch-off and quiet-active switch-on activity and the times for this on and off switch can be directly determined from the sunspot time-series without performing Hilbert transform. The switch-off and switch-on of activity can be mapped from the clock back into the time-domain to create a cycle-by-cycle chart of activity, which can be useful for space weather assessment.

Sivadas and Sibeck study how simultaneous measurements of different L1 solar wind monitors differ due spatial and temporal structure of solar wind. They point out that this inherent uncertainty in L1 solar wind measurements may lead to bias in various studies utilizing correlations between solar wind and magnetospheric variables. By numerical experiments Sivadas and Sibeck show that this so-called regression bias may lead to an

apparent underestimation of magnetospheric response to extremes in solar wind driving for all popularly used regression analysis methods.

Chepuri et al. examine a large number of low-latitude boundary layer crossings by the Magnetospheric Multiscale (MMS) satellites to analyze the fluxes of energetic (>30 keV) electrons and whistler-mode chorus waves. They find that enhancements of energetic electrons and whistler-mode waves are often associated with signatures of magnetic reconnection. However, they point out that more research is needed to uncover whether these statistical relationships indicate causality.

Farrugia et al. study the effect of a solar wind directional discontinuity (DD) on the Earth's magnetosphere on 10 January 2004 using simultaneous observations from four spacecraft, namely Geotail, Cluster, Polar, and DMSP. The passage of the solar wind DD leads to the formation of the complicated structures in the magnetosphere even though the geomagnetic activity is relatively quiet, AE index is ~ 0 nT and Sym-H ~−10 nT. These structures include compression and dilation of the magnetosphere, deformation of the postnoon magnetopause, magnetotail flapping and twisting, strong tailward flow (~680 km/s) at a distant tail (~−230 Re). At the nightside ionosphere, near the poleward edge of the auroral oval, there is evidence of strong sunward flow (3 km/s) accompanied by a pair of upward and downward field-aligned currents (FACs).

Reistad et al. show that magnetospheric substorms are stronger and more frequent when IMF By and the Earth's magnetic dipole tilt have opposite signs. That is, substorm activity is enhanced for By > 0 during negative dipole tilt (NH winter) and *vice versa* during positive dipole tilt (NH summer). Reistad et al. show that this so-called explicit IMF By dependence is systematically seen in several, independent substorm lists. The physical mechanism of the By dependence is currently not fully understood. Reistad et al. suggest that the By dependence of magnetospheric substorms could result from a similar By dependence of the dayside reconnection rate.

Pulkkinen et al. perform 131 simulations of geomagnetic storms using the University of Michigan Space Weather Modeling Framework Geospace configuration. The framework comprises a set of numerical models able to solve the 3-D extended MHD equations to describe and predict different processes in space plasma. The study focuses on modeling the parameters characterizing the condition of the magnetosphere like the geomagnetic indices, which are directly related to solar wind drivers, magnetopause locations, and the cross-polar cap potential. The simulated results are generally in a good agreement with those observed. Meanwhile, it is found that the Geospace simulation consistently underestimates AL index, and significantly gives smaller distances from the Sun-Earth line to the lobe boundary in comparison with the empirical model in the conditions of the increased dynamic solar wind pressure. The article highlights the usability of geomagnetic indices and constructiing solar wind drivers of geomagnetic storms.

Borovsky re-examines the well-known positive correlation between the amplitude of magnetic-field fluctuations (turbulence) in the upstream solar wind and the level of geomagnetic activity. He re-confirms those correlations, but cautions the research community that the "turbulence effect" on magnetospheric activity may not be physically real.

Borovsky re-investigates the effect of noise on solar-wind/magnetosphere coupling studies by adding noise to real solar-wind and geomagnetic-activity data. This study re-confirms that noise changes the functional forms of best-fit driver functions, again obscuring the physics of how the magnetosphere is driven by the solar wind.

Borovsky uses artificial-data "gedankenexperiments" to explore the effect of noise in the data on correlation analysis between the time-dependent solar wind and the time-dependent geomagnetic activity. Noise is found to alter best-fit formulas for solar-wind driver functions, obscuring the physics of solar-wind driving.

Borovsky points out that there are 3 dawn-dusk aberrations to the solar wind at the Earth: one caused by the orbit of the Earth about the Sun, one caused by the propatation of solar-wind structure along the Parker spiral direction, and one associated with a systematic non-radial flow of the solar wind at 1 AU. These 3 aberrations degrade the quality of a solar-wind monitor at L1.

Gokani et al. discuss how solar drivers and geomagnetic storms affect the loss of high energy electrons from the outer radiation belt. They analyze 103 intense geomagnetic storms with Dst ≤ −100 nT in 1996–2019 and, using the superposed epoch analysis, find that the flux depletions of electrons having energies >0.6 MeV and >0.8 MeV at the geostationary orbit starts with the main phase of the storm and can reach over one order of magnitude. No solar cycle dependence is found. Effects of the most geoeffective solar drivers, namely coronal mass ejections (CMEs) and corotating interaction regions (CIRs), are investigated. Interplanetary coronal mass ejections (ICMEs) are divided into sub-structures and tested for the impact of each on the radiation belt electron flux. The authors conclude that the flux decreases are larger in the sheath-related storms, which may be due to the enhanced dynamic pressure and ULF wave power. A comparison between the radiation belt electron depletion caused by ICMEs and CIRs shows that it is more pronounced in the latter case, contrary to previous observations. The role of different solar drivers, such as solar wind conditions, the pressure, the speed, the density, the electric field, and the interplanetary magnetic field vertical component in causing radiation belt energetic electron flux decrease is also discussed.

Borovsky and Runov investigate the possibility that the energetic strahl electron population of the solar wind might be the ultimate origin of the seed electron population of the Earth's electron radiation belt, with the strahl electrons becoming the suprtathermal electron population of the magnetotail plasma sheet, electrons which are injected into the Earth's dipole by substorms.

Kondrashov et al. describe a machine learning technique to predict plasmaspheric hiss spectral classes ("no hiss", "regular hiss", and "low-frequency hiss") from the Van Allen Probes data. The authors create a random forests model which is found to be more accurate, compared to the existing unsupervised machine learning self-organizing map method. The highest scores detected by the model often match the distribution of the classes in the data set, which explains the model's high predictive skill. It is shown that predictors like magnetospheric and solar wind conditions only improve the predictions by a very small amount while the distinct locations of a given spectral class play a major role in determining the prediction's accuracy.

Lockwood and Cowley carry out a comprehensive analysis of non-equilibrium conditions of the magnetosphere-ionosphere-thermosphere system. The most important phenomena, such as magnetic reconnection and flux transport, occur when the system is not in equilibrium, therefore the corresponding processes require better understanding. It is shown that even if the solar wind driving does not change, the magnetosphere-ionosphere system can still display variations depending on time of year and UT owing to the Earth dipole tilt combined with other effects such as motions of the geomagnetic poles in a geocentric frame, the tail geometry, and ionospheric conductivity. This means that equilibrium is not just a function of the amount of open flux in the system. The study suggests that if one tries to map electric fields from interplanetary space to the ionosphere, the results are only accurate under steady-state conditions that can be achieved by taking data over long timescales and averaging out fluctuations. It is also discussed how the Expanding Contracting Polar Cap (ECPC) model may be the most accurate in predicting the magnetospheric response to the solar wind variability. In particular, it is found that the convection response and the integrated flux transport over the polar cap are higher for the high solar wind dynamic pressure cases. According to ECPC, enhanced solar wind dynamic pressure leads to a faster response time of the magnetosphere-ionosphere system since it controls the pressure in the magnetosheath that, in turn, determines how quickly the system returns towards equilibrium.

Partamies et al. study 68 events of high-latitude pulsating aurora (PsA) events using the optical observatory at Svalbard at 75° magnetic latitude (MLAT). They find that the high-latitude PsA events, which tend to occur between 5 and 11 magnetic local time (MLT), are associated with lower geomagnetic activity, weaker solar wind driving, lower ionospheric electron density than those with the low-latitude PsA events (located in the equatorward portion of the auroral oval). They conclude that the high-latitude PsA is dominated by a sub-type called Amorphous Pulsating Aurora (APA) and not likely to cause direct changes in the chemical composition of the mesosphere.

Dredger et al. present a study in which they investigate the connection of the field-aligned currents in the polar cap and the currents generated at the bow shock using MMS, AMPERE, and DMSP observations during a period of strong IMF By on 13 November 2015. The FAC flows downward and upward in the northern and southern polar cap, respectively while the bow shock current also has the same south-to-north polarity. They compare the magnitudes and polarities of the bow shock and field-aligned currents in the observations with those from the MHD simulation of the same event. They conclude that taken together, the observations and simulation support the hypothesis that the bow shock current, at least partially, closes through the ionosphere.

Bland et al. determine the spatial extent of energetic (>30 keV) electron precipitation during three substorms using cosmic noise absorption (CNA), the Super Dual Auroral Radar Network (SuperDARN) and very low frequency (VLF) measurements. They show that energetic electron precipitation extends significantly further equatorward than predicted by current empirical models, even during moderate geomagnetic activity. These results show that more research is needed to understand spatial distribution of energetic electron precipitation and its atmospheric response.

Author contributions

All authors listed have made a substantial, direct, and intellectual contribution to the work and approved it for publication. All authors performed the research and wrote the manuscript.

Funding

SW was supportted by NASA grants 80NSSC20K0704, 80NSSC21K1678, 80NSSC22K0515, 80NSSC19K0843, 80NSSC20K0188, 80NSSC20k0355, 80NSSC22K0304, and 80NSSC21K1321. JB was supported at the Space Science Institute by the NSF GEM Program via grant AGS-2027569 and by the NASA HERMES Interdisciplinary Science Program via grant 80NSSC21K1406. LH was supported by the Academy of Finland Postdoctoral Researcher Grant (No. 322459).

Acknowledgments

The authors of this editorial were honored to be able to oversee this Research Topic focused on the solar wind–magnetosphere interactions. The authors thank George Balasis, Xochitl Blanco-Cano, Marian Lazar, Francesco Malara, David Ruffolo, and Luca Sorriso-Valvo for their help with editorial duties. The authors also thank the many reviewers of these articles: Richard Boynton, Brandon Burkholder, Gian Luca Delzanno, Matteo Faganello, Katherine Garcia-Sage, Adrian Grocott, Rullong Guo, LH, Jia Huang, Zhenguang Huang, Nickolay Ivchenko, Caitriona Jackman, Kyung-Chan Kim, Jun Liang, Mike Lockwood, Ryan MacGranaghan, Scott McIntosh, Robert McPherron, Adam Michael, Elizabeth Mitchell, Agnit Mukhopadhyay, Bibin Ni, Adnane Osmane, Sampad Kumar Panda, Steven Petrinec, Arthur Richmond, Adriana Settino, Xiaochen Shen, David R. Shklyar, David Sibeck, Mikhail Sitnov, Weijie Sun, Antonio Vecchio, Brian Walsh, Tieyan Wang, Michael Wiltberger, and Chongjing Yuan.

Conflict of interest

The authors declare that the research was conducted in the absence of any commercial or financial relationships that could be construed as a potential conflict of interest.

Publisher's note

References

Akasofu, S. I. (1981). Energy coupling between the solar wind and the magnetosphere. *Space Sci. Rev.* 28, 121–190. doi:10.1007/BF00218810

Borovsky, J. E. (2020). What magnetospheric and ionospheric researchers should know about the solar wind. *J. Atmos. Solar-Terrestrial Phys.* 204, 105271. doi:10.1016/j.jastp.2020.105271

Gonzalez, W. D., Tsurutani, B. T., and Clúa de Gonzalez, A. L. (1999). Interplanetary origin of geomagnetic storms. *Space Sci. Rev.* 88, 529–562. doi:10.1023/A:1005160129098

Johnson, J. R., Wing, S., and Delamere, P. A. (2014). Kelvin helmholtz instability in planetary magnetospheres. *Space Sci. Rev.* 184, 1–31. doi:10.1007/s11214-014-0085-z

Jordanova, V. K. (2003). New insights on geomagnetic storms from model simulations using multi-spacecraft data. *Space Sci. Rev.* 107, 157–165. doi:10.1023/A:1025575807139

Kilpua, E. K. J., Balogh, A., von Steiger, R., and Liu, Y. D. (2017). Geoeffective properties of solar transients and stream interaction regions. *Space Sci. Rev.* 212, 1271–1314. doi:10.1007/s11214-017-0411-3

Rostoker, G., Akasofu, S. I., Baumjohann, W., Kamide, Y., and McPherron, R. L. (1988). The roles of direct input of energy from the solar wind and unloading of stored magnetotail energy in driving magnetospheric substorms. *Space Sci. Rev.* 46, 93–111. doi:10.1007/BF00173876

Watermann, J., Wintoft, P., Sanahuja, B., Saiz, E., Poedts, S., Palmroth, M., et al. (2009). Models of solar wind structures and their interaction with the Earth's space environment. *Space Sci. Rev.* 147, 233–270. doi:10.1007/s11214-009-9494-9

Wing, S., Johnson, J. R., Chaston, C. C., Echim, M., Escoubet, C. P., Lavraud, B., et al. (2014). Review of solar wind entry into and transport within the plasma sheet. *Space Sci. Rev.* 184, 33–86. doi:10.1007/s11214-014-0108-9

Zhang, H., Zong, Q., Connor, H., Delamere, P., Facskó, G., Han, D., et al. (2022). Dayside transient phenomena and their impact on the magnetosphere and ionosphere. *Space Sci. Rev.* 218, 40. doi:10.1007/s11214-021-00865-0

frontiers in Astronomy and Space Sciences

BRIEF RESEARCH REPORT
published: 04 March 2022
doi: 10.3389/fspas.2022.867282

Noise, Regression Dilution Bias, and Solar-Wind/Magnetosphere Coupling Studies

Joseph E. Borovsky *

Space Science Institute, Boulder, CO, United States

Using numerical experiments, the effects of noise in the solar-wind and magnetospheric data on fits to the data are examined. In particular, the impact of noise amplitude on the functional forms of best-fit solar-wind driver functions is explored. The presence of noise (measurement error) will make it difficult to use solar wind and magnetosphere data to uncover (or confirm) the formula that describes the physics of the driving of the magnetosphere.

Keywords: magnetosphere, solar wind, geomagnetic activity, geomagnetic indices, solar wind magnetosphere coupling, space weather

OPEN ACCESS

Edited by:
David Ruffolo,
Mahidol University, Thailand

Reviewed by:
Robert McPherron,
Los Angeles County, California, United States
Zhenguang Huang,
University of Michigan, United States

***Correspondence:**
Joseph E. Borovsky
jborovsky@spacescience.org

Specialty section:
This article was submitted to Space Physics, a section of the journal Frontiers in Astronomy and Space Sciences

Received: *31 January 2022*
Accepted: *21 February 2022*
Published: *04 March 2022*

Citation:
Borovsky JE (2022) Noise, Regression Dilution Bias, and Solar-Wind/Magnetosphere Coupling Studies. Front. Astron. Space Sci. 9:867282. doi: 10.3389/fspas.2022.867282

INTRODUCTION

Solar-wind/magnetosphere coupling is often studied by examining "driver functions" created from multiple solar-wind variables and testing how well the driver functions do in statistically describing the time-dependent activity of the Earth's magnetosphere-ionosphere system, with that activity typically measured with a single geomagnetic index. Often the goodness of the driver function is measured by the magnitude of the Pearson linear-correlation coefficient between the time-dependent solar-wind driver function and the time-dependent geomagnetic index. Correlation coefficients of 0.5–0.8 are typical.

Associated with the linear correlation, a least-squares linear-regression fit to the geomagnetic-index values as a function of the driver-function values is often made. In a plot (for example, **Figure 1**)of the geomagnetic index (vertical) versus the solar-wind driver function (horizontal), the least squares fit is based on minimizing the vertical errors from a line on the plot. In a sense, this least-squares linear-regression fit is the best fit for predicting the value of the geomagnetic index (vertical) knowing the value of the driver (horizontal).

In this report, artificial data sets are used to explore the effects of noise in the data for the study of solar-wind/magnetosphere coupling. For simplicity and clarity, the artificial data sets employed will not involve time lags as the actual solar-wind and magnetospheric data do.

REGRESSION DILUTION BIAS

Data that is imperfectly correlated leads to a phenomenon denoted as "regression dilution bias" (e.g., Liu, 1988; Hutcheon et al., 2010) or as "attenuation by errors" (e.g., Spearman, 1904; Bock and Petersen, 1975). Basically, the smaller the Pearson correlation coefficient r_{corr}, the shallower the slope of the linear regression fit: that is the systematic "bias". Hence, the larger the noise in the data, the lower the correlation coefficient, and the shallower the slope of the linear-regression fit. Additionally for data points x versus y, the linear-regression fit formula obtained for y(x) (y fitted as a function of x) differs from the fit formula for x(y) (x fitted as a function of y).

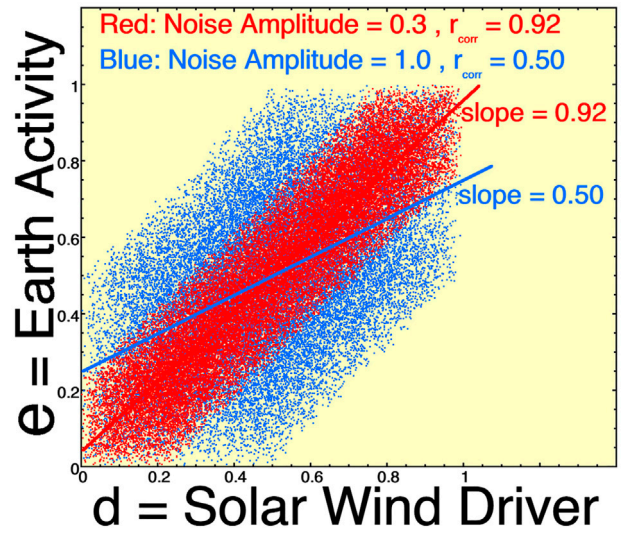

FIGURE 1 | A scatterplot of two sets of data (d,e) with two different amounts of noise in the data. Only every 100th data point is plotted.

In some sense a better fit to the data is a "major-axis linear-regression fit" (Riggs et al., 1978; Warton et al., 2006), also known as a "total least squares fit" (Golub and Van Loan, 1980) or a "Gaussian fit" (Borovsky et al., 1998): this fit minimizes the perpendicular distances to the line rather than just minimizing the vertical distances to the line. If you were to "eyeball" a scatterplot and draw a line through the group of points, your line would approximate the major axis fit and would have a slope steeper than the mathematical linear-regression least-squares fit.

Figure 1 displays some of these concepts with artificial data. Data points e (Earth activity, vertical) are plotted as a function of d (solar wind driver, horizontal). The data sets each are comprised of 300,000 points (d,e), although only every 100th point is plotted. The core data set (d_o,e_o) is not plotted, but it is created as follows. d_o (solar-wind driver) is a box-car distribution of random numbers between 0 and 1. Then e_o (Earth) is created as $e_o = d_o$. If e_o were to be plotted as a function of d_o, all points would lie on the line e = d, the slope of the linear-regression fit would be 1.0, and the Pearson correlation coefficient would be $r_{corr} = 1.0$. The red points in **Figure 1** are created by adding noise (boxcar random numbers) to both d_o and e_o where the boxcar noise values go from -0.15 to +0.15. The d and e distributions ($d = d_o$ + noise and $e = e_o$ + noise) are then "standardized" so that they go from values of 0 to values of 1. Similarly the blue points in **Figure 1** are created by adding larger-amplitude noise to the d_o and e_o points, where the boxcar noise goes from -0.25 to +0.25, and the distributions are "standardized" after the noise is added. Least-square linear regression fits are performed and plotted as the two lines: a red line for the red points and a blue line for the blue points. For the red points the fit slope is 0.92 and for the more-noisy blue points the fit slope is 0.5. Recall that the "true answer" if there was no noise in the data would be a slope of 1.0. As noted in the scatterplot of **Figure 1**, with increasing noise the Pearson linear correlation coefficient r_{corr} is reduced.

If the physics of the solar wind d driving the magnetosphere e is e = d as described by the $e_o = d_o$ points, then noise in the variables in **Figure 1** is yielding systematically different formulas for the driving: e = 0.92d and e = 0.5d. With increasing inaccuracy of the data, the interpretation of the fit formulas is that the solar-wind driving of the earth is weaker than it should be: the increase in Earth activity associated with an increase in driving is lessened.

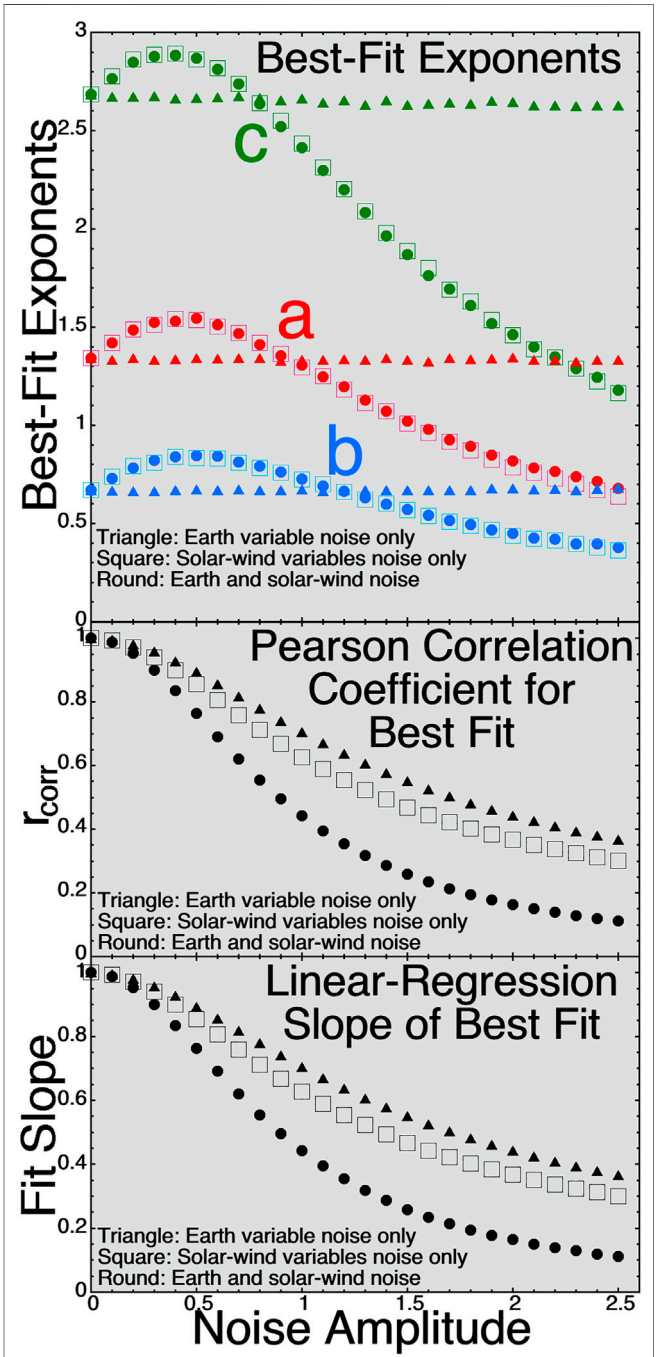

FIGURE 2 | For a driver function of the form $d = v_1^a v_2^b v_3^c$ for three independent solar-wind variables v_1, v_2, and v_3, the exponents **(A–C)** are solved for as a function of time *via* an evolutionary algorithm that maximizes the Pearson linear correlation between d and e.

EFFECT OF NOISE ON A BEST-FIT FORMULA

The solar-wind driver functions are mathematical combinations of solar wind variables. The functional forms used are most often multiplicative combinations of solar-wind variables with non-unity exponents on some of the variables (cf. Table 1 of Baker, 1986, Table 1 of Newell et al., 32,007, Table 1 of Balikhin et al., 2010, Table 1 of Borovsky, 2013), or they can be linear combinations of solar wind variables (Borovsky and Denton, 2018; Borovsky, 2021), or they can be time integrals of solar-wind variables (Borovsky, 2017). We don't know the "correct" functional form of the solar-wind driver function for the Earth, so we often look for the solar-wind function that gives the best correlation with geomagnetic indices (e.g., Newell et al., 2007; Borovsky, 2014; McPherron et al., 2015). Let's ask whether noise in the data changes those combinations, i.e., whether noise changes the functional form of a best-fit solar-wind formula to describe the Earth activity.

For a mathematical gedanken experiment, let's suppose we know how the driving works and can describe it with a solar wind formula. **Figure 2** explores how noise in the solar-wind-magnetosphere data can change the functional form of best-fit solar-wind driver functions. As in **Figure 1** a core data set (d_o,e_o) is created, where here the solar-wind driver function d_o is constructed from three independent solar-wind variables v_{1o}, v_{2o}, and v_{3o} represented by three sets of 100,000 random numbers. The driver function will be taken to have a functional form like the Newell driver (Newell et al., 2007) $d_o = v_{1o}^{4/3}v_{2o}^{2/3}v_{1o}^{8/3}$. (The Newell function is $v_{sw}^{4/3}B_{sw}^{2/3}\sin^{8/3}(\theta_{clock}/2)$.) In the reference data set (d_o,e_o) of 100,000 point pairs the Earth reaction is taken to be $e_o = d_o$. Let's assume d_o is the driver function that describes the physics of the driving and e_o is the real reaction of the Earth to d_o. As was the case in **Figure 1**, noise will be added to d_o and e_o to make various noisy data sets (d,e). The added noise are random numbers. The "noise amplitude" is the standard deviation of the noise-number distribution divided by the standard deviation of the variable to which the noise is added. The noise will be added in three different manners: 1) noise added only to e_o (vertical noise on the e-versus-d scatter plot), 2) noise added only to v_{1o}, v_{2o}, and v_{3o} (horizontal noise on the e-versus-d scatter plot), and 3) noise added to both the vertical and the horizontal. For each noisy data set v_1, v_2, v_3, and e the following calculation is made. An evolutionary algorithm (genetic algorithm) (cf. Borovsky, 2017; Borovsky, 2020a) is run to solve for the three exponents a, b, and c such that the Pearson correlation between the driver function $d = v_1^a v_2^b v_3^c$ and the earth function e is maximum. The algorithm randomly changes the values of a, b, and c: if a random change produces a driver $d = v_1^a v_2^b v_3^c$ with a larger correlation coefficient r_{corr}, then the change is accepted: if the random change produces a lower correlation coefficient, then the change is rejected and the formula is reverted back to the pre-change form. The algorithm evolves a, b, and c to a local maximum in r_{corr}. There is no guarantee that there is only one local maximum, but whenever the algorithm has been run with drastically different initial values of a, b, and c it evolves to the same final set of a, b, and c values. In the top panel of **Figure 2** the values of a, b, and c that give the maximum correlation are plotted as a function of the amplitude of the noise added to v_{1o}, v_{2o}, v_{3o}, and e_o. The three shapes of the points correspond to the three separate ways the noise was added. In the middle panel of **Figure 2** the maximum correlation coefficient r_{corr} for that amount of noise obtained by the algorithm between $d = v_1^a v_2^b v_3^c$ and e for the best-fit a, b, and c values is plotted. As expected, the correlation coefficient r_{corr} decreases with increasing noise amplitude. Note however in the top panel that the best-fit values of a, b, and c vary with the noise amplitude if there is noise in the solar-wind variables (round and hollow-square points). Recall that the answer in the absence of noise was a = 4/3, b = 2/3, and c = 8/3 such that $d_o = v_{1o}^{4/3}v_{2o}^{2/3}v_{1o}^{8/3}$. Lets call d_o the formula describing the physics of the solar-wind driving the magnetosphere. As **Figure 2** demonstrates, with noise (which there always is in measurements of the solar wind for the real magnetosphere) the data yields a different formula from the one that describes the "physics". The changing of the values of a, b, and c in the driver formula $d = v_1^a v_2^b v_3^c$ is what this report considers as a changing of the functional form of the driver function caused by noise.

In the bottom panel of **Figure 2** the slopes of linear-regression fits to the e values as functions of the best-fit d values are plotted as functions of the noise amplitude. (Both d and e are standardized here, with mean values of 0 and standard deviations of 1.) The slope values in the bottom panel track the correlation coefficients in the middle panel, commensurate with the regression-dilution-bias effect. I.e., for the linear best fit of e by $v_1^a v_2^b v_3^c$, the coefficient in front of $v_1^a v_2^b v_3^c$ decreases with increasing noise.

Note that if there is vertical-only noise on the Earth measure (geomagnetic index) e but not in the solar wind, the coefficients obtained would not change with noise. However, the correlation r_{corr} decreases with noise (middle panel of **Figure 2**) and the regression dilution bias still occurs with the linear-regression slopes decreasing with noise amplitude (bottom panel of **Figure 2**) interpreted as lessened Earth reaction for an increased driver strength.

As a preview of future work, adding noise to the solar-wind variables in real data [i.e., OMNI2, King and Papitashvili (2005)] indeed changes the functional form of the best-fit solar-wind driver. Fits of the form $v_{sw}^a B_{sw}^b \sin^c(\theta_{clock}/2)$ to various time-lagged geomagnetic indices (AE, AL, AU, Kp, Hp60, PCI) find that adding noise to any one of the three solar-wind variables changes the best-fit values of all three exponents a, b, and c. Depending on the geomagnetic index that is being fit, the best-fit values of a, b, or c can either decrease with added noise or increase with added noise. In agreement with the triangle points in the top panel of **Figure 2**, adding noise only to the geomagnetic index does not change the best-fit values of a, b, or c in a real data set. Real solar-wind data will be explored in a future report.

SUMMARY

The functional form obtained for the best fit solar-wind driver d depends on (at least) two things. It is a function of how the driving works. It is also a function of noise in the measurements. If our goal is to use real solar-wind/magnetosphere data to uncover or to confirm the formula that tells us the physics of the driving, we have trouble because of there always being noise in the data. One

source of error in the solar-wind and magnetosphere data is the fact that the solar wind that hits an upstream monitor is not the same solar wind that hits the earth: this error has been expounded upon (Borovsky, 2018; Borovsky, 2020b; Walsh et al., 2019; Burkholder et al., 2020). Another source of error is that geomagnetic indices are only indirect measures of the reaction of the earth to the solar wind. A future research effort might involve 1) obtaining a best-fit driver formula from the real data, 2) assessing the amplitude and properties of the noise in the real data, and 3) attempting to correct the formula for the effects of the noise.

DATA AVAILABILITY STATEMENT

The original contributions presented in the study are included in the article/Supplementary Material, further inquiries can be directed to the corresponding author.

AUTHOR CONTRIBUTIONS

The author confirms being the sole contributor of this work and has approved it for publication.

FUNDING

JB was supported by the NSF GEM Program *via* grant AGS-2027569, by the NASA HERMES Interdisciplinary Science Program *via* grant 80NSSC21K1406, and by the NASA Heliophysics Mission Concept Study Program *via* award 80NSSC22K0113.

ACKNOWLEDGMENTS

The author wishes to thank Gian Luca Delzanno for helpful conversations.

REFERENCES

Baker, D. N. (1986). Statistical Analyses in the Study of Solar Wind-Magnetosphere Coupling. in *Solar Wind-Magnetosphere Coupling*, Y. Kamide and J. A. Slavin (eds.), p. 17, 38. Terra Scientific, Tokyo. doi:10.1007/978-94-009-4722-1_2

Balikhin, M. A., Boynton, R. J., Billings, S. A., Gadalin, M., Ganushkina, N., Coca, D., et al. (2010). Data Based Quest for Solar Wind-Magnetosphere Coupling Function. *Geophys. Res. Lett.* 37, L24107. doi:10.1029/2010gl045733

Bock, R. D., and Petersen, A. C. (1975). A Multivariate Correction for Attenuation. *Biometrika* 62, 673–678. doi:10.1093/biomet/62.3.673

Borovsky, J. E. (2020a). A Survey of Geomagnetic and Plasma Time Lags in the Solar-Wind-Driven Magnetosphere of Earth. *J. Atmos. Solar-Terrestrial Phys.* 208, 105376. doi:10.1016/j.jastp.2020.105376

Borovsky, J. E. (2014). Canonical Correlation Analysis of the Combined Solar Wind and Geomagnetic index Data Sets. *J. Geophys. Res. Space Phys.* 119, 5364–5381. doi:10.1002/2013ja019607

Borovsky, J. E., and Denton, M. H. (2018). Exploration of a Composite index to Describe Magnetospheric Activity: Reduction of the Magnetospheric State Vector to a Single Scalar. *J. Geophys. Res. Space Phys.* 123, 7384–7412. doi:10.1029/2018ja025430

Borovsky, J. E. (2021). Is Our Understanding of Solar-Wind/Magnetosphere Coupling Satisfactory? *Front. Astron. Space Sci.* 8, 634073. doi:10.3389/fspas.2021.634073

Borovsky, J. E. (2013). Physical Improvements to the Solar Wind Reconnection Control Function for the Earth's Magnetosphere. *J. Geophys. Res. Space Phys.* 118, 2113–2121. doi:10.1002/jgra.50110

Borovsky, J. E. (2018). The Spatial Structure of the Oncoming Solar Wind at Earth and the Shortcomings of a Solar-Wind Monitor at L1. *J. Atmos. Solar-Terrestrial Phys.* 177, 2–11. doi:10.1016/j.jastp.2017.03.014

Borovsky, J. E., Thomsen, M. F., and Elphic, R. C. (1998). The Driving of the Plasma Sheet by the Solar Wind. *J. Geophys. Res.* 103, 17617–17639. doi:10.1029/97ja02986

Borovsky, J. E. (2017). Time-integral Correlations of Multiple Variables with the Relativistic-Electron Flux at Geosynchronous Orbit: The strong Roles of the Substorm-Injected Electrons and the Ion Plasma Sheet. *J. Geophys. Res.* 122, 11961. doi:10.1002/2017ja024476

Borovsky, J. E. (2020b). What Magnetospheric and Ionospheric Researchers Should Know about the Solar Wind. *J. Atmos. Solar-Terrestrial Phys.* 204, 105271. doi:10.1016/j.jastp.2020.105271

Burkholder, B. L., Nykyri, K., and Ma, X. (2020). A Multispacecraft Solar Wind Monitor. *J. Geophys. Res.* 125, e2020JA027978. doi:10.1029/2020ja027978

Golub, G. H., and Van Loan, C. F. (1980). An Analysis of the Total Least Squares Problem. *SIAM J. Numer. Anal.* 17, 883–893. doi:10.1137/0717073

Hutcheon, J. A., Chiolero, A., and Hanley, J. A. (2010). Random Measurement Error and Regression Dilution Bias. *BMJ* 340, c2289–1406. doi:10.1136/bmj.c2289

King, J. H., and Papitashvili, N. E. (2005). Solar Wind Spatial Scales in and Comparisons of Hourly Wind and ACE Plasma and Magnetic Field Data. *J. Geophys. Res.* 110, 2104. doi:10.1029/2004ja010649

Liu, K. (1988). Measurement Error and its Impact on Partial Correlation and Multiple Linear Regression Analyses1. *Am. J. Epidemiol.* 127, 864–874. doi:10.1093/oxfordjournals.aje.a114870

McPherron, R. L., Hsu, T.-S., and Chu, X. (2015). An Optimum Solar Wind Coupling Function for theALindex. *J. Geophys. Res. Space Phys.* 120, 2494–2515. doi:10.1002/2014ja020619

Newell, P. T., Sotirelis, T., Liou, K., Meng, C.-I., and Rich, F. J. (2007). A Nearly Universal Solar Wind-Magnetosphere Coupling Function Inferred from 10 Magnetospheric State Variables. *J. Geophys. Res.* 112, A01206. doi:10.1029/2006ja012015

Riggs, D. S., Guarnieri, J. A., and Addelman, S. (1978). Fitting Straight Lines when Both Variables Are Subject to Error. *Life Sci.* 22, 1305–1360. doi:10.1016/0024-3205(78)90098-x

Smith, R. J. (2009). Use and Misuse of the Reduced Major axis for Line-Fitting. *Am. J. Phys. Anthropol.* 140, 476–486. doi:10.1002/ajpa.21090

Spearman, C. (1904). The Proof and Measurement of Association between Two Things. *Am. J. Psychol.* 15, 72. doi:10.2307/1412159

Walsh, B. M., Bhakyapaibul, T., and Zou, Y. (2019). Quantifying the Uncertainty of Using Solar Wind Measurements for Geospace Inputs. *J. Geophys. Res. Space Phys.* 124, 3291–3302. doi:10.1029/2019ja026507

Warton, D. I., Wright, I. J., Falster, D. S., and Westoby, M. (2006). Bivariate Line-Fitting Methods for Allometry. *Biol. Rev.* 81, 259. doi:10.1017/s1464793106007007

Conflict of Interest: The author declares that the research was conducted in the absence of any commercial or financial relationships that could be construed as a potential conflict of interest.

Publisher's Note: All claims expressed in this article are solely those of the authors and do not necessarily represent those of their affiliated organizations, or those of the publisher, the editors and the reviewers. Any product that may be evaluated in this article, or claim that may be made by its manufacturer, is not guaranteed or endorsed by the publisher.

frontiers | Frontiers in Astronomy and Space Sciences

HYPOTHESIS AND THEORY
published: 01 June 2022
doi: 10.3389/fspas.2022.930162

Is the Solar Wind Electron Strahl a Seed Population for the Earth's Electron Radiation Belt?

Joseph E. Borovsky[1]* *and Andrei Runov*[2]

[1]Space Science Institute, Boulder, CO, United States, [2]Department of Earth, Planetary, and Space Sciences, University of California, Los Angeles, Los Angeles, CA, United States

1) Since the outer electron radiation belt is lost on occasion, the radiation belt needs seed electrons to rebuild. 2) The clear candidate for that seed population is energetic substorm-injected electrons in the dipolar magnetosphere. 3) The energetic substorm-injected electrons in the dipole come from the suprathermal electron population in the magnetotail plasma sheet, delivered by substorms. Scenario (1)–3) begs the question: Where do these magnetotail suprathermal electrons come from? We are hypothesizing that one source (perhaps the dominant source) is the energetic field-aligned electron strahl in the solar wind, which are electrons fresh from the solar corona.

Keywords: radiation belt, strahl, plasma sheet, polar rain, magnetosphere

OPEN ACCESS

Edited by:
Luca Sorriso-Valvo,
Institute for Space Physics, Sweden

Reviewed by:
David R. Shklyar,
Space Research Institute (RAS), Russia
Jia Huang,
University of Michigan, United States

***Correspondence:**
Joseph E. Borovsky
jborovsky@spacescience.org

Specialty section:
This article was submitted to Space Physics, a section of the journal Frontiers in Astronomy and Space Sciences

Received: *27 April 2022*
Accepted: *18 May 2022*
Published: *01 June 2022*

Citation:
Borovsky JE and Runov A (2022) Is the Solar Wind Electron Strahl a Seed Population for the Earth's Electron Radiation Belt? Front. Astron. Space Sci. 9:930162. doi: 10.3389/fspas.2022.930162

OVERVIEW

In this Hypothesis paper we will explore the possibility that strahl electrons in the solar wind at Earth follow the pathway into the magnetosphere that is: solar wind → lobe → polar rain → plasma sheet → substorm-injected electrons → electron radiation belt.

It is a reasonable hypothesis that the energetic electron strahl of the solar wind contributes as a source population for the Earth's outer electron radiation belt. 1) The strahl is seen on lobe field lines and it reaches the polar-cap atmosphere to create the polar-rain aurora (Fairfield and Scudder, 1985). The intensity of the polar-rain aurora is modulated by the intensity of the strahl in the solar wind (Hershbach and Zhang, 2021). 2) Lobe field lines are captured into the magnetotail plasma sheet via the action of the distant reconnection site and these field lines have energetic strahl electrons on them (Zhang and Wing, 2015). 3) The magnetotail plasma sheet is observed to have a suprathermal electron population (Christon et al., 1989; Runov et al., 2018). 4) The suprathermal electron population of the magnetotail plasma sheet becomes the substorm-injected electron population in the dipolar magnetosphere as substorms transport and adiabatically energize this population (Birn et al., 1998, 2014). 5) The substorm-injected electrons are widely considered to be the seed population for the electron radiation belt (Jaynes et al., 2015; Boyd et al., 2016; Borovsky and Valdivia, 2018).

This hypothesis has the potential to uncover another piece of the M-I-T system and how it is driven by the solar wind, and in fact by the solar corona. This hypothesis, if accurate, could have a transformative impact on our system-science understanding of the solar-wind-driven magnetosphere of the Earth (Borovsky and Valdivia, 2018) and could contribute to electron systems science (Vershcaren et al., 2021). This could lead to an increased understanding of the controlling factors for space weather at Earth and an improved ability to predict the evolution of the electron radiation belt.

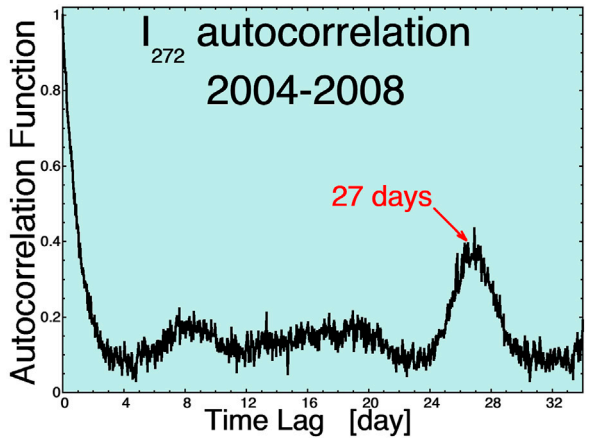

FIGURE 1 | The autocorrelation function of the hourly strahl-intensity index I_{272}. Note the autocorrelation time (1/e method) is about 26 h and note the 27-day recurrence of the correlation indicating a 27-day periodicity in the I_{272} time series.

THE ELECTRON STRAHL IN THE SOLAR WIND

The solar wind has three electron populations (Boldyrev et al., 2019; Bercic et al., 2020): the (cool) core, the hot isotropic halo, and the energetic field-aligned strahl. The strahl is a field-aligned distribution of electrons with a broad range of energies from 100s of eV to a few-keV. The strahl is the hot-electron population of the solar corona escaping along magnetic-field lines out into the heliosphere. The strahl is sometimes referred to as the solar-wind heat flux (e.g., Gary et al., 1975). Strahl electrons move rapidly along the field: a 500-eV strahl electron has a field-aligned velocity of 1.3×10^9 cm/s, which is 2 R_E/s. At 1 AU the observed strahl electrons left the Sun about 3 h ago, whereas the solar-wind plasma is about 100 h old. At 1 AU the core represents about 90% of the electron density, the halo about 7%, and the strahl on average about 3% (Stverak et al., 2009), although the strahl fractional density can vary greatly with time. At 1 AU the field-aligned strahl is several degrees wide (Fitzenreiter et al., 1998; de Koning et al., 2007).

The spaghetti magnetic-flux-tube structure of the solar wind (Borovsky, 2008, 2010) forms a ductwork for the outward moving strahl (Borovsky et al., 2021). As the various flux tubes pass the Earth the intensity of the strahl can change from tube to tube (Gosling et al., 2004; Borovsky, 2020a, 2021). This results in intensity changes on 10-min timescales at Earth as the various solar-wind magnetic flux tubes advect past the Earth (Borovsky, 2020b). Additionally, the strahl intensity varies systematically on a few-day timescale as the different types of solar-wind plasma pass the Earth (Borovsky, 2018). An hourly-averaged 272-eV strahl-intensity index I_{272} at Earth has been created (Borovsky, 2017). I_{272} is $\log_{10}$ (f (272)) where f (272) is the phase-space density of the strahl at 272 eV: I_{272} is a proxy for the flux of the strahl, but future studies should use the total integral of the strahl to properly calculate its flux. There is a 27-day periodicity to the intensity of the strahl at Earth; this can be seen in the autocorrelation function of I_{272} plotted in **Figure 1**. The intensity of the electron strahl can be used as an indicator of the magnetic connection from the Earth to the Sun (Borovsky, 2021). The strahl is most intense in corotating interaction regions and the beginnings of high-speed streams (Borovsky and Denton, 2016), which at Earth are the times when the electron radiation belt becomes most intense (Borovsky and Denton, 2010).

THE STRAHL IN THE LOBES

The electron strahl is seen in the magnetosheath, both in the near-Earth magnetosheath (Terasawa et al., 2000; Kasaba et al., 2000) and in the distant-tail magnetosheath (Aaker et al., 1986). The strahl electrons are commonly seen throughout the lobes at energies of 100s of eV to a few keV (e.g., Fairfield and Scudder, 1985; Aaker et al., 1986).

Figure 2 is a noon-midnight meridional cut from a global MHD simulation of the solar-wind-driven magnetosphere examining the magnetic connection from the solar wind into the magnetosphere. The IMF is purely southward in this simulation and magnetic-field lines are shown in light green. The time labels at the top of the figure indicate the time that has passed since the various solar-wind magnetic-field lines became connected into the magnetosphere via dayside reconnection.

In each flux tube at 1 AU the strahl moves out from the Sun as a steady stream (heat flux) of electrons. When a particular tube passes a solar-wind monitor, the strength of the stream in that tube is gauged by I_{272}. As that tube passes the Earth and its magnetic connection to the magnetosphere changes, the strahl flux in that tube should remain the same. Hence, when comparing lobe observations of the strahl with solar-wind observations of the strahl, a time lag in the solar-wind observations must be accounted for. The time lags are owed to temporal changes in where that tube connects into the magnetosphere. Mirroring strahl electrons are lost to the solar wind on polar-cap flux tubes that are open, and mirroring strahl electrons are captured on closed flux tubes.

Conserving the first adiabatic invariant, the narrow field-aligned strahl in the solar wind has no difficulty going from the solar wind into the lobes. If the field strength in the lobes is ~30 nT and the field strength in the solar wind is ~5 nT, then electrons with pitch angles up to ~23° can enter the stronger field of the lobes. Scatter-free transport of the strahl into the lobes is also expected: unless a strahl-electron gyroradius r_{ge} is $r_{ge} > 0.1\ r_{curve}$ (Borovsky et al., 2022a,b), where r_{curve} is the radius of curvature of a field line, there will be no scattering. At 5 nT a 500-eV electron has $r_{ge} \sim 1$ km and field-line radii of curvatures of 10 km are not expected in the connection of the solar-wind magnetic field into the magnetosphere depending on the spacecraft location in the lobes.

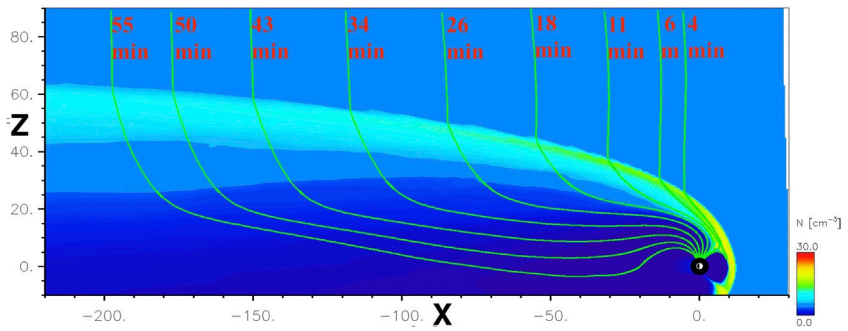

FIGURE 2 | A number-density snapshot from an LFM (Lyon et al., 2004) simulation (Joe_Borovsky_081,121_1) at the CCMC with a purely southward IMF: the bow shock is in yellow, the magnetotail is dark blue. Nine open field lines (light green) are traced from the polar cap into the solar wind. The labels (red) are the times since that particular solar-wind flux tube passed a solar-wind monitor at the nose of the bow shock. The solar wind velocity vector is tilted southward (v_x = −400 km/s and v_z = −66 km/s) to wind-sock move the magnetotail downward (1) to keep the distant magnetotail from flaring out of the simulation domain and (2) to push the northern high-latitude magnetopause onto a higher-resolution region of the simulation grid.

Note in **Figure 2** that most of the solar-wind magnetic-field lines connecting into the lobes (and into the polar cap) pass through the distant bow shock, where the shock compression ratio is weak (Greenstadt et al., 1990; Bennett et al., 1997). For these distant field lines, the strahl population should be little effected by passage through the weak bow shock.

POLAR RAIN AURORA

As solar-wind magnetic-field lines become connected to the Earth, the electron strahl creates the polar-rain aurora in the northern polar ionosphere when the IMF is in an away sector and in the southern polar ionosphere when the IMF is in a toward sector (Fairfield and Scudder, 1985; Newell and Meng, 1990; Wing et al., 1996; 2001; 2005). The intensity of polar-rain aurora is correlated with intensity of the strahl in the solar wind (Hong et al., 2012; Hershbach and Zhang, 2021), hence, polar-rain observations can provide a good estimate of the strahl population in the lobe and in the plasma sheet. The polar rain is structured, similar to the structured strahl population of the solar wind (Borovsky, 2020a).

As seen from the solar wind, the atmospheric loss cone for the Earth's polar caps is quite small and so not all of the strahl electrons are able to hit the atmosphere and make aurora. For instance, if the field strength in the solar wind is 5 nT = 5×10^{-5} G, then the loss cone for the 0.5-G field of the polar cap is about 0.6°. Strahl electrons outside of the loss cone will mirror above the atmosphere.

As indicated in **Figure 2**, time lags of 0–2 h are expected between the solar wind and the ionosphere owing to flux-tube advection past the Earth, with the time delays shorter in the sunward portions of the polar cap and longer in the nightside polar cap (cf. **Figure 2**).

In matching the energy spectra of the polar-rain electrons with the solar wind, evidence of field-aligned potentials has been seen (e.g., Fairfield et al., 2008; Wing et al., 1996; 2001; 2005; 2015). Polar rain intensity or energy flux sometimes shows a negative gradient from the dayside to the nightside, which can be partly attributed to the retarding potential (Newell et al., 1996; Fairfield et al., 2008; Wing et al., 1996; 2001; 2005; 2015). However, this negative gradient is not always seen for the reasons that are not entirely clear (Newell and Meng, 1990);

THE PLASMA SHEET SUPRATHERMAL-ELECTRON POPULATION

The pathway from the electron strahl in the solar wind to the electron strahl in the lobes (where the strahl electrons create the polar-rain aurora) is well established. Then next step in the pathway to the radiation belt is not well established. It is imperative to initiate a research effort 1) to quantify how much of the plasma-sheet suprathermal-electron distribution is owed to the strahl (and halo) electrons of the solar wind and 2) to determine whether there are other candidate sources for the plasma-sheet suprathermal-electron population (Other sources, e.g., recirculation of electrons from the dipolar magnetosphere into the tail, have been documented for much-higher-energy electrons (Borovsky and Denton, 2011; Walsh et al., 2012).).

The suprathermal-electron population of the Earth's plasma sheet has been well documented (e.g., Christon et al., 1989, 1991; Runov et al., 2018; Stepanov et al., 2021). At 60 R_E the suprathermal electron population has energies above about 200 eV (Runov et al., 2018). Measurements of the shapes of velocity distribution functions, phase-space densities, and sudden temporal/spatial changes in the population need to be made. Occurrence distributions of the properties of the suprathermal electrons in the magnetotail plasma sheet need to be compared with occurrence distributions of the electron properties in the lobes and in the solar wind. Occurrence distributions such as the phase-space density at constant μ (μ = $v_\perp^2/B$ being the first adiabatic invariant) are particularly revealing. Simulations of the field-aligned strahl electron population through the nightside-reconnection process may be informative: the simulations should provide information about the likelihood of pitch-angle scattering at thin current sheets and

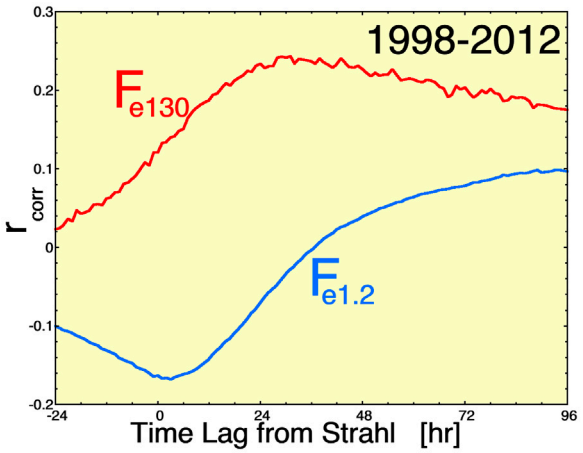

FIGURE 3 | The correlation time-lag behavior between the strahl intensity in the solar wind and (red) the peak flux of 130-keV electrons at geosynchronous orbit and (blue) the peak flux of 1.2-MeV radiation-belt electrons at geosynchronous orbit. 11,020 hourly data points were used. The modest, but nonzero, levels of correlation indicate that strahl intensity is not the only controller of these magnetospheric quantities.

at the reconnection site and about energy-anisotropy evolution in the collapsing Earthward field lines after reconnection.

Besides entry from the solar wind into the magnetotail plasma sheet from the lobe via nightside reconnection, solar-wind electron populations can also enter into the magnetotail plasma sheet *via* the low-latitude boundary layer (LLBL).

For the lobe-reconnection pathway, the best estimate of the strahl electrons that enter the nightside closed magnetosphere may be obtained from the polar rain electrons where the polar rain meets the open-closed boundary of the nightside oval (Newell and Meng, 1990; Wing and Zhang, 2015).

SUBSTORM-INJECTED ELECTRONS

It is well established that the population of energetic substorm-injected electrons in the dipolar magnetosphere is directly related to the suprathermal electron population in the magnetotail plasma sheet, delivered into the dipolar region by the strong electric fields of magnetospheric substorms (Birn et al., 1997, 1998, 2004, 2014).

Using the hourly multispacecraft substorm-injected-electron index F_{e130} (Borovsky and Yakymenko, 2017) that is based on SOPA measurements (Belian et al., 1992) from geosynchronous orbit and using the hourly I_{272} strahl-intensity index (Borovsky, 2017) that is based on ACE measurements in the solar wind, the red curve in **Figure 3** plots the time-lagged Pearson linear correlation coefficient between I_{272} and F_{e130}. The peak correlation occurs when the F_{e130} substorm-injected-electron intensity is lagged by about 1 day from the solar-wind I_{272} strahl-intensity index.

SEED ELECTRONS FOR THE RADIATION BELT

It is commonly accepted that the energetic substorm-injected electron population in the dipolar magnetosphere is the seed population for the Earth's electron radiation belt (Jaynes et al., 2015; Boyd et al., 2016; Borovsky and Valdivia, 2018), with the substorm-injected electrons energized primarily by whistler-mode chorus waves, with the chorus waves driven by lower-energy injected electrons. It is well known that the intensity of the electron radiation belt is statistically strongly connected to the time history of the intensity of substorm electron injections (Simms et al., 2016; Borovsky, 2017). Borovsky (2017) found a Pearson correlation coefficient of +74% between the multispacecraft flux $F_{e1.2}$ of 1.2-MeV radiation-belt electrons and the 62-h time integral of the F_{e130} flux of substorm-injected electrons.

The blue curve of **Figure 3** plots the time-lagged Pearson linear correlation coefficient between the strahl electron intensity index I_{272} in the solar wind and the 1.2-MeV radiation-belt flux index $F_{e1.2}$ at geosynchronous orbit: a peak in the correlation coefficient occurs when the radiation-belt index $F_{e1.2}$ is lagged by about 4 days.

THE FUTURE

A project is needed that will verify and quantify a long chain of events that leads to a seed population of energetic electrons for the Earth's electron radiation belt: solar wind → lobe → polar rain → plasma sheet → injected electrons → radiation belt. Of particular interest is determining the relative contribution of strahl to the seed population through each stage of the proposed pathway. It will be important distinguished the strahl electron population from other electron populations by comparing phase-space densities for consistency in the various steps of the strahl's pathway and by correlating the strengths of the various populations.

The project goals would be the following. 1) To determine whether (and by how much) the solar-wind electron strahl (and halo) acts as a seed population for the Earth's electron radiation belt. 2) To determine the controlling factors for this process. 3) To trace the electron strahl from the solar wind, into the lobe, into the polar-cap ionosphere (polar rain), into the magnetotail plasma sheet. The suprathermal electrons of the plasma sheet have already been traced into substorm injections in the dipole, and evolving into the electron radiation belt has been examined.

A project pursuing this unique hypothesis could have a transformative impact.

DATA AVAILABILITY STATEMENT

The original contributions presented in the study are included in the article/Supplementary Material, further inquiries can be directed to the corresponding author.

AUTHOR CONTRIBUTIONS

JB initiated this project and JB and AR researched and wrote the manuscript.

FUNDING

JB was supported by the NSF GEM Program via grant AGS-2027569 and by the NASA HERMES Interdisciplinary Science Program *via* grant 80NSSC21K1406. AR was supported by the NASA HERMES Interdisciplinary Science Program *via* grant 80NSSC21K1407.

ACKNOWLEDGMENTS

The authors thank Joachim Birn, Yuri Shprits, and Simon Wing for helpful conversations.

REFERENCES

Aaker, D. N., Bame, S. J., Feldman, W. C., Gosling, J. T., Zwickl, R. D., Slavin, J. A., et al. (1986). Strong Electron Bidirectional Anisotropies in the Distant Tail: ISEE 3 Observations of Polar Rain. *J. Geophys. Res.* 91, 5637–5662. doi:10.1029/JA091iA05p05637

Belian, R. D., Gisler, G. R., Cayton, T., and Christensen, R. (1992). High-Zenergetic Particles at Geosynchronous Orbit during the Great Solar Proton Event Series of October 1989. *J. Geophys. Res.* 97, 16897. doi:10.1029/92ja01139

Bennett, L., Kivelson, M. G., Khurana, K. K., Frank, L. A., and Paterson, W. R. (1997). A Model of the Earth's Distant Bow Shock. *J. Geophys. Res.* 102, 26927–26941. doi:10.1029/97ja01906

Bercic, L., Larson, D., Whittlesey, P., Maksimovic, M., Badman, S. T., Landi, S., et al. (2020). Coronal Electron Temperature Inferred from the Strahl Electrons in the Inner Heliosphere: Parker Solar Probe and Helios Observations. *Astrophys. J.* 892, 88. doi:10.3847/1538-4357/ab7b7a

Birn, J., Runov, A., and Hesse, M. (2014). Energetic Electrons in Dipolarization Events: Spatial Properties and Anisotropy. *J. Geophys. Res. Space Phys.* 119, 3604–3616. doi:10.1002/2013ja019738

Birn, J., Thomsen, M. F., Borovsky, J. E., Reeves, G. D., McComas, D. J., and Belian, R. D. (1997). Characteristic Plasma Properties during Dispersionless Substorm Injections at Geosynchronous Orbit. *J. Geophys. Res.* 102, 2309–2324. doi:10.1029/96ja02870

Birn, J., Thomsen, M. F., Borovsky, J. E., Reeves, G. D., McComas, D. J., Belian, R. D., et al. (1998). Substorm Electron Injections: Geosynchronous Observations and Test Particle Simulations. *J. Geophys. Res.* 103, 9235–9248. doi:10.1029/97ja02635

Birn, J., Thomsen, M. F., and Hesse, M. (2004). Electron Acceleration in the Dynamic Magnetotail: Test Particle Orbits in Three-Dimensional Magnetohydrodynamic Simulation Fields. *Phys. of Plasmas* 11, 1825–1833. doi:10.1063/1.1704641

Boldyrev, S., and Horaites, K. (2019). Kinetic Theory of the Electron Strahl in the Solar Wind. *MNRAS* 489, 3412–3419. doi:10.1093/mnras/stz2378

Borovsky, J. E., Delzanno, G. L., and Yakymenko, K. N. (2022a). Pitch-Angle Diffusion in the Earth's Magnetosphere Organized by the Mozer-Transformed Coordinate System. *Front. Astron. Space Sci.* 9, 810792. doi:10.3389/fspas.2022.810792

Borovsky, J. E., and Denton, M. H. (2011). Evolution of the Magnetotail Energetic-Electron Population during High-Speed-Stream-Driven Storms: Evidence for the Leakage of the Outer Electron Radiation Belt into the Earth's Magnetotail. *J. Geophys. Res.* 116, A12228. doi:10.1029/2011ja016713

Borovsky, J. E., and Denton, M. H. (2010). On the Heating of the Outer Radiation Belt to Produce High Fluxes of Relativistic Electrons: Measured Heating Rates for High-Speed-Stream-Driven Storms. *J. Geophys. Res.* 115, A12206. doi:10.1029/2010ja015342

Borovsky, J. E., and Denton, M. H. (2016). The Trailing Edges of High-Speed Streams at 1 AU. *J. Geophys. Res. Space Phys.* 121, 6107–6140. doi:10.1002/2016ja022863

Borovsky, J. E. (2021). Exploring the Properties of the Electron Strahl at 1 AU as an Indicator of the Quality of the Magnetic Connection between the Earth and the Sun. *Front. Astron. Space Sci.* 8, 646443. doi:10.3389/fspas.2021.646443

Borovsky, J. E., Halekas, J. S., and Whittlesey, P. L. (2021). The Electron Structure of the Solar Wind. *Front. Astron. Space Sci.* 8, 69005. doi:10.3389/fspas.2021.690005

Borovsky, J. E. (2018). On the Origins of the Intercorrelations Between Solar Wind Variables. *JGR Space Phys.* 123, 20–29. doi:10.1002/2017ja024650

Borovsky, J. E. (2010). On the Variations of the Solar-Wind Magnetic Field about the Parker-spiral Direction. *J. Geophys. Res.* 115, A09101. doi:10.1029/2009ja015040

Borovsky, J. E. (2008). The Flux-Tube Texture of the Solar Wind: Strands of the Magnetic Carpet at 1 AU? *J. Geophys. Res.* 113, A08110. doi:10.1029/2007ja012684

Borovsky, J. E. (2020a). The Magnetic Structure of the Solar Wind: Ionic Composition and the Electron Strahl. *Geophys. Res. Lett.* 47, e2019GL084586. doi:10.1029/2019gl084586

Borovsky, J. E. (2017). Time-integral Correlations of Multiple Variables with the Relativistic-Electron Flux at Geosynchronous Orbit: The Strong Roles of the Substorm-Injected Electrons and the Ion Plasma Sheet. *J. Geophys. Res.* 122, 11961. doi:10.1002/2017ja024476

Borovsky, J. E., and Valdivia, J. A. (2018). The Earth's Magnetosphere: A Systems Science Overview and Assessment. *Surv. Geophys* 39, 817–859. doi:10.1007/s10712-018-9487-x

Borovsky, J. E. (2020b). What Magnetospheric and Ionospheric Researchers Should Know about the Solar Wind. *J. of Atmos. and Solar-Terrestrial Phys.* 204, 105271. doi:10.1016/j.jastp.2020.105271

Borovsky, J. E., Yakymenko, K. N., and Delzanno, G. L. (2022b). Modification of the Loss Cone for Energetic Particles in the Earth's Inner Magnetosphere. *J. Geophys. Res.* 127:e2021JA030106. in press. doi:10.1029/2021JA030106

Borovsky, J. E., and Yakymenko, K. (2017). Systems Science of the Magnetosphere: Creating Indices of Substorm Activity, of the Substorm-Injected Electron Population, and of the Electron Radiation Belt. *J. Geophys. Res.* 122, 10012. doi:10.1002/2017ja024250

Boyd, A. J., Spence, H. E., Huang, C. L., Reeves, G. D., Baker, D. N., Turner, D. L., et al. (2016). Statistical Properties of the Radiation Belt Seed Population. *J. Geophys. Res. Space Phys.* 121, 7636–7646. doi:10.1002/2016ja022652

Christon, S. P., Williams, D. J., Mitchell, D. G., Frank, L. A., and Huang, C. Y. (1989). Spectral Characteristics of Plasma Sheet Ion and Electron Populations during Undisturbed Geomagnetic Conditions. *J. Geophys. Res.* 94, 13409. doi:10.1029/ja094ia10p13409

Christon, S. P., Williams, D. J., Mitchell, D. G., Huang, C. Y., and Frank, L. A. (1991). Spectral Characteristics of Plasma Sheet Ion and Electron Populations during Disturbed Geomagnetic Conditions. *J. Geophys. Res.* 96, 1–22. doi:10.1029/90ja01633

de Koning, C. A., Gosling, J. T., Skoug, R. M., and Steinberg, J. T. (2007). Energy Dependence of Electron Pitch Angle Distribution Widths in Solar Bursts. *J. Geophys. Res.* 112, A04101. doi:10.1029/2006ja011971

Fairfield, D. H., and Scudder, J. D. (1985). Polar Rain: Solar Coronal Electrons in the Earth's Magnetosphere. *J. Geophys. Res.* 90, 4055. doi:10.1029/ja090ia05p04055

Fairfield, D. H., Wing, S., Newell, P. T., Ruohoniemi, J. M., Gosling, J. T., and Skoug, R. M. (2008). Polar Rain Gradients and Field-Aligned Polar Cap Potentials. *J. Geophys. Res.* 113, A10203. doi:10.1029/2008JA013437

Fitzenreiter, R. J., Ogilvie, K. W., Chornay, D. J., and Keller, J. (1998). Observations of Electron Velocity Distribution Functions in the Solar Wind by the WIND Spacecraft: High Angular Resolution Strahl Measurements. *Geophys. Res. Lett.* 25, 249–252. doi:10.1029/97gl03703

Gary, S. P., Feldman, W. C., Forslund, D. W., and Montgomery, M. D. (1975). Electron Heat Flux Instabilities in the Solar Wind. *Geophys. Res. Lett.* 2, 79–82. doi:10.1029/gl002i003p00079

Gosling, J. T., de Koning, C. A., Skoug, R. M., Steinberg, J. T., and McComas, D. J. (2004). Dispersionless Modulations in Low-Energy Solar Electron Bursts and Discontinuous Changes in the Solar Wind Electron Strahl. *J. Geophys. Res.* 109, A05102. doi:10.1029/2003ja010338

Greenstadt, E. W., Traver, D. P., Coroniti, F. V., Smith, E. J., and Slavin, J. A. (1990). Observations of the Flank of Earth's Bow Shock to −110 REby ISEE 3/ICE. *Geophys. Res. Lett.* 17, 753–756. doi:10.1029/gl017i006p00753

Herschback, D. M., and Zhang, Y. (2021). Spatial Structures in Solar Wind Superthermal Electrons and Polar Rain Aurora. *J. Atmos. Solar.-Terr. Phys.* 218, 105633. doi:10.1016/j.jastp.2021.105633

Hong, J., Lee, J. J., Min, K. W., Kim, V. P., and Hegai, V. V. (2012). Variations in Polar Rain Flux According to IMF Geometries Observed by STSAT-1. *Adv. Space Res.* 50, 221–227. doi:10.1016/j.asr.2012.03.031

Jaynes, A. N., Baker, D. N., Singer, H. J., Rodriguez, J. V., Lota'aniu, T. M., ali, A. F., et al. (2015). Source and Seed Populations for Relativistic Electrons: Their Roles in Radiation Belt Changes. *J. Geophys. Res. Space Phys.* 120, 7420–7254. doi:10.1002/2015ja021234

Kasaba, Y., Terasawa, T., Tsubouchi, K., Mukai, T., Saito, Y., Matsumoto, H., et al. (2000). Magnetosheath Electrons in Anomalously Low Density Solar Wind Observed by Geotail. *Geophys. Res. Lett.* 27, 3253–3256. doi:10.1029/2000gl000086

Lyon, J. G., Fedder, J. A., and Mobarry, C. M. (2004). The Lyon-Fedder-Mobary (LFM) Global MHD Magnetospheric Simulation Code. *J. Atmos. Solar Terr. Phys.* 66, 1333. doi:10.1016/j.jastp.2004.03.020

Newell, P. T., Feldstein, Y. I., Galperin, Y. I., and Meng, C.-I. (1996). Morphology of Nightside Precipitation. *J. Geophys. Res.* 101, 10737–10748. doi:10.1029/95JA03516

Newell, P. T., and Meng, C.-I. (1990). Intense keV Energy Polar Rain. *J. Geophys. Res.* 95, 7869–7879. doi:10.1029/JA095iA06p07869

Runov, A., Angelopoulos, V., Artemyev, A. V., Lu, S., and Zhou, X.-Z. (2018). Near-Earth Reconnection Ejecta at Lunar Distances. *J. Geophys. Res. Space Phys.* 123, 2736–2744. doi:10.1002/2017JA025079

Simms, L. E., Engebretson, M. J., Pilipenko, V., Reeves, G. D., and Clilverd, M. (2016). Empirical Predictive Models of Daily Relativistic Electron Flux at Geostationary Orbit: Multiple Regression Analysis. *J. Geophys. Res. Space Phys.* 121, 3181–3197. doi:10.1002/2016ja022414

Stepanov, N. A., Sergeev, V. A., Sormakov, D. A., Andreeva, V. A., Dubyagin, S. V., Ganushkina, N., et al. (2021). Superthemal Proton and Electron Fluxes in the Plasma Sheet Transition Region and Their Dependence on Solar Wind Parameters. *J. Geophys. Res. Space Phys.* 126, e2020JA028580. doi:10.1029/2020ja028580

Stverak, S., Maksimovic, M., Travnicek, P. M., Marsch, E., Fazakerley, A. N., and Scime, E. E. (2009). Radial Evolution of Nonthermal Electron Populations in the Low-Latitude Solar Wind: Helios, Cluster, and Ulysses Observations. *J. Geophys. Res.* 114, A04104. doi:10.1029/2008JA013883

Terasawa, T., Kasaba, Y., Tsubouchi, K., Mukai, T., Saito, Y., Frank, L. A., et al. (2000). GEOTAIL Observations of Anomalously Low Density Plasma in the Magnetosheath. *Geophys. Res. Lett.* 27, 3781–3784. doi:10.1029/2000gl000087

Verscharen, D., Wicks, R. T., Alexandrova, O., Bruno, R., Burgess, D., Chen, C. H. K., et al. (2021). A Case for Electron-Astrophysics. *Exp. Astrophys.* doi:10.1007/s10686-09761-5

Walsh, b. M., Haaland, S. E., Daly, P. W., Kronberg, E. A., and Fritz, T. A. (2012). Energetic Electrons along the High-Latitude Magnetopause. *Ann. Geophys.* 30, 1003–1013. doi:10.5194/angeo-30-1003-2012

Wing, S., Fairfield, D. H., Johnson, J. R., and Ohtani, S. I. (2015). On the Field-aligned Electric Field in the Polar Cap. *Geophys. Res. Lett.* 42, 5090–5099. doi:10.1002/2015GL064229

Wing, S., Newell, P. T., and Meng, C.-I. (2005). Cusp Modeling and Observations at Low Altitude. *Surv. Geophys* 26, 341–367. doi:10.1007/s10712-005-1886-0

Wing, S., Newell, P. T., and Onsager, T. G. (1996). Modeling the Entry of Magnetosheath Electrons into the Dayside Ionosphere. *J. Geophys. Res.* 101, 13155–13167. doi:10.1029/96JA00395

Wing, S., Newell, P. T., and Ruohoniemi, J. M. (2001). Double Cusp: Model Prediction and Observational Verification. *J. Geophys. Res.* 106, 25571–25593. doi:10.1029/2000ja000402

Wing, S., and Zhang, Y. L. (2015). The Nightside Magnetic Field Line Open-Closed Boundary and Polar Rain Electron Energy-Latitude Dispersion. *Ann. Geophys.* 33, 39–46. doi:10.5194/angeo-33-39-2015

Zhang, Y., and Wing, S. (2015). Determining Magnetotail Reconnection Location from Polar Rain Energy Dispersion. *J. of Atmos. and Solar-Terrestrial Phys.* 130-131, 75–80. doi:10.1016/j.jastp.2015.05.009

Conflict of Interest: The authors declare that the research was conducted in the absence of any commercial or financial relationships that could be construed as a potential conflict of interest.

Publisher's Note: All claims expressed in this article are solely those of the authors and do not necessarily represent those of their affiliated organizations, or those of the publisher, the editors and the reviewers. Any product that may be evaluated in this article, or claim that may be made by its manufacturer, is not guaranteed or endorsed by the publisher.

frontiers | Frontiers in Astronomy and Space Sciences

BRIEF RESEARCH REPORT
published: 06 June 2022
doi: 10.3389/fspas.2022.917163

The Triple Dusk-Dawn Aberration of the Solar Wind at Earth

*Joseph E. Borovsky**

Space Science Institute, Boulder, CO, United States

In this Brief Report it is pointed out that there are three dusk-dawn aberrations of the solar-wind plasma and magnetic structure approaching Earth and the magnitudes of these aberrations are estimated for various solar-wind types monitored from L1. Solar-wind monitors closer to the Earth than L1 would have superior performances.

Keywords: solar wind, magnetosphere, solar wind monitor, solar wind magnetosphere coupling, space weather

OPEN ACCESS

Edited by:
Xochitl Blanco-Cano, National Autonomous University of Mexico, Mexico

Reviewed by:
Steven Petrinec, Lockheed Martin Solar and Astrophysics Laboratory (LMSAL), United States
Ryan McGranaghan, Atmospheric and Space Technology Research Associates, United States

***Correspondence:**
Joseph E. Borovsky
jborovsky@spacescience.org

Specialty section:
This article was submitted to Space Physics, a section of the journal Frontiers in Astronomy and Space Sciences

Received: *10 April 2022*
Accepted: *20 May 2022*
Published: *06 June 2022*

Citation:
Borovsky JE (2022) The Triple Dusk-Dawn Aberration of the Solar Wind at Earth. Front. Astron. Space Sci. 9:917163. doi: 10.3389/fspas.2022.917163

The solar-wind plasma and its magnetic structure that hit an L1 monitor on the Sun-Earth line will on average pass duskward of the Earth's magnetosphere. This is depicted in **Figure 1** with L1 at the top of the sketch and with the shape of the magnetosphere drawn in blue using the Lin et al. (2010) magnetopause model (eq. (3) of Lin et al. (2010) with r_o = 10.8 R_E, m = 0.1, and β = −1.1).

The solar-wind velocity vector at 1 AU varies with time by about ±5° in both the dawn-dusk and north-south directions (cf. Borovsky 2012; Borovsky, 2018). With L1 being 235 R_E upstream from the Earth (cf. **Figure 1**), the ±5° time variation of the flow vector corresponds to a ±20.5 R_E time variation in the location at Earth of a flow streamline passing through an L1 monitor. The timescales of these velocity-vector changes can be slow (e.g., the days-long variations about stream interfaces discussed below) or fast [e.g., the 98 km/s change in the solar-wind velocity vector over 3 s shown in Fig. 6b of Borovsky (2020a)].

In addition to this variation in the streamline location at Earth, there is a systematic triple aberration (shift) in the dawn-dusk direction. The plasma flow of the solar wind experiences the first two aberrations and the magnetic structure of the solar wind experiences all three aberrations. The origins of the triple aberration are as follows.

(1) The motion of the Earth around the Sun. The 29.8 km/s dawnward motion of the Earth in its orbit (black arrow in **Figure 1**) means that for a perfectly radial solar-wind flow with a speed v_{sw} hitting L1 at the Sun-Earth line will have a streamline that passes the Earth on the dusk side by a distance of (235 R_E) (29.8/v_{sw}) (e.g., Fairfield, 1993). For v_{sw} = 350 km/s this distance is 20 R_E and for v_{sw} = 650 km/s this distance is 10.8 R_E (cf. **Table 1**). In Borovsky (2018) the variability of this first aberration owing to the variability of the solar-wind flow vector is examined in comparison with the typical structure sizes of the solar wind magnetic field (10's of R_E to 100 R_E): cf. Fig. 5 of Borovsky (2018).
(2) The non-radial average flow vector of the solar wind. Using multiple spacecraft at 1 AU, Nemecek et al., (2020a) found a systematic nonradial component to the proton-solar-wind flow that tends to be in the direction of the solar rotation [see also Pizzo et al., (1983) and Finlay et al., (2019)]. As noted in **Table 1**, this systematic flow is ~10 km/s dawnward for slow solar wind and is ~5 km/s duskward for mid-range solar-wind speed. Note that there are also very large ~40 km/s dawn-dusk flows at Earth associated with stream interfaces (Gosling et al., 1978): for slow-to-fast (leading-edge) stream interfaces the solar-wind flow is strongly dawnward on the day before the interface passes the Earth and the flow is strongly duskward on the day after the passage of the interface [cf. Fig. 4b of Borovsky and Denton (2010)] and for fast-to-slow (trailing-edge) stream interfaces the solar-wind flow is systematically duskward for about 3 days prior to the interface passage and the flow is systematically dawnward for about 3 days after the interface passage [cf. Fig. 14b of Borovsky and

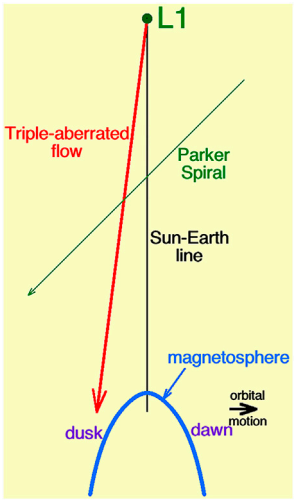

FIGURE 1 | A sketch of a net duskward aberration (red arrow) from a monitor at L1 (green).

Denton (2016)]. As noted in **Table 1**, the Nemecek et al., (2020a) 10 km/s dawnward velocity in a 350 km/s wind yields an offset of 6.7 R_E for the streamline at Earth.

(3) The magnetic structure of the heliosphere moves out from the Sun along the Parker spiral faster than the proton flow. In the Alfvenic fast wind and in the Alfvenic slow wind, the magnetic structure of the heliosphere moves outward from the Sun at a speed of about 0.7 v_A along the Parker-spiral direction relative to the proton flow (Borovsky, 2020b; Nemecek et al., 2020b). [Alfvénic wind has strong temporal correlations between the flow vector **v**(t) and the magnetic-field vector **B**(t).] A nominal 45° Parker-spiral orientation is sketched as the green arrow in **Figure 1**. For v_{sw} in the range 500–650 km/s, the mean Alfven speed in the OMNI2 data set (King and Papitashvili, 2005) is v_A = 73 km/s. Accounting for the angle of the Parker spiral from the Sun-Earth line (39° for 500 km/s and 32° for 650 km/s) the aberration of the magnetic structure is estimated to be 31.7 km/s duskward for 500 km/s Alfvenic solar wind and 27.1 km/s for 650 km/s Alfvenic solar wind (cf. **Table 1**). These aberrations yield "streamline" duskward displacements of 14.9 R_E and 9.8 R_E. Note that the alpha particles of the solar wind are approximately at rest in the reference frame moving with the magnetic structure (Nemecek et al., 2020b), so the alpha-particle flow has the same aberration as the magnetic structure. Also note that at 1 AU the instantaneous magnetic-field direction varies by about ±45° with respect to the calculated Parker-spiral direction [cf. Table 1 of Borovsky (2010)], but the magnetic structure moves in the mean-field direction which is the calculated Parker-spiral direction.

These aberrations are on the order of the 10s-of-R_E magnetic structure sizes in the background Parker-spiral solar wind at 1 AU (Borovsky, 2008; 2018).

Assuming a radial proton flow, the magnitude of the first aberration is straightforward to calculate with the formula

TABLE 1 | Estimates of the dusk-dawn aberrations of the proton plasma and the magnetic structure for typical solar wind types.

Solar wind	Aberration 1	Aberration 2	Aberration 3	Total Aberration
350 km/s non-Alfvenic	Duskward 29.8 km/s 20.0 R_E	dawnward 10 km/s 6.7 R_E	0 km/s 0 R_E	duskward 13.3 R_E
500 km/s non-Alfvenic	Duskward 29.8 km/s 14.0 R_E	duskward 5 km/s 2.4 R_E	0 km/s 0 R_E	duskward 16.4 R_E
500 km/s Alfvenic	Duskward 29.8 km/s 14.0 R_E	Duskward 5 km/s 2.4 R_E	duskward 31.7 km/s 14.9 R_E	duskward 31.3 R_E
650 km/s Alfvenic	Duskward 29.8 km/s 10.8 R_E	?	duskward 27.1 km/s 9.8 R_E	duskward 20.6 R_E

($29.8/v_{sw}$): if the flow is not radial the correction to the first aberration is very small. The second aberration (caused by the non-radial flow) is very variable with time: with a ±5° variation in the flow vector this is a ~ ±20-R_E variation at Earth. The variability of the third aberration has yet to be explored: the Parker-spiral direction varies according to the known formula ($405/v_{sw}$) however the statistics of the magnetic-structure velocity vector with respect to the Parker-spiral direction have not been studied.

The aberration problem from L1 gets better or worse depending on the location of the solar-wind monitor about the L1 point. And during the systematic large deflections of the solar wind in the days around the passages of stream interfaces, the aberration problem gets worse.

There have been a number of recent criticisms of using L1 monitoring for solar-wind/magnetosphere coupling studies (Sandahl et al., 1996; Ashour-Abdalla et al., 2008; Borovsky, 2018, 2020a; Walsh et al., 2019; Burkholder et al., 2020) and several estimates of the solar-wind errors between L1 and Earth (Crooker et al., 1982; Ridley, 2000; Weimer et al., 2002; Mailyan et al., 2008; Case and Wild, 2012). These criticisms and error calculations were based on the temporal flow deviations of the solar wind, the magnetic-structure scalesizes in the solar wind, and cross correlations between L1 measurements and near-Earth measurements.

In studying the driving of the Earth by the solar wind, recent work indicates that errors in the solar-wind values make it difficult to uncover or confirm the physics of the driving. In particular in data-analysis studies the "best fit" formulas obtained by optimizing correlations change depend on the amount of noise in the solar wind measurements (Borovsky, 2022; Sivadas et al., 2022).

To make needed progress in understanding solar-wind/magnetosphere interaction, a call is made for solar-wind monitors much closer to the Earth than L1. A study to optimize the monitor mission is needed. One suggestion would be multiple spacecraft in IMP-type circular orbits (r ~ 30 R_E) wherein one of the spacecraft would always be in the upstream solar wind.

DATA AVAILABILITY STATEMENT

The original contributions presented in the study are included in the article/Supplementary Material, further inquiries can be directed to the corresponding author.

AUTHOR CONTRIBUTIONS

The author confirms being the sole contributor of this work and has approved it for publication.

FUNDING

JEB was supported by the NSF GEM Program via grant AGS-2027569 and by the NASA HERMES Interdisciplinary Science Program via grant 80NSSC21K1406.

ACKNOWLEDGMENTS

The author thanks Bob McPherron, Zdenek Nemecek, and Nithin Sivadas for helpful conversations.

REFERENCES

Ashour-Abdalla, M., Walker, R. J., Peroomian, V., and El-Alaoui, M. (2008). On the Importance of Accurate Solar Wind Measurements for Studying Magnetospheric Dynamics. *J. Geophys. Res.* 113, A08204. doi:10.1029/2007ja012785

Borovsky, J. E., and Denton, M. H. (2010). Solar-wind Turbulence and Shear: A Superposed-Epoch Analysis of Corotating Interaction Regions at 1 AU. *J. Geophys. Res.* 115, A10101. doi:10.1029/2009ja014966

Borovsky, J. E., and Denton, M. H. (2016). The Trailing Edges of High-Speed Streams at 1 AU. *J. Geophys. Res. Space Phys.* 121, 6107–6140. doi:10.1002/2016ja022863

Borovsky, J. E. (2022). Noise, Regression Dilution Bias, and Solar-Wind/magnetosphere Coupling Studies. *Front. Astron. Space Sci.* 9, 867282. doi:10.3389/fspas.2022.867282

Borovsky, J. E. (2020b). On the Motion of the Heliospheric Magnetic Structure through the Solar Wind Plasma. *J. Geophys. Res. Space Phys.* 125, e2019JA027377. doi:10.1029/2019JA027377

Borovsky, J. E. (2010). On the Variations of the Solar Wind Magnetic Field about the Parker Spiral Direction. *J. Geophys. Res.* 115, A09101. doi:10.1029/2009ja015040

Borovsky, J. E. (2012). The Effect of Sudden Wind Shear on the Earth's Magnetosphere: Statistics of Wind-Shear Events and CCMC Simulations of Magnetotail Disconnections. *J. Geophys. Res.* 117, A06224. doi:10.1029/2012ja017623

Borovsky, J. E. (2008). The Flux-Tube Texture of the Solar Wind: Strands of the Magnetic Carpet at 1 AU? *J. Geophys. Res.* 113, A08110. doi:10.1029/2007ja012684

Borovsky, J. E. (2018). The Spatial Structure of the Oncoming Solar Wind at Earth and the Shortcomings of a Solar-Wind Monitor at L1. *J. Atmos. Solar-Terrestrial Phys.* 177, 2–11. doi:10.1016/j.jastp.2017.03.014

Borovsky, J. E. (2020a). What Magnetospheric and Ionospheric Researchers Should Know about the Solar Wind. *J. Atmos. Solar-Terrestrial Phys.* 204, 105271. doi:10.1016/j.jastp.2020.105271

Burkholder, B. L., Nykyri, K., and Ma, X. (2020). A Multispacecraft Solar Wind Monitor. *J. Geophys. Res.* 125, e2020JA027978. doi:10.1029/2020ja027978

Case, N. A., and Wild, J. A. (2012). A Statistical Comparison of Solar Wind Propagation Delays Derived from Multispacecraft Techniques. *J. Geophys. Res.* 117, A02101. doi:10.1029/2011ja016946

Crooker, N. U., Siscoe, G. L., Russell, C. T., and Smith, E. J. (1982). Factors Controlling Degree of Correlation between ISEE 1 and ISEE 3 Interplanetary Magnetic Field Measurements. *J. Geophys. Res.* 87, 2224–2230. doi:10.1029/ja087ia04p02224

Fairfield, D. H. (1993). Solar Wind Control of the Distant Magnetotail: ISEE 3. *J. Geophys. Res.* 21265, 21276.

Finlay, A. J., Hewitt, A. L., Matt, S. P., Owens, M., Pinto, R. F., and Reville, V. (2019). Direct Detection of Solar Angular Momentum Loss with the Wind Spacecraft. *Astrophys. J. Lett.* 885, L30.

Gosling, J. T., Asbridge, J. R., Bame, S. J., and Feldman, W. C. (1978). Solar Wind Stream Interfaces. *J. Geophys. Res.* 83, 1401. doi:10.1029/ja083ia04p01401

King, J. H., and Papitashvili, N. E. (2005). Solar Wind Spatial Scales in and Comparisons of Hourly Wind and ACE Plasma and Magnetic Field Data. *J. Geophys. Res.* 110, 2104. doi:10.1029/2004ja010649

Lin, R. L., Zhang, X. X., Liu, S. Q., Wang, Y. L., and Gong, J. C. (2010). A Three-Dimensional Asymmetric Magnetopause Model. *J. Geophys. Res.* 115, A04207. doi:10.1029/2009ja014235

Mailyan, B., Munteanu, C., and Haaland, S. (2008). What Is the Best Method to Calculate the Solar Wind Propagation Delay? *Ann. Geophys.* 26, 2383–2394. doi:10.5194/angeo-26-2383-2008

Nemecek, Z., Durovcova, T., Safrankova, J., Nemec, F., Matteini, L., StansbyJantizek, D. N., et al. (2020b). What Is the Solar Wind Frame of Reference? *Astrophys. J.* 889, 163.

Nemecek, Z., Durovcova, T., Safrankova, J., Richardson, J. D., Simunek, J., and Stevens, M. L. (2020a). (Non)radial Solar Wind Propagation through the Heliosphere. *Astrophys. J. Lett.* 897, L39.

Pizzo, V., Schwenn, R., Marsch, E., RosenbauerMuhlhauser, H., Muehlhaeuser, K.-H., and Neubauer, F. M. (1983). Determination of the Solar Wind Angular Momentum Flux from the HELIOS Data - an Observational Test of the Weber and Davis Theory. *ApJ* 271, 335–354. doi:10.1086/161200

Ridley, A. J. (2000). Estimations of the Uncertainty in Timing the Relationship between Magnetospheric and Solar Wind Processes. *J. Atmos. Solar-Terrestrial Phys.* 62, 757–771. doi:10.1016/s1364-6826(00)00057-2

Sandahl, I., Lundstedt, H., Koskinen, H., and Glassmeir, K.-H. (1996). On the Need for Slar Wind Monitoring Close to the Magnetosphere. *Asp. Conf. Ser.* 95, 300.

Sivadas, N., Sibeck, D., Subramanyan, V., Wlach, M.-T., Murphy, K., and Halford, A. (2022). *Uncertainty in Solar Wind Forcing Explains Polar Cap Potential Saturation*. Cornell University, Ithaca New York, United States: arXiv:2201.0217v1. doi:10.48550/arXiv.2201.02137

Walsh, B. M., Bhakyapaibul, T., and Zou, Y. (2019). Quantifying the Uncertainty of Using Solar Wind Measurements for Geospace Inputs. *J. Geophys. Res. Space Phys.* 124, 3291–3302. doi:10.1029/2019ja026507

Weimer, D. R., Ober, D. M., Maynard, N. C., Burke, W. J., Collier, M. R., McComas, D. J., et al. (2002). Variable Time Delays in the Propagation of the Interplanetary Magnetic Field. *J. Geophys. Res.* 107, 1210. doi:10.1029/2001ja009102

Conflict of Interest: The author declares that the research was conducted in the absence of any commercial or financial relationships that could be construed as a potential conflict of interest.

Publisher's Note: All claims expressed in this article are solely those of the authors and do not necessarily represent those of their affiliated organizations, or those of the publisher, the editors and the reviewers. Any product that may be evaluated in this article, or claim that may be made by its manufacturer, is not guaranteed or endorsed by the publisher.

frontiers | Frontiers in Astronomy and Space Sciences

ORIGINAL RESEARCH
published: 23 June 2022
doi: 10.3389/fspas.2022.926660

A Statistical Study of Magnetopause Boundary Layer Energetic Electron Enhancements Using MMS

S. N. F. Chepuri[1], A. N. Jaynes[1], D. N. Baker[2], B. H. Mauk[3], I. J. Cohen[3], T. Leonard[2], D. L. Turner[3], J.B. Blake[4], J.F. Fennel[4] and T. D. Phan[5]*

[1]Department of Physics and Astronomy, University of Iowa, Iowa City, IA, United States, [2]Laboratory of Atmospheric and Space Physics, University of Colorado Boulder, Boulder, CO, United States, [3]The Johns Hopkins University Applied Physics Laboratory, Laurel, MD, United States, [4]Space Science Applications Laboratory, El Segundo, CA, United States, [5]Space Sciences Laboratory, University of California, Berkeley, Berkeley, CA, United States

We took a survey of boundary layer (or low-latitude boundary layer) crossings by the Magnetospheric Multiscale (MMS) mission. Out of 250 total crossings, about half showed enhancements of high-energy (> 30 keV) electrons in the FEEPS sensor and a little less than half of those energetic electron events had whistler-mode waves present. Energetic electron enhancements were more likely to be present at magnetic local times closer to noon and at distances of less than about 20 Earth radii, but there was seemingly no correlation with magnetic latitude. For almost all of these events, the pitch angles of the FEEPS electrons were peaked at 90° or isotropic, not field-aligned. Most of the events for which we had data to make a determination showed either direct or indirect evidence of reconnection. Overall, energetic electron enhancements are a fairly common occurrence and there appears to be some connection between whistler waves, energetic electron enhancements, and reconnection, whether it is a direct link or some other process affecting all of them.

Keywords: boundary layer, energetic electrons, whistler waves, magnetosphere, MMS

OPEN ACCESS

Edited by:
Lauri Holappa,
University of Oulu, Finland

Reviewed by:
Ruilong Guo,
Shandong University, China
Tieyan Wang,
Rutherford Appleton Laboratory, United Kingdom

****Correspondence:***
S. N. F. Chepuri
sanjay-chepuri@uiowa.edu

Specialty section:
This article was submitted to Space Physics, a section of the journal Frontiers in Astronomy and Space Sciences

Received: *22 April 2022*
Accepted: *02 June 2022*
Published: *23 June 2022*

Citation:
Chepuri SNF, Jaynes AN, Baker DN, Mauk BH, Cohen IJ, Leonard T, Turner DL, Blake JB, Fennel JF and Phan TD (2022) A Statistical Study of Magnetopause Boundary Layer Energetic Electron Enhancements Using MMS. Front. Astron. Space Sci. 9:926660. doi: 10.3389/fspas.2022.926660

INTRODUCTION

The boundary layer (or low-latitude boundary layer) is the region of the magnetosphere just inside the magnetopause. It contains a mixture of solar wind plasma from the magnetosheath and magnetosphere plasma. Energetic electrons have been observed in the boundary layer but not often enough to draw broad conclusions about the characteristics of those events. The study presented here found that energetic electrons occurred about half of the time we passed through the boundary layer and colocated whistler-mode waves were observed a little less than half the time. Although we only observed direct evidence of reconnection in the immediate vicinity of whistler waves a few times, we found indications that reconnection was likely occurring, which fits with the common association of whistler waves with reconnection.

There has long been evidence of energetic electrons > 10s of keV in the boundary layer region of the magnetosphere. Starting with Geotail, observations with newer instruments have found these electrons at increasingly higher energies and in many different regions, such as the nightside magnetosheath (Sarafopoulos et al., 2000), high and low latitudes of the dayside magnetosphere boundary layer (Dunlop et al., 2008), and the high latitude magnetopause (Walsh et al., 2012). Jaynes et al. (2016) observed energetic electrons at over 100 keV in the vicinity of the dayside reconnection

region exhibiting 90° peaked, or trapped, pitch angle distributions, using the Magnetospheric Multiscale (MMS) mission just in the first few months of the mission. Dunlop et al. (2008) found a pitch angle distribution that was more isotropic closer to the magnetopause, but it transitioned to a distribution with complex dynamics, leading to inconclusive signatures. Walsh et al. (2012) also found cases both where electrons were field-aligned and trapped in the high-latitude magnetopause. Jaynes et al. (2016) found a field-aligned flow at the time of reconnection, but a distribution that was highly peaked at 90° shortly after when whistler-mode and electrostatic waves were present.

Electron acceleration has previously been connected to wave activity associated with magnetic reconnection (Drake et al., 2006; Pritchett, 2008; Fu et al., 2019) or with cusp energization, which has been observed in the magnetosheath, a region where energetic electrons have been studied more thoroughly (Nykyri et al., 2012). Nykyri et al. (2012) found high energy particles in the cusp diamagnetic cavity with pitch angles around 90°. Reconnection converts magnetic energy into kinetic energy, which transports solar energy into the magnetosphere and also allows solar wind particles to mix with magnetospheric particles (Dungey, 1961). This process could be mediated by whistler-mode waves, which has been shown both theoretically (Mandt et al., 1994) and experimentally (Deng and Matsumoto, 2001). This follows the longstanding theoretical and observational evidence that connects whistler wave excitation with magnetic reconnection (Fujimoto and Sydora, 2008; Graham et al., 2016). These whistler-mode waves propagate away from the site of reconnection (the X-line) so we would expect to see them in the region of reconnection, not necessarily just at the source (Tang et al., 2013). Whistler waves have also been more widely observed in the inner magnetosphere and have been connected to the precipitation of energetic electrons (Yahnin et al., 2019). There are detailed models of how whistler waves accelerate electrons in the radiation belt in addition to precipitating electrons (Trakhtengerts et al., 2003; Demekhov et al., 2006). Even though these processes occur in a different region of the magnetosphere there could be similarities to these VLF events with energetic electrons in the boundary layer. Therefore, whistler-mode waves are something to look for when investigating electron enhancements, and since they propagate between around 0.1 and 1 times the electron cyclotron frequency and they exhibit narrow-band power, we can easily identify them in the data (Wilder et al., 2016).

Most of the observations summarized above were case studies of only one or a few events as opposed to a wide-ranging survey of these events as a whole. In this paper, we will take that wider view. By studying a large number of boundary layer crossings, we will determine how common events with energetic electrons and whistler-mode waves are and then search for properties these events have in common.

INSTRUMENTATION

Launched in 2015, NASA's Magnetospheric Multiscale (MMS) mission has unprecedentedly high-resolution, especially its burst mode data (Burch et al., 2016). The mission consists of four spacecraft, although we only used data from one (MMS 1) because the spatial difference between the spacecraft was smaller than the scale at which we would expect to see a meaningful difference in the energetic electron data given their large gyroradii. The mission changed its orbit from a lower-apogee orbit that skimmed through the boundary layer at apogee to a higher-apogee orbit that passes through the boundary layer more quickly at the end of 2016. Our dataset runs from 2016 to 2020, so we include some data from both orbits.

All four MMS spacecraft have a wide range of instruments to measure both field and particle data. We used several instruments from the FIELDS suite onboard (Torbert et al., 2016a): the flux gate magnetometer (FGM) (Russell et al., 2016), the electron drift instrument (EDI) (Torbert et al., 2016b), the search coil magnetometer (SCM) (Le Contel et al., 2016), and the electric field double probe (EDP) (Ergun et al., 2016; Lindqvist et al., 2016). Additionally, we used the Fast Plasma Investigation (FPI) (Pollock et al., 2016) and, from the Energetic Particle Detector suite (Mauk et al., 2016), the Fly's Eye Electron Proton Spectrometer (FEEPS) (Blake et al., 2016). The FEEPS sensor has six heads, each of which has two eyes. Of the 12 eyes for each FEEPS, nine are for electrons and three for ions. FEEPS covers an energy range of 25–650 keV for electrons and each MMS spacecraft has two FEEPS sensors that combine to give a solid-angle coverage of over 3π sr. These data were used to identify boundary layer regions as well as find the occurrences of energetic electron enhancements and to look for waves during the electron enhancement events.

DATA

Example Boundary Layer Crossing Event

In order to get a sample, we used the SITL reports to pick out boundary layer observations. The SITL (scientist in the loop) model is the method by which MMS decides what data to download. A SITL looks at all the low resolution data and flags it if they see something interesting. Then, they write a brief report mentioning why that data was noteworthy and the high resolution data is downloaded. MMS has two data types: low resolution "survey" data and high resolution "burst" data. For example, for the FEEPS instrument, burst mode acquires 64 samples per spin, which would be 0.3125 s per sample for a 20 s spin period, compared to the fast survey mode which only has a sample rate of eight per spin (Blake et al., 2016). This eightfold increase in time resolution in the burst data is crucial to our study because boundary layer crossings and FEEPS enhancements can be for very brief periods of time and would be averaged out in the lower resolution data. Therefore, we were limited to burst data, which we only have access to for the exact times a SITL asks for it. After downloading all the reports, we used a string search to find any time the SITL flagged a boundary layer crossing. We searched through every available SITL report, which covered April 2016-1 May 2020.

For each of these crossings, we graphed several variables from various instruments on MMS to confirm that this event was in fact a boundary layer crossing (**Figure 1**). Panel a) shows the

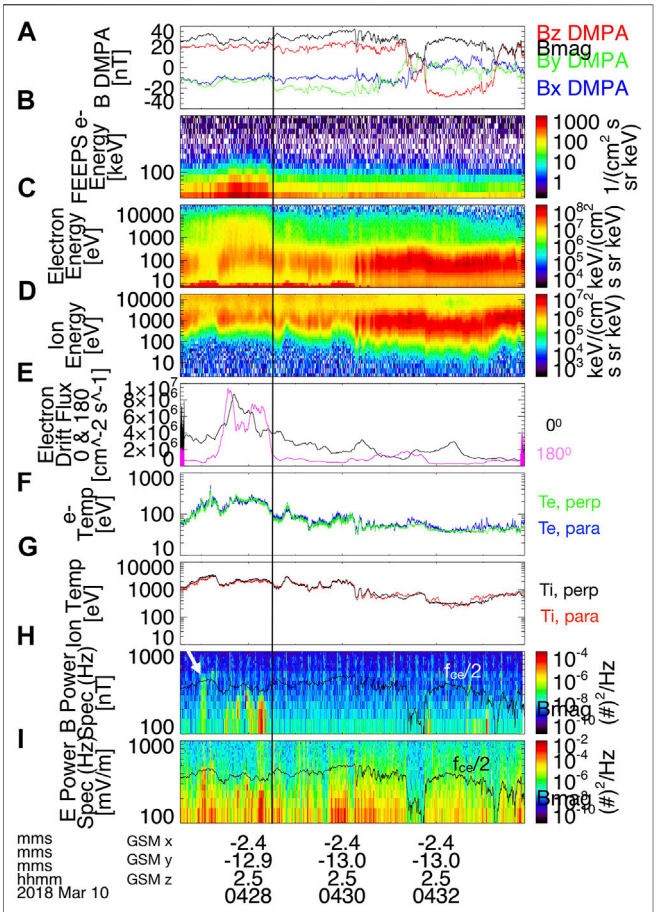

FIGURE 1 | An example of a boundary crossing event containing whistler waves at 04:26 on 10 March 2018. **(A)** Magnetic field in DMPA coordinates, **(B)** FEEPS electron energies, **(C)** Lower-energy electron energies, **(D)** Lower-energy ion energies, **(E)** Flux of background thermal electrons looking at 0° (black) and 180° (pink), **(F)** Parallel (blue) and perpendicular (green) electron temperatures, **(G)** Parallel (red) and perpendicular (black) ion temperatures, **(H)** Magnetic field power spectral density, **(I)** Electric field power spectral density. For the last two panels, the half electron cyclotron frequency is plotted. The vertical line shows the end of the boundary layer crossing with FEEPS enhancements while the arrow points to the whistler waves.

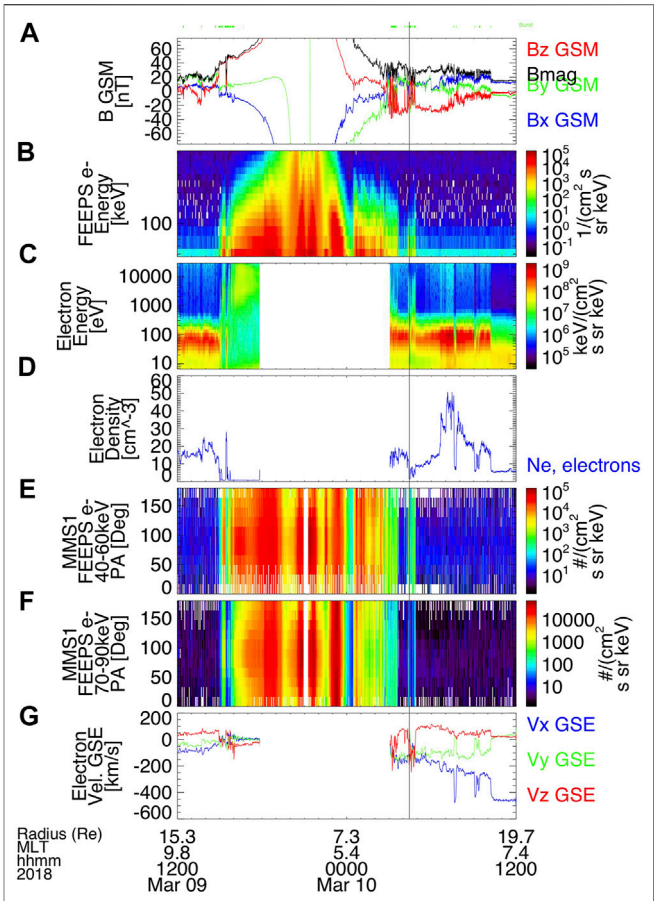

FIGURE 2 | A full day plot of the same event as above, going from 12:00 on 9 March 2018 to 12:00 on March 10. **(A)** Magnetic field in GSM coordinates, **(B)** FEEPS electron energies, **(C)** Lower-energy electron energies, **(D)** electron density, **(E)** Pitch angle distribution of FEEPS electrons in the 40–60 keV range, **(F)** Pitch angle distribution of FEEPS electrons in the 70–90 keV range, **(G)** Electron velocity components in GSE coordinates. The lime green bars on top indicate where burst mode data is available and the gaps in the middle are from the FPI instruments turning off in the inner magnetosphere. The vertical line indicates where **Figure 1** begins, which is located at a distance of 13.4 R_e.

magnetic field, both the components and total magnitude, in Despun Major Principal Axis of inertia (DMPA) coordinates, which is considered "near-GSE" (Leinweber et al., 2016). Panel b) shows the FEEPS intensity of electrons at different energies. Panels c) and d) are the intensity of background thermal electrons and ions, respectively, at different energies. Panel e) compares the flux of background thermal electrons in two opposite directions, while f) and g) show the electron and ion temperatures, respectively, in both the parallel and perpendicular directions. Finally, panels h) and i) are the magnetic field and electric field power spectra with half of the electron cyclotron frequency plotted for reference. The indicators of a boundary layer crossing were a slowly varying magnetic field as measured by the FGM, a mixture of higher energy plasma (electrons and ions) and lower energy plasma showing the mixture of magnetosheath and magnetosphere plasma using the FPI, and divergence between the flux of lower-energy electrons at 0° and 180° using the EDI. These parameters were examined visually to confirm that the observation did in fact pass through the boundary layer. In cases where we did find evidence of a boundary layer crossing, next we looked for enhancements in the intensity of high energy electrons from FEEPS, where there was an order of magnitude increase in the FEEPS intensity inside the boundary layer excluding the lowest energy channel. Finally, when there were FEEPS enhancements, we took power spectra of the electric and magnetic fields on EDP and SCM data to see if there was any evidence of whistler-mode waves at around half of the electron cyclotron frequency.

Looking at these indicators on **Figure 1**, the magnetic field in panel a) is relatively slowly-varying from the start of the data until around 04:30, although not as smooth as often seen in other

events. Panel b) shows a FEEPS enhancement from about 04:27:00–04:28:30. The low energy electrons are present in panel c) throughout the time covered in this graph, but the high energy thermal electron population is only consistently present until around 04:28:30, so this is when the boundary layer crossing is over, as indicated by the vertical black line. After that, there are a few instances where the higher energy thermal electrons in the FPI data in panel c) are measured momentarily but they immediately disappear each time. These are instances where we briefly enter the boundary layer but not for long enough to collect any data from that entry. In panel e), the black line showing the flux at 0° and the pink line showing the flux at 180° are very different and do not follow the same path during the boundary layer crossing, but converge once we leave the boundary layer. In panels h) and i), there are waves at about half of the electron cyclotron frequency (the line plotted over the spectrum) at about 04:27, as indicated by the arrow. There is also noise throughout at low frequencies, but that is not relevant to our study. In order for an event to be counted as one with FEEPS enhancements and waves, we looked for any wave activity in the relevant range between f_{ce} and 0.1 f_{ce}. We looked for signatures in both the electric and magnetic fields, unless there was broadband activity obscuring the whistler in the electric field, in which case magnetic field alone sufficed. To be counted, the wave activity only needed to last about 5 s, which is long enough to be longer than random noise and could have any amount of overlap with the energetic electrons or be immediately preceding or succeeding the electrons.

Figure 2 shows a wider view of this event where we can see an entire orbit. Panels a)-c) are the same as in **Figure 1**, showing magnetic field in GSM coordinates, FEEPS electron energies, and background thermal electron energies, respectively. Panel d) shows the electron density and panels e) and f) show the pitch angle distributions of FEEPS electrons at 40–60 and 70–90 keV, respectively. Finally, panel g) shows the components of the electron velocity in GSE coordinates. The data missing from the middle section is because FPI instruments turn off in the inner magnetosphere, but this does not affect our analysis. The magnetic field peak and high levels in FEEPS intensity show when the spacecraft is in the inner magnetosphere, but once it leaves that region, the FEPPS levels drop to 0, until the spike when the event shown in **Figure 1** takes place. The mixed population of background electrons from FPI in panel c) show that this increase in energetic electron precisely corresponds with the time when the spacecraft is in the boundary layer, showing that this effect is localized to the boundary layer.

Statistical Results

Having examined every event, we sorted them into three groups: events with FEEPS enhancements and whistler waves, events with FEEPS enhancements but no waves, and boundary layer crossings without FEEPS enhancements. There were a total of 250 boundary layer crossings, 121 of which (48%) showed FEEPS enhancements, and 47 of which (19% of the total boundary layer crossings and 39% of the FEEPS events) had waves. We then graphed different parameters for all the boundary layer crossings. We looked at the location in GSM coordinates (**Figure 3**) and saw that most of the boundary layer crossings were on the dayside. Except for a cluster of boundary layer only events at high latitudes

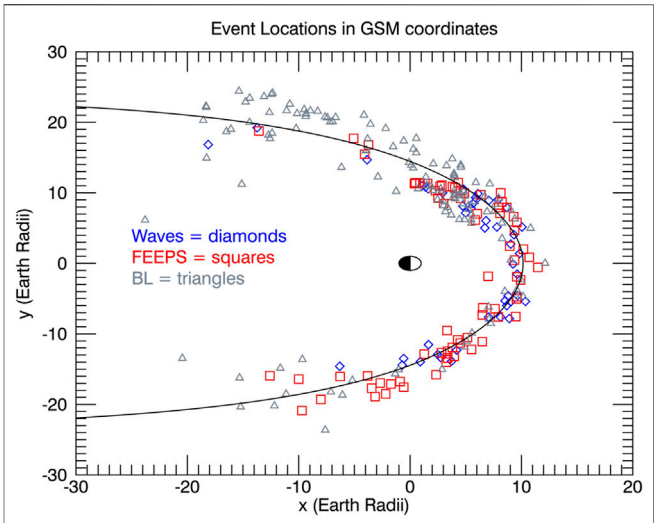

FIGURE 3 | A scatter plot of x and y position of boundary layer crossings in GSM coordinates. The blue diamonds represent events with FEEPS enhancements and whistler waves, the red squares are events with FEEPS enhancements but no waves, and the gray triangles are boundary layer crossings with no FEEPS enhancements. The black line shows a typical magnetopause using a model and average data from Lin et al. (2010).

on the night side, events with FEEPS enhancements and events without were evenly distributed throughout other locations. The data points are plotted along with a typical magnetopause location for reference, using a model from Lin et al. (2010). The inputs for the model are solar wind dynamic pressure, solar wind magnetic pressure, IMF B_z, and corrected dipole tilt. Lin et al. (2010) give average values for 2,708 magnetopause crossings of P_d = 2.77 nPa, P_m = 0.01939 nPa, and B_z = −0.23 nT, and we used a dipole tilt of 0.

We also made histograms of the boundary layer crossings for magnetic local time, magnetic latitude, and radius (**Figure 4**). Panels a), d), and g), show the amount of burst data gathered by MMS throughout the time period of this study, binned by magnetic local time, magnetic latitude, and distance, respectively. Panels, b), e), and h) show the same parameters but just for boundary layer crossings, where the gray bar shows the amount of boundary layer crossings with no FEEPS enhancements and the red and blue bar shows crossings with enhancements. Finally, panels c), f), and i) show the ratio of total boundary layer crossings in that bin that have FEEPS enhancements. From panels b) and c), it is clear that FEEPS enhancements are more common for boundary layer crossings closer to noon or slightly on the dawn side, while the crossings farther away on the flanks see energetic electrons less often. Looking at the magnetic latitude in panels e) and f), there doesn't seem to be much correlation with how often we see enhancements. Additionally, comparing panel e) to panel d), it is clear that the lowest latitude bin in panel e) has many more events because of the orbit of MMS spends more time at those latitudes and not because of any physical reason. Finally, from panels h) and i), events with FEEPS enhancements are more common at distances that are closer to the Earth; for events that are farther

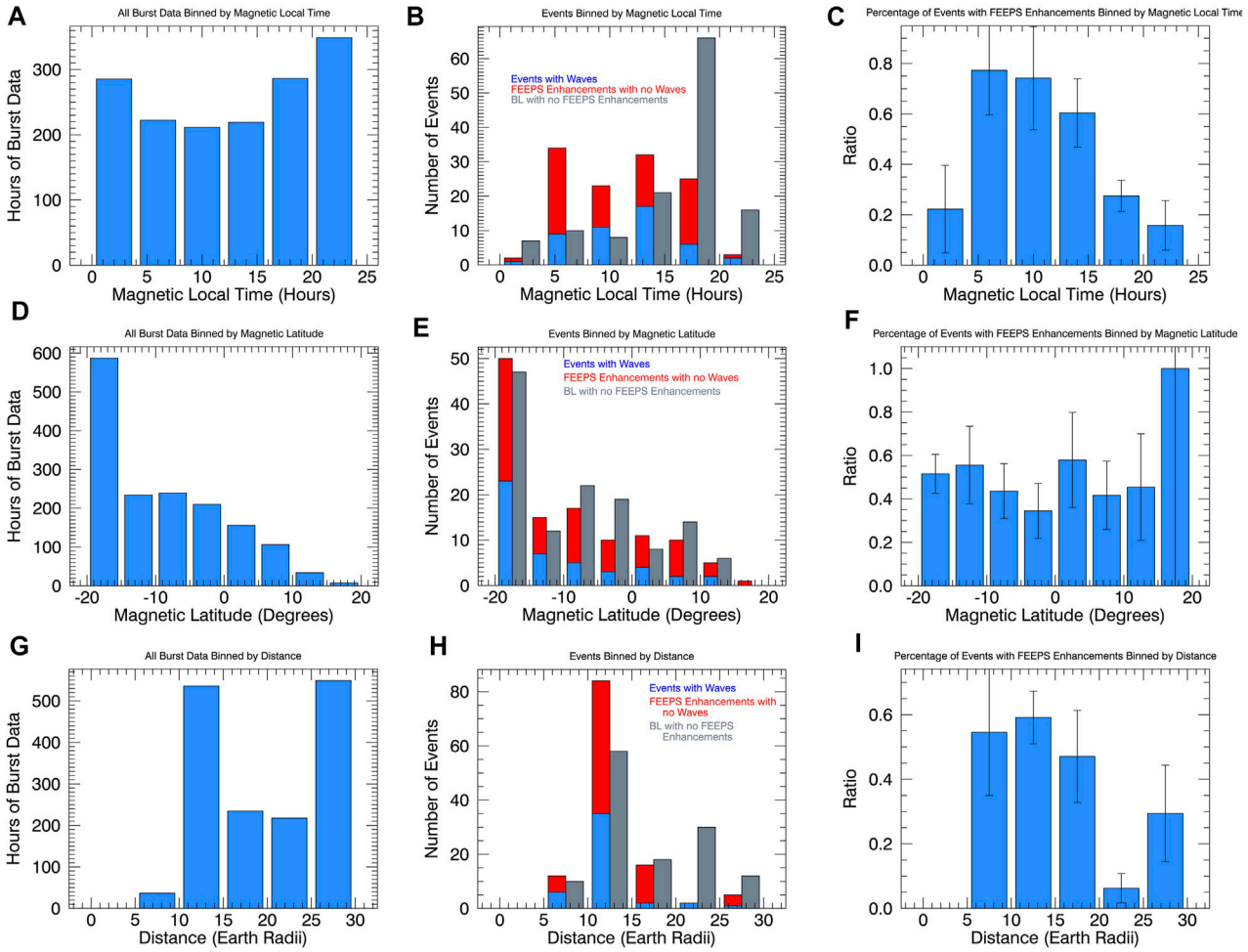

FIGURE 4 | Bar plots comparing boundary layer crossings with FEEPS energetic electron enhancements and those without for different parameters. In the middle, the red and blue bar represents events with FEEPS enhancements (without and with whistler waves respectively) and the gray bar is crossings without FEEPS enhancements. **(B)** is magnetic local time, **(E)** is magnetic latitude, and **(H)** is distance. On the right is the same data graphed as percentage of total events that had FEEPS enhancements, with **(C)** Magnetic local time, **(F)** Magnetic latitude, **(I)** Distance. On the left is the same parameters for all burst data gathered by MMS in the relevant time period, with again **(A)** Magnetic local time, **(D)** Magnetic latitude, **(G)** Distance. Error bars derived using Poisson statistics, assuming a $\sqrt{N}$ uncertainty associated with each bin of N events.

out that about 20 Earth radii, FEEPS enhancements are very rare. The error bars in panels c), f), and i) were derived using Poisson statistics, assuming that each bin of N events, either with or without enhancements has $\sqrt{N}$ uncertainty associated with it, and then propagating that uncertainty through taking the ratio.

The last aspect of these events we wanted to study was the pitch angle of the FEEPS electrons and evidence of reconnection in the vicinity (as a potential driver of whistler waves), as shown in **Figure 5**. Panels a) and b) show the FEEPS intensity and background thermal electron intensity for reference to show when the spacecraft is passing through the boundary layer and measuring energetic electrons. Panels c) and d) show pitch angle distributions at two different energy bands for FEEPS electrons, and panel e measures each component of the velocity in Geocentric Solar Ecliptic (GSE) coordinates. If pitch angle was centered around 0°/180°, then these electrons would be traveling into the boundary layer or from a different region in the boundary layer along the field lines, otherwise they would be locally produced. We found a distribution peaked around 90° or isotropic the vast majority of the time, only 10 events showed a field aligned pitch angle. To examine the connection between whistler waves (and thus enhancements) and reconnection, we examined the velocity moment. A reconnection jet would be associated with a sudden reversal in velocity from highly negative to highly positive (or vice-versa) in one dimension that is not mirrored in the other two or, more commonly but still rare, a spike from near zero to a high value. Features that looked like reconnection jets were very rare and we only found this in seven events. However, a reversal like this would only show up right at the point of reconnection. Zooming out around events, we saw a velocity moment maximum above 200 km/s within a few minutes for almost every event, suggesting reconnection nearby. Looking

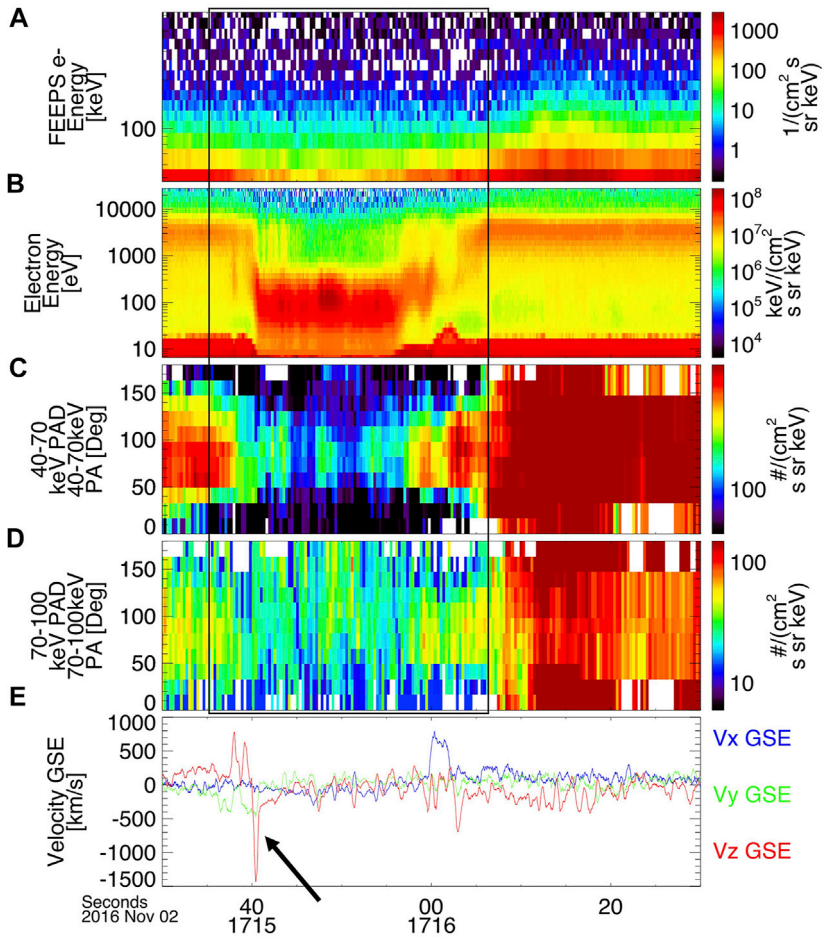

FIGURE 5 | An example of a boundary crossing event that showed evidence of reconnection at 17:15 on 2 November 2016. **(A)** FEEPS electron energies, **(B)** background thermal electron energies, **(C)** Pitch angle distribution at 40–70 keV, **(D)** Pitch angle distribution at 70–100 keV, **(E)** Electron velocity components in GSE coordinates. The box shows the time of the boundary layer crossing and the arrow points to the velocity reversal suggestive of a reconnection jet.

at these events in more detail, there was only clean enough data to make a more definitive determination in a small subset of events, where there was a stable entry into the magnetosheath to determine if a velocity jet during a boundary layer crossing is in fact over ~ 100 km/s different than the magnetosheath velocity. Of those, over 90% showed some evidence of reconnection. This was either directly from jets in the ion and/or electron v_z flow, or indirectly from magnetic flux ropes, which are generated by reconnection, though not necessarily locally. In contrast, only about 55% of boundary layer crossings without FEEPS enhancements should signatures of reconnection. Therefore there appears to be some connection between whistler waves, electron enhancements, and reconnection, whether it is a direct link or some other process affecting all of them.

DISCUSSION

Overall, we found that enhancements of energetic electrons in the boundary layer was a common phenomenon but far from ever-present. Also, although both energetic electrons and whistler waves are thought to be common results of reconnection, we only found waves less than half the time we found energetic electrons. However, if waves are generated by the distribution of magnetospheric electrons as suggested by Graham et al. (2016), then it fits that events with waves would be a subset of events with electron enhancements. These events were more common on the dayside and when the boundary layer is relatively close to the Earth, which could relate to asymmetries in the boundary layer (Dunlop et al., 2008). For the distance away from the Earth, the boundary layer is often closer when there is stronger solar driving pushing the magnetosphere closer to Earth and it is possible that this also drives processes such as reconnection that create energetic electrons to happen more often. To test this hypothesis, we examined the disturbance storm time (Dst) index, a general indication of geomagnetic activity that has a more negative value when solar driving is stronger. We found no meaningful difference between events with FEEPS enhancements and boundary layer crossings without, taking the Dst index to the nearest hour. Boundary layer crossings without FEEPS

enhancements had an average Dst index of -13.9 and crossings with enhancements had an average of -12.6. However, with standard deviations of 18.4 and 13.5 respectively, these differences are not significant. Similarly, there was no meaningful difference in the auroral electrojet (AE) index, another indicator of geomagnetic activity. Another possible explanation for this is that distance and magnetic local time (MLT) are not independent. Further down the flanks, the magnetopause and therefore the boundary layer is farther away from the Earth, so this pattern in the distance could be a different manifestation of the MLT pattern. The direction of the interplanetary magnetic field (IMF) could also be a factor in reconnection occurring. The IMF was rapidly flipping back and forth between northward and southward for many events, but we examined whether there was a southward IMF at any point within 15 min of a boundary layer crossing. Of events with no FEEPS enhancements, 87 out of 128 (68%) had a southward IMF, while it was 87 out of 119 (73%) for events with FEEPS enhancements. Splitting up the events with FEEPS enhancements, 52 out of 73 (71%) without waves had a southward IMF and 35 out of 46 (76%) with waves did. Although there is a small increase in events with southward IMF for FEEPS enhancements and waves, considering the ambiguities in determining whether a southward IMF did affect reconnection at a relevant time for our observations, it is difficult to say this relationship is meaningful.

Although we did not find many instances of reconnection jets, that is expected since that is a much more localized effect than the waves or energetic electrons which can travel and cover a wider area. We found many cases where there was likely reconnection nearby, so it still could be a relevant process even if we could not measure it directly. To investigate the driver of these whistler waves, we searched for temperature anisotropy (Artemyev et al., 2016) and beam anisotropy in our data (Wilder et al., 2019). We found some cases of each type of anisotropy in our dataset, though the majority of the events had neither and most of the temperature anisotropies we found were small enough that it is debatable whether that would be sufficient to drive waves, so examining the process that is driving the waves still requires further study. We also saw 90° peaked electrons in almost every event, only rarely finding field-aligned electrons. Whistler waves have been shown to trap electrons and create this kind of peaked distribution using multiple mechanisms, including in cases where the waves were generated elsewhere and traveled into a different region (Kellogg et al., 2010). Additionally, electrons can be trapped by the geometry of reconnection without the direct presence of whistler waves (Egedal et al., 2008). This is crucial for our results because 90° peaked electrons were prevalent in events that did not have waves as well as those that did. For the few events with field-aligned electrons, escape across the magnetopause along field lines could be one possible mechanism that is occurring(Cohen et al., 2017).

Phase trapping is one mechanism by which particles and waves interact and is not a stochastic process, so it can affect the particle's pitch angle as well as its energy within one interaction. Phase trapping occurs when a particle becomes trapped inside a magnetic island and moves along with the wave for a time, which has a significant effect on the particle's energy and/or pitch angle in a short amount of time. This has been considered a candidate for accelerating electrons, at least in other regions of the magnetosphere (Albert, 2002). Using data from this study, simulations can be run for individual events to examine phase trapping as an acceleration mechanism in the boundary layer. Although electron cyclotron resonance is a common mechanism that energizes electrons elsewhere in the magnetosphere, whistler waves in the boundary layer would not be a good candidate for that type of process since they are generally only present for a timescale on the order of seconds to a few minutes, so there would not be enough time for them to be energized to this level by cyclotron resonance. Additionally, these whistler waves have been shown to be highly nonlinear (Wilder et al., 2016) which leaves open the possibility for other methods of acceleration such as phase trapping. Overall, energetic electron enhancements are a fairly common occurrence and are likely correlated with reconnection.

DATA AVAILABILITY STATEMENT

Publicly available datasets were analyzed in this study. This data can be found here: https://lasp.colorado.edu/mms/sdc/public/about/browse-wrapper/ http://cdaweb.gsfc.nasa.gov/istp_public/.

AUTHOR CONTRIBUTIONS

AJ was Ph. D. advisor for the first author and contributed to work. DT advised on data products and analysis. DB and TL contributed expertise on the FEEPS instrument. BM, IC, JB, and JF gave advice on data usage. TP helped with interpretation for reconnection related events.

FUNDING

This work was supported by funding from the MMS mission, under NASA contract NNG04EB99C.

REFERENCES

Albert, J. M. (2002). Nonlinear Interaction of Outer Zone Electrons with Vlf Waves. *Geophys. Res. Lett.* 29, 1–2. doi:10.1029/2001gl013941

Artemyev, A., Agapitov, O., Mourenas, D., Krasnoselskikh, V., Shastun, V., and Mozer, F. (2016). Oblique Whistler-Mode Waves in the Earth's Inner Magnetosphere: Energy Distribution, Origins, and Role in Radiation Belt Dynamics. *Space Sci. Rev.* 200, 261–355. doi:10.1007/s11214-016-0252-5

Blake, J. B., Mauk, B. H., Baker, D. N., Carranza, P., Clemmons, J. H., Craft, J., et al. (2016). The Fly's Eye Energetic Particle Spectrometer (FEEPS) Sensors for the Magnetospheric Multiscale (MMS) Mission. *Space Sci. Rev.* 199, 309–329. doi:10.1007/s11214-015-0163-x

Burch, J. L., Moore, T. E., Torbert, R. B., and Giles, B. L. (2016). Magnetospheric Multiscale Overview and Science Objectives. *Space Sci. Rev.* 199, 5–21. doi:10.1007/s11214-015-0164-9

Cohen, I. J., Mauk, B. H., Anderson, B. J., Westlake, J. H., Sibeck, D. G., Turner, D. L., et al. (2017). Statistical Analysis of Mms Observations of Energetic Electron Escape Observed At/beyond the Dayside Magnetopause. *J. Geophys. Res. Space Phys.* 122, 9440–9463. doi:10.1002/2017ja024401

Demekhov, A. G., Trakhtengerts, V. Y., Rycroft, M. J., and Nunn, D. (2006). Electron Acceleration in the Magnetosphere by Whistler-Mode Waves of Varying Frequency. *Geomagn. Aeron.* 46, 711–716. doi:10.1134/s0016793206060053

Deng, X. H., and Matsumoto, H. (2001). Rapid Magnetic Reconnection in the Earth's Magnetosphere Mediated by Whistler Waves. *Nature* 410, 557–560. doi:10.1038/35069018

Drake, J. F., Swisdak, M., Che, H., and Shay, M. A. (2006). Electron Acceleration from Contracting Magnetic Islands during Reconnection. *Nature* 443, 553–556. doi:10.1038/nature05116

Dungey, J. W. (1961). Interplanetary Magnetic Field and the Auroral Zones. *Phys. Rev. Lett.* 6, 47–48. doi:10.1103/physrevlett.6.47

Dunlop, M., Taylor, M., Bogdanova, Y., Shen, C., Pitout, F., Pu, Z., et al. (2008). Electron Structure of the Magnetopause Boundary Layer: Cluster/double Star Observations. *J. Geophys. Res. Space Phys.* 113. doi:10.1029/2007ja012788

Egedal, J., Fox, W., Katz, N., Porkolab, M., Øieroset, M., Lin, R., et al. (2008). Evidence and Theory for Trapped Electrons in Guide Field Magnetotail Reconnection. *J. Geophys. Res. Space Phys.* 113. doi:10.1029/2008ja013520

Ergun, R. E., Tucker, S., Westfall, J., Goodrich, K. A., Malaspina, D. M., Summers, D., et al. (2016). The Axial Double Probe and Fields Signal Processing for the Mms Mission. *Space Sci. Rev.* 199, 167–188. doi:10.1007/s11214-014-0115-x

Fu, H. S., Peng, F. Z., Liu, C. M., Burch, J. L., Gershman, D. G., and Le Contel, O. (2019). Evidence of Electron Acceleration at a Reconnecting Magnetopause. *Geophys. Res. Lett.* 46, 5645–5652. doi:10.1029/2019gl083032

Fujimoto, K., and Sydora, R. D. (2008). Whistler Waves Associated with Magnetic Reconnection. *Geophys. Res. Lett.* 35. doi:10.1029/2008gl035201

Graham, D. B., Vaivads, A., Khotyaintsev, Y. V., and André, M. (2016). Whistler Emission in the Separatrix Regions of Asymmetric Magnetic Reconnection. *J. Geophys. Res. Space Phys.* 121, 1934–1954. doi:10.1002/2015ja021239

Jaynes, A. N., Turner, D. L., Wilder, F. D., Osmane, A., Baker, D. N., Blake, J. B., et al. (2016). Energetic Electron Acceleration Observed by Mms in the Vicinity of an X-Line Crossing. *Geophys. Res. Lett.* 43, 7356–7363. doi:10.1002/2016gl069206

Kellogg, P. J., Cattell, C. A., Goetz, K., Monson, S., and Wilson, L., III (2010). Electron Trapping and Charge Transport by Large Amplitude Whistlers. *Geophys. Res. Lett.* 37.

Le Contel, O., Leroy, P., Roux, A., Coillot, C., Alison, D., Bouabdellah, A., et al. (2016). The Search-Coil Magnetometer for Mms. *Space Sci. Rev.* 199, 257–282.

Leinweber, H. K., Bromund, K. R., Strangeway, R. J., and Magnes, W. (2016). *The MMS Fluxgate Magnetometers Science Data Products Guide*. Springer.

Lin, R., Zhang, X., Liu, S., Wang, Y., and Gong, J. (2010). A Three-Dimensional Asymmetric Magnetopause Model. *J. Geophys. Res. Space Phys.* 115. doi:10.1029/2009ja014235

Lindqvist, P.-A., Olsson, G., Torbert, R. B., King, B., Granoff, M., Rau, D., et al. (2016). The Spin-Plane Double Probe Electric Field Instrument for Mms. *Space Sci. Rev.* 199, 137–165. doi:10.1007/s11214-014-0116-9

Mandt, M. E., Denton, R. E., and Drake, J. F. (1994). Transition to Whistler Mediated Magnetic Reconnection. *Geophys. Res. Lett.* 21, 73–76. doi:10.1029/93gl03382

Mauk, B., Blake, J., Baker, D., Clemmons, J., Reeves, G., Spence, H. E., et al. (2016). The Energetic Particle Detector (Epd) Investigation and the Energetic Ion Spectrometer (Eis) for the Magnetospheric Multiscale (Mms) Mission. *Space Sci. Rev.* 199, 471–514.

Nykyri, K., Otto, A., Adamson, E., Kronberg, E., and Daly, P. (2012). On the Origin of High-Energy Particles in the Cusp Diamagnetic Cavity. *J. Atmos. solar-terrestrial Phys.* 87-88, 70–81. doi:10.1016/j.jastp.2011.08.012

Pollock, C., Moore, T., Jacques, A., Burch, J., Gliese, U., Saito, Y., et al. (2016). Fast Plasma Investigation for Magnetospheric Multiscale. *Space Sci. Rev.* 199, 331–406.

Pritchett, P. L. (2008). Energetic Electron Acceleration during Multi-Island Coalescence. *Phys. Plasmas* 15, 102105. doi:10.1063/1.2996321

Russell, C. T., Anderson, B. J., Baumjohann, W., Bromund, K. R., Dearborn, D., Fischer, D., et al. (2016). The Magnetospheric Multiscale Magnetometers. *Space Sci. Rev.* 199, 189–256. doi:10.1007/978-94-024-0861-4_8

Sarafopoulos, D. V., Athanasiu, M. A., Sibeck, D. G., McEntire, R. W., Sarris, E. T., and Kokubun, S. (2000). Energetic Proton and Electron Dispersion Signatures in the Nightside Magnetosheath Supporting Their Leakage Out of the Magnetopause. *J. Geophys. Res.* 105, 15729–15739. doi:10.1029/2000ja900041

Tang, X., Cattell, C., Dombeck, J., Dai, L., Wilson, L. B., III, Breneman, A., et al. (2013). Themis Observations of the Magnetopause Electron Diffusion Region: Large Amplitude Waves and Heated Electrons. *Geophys. Res. Lett.* 40, 2884–2890.

Torbert, R. B., Russell, C. T., Magnes, W., Ergun, R. E., Lindqvist, P.-A., LeContel, O., et al. (2016a). The Fields Instrument Suite on Mms: Scientific Objectives, Measurements, and Data Products. *Space Sci. Rev.* 199, 105–135. doi:10.1007/s11214-014-0109-8

Torbert, R. B., Vaith, H., Granoff, M., Widholm, M., Gaidos, J. A., Briggs, B. H., et al. (2016b). The Electron Drift Instrument for Mms. *Space Sci. Rev.* 199, 283–305. doi:10.1007/s11214-015-0182-7

Trakhtengerts, V. Y., Rycroft, M., Nunn, D., and Demekhov, A. (2003). Cyclotron Acceleration of Radiation Belt Electrons by Whistlers. *J. Geophys. Res. Space Phys.* 108, 1. doi:10.1029/2002ja009559

Walsh, B. M., Haaland, S. E., Daly, P. W., Kronberg, E. A., and Fritz, T. A. (2012). Energetic Electrons along the High-Latitude Magnetopause. *Ann. Geophys.* 30, 1003–1013. doi:10.5194/angeo-30-1003-2012

Wilder, F. D., Ergun, R. E., Hoilijoki, S., Webster, J., Argall, M. R., Ahmadi, N., et al. (2019). A Survey of Plasma Waves Appearing Near Dayside Magnetopause Electron Diffusion Region Events. *J. Geophys. Res. Space Phys.* 124, 7837–7849. doi:10.1029/2019ja027060

Wilder, F., Ergun, R., Goodrich, K., Goldman, M., Newman, D., Malaspina, D., et al. (2016). Observations of Whistler Mode Waves with Nonlinear Parallel Electric Fields Near the Dayside Magnetic Reconnection Separatrix by the Magnetospheric Multiscale Mission. *Geophys. Res. Lett.* 43, 5909–5917.

Yahnin, A. G., Titova, E. E., Demekhov, A. G., Yahnina, T. A., Popova, T. A., Lyubchich, A., et al. (2019). Simultaneous Observations of Emic Waves, Elf/vlf Waves, and Energetic Particle Precipitation during Multiple Compressions of the Magnetosphere. *Geomagn. Aeron.* 59, 668–680. doi:10.1134/s0016793219060148

Conflict of Interest: The authors declare that the research was conducted in the absence of any commercial or financial relationships that could be construed as a potential conflict of interest.

Publisher's Note: All claims expressed in this article are solely those of the authors and do not necessarily represent those of their affiliated organizations, or those of the publisher, the editors and the reviewers. Any product that may be evaluated in this article, or claim that may be made by its manufacturer, is not guaranteed or endorsed by the publisher.

frontiers | Frontiers in Astronomy and Space Sciences

ORIGINAL RESEARCH
published: 04 July 2022
doi: 10.3389/fspas.2022.924976

Regression Bias in Using Solar Wind Measurements

Nithin Sivadas[1,2]* *and David G. Sibeck*[1]

[1]Space Weather Laboratory, NASA Goddard Space Flight Center, Greenbelt, MD, United States, [2]Department of Physics, The Catholic University of America, Washington DC, MD, United States

Simultaneous solar wind measurements from the solar wind monitors, WIND and ACE, differ due to the spatial and temporal structure of the solar wind. Correlation studies that use these measurements as input may infer an incorrect correlation due to uncertainties arising from this spatial and temporal structure, especially at extreme and rare solar wind values. In particular, regression analysis will lead to a regression function whose slope is biased towards the mean value of the measurement parameter. This article demonstrates this regression bias by comparing simultaneous ACE and WIND solar wind measurements. A non-linear regression analysis between them leads to a perception of underestimation of extreme values of one measurement on average over the other. Using numerical experiments, we show that popular regression analysis techniques such as linear least-squares, orthogonal least-squares, and non-linear regression are not immune to this bias. Hence while using solar wind parameters as an independent variable in a correlation or regression analysis, random uncertainty in the independent variable can create unintended biases in the response of the dependent variable. More generally, the regression to the mean effect can impact both event-based, statistical studies of magnetospheric response to solar wind forcing.

Keywords: uncertainty, regression to the mean, solar wind magnetosphere coupling, space weather, regression dilution bias, noise

OPEN ACCESS

Edited by:
Joseph E. Borovsky,
Space Science Institute, United States

Reviewed by:
Brian Walsh,
Boston University, United States
Mike Lockwood,
University of Reading, United Kingdom

***Correspondence:**
Nithin Sivadas
sivadas@cua.edu

Specialty section:
This article was submitted to Space Physics, a section of the journal Frontiers in Astronomy and Space Sciences

Received: *21 April 2022*
Accepted: *01 June 2022*
Published: *04 July 2022*

Citation:
Sivadas N and Sibeck DG (2022) Regression Bias in Using Solar Wind Measurements. Front. Astron. Space Sci. 9:924976. doi: 10.3389/fspas.2022.924976

1 INTRODUCTION

The Earth's magnetosphere-ionosphere system is primarily driven by the solar wind. Hence, measurements of the solar wind and their interpretation are crucial in our attempt to understand the near-Earth space environment. At the time of writing this report, two spacecraft, ACE and WIND, have been measuring solar wind parameters for over 20 years from outside the magnetospheric bow shock. Many event-based studies, statistical studies, and simulations use these measurements as input. Many assume that the solar wind measured by these monitors situated at the L1 Lagrange point ultimately drives the magnetosphere system.

However, comparing measurements of the solar wind time-shifted to the bow shock shows random differences between the spacecraft (King and Papitashvili, 2005). These differences are expected because the satellites depending on their orbits, can be separated by significant distances (~ 10 to $400\ R_E$), and solar wind parameters vary over those length scales (e.g., Borovsky, 2018). There is also a random uncertainty in the solar wind propagation times to the bow shock, leading to a mismatch in measurements from different satellites (e.g., Case and Wild, 2012). Additionally, uncertainties stem from the fact that the solar wind parameters at the bow shock are not what drives the geospace system, it is modified by the shock and the magnetosheath before it interacts with the magnetosphere (Walsh et al., 2019).

In this manuscript, we refer to these uncertainties as measurement uncertainties. They arise from *a problem of definition* (Taylor, 1982), as the solar wind parameters that affect the magnetosphere are not clearly nor easily defined. We must stress that this type of error is distinct from instrument error. In fact, the solar wind measurements made in the vicinity of the spacecraft ACE or WIND could be exact. Even so, they are not an accurate estimate of the solar wind parameters impacting the magnetosphere at a given time, nor are they a perfect estimate of the solar wind measured by each other time-shifted to the bow shock. Such uncertainties pose challenges in interpreting the result of any study that explores how the solar wind affects the Earth's response.

For instance, at times, in event-based studies, the estimated solar wind driver from L1 measurements may not be driving the magnetosphere-ionosphere response being investigated. However, one may believe that multi-event and large-scale statistical studies can avoid this difficulty posed by random errors and provide us with the average response of the planet to solar wind driving. The reasoning goes that "underestimates will cancel overestimates" for random errors when estimating averages. Such studies belong to the class of regression analysis, where average associations and relationships between solar wind parameters and geomagnetic parameters are inferred from observations. In fact, many modern machine learning studies are non-parametric non-linear regression analysis carried out for multiple variables using large data sets (Louppe, 2014; Camporeale, 2019). The core idea of these techniques is to extract the conditional probability distribution of the response given values of the driver (or usually the moments of the conditional distribution). However, in this article, we note that underestimates will not cancel overestimates when solar wind parameters with random errors are used as *input* or *independent variables* in regression analysis. When we don't account for these random uncertainties, there will be a bias in the inferred relationship between driver and response, especially for rare or extreme values. We refer to this bias as regression bias in this manuscript. It is associated with the statistical phenomenon of regression dilution bias, regression attenuation, and the regression towards the mean (e.g., Fuller, 1987; Frost and Thompson, 2000; Barnett et al., 2005; Carroll et al., 2006). We must note here that there are also other sources of regression bias, in particular, data gaps as shown by Lockwood et al. (2019), which are usually ignored but can have a considerable effect.

Borovsky (2022) discusses regression bias in the context of functional forms of solar wind driver functions. There are several different formulations of solar wind driver functions in literature, each attempting to describe solar wind coupling with the Earth's magnetosphere accurately (Lockwood and McWilliams, 2021). However, Borovsky (2022) notes that when formulating the functional form of drivers, we must take into account the uncertainty in measurements and, in particular, the bias that they create in linear least-square fits on solar wind and magnetospheric data. If we do not, we risk misinterpreting the bias caused by uncertainties as a physical effect.

In this report, we show direct evidence for such regression biases by comparing measurements of the solar wind propagated to the bow shock made by two spacecraft via a simple non-linear regression analysis (i.e., calculating the conditional expectation of one spacecraft measurement given the other). If the solar wind monitors all measured the same value, the average measurement of one spacecraft given the measurement of the other (regression curve) would be a straight line with a 45° slope. However, since their measurements differ, albeit randomly, we observe a bias in the slope of the regression curve such that it bends towards the mean of the independent variable. The bias can be severe at extreme values.

Before presenting the evidence for this bias from solar wind measurements in **Section 3**, we first demonstrate the effect of uncertainty in creating regression bias in **Section 2**. Readers who are familiar with the regression to the mean effect can skip to **Section 3**. In **Section 4**, we discuss the implications of these results and conclude with a summary in **Section 5**.

2 REGRESSION TO THE MEAN

Like Borovsky (2022), we first construct a mathematical thought experiment where we suppose we have a measurement described by a random variable X, which is related to another measurement described by W. For simplicity, let us assume that when devoid of any measurement uncertainty, these two measurements are equal to each other $W = X$, i.e., W and X are entirely correlated.

Initially, we assume the random variable X is described by a normal probability distribution function (with mean 0 and standard deviation 3). As expected, **Figure 1A** shows that a scatter plot of W vs. X lies along a straight line. This line is referred to as the line of equality through the manuscript.

However, when the relationship between the two variables is unknown, it is common to rely on regression analysis to infer their relationship. Regression analysis is a broad category of techniques used to find an association between two or more variables. Linear regression is the most familiar type of regression analysis, especially the method of ordinary linear least-squares that minimizes the sum of squared differences between the data points and a unique line on the plot. Suppose the relationship between W and X is linear. In that case, the best predictor of W given X is a line $\beta X + c$ where the slope β and the intercept c are chosen to minimize the mean squared error between the vertical distance of the data and line from the x-axis. If we do not assume the relationship between W and X to be linear, then the function that minimizes the mean squared error between the vertical distance of itself and the data is $\hat{W} = E(W|X)$ (Carroll et al., 2006). When W and X are jointly normally distributed, $E(W|X)$ becomes linear in X and coincides with the ordinary linear-least squares estimate. Hence, this manuscript uses the more general non-linear regression technique of estimating the conditional expectation to uncover the functional relationship between W and X.

An approximate and common method of calculating the conditional expectation $E(W|X)$ is to bin the data along the "independent" variable X and average the values of the "dependent" variable W within each bin. In this article, we use this method to estimate the conditional expectation, which we

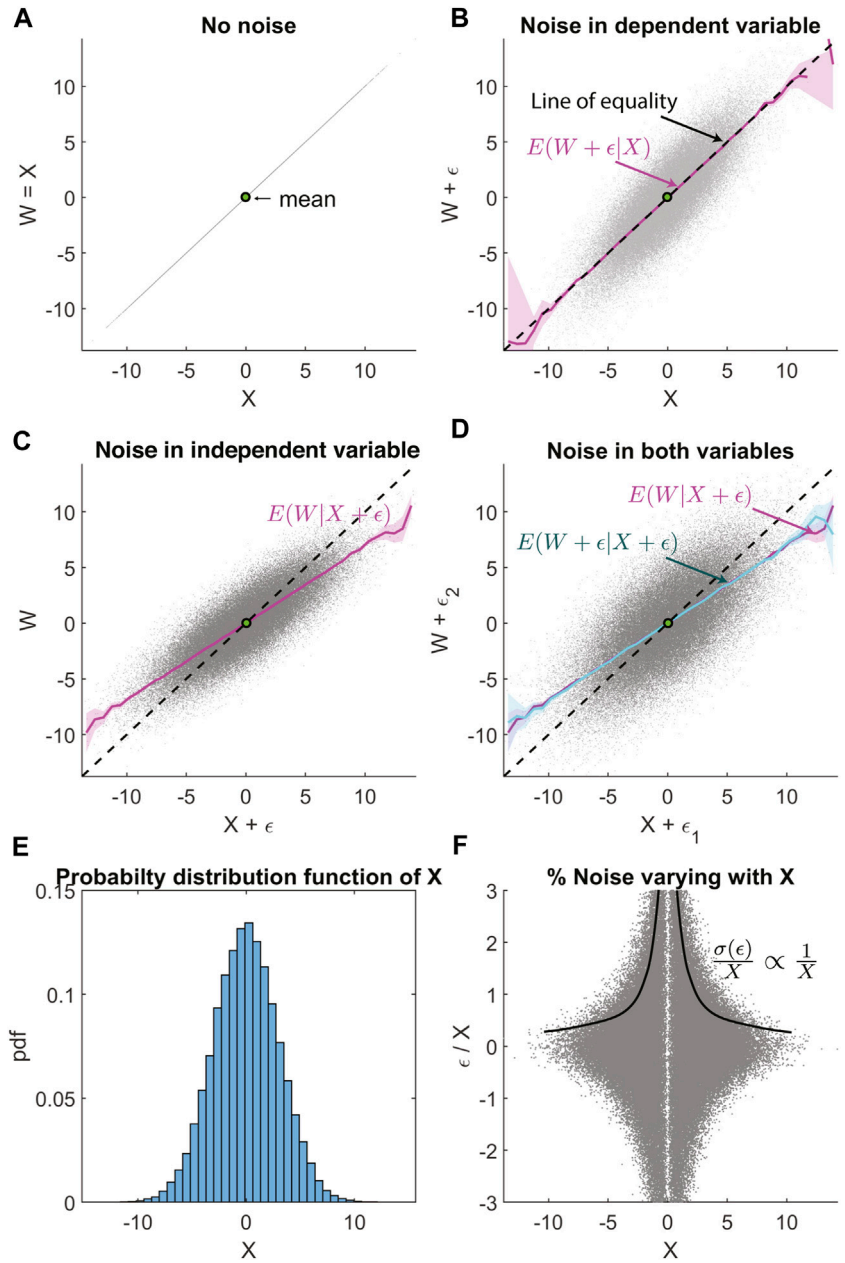

FIGURE 1 | Regression bias in non-linear regression analysis between normally distributed random variables, with uncorrelated Gaussian noise. **(A)** Scatter plot of W vs. X, where X is a normally distributed random variable and W = X. **(B)** Uncorrelated Gaussian noise ϵ is added to W. Magenta line shows the conditional expectation $E(W+\epsilon|X)$. The dashed black line is the line of equality. **(C)** Uncorrelated Gaussian noise added only to X, with the magenta line $E(W|X+\epsilon)$ showing regression bias. **(D)** Uncorrelated Gaussian noise is added to both W and X, with regression bias in $E(W+\epsilon|X+\epsilon)$ is visible in the cyan line. This overlaps with the magenta line that shows $E(W|X+\epsilon)$ for comparison. **(E)** Probability distribution function X showing the normal distribution with zero mean and standard deviation 3. **(F)** The fractional error ϵ/X that is varying inversely with X, as $\sigma(\epsilon) = constant$.

also refer to as the regression function or regression curve. This method of plotting the conditional expectation is used regularly in space physics. It is, in some instances, quite similar to the running average used by Borovsky (2021b), taken along the vertical axis for data sorted according to the magnitude of the parameter on the horizontal axis. Unlike the method of fitting functions, which gives equal weight to all data points, thereby restricting the fit to be dominated by the range of parameters with most points, calculating the conditional expectation through binning gives equal weight to every bin, and hence the non-linear function derived from it applies to the full range.

True values of W and X are always unavailable since we inevitably have some uncertainty ϵ in the measurements of these random variables. The source of this uncertainty can be

instrumental error, our assumptions about what X or W actually measures, and uncertainty in the temporal association of the two parameters.

In **Figure 1B**, we add uncertainty ϵ in the dependent variable W. ϵ is also normally distributed with mean 0 and standard deviation 2. We used the Marsaglia and Tsang (1984) method to generate the random numbers. The data points now have a vertical spread about the line of equality as expected. And the non-linear regression function $E(W|X)$ is also along the line of equality, giving us back the true relationship between W and X as the noise in W is averaged away.

In **Figure 1C**, we keep W free of uncertainty while including the same uncertainty ϵ in the independent variable X. Now, the regression function $E(W|X)$ has a slope biased to a lower value. The conditional expectation coincides with the linear least-squares fit, and it happens because W and $X + \epsilon$ are jointly normally distributed. This bias is referred to as regression dilution bias for linear regression. This article uses the term regression bias and it includes biases caused even in non-linear regression, unlike "regression dilution bias" which is commonly used to describe biases observed for linear least-squares regression. The regression bias is a result of the "regression to the mean" effect. We explain these two important phrases found in statistics literature as follows.

1. **Regression Dilution Bias**: If the relationship between W and X is linear $W = \beta X + c$, and we only have access to the error-prone measurement $X^* = X + \epsilon$, then $W = \beta(X^* - \epsilon) + c$. Hence, the minimum mean squared estimate of the slope for the best linear prediction is

$$\hat{\beta} = \frac{cov(X^*, W)}{var(X^*)}$$

It follows that,

$$\hat{\beta} = \frac{cov(X + \epsilon, \beta X + c)}{var(X + \epsilon)} = \beta \frac{\sigma_X^2}{\sigma_X^2 + \sigma_\epsilon^2} = \beta\lambda$$

. Where λ is known as the attenuation factor, and $0 < \lambda < 1$ because σ_X^2 and σ_ϵ^2 are non-negative. This quantifies how the slope of the linear least-squares regression function reduces when there is uncertainty in the independent variable. Note that here it is assumed that X is uncorrelated with ϵ and c. If we can calculate λ then the regression bias can be corrected by dividing the biased slope with it. However, for non-linear regression the same technique will not work. Several commonly used methods to correct regression bias are discussed in Carroll et al. (2006).

2. **Regression to the mean**: A more fundamental explanation of the regression bias is the fact that measured extreme values are more likely to be values that are closer to the mean but are mistaken to be extreme due to uncertainty or measurement error (Barnett et al., 2005). In **Figure 2**, we show the probability density function of X—the true value we are attempting to measure. When a specific value of X occurs, our attempt to measure it with some uncertainty ϵ is shown with the conditional probability density function $pdf(X^*|X = 2)$ and $pdf(X^*|X = 4)$. These conditional probability density functions (in blue and red) show the probability that the true values $X = 2$ or $X = 4$, when measured, will appear as any other value X^* on the real-line due to measurement error ϵ. When we measure $X^* = 3$, the true value could be either $X = 3$ or any other value on the real line. However, the points where the conditional probability density functions intersect the vertical line $X^* = 3$ show that it is more probable for $X^* = 3$ to be actually $X = 2$ than $X = 3$ or $X = 4$. In fact, it is less probable that the true value of the measurement $X^* = 3$ is $X = 4$ than $X = 3$ or $X = 2$. This is because it is much more likely for the mean value of a stochastic process to occur than an extreme value. The exact manner in which these biases happen depends on the nature of the measurement errors, the regression model, and the nature of the random variable or stochastic process.

The regression bias, quantified by the attenuation factor in the linear least-squares regression, is unaffected by uncertainty in the dependent variable W. This was seen in **Figure 1B** as $E(W + \epsilon|X)$ is unbiased. As a result, in **Figure 1D**, when we add uncertainty in both the dependent variable W and the independent variable X, the bias in the regression function $E(W + \epsilon|X + \epsilon)$ remains the same as that observed in **Figure 1C**. An interesting consequence of this is that the reverse regression function $E(X + \epsilon|W + \epsilon)$ will also have the same bias as $E(W + \epsilon|X + \epsilon)$. If we interpret these regression functions without accounting for the regression bias, they appear to result in contradictory inferences. $E(W + \epsilon|X + \epsilon)$ will imply that, on average, for extreme values, W^* is an underestimate of X^*, while $E(X + \epsilon|W + \epsilon)$ implies the opposite, that on average X^* is an underestimate of W^*. This contradiction is an indicator of the existence of regression bias and that the nature of uncertainty in both variables is similar.

Figure 1E shows that the probability distribution function of X is a Gaussian, and **Figure 1F** shows how the percentage of uncorrelated Gaussian noise ϵ with respect to X varies with X. In this case, the noise fraction varies inversely with X ($\sigma(\epsilon|X = x)/X \propto 1/X$), since $\sigma(\epsilon|X = x) = constant$. This depiction of the nature of measurement uncertainty will be useful as we demonstrate how the regression bias is affected by the uncertainty that is correlated with X below.

When X is not normally distributed but instead is log-normally distributed (**Figures 3A,B,E**), then the non-linear regression bias is no longer linear (**Figures 3C,D**). The log-normally distributed random number is generated by the transformation of a normally distributed random number generated by the Marsaglia and Tsang (1984) method. Here we have ensured that the error ϵ is still a zero-mean Gaussian with a standard deviation of 2, and it is uncorrelated with X or W (**Figure 3F**). The non-linearity is substantial, close to the mean value shown by the green dot, and the slope bends away from the line of equality towards the mean.

When X is log-normally distributed (**Figures 4A,B,E**), and the error ϵ is correlated with X (**Figure 4F**) then the non-linear regression bias is even more non-linear, especially at extreme values (**Figures 4C,D**). The layout of **Figure 4** is the same as **Figure 1**. The uncertainty ϵ is made to be proportional to $|X|^2$;

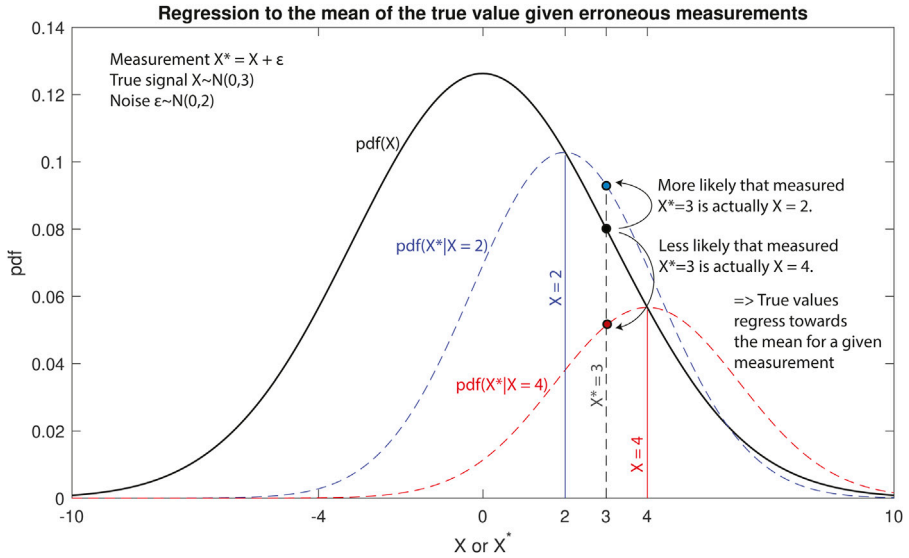

FIGURE 2 | Demonstrating regression to the mean of the true value of an erroneous measurement. The black line is the underlying probability distribution of a random variable X. An erroneous measurement of X is $X^* = X + \epsilon$, where ϵ is uncorrelated Gaussian noise. One such measurement, $X^* = 3$, is represented using the black dashed line. The likelihood that the true value X is also 3 is represented by the black filled circle on $pdf(X)$. The blue dashed line is the conditional probability density function $pdf(X^*|X = 2)$, and it intersects line $X^* = 3$ at the blue-filled circle, which represents the likelihood that the true value X is 2. Similarly, the red dashed line is the $pdfX^*|X = 4$, which intersects line $X^* = 3$ at the red-filled circle, which represents the likelihood that the true value X is 4 given the measurement $X^* = 3$. From the relative positions of the circles, we can conclude that it is more likely for the true value to be closer to the mean value of X than $X = 3$ or 4 or higher.

hence the noise fraction shown in **Figure 4F** increases linearly with X. This leads to a substantial non-linear bias in the non-linear regression function at values far away from the mean. The slope is biased away from the line of equality towards the mean value shown by the green dot. If we did not realize this as regression bias, then it is possible to misinterpret that $E(W|X^*)$ saturates with increasing X^* and misattribute it to a physical cause or systematic instrument bias.

By definition, the log-normal distribution X can be transformed to another random variable $Z = \log X$ which is normally distributed. Hence, if we know that the independent and dependent variables are jointly log-normally distributed, we can, in principle, take its logarithm and carry out a linear least-squares regression. For example one can estimate the coefficients of the linear regression function $\log W = \beta \log X + c$ and then transform them back to the W vs. X coordinate system. The procedure was carried out by King and Papitashvili (2005) for solar wind density and temperature as they are log-normally distributed to estimate systematic biases between ACE and WIND measurements. However, as shown in **Figures 5A–D**, this log-linear least-squares fit (blue-line) also tracks the non-linear regression function (magenta line) reasonably well for all combination of uncertainties in W and X. This implies that the log-linear least-squares fit is susceptible to regression bias created by the log-normality of the independent variable and uncertainty in its measurements. Hence using the log-linear least-squares approach may result in misattributing regression bias to systematic biases between the space monitors.

A relatively popular method considered to be capable of avoiding regression bias is the orthogonal regression function. The orange line in **Figures 5A–D** is the orthogonal linear regression fit for the corresponding data set. And it retrieves the true relationship between X and W in the case where the same error ϵ is present in both variables. This is because orthogonal linear regression minimizes the sum of the squared orthogonal distances between all (W, X) points and a unique line, and it has an unbiased slope only when the uncertainty in both variables is equal. A more general orthogonal regression method (total least squares regression) includes the information on the ratio of uncertainties in both W and X and can correct the regression bias much more effectively. In general, to correct the regression bias, we need to possess a quantitative knowledge of the uncertainty in X and W—not just the probability distribution of ϵ but also the conditional probability distribution $pdf(\epsilon|X)$ (e.g., Morley et al., 2018).

Uncertainties are commonly characterized by referring to the standard deviation or variance of $X^* - \langle X^* \rangle = \epsilon$. However, the severity of the regression bias cannot be judged solely on a parameter like the standard deviation or variance of the noise ϵ. It is affected by the nature of the correlation of ϵ with X and even other variables that may, in turn, affect X. **Figure 6** provides a demonstration of this argument. The top and bottom panels show regression bias in the non-linear regression of W vs. $X + \epsilon$, where W and X have the same log-normal distributions. The only difference between the top and bottom panels is the uncertainty in the independent variable X, which is a function of $\epsilon_1(X) \propto X^2$ for the top while $\epsilon_2(X) = constant$ for the bottom panel. Therefore the noise fraction $\epsilon_1/X \propto X$ and $\epsilon_2/X \propto 1/X$ as seen in **Figures 6B,E** respectively. The rightmost column (**Figures 6C,F**) shows plots of the marginal distribution of the noise ϵ_1 and ϵ_2 i.e., $pdf(\epsilon_1)$

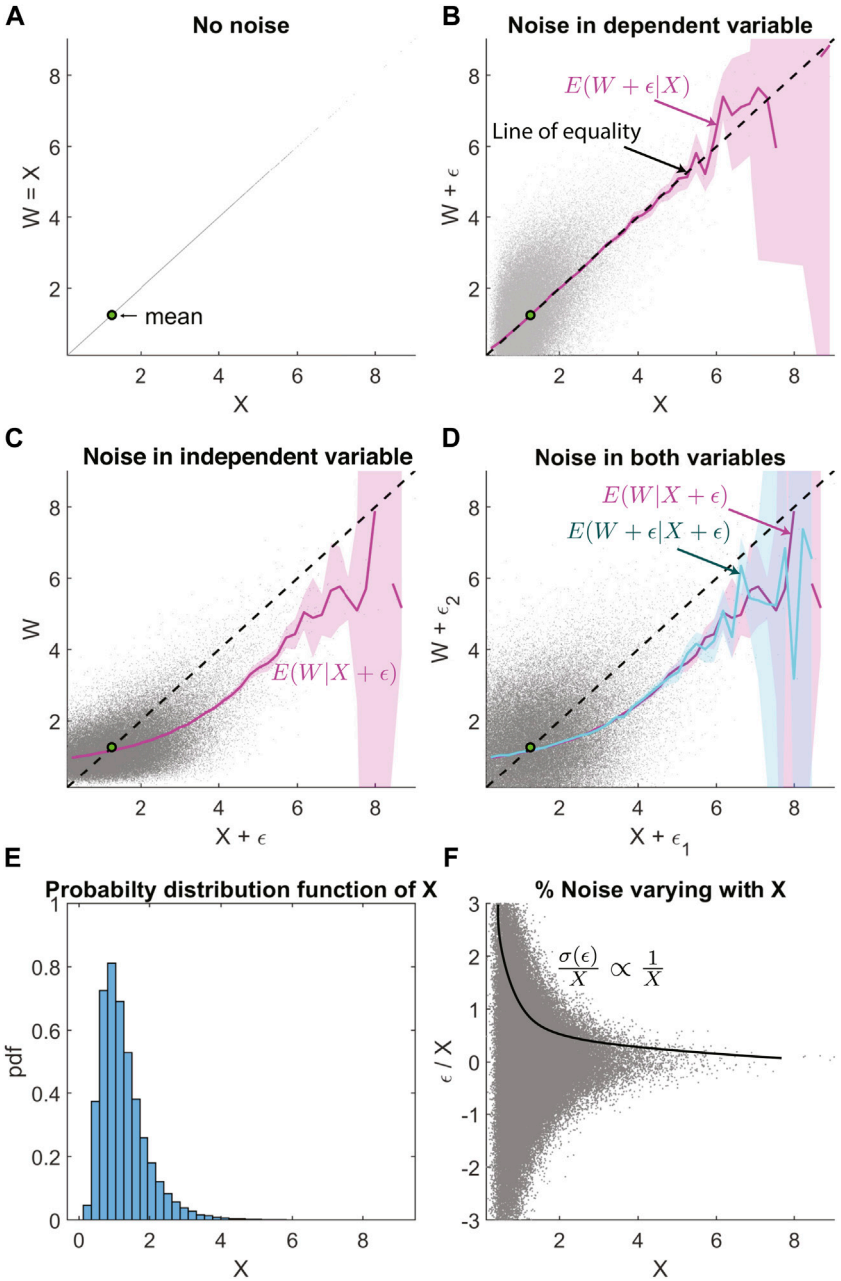

FIGURE 3 | Similar layout as **Figure 1**, but with log-normal distribution and uncorrelated noise. **(A)** Scatter plot of W vs. X, where X is a log-normally distributed random variable and W = X. **(B)** Uncorrelated Gaussian noise ϵ is added to *W*. Magenta line shows the conditional expectation $E(W+\epsilon|X)$. The dashed black line is the line of equality. **(C)** Uncorrelated Gaussian noise added only to *X*, with the magenta line $E(W|X+\epsilon)$ showing regression bias. **(D)** Uncorrelated Gaussian noise is added to both *W* and *X*, with regression bias in $E(W+\epsilon|X+\epsilon)$ is visible in the cyan line. This overlaps with the magenta line that shows $E(W|X+\epsilon)$ for comparison. **(E)** Probability distribution function *X* showing the log-normal distribution. **(F)** The fractional error $\sigma(\epsilon)/X$ that is varying inversely with *X*, as $\sigma(\epsilon)$ = *constant*.

and $pdf(\epsilon_2)$. Here the common metric used to quantify unbiased noise, the standard deviation, has the value of 0.5 for ϵ_1 and 1 for ϵ_2. Since $\sigma(\epsilon_1) < \sigma(\epsilon_2)$ one may assume that there is less noise in *X* for the top panel than the bottom, and hence less regression bias. This is true close to the mean; however, further away from the mean, the regression bias is more severe for panel 1 (**Figure 6A**) than panel 2 (**Figure 6D**) as ϵ_1 is correlated with *X* while ϵ_2 is not.

3 COMPARING SOLAR WIND MONITORS

The previous section demonstrates that uncertainty in the independent variable can lead to a bias in the regression function. Such biases are unavoidable whether we use non-linear regression, linear least-squares regression, or orthogonal linear regression. However, we can correct the bias with a quantitative

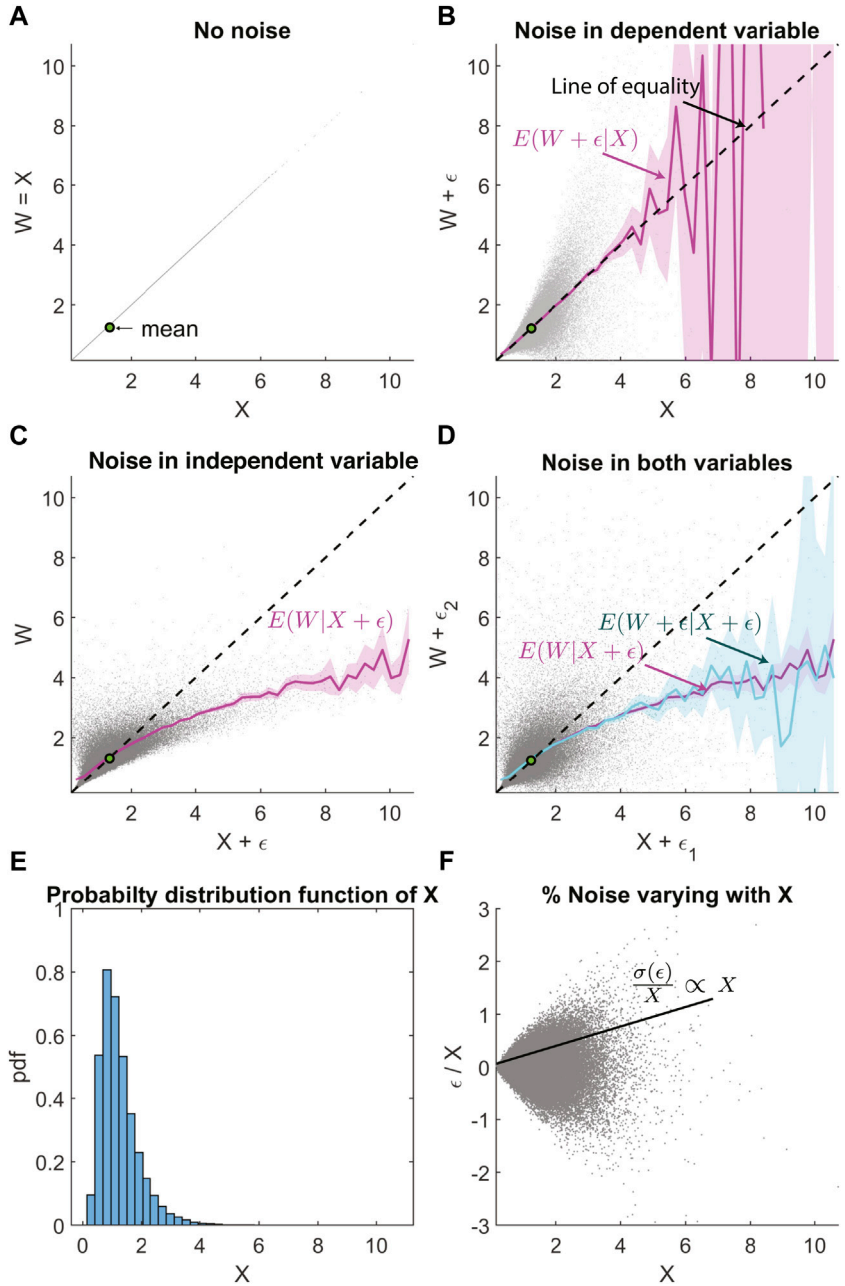

FIGURE 4 | Similar layout as **Figure 1**, but with log-normal distribution and correlated noise such that $\sigma(\epsilon) \propto X^2$. **(A)** Scatter plot of W vs. X, where X is a log-normally distributed random variable and W = X. **(B)** Correlated Gaussian noise ϵ is added to *W*. Magenta line shows the conditional expectation $E(W+\epsilon|X)$. The dashed black line is the line of equality. **(C)** Correlated Gaussian noise added only to *X*, with the magenta line $E(W|X+\epsilon)$ showing regression bias. **(D)** Correlated Gaussian noise is added to both *W* and *X*, with regression bias in $E(W+\epsilon|X+\epsilon)$ is visible in the cyan line. This overlaps with the magenta line that shows $E(W|X+\epsilon)$ for comparison. **(E)** Probability distribution function *X* showing the log-normal distribution. **(F)** The fractional error is proportional to *X*.

knowledge of the uncertainties, its direct or indirect correlation with the independent variable, and the probability distribution underlying the independent variable. In this section, we show regression biases in comparisons between solar wind monitors and suggest that at least part of these results are from random uncertainty in solar wind measurements rather than systematic instrument biases.

The solar wind monitors we use are the ACE and WIND satellites. They mostly measure solar wind plasma and magnetic fields upstream of the Earth's magnetospheric bow shock. We use 1-min spacecraft-specific data compiled by the OMNI database, which are time-shifted using a propagation model to the bow shock. Following is a look at non-linear

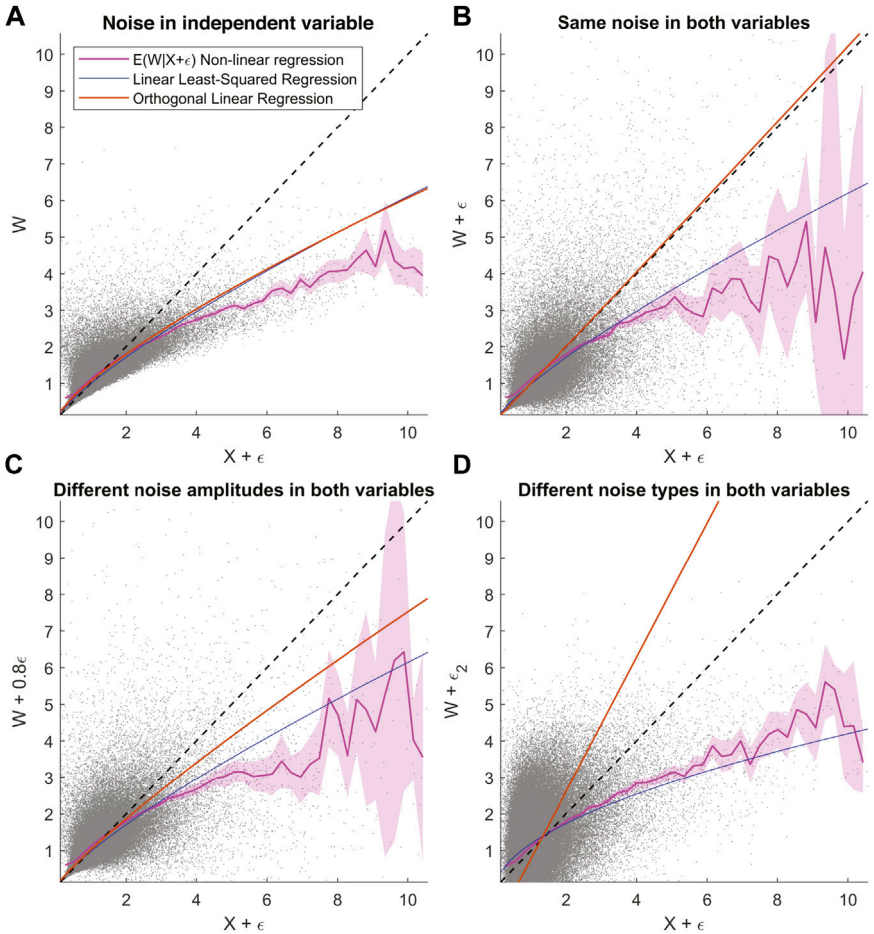

FIGURE 5 | Comparing the effect of regression to the mean on non-linear regression, linear least-squares regression, and orthogonal regression function. Similar to **Figure 4**, X is log-normally distributed with $W = X$, and ϵ is Gaussian uncertainty that is correlated with X such that $\sigma(\epsilon) \propto X^2$. **(A)** Shows different regression fits on data with uncertainty added only to X. **(B)** Shows the same with added uncertainty and the same characteristics on both X and W. **(C)** Shows the same but with slightly less uncertainty added to W compared to X. **(D)** Shows the same plot with uncorrelated Gaussian uncertainty ϵ_2 added to W, while correlated Gaussian uncertainty ϵ as in B is added to X.

regression between ACE and WIND measurements of multiple solar wind parameters. They should lie along the line of equality if both spacecraft measure the same solar wind plasma and magnetic field on average without uncertainty. However, that is not the case. Substantial regression biases towards the mean of the parameter can be observed for extreme values, especially when the monitors are far apart.

3.1 Solar Wind Velocity V_y and V_z

Figures 7A,B show scatter plots of time-shifted solar wind velocity components along the Z-GSE direction measured simultaneously by ACE and WIND spacecraft over 20 years. The black dashed line is the line of equality with a 45° slope, along which we would expect an unbiased ACE and WIND measurement to lie. However, a non-linear regression of ACE V_z GSE measurements given WIND V_z GSE and vice versa, shown by the magenta line, has a slope reduced towards the mean. The regression curve in **Figures 7A, B** seem to suggest a contradiction. The former suggests that ACE underestimates V_z GSE on average compared to WIND for extreme values. However, the latter suggests that WIND underestimates V_z GSE on average compared to ACE. We can explain the contradiction if we suppose that the biases of these regression curves come from similar uncertainty in both ACE and WIND measurements, as discussed concerning **Figure 1D** in the previous section. And since systematic measurement bias cannot lead to contradictory regression curves, the regression bias in **Figure 7** cannot possibly arise from systematic biases in the ACE and WIND measurements. However, we cannot rule out the existence of systematic measurement bias without a more careful analysis of quantifying random uncertainties. **Figures 7C,D** shows similar regression bias in ACE and WIND measurements of V_y GSE. At large values of ACE $V_y \sim$ 200 km/s, on average WIND measures a $\langle V_y^{WIND} | V_y^{ACE} \rangle \sim$ 150 km/s which is an underestimate of around ~ 25%.

3.2 Solar Wind IMF B_z

The primary cause of this non-trivial regression bias is the uncertainty stemming from the spatial and temporal separation of the measurements. As a result, both spacecraft

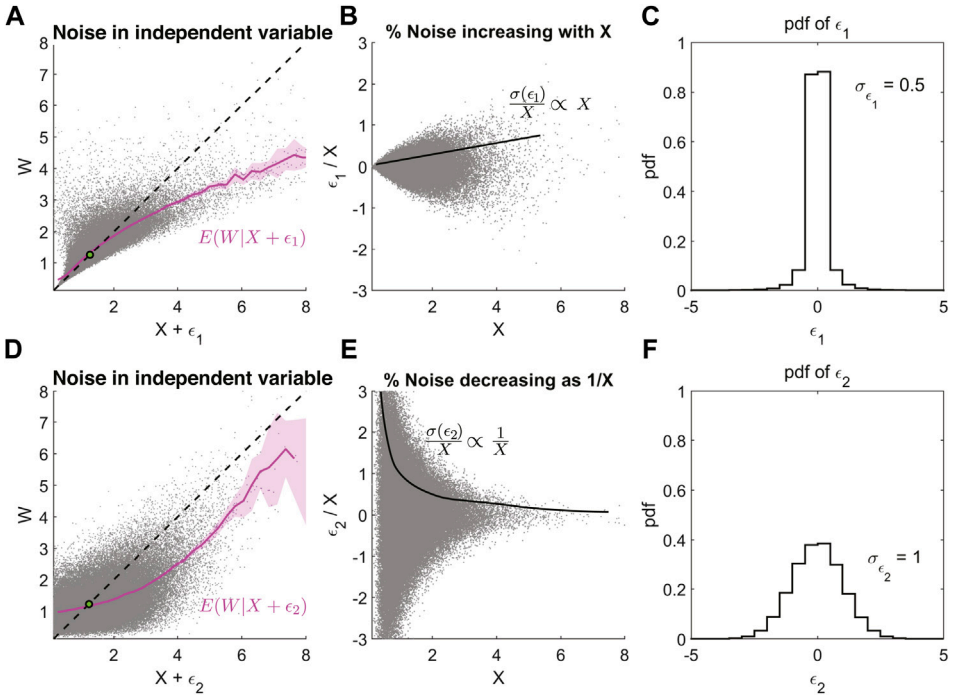

FIGURE 6 | The severity of the regression bias at extremes is not determined only by the standard deviation of the uncertainty ϵ. It is also necessary to know how the noise is correlated with the independent variable. **(A)** Magenta line is the $E(W|X+\epsilon_1)$ where ϵ_1 is correlated Gaussian noise. **(B)** Fractional error or noise ϵ_1/X increasing linearly with X, since $\sigma(\epsilon_1) \propto X^2$. **(C)** The marginal probability distribution of ϵ_1, with the standard deviation of $\epsilon_1 = 0.5$. **(D)** Same as **(A)** but with uncorrelated Gaussian noise ϵ_2 added to X. **(E)** Fractional error or noise ϵ_2/X decreasing as $1/X$, since $\sigma(\epsilon_2) = constant$. **(F)** The marginal probability distribution of ϵ_2, with the standard deviation of $\epsilon_2 = 1$.

do not see the same solar wind magnetic field or plasma most of the time. A useful measure of whether a downstream spacecraft measures the same plasma element previously seen by an upstream spacecraft is the impact parameter (IP). For WIND and ACE, the impact parameter (IP) is the "minimum distance experienced between WIND moving at 30 km/s in Y and plasma element moving at 390 km/s in X" (King and Papitashvili, 2005; Papitashvili, 2005).

Figures 8A,C plots ACE vs. WIND measurements of B_z GSM and vice-versa for all data points in the year 2002. In 2002, WIND was not yet parked onto its L1 orbit, and as a result, the IP between ACE and WIND is significant for most measurements. **Figures 8B,D** plot the regression between ACE and WIND B_z and vice versa for IP less than 60 R_E, implying that they both likely see similar solar wind plasma. An IP of less than $60R_E$ is considered to be the minimum separation for which WIND and ACE will see similar plasma and magnetic fields (King and Papitashvili, 2005). In this case, the regression bias is substantially reduced, as the regression curves almost align with the line of equality. This indicates that regression biases can exacerbate while using ACE and WIND data when they are far away from each other (IP > $60R_E$). Between 1998 and 2021, the percentage of available time-shifted 1-minute ACE and WIND measurements where IP is less than $60R_E$ is about ~30%. Hence for ~70% of the time, the two spacecraft don't measure the same plasma or field.

3.3 Solar Wind Proton Number Density *N*

Figure 9 shows the solar wind proton number density comparison between ACE and WIND measured during two time periods: column 1–1998 to 2001 pre solar maximum and column 2–2002 to 2005 post solar maximum. The dotted black line is the line of equality, while the magenta line is the non-linear regression function, and the blue line is the same but only includes measurements with ACE-WIND IP less than 60 R_E. The first panel shows the regression function of ACE given WIND measurements, while the second panel plots the reverse: WIND given ACE measurements. We see that there is a regression bias with a decreasing slope with increasing density for **Figures 9A–D**. The bias is more severe further away from the mean of the density measurements. From the density of the scatter plots, we can see that there are fewer proton number density measurements overall in the years 2002–2005 as compared to 1998 to 2001. Indicating that the underlying probability distribution of the proton number density can indeed change with the solar cycle, and regression bias can be time-dependent. Reducing the IP does not seem to change the regression function much, except for **Figure 9D**, where it has a substantial effect on making the regression function align with the line of equality. This could suggest that even the random uncertainty in measuring the solar wind parameters may change depending on the periods of the measurements, as the spacecraft's relative location also vary with time.

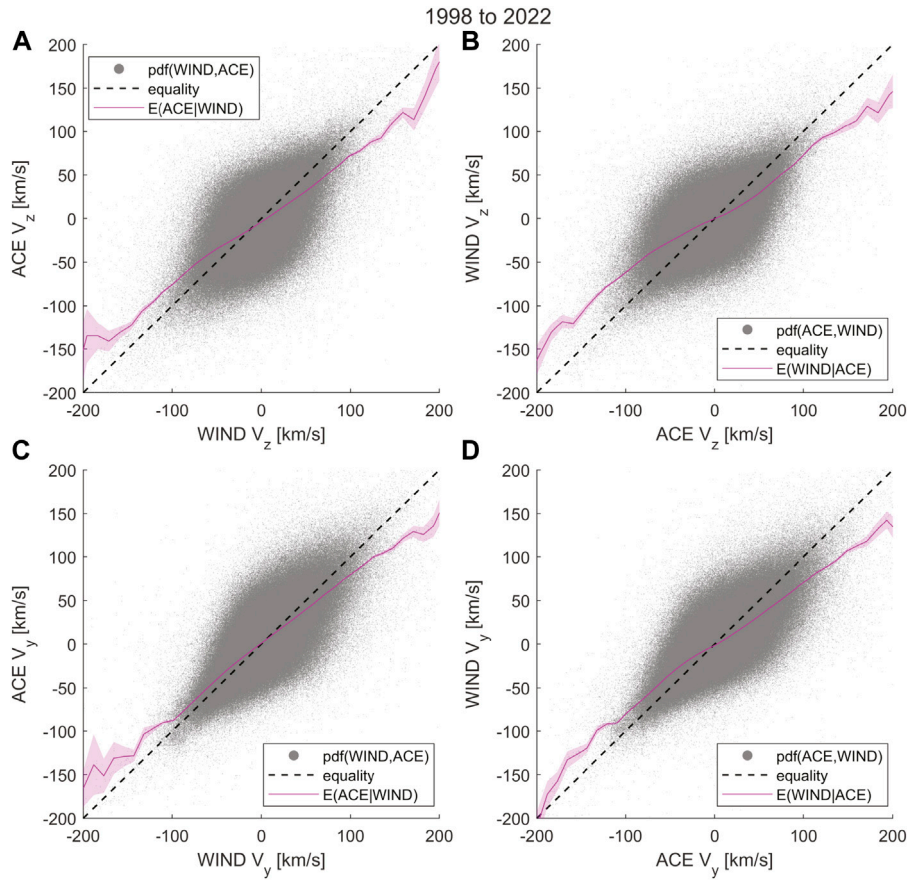

FIGURE 7 | Regression bias in solar wind velocity V_z and V_y in GSE coordinates. **(A)** Shows a scatter plot of 1-min resolution propagation delay-corrected ACE *Vz* vs. WIND V_z. The dashed black line is the line of equality, and the magenta line is the conditional expectation $E\,(V_z^{ACE}|V_z^{WIND})$ or the regression function. **(B)** Shows the same but reverse. The scatter plot is of WIND V_z vs. ACE V_z. However, the magenta line is the reverse regression function $E\,(V_z^{WIND}|V_z^{ACE})$. **(C)** Is the same as **(A)** but for the y-component of the solar wind velocity. **(D)** Is the same as **(B)** but for the y-component of velocity as well.

For the regression functions shown here, the non-linear decrease in the slope with increasing density is due to the log-normal distribution of density, similar to the numerical experiment described in **Figure 4**. According to King and Papitashvili (2005) ACE proton number densities are systematically larger than WIND number densities by up to 18% for higher solar wind speeds. They carried out a log-linear least squares regression, only for WIND vs. ACE and not the reverse. The systematic bias they estimate for higher solar wind speeds suggests ACE overestimates the densities. Curiously this bias is in the same direction we'd expect if the systematic bias was regression bias instead. However, our analysis in this article does not quantitatively delineate the two biases, as it requires careful correction of the regression bias.

3.4 Solar Wind IMF Clock Angle θ_{cl}

The IMF clock angle is an essential solar wind parameter determining the extent of solar wind energy coupling to the magnetosphere. The rate of the day-side reconnection, in part, is influenced by the relative orientation of the solar wind magnetic field direction (modified by the magnetosheath). For example, in simple magnetic reconnection models, two oppositely directed magnetic fields brought together by moving plasma drive reconnection. Hence, a southward IMF can generally trigger day-side reconnection at the sub-solar point, while a northward IMF does not. As a result, many proposed solar wind driver functions, which estimate the energy coupling between the solar wind and the magnetosphere, are some functions of the IMF clock angle (Newell et al., 2007; Borovsky, 2008; Lockwood and McWilliams, 2021).

The IMF clock angle is defined as the angle between the IMF vector projected on the GSM Y-Z plane and the geomagnetic north: $\theta_{cl} = atan2(B_Y, B_Z)$ where $-180^\circ < \theta_{cl} < 180^\circ$. In this manuscript, we have constructed θ_{cl} to range from 0° to 360° with 0° pointing towards B_Z north. In **Figure 10A**, we compare 1 min-resolution measurement of the ratio B_Y/B_Z of ACE vs. WIND and plot the conditional expectation of the ACE B_Y/B_Z given WIND B_Y/B_Z (magenta line). The blue line is the same non-linear regression function but with measurements where ACE and WIND have an impact parameter less than 60 R_E. **Figure 10C**

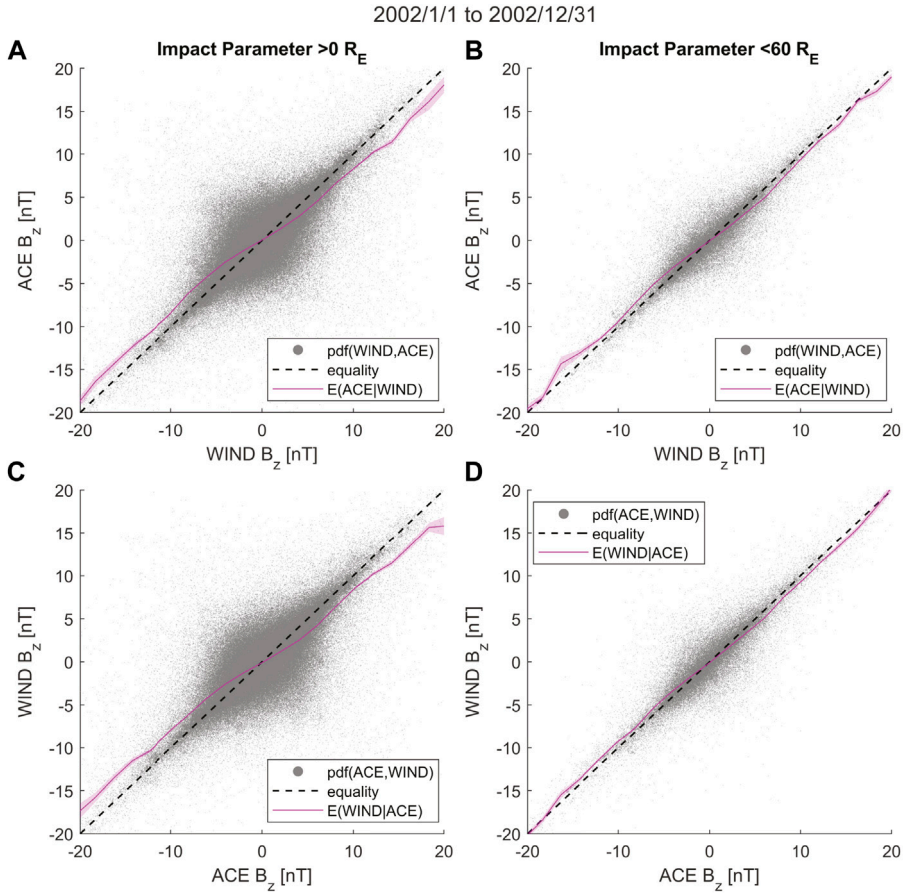

FIGURE 8 | Regression bias in solar wind magnetic field Z-GSM component. The bias reduces when filtering the data used by reducing the impact parameter (IP) between ACE and WIND. **(A)** Shows a scatter plot of simultaneous 1-min resolution propagation delay-corrected ACE B_z vs. WIND B_z. The measurements used were from the year 2002. The dashed black line is the line of equality, and the magenta line is the conditional expectation $E\,(B_z^{ACE}|B_z^{WIND})$ or the regression function showing the regression bias. **(B)** The same plot as **(A)** showing considerably less regression bias by restricting the measurements to time instances when IP $< 60R_E$ **(C)** Same as **(A)** but reversing the regression function to plot $E\,(B_z^{WIND}|B_z^{ACE})$. **(D)** Same plot as **(C)** showing less regression bias by restricting the measurements to time instances when IP between ACE and WIND is less than $60R_E$.

plots the reverse regression of WIND vs. ACE. Both plots show regression bias towards the mean for extreme values (for $|B_y/B_z| \sim > 2$). Large values of the B_Y/B_Z ratio are mostly a result of small B_Z values. The latter corresponds to ~ 90° or ~ 270° clock angle. The uncertainty increases with the magnitude of the ratio, and as a result, a clear non-linear bias (almost a "saturation") in the regression curve is visible. This example demonstrates that irrespective of the physical significance of the solar wind parameters, some functions of the parameters can have significantly more uncertainty, especially when ratios of measurements are involved.

Figures 10B,D show the ACE vs. WIND regression curve of the IMF clock angle and its reverse, respectively. Though the measurements span 0°–360°, the plot only shows the clock angles 0°–90° to highlight the bias in the regression curve, which has a slope that increases from the line of equality and then decreases. The regression bias reduces when the impact parameter is limited to less than 60 R_E in both plots. The conditional expectation is calculated using directional statistics, as an arithmetic mean is inappropriate for angles. Here the mean is calculated by first converting the IMF clock angle into a complex number through Euler's formula to consider how angles wrap around 360°. Then the arithmetic mean is calculated of the resulting complex numbers. This value is then converted back to an angle to obtain the conditional expectation.

To explore the nature of the bias in detail, **Figure 11** plots the regression bias in polar coordinates. **Figure 11A** shows the probability density function of the IMF clock angle as measured by ACE from 1998 to 2022 along the radial axis. The polar angle coordinates represent θ_{cl}^{ACE} for all panels of 11. The pdf is bi-modal and peaks around ~ 90° and ~ 270° and has two local minima around ~ 0^0 and ~ 180°. **Figure 11B** plots the regression bias - the deviation of the regression function $E\,(\theta_{cl}^{WIND}|\theta_{cl}^{ACE})$ from the line of equality shown in **Figure 10D** (magenta line). The blue line is the same calculation but limited to measurements where the WIND and ACE spacecraft are within an IP less than 60 R_E. When the distances

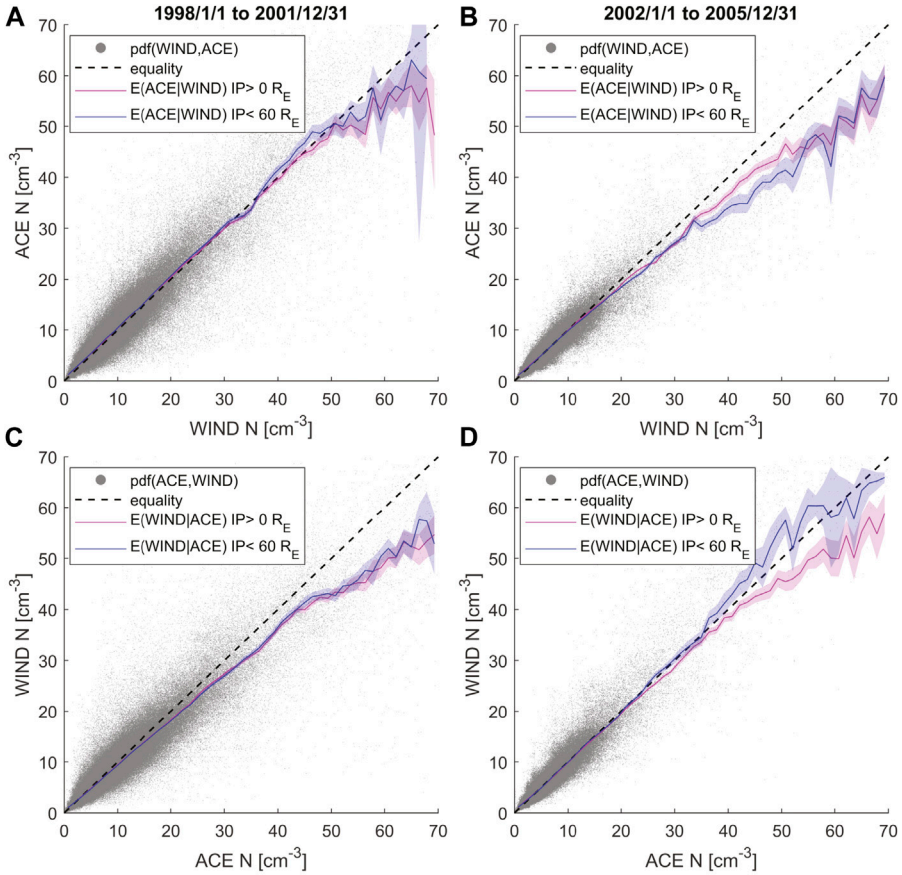

FIGURE 9 | Regression bias in solar wind proton density. It reduces when filtering the data to IP < 60R_E and is different for different solar cycle periods. **(A)** Shows the regression function $E(N^{ACE}|N^{WIND})$ in magenta, and the same restricted to only data with IP < 60R_E in blue. The data spans 1998 to 2001. **(B)** Shows the same plots but for the years 2002–2005. **(C)** Shows the reverse regression of **(A)**: $E(N^{WIND}|N^{ACE})$, and reveals similar bias towards the mean value. **(D)** Shows the reverse regression of **(B)**. However, when we filter the data to only IP < 60R_E, it results in a regression function closer to the line of equality.

between the monitors are lower, the regression bias is lower for all ACE IMF clock angles.

The regression bias is at a highest of ~ + 7° around θ_{cl}^{ACE} ~ 30°, which means the regression bias pushes the average value of $E(\theta_{cl}^{WIND}|\theta_{cl}^{ACE})$ towards the more likely ~ 90° clock angle. The bias, in fact, disappears close to the pdf maxima at ~ 90°. The green line marks the angles of zero bias. The bias then goes negative for clock angles greater than ~ 90° and less than ~ 180°. The negative bias drags the regression curve values $E(\theta_{cl}^{WIND}|\theta_{cl}^{ACE})$ back towards the pdf maxima at ~ 90°. The behavior of the bias is similar to the solar wind parameters we considered previously. Except here, it is the "regression towards the local maxima in the probability distribution" instead of "regression to the mean." Previous probability distributions discussed in this manuscript only had a single local maximum (indicating the most probable value), which was also near the mean.

Close to the local pdf minimum ~ 180° corresponding to southward IMF, the regression bias goes to zero again and then transitions to a more positive bias pushing the regression curve towards the second pdf maximum at ~ 270°. The same pattern repeats as the bias goes to zero and then negative, dragging the curve back to the second pdf maximum at ~ 270° and then to zero once more at the local pdf minimum near θ_{cl}^{ACE} ~ 0°. The reason for the positive bias is that more likely and higher IMF clock angles push the curve forward. In comparison, the negative bias happens as more likely, but lower IMF clock angles drag the curve backward. Zero bias occurs in the transitions when the regression curve is at a value close to the local pdf maximum. It also happens close to a local pdf minimum, where the more likely higher IMF values on one of its sides and more likely lower IMF values on the opposite side cancel each other's effects on the regression curve.

Figure 11D plots the bias in the IMF clock angle regression curve of ACE vs. WIND (magenta line) and its reverse (blue line). The same cycle of positive and negative bias as **Figure 11B** is seen for both the regression curves. However the positive bias is lesser and negative bias is greater for $E(\theta_{cl}^{ACE}|\theta_{cl}^{WIND})$ as compared to $E(\theta_{cl}^{WIND}|\theta_{cl}^{ACE})$. One important aspect to note regarding IMF clock angle comparisons between ACE and WIND is the

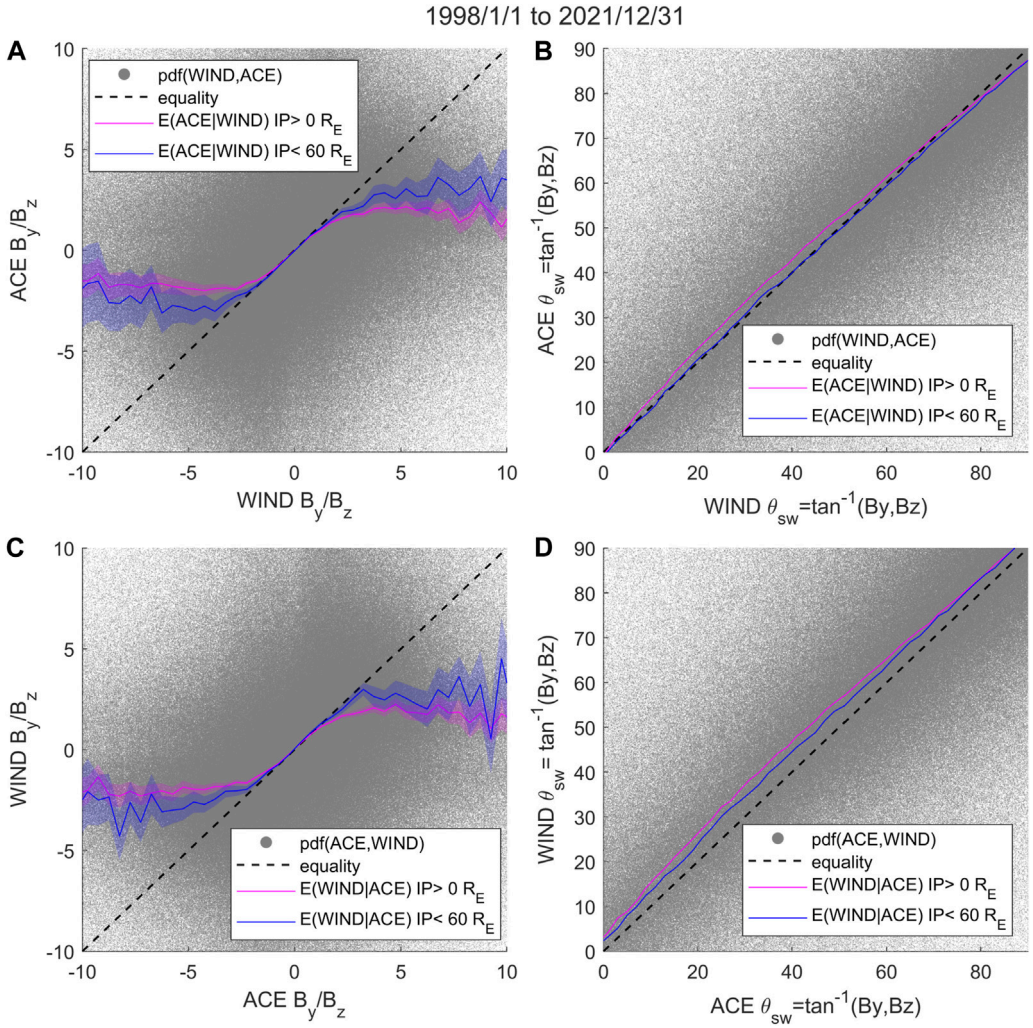

FIGURE 10 | Regression bias in Solar Wind IMF Clock Angle. **(A)** Regression function $E\left(ACE\frac{B_y}{B_z}|WIND\frac{B_y}{B_z}\right)$ is shown with the magenta line. Blue line plots the same with only measurements where ACE and WIND have an impact parameter less than $60R_E$. **(B)** Shows the regression function $E\left(\theta_{cl}^{ACE}|\theta_{cl}^{WIND}\right)$ using the magenta line. Blue line plots the same regression function for measurements with an IP less than $60R_E$. **(C)** Shows the reverse regression of **(A)**. **(D)** Shows the reverse regression of **(B)**.

variability in the clock angle observed by one satellite with respect to the other.

Figure 11C shows the standard deviation of WIND measurements of the IMF clock angle given ACE measurements of the same (shown in the magenta curve). The maximum uncertainty in the IMF clock angle measurements occurs when ACE measures northward and southward IMF B_z ($\theta_{cl}^{ACE} \sim 0°$ and $\theta_{cl}^{ACE} \sim 180°$) respectively. The magnitude of this uncertainty is high at about ~ 45°, and still high at its minimum, as ~ 35°. The blue line is the same curve but restricted to only measurements when WIND and ACE have an impact parameter less than 60°. This reduces the uncertainty, consistent with the reduction in the regression bias as seen in **Figures 11B,D**. However, the uncertainty in the IMF clock angle observed by WIND for a given measurement by ACE still does not go below ~ 30°. Functions of the clock angle will result in different joint probability distribution functions, and as a result will exhibit a different regression bias. An example for the function $\sin^2(\theta_{cl}/2)$ is shown in **Supplementary Figure S1**.

3.5 Solar Wind Driver Function E_{sw}

$E_{sw} = V_{sw}B_{South}^{GSM}$ is the interplanetary electric field and a simple solar wind driver or coupling function used frequently in literature (McPherron et al., 2013; Lockwood and McWilliams, 2021). Unlike McPherron et al. (2013), we do not use a half-wave rectified function where $B_s(B_z >= 0) = 0$ and $B_s(B_z < 0) = -B_z$, instead we define $B_{South}^{GMS} = -B_Z^{GMS}$. E_{sw} is, therefore, the product of solar wind velocity and negative IMF B_z in GSM coordinates. **Figure 12** compares ACE E_{sw} estimates with WIND E_{sw} and vice versa during 2002. Although the regression is carried out through the entire range of E_{sw}, the figure shows only $E_{sw} > 0$ as it is the dawn-dusk component of the solar wind electric field. In 2002, the WIND spacecraft was far from L1 and had not yet arrived at the L1 orbit. The non-linear regression curves in both show a bias

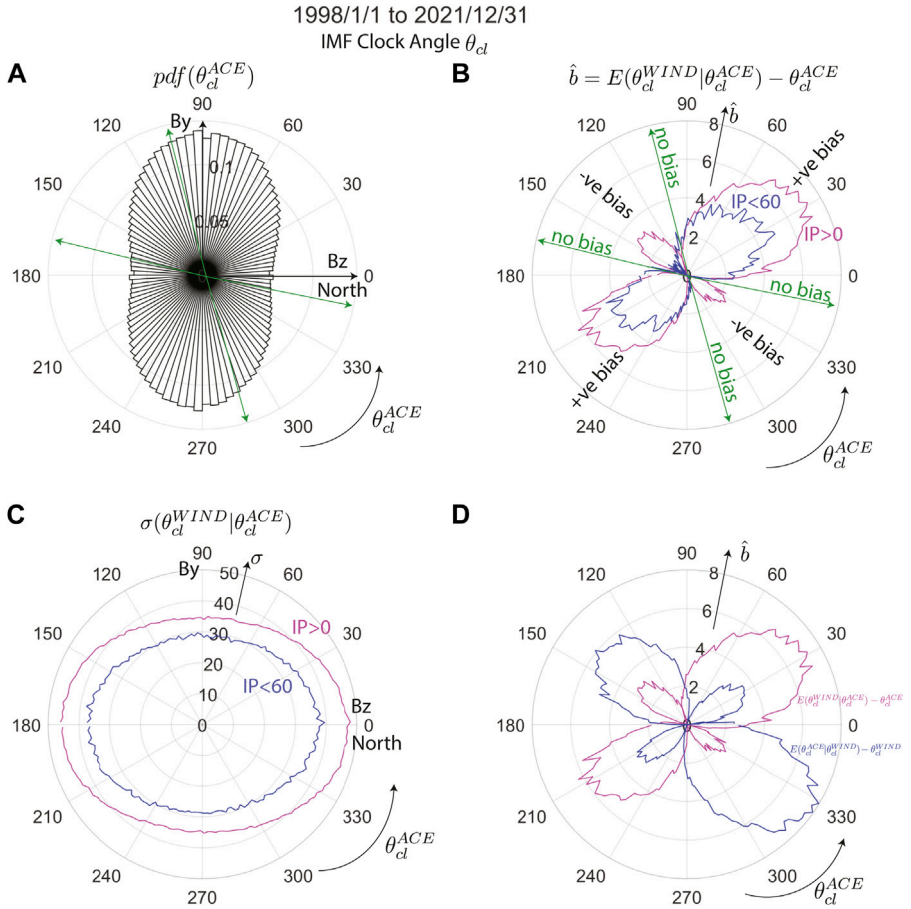

FIGURE 11 | Polar plots of regression bias in solar wind IMF clock angle. **(A)** Circular probability density function of IMF clock angle, defined as $\theta_{cl} = \tan^{-1}(B_y^{GSM}, B_z^{GSM})$. The angle coordinate is the ACE clock angle, and radial direction gives the pdf value. 0° is North and 180° is South. The green lines represent angles where the regression function $E(\theta_{cl}^{WIND}|\theta_{cl}^{ACE})$ has no bias. The lines run close to the local maxima and minima of the circular pdf. **(B)** The magenta line shows the regression bias $\hat{b} = E(\theta_{cl}^{WIND}|\theta_{cl}^{ACE}) - \theta_{cl}^{ACE}$ varying with the ACE clock angle. The blue line shows the same but only using measurements where the impact parameter is less than $60R_E$, implying ACE and WIND are likely measuring similar plasma. **(C)** The magenta line shows the standard deviation of WIND clock angle measurements given a measured ACE clock angle: $\sigma(\theta_{cl}^{WIND}|\theta_{cl}^{ACE})$. The blue line shows the same but only using measurements with impact parameter less than $60R_E$. **(D)** Compares the regression bias $\hat{b} = E(\theta_{cl}^{WIND}|\theta_{cl}^{ACE}) - \theta_{cl}^{ACE}$ with the bias in the reverse regression $\hat{b} = E(\theta_{cl}^{ACE}|\theta_{cl}^{WIND}) - \theta_{cl}^{WIND}$.

with a lower slope from 0 to 15 mV/m. At higher values of the driver, the number of data points is fewer, and hence there is substantial uncertainty in the regression curves. However, we observe a non-linear decrease in the average WIND E_{sw} measurements in **Figure 12B** from 15 mV/m and higher values of the ACE E_{sw} measurements (magenta line). The regression function has considerably less bias when restricted to measurements where the impact parameter is less than $60R_E$, suggesting that the bias is entirely a result of the spatial separation between the monitors.

For example, consider the data points highlighted using larger dots in **Figure 12B**. Here ACE measures E_{sw} values between 15 and 20 mV/m and WIND measures some of it to be much lower - between ~ 0 to ~ $5mV/m$. Most of these data points occur on a particular day, 23 May 2002, between 12:14 UT and 16:41 UT, as shocks from multiple Coronal Mass Ejections (CMEs) left the Sun on 22 May 2002. However, the impact parameter between WIND and ACE was ~265 R_E, with WIND being far away from ACE (~ $280R_E$) towards the dusk-side of the YZ plane, clearly measuring different solar wind plasma and field. And since the probability of occurrence of low E_{sw} is much higher than the rarer CME-induced high value of E_{sw}, WIND is more likely to see a smaller E_{sw} (due to their high probability of occurrence) than ACE which is measuring a high value (with a low probability of occurrence). The bias caused by this event is removed easily by filtering for measurements with impact parameters less than 60 R_E. Similar regression bias is observed with other solar wind driver functions as well. An example of the bias in the merging electric field $E_m = V_{sw}B_T \sin^2\theta_{cl}/2$ is shown in the **Supplementary Figure S2**. Here V_{sw} is the solar wind speed

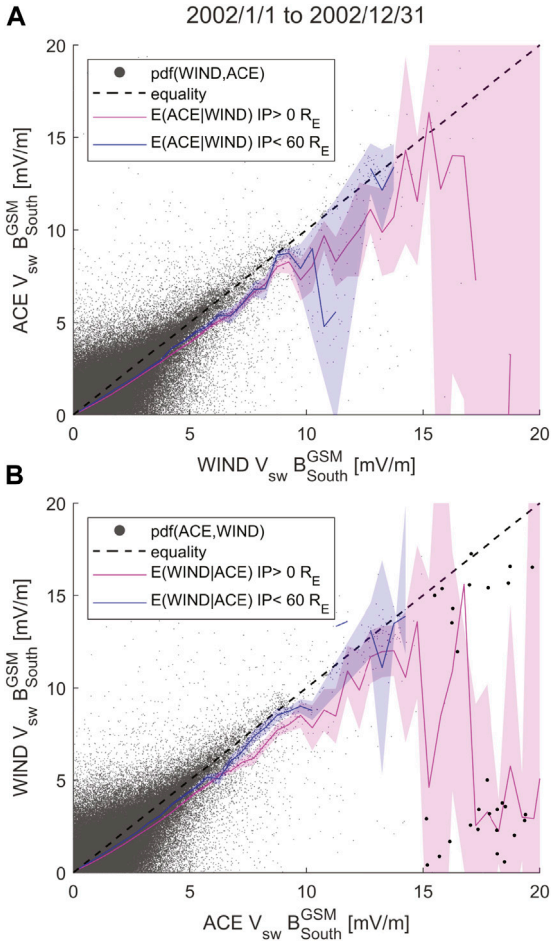

FIGURE 12 | Regression bias in solar wind driver function $E_{sw} = V_{sw}B_{south}$, where $B_{south} = -B_Z^{GSM}$. **(A)** The magenta line plots the regression function $E\,(E_{sw}^{ACE}|E_{sw}^{WIND})$ using measurements in 2002. The blue line is the same but limited to measurements where the IP $< 60R_E$ between ACE and WIND. **(B)** Plots the reverse regression function $E\,(E_{sw}^{WIND}|E_{sw}^{ACE})$ in magenta, and the same curve with IP $< 60R_E$ between the spacecrafts. Note that the regression bias at extreme values here is a result of the fact that the IP between WIND and ACE were as large $\sim 265R_E$. The data points with ACE $V_{sw}B_{south}$ between 15 and 20 mV/m are highlighted with larger dots.

in km/s, and $B_T = \sqrt{B_y^2 + B_z^2}$ is the transverse magnitude of the interplanetary magnetic field in nT and GSM coordinates.

4 DISCUSSION

Results in section 3 show that regression bias exists for important solar wind parameters like IMF B_z, clock angle θ_{cl} and solar wind proton number density N. Many other parameters also exhibit such regression biases, especially for extreme values of their measurements. Hence if we do not carefully account for random uncertainties in the solar wind parameters, any effort to identify instrument biases by comparing data sets may misinterpret regression bias as systematic instrument bias.

Uncertainties in complex parameters such as solar wind driver functions, which are a combination of solar wind parameters, may be correlated with the parameter's value. Consider the example of the merging electric field: $E_m = VB_T \sin^2\theta_{cl}/2$. An uncertainty $\Delta\theta$ in θ_{cl}, will result in an erroneous merging electric field $E_m^* = VB_T \sin^2(\theta_{cl} + \Delta\theta)/2$. For small θ_{cl} and $\Delta\theta$, $E_m^* \sim VB_T(\theta_{cl} + \Delta\theta)^2/4$ and $E_m = VB_T\theta_{cl}^2/4$. This implies

$$E_m^* - E_m \sim \frac{VB_T\theta_{cl}^2}{4}\frac{\Delta\theta}{\theta_{cl}}\left[2 + \frac{\Delta\theta}{\theta_{cl}}\right] = E_m \cdot f\left(\frac{\Delta\theta}{\theta_{cl}}\right)$$

Therefore, the uncertainty in the merging electric field: $E_m^* - E_m$ is correlated with E_m for a given fractional uncertainty of a small IMF clock angle. **Section 2** showed that uncertainties correlated with the parameters' magnitude could lead to non-linear regression biases in the regression functions. Such uncertainties that vary with the parameter's magnitude are called heteroscedastic/heteroskedastic errors. In regression analysis, especially linear regression, this manifests as variations in the residuals of the regression function or fit. Hence, it is helpful to enlist simple statistical tests to evaluate whether a heteroscedastic error exists in the measurements. A straightforward demonstration of testing for heteroscedasticity in linear regression by plotting residual errors with increasing fitted parameter value is shown in Section 6 of (Lockwood et al., 2006).

Many solar wind driver functions are empirically constructed formulas and are not necessarily derived from physical principles. Hence true solar wind driver functions may be biased or different in a random sense or both. It is easy to imagine that the estimate of the solar wind drivers using upstream solar wind monitors differs randomly from the platonic "true" driver function that affects the Earth's response. Suppose the driver function is in the form of the merging electric field. In that case, random uncertainty in one of the parameters can lead to correlated uncertainties in the merging electric field. However, if, instead, they are in the form of a sum of parameters like $V_{sw} + 56B_z$ (Borovsky, 2014), then the uncertainties will not be correlated with the magnitude of the driver. Hence, one may expect less regression bias. This could be the reason why the above unphysical solar wind driver formula has better correlations with geomagnetic activity than all other standard solar-wind functions (Newell et al., 2007; Borovsky, 2008; Borovsky, 2021a). Hence, the uncertainty in the solar wind driver functions and the regression bias it causes may be contributing to the math-versus-physics dilemma discussed by Borovsky (2021a). Once we account for the uncertainties, the physics-based formula may be more correlated than the other unphysical math-based ones.

Random uncertainties in the solar wind drivers are not just limited to spatial and temporal uncertainty in the solar wind measurements and instrumental errors (Lockwood, 2022). (Though these are likely the primary source of uncertainties in ACE and WIND measurements used in this manuscript.) Another important source of error is

the effect of bow shock and magnetosheath on the solar wind IMF at the day-side. For example, Coleman (2005) shows a ~ 30° uncertainty in the IMF clock angle between spacecraft in the magnetosheath and L1, with a substantial increase in this uncertainty along the flanks of the magnetosheath and with increasing dynamic pressure. As a result, the day-side reconnection rate and its extent may vary substantially for a given L1 monitor estimate of the solar wind driver.

Borovsky (2022) proposes that the functional form of the solar wind drivers ought to be constructed taking into account the uncertainties and the regression bias it creates. We believe this is crucial, as otherwise, regression bias in regression analysis of the driver functions and earth's response may be misinterpreted as caused by physical processes rather than uncertainty. Machine-learning-based models that use non-parametric non-linear regression analysis may also be susceptible to such biases. With the recent proliferation of many such models in space physics, we believe these biases are important to consider. A plausible example of regression bias, either partially or wholly misunderstood as caused by physical processes, could be the saturation of the polar cap potential and other geomagnetic indices (Borovsky, 2021b).

The "regression towards the mean effect" may not only be relevant to statistical regression analysis. It affects individual studies of extreme solar wind driving and the Earth's response to it. The reason for this is that the regression bias affects the entire conditional probability distribution of the measurements being compared. Hence, when we infer the Earth's response to an extreme solar wind driving, it is likely that the actual value of the solar wind driver is lower and closer to its mean value. Hence, we may be underestimating the effect of the solar wind driving of geomagnetic activity even for a single event or case study.

A more precise way to describe the "regression towards the mean effect" is perhaps apparent in **Figure 11**. Here the distribution is bi-modal and has two regions of high probability in the parameter space (~ 90° and ~ 270°). In such scenarios, it becomes clear that when there is a measurement uncertainty, the parameter's actual value is biased towards the most likely value in the parameter space. Therefore, there can be regions within the parameter space where the biases in opposite directions cancel out—leading to zero bias in some areas, making regression bias more complex than just a simple regression to the mean.

The natural question from our analysis is what we can do to correct or mitigate regression bias. Two primary directions here are 1) to quantify the uncertainty and calibrate the data to compensate for the bias, or 2) to improve the quality of the data by reducing uncertainty. For the case of ordinary linear least-squares regression, orthogonal regression that considers uncertainty in both dependent and independent variables can correct the bias. However, for non-linear regression, these methods may be insufficient. Therefore a careful analysis of correlated uncertainties and stochastic properties of the measured parameters are necessary to construct error models that estimate the regression bias. After this, one can apply the technique of regression calibration to the uncertain measurements and calculate the likely true values to correct for the bias in the inferred relationship. Many more techniques exist and are discussed extensively in Carroll et al. (2006).

The main challenge to constructing error models to carry out regression calibration is quantifying the uncertainties in the measurement parameters. In most cases, the uncertainties involved are not just instrumental errors but uncertainties that stem from the implicit assumptions made in interpreting measurements. For example, in the case of the solar wind driver functions—random uncertainties stem from our assumptions of: 1) solar wind propagation models, 2) solar wind structure, 3) solar wind interaction with bow-shock and magnetosheath plasma, 4) valid solar wind and magnetosphere state parameters. More assumptions may exist, but the first step towards quantifying random uncertainty in solar wind parameters (including driver functions) is to identify the assumptions and then estimate their contribution to the uncertainty through physics or mathematical models.

5 SUMMARY

We used simple numerical experiments to demonstrate the statistical phenomenon of regression towards the mean, which leads to biases in the correlation between measurement parameters. We showed evidence for such biases while comparing simultaneous 1-min resolved propagation delay-corrected ACE and WIND measurements of several solar wind parameters upstream of the magnetosphere bow-shock. The regression biases were significant for extreme values of the measurement parameters. For example when WIND measures V_y^{GSE} of 200 km/s, ACE measures only 150 km/s on average, a ~ 25% reduction. A similar reduction of ~ 20% or more is observed in average WIND measurements of IMF B_z^{GSM}, proton number density N and IMF Clock angle when ACE measures a $B_z^{GSM} = 20$ nT, $N = 70\,cm^{-3}$ and $\theta_{cl} = 30^{\circ}$respectively. This regression bias reduces when selecting measurements where ACE and WIND are nearby and in similar solar wind plasma.

These results suggest that regression biases may exist in statistical and event-based solar-wind/magnetosphere coupling studies, where the magnetosphere's response to solar wind driving is inferred from measurements. The bias may become significant for rare and extreme driving conditions and if the uncertainties in the driver functions correlate with the solar wind strengths. We can reliably correct the regression bias only by knowing the stochastic properties of the parameters used in the study and their uncertainties. Not accounting for the effect of these uncertainties may lead to misinterpreting the bias (which can sometimes be non-linear) as systematic measurement bias or physical processes. One such possible misinterpretation could be the saturation of geomagnetic

indices observed with increasing solar wind driving (Borovsky, 2021b).

DATA AVAILABILITY STATEMENT

The datasets analyzed for this study, and the corresponding MATLAB code used to visualize the plots in this article can be found in the repository https://doi.org/10.5281/zenodo.6604150. For non-MATLAB users, the code and its output is accessible as HTML files in the repository. All data we have used is publicly available. We thank GSFC/SPDF OMNIWeb service for the spacecraft specific 1 min resolution data sets of WIND and ACE measurements propagated to the bow shock. This can be accessed from https://spdf.gsfc.nasa.gov/pub/data/omni/high_res_omni/sc_specific/.

AUTHOR CONTRIBUTIONS

NS conceptualized this project, performed the analysis, and wrote the manuscript. DS supervised and conceptualized the work, and reviewed the manuscript.

FUNDING

NASA Cooperative Agreement 80NSSC21M0180G: Partnership for Heliophysics and Space Environment Research (NS) NASA Heliophysics Participating Investigator Program under Grant WBS516741.01.24.01.03 (DS).

ACKNOWLEDGMENTS

We thank Bob Robinson at the Catholic University of America for discussions and support. We also wish to acknowledge Joe Borovsky, Maria-Theresia Walach, Varsha Subramanyan, Dogacan Ozturk, Banafsheh Ferdousi, Gonzalo Cucho-Padin and Abigail R. Azari for valuable discussions.

SUPPLEMENTARY MATERIAL

The Supplementary Material for this article can be found online at: https://www.frontiersin.org/articles/10.3389/fspas.2022.924976/full#supplementary-material

REFERENCES

Barnett, A. G., van der Pols, J. C., and Dobson, A. J. (2005). Regression to the Mean: What it is and How to Deal with it. *Int. J. Epidemiol.* 34, 215–220. doi:10.1093/IJE/DYH299

Borovsky, J. E. (2014). Canonical Correlation Analysis of the Combined Solar Wind and Geomagnetic Index Data Sets. *J. Geophys. Res. Space Phys.* 119, 5364–5381. doi:10.1002/2013JA019607

Borovsky, J. E. (2021a). Is Our Understanding of Solar-Wind/Magnetosphere Coupling Satisfactory? *Front. Astron. Space Sci.* 8, 5. doi:10.3389/FSPAS.2021.634073/BIBTEX

Borovsky, J. E. (2022). Noise, Regression Dilution Bias, and Solar-Wind/Magnetosphere Coupling Studies. *Front. Astron. Space Sci.* 9, 45. doi:10.3389/fspas.2022.867282

Borovsky, J. E. (2021b). On the Saturation (or not) of Geomagnetic Indices. *Front. Astron. Space Sci.* 8, 175. doi:10.3389/FSPAS.2021.740811/BIBTEX

Borovsky, J. E. (2008). The Rudiments of a Theory of Solar Wind/magnetosphere Coupling Derived from First Principles. *J. Geophys. Res.* 113, 8228. doi:10.1029/2007JA012646

Borovsky, J. E. (2018). The Spatial Structure of the Oncoming Solar Wind at Earth and the Shortcomings of a Solar-Wind Monitor at L1. *J. Atmos. Sol.-Terr. Phys.* 177, 2–11. doi:10.1016/j.jastp.2017.03.014

Camporeale, E. (2019). The Challenge of Machine Learning in Space Weather: Nowcasting and Forecasting. *Space Weather* 17, 1166–1207. doi:10.1029/2018SW002061

Carroll, R. J., Ruppert, D., Stefanski, L. A., and Crainiceanu, C. M. (2006). *Measurement Error in Nonlinear Models: A Modern Perspective, Second Edition*. Baco Raton: Chapman & Hall/CRC, 1–455.

Case, N. A., and Wild, J. A. (2012). A Statistical Comparison of Solar Wind Propagation Delays Derived from Multispacecraft Techniques. *J. Geophys. Res.* 117, 2101. doi:10.1029/2011JA016946

Coleman, I. J. (2005). A Multi-Spacecraft Survey of Magnetic Field Line Draping in the Dayside Magnetosheath. *Ann. Geophys.* 23, 885–900. doi:10.5194/ANGEO-23-885-2005

Frost, C., and Thompson, S. G. (2000). Correcting for Regression Dilution Bias: Comparison of Methods for a Single Predictor Variable. *J. R. Stat. Soc. A* 163, 173–189. doi:10.1111/1467-985x.00164

Fuller, W. A. (1987). *Measurement Error Models*. New York: John Wiley & Sons. doi:10.1002/9780470316665

King, J. H., and Papitashvili, N. E. (2005). Solar Wind Spatial Scales in and Comparisons of Hourly Wind and Ace Plasma and Magnetic Field Data. *J. Geophys. Res.* 110, 2104. doi:10.1029/2004JA010649

Lockwood, M., Bentley, S. N., Owens, M. J., Barnard, L. A., Scott, C. J., Watt, C. E., et al. (2019). The Development of a Space Climatology: 1. Solar Wind Magnetosphere Coupling as a Function of Timescale and the Effect of Data Gaps. *Space Weather* 17, 133–156. doi:10.1029/2018sw001856

Lockwood, M., and McWilliams, K. A. (2021). On Optimum Solar Wind-Magnetosphere Coupling Functions for Transpolar Voltage and Planetary Geomagnetic Activity. *JGR Space Phys.* 126, e2021JA029946. doi:10.1029/2021JA029946

Lockwood, M., Rouillard, A. P., Finch, I., and Stamper, R. (2006). Comment on "The IDV Index: Its Derivation and Use in Inferring Long-Term Variations of the Interplanetary Magnetic Field Strength" by Leif Svalgaard and Edward W. Cliver. *J. Geophys. Res.* 111, A09109. doi:10.1029/2006JA011640

Lockwood, M. (2022). Solar Wind-Magnetosphere Coupling Functions: Pitfalls, Limitations, and Applications. *Space Weather* 20, e2021SW002989. doi:10.1029/2021SW002989

Louppe, G. (2014). Understanding Random Forests: From Theory to Practice. PhD Thesis.

Marsaglia, G., and Tsang, W. W. (1984). A Fast, Easily Implemented Method for Sampling from Decreasing or Symmetric Unimodal Density Functions. *SIAM J. Sci. Stat. Comput.* 5, 349–359. doi:10.1137/0905026

McPherron, R. L., Baker, D. N., Pulkkinen, T. I., Hsu, T.-S., Kissinger, J., and Chu, X. (2013). Changes in Solar Wind-Magnetosphere Coupling with Solar Cycle, Season, and Time Relative to Stream Interfaces. *J. Atmos. Sol.-Terr. Phys.* 99, 1–13. doi:10.1016/j.jastp.2012.09.003

Morley, S. K., Welling, D. T., and Woodroffe, J. R. (2018). Perturbed Input Ensemble Modeling with the Space Weather Modeling Framework. *Space Weather* 16, 1330–1347. doi:10.1029/2018sw002000

Newell, P. T., Sotirelis, T., Liou, K., Meng, C.-I., and Rich, F. J. (2007). A Nearly Universal Solar Wind-Magnetosphere Coupling Function Inferred from 10 Magnetospheric State Variables. *J. Geophys. Res.* 112, 1206. doi:10.1029/2006JA012015

[Dataset] Papitashvili, N. (2005). *Impact Parameters between a Pair of Objects*. Greenbelt: NASA.

Taylor, J. R. J. R. (1982). *An Introduction to Error Analysis: The Study of Uncertainties in Physical Measurements*. Sausalito, California: University Science Books.

Walsh, B. M., Bhakyapaibul, T., and Zou, Y. (2019). Quantifying the Uncertainty of Using Solar Wind Measurements for Geospace Inputs. *J. Geophys. Res. Space Phys.* 124, 3291–3302. doi:10.1029/2019JA026507

Conflict of Interest: The authors declare that the research was conducted in the absence of any commercial or financial relationships that could be construed as a potential conflict of interest.

Publisher's Note: All claims expressed in this article are solely those of the authors and do not necessarily represent those of their affiliated organizations, or those of the publisher, the editors and the reviewers. Any product that may be evaluated in this article, or claim that may be made by its manufacturer, is not guaranteed or endorsed by the publisher.

frontiers | Frontiers in Astronomy and Space Sciences

REVIEW
published: 04 July 2022
doi: 10.3389/fspas.2022.908571

Magnetosphere-Ionosphere Coupling: Implications of Non-Equilibrium Conditions

Mike Lockwood[1]* *and Stan W. H. Cowley*[2]

[1]Department of Meteorology, University of Reading, Reading, United Kingdom, [2]Department of Physics and Astronomy, Leicester University, Leicester, United Kingdom

The response times of the coupled magnetosphere-ionosphere-thermosphere system are, on average, greater than the autocorrelation timescales of solar wind forcing. This means that the system is rarely, if ever, in equilibrium. Departures from equilibrium are a key component of the Expanding-Contracting Polar Cap (ECPC) model of convection excitation in both the magnetosphere and ionosphere, driven by the Dungey reconnection cycle of opening and re-closing magnetospheric field lines. Averaging over sufficiently long timescales reduces data to the equivalent of steady-state conditions, which hides the physical mechanisms involved and allows us to map electric fields from interplanetary space to the ionosphere–but this is not valid, either physically or generally, because of magnetic induction effects. Only for transient phenomena on sufficiently short timescales do the mechanisms associated with non-equilibrium fully manifest themselves. Nevertheless, because of both ever-changing solar wind conditions and Earth's dipole tilt, eccentricity and rotation, the magnetosphere is always tending towards a perpetually-evolving equilibrium configuration and there are important implications of transient events for understanding the general behavior of the coupled magnetosphere-ionosphere-thermosphere system and its response to solar wind forcing. We here discuss one example: as a consequence of the importance of departures from equilibrium inherent in the ECPC model, the solar wind dynamic pressure P_{SW} influences the magnetosphere-ionosphere convection response to the generation of open field lines by reconnection in the dayside subsolar magnetopause. We here demonstrate this effect in a statistical survey of observations and show that it is as predicted by the ECPC model and that, through it, P_{SW} has an influence on flux transport in the magnetosphere-ionosphere system.

Keywords: solar wind, magnetosphere, magnetopause, coupling, reconnection, equilibrium, response times, expanding-contracting polar cap

OPEN ACCESS

Edited by:
Joseph E Borovsky,
Space Science Institute, United States

Reviewed by:
Adnane Osmane,
University of Helsinki, Finland
Arthur Richmond,
National Center for Atmospheric Research (UCAR), United States
Adrian Grocott,
Lancaster University, United Kingdom

***Correspondence:**
Mike Lockwood
m.lockwood@reading.ac.uk

Specialty section:
This article was submitted to Space Physics, a section of the journal Frontiers in Astronomy and Space Sciences

Received: *30 March 2022*
Accepted: *19 May 2022*
Published: *04 July 2022*

Citation:
Lockwood M and Cowley SWH (2022) Magnetosphere-Ionosphere Coupling: Implications of Non-Equilibrium Conditions. Front. Astron. Space Sci. 9:908571. doi: 10.3389/fspas.2022.908571

INTRODUCTION

The Development of Solar Wind-Magnetosphere Coupling Science

The concept of what we now call Earth's magnetosphere was first introduced by Chapman and Ferraro (1931), who envisaged geomagnetic storms as being caused by plasma clouds ejected by the Sun impacting upon Earth's magnetic field and confining it in space. This accords with modern understanding of the effect of Coronal Mass Ejections (CMEs). However, because Chapman and

Ferraro considered the solar wind to be absent during the intervals between the events, this meant that they envisaged the confined geomagnetic field as a transient, storm-time condition and not the persistent feature that we now know the magnetosphere to be. Paradoxically, they applied equilibrium concepts to these transient compressions, with the magnetic pressure of the geomagnetic field envisaged as balancing the dynamic pressure of the plasma cloud in a series of evolving equilibria. Later, multi-spacecraft observations showed the locations and motions of the magnetospheric boundary (the magnetopause), caused by changing solar wind dynamic pressure, did agree to first order with Chapman and Ferraro's concept of evolving equilibria (e.g., Farrugia et al., 1989).

Chapman and Ferraro knew nothing of the existence of the interplanetary magnetic field (IMF), the discovery of which was not made until the space age, when it was detected by the Pioneer-5 spacecraft (Coleman et al., 1960). There had been indications of its existence in the early 1950s from Forbush decreases in Galactic Cosmic Rays and from the propagation time of Solar Cosmic Rays (now called Solar Energetic Particles) seen following solar flares by neutron monitors (*see* Parker, 2001). However, even before this, several scientists had been certain enough of the existence of an IMF to be thinking about its terrestrial implications, including Fred Hoyle, his PhD student Jim Dungey (*see* Cowley, 2016), and Hannes Alfvén (1950a). How near-Earth IMF could be generated by the Sun and solar wind was understood from Alfvén's formulation of magnetohydrodynamics (MHD) (Alfvén, 1950b) which in the "ideal MHD" limit shows that the solar wind drags the "frozen-in" solar coronal magnetic field with it to give, on average, the Parker spiral configuration of the IMF (Parker, 1958). It became recognized that the solar wind, and hence the frozen-in IMF, was an ever-present feature because of the continuous nature of its action on comet tails (Hoffmeister, 1943; Ahnert, 1943; Biermann, 1951). The role of the north-south IMF component in the coupling of energy and momentum into the magnetosphere from the solar wind, was postulated by Dungey (1950, 1961). He introduced the concept of magnetic reconnection which, through a breakdown in ideal MHD at thin current sheets, generates open field lines that thread the magnetopause, and then closes them again in the cross-tail current sheet. A snapshot of the Dungey cycle during southward IMF, showing open and closed field lines and the reconnection sites in the noon-midnight meridian plane is shown schematically in Part **A** of **Figure 1**. Dungey still applied inherently steady, equilibrium concepts to this "Dungey cycle" as he saw antisunward transport of frozen-in flux in the polar ionosphere on open field lines as being due to interplanetary electric field (the electric field in the Earth's frame due to the motion of the solar wind with its frozen-in magnetic field) mapped down to the ionosphere. This concept of mapped interplanetary electric field (e.g., Volland, 1973; Stern, 1975a) has been widely used in the interpretation of results from both observations and numerical MHD models and even in the derivation and use of some indices, such as the polar cap index (Stauning, 2022). This would be valid for fully steady-state conditions when the rate of change in the magnetic field is everywhere zero: by Faraday's law, steady state means that the electric field is curl-free and would, in this special case only, map from interplanetary space, through the magnetosheath and magnetosphere, to the ionosphere.

Dungey's seminal schematic (the origin of **Figure 1A**) showing how reconnection between the IMF and the geomagnetic field would drive the magnetospheric and ionospheric circulation of plasma and frozen-in magnetic field (flow that we call convection), was included in his 1950 PhD thesis (Dungey, 1950), but was not published in the open literature until 1961. In that year, Axford and Hines (1961) proposed a second, unspecified, mechanism could also cause the solar wind flow to excite magnetospheric and ionospheric convection. The key difference was that Axford and Hines proposed the forcing acted on closed field lines and this is now referred to as a "viscous-like interaction" and, being unspecified in nature, this name effectively means "anything but reconnection." Kelvin-Helmholtz wave-breaking on the magnetopause is one proposed mechanism. The key and observable difference between reconnection-driven and non-reconnection-driven convection is that reconnection transfers magnetic flux and frozen-in plasma antisunward over the poles and out of the magnetospheric equatorial plane and hence, in that plane only the sunward return motion of re-closed field lines and frozen-in plasma is seen. On the other hand, for any viscous-like interaction both the antisunward and sunward transport must be seen in the equatorial plane. This difference was used to show that the contribution of the viscous-like interaction was relatively minor (Cowley, 1982). The same conclusion was reached from studies of the dependence of the observed convection voltage in the polar cap (the transpolar voltage Φ_{PC}, a.k.a. the cross-cap potential difference) on the north-south IMF component, B_Z, in the Geocentric Solar Magnetospheric frame of reference (GSM, in which the X axis points towards the Sun and the Z axis is the projection of Earth's magnetic axis onto the YZ plane): larger values of Φ_{PC} were only found when the IMF pointed southward ($B_Z < 0$), the orientation that gives greatest rate of opening of field lines. During intervals of $B_Z > 0$ (northward IMF) observed antisunward transport voltages were considerably smaller (*see* review by Cowley, 1984). However, the assumption that all antisunward convection in the polar cap during northward IMF must be caused by a viscous-like mechanism is far from correct. Studies using data from satellites (Wygant et al., 1983) and radar networks (Lockwood and McWilliams, 2021a) have shown a large range of transpolar voltages can exist during northward IMF intervals but the largest values are at times of enhanced auroral electrojet activity and these largest values decay with time since the IMF turned northward, revealing a residual effect of the prior interval of southward IMF. This is explained by the Expanding-Contracting Polar Cap (ECPC) model of convection excitation discussed below (Cowley and Lockwood, 1992) which shows how and why effects of continuing nightside reconnection, closing residual open field lines generated during a prior period of southward IMF, are often wrongly attributed to a viscous-like mechanism, which consequently explains only about 10 kV of antisunward flux transport, and very probably less, compared to the larger reconnection-driven antisunward transfer rates of up to about 150 kV.

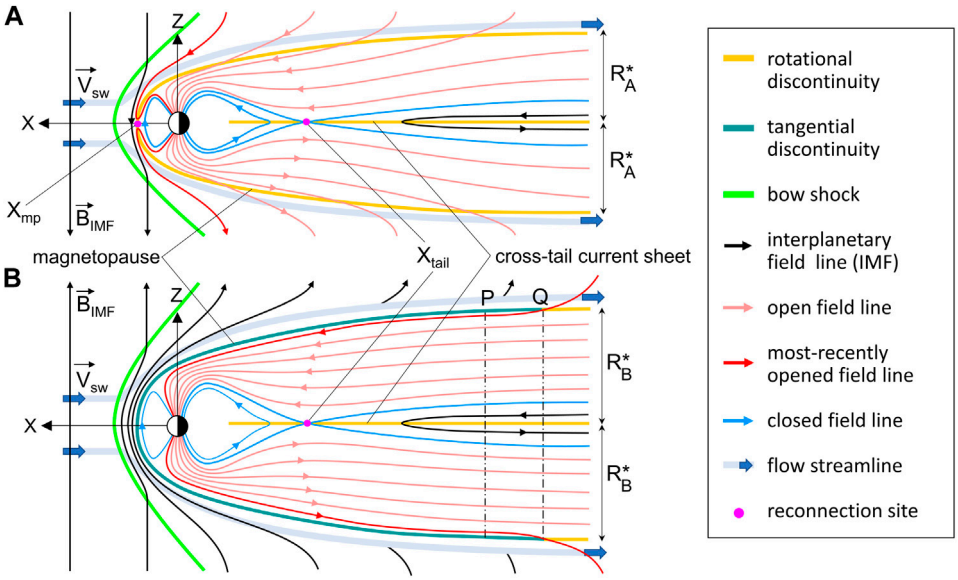

FIGURE 1 | Noon-midnight meridian cuts of the magnetosphere, viewed from the from the dusk flank: the *X* (sunward) and *Z* (northward) axes in the Geocentric Solar Magnetospheric frame (GSM, in which the *X* axis points towards the Sun and the *Z* axis is the projection of Earth's magnetic axis onto the *YZ* plane) are shown. Parts **(A)** and **(B)** are for times t_A and t_B when the IMF was southward and northward respectively where $t_B > t_A$, and the IMF has been northward for all the interval $t_A < t \leq t_B$. In **A** the southward-directed interplanetary magnetic field (IMF) gives magnetic shear across the dayside magnetosphere, and this drives magnetic reconnection at X_{mp} between closed geomagnetic field lines (in blue) and (shocked) interplanetary field lines (in black), and thereby generating open field lines that thread the magnetopause current sheet (in red/pink: most open field lines are shown in pink but the most recently opened one is shown in darker red). Open field lines threading the magnetopause current sheet make it a rotational discontinuity, shown in orange. Open-field lines are re-closed by reconnection at X_{tail} in the cross-tail current sheet (also a rotational discontinuity and so also shown in orange). In part **(B)**, the northward pointing IMF means that reconnection in the subsolar magnetopause has ceased and the because the northward IMF has persisted for a long interval ($t_B - t_A$), the last field line to be opened (in red) has been swept a large distance in the $-X$ direction by the solar wind flow (a typical solar wind speed of 400 kms^{-1} corresponds to $150R_E$ per hour (where $1R_E$ is a mean Earth radius = 6370 km). In comparison, the dayside magnetopause is typically at *X* of between $10R_E$ and $15R_E$ and so, given we here consider intervals ($t_B - t_A$) of several hours, the *X* axis in the tail is necessarily greatly compressed in these schematics. In part **(B)**, most of the magnetopause is now a tangential discontinuity (shown in dark green) and is only threaded by open flux at the most negative *X* values shown. Note that three of the northward-pointing IMF/magnetosheath field lines are shown as remaining in the non-midnight meridian, being draped over the nose of the magnetosphere, but two others are moving round the dawn or dusk flank, out of the plane of the diagram. The appending of open field lines to the tail by the solar wind flow between the times t_B and t_A has flared the tail, increasing its asymptotic radius from R^*_A to R^*_B. The point where the last field lines to be opened thread the magnetopause have, by the time t_B, reached the tail cross-section shown by the vertical black dot-dash line labelled Q (at $X = X_Q$) and all open field lines are parallel to the solar wind flow by the tail cross section labelled P (at $X = X_P$). Earthward of the $X = X_P$, the solar wind flow is no longer generating field-perpendicular convection.

In most early papers, the concept of a steady equilibrium, or at least an evolving series of equilibria, was applied. Only with a growing understanding of the substorm cycle did it become clear that the magnetospheric response to the solar wind forcing was not, in general, a steady-state one (McPherron, 1979). In these studies, non-steady conditions are applied to the Dungey cycle, with the rate at which open flux is generated during the substorm growth phases (i.e., the voltage Φ_D along the reconnection X-line in the dayside magnetopause, labelled X_{mp} where it crosses the noon-midnight plane in **Figure 1A**) exceeding the rate at which the open flux is lost (the voltage Φ_N along the nightside reconnection X-line in the cross-tail current sheet at which open field lines are re-closed, labelled X_{tail} in **Figure 1A**). The converse applies during the expansion and recovery phases when $\Phi_N > \Phi_D$. In general, imbalance between Φ_D and Φ_N makes the open flux F_o change at a rate

$$dF_o/dt = (\Phi_D - \Phi_N) \quad (1)$$

This equation can be seen as a statement of continuity of open flux or, alternatively, of Faraday's law (in integral form) applied to any closed loop that surrounds the open flux region.

Because the ionosphere is incompressible, in the sense that the magnetic field there is approximately constant, this means that the region of open flux there (that we here term the "polar cap") expands and contracts in area (Holzer et al., 1986). Open flux is rapidly swept into the tail by the solar wind flow during the substorm growth phase, making the magnetic flux in the tail lobes increase until the onset of the expansion phase, after which it decreases again (Caan et al., 1973, 1978; McPherron et al., 1993): as a result, steady-state, curl-free electric field does not apply. Siscoe and Huang (1985) introduced an important concept for understanding and interpreting the pattern of convection flows driven in the ionosphere, namely the effect of the movement of non-reconnecting ("adiaroic") segments of the open polar cap boundary associated with this expansion and contraction of the polar cap. This understanding is also based on the fact that the

ionosphere is incompressible and so there are negligible sources or sinks of flow. This time-dependent behavior reveals that mapping electric field from interplanetary space is not the mechanism by which solar wind energy and momentum is coupled into the magnetosphere and polar ionosphere and only when we average on timescales long enough that the dayside and nightside reconnection voltages become the same does the concept of electric field mapping give a valid answer.

Our paper from 30 years ago this year (Cowley and Lockwood, 1992) provided an alternative to the idea of mapping electric fields by discussing a mechanism that applied on shorter timescales as well as on longer timescales. This paper introduced what we called the "Expanding Contracting Polar Cap" model (ECPC–or "easy-peasy") of how reconnection drives flow in the magnetosphere-ionosphere system and the ionosphere in particular (Lockwood, 1993). The model was developed by taking the above concepts of non-steady flux transport driven by differing time-dependent reconnection voltages Φ_D and Φ_N, ionospheric incompressibility, moving adiaroic boundaries and solar wind dynamic pressure compression of the magnetosphere: it was applied to explain observations made using the EISCAT incoherent scatter radars of the ionospheric flow response to sudden southward turnings of the IMF.

The Dungey cycle is well observed in ionospheric convection (e.g., Zhang et al., 2015 and references therein). The ECPC model is a conceptual model of how reconnection drives this ionospheric convection. Momentum is transferred from the outer magnetosphere down to the F-region ionosphere by matched pairs of oppositely-directed field-aligned currents connected by Pedersen currents (Southwood, 1987), but this does not answer the question of what determines the intensity of those currents and where they occur, and hence the speed and pattern of ionospheric convection. In steady-state there are no inductive effects and so that question is answered by mapping the interplanetary electric field into the polar cap ionosphere down open magnetic field lines. However, induction effects mean that this cannot be applied to non-steady conditions and the ECPC model provides the required understanding by considering the magnetosphere-ionosphere response to changes in the tangential and normal stresses applied to the magnetosphere by changing the total open flux in the system. Hence ECPC is a conceptual model of the how electric fields and voltages of interplanetary space (in the Earth's frame of reference) are transferred into the magnetosphere and ionosphere: it generalizes the commonly-used (often tacitly used) assumption of mapped electric fields to which it reduces in the special case of steady state. Details of the ECPC concept are reprised in **Section 3** of this paper. Note that because it deals only with reconnection-driven flow, the ECPC model does not consider viscous-like mechanisms acting on closed field lines and that can operate simultaneously with the reconnection-driven flow. Having said that, as mentioned above, ECPC does have implications for our understanding of viscous-like mechanisms because it shows that much or even all of the ionospheric voltage often ascribed to them can be due to continuing tail reconnection after the IMF has turned northward. Note also that the concepts of non-steady electric field mapping inherent in ECPC would also apply to any electric fields generated on closed field lines near the magnetopause by a viscous-like mechanism. In this paper, we explore a point that has not been considered before, namely the implications of the ECPC model for how the dynamic pressure of the solar wind influences the convection response to changes in the rate of production of open flux by magnetic reconnection in the dayside magnetopause induced by IMF orientation changes.

Figure 1B helps us define some terms and principles. It is a parallel schematic to **Figure 1A**, but is for northward IMF and considerable time (t_B–t_A) after the IMF last pointed southward. Antisunward motion of open flux in the interval (t_B–t_A), in the absence of any magnetopause reconnection, would turn the dayside magnetopause and near-Earth tail magnetopause from a Rotational Discontinuity (i.e., it is threaded by the open flux) into a Tangential Discontinuity (which is not threaded by open flux). In both parts of **Figure 1**, we can see the "tail flaring"–meaning the increase in the cross-section tail radius, R with increasingly negative X coordinates, until a maximum "asymptotic" limit is reached ($R = R^*$). Comparison of **Figure 1A** and **Figure 1B** also highlights a second meaning of the term "tail flaring" that has been used in the literature, namely the increase in R with time at a given X due to open flux being appended to the tail. To distinguish these spatial and temporal uses of the word flaring, we here refer to the spatial effect as the "tail flaring" and the temporal effect as the "an increase in the tail flaring." The asymptotic limit is a somewhat simplified concept as the pressure of draped interplanetary field lines means that the tail tends to be flattened and the effect of the IMF B_Y component twists the cross-tail current sheet out of the XY plane (Sibeck and Lin, 2014). In addition, there is the slight tail aberration due Earth's motion in the $-Y$ direction and the solar wind flow close to the $-X$ direction. Nevertheless, to first order, $R = R^*$ is reached when the tail magnetopause becomes aligned with the solar wind flow so that, in equilibrium, the lobe magnetic pressure equals the static pressure of interplanetary space and the dynamic pressure is no longer constraining the magnetopause. Hence beyond the asymptotic limit, the equilibrium lobe field is set by the interplanetary static pressure and adding more open flux only causes the tail flaring to increase (i.e., R at a given X rises) and does not cause field perpendicular motion in the magnetosphere (the lobe field remains constant). Conversely, removing open flux (by tail reconnection and its exhaust in the $-X$ direction along the current sheet) reduces R and the tail flaring and does cause field-perpendicular convection throughout the lobes and towards the current sheet, even though the lobe field strength remains constant and set by the static pressure of interplanetary space.

Mapping Electric Fields From Interplanetary Space to the Ionosphere

The previous section makes the point that a key component of the ECPC model is the fact that electric field does not map down open field lines from interplanetary space into the ionosphere for anything other than steady-state conditions. To define specifically what we mean by "steady-state mapping" consider

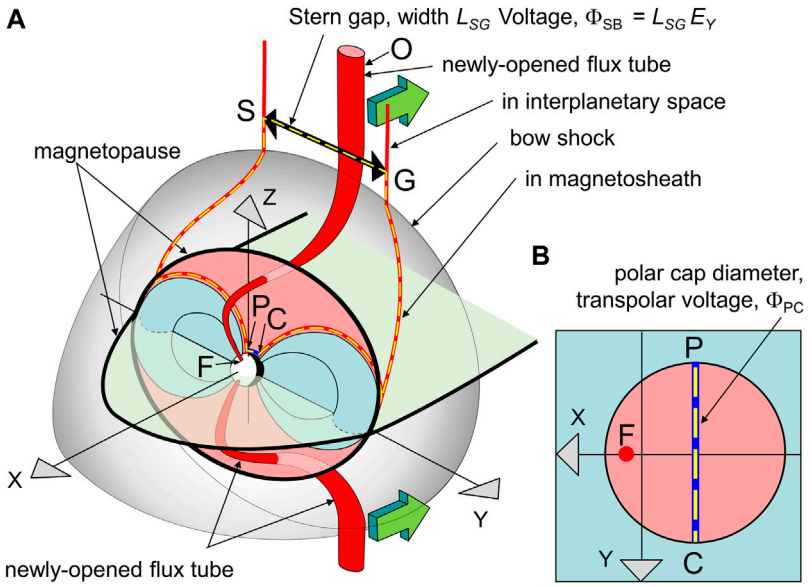

FIGURE 2 | Schematic illustrating how interplanetary voltages and electric fields are decoupled from those in the ionosphere by the inductive effects of growth or decay of magnetic fluxes threading parts of the magnetosphere: in this case the lobe flux is growing during a substorm growth phase as newly-opened field lines like OF are appended to the tail lobe by the solar wind flow (green arrows) and so thread the loop PSGC, shown by the yellow dashed line, that is fixed in the *XYZ* GSM frame shown. Part **(A)** is a view of the magnetosphere from the northern hemisphere, mid-afternoon sector and pink and light blue areas show, respectively, open and closed field line areas in the GSE *YZ* plane. Part **(B)** is looking down on the northern hemisphere polar cap and, again, pink and light blue areas show, respectively, open and closed field line areas. Red lines are selected open flux tubes.

two points on open field lines a distance L_{SW} apart in interplanetary space, between which there is an electric field E_{SW} applied in a geocentric frame. These points map magnetically down the open magnetic field lines into the ionosphere, to two points that are L_i apart, between which the electric field is E_i in the same frame of reference. Steady-state mapping of a (curl-free) electric field would mean that $E_i = E_{SW}(L_{SW}/L_i)$ in the ionosphere: in other words, the voltage difference between the two field lines in the ionosphere, $E_i\ L_i$, is equal to that in interplanetary space, $E_{SW}\ L_{SW}$. In this section, we outline some observations that specifically discriminate between the ECPC model and this steady-state electric-field mapping concept. Because steady-state applies for data that is averaged over sufficient timescales, many scientists do not see the need to allow for the effects of a breakdown of steady-state mapping: we here stress how and why it is inadequate, being a consequence of averaging rather than a physical mechanism.

The reason why electric field does not, in general, map down open field lines can be seen from application of Faraday's induction law to the tail lobes. **Figure 2** is based on similar schematics in Lockwood and Cowley (1992) and Lockwood and Morley (2004) and part **A** shows the magnetosphere and part **B** the polar ionosphere, with closed field lines occupying the pale blue areas and open field lines in the pink areas. During strong substorms, the near-Earth lobe field can increase during the growth phase from about 30 to 40 nT in about Δt = 25 min (e.g., McPherron et al., 1993). Assuming that the lobes are semi-circular in cross section with a (constant) radius 15 R_E (a mean Earth radius, $1R_E$ = 6370 km), this means that the magnetic flux in one lobe, F_L, increases from about 0.4 GWb to about 0.6 GWb and, by Faraday's law, such a rise of ΔF_L = 0.2 GWb corresponds to an e.m.f. around any closed loop surrounding the lobe of $\Delta F_L/\Delta t$ = 133 kV. This gives an order of magnitude estimate of the possible voltage decoupling between interplanetary space and the ionosphere caused by induction. Because some of the open polar cap flux F_o threads the dayside magnetopause, in general F_L will be smaller than F_o; however, F_L will still be a significant fraction of F_o because open flux is swept into the tail on short timescales compared to the time lag between opening and closure of a given field line. Surveys by Milan et al. (2007) and Boakes et al. (2009) found a distribution of F_o between 0.2 and 0.9 GWb with a mode value near 0.4 GWb and a mean of 0.46 GWb. The smallest estimated F_o that we know of is for the "nearly closed" magnetosphere observed by Wang et al. (2022) for which F_o was estimated to have fallen to about 0.08 GWb. Substorm onsets are typically initiated when F_o reaches about 0.7 GWb (Milan et al., 2008) but larger values, up to about 1.1 GWb, have been deduced in sawtooth events and steady convection events (DeJong et al., 2007; Lockwood et al., 2009; Brambles et al., 2013). It has been estimated that in large superstorms, F_o saturates near 1.2 GWb (Mishin and Karavaev, 2017). For all these F_o estimates, the inferred changes in tail lobe flux ΔF_L during substorms, sawtooth events, and steady convection events are significant fractions of the increases in the total open polar cap flux, ΔF_o.

Open field lines, by definition, thread the magnetopause. They then thread the magnetosheath and the bow shock and define a region called the "Stern Gap" in interplanetary space (the name

originated from a NASA Technical report (Stern, 1975b) in which this region was actually called a "window"). The red lines PS and CG in **Figure 2** are the open field lines closest to, respectively, the dawn and dusk flanks of the magnetosphere and so define the full extent (in the *Y* dimension) of both the Stern Gap, SG, and the polar cap, PC, in the ionosphere. The yellow dashed line is a closed loop PSGC round the lobe, which is fixed in the GSM frame of reference. Faraday's law (in integral form) applied to this loop gives

$$\oint_{PSGC} \vec{E}.\overrightarrow{dl} = \Phi_{PS} + \Phi_{SG} + \Phi_{GC} + \Phi_{CP} = d \oint_{PSGC} \vec{B}.\overrightarrow{dA} \Big/ dt = dF_T/dt \quad (2)$$

Where F_T is the total magnetic flux threading the loop and Φ_{AB} is the voltage between generic points A and B. If there are no changes in the magnetosheath, the flux of sheath field threading the loop remains constant and so $dF_T/dt = dF_L/dt$, where F_L is the flux in the lobe. The segments of the loop PS and GC are everywhere aligned with the magnetic field. In ideal MHD, the field-aligned potential drops Φ_{PS} and Φ_{GC} are zero and so, although field lines at these segments of the loop are convecting, the electric field associated with that motion is field-perpendicular and so also perpendicular to the loop segments (i.e., $\underline{\boldsymbol{E}}.\ \underline{\mathbf{dl}} = 0$ along the PS and GC segments of the loop). One cannot explain the magnitude of the decoupling of the voltages across SG and PC by invoking a static situation and field-aligned potential differences. Information of field-parallel electric fields comes from energies of field-aligned beams of accelerated ions and electrons (upgoing or downgoing) seen both above and below the acceleration region (*see* review by Marklund and Lindqvist, 2021). To be effective in generating these beams, the potential drops need to be present for at least the flight time of the particles across them and are referred to as "quasi-static." Hence there is debate between the relative influence of electric fields in Alfvén wave phenomena (e.g., Watt et al., 2005) and longer-lived structures giving field-parallel potential drops (such as proposed double layers) and so it is not clear how persistent they are on timescales of convection and hence to what extent they are averaged out on such timescales. However, the largest values are typically 1–3 kV in the auroral oval (Marklund and Lindqvist, 2021) and about a 10th of this inside the polar cap (Hosokaw et al., 2020). These values are considerably smaller than both the typical field-perpendicular voltages Φ_{PC} (= $-\Phi_{CP}$) of 50–150 kV (e.g., Lockwood and McWilliams, 2021a) and the typical scale of the electromotive force around the loop PSGC inferred above ($dF_L/dt = 1.33 \times 10^5$ Wb s^{-1} = 133 kV). Hence, to first order, even without the averaging effect of their quasi-static nature, we can discount quasi-static field parallel potential drops. This gives

$$\Phi_{SG} - \Phi_{PC} = dF_L/dt \quad (3)$$

Hence only in steady state, when $dF_L/dt = 0$, does $\Phi_{PC} = \Phi_{SG}$ and the interplanetary voltage maps into the ionosphere. Numerical MHD models of the magnetosphere provide evidence for the magnitude of decoupling of the Stern gap voltage Φ_{SG} and the transpolar voltage Φ_{PC} indicated by **Eq. 3**. For example, Gordeev et al. (2017) compare the predictions of three different models following a southward turning of the IMF, after which B_Z is held steady at −5 nT with a solar wind speed $V_{SW} = -V_X = 600$ km s^{-1}. From $\underline{\boldsymbol{E}} = -\underline{\boldsymbol{V}} \times \underline{\boldsymbol{B}}$, the dawn-to-dusk interplanetary electric field is $E_Y = V_X B_Z = +3$ mVm^{-1} after the southward turning (where V_X is the solar wind velocity in the +*X* direction so $V_X < 0$ and $E_Y > 0$ for $B_Z < 0$). Note that even if the E_Y arriving at Earth changes with time, all field lines opened at a given E_Y keep that value for their entire transit over the polar cap because neither V_X nor B_Z change significantly for each field line in the relevant extent of interplanetary space. We here just use the results from the BATSRUS model to illustrate the point about how E_Y maps to the ionosphere. The model predicts that the tail flux rises almost linearly in the resulting substorm growth phase from 0.4 to 0.6 GWb over an interval 25 min long giving dF_L/dt = 133 kV (as estimated above for a typical substorm from magnetic field observations in the tail lobe). The rise is caused by newly-opened field lines, such as OF in **Figure 2**, being transferred antisunward along the Stern Gap from the dayside to the nightside, the rate of flux transfer being Φ_{SG}, while their ionospheric footpoints are not moved across the polar cap diameter PC. In fact, Φ_{SG} will exceed this value of dF_L/dt as some tail lobe flux is lost by reconnection in the cross tail current sheet and convected sunward out of the tail as closed flux. The tail reconnection site is not immediately influenced by the increase in magnetopause reconnection as it takes time for any information about the southward turning to reach it; hence we can assume this loss of lobe flux carries on at the rate of 21 kV which was the modelled quasi-steady value before the southward IMF turning. This means that Φ_{SG} is approximately 133 + 21 = 154 kV, giving a Stern gap width of $L_{SG} = \Phi_{SG}/E_Y = 8.1\ R_E$, which is a realistic value. Substorm onset in the model occurs about 30 min after the southward turning and during that interval, the model predicts that the ionospheric transpolar voltage rises from 21 to 93 kV. Hence at no time in the growth phase does the interplanetary electric field or voltage map from interplanetary space to the ionosphere in these simulations. The other models tested by Gordeev et al. (2017) show the same general behavior.

Possibly the most straightforward evidence for the need for something like the ECPC model is that transpolar voltage Φ_{PC} depends both on the prevailing IMF B_Z component (and hence the dawn-dusk interplanetary electric field, $E_Y = -V_{SW} B_Z$) and on the *AL* auroral electrojet index. This is demonstrated in the contour plot from 25 years of SuperDARN Φ_{PC} data shown in **Figure 3** (this is a version of the −*AL* versus B_Z contour plot for the same dataset presented in Figure 8 of Lockwood and McWilliams (2021a) but uses E_Y along the *x*-axis instead of B_Z). The diagonal orientation of the contours shows that, in general, Φ_{PC} increases both with E_Y at a fixed *AL* and with −*AL* at a fixed E_Y. For northward IMF ($E_Y < 0$), the contours become almost horizontal showing a dominant dependence on −*AL*: for southward IMF ($E_Y > 0$) both have an influence but at the largest E_Y the contours become almost vertical, indicating E_Y is the dominant influence. Hence the plot shows Φ_{PC} increases with auroral electrojet strength, quantified by −*AL*, at all but the largest E_Y and that for northward IMF ($E_Y < 0$), Φ_{PC} depends almost entirely on *AL*. If the interplanetary electric field always mapped

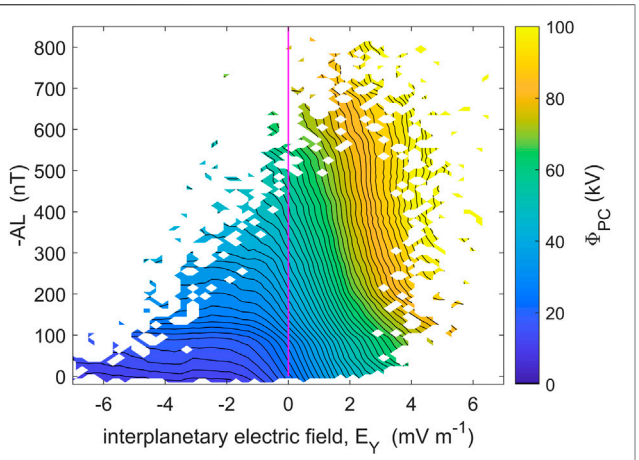

FIGURE 3 | Contours of average transpolar voltage, Φ_{PC}, observed over 25 years by the northern hemisphere SuperDARN radar network (Lockwood and McWilliams, 2021a) as a function of the dawn-dusk interplanetary electric field, E_Y, and the auroral electrojet index, $-AL$.

to the ionosphere, as predicted by steady-state, then Φ_{PC} would be equal to the voltage across the Stern gap $\Phi_{SG} = E_Y L_{SG}$ where L_{SG} is the width (in the Y dimension) of the Stern gap. This value would then persist on those field lines until they were closed again. Hence the only way that mapped electric fields could explain the observed dependence on both $-AL$ and E_Y in **Figure 3** is if L_{SG} increased monotonically with $-AL$. Given that L_{SG} is set by the length of the magnetopause reconnection X-line and the field line draping in the magnetosheath and AL is determined by processes in the near-Earth tail and that information takes time to travel between the two regions, there can be no mechanism that could give such a relationship. Strictly speaking, this argument shows that application of steady-state mapping of the electric field cannot explain **Figure 3**. However, we also note that the ECPC model is the only proposed alternative to steady-state mapping in the literature. In addition, substorm theories and observations show there is a monotonic average relationship between $-AL$ and Φ_N and the polar cap contraction that Φ_N causes (Milan et al., 2009a; Lockwood et al., 2009; Mooney et al., 2020; Milan et al., 2021) and simultaneous lobe field decreases at well-separated locations (Caan et al., 1978; McPherron et al., 1993). The $-AL$ index can therefore be considered to be a proxy indicator of Φ_N. Hence **Figure 3** shows that Φ_N and Φ_D are separate contributors to Φ_{PC} which is a central prediction of the ECPC model.

Another key piece of evidence is the behavior of transpolar voltage Φ_{PC} after the IMF returns northward following a period of southward IMF. A northward turning of the IMF ceases the production of new opened field lines, or at least reduces their rate of production, but does not remove pre-existing ones. The open field lines generated during the prior southward IMF interval remain open until they are closed by reconnection in the cross tail current sheet and their interplanetary E_Y, L_{SG} and Φ_{SG} values all stay constant all that time. Hence if steady-state mapping applied, Φ_{PC} would also remain constant and then drop rapidly as the last-to-be-opened field lines are re-closed. This is not what is observed (Wygant et al., 1983; Lockwood et al., 2006; Lockwood and McWilliams, 2021a): rather, a range of Φ_{PC} values are observed between almost zero and largest values that decay exponentially with time after the northward turning and that depend on the $-AL$ value. This is a prediction of the ECPC model because one substorm expansion does not remove all the extra lobe magnetic flux that is built up during the prior growth phase and so one isolated growth phase can generate a string of subsequent substorm expansions of declining amplitude, each giving a peak in Φ_{PC} due to an associated rise in the reconnection voltage in the cross-tail current sheet, Φ_N. Northward-IMF intervals are often thought of as giving an equilibrium to which the magnetosphere returns because they give geomagnetically quiet conditions. This is not the case. During these intervals the interplanetary electric field points from dusk to dawn ($E_Y < 0$) and reconnection taking place poleward of the magnetic cusps, near the sunward edges of the tail lobe magnetopause boundary, gives penetration of that negative E_Y into the magnetosphere (e.g., Lockwood and Moen, 1999). The tail never decays away completely and so, at the same time as the lobe reconnection, magnetic shear remains across the cross-tail current sheet and reconnection there can only give either $E_Y > 0$ or, if it ceases, $E_Y = 0$. In both scenarios, there is a curl in electric field and so this is a slow decline of the lobe field and not steady state (Lockwood, 2019). That decline can be understood because any ongoing reconnection in the cross-tail current sheet causes a loss of open flux and reconnection taking place at the sunward edge of both lobes can also cause a loss of dayside open flux, giving a "horse-collar" auroral form, with a teardrop-shaped open polar cap with most remaining open flux confined to the nightside (Lockwood and Moen, 1999; Imber et al., 2006; Milan et al., 2020). The most extreme example of this was observed by Wang et al. (2022), but even in this case a residual open flux of about 0.08 GWb remained. Hence, as far as we can tell, the magnetosphere is never subject to a long enough period of strongly northward IMF that it becomes completely closed and so northward IMF conditions, although geomagnetically quiet, give a slow decline of the lobe fields rather than an equilibrium steady state.

A more complex test of the ECPC model was provided by Soterelis et al. (2017). These authors showed that when the polar cap is expanding the observed transpolar voltage correlates best (correlation coefficient $r = 0.86$) with the solar wind/IMF driving, integrated over the previous 10 min (compared to $r = 0.57$ for when the polar cap is contracting). On the other hand, when the polar cap is contracting the transpolar voltage correlates best ($r = 0.87$) with averages of solar wind/IMF driving over the previous 90 min (compared with 0.51 for when the polar cap is expanding). This is consistent with the ECPC model and also specifically inconsistent with the idea that electric field maps from the solar wind and magnetosheath to the ionosphere for which correlations would not depend on whether the polar cap was expanding or contracting.

Note that polar cap expansion (when $\Phi_D > \Phi_N$) and contraction (when $\Phi_N > \Phi_D$) are both observed and the transpolar voltage is

raised during both, by the increased Φ_D and by increased Φ_N, respectively (Lockwood, 1993; Milan, 2004; Hubert et al., 2006a; Hubert et al., 2006b; Lockwood et al., 2009; Milan et al., 2009b; 2021), consistent with the ECPC model. For electric field mapping transpolar voltage would be set by Φ_{SG} only.

Applications of the ECPC model have been predominantly in describing transient effects. In particular, it has been widely used to investigate the ionospheric signatures of Flux Transfer Events (FTEs: burst of enhanced reconnection voltage in the dayside magnetopause) (Cowley et al., 1991; Smith and Lockwood, 1996; Milan et al., 2016) and convection during the substorm cycle (Milan et al., 2021). It has also been applied to the magnetospheres of other planets (e.g., Cowley et al., 2005). Here we are making a somewhat different point. Because the magnetosphere is rarely, if ever, in a steady-state equilibrium, some part or all of it is always responding to prior variations in the solar wind (Lockwood, 2022b) which means the ECPC concept will always have some relevance. We here investigate this idea in relation to the observed effects of solar wind dynamic pressure on transpolar voltage and geomagnetic activity.

Effects of Solar Wind Dynamic Pressure

Equilibrium concepts balance the dominant magnetic pressure in the magnetosphere with the dominant pressure in interplanetary space, which, for the near-Earth magnetopause, is the dynamic pressure of the solar wind flow ($P_{SW} = m_{SW}N_{SW}V_{SW}^2 = \rho_{SW}V_{SW}^2$, where m_{SW} is the mean ion mass, N_{SW} the number density, ρ_{SW} is the solar wind mass density and V_{SW} the solar wind speed).

A number of papers have indicated that solar wind dynamic pressure has an influence in flux transport through the magnetosphere and on geomagnetic activity (e.g., Lukianova, 2003; Lee et al., 2004; Boudouridis et al., 2005; Stauning & Troshichev, 2008; Lockwood et al., 2020b; Lockwood et al., 2020c): this is beyond, and separate from, the known generation of transient filamentary field aligned currents and travelling convection vortices (e.g., Glassmeier and Heppner, 1992; Lühr et al., 1996). These "TCV" events are caused by filamentary pairs of field aligned currents generated by the magnetopause deformation but they move laterally (along the line between the two currents) which means that although flow is generated, there is no net effect as they pass through and do not add to the convection cycle. There are physical reasons to expect both the dayside and the nightside reconnection voltages (respectively, Φ_D and Φ_N) to be enhanced by increased solar wind dynamic pressure P_{SW}. In both cases, the compression brought about by greater P_{SW} should increase the magnetic shear across the current sheet and so would be expected to enhance the reconnection rate: an effect that has been identified in global MHD model simulations (e.g., Palmroth et al., 2004). However, in observational studies it is not clear how much of the response is a TCV.

One caveat to this idea is that the nightside reconnection must be taking place at a GSM X-coordinate at which the tail is still flaring (i.e., $dR/dX < 0$), which enables the dynamic pressure to squeeze the tail lobe and so increase the field there (Caan et al., 1973) and hence the cross-tail current (Lockwood, 2013). Scurry and Russell (1991) inferred statistically that dayside reconnection voltage Φ_D was enhanced by increased P_{SW} using the *am* geomagnetic activity index as a proxy for the reconnection rate (we will discuss the validity of this below). Transient responses to individual events in which P_{SW} increases suddenly include a rise in Φ_D (e.g., Boudouridis et al., 2007), a rise in Φ_N (Boudouridis et al., 2008a) and hence a rise in Φ_{PC} (Boudouridis et al., 2008b). Karlsson et al. (2000) reported events in which the energy content of the near-Earth tail was reduced following decreases in P_{SW} at the end of a substorm growth phase, inferring that they even caused quenching of any substorm expansion that had recently begun. These authors deduced that reducing P_{SW} can also reduce Φ_N. Conversely, increases in P_{SW} have been seen to trigger onsets of full substorm expansion phases (Schieldge and Siscoe, 1970; Kokubun et al., 1977; Yue et al., 2010) consistent with the idea that increased P_{SW} can increase Φ_N. In some cases, a rise in Φ_N due to increases in P_{SW} has been inferred from a loss of open flux as aurora on closed field lines expands into what appears to have been open flux (Hubert et al., 2006a; b). Various observational studies suggest that increases in P_{SW} cause an enhancement in general magnetospheric convection and in field-aligned current systems as well as enhanced geomagnetic activity (e.g., Lukianova, 2003; Lee et al., 2004; Hubert et al., 2006b; Boudouridis et al., 2008a; Stauning and Troshichev, 2008). This phenomenon has also been modelled using global MHD models of the magnetosphere as being caused by rises in both Φ_D and Φ_N induced by rises in P_{SW} (Palmroth et al., 2004; Ober et al., 2006; Connor et al., 2014; Lockwood et al., 2020b).

Many of these studies relate to the effects of sudden rises or falls in P_{SW} and from the transient responses it is not clear what influence different constant levels of P_{SW} have on the overall average reconnection voltages, flux circulation through the magnetosphere and on the overall level of geomagnetic activity. The observed "McIntosh" (a.k.a. "equinoctial") pattern of the average *am* geomagnetic index with time-of-day and time-of-year, associated with the dipole tilt, has been shown to have an amplitude that is proportional to the value of P_{SW} (Lockwood et al., 2020a). This geomagnetic effect has been reproduced using global MHD modelling by Lockwood et al. (2020c) and explained by the effectiveness with which P_{SW} can squeeze the tail and how that varies with the dipole tilt. This shows a strong influence of P_{SW} on geomagnetic activity. Lockwood et al. (2020b) show that P_{SW} has a distinct influence on geomagnetic activity from that of the estimated power input on the magnetosphere, P_α (*see* Lockwood, 2019), despite the fact that they share common dependencies on N_{SW}, m_{SW} and V_{SW}. We here use the estimate of the power input $P_\alpha = B^{2\alpha}V_{SW}^{(7/3-2\alpha)}\rho_{SW}^{(2/3-\alpha)} sin^4(\theta_{GSM}/2)$, where B is the IMF magnitude, and θ_{GSM} the IMF clock angle in the GSM frame of reference (Vasyliunas et al., 1982). Hence although $P_{SW} = \rho_{SW} V_{SW}^2$, the best-fit coupling exponent of $\alpha = 0.44$ found by Lockwood et al. (2020b) means that P_α is proportional to $\rho_{SW}^{0.227}V_{SW}^{1.453}$ and it has an additional dependence on the IMF strength and orientation. Specifically, Lockwood et al. (2020b) show that the geomagnetic activity level generated per unit P_α depends on P_{SW} (and on Earth's dipole tilt and hence time of year and Universal Time). What was unclear from this study was to what extent this

is caused by enhanced flux transport through the magnetosphere (and hence transpolar voltage) or by enhanced energy storage in a compressed geomagnetic tail.

Lockwood and McWilliams (2021b) and Lockwood (2022a) studied best-fit coupling functions for simultaneous Φ_{PC}, *SML* and *am* data for 1996–2020 and found optimum exponents *b* for a mass density term ($\rho_{SW}{}^{b}$) of 0.02, 0.06, and 0.36 for Φ_{PC}, *SML* and *am,* respectively. We mention the *am* index here for two reasons. Firstly, Scurry and Russell (1991) used *am* as a proxy to infer that dayside reconnection voltage Φ_D was enhanced by increased P_{SW}. Secondly *am* has the most uniform response in terms of time-of-day and and time-of-year of all geomagnetic indices (Lockwood et al., 2019a) and is genuinely planetary: however, it has the disadvantage that it is has only a 3-hourly cadence. The best-fit exponent *b* for the *SML* and *AL* indices was found to be essentially identical by Lockwood and McWilliams (2021b) and Lockwood (2022a). These values for *b* are very similar to those found in other studies using *AL* (e.g., McPherron et al., 2015). The low value of *b* for Φ_{PC} accords with the highly successful coupling function for transpolar voltage of Boyle et al. (1997), which makes no allowance for ρ_{SW} (i.e., $b = 0$) whereas other coupling functions designed to predict geomagnetic activity have non-zero exponents *b* (*see* Lockwood and McWilliams, 2021b and references therein). Hence these statistical studies suggest that P_{SW} has a significant effect on geomagnetic activity indices such as *AL*, *SML* and *am* but a smaller effect (if any) on flux transport and transpolar voltage, Φ_{PC}.

Some clarification of the effects of higher constant solar wind dynamic pressure P_{SW} (as opposed to transient increases in P_{SW}) is brought by **Figure 4**, which is from the survey of 25 years of data by Lockwood and McWilliams (2021a) and shows contour plots of average values (normalized by the parameter standard deviation) as a function of IMF B_Z along the *x* axis and P_{SW} (normalized to the overall mean value $<P_{SW}>$) along the *y* axis. The values of B_Z and P_{SW} are 15-min boxcar means for the same intervals as the terrestrial indices, using the derived optimum propagation lag. Parts **A**, **B** and **C** are for *am*, *AL* and Φ_{PC}, respectively. In general, the contours for all three slope diagonally, showing mean values increase with increasingly negative B_Z at a fixed P_{SW} and with increasing P_{SW} at a fixed B_Z. However, the plots are not identical in form. For *am* the contours are the most inclined to the vertical and are inclined at all B_Z; for *AL* and Φ_{PC} the contours are less inclined to the vertical and, indeed, for strongly southward IMF become vertical. Hence Φ_{PC} and *AL* have a weaker dependence on P_{SW} than *am* and one that is mainly significant for northward IMF or weakly southward IMF. Note that, whereas Figure 11 of Lockwood and McWilliams (2021a) the colour scale used was absolute values of the parameter means, in **Figure 4** they have been normalized to the standard deviation, SD, of the parameter. It can be seen that the amplitude of the pattern is a smaller fraction of the overall variability for *AL* and a larger fraction for Φ_{PC}. However, it is not possible to draw a physical conclusion from these pattern amplitude differences because of the different construction of the three indices used: all values

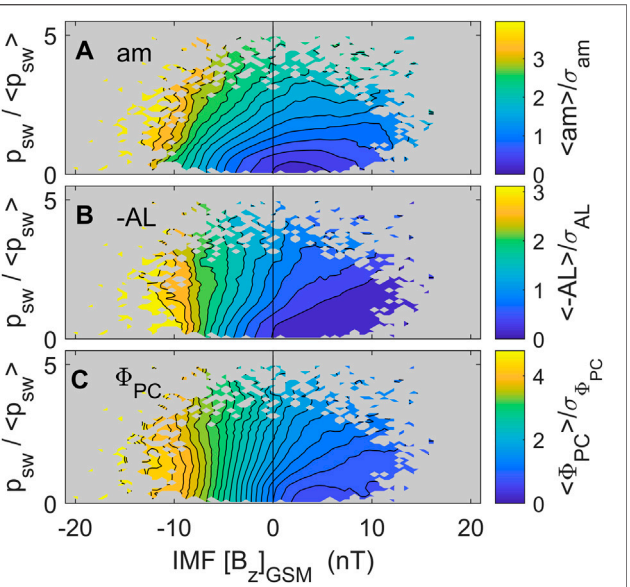

FIGURE 4 | Variations with IMF B_Z in the GSM frame and solar wind dynamic pressure, P_{SW}, of: **(A)** the *am* planetary geomagnetic index; **(B)** the *–AL* auroral electrojet index; and **(C)** the transpolar voltage, Φ_{PC}. All data are simultaneous with the valid Φ_{PC} samples from 1996 to 2020. The *x* axis is north-south IMF component (B_Z, defined as positive northward) in the GSM frame of reference and the *y* axis is the normalized solar wind dynamic pressure, $P_{SW}/< P_{SW} >$ where $P_{SW} = m_{SW}N_{SW}V_{SW}{}^2$, m_{SW} is the mean ion mass, N_{SW} is the number density and V_{SW} is the speed of the solar wind. The normalizing factor $< P_{SW} >$ is the mean for all data. The *–AL*, Φ_{PC} and P_{SW} data are all 15-min boxcar running means of 1-min data whereas the *am* data are linearly interpolated to the time of the hourly Φ_{PC} sample and the mean value in each B_Z - normalized P_{SW} bin, divided by the parameter SD is plotted: the absolute values were presented in Figure 11 of Lockwood and McWilliams (2021a). Grey areas are where data are too sparse for contours to be fitted.

are 15-min boxcar means of 1 min values but there the similarities end. For *AL* we have used raw 1-min values which gives a high SD σ_{AL}; for the *am* index we are using interpolated values from maximum range values (over 3-h intervals) of 3-hourly cadence and for Φ_{PC} we are using interpolated values from hourly integrations of 2-min data. What is significant in **Figure 4** is the similarities and differences in the form of the pattern and the evidence for an effect of P_{SW} at all but the largest negative B_Z. In this paper, we use the ECPC model of flow excitation of Cowley and Lockwood (1992) to look at the implications of the effect of P_{SW} on these magnetospheric state indicators.

DATA EMPLOYED

We here use 1-min interplanetary data from the Omni2-dataset (King, and Papitashvili, 2005) from 1996 onwards when data gaps are both rarer and shorter (Lockwood et al., 2019b). To estimate the dynamic pressure P_{SW} and the power input into the magnetosphere P_α, we need the solar wind mass density ρ_{SW} which we estimate by

neglecting ions heavier than Helium and using observations of the Helium abundance at the highest resolution available (either 5 min, 15 min or 1 h) and linearly interpolating to minute values.

These data are compared to a number of magnetospheric state indicators. We use 1-min data on the auroral electrojet from the SuperMAG *SML* index (Newell and Gjerloev, 2011) which is constructed the same way as the *AL* auroral electrojet index (Davis and Sugiura 1966). Specifically, for both of these two indices, magnetograms of the horizontal components from the stations used are superimposed and the lower envelope defines the index. Like *AL*, *SML* is a measure of the strength of the nightside westward auroral electrojet. The difference between *SML* and *AL* is that all available stations in the northern hemisphere at middle and high latitudes are used (typically 100 in number) instead of the ring of 12 auroral stations used to construct *AL*. This means is has a more unform response with Universal Time than *AL* because it does not have the large longitudinal gaps (on average 30° in width) that cause such problems for *AL*. In addition, by having stations at lower latitudes, *SML* avoids the problem that *AL* suffers from that at large activities the auroral oval expands to lower latitudes than the stations, reducing the response. Both *SML* and *AL* are from observations in the northern hemisphere only which means they have a strong annual variation due to the axial tilt of the Earth and the effect that has on ionospheric conductivities. A comparison of the performance of *SML* and *AL* has been presented by Bergin et al. (2020). Results for *SML* and *AL* were here found to be similar in all important respects and we here show only the results for *SML*. For a monitor of (mainly) the ring current, we here use the SuperMAG *SMR* index (Newell and Gjerloev, 2012) that is based on the *SYM-H* index and compiled from the baseline-subtracted northward component of the geomagnetic field from all available ground magnetometer stations at geomagnetic latitudes between −50 and +50° (again typically 100 in number). An inverse cosine correction for magnetic latitude is then applied and it is averaged globally. Bergin et al. (2020) compare the performance of *SMR* and the frequently-employed *Dst* index. Both *SMR* and *SML* are available at 1-miute integrations which enables us to process them in the same way as we do the interplanetary data.

We also make some use of the planetary *am* geomagnetic index (Mayaud, 1980). This index is a range index (between maximum and minimum values of the horizontal field component) taken over 3-h intervals; a time resolution that makes unsuitable for, for example, superposed epoch studies on timescales of a day and less. However, the use of uniform rings of mid-latitude stations in both hemispheres, and the adoption of weighting functions to allow for necessary longitudinal gaps because of oceans, makes the response of the *am* index truly planetary in nature and exceptionally uniform in time-of-year and time-of-day response (Lockwood et al., 2019a): we employ *am* when these characteristics are most important.

In addition to these geomagnetic indices, we use the transpolar voltage Φ_{PC} derived from the SuperDARN radar network. A dataset of hourly averages of 2-min integrations over the past 25 years has been generated by Lockwood and McWilliams (2021a). However, unlike the above geomagnetic indices, it cannot be used as a continuous data series. The reason is that the "map-potential" method used to derive Φ_{PC} is a data assimilation technique employing a model of the ionospheric convection pattern, driven by the IMF orientation in the upstream solar wind (Ruohoniemi and Baker, 1998; Provan et al., 2002). Lockwood and McWilliams (2021a) tested these SuperDARN Φ_{PC} estimates against values from satellite overpasses and found that an average number of radar echoes for the thirty 2-min pre-integrations in each hour must exceed 255 for the influence of the model in the Φ_{PC} data to be reduced to an undetectable level. This condition left 65,133 usable hourly mean Φ_{PC} values, about one third of the total obtained over 25 years. Despite not being a continuous record and despite the fact that it is only of hourly time resolution, these data are included in the present study because magnetic flux transport (i.e., voltage) is known to be a key and fundamental part of the coupling of solar wind mass, momentum and energy into the magnetosphere and Lockwood and McWilliams (2021b) and Lockwood (2022b) have shown it has a significantly different behavior to geomagnetic indices.

THE NON-EQUILIBRIUM NATURE OF THE MAGNETOSPHERE

Milan et al. (2021) make the point that if interplanetary conditions vary slowly enough, the magnetosphere-ionosphere system can evolve through a series of quasi-steady-state equilibria. We can quantify roughly what "slowly" means in this context from their Figure 8: for small polar caps (initial open flux $F_o \approx 0.4$ GWb) it means rises in dayside reconnection voltages Φ_D of <25% in 2 h; for mid-sized polar caps ($F_o \approx 0.5$ GWb) it means Φ_D rises of <30% in 2 h; and for large polar caps ($F_o \approx 0.6$ GWb) it means Φ_D rises of <35% in 2 h. To investigate how likely this is to occur, **Figure 5** studies the normalized autocovariance functions (a.c.f.s) of various parameters. To ensure that we compare like-with-like we use parameters that have only one polarity because the a.c.f. of, for example, the IMF B_Z component would be different from that of, for example, the *am* index because it has both positive and negative whereas *am* is only positive. Hence instead of B_Z, we use the IMF orientation factor $B_\perp \sin^4(\theta/2)$ (where $B_\perp$ is the transverse component of the IMF perpendicular to the Sun-Earth line, $B_\perp = (B_Y^2+B_Z^2)^{1/2}$, and θ is the IMF clock angle defined as $\theta = \arctan(|B_Y|/B_Z)$, B_Y and B_Z being the Y and Z components of the IMF in the GSM frame). We also use the half-wave rectified dawn-dusk electric field E_Y' (where $E_Y' = E_Y$ for $E_Y > 0$ and $E_Y' = 0$ for $E_Y \le 0$). In addition, we use a pressure-corrected SuperMAG *SMR* index that only has negative values: the pressure correction uses the form that Burton et al. (1975) proposed for the *Dst* index, namely $SMR^* = SMR - \gamma P_{SW}^{1/2} - \beta$ with derived coefficients $\gamma = 31.45$ nT nPa$^{-1/2}$ and $\beta = 11.51$ nT that give the peak linear correlation coefficient of 0.9 between hourly values of *SMR** and the pressure-corrected *Dst* index, *Dst**. (Note that we also used the raw *SMR* index and the a.c.f.s for

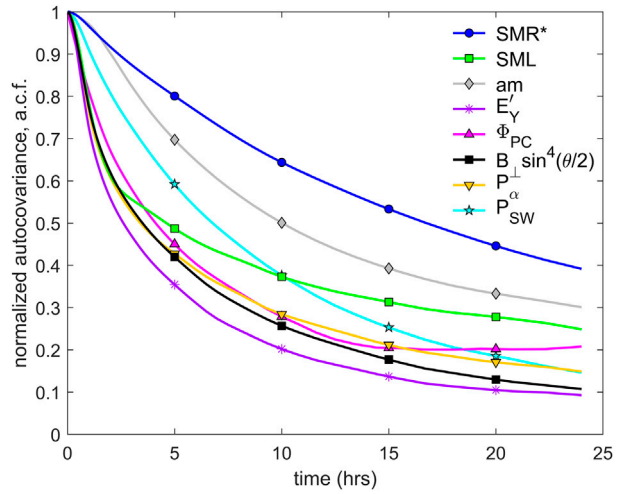

FIGURE 5 | Normalized autocovariance functions of 60-point (hourly) 1-min values of: (black line with filled square symbols) an estimate of the geoeffective IMF component of the interplanetary magnetic field, $B_{\perp}\sin^4(\theta/2)$; (purple with asterisk symbols) the half-wave rectified dawn-dusk component of the interplanetary magnetic field, E_Y' (where $E_Y' = E_Y$ when $E_Y' > 0$ and $E_Y' = 0$ when $E_Y < 0$); (cyan with star symbols) the solar wind dynamic pressure, P_{SW}; (mauve with upward-pointing triangle symbols) the transpolar voltage measured by the SuperDARN radar array, Φ_{PC} (1 min values, obtained from linear interpolation between hourly values are used); (gray with diamond symbols) the *am* geomagnetic index (1 min values, obtained from linear interpolation between 3-hourly values are used); (green with open squares) the SuperMAG *SML* auroral electrojet index; (blue with circle symbols) the pressure-corrected SuperMAG geomagnetic index *SMR** (dominated by the effect of the ring current). All curves are for all available data for 1996–2019, inclusive. Note that the symbols have been added at intervals of 5 h to help distinguish between the different color lines. but a.c.f.s were computed for lags 1 min apart.

*SMR** and *SMR* were very similar indeed because positive excursions of *SMR* are short and small compared to negative ones). In addition, we try to use the same integration and averaging timescales for the data as far as is possible. For the solar wind and IMF parameters, the *SMR** index and the *SML* index we use 1-min integrations of data that are smoothed into hourly means using 60-point running (boxcar) means, before taking the autocovariance. The Φ_{PC} data are slightly different being initially 2-min integrations and the *am* data are necessarily radically different being originally range values in 3-h windows.

The most variable (lowest persistence and shortest autocorrelation timescale) is the interplanetary electric field E_Y'. The a.c.f. for the IMF orientation factor $B_{\perp}\sin^4(\theta/2)$ and the estimated power input to the magnetosphere P_{α} are similar but show slightly greater persistence than E_Y'. The least variable (highest persistence and longest autocorrelation timescale) of those shown is the *SMR** geomagnetic index, which is dominated by the ring current. Of the terrestrial indices shown, the order of increasing variability is *SMR**, *am*, Φ_{PC} and *SML*. Note that persistence, as quantified by autocovariance and autocorrelation is a measure of average behavior and individual cases can differ considerably from the average. All of these terrestrial indices are less variable on average than the key driving solar wind parameters, namely: the IMF orientation factor, the half-wave rectified dawn-dusk interplanetary electric field E_Y' and the estimated power input to the magnetosphere, P_{α}. The solar wind dynamic pressure has greater persistence because of its dependence on higher-persistence parameters, the solar wind flow speed, mean ion mass and number density (Lockwood, 2022).

Figure 5 demonstrates that the key driving solar wind parameters tend to change faster than the terrestrial state indicators can respond and so the magnetosphere will, in general, not have time to reach equilibrium with the solar wind.

However, there is a caveat we must place on this analysis. The interplanetary parameters are point values from a single spacecraft whereas the magnetosphere will respond to solar wind impacting over an extended area (in the *YZ* plane) of unknown size. Spatial structure within that area would make the point interplanetary values more variable in time than is the area-averaged values that the magnetosphere responds to. There is very little data pertaining to such an effect and much of it of only quite distant relevance. Walsh et al. (2019) and Lockwood (2022a) have studied the correlations (at optimum propagation lags) between L1 values of interplanetary parameters and coupling functions and those evaluated from near-Earth observations by spacecraft in the magnetosheath and undisturbed solar wind. There are distributions of correlations because the solar wind that passes over the L1 spacecraft may miss the near-Earth craft and/or because conditions can change during the transit between the two and/or there are variations in the propagation delay. Walsh et al. (2019) show that the difference in magnetic field clock-angle θ measured at the two locations, Δθ, increases with the distance of the L1 craft from the Sun-Earth line, R_{XY} showing an effect of spatial structure in the *YZ* plane. The effect is modest, the SD of Δθ increasing by about 1% per $1R_E$ increase in R_{XY}, but nevertheless present. On the other hand, Lockwood (2022b) shows that the distributions of correlations (for 1-min, 10-min and 1-h averages) between an L1 coupling functions and auroral activity indices were only degraded at R_{XY} exceeding about $80R_E$. Together, these results indicate that there is very likely to be an effect of spatial averaging in the correlations between L1 craft and terrestrial space weather activity. However, directly-relevant evidence that the spatial averaging effect is relatively minor comes from **Figure 5** itself. Such an effect would necessarily influence all internal magnetospheric responses at all lags. The autocovariance function of the *SML* index is therefore interesting because at lags below about 2 h it falls essentially as rapidly with lag as the interplanetary factors that are strongly influenced by IMF orientation ($B_{\perp}\sin^4(\theta/2)$, E_Y' and estimated power input into the magnetosphere, P_{α}). At lags above 2 h, the a.c.f. for *SML* does become larger than for these interplanetary factors, but because the difference is very small at low lags, this must be predominantly because of delayed magnetospheric responses (for example, due to energy stored in the geomagnetic tail or the particle and energy content of the ring current) and not due to the averaging effect of spatial structure in near-Earth interplanetary

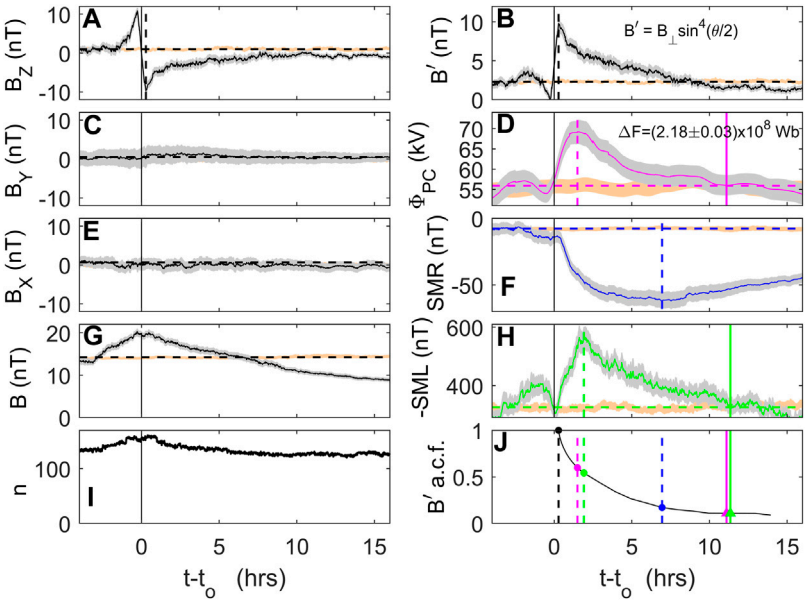

FIGURE 6 | Superposed epoch study of responses to southward turnings in the IMF. A total of 160 southward turning events (at time t_o) were identified in the data for 1996–2019 (inclusive) from times when 30-min running means of 1-min values of the northward IMF component, B_Z, turned from positive to negative with a decrease in successive values exceeding 0.75 nT. The line in each panel gives the mean of 1-min values at epoch time ($t - t_o$) and the gray area around it is plus and minus one standard error in the mean. The left hand panels are for the IMF and parts **(D–J)** of the right hand panels are about the magnetospheric response. From top to bottom the left hand panels are for: **(A)** the IMF B_Z component; **(C)** the IMF B_Y component; **(E)** the IMF B_X component and **(G)** the IMF magnitude, B. Panel **(I)** shows the number of samples n at each ($t - t_o$). The top right-hand panel, **(B)**, is for the IMF factor $B' = B_\perp \sin^4(\theta/2)$ where (where $B_\perp = (B_Y^2+B_Z^2)^{1/2}$, and θ is the IMF clock angle defined as $\theta = \arctan(|B_Y|/B_Z)$. Panel **(D)** is for the transpolar voltage Φ_{PC}; **(F)** the *SMR* geomagnetic index; and **(H)** the *SML* geomagnetic index. The bottom panel, **(J)**, shows the a.c.f of $B' = B_\perp \sin^4(\theta/2)$ for the subset of data contributing to the superposed epoch events, starting from the time of peak B' to illustrate the probability that the IMF factor has changed from its peak value after the southward turning. Vertical dashed lines mark the epoch times at which the mean disturbance peaks and vertical solid colored lines mark the times the parameter returns to its pre-event level (only shown for Φ_{PC} and *SML* because this is greater than 1 day for *SMR* and so off scale). These vertical lines are repeated in part **(J)**. For all superposed epoch panels, the mean observed over a pre-event calibration period of $-4 \le (t - t_o) < -2$ h is shown by the horizontal line. The orange bands is the same as the grey ones, but from a random event time selection procedure repeated 500 times and then averaged using the same number of event epoch times. This has been normalized by multiplying by the ratio of the calibration period means for the observed and the randomly-selected events so that the magnitude of the observed event response can be evaluated.

space inherent in solar wind-magnetosphere coupling that would have an effect at all lags.

Figure 5 does not say anything explicitly about the response lags and evolution times of the magnetosphere. To study their influence, **Figure 6** presents a superposed-epoch study of the response to southward turnings of the IMF. These are here defined as when the 30-min means of IMF B_Z, $< B_Z >_{30min}$, change from positive to negative with a decrease in successive $< B_Z >_{30min}$ values of exceeding 0.75 nT. This definition of a southward turning was chosen as a compromise between selecting large amplitude events and having a large number of events. Various values of this threshold and averaging timescale were adopted in a sensitivity study and the character of the responses in superposed epoch plots was always the same and only differed in amplitude: response lags only differed by 5 min at most, which can be used as a general uncertainty estimate. The above definition yielded 160 distinct usable events (at times t_o) of near-continuous data for all parameters from the years 1996–2019, inclusive. One-minute values at epoch times (t–t_o) are then averaged together. In the case of Φ_{PC}, these 1-min values were linearly interpolated from the hourly data. Values are excluded for which $(t_o - t) \ge (t_o - t_o')$ or $(t - t_o) \ge (t_o'' - t_o)$, where t_o' and t_o'' are the times of the events, respectively, preceding or after the one at time t_o. This means that sample numbers n are lower at larger $|t - t_o|$. **Figure 6I** shows the variation of n with ($t - t_o$): by ($t - t_o$) = 16 h n falls from 160 to 120, much of that fall occurring at small ($t - t_o$) because of a tendency for large southward-turning events to cluster. Note there is also some noise in the variation of n caused by short data gaps.

The top left panel, **A**, of **Figure 6** shows the average variation of B_Z (in GSM) around the events and shows that, on average, B_Z reaches is maximum southward value about 15 min after the southward turning and then returns towards zero with an approximately $(1\text{-}e^{-t/\tau})$ variation and an e-folding timeconstant $\tau \approx 2$ h. This plot also reminds us that strong southward turnings tend to be preceded by strong northward IMF. Panels **C** and **E** show there is almost no net signature of these events in the other two IMF components and Panel **G** shows the IMF magnitude B peaks at the time of the southward turnings, an effect of selecting large swings in B_Z. Panel **B** also presents IMF data and shows the

factor $B' = B_{\perp}\sin^4(\theta/2)$ that is designed to be a monotonic, unipolar indicator of solar wind coupling (Lockwood and McWilliams, 2021b; Lockwood, 2022b) that peaks when the southward component is strongest.

Panels **D**, **F** and **H** show the lagged response of magnetospheric state indicators Φ_{PC}, *SMR* and *SML* for which the peak in average disturbance associated with the southward turning is at $(t–t_o)$ of 1.5, 6.9 and 2.0 h, respectively. Pre-event conditions are taken to be the mean over the interval $-4\text{ h} < (t–t_o) \leq -2\text{ h}$, shown by the horizontal dashed lines. The return to these pre-event conditions takes, respectively, 11.0 h, several days (off scale) and 11.3 h, for Φ_{PC}, *SMR* and *SML*. The bottom right panel, **J**, shows the a.c.f. of the IMF $B' = B_{\perp}\sin^4(\theta/2)$ factor with lag zero at the time of peak negative B_Z, which gives us an indicator of the probable change of the IMF coupling factor component from the peak southward values in the event by the time that the terrestrial state indicators are reaching their peak disturbance level or have returned to pre-event values. Note that this a.c.f is derived for only the data that contributed to the superposed epoch plots and it falls somewhat more rapidly with lag than that shown in **Figure 5** for the same parameter but for the whole dataset. This means the IMF coupling function factor B' varies somewhat more rapidly around times of large southward turnings. **Figure 6** shows that the solar wind forcing is always likely to have changed by the time peak disturbance is reached and almost certain to have by the time the system takes to return to pre-disturbance levels. For these reasons we should regard the magnetosphere-ionosphere-thermosphere system as usually a non-equilibrium system.

If we integrate the excess Φ_{PC} above the pre-event level between $(t–t_o) = 0$ and $(t–t_o) = 11.0$ h (the epoch time at which the average Φ_{PC} returns to its pre-event level) we get the average open flux generated and transported over the polar cap following the southward turning is about $\Delta F = 0.218$ GWb. As discussed earlier, this is typical of the antisunward transport seen in substorm growth phases in both observations and models.

THE EXPANDING-CONTRACTING POLAR CAP (ECPC) MODEL AND DEPARTURES FROM EQUILIBRIUM

Because electric fields do not, in general, map from interplanetary space to the ionosphere, we need to re-consider why magnetopause and tail reconnection drive ionospheric convection. This was why, 30 years ago this year, we introduced the Expanding-Contracting Polar Cap (ECPC) model (Cowley and Lockwood, 1992). To do this, we introduced the concept of a zero-flow equilibrium magnetospheric configuration for a given amount of open flux, F_o. If such an equilibrium is ever attained is unlikely: there have been times when something close to it appears to have been reached (e.g., Farrugia et al., 2007); however, it is not necessary to know if equilibrium is ever attained. Note this is separate to the question of whether or not the magnetosphere ever loses all open flux and becomes fully closed: that would be the special case of a no-flow equilibrium for open flux $F_o = 0$.

In a "gedanken experiment," consider what would happen in the hypothetical case that reconnection ceased completely, in both the dayside magnetopause and the cross tail current sheet, at a time when the open magnetospheric flux was F_o. Without any reconnection, that open flux value remains constant thereafter. All open flux would be soon removed from the dayside and appended to the tail by the solar wind flow. Pressure equilibrium would become possible between the eroded dayside magnetic flux and the dayside magnetosheath which would depend on the solar wind dynamic pressure and on how much open flux had been removed and appended to the tail (i.e., on the value of the open flux F_o). Because the open field lines are embedded in the solar wind flow they would be extended antisunward and so in the near-Earth and middle tail they would eventually become aligned with the solar wind velocity. Consider the last field line to be opened before the reconnection ceased and let Q be the point where it passes through the magnetopause and P be the point where it becomes parallel to the solar wind flow in the tail lobe–the X coordinates of these points are marked in **Figure 1B**. The field line passing through the point Q is moving antisunward and in interplanetary space it experiences the same dawn-dusk electric field E_Y that it did when it was opened. To first order, the point P is where the tail reaches is asymptotic radius R^* (Nakamura et al., 1997; Tsyganenko, 2013; Liu, et al., 2015), and also where the lobe field strength falls to an almost constant value (Fairfield and Jones, 1996; Slavin et al., 1983). Both of these typically occur at $X = X_P$ between about $-60R_E$ and $-120R_E$. Using a typical solar wind speed of 400 km s^{-1}, MHD simulations show it takes open field lines of order an hour after opening to reach these distances down the tail. Hence for there to be no open field lines threading the magnetopause sunward of Q (as in **Figure 1B**) requires the IMF be northward (and potentially quite strongly northward to shut off all reconnection that opens closed field lines) for at least about 1 h. At P the antisunward motion of open field lines threading the magnetopause at Q (or further down the tail) is not causing any field-perpendicular motion and so the electric field there is zero. This means that there are changes in the field in the furthest tail (between P and Q) that inductively decouple the electric fields and the solar wind flow is driving no flow sunward of P. As Q moves away from the Earth so does P and both attain velocities in the $-X$ direction that are super-Alfvénic and so information about the tail beyond P cannot propagate back to the near-Earth and middle tail. Hence equilibrium is established sunward of P even though tailward of P is not in equilibrium. Because pressure equilibrium sunward of P is established between the magnetosheath and the tail magnetosphere, all flow in the magnetosphere sunward of P ceases. Again, the details of this equilibrium will depend on the solar wind pressure and on the open flux F_o (e.g., Lin et al., 2010; Liu et al., 2015). Hence we arrive at the concept of a zero-flow equilibrium in the magnetosphere-ionosphere system, for a given value of open flux, F_o.

Note that this "no-flow equilibrium" in the complete absence of both magnetopause and tail reconnection will be rarely be achieved, and may never be so fully. The reason is that even after the most prolonged periods of northward IMF, the tail never goes away and so locations in the cross tail current sheet where there is

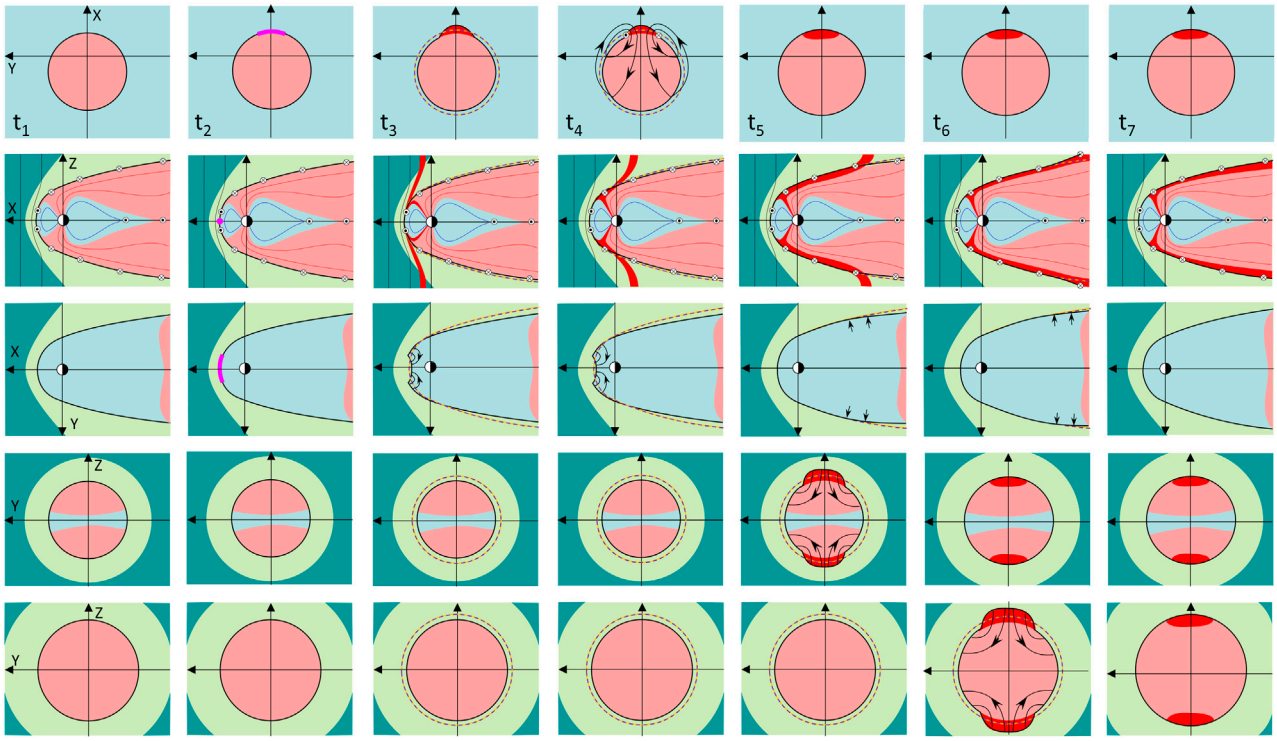

FIGURE 7 | Schematics of the expanding-contracting polar cap (ECPC) model predictions of the evolution of the magnetosphere-ionosphere system in response to an isolated pulse of magnetopause reconnection, generating newly-opened flux, shown in red. The colored regions and lines are defined in the legend to **Figure 8**. The seven columns are for increasing times from t_1 to t_7. Axes in the GSM frame are defined in the left-hand plot for each row. From top to bottom rows show: the ionospheric polar cap looking down from above, the pink area being open field lines and the pale blue being closed; the magnetosphere viewed from the dusk flank with dark green showing the undisturbed solar wind and light green showing the magnetosheath; the equatorial magnetosphere viewed from the north; the cross-section of the near-Earth tail viewed from downstream from the Earth; and the cross-section of the middle tail viewed from downstream from the Earth. Black lines with arrows show flows, mauve lines and dots an active reconnection site or its ionospheric footpoint; mauve and orange dashed lines show the equilibrium location of the open-closed and magnetopause boundaries for the amount of open flux. In some cases, this is not seen because the boundary in question is at its equilibrium location, in which case it is covered by the black line that shows the current location of the boundary. In the second row, the magnetopause and cross-tail current directions are shown. Note that at times t_5 and t_6 in the equatorial plane (row 3) only short arrows are used to denote the flows associated with the tail flaring increase in, respectively, the mid tail and (at the later time) the further tail. That is because, as shown for the mid-tail cross section at time t_5 (row 4. column 5) and for the further tail cross section at time at time t_6 (row 5, column 6), these flows originate at higher latitudes in both lobes and only descend into the equatorial plane close to the magnetopause.

magnetic shear between oppositely-directed open flux are probable, which means that tail reconnection that closes open flux is probable, even if at a very low voltage.

The key point is not if such a zero-flow equilibrium is ever achieved or not: it is that perturbations by reconnection in either the dayside magnetopause or in the cross tail current sheet will, respectively increase or decrease F_o and, in general, will take the magnetosphere away from that equilibrium. Hence both will excite convection as the magnetosphere-ionosphere system tends towards the equilibrium condition for the prevailing F_o. The observation that convection appears to never completely die away is an indicator that these no-flow equilibria are almost never achieved.

Figures 7, **8** show the sequence of events following, respectively, an isolated burst of reconnection in the dayside magnetopause current sheet and in the cross-tail current sheet. **Figure 7** therefore looks at the flow induced by the open flux being increased by an amount ΔF_o and **Figure 8** at the flow induced by the open flux being decreased by ΔF_o. For simplicity we consider the IMF B_Y component to be zero.

At time t_1, the first column in **Figure 7**, we consider the magnetosphere-ionosphere system in an equilibrium state for an open flux F_o. As explained above, this may never actually occur. The rows in **Figure 7**, from top to bottom, show: the polar caps looking down from above; the ZX plane of the magnetosphere (i.e., a noon-midnight meridian cross section), viewed from the dusk side; the XY plane of the magnetosphere (the equatorial cross section), viewed from the north; a ZY plane at $X = X_1$ (a cross-section cut of the near-Earth tail) viewed from the far tail; and a ZY plane at $X = X_2$ where $|X_2| > |X_1|$ (a cross-section cut of the middle tail) viewed from the far tail. Pre-existing closed flux is colored light blue and pre-existing open flux is shaded pink. The undisturbed solar wind, outside the bow shock, is shaded dark green and the magnetosheath is in pale green.

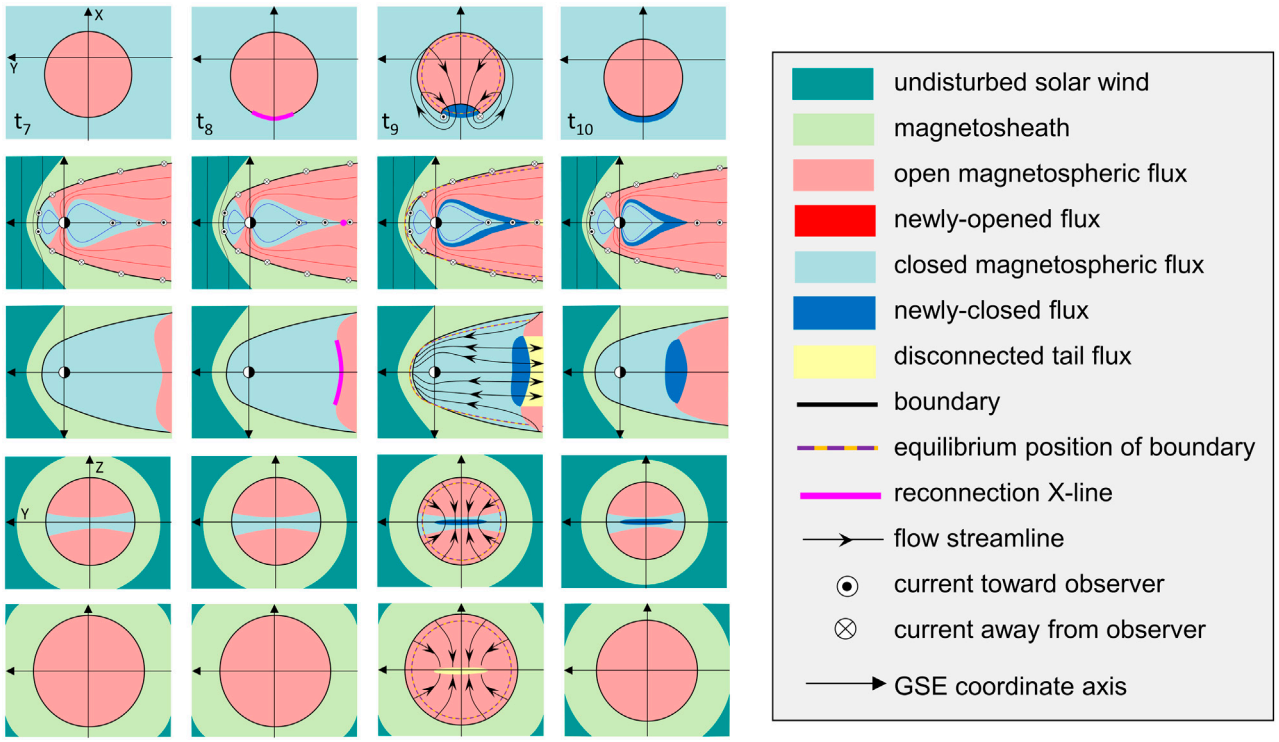

FIGURE 8 | Same a **Figure 7** but showing the response (at times t_7 - t_{10}) to the closure of open flux by a burst of reconnection in the cross-tail current sheet. The newly-closed flux is shown in dark blue.

At time t_1 there is no magnetospheric flow, by definition, because the magnetosphere system is at its zero-flow equilibrium state. At time t_2 a subsolar reconnection X-line forms, shown by the mauve line (this appears as a mauve dot in the *XZ* plane and in the view of the ionosphere the mauve line is the magnetic footprint of the X-line). Reconnection at this X-line starts just after t_2 and persists until time t_3 when it ceases, by which time it has generated an open flux ΔF_o (and hence the average reconnection voltage is $\Delta F_o/\{t_3 - t_2\}$). The newly-opened flux generated by this reconnection burst is colored red.

Initially no flow that contributes to convection circulation and the Dungey cycle commences in the ionosphere. (However, there are likely to be oscillatory flows associated with transient filamentary field aligned currents and phenomena such as Alfvén waves). While the newly-opened flux tube threads the dayside magnetopause, the magnetopause current $\underline{\mathbf{J}}$ is from dawn-to-dusk and the point where it threads the magnetopause moves poleward under the so-called magnetic "tension" force in the reconnection outflow jet. This tension force acts normal to the newly-opened field lines only where they are curved and in such a way as to straighten them. (The name tension is somewhat misleading because, unlike a taught wire or elastic band, the force must necessarily disappear once the field line has straightened). In addition, it causes flow only where there is insufficient magnetic or plasma pressure to oppose the straightening of the field lines: this must necessarily be the case in the dayside magnetopause when the field line curvature has suddenly been created by the reconnection process. In summary, while the field line is only shortening there is no new poleward force on the ionospheric footpoint of the newly-open field lines (in the cusp region). Hence new open flux has been generated but poleward flow does not commence until the field line has straightened (after which the newly opened flux is moving poleward because of the magnetosheath flow). Consequently, the dayside ionospheric open-closed field line boundary must migrate equatorward. We expect the delay before ionospheric flow starts to be shorter if the reconnection site is at higher latitudes as the field lines have less distance to travel before they straighten. We also expect the delay to be greater/shorter in the summer/winter hemisphere, respectively, because the dipole tilt favors reconnection sites that are shifted from the subsolar point to higher latitudes in the winter hemisphere (*see* Lockwood et al., 2020c and references therein). This means that not only do newly-opened field lines in the summer/winter hemisphere have to travel longer/shorter distances around the magnetopause before they straighten, but initially the tension force is antiparallel/parallel to a component of the magnetosheath flow.

This delay and the consequent erosion of the dayside ionospheric open-closed boundary must occur to some degree.

The reason is that it takes at least an Alfvén wave travel time down the dayside field lines (t_f, typically a minute) before there can be any response in the ionosphere and in that time the topological open-closed boundary must erode equatorward. The magnetic flux in this erosion is $t_f\,\Delta\Phi_D$ and so it covers an area in the ionosphere of $\{t_f\,\Delta\Phi_D\}/B_i$ where B_i is the ionospheric magnetic field strength and $\Delta\Phi_D$ is the increase in magnetopause reconnection voltage. The fact that the stress balance in the ionosphere does not change initially adds an additional delay δt before ionospheric flow commences and the eroded area is $\{(t_f + \delta t)\Delta\Phi_D\}/B_i$. Lu et al. (2002) used flows inferred from magnetometer network data in response to a sudden southward turning and estimate that $(t_f+\delta t)$ is 9 min. Throp et al. (2005) and Lockwood et al. (2006) studied the response to a more gradual southward turning (a rotation in clock angle) using global images of the proton aurora and observations of flows from the SuperDARN radar network. The eroded area after the IMF turned southward could be monitored directly in the proton aurora due to solar wind protons precipitating down the newly-opened field lines and was clearly and directly observed. Even for this gradual southward turning event, Lockwood et al. (2006) find $(t_f+\delta t)$ = 9.7 min with an uncertainty range (at the 80% confidence level) of between 8.4 and 10.9 min. The ionospheric flows seen in both events, with new flow cells initially centered on the dayside, were consistent with those predicted by the ECPC model (**Figure 7** at time t_4) and were modelled by Lockwood et al. (2006) using the quantitative implementation of ECPC by Lockwood and Morley (2004). This delay and patterns of flow were first reported by Lockwood and Cowley (1992) using data from the CDAW-6 interval, an example for which $(t_f+\delta t)$ was 12.5 min.

In contrast to the lagged response in the ionosphere, flows commence in the equatorial dayside magnetosphere immediately the reconnection starts. Sunward flows in the magnetosphere are inflows to the reconnection site and continue to allow the dayside magnetopause to relax back sunward where it has been eroded Earthward by the poleward removal of the opened flux along the magnetopause.

After time t_3 the magnetopause reconnection ceases and so the open flux remains constant at $(F_o + \Delta F_o)$ and the equilibrium location of the magnetopause has changed, now having reduced flux on the dayside but more flux in the tail. Because the ionosphere is incompressible the equilibrium polar cap is larger and drawn here as remaining circular, which we can consider to be the minimum energy configuration with the surrounding closed field line region. The new equilibrium locations of the magnetopause and the OCB in the ionosphere are shown by mauve and orange dashed lines. The reconnection burst leaves the ionospheric open-closed boundary around noon equatorward of its new equilibrium position but everywhere else poleward of it. At the time t_4 ionospheric flows have begun which are poleward around noon and equatorward at all other local times–these are flows that bring the OCB back towards its new equilibrium location. Note at this time, the equilibrium location of the tail magnetopause has flared outward but no flow has commenced because the newly open flux has not yet reached $X = X_1$. This happens at time t_5 by when almost all ionospheric flow has ceased because the OCB is now close to its new equilibrium position. As soon as the newly open flux arrives at $X = X_1$ it forms bulges on the magnetopause that the pressure of the magnetosheath flattens giving the flows shown which bring the magnetopause back towards its new equilibrium location. Some time later (at time t_6) this sequence is repeated at $X = X_2$ when the newly-open flux has reached that far down the tail. By the time t_7 all flow has ceased because both the OCB and the magnetopause have reached their new equilibrium locations, at least for the range of the X coordinate covered by the schematics.

Figure 8 shows the corresponding sequence for a burst of tail reconnection. If we continue from t_7 in **Figure 7**, we start from an equilibrium magnetosphere for an open flux $(F_o + \Delta F_o)$. At time t_8 a reconnection X-line forms in the cross tail current sheet (mauve line): this time will usually be close to onset of the expansion phase of a substorm cycle. Between t_7 and t_8 this reconnection line closes a flux of ΔF_o (an average reconnection voltage of $\Delta F_o/\{t_8 - t_7\}$), returning the open flux to F_o. Equilibrium for this open flux has less magnetic flux in the tail and more on the dayside. The dark blue patch is the newly closed field flux. Flows in the ionosphere and magnetosphere are to bring the existing locations of boundaries from their present position toward the equilibrium positions for the new open flux F_o.

Note that at no time in this gedanken experiment has steady-state mapping of electric field been invoked, and so inductive changes in the magnetospheric magnetic field configuration have been allowed, whereas they are not allowed if electric fields are mapped. And yet flows and changes in the ionosphere have been generated by the reconnection processes occurring in the magnetosphere.

EFFECTS OF SOLAR WIND DYNAMIC PRESSURE

We have reprised our description of the ECPC model in the previous section to make an important point. If one adopts a non-physical mechanism by mapping electric fields in non-steady situations one will make incorrect deductions if the assumed steady state does not fully apply. From the response times and lags, we can infer that the magnetosphere will almost always be recovering from a prior change in solar wind driving and so, rather being in steady state, it is almost permanently recovering from a prior change in either solar wind driving or in the configuration of both the dayside and near-Earth tail from the ever-changing geomagnetic axis tilt (and, in general, its offset from the origin in a geocentric frame) as Earth rotates (Lockwood et al., 2020c, 2021).

The ECPC scenario discussed in the previous section makes an interesting prediction. If we generate a given amount of newly-opened flux, it is the pressure in the magnetosheath at the magnetopause that determines how quickly the system would return towards the new equilibrium location as it is ultimately this pressure that drives the magnetospheric motions that act towards restoring the no-flow equilibrium for the new amount of open flux. The resulting changes in the magnetospheric configuration are communicated to the ionosphere through the field-perpendicular pressure balance between closed field lines and

open field lines and it is this that determines where the field-aligned currents form and what magnitude they have. The pressure on the magnetopause depends on the dynamic pressure of the upstream solar wind: this applies throughout the dayside and in the near-Earth and middle tail where the tail is still flaring (i.e., where the tail radius increases with increasingly negative X). Hence the ECPC concept predicts that the response time of the magnetosphere-ionosphere system will be shorter if the wind dynamic pressure is greater because the restoring force per unit area is greater for a larger P_{SW} for a given F_o and ΔF_o.

Sorting by Solar Wind Dynamic Pressure, P_{SW}

To look for such an effect, we here divide the 160 examples of southward turnings used to compile **Figure 6** into two subsets of 80 samples each. To do that, we used the dynamic pressure P_{SW}, averaged over the 3 h after the southward turning, $<P_{SW}>_{(0-3h)}$. An interval of 3 h was chosen because it is enough to cover most of the length of the tail where it is increasing in radius with -X and so P_{SW} has an influence on pressure balance at the magnetopause. It was found a threshold value of $<P_{SW}>_{(0-3h)}$ of 6.5 nPa divided the southward turning events into two equal-sized datasets of 80 events each. The superposed epoch study shown in **Figure 6** was then repeated for the $<P_{SW}>_{(0-3h)} \geq 6.5$ nPa and $<P_{SW}>_{(0-3h)} <$ 6.5 nPa subsets: the results are shown by, respectively, the left and right columns in **Figure 9**. The top four rows shows parameters presented in **Figure 6**, but the bottom row is for P_{SW}. Panels **A**–**E** are for the high-pressure cases, panels **F**–**J** for the low-pressure cases.

Panels **E** and **J** show the effect of the high-P_{SW} versus low-P_{SW} sort on the average variation of P_{SW} during these events: the high-pressure events show a pronounced peak in average P_{SW} at the time of the southward turning (panel **E**) that is almost completely absent in the averages for the low pressure events (panel **J**): indeed, for the low-pressure events, P_{SW} falls below the average value seen before the southward turning for all positive (t–t_o), whereas for the high-pressure events this only happens at (t–t_o) > 4 h. Panels **A** and **F** show that the average behavior of the IMF B_Z component is very similar for these two event subsets. However, the other panels show a markedly different responses in the magnetospheric state indicators. To enable us to contrast high and low pressure cases, the responses in the terrestrial indices are re-plotted in **Figure 10**. These variations are the same data as shown in parts **C** - **H** of **Figure 9** but in each case, the changes relative to the pre-event mean, $\Delta\Phi_{PC}$, ΔSMR and ΔSML, are plotted.

Comparing panels **B** and **G** of **Figure 9** (and panel **A** of **Figure 10**) we see that the amplitude of the transpolar voltage Φ_{PC} response is greater for the case of high-P_{SW} data subset. However, the response for the low-P_{SW} data subset lasts longer: it takes 13.8 h before the average Φ_{PC} is returned to pre-event levels, whereas this takes just 6.3 h for the high-P_{SW} dataset. If we integrate the mean additional Φ_{PC} (over the pre-event levels) after the events, we obtain an estimate of the average extra flux transported over the polar cap caused by the southward turning: for the high-P_{SW} cases it is $\Delta F = 0.225 \pm 0.004$ GWb and for the

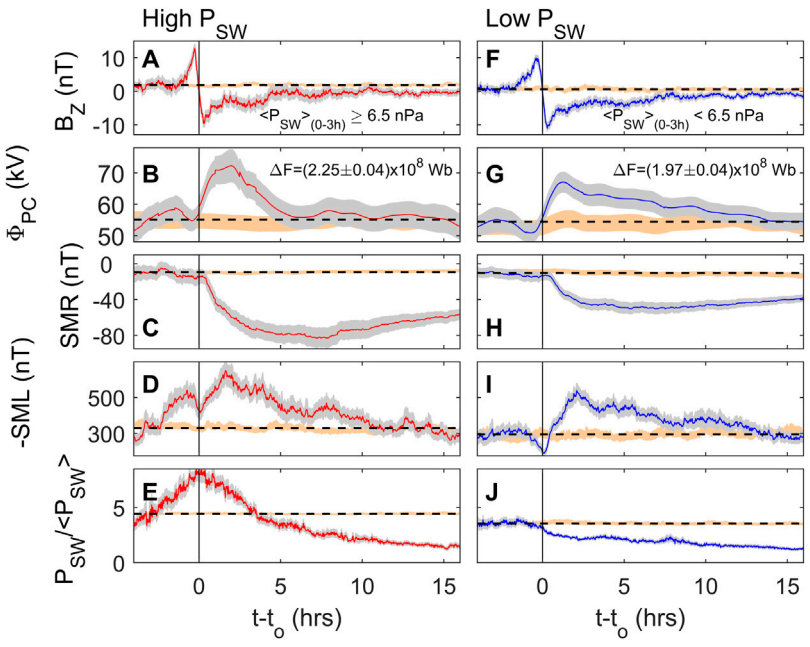

FIGURE 9 | Superposed epoch study illustrating the effect of solar wind dynamic pressure, P_{SW}, on the events discussed in **Figure 5**. The southward turning are divided into two sets with P_{SW}, averaged over the 3 h after the southward turning, $< P_{SW} >_{(0-3h)}$, exceeding or less than 6.5 nPa, that being the threshold that divides the data into two equal sets of 80 events. The format is as in **Figure 5** with left hand panels (and red lines) for $< P_{SW} >_{(0-3h)} \geq 6.5$ nPa and right-hand columns (and blue lines) for $< P_{SW} >_{(0-3h)} <$ 6.5 nPa. The bottom panels are the superposed epoch plots of the solar wind dynamic pressure, P_{SW}.

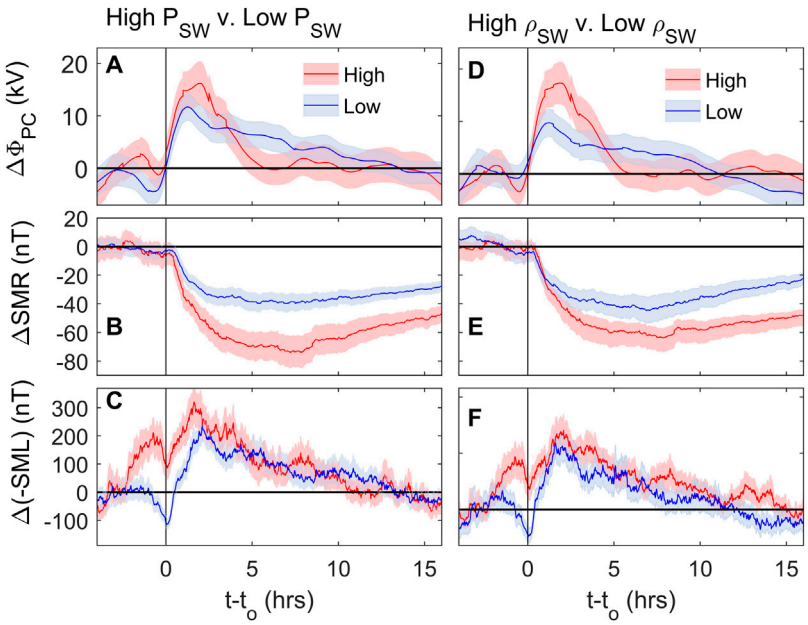

FIGURE 10 | Comparison of the terrestrial responses to the southward turning events of the IMF for (left column, parts **A**, **B** and **C**) high- and low-solar wind dynamic pressure P_{SW} and (right column, parts **D**, **E** and **F**) high- and low-solar wind mass density ρ_{SW}. In both cases red lines with pink uncertainty bands are for the "high" event subset and blue lines with pale blue uncertainty bands are for the "low" cases. Rows from top to bottom are for (**A** and **D**) transpolar voltage Φ_{PC}, (**B** and **E**) the *SMR* index, (**C** and **F**) the *SML* index. Note that these plots are similar to those in (left column) **Figure 9** and (right column) **Figure 12** and are plotted here with high and low cases on a single panel to allow comparison. However, they are not quite the same as, to allow comparison, the pre-event means have here been subtracted from the values at general elapsed time (t-t_o) to show the response and so the plots show the changes in Φ_{PC}, *SMR* and *SML*, denoted by $\Delta\Phi_{PC}$, Δ*SMR* and Δ*SML*, respectively.

low-P_{SW} case it is 0.197 ± 0.004 GWb. A large contribution to these uncertainties comes from the uncertainty in the average pre-event voltage. These two values are very similar, but there is a difference of 0.028 ± 0.008 GWb. The origins of this difference are discussed in **Section 6**. However, the main point we want to stress in this section is that there is a marked difference in how this integrated flux transport is manifest in the ionosphere with larger-amplitude but shorter-duration burst of voltage for the high-P_{SW} data subset. This effect of P_{SW} is well predicted by the ECPC model, as discussed above.

There is a greater difference in the effects on the *SMR* geomagnetic activity index between the high-P_{SW} and low-P_{SW} cases: the average response to the southward turning event in the *SMR* index data (panels **C** and **H** of **Figure 9** and panel **B** of **Figure 10**) is considerably weaker for the low-P_{SW} cases. The same effect is seen, but much less marked, in *SML* from comparison of panels **D** and **H** of **Figure 9** (and panel **C** of **Figure 10**) that shows the response in the *SMR* index is consistently weaker for the low-P_{SW} cases.

Before discussing these results in greater detail, we should also look at the average variations in other interplanetary variables during these events. These are shown in **Figure 11**. Panels **B** and **G** show the solar wind number density, N_{SW}, which has very similar variations to those for P_{SW} (shown in the bottom panels of **Figure 9**). However, there are also variations in the mean ion mass of the solar wind, m_{SW} (panels **C** and **H**) and the solar wind speed, V_{SW} (panels **D** and **I**) that contribute. These variations are consistent with the large IMF southward turning events being caused mainly by impacts of coronal mass ejections or the compressions in interaction regions ahead of fast flow streams.

The difference in the variations of average V_{SW} for the two sets of cases (seen in the comparison of panels **D** and **I** of **Figure 11**) is significant for three reasons. Firstly, it has an influence on the interplanetary electric fields, $E_Y = -V_X B_Z$. Panels **A** and **F** of **Figure 11** contrast the variations of the half-wave rectified dawn-to-dusk electric field, E_Y' (the rationale for using half-wave rectification is that subsolar reconnection is greatly reduced in rate when the IMF points northward). The higher average V_{SW} for the high-P_{SW} cases has a marked effect and although the average E_Y' variation is very similar in form for the two cases, it is of smaller amplitude for the low-P_{SW} cases. The second effect of V_{SW} is on variations of the estimated power input to the magnetosphere, P_α. Because power in the solar wind is delivered predominantly in the form of kinetic energy of the particles (Lockwood, 2019), the solar wind speed also influences the power input to the magnetosphere. Panels **E** and **J** show P_α, P_α/P_o, as a ratio of its overall mean value $P_o = \langle P_\alpha \rangle_{all}$. The third effect of V_{SW} is on the time taken for newly-opened field lines to be appended to the tail: for the average speeds shown in **Figure 11**, the open field lines in the Stern Gap have, on average, moved 283 R_E antisunward after 1 h for the low-P_{SW} cases but 334R_E for the high-P_{SW} cases. Hence there are a number of effects of varying P_{SW} that are actually caused by solar wind

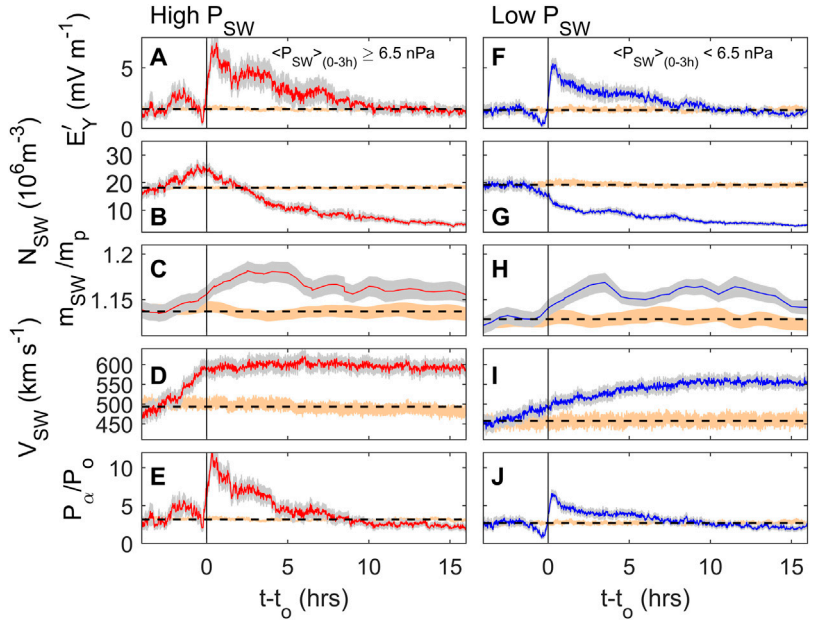

FIGURE 11 | Superposed epoch study of the interplanetary conditions for the events studied in **Figure 9**. The left hand column are for the 80 high-P_{SW} southward turnings of the IMF and the right hand panels for the low-P_{SW} set. From top to bottom panels are for: (**A** and **F**) the half-wave rectified dawn-to-dusk electric field, E_Y'; (**B** and **G**) the solar wind number density, N_{SW}; (**C** and **H**) the solar wind mean ion mass in amu m_{SW}/m_p; (**D** and **I**) the solar wind speed, V_{SW}; and (**E** and **J**) the estimated power input into the magnetosphere, P_α, as a ratio of its overall mean value, P_o, as computed by the procedure and formulae of Vasyliunas et al. (1982).

speed V_{SW} rather than being specifically caused by pressure effects.

Sorting by Solar Wind Mass Density, ρ_{SW}

To eliminate the potential additional effects of solar wind speed V_{SW} on the sorting criterion we here repeat **Figures 9** and **11**, but divide the data into two equal size datasets by the mass density of the solar wind $\rho_{SW} = m_{SW}.N_{SW}$. This influences the dynamic pressure $P_{SW} = \rho_{SW}V_{SW}^2$ and the power input to the magnetosphere $P_\alpha = B^{2\alpha}V_{SW}^{(7/3-2\alpha)}\rho_{SW}^{(2/3-\alpha)}sin^4(\theta_{GSM}/2)$. The results are shown in **Figures 12** and **13**. The high ρ_{SW} and low ρ_{SW} terrestrial responses are compared in the right-hand panels of **Figure 10**. Comparing parts **D** and **I** in **Figure 13** we can see this gives more similar (but not identical) variations in V_{SW} and hence the E_Y' variations (Panels **A** and **F**) and the P_α variations (Panels **E** and **J**) are also much more similar than they are for the P_{SW} sort shown in **Figure 11**. In fact, for this sort, the low-ρ_{SW} cases give very slightly higher average V_{SW}, E_Y' and P_α after the event. Note that differences in the V_{SW} variations have not been eliminated by moving from a P_{SW} sort to a ρ_{SW} sort, however they have been reduced and we know V_{SW} did not enter into the event selection and that remaining effects are caused by inter-relations between the parameters of interplanetary space. Comparison of parts **C** and **H** of **Figure 12** (panel **E** of **Figure 10**) and of parts **D** and **I** of **Figure 12** (panel **F** of **Figure 10**) show that the geomagnetic responses are more similar for the data sorted by ρ_{SW} than they were for P_{SW}, but that the response to the southward turning is still larger for the high-ρ_{SW} cases than for the low-ρ_{SW} cases. Panels **B** and **G** of **Figure 11** (panel **D** of **Figure 10**) show that the extra magnetic flux transport following the southward turning is again similar in the high-ρ_{SW} and low-ρ_{SW} cases, being 0.199 ± 0.004 GWb per event, on average, for the high-ρ_{SW} cases and 0.186 ± 0.004 GWb per event for the low-ρ_{SW} cases. As for the high- and low-P_{SW} cases the difference between the two sets of events, in terms of total flux transport, is still very small, but it does appear to be larger than uncertainties. This is discussed further in **section 6**. The same behavior for Φ_{PC} is seen as in **Figure 9**, with the high-ρ_{SW} cases giving a larger-amplitude but shorter-duration response than the low-ρ_{SW} cases, but the total flux transport being only marginally greater for the high-ρ_{SW} cases.

DISCUSSION AND CONCLUSION

Induction effects associated with magnetic field changes in the magnetosphere mean that mapping electric fields from interplanetary space to the ionosphere is only valid for steady-state conditions. Steady state can be achieved in data series if we average over long enough timescales. From the statistical analyses of Milan et al. (2021) this implies averaging over about 4 h in the cases of substorms but over of order 12 h for steady convection events or sawtooth events. In addition, as discussed below, the rotation of the Earth means that equilibrium concepts are only really valid when averaging over a whole number of days.

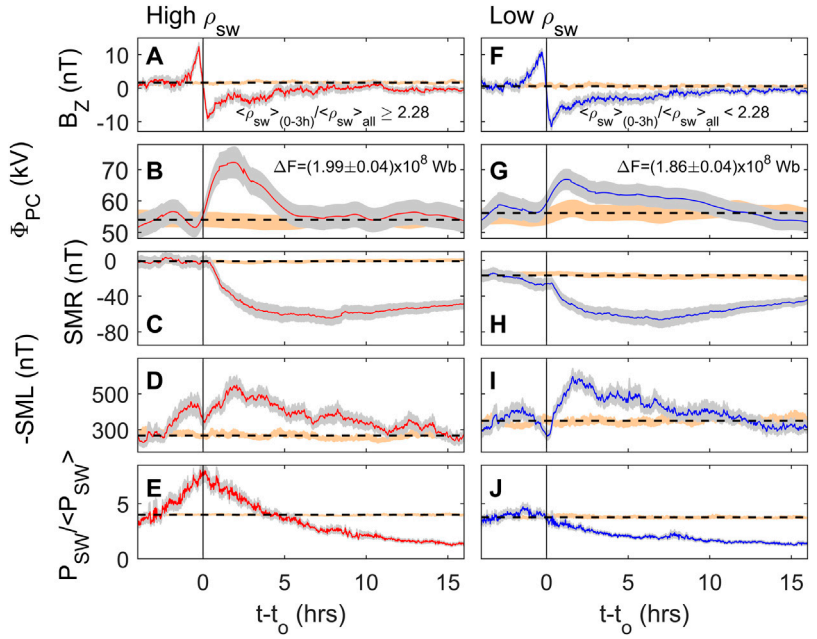

FIGURE 12 | The same as **Figure 9** but with the 160 southward turning events sorted by the solar wind mass density, ρ_{SW}. The left hand panel are for the events with normalized ρ_{SW} over the subsequent 3 h $<\rho_{SW}>_{0-3h}/<\rho_{SW}>_{all}$ (where $<\rho_{SW}>_{all}$ is the mean value for all data) greater than or equal to the median value for the events of 2.58; the right-hand panel are for the events with $<\rho_{SW}>_{0-3h}/<\rho_{SW}>_{all} < 2.58$.

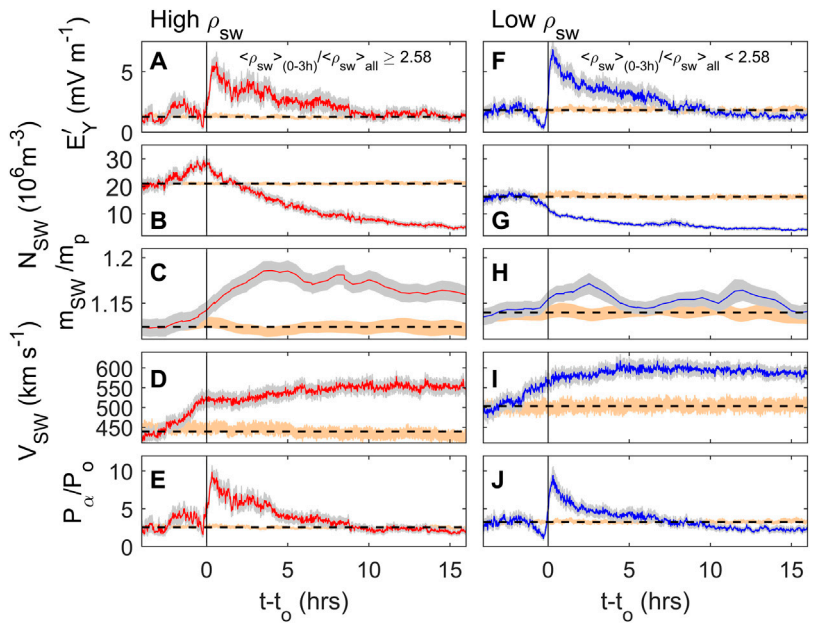

FIGURE 13 | The same as **Figure 11** but with the 160 southward turning events sorted by the solar wind mass density, ρ_{SW} as in **Figure 12**.

Effects of Solar Wind Dynamic Pressure on Convection Response

We have used superposed epoch studies of 160 clear southward turnings of the IMF that give near-continuous data in all parameters. The transpolar voltage data for all subsets of these events show that they cause an average of close to 0.2 GWb of additional magnetic flux transfer from the dayside to the nightside. As discussed in the introduction,

this value is consistent with the total rise in tail lobe field seen in substorm growth phases (e.g., McPherron et al., 1993), as well as with numerical global MHD model simulations of the effects of strong southward turnings of the IMF (Gordeev et al., 2017), with inferences from polar cap expansion and contraction seen in global auroral images (Milan et al., 2003; 2012) and with the latitudinal variations of the locations of the Region 1 field-aligned current sheets (Clausen et al., 2012; Milan et al., 2021).

Subdividing the southward turnings into two datasets of 80 cases each using the solar wind dynamic pressureP_{SW}, averaged over the 3 h after the southward turning, has allowed us to look for an effect of dynamic pressure on these strongly southward IMF events. We note that **Figure 4C** shows dynamic pressure increases transpolar voltage for northward-IMF conditions but as the IMF becomes more southward the effect diminishes and is not present for the most southward IMF. Also, note that by taking averages over 3 h we are looking at the effect of the average dynamic pressure and not the transient effects of pressure increases that are complicated by transient phenomena such as travelling convection vortices. We find that the integrated flux transport over the polar cap is only slightly greater in the high-P_{SW} cases, being 0.225 ± 0.004 GWb compared with 0.197 ± 0.004 GWb for the low-P_{SW} cases. The difference is therefore small but significant. To check that this is not associated with the solar wind speed influence on the interplanetary electric field, we repeated the analysis using the mass density of the solar wind, ρ_{SW}, again averaged over the 3 h after the southward turning and again dividing the data into two subsets of 80 cases. The integrated flux transport over the polar cap was only marginally higher for the high-ρ_{SW} cases, being 0.199 ± 0.004 GWb compared to 0.186 ± 0.004 GWb for the low-ρ_{SW} cases. Hence sorting using high- and low-ρ_{SW}, the same sense of difference is seen as for the P_{SW} sort. The difference in total flux transport caused was 0.013 ± 0.006 GWb (a 7% increase for the high-ρ_{SW} cases relative to the low-ρ_{SW} cases). Lockwood and McWilliams (2021b) found that the optimum coupling function for transpolar voltage Φ_{PC} depended only very weakly on ρ_{SW}, finding a ${\rho_{SW}}^b$ dependence with the best-fit exponent of $b = 0.018$. The high ρ_{SW} dataset gives $[\rho_{SW}]_{hi}/<\rho_{SW}>_{all} = 3.72$ whereas $[\rho_{SW}]_{lo}/<\rho_{SW}>_{all} = 1.48$ which predicts a factor $([\rho_{SW}]_{hi}/[\rho_{SW}]_{lo})^b = 1.02$ (a 2% increase). Hence the increase in total flux transport found here for the high ρ_{SW} cases is somewhat larger that we would expect from the optimum coupling function of Lockwood and McWilliams (2021b). An explanation of this discrepancy is provided by **Figure 13** that shows that, due to correlations between interplanetary parameters, the solar wind velocity V_{SW} is also higher after for the high ρ_{SW} cases with a ratio of average values after the event of about $[V_{SW}]_{hi}/[V_{SW}]_{lo} \approx 580/520$ and using the ${V_{SW}}^a$ (with exponent $a = 0.55$) dependence found by Lockwood and McWilliams (2021b), this gives a factor $([V_{SW}]_{hi}/[V_{SW}]_{lo})^a = 1.05$ (a 5% increase). Hence a larger part of the increase in total flux transport after the event (about 5% of the 7%) can be attributed to the fact that V_{SW} is somewhat higher after the high ρ_{SW} cases. However, there is an additional 2% that does appear to be associated with the increased ρ_{SW} and that is consistent with the coupling function prediction of Lockwood and McWilliams (2021b). We conclude increased solar wind mass density does (very slightly) increase the magnetopause reconnection voltage through increased reconnection rate and/or increased length of the reconnection X-line, as proposed by Scurry and Russell (1991). The effect of increased mass density would be to reduce the cross-section radius of the dayside magnetosphere which we might expect to also reduce the length of the reconnection X-line. Therefore, is seems likely that any effect on Φ_D would be through increased magnetic shear across the dayside magnetopause elevating the reconnection rate along the X-line or *via* the same effect of increased lobe field on the tail reconnection Φ_N.

However, the dominant effect of increased P_{SW} (one that is almost identical in the high/low ρ_{SW} analysis) in that there is a marked effect on the time profile of the flux transfer. For the high-P_{SW} cases, the transpolar voltage is enhanced to larger values soon after the southward turning, but elevated values persist for a shorter time. This effect is predicted by the ECPC model because it is the dynamic pressure that generates the pressure on the newly opened flux that drives the flow acting to return the magnetosphere towards the new equilibrium for the new open flux. The effect defined here is predicted by the ECPC model and cannot arise if electric fields are mapped from interplanetary space to the ionosphere: we know of no other model that can explain it.

The ECPC Model and Effects of Earth Rotation With a Tilted and Eccentric Dipole Axis

We note that, although this effect has been defined using the transient response to southward IMF turnings, the ECPC model has still important implications for understanding solar-wind magnetosphere coupling under even constant interplanetary solar wind conditions. Lockwood et al. (2021) have recently used the ECPC model to closely match all features of the observed fraction-of-year (*f*) - Universal Time (*UT*) pattern of geomagnetic activity (called the "McIntosh" or "equinoctial" pattern). This is seen in the *am* index (and there are corresponding patterns in its two hemispheric sub-indices *an* and *as*). As mentioned earlier, Lockwood et al. (2019a) show that *am* is the most suitable index to use in this context as it is genuinely global and has the most uniform *f-UT* response. Lockwood et al. (2021) show that there are four effects at work in generating this *f-UT* pattern: *1*) the Russell and McPherron (1973) effect of the dipole tilt on the magnetic shear, and hence reconnection rate, at the dayside magnetopause; *2*) the dipole tilt effect on polar ionospheric conductivities; *3*) the dipole tilt effect on the tail geometry; and *4*) the diurnal motions of the geomagnetic poles in a geocentric frame as the Earth rotates. Effects (2) and (3) are dominated by the effect of the dipole tilt on the ability of the solar wind dynamic pressure to squeeze the tail and together they give the basic McIntosh form that varies in amplitude with P_{SW} (Lockwood et al., 2020b, 2021). This is complicated by effect (1), but combining effects (1), (2) and (3) gives does not give the total *UT* variation (averaged over all times of year, *f*) that is seen in geomagnetic activity (Russell, 1989). This is because adding the Russell-McPherron effect to the other two causes *UT* variations in

both the March and September equinox peaks in geomagnetic activity, but these *UT* variations are in antiphase and so cancel each other when averages over all times of year (all *f*) are taken.

Lockwood et al. (2021) show that the observed *UT* variation is consistent with an effect of the diurnal pattern of sunward and antisunward motion of the geomagnetic poles caused by Earth's rotation and the offset of the geomagnetic poles from the rotational axis. This rotation is different in the two poles because of the eccentricity of Earth's dipole axis which does not pass through the center of the Earth. As described by Lockwood et al. (2021), the effect is caused by a motion of the ionospheric polar caps, as a whole, toward and away from the Sun in a geocentric frame (the frames in which the interplanetary electric field is quantified). When a given polar cap (including its diameter, PC) is moving toward/away from the Sun, the transpolar voltage Φ_{PC} is increased/decreased in the geocentric frame (the same frame in which the interplanetary electric field and Stern Gap voltage Φ_{SG} are measured): by **Eq. 1**, this increases/decreases the rate of increase in the tail lobe flux in that hemisphere, dF_L/dt. In this context, it should be noted that the open flux F_o must always be identical in the two hemispheres but, at any X coordinate, the open flux divides into the flux F_d that threads the magnetopause sunward of X and the lobe flux that threads the tail cross-section at that X, F_L. Transfer from the dayside into the lobe (i.e., conversion of F_d into F_L for a given X) is faster for the polar cap that is tipped away from the Sun than the one that is tipped toward the Sun. Hence although F_o is the same in the two hemispheres F_L and dF_L/dt are both generally different in the two hemispheres. This effect of dipole tilt has been demonstrated using an MHD model of the magnetosphere (Lockwood et al., 2020c). The Earth's rotation and the offset geomagnetic poles from the rotational axis therefore cause a diurnal cycle with 12 h in which dF_L/dt was lower in one hemisphere followed by 12 h in which it was lower in the other. The alternate faster loading of the tail in one hemisphere then the other would average out if the offset of the geomagnetic pole from the rotational axis were the same in the two hemispheres; however, it is much larger in the southern hemisphere which leaves a net effect of the Earth's eccentric tilted dipole and causes the marked *UT* variation in global geomagnetic activity that is superposed on the dipole tilt pattern to give the total McIntosh pattern. Adding this effect to effects (1), (2) and (3), Lockwood et al. (2021) obtained a very close match to the observed *f*-*UT* patterns for *am* index and its hemispheric sub-indices, *an* and *as*. This effect would not happen if electric field just mapped from the solar wind to the ionosphere and the explanation of the UT variation of geomagnetic activity depends upon the application of the ECPC model.

Hence the equilibrium that the magnetosphere-ionosphere system is constantly in the process of returning toward is not just a function of the amount of open flux in the system, it also depends on both time-of-year, *f*, and the Universal Time, *UT*, through the dipole tilt effects and the (different and antiphase) motions of the geomagnetic poles in a geocentric frame. Hence, even if the solar wind driving is completely constant with time, the response of the magnetosphere-ionosphere-thermosphere system will not be and the ECPC model of that response is still required.

Applications and Limitations of ECPC

Looking at the potential future applications of the conceptual ECPC model we have to also think about its limitations. It is obviously not a full model of the magnetosphere and so there is a wide variety of phenomena that it does not predict. It is a conceptual model and therefore, its major use in quantitative predictions will be in conjunction with other models. Before the present paper looking at pressure effects on convection responses, ECPC has had four main applications. The first has been quantitative in the application of Faraday's law to the open-closed field line boundary in the ionospheric polar cap and its use in understanding and exploiting observations of changes in the area of the polar cap (e.g., Milan et al., 2021 and references therein), particularly during substorm cycles, steady convection events and sawtooth events. A second specific application has been in the interpretation of ionospheric signatures of flux transfer events (transient increases in the magnetopause reconnection voltage, Φ_D) which has grown from the initial papers by Southwood (1987) and Cowley et al. (1991) (*see* reviews by Smith and Lockwood, 1996 and Milan et al., 2016). More recently, ECPC has been applied to understanding UT and time-of year variations in geomagnetic activity and transpolar voltage, as discussed in **section 6.2**. The fourth application is less specific and has been more qualitative in aiding the avoidance of incorrect assumptions about how electric fields map down field lines in interpretations of observations or model simulations of time-dependent events (e.g., Lockwood et al., 2020c).

Because it is an application of the principles of MHD and of Maxwell's equations, all behavior predicted by ECPC should, in principle, also be predicted by numerical MHD models of the magnetosphere. However, there are highly complex issues in ensuring that the lower ionospheric boundary in these models is fully self-consistent with the simulated magnetosphere: the lower boundary of most MHD models has to be at considerably greater altitudes (typically $2R_E$) than the real ionosphere for numerical reasons. A commonly used method to determine the spatial distribution of potential in this ionospheric boundary is to solve a Poisson equation using current continuity in the ionosphere (e.g., Raeder et al., 2001; Ridley et al., 2002; Lyon et al., 2004; Wiltberger et al., 2004). However, Lockwood (1993) pointed out that it is not adequate to just impose a pattern of convection on the ionosphere. The reason is that expanding and contracting an ionospheric convection pattern (without consideration of what are open and what are closed field lines or some other equivalent safeguard) will result in, respectively, closed field lines incorrectly migrating antisunward and open field lines incorrectly moving sunward in the ionosphere. The ECPC does not allow this and so provides a method that could ensure this does not occur; however, this has yet to be exploited in this context.

AUTHOR CONTRIBUTIONS

ML and SC co-wrote the text. ML developed the schematics from SC's originals and also generated the autocorrelations and superposed epoch analysis.

FUNDING

The work of ML at Reading University is supported by the UK Science and Technology Facilities Council (STFC) consolidated grant number ST/R000921/1 and the work of SWHC at Leicester University by STFC Grant number ST/N000749/1.

ACKNOWLEDGMENTS

The work on ML at Reading University was supported by STFC consolidated grant number ST/M000885/1 and by the SWIGS NERC Directed Highlight Topic Grant number NE/P016928/1/. The work of SWHC at Leicester University by STFC Grant number ST/N000749/1. The authors thank Steve Milan and Joe Borovsky for many helpful conversations. The authors acknowledge the use of data from the SuperDARN project and particularly thank Kathryn McWilliams of University of Saskatchewan for processing the data. SuperDARN is a collection of radars funded by national scientific funding agencies of Australia, Canada, China, France, Italy, Japan, Norway, South Africa, United Kingdom and the United States of America. In addition, we are grateful to the staff of the Space Physics Data Facility, NASA/Goddard Space Flight Center, who prepared and made available the OMNI2 dataset used and of L'École et Observatoire des Sciences de la Terre (EOST), a joint of the University of Strasbourg and the French National Center for Scientific Research (CNRS), and the International Service of Geomagnetic Indices (ISGI) for making the *am* index data available. They are also grateful to the many groups who built and operated the instruments that have monitored near-Earth interplanetary space, particularly on the spacecraft ACE and Wind, and to the SuperMAG project for the *SML* and *SMR* indices and acknowledge the following projects and PIs: Intermagnet; USGS, Jeffrey J. Love; CARISMA, PI Ian Mann; CANMOS; The S-RAMP Database, PI K. Yumoto and K. Shiokawa; The SPIDR database; AARI, PI Oleg Troshichev; The MACCS program, PI M. Engebretson, Geomagnetism Unit of the Geological Survey of Canada; GIMA; MEASURE, UCLA IGPP and Florida Institute of Technology; SAMBA, PI Eftyhia Zesta; Chain, PI K. Yumoto; SAMNET, PI Farideh Honary; The institutes who maintain the IMAGE magnetometer array, PI Eija Tanskanen; PENGUIN; AUTUMN, PI Martin Connors; DTU Space, PI Rico Behlke; South Pole and McMurdo Magnetometer, PI's Louis J. Lanzarotti and Alan T. Weatherwax; ICESTAR; RAPIDMAG; PENGUIn; British Antarctic Survey; McMac, PI Peter Chi; BGS, PI Susan Macmillan; Pushkov Institute of Terrestrial Magnetism, Ionosphere and Radio Wave Propagation (IZMIRAN); GFZ, PI Juergen Matzka; MFGI, PI B. Heilig; IGFPAS, PI J. Reda; University of L'Aquila, PI M. Vellante; BCMT, V. Lesur and A. Chambodut; Data obtained in cooperation with Geoscience Australia, PI Marina Costelloe; and the SuperMAG, PI Jesper W. Gjerloev.

REFERENCES

Ahnert, P. (1943). Der Komet 1942 G (Whipple-Fedtke). *Z. Astrophys.* 22, 288.

Alfvén, H. (1950b). *Cosmical Electrodynamics*. Oxford: Clarendon Press.

Alfvén, H. (1950a). Discussion of the Origin of the Terrestrial and Solar Magnetic Fields. *Tellus* 2, 74–82. doi:10.3402/tellusa.v2i2.8540

Axford, W. I., and Hines, C. O. (1961). A Unifying Theory of High-Latitude Geophysical Phenomena and Geomagnetic Storms. *Can. J. Phys.* 39 (10), 1433–1464. doi:10.1139/p61-172

Bergin, A., Chapman, S. C., and Gjerloev, J. W. (2020). A E, D S T, and Their SuperMAG Counterparts: The Effect of Improved Spatial Resolution in Geomagnetic Indices. *J. Geophys. Res. Space Phys.* 125, e2020JA027828. doi:10.1029/2020JA027828

Biermann, L. (1951). Kometschweife und solare Korpuskularstrahlung. *Z. Astrophys.* 29, 274.

Boakes, P. D., Milan, S. E., Abel, G. A., Freeman, M. P., Chisham, G., and Hubert, B. (2009). A Statistical Study of the Open Magnetic Flux Content of the Magnetosphere at the Time of Substorm Onset. *Geophys. Res. Lett.* 36, L04105. doi:10.1029/2008gl037059

Boudouridis, A., Lyons, L. R., Zesta, E., and Ruohoniemi, J. M. (2007). Dayside Reconnection Enhancement Resulting from a Solar Wind Dynamic Pressure Increase. *J. Geophys. Res.* 112, a–n. doi:10.1029/2006JA012141

Boudouridis, A., Lyons, L. R., Zesta, E., Ruohoniemi, J. M., and Lummerzheim, D. (2008a). Nightside Flow Enhancement Associated with Solar Wind Dynamic Pressure Driven Reconnection. *J. Geophys. Res.* 113, a–n. doi:10.1029/2008JA013489

Boudouridis, A., Zesta, E., Lyons, L. R., Anderson, P. C., and Ridley, A. J. (2008b). Temporal Evolution of the Transpolar Potential after a Sharp Enhancement in Solar Wind Dynamic Pressure. *Geophys. Res. Lett.* 35, L02101. doi:10.1029/2007GL031766

Boyle, C. B., Reiff, P. H., and Hairston, M. R. (1997). Empirical Polar Cap Potentials. *J. Geophys. Res.* 102 (A1), 111–125. doi:10.1029/96JA01742

Brambles, O. J., Lotko, W., Zhang, B., Ouellette, J., Lyon, J., and Wiltberger, M. (2013). The Effects of Ionospheric Outflow on ICME and SIR Driven Sawtooth Events. *J. Geophys. Res. Space Phys.* 118, 6026–6041. doi:10.1002/jgra.50522

Burton, R. K., McPherron, R. L., and Russell, C. T. (1975). An Empirical Relationship between Interplanetary Conditions and Dst. *J. Geophys. Res.* 80 (31), 4204–4214. doi:10.1029/ja080i031p04204

Caan, M. N., McPherron, R. L., and Russell, C. T. (1973). Solar Wind and Substorm-Related Changes in the Lobes of the Geomagnetic Tail. *J. Geophys. Res.* 78 (34), 8087–8096. doi:10.1029/ja078i034p08087

Caan, M. N., McPherron, R. L., and Russell, C. T. (1978). The Statistical Magnetic Signature of Magnetospheric Substorms. *Planet. Space Sci.* 26 (3), 269–279. doi:10.1016/0032-0633(78)90092-2

Chapman, S., and Ferraro, V. C. A. (1931). A New Theory of Magnetic Storms. *J. Geophys. Res.* 36 (3), 171–186. doi:10.1029/TE036i003p00171

Clausen, L. B. N., Baker, J. B. H., Ruohoniemi, J. M., Milan, S. E., and Anderson, B. J. (2012). Dynamics of the Region 1 Birkeland Current Oval Derived from the Active Magnetosphere and Planetary Electrodynamics Response Experiment (AMPERE). *J. Geophys. Res.* 117, a–n. doi:10.1029/2012JA017666

Coleman, P. J., Davis, L., and Sonett, C. P. (1960). Steady Component of the Interplanetary Magnetic Field: Pioneer V. *Phys. Rev. Lett.* 5 (2), 43–46. doi:10.1103/physrevlett.5.43

Connor, H. K., Zesta, E., Ober, D. M., and Raeder, J. (2014). The Relation between Transpolar Potential and Reconnection Rates during Sudden Enhancement of Solar Wind Dynamic Pressure: OpenGGCM-CTIM Results. *J. Geophys. Res. Space Phys.* 119, 3411–3429. doi:10.1002/2013JA019728

Cowley, S. W. H. (1991). Acceleration and Heating of Space Plasmas—Basic Concepts. *Ann. Geophys.* 9, 176–187.

Cowley, S. W. H., Badman, S. V., Bunce, E. J., Clarke, J. T., Gérard, J.-C., Grodent, D., et al. (2005). Reconnection in a Rotation-Dominated Magnetosphere and its Relation to Saturn's Auroral Dynamics. *J. Geophys. Res.* 110, A02201. doi:10.1029/2004JA010796

Cowley, S. W. H., Freeman, M. P., Lockwood, M., and Smith, M. F. (1991). "The Ionospheric Signature of Flux Transfer Events," in *CLUSTER - Dayside Polar Cusp*. *ESA SP-330*. Editor C. I. Barron (Nordvijk, Netherlands: European Space Agency Publications), 105–112.

Cowley, S. W. H. (2016). Hoyle and the Magnetosphere. *A&G* 57 (1), 1.12. doi:10.1093/astrogeo/atw033

Cowley, S. W. H., and Lockwood, M. (1992). Excitation and Decay of Solar-wind Driven Flows in the Magnetosphere-ionosphere System. *Ann. Geophys* 10, 103–115. Available at: http://www.personal.reading.ac.uk/~ym901336/pdfs/92_CowleyandLockwood_1992.pdf.

Cowley, S. W. H. (1984). "Solar Wind Control of Magnetospheric Convection," in *Achievements of the International Magnetospheric Study (IMS), Proceedings of an International Symposium, Graz, Austria, 26-28 June 1984, ESA-SP-217*. Editors B. Battrick and E. J. Rolfe (Paris, France: European Space Agency), 483. ISSN 0379-6566.

Cowley, S. W. H. (1982). The Causes of Convection in the Earth's Magnetosphere: A Review of Developments during the IMS. *Rev. Geophys.* 20 (3), 531–565. doi:10.1029/RG020i003p00531

Davis, T. N., and Sugiura, M. (1966). Auroral Electrojet Activity Index *AE* and its Universal Time Variations. *J. Geophys. Res.* 71 (3), 785–801. doi:10.1029/JZ071i003p00785

DeJong, A. D., Cai, X., Clauer, R. C., and Spann, J. F. (2007). Aurora and Open Magnetic Flux during Isolated Substorms, Sawteeth, and SMC Events. *Ann. Geophys.* 25, 1865–1876. doi:10.5194/angeo-25-1865-2007

Dungey, J. W. (1961). Interplanetary Magnetic Field and the Auroral Zones. *Phys. Rev. Lett.* 6, 47–48. doi:10.1103/physrevlett.6.47

Dungey, J. W. (1950). *Some Researches in Cosmic Magnetism*. PhD thesis (Cambridge: Cambridge University).

Fairfield, D. H., and Jones, J. (1996). Variability of the Tail Lobe Field Strength. *J. Geophys. Res.* 101 (A4), 7785–7791. doi:10.1029/95JA03713

Farrugia, C. J., Freeman, M. P., Cowley, S. W. H., Southwood, D. J., Lockwood, M., and Etemadi, A. (1989). Pressure-driven Magnetopause Motions and Attendant Response on the Ground, Planet. *Space Sci.* 37, 589-608. doi:10.1016/0032-0633(89)90099-8

Farrugia, C. J., Grocott, A., Sandholt, P. E., Cowley, S. W. H., Miyoshi, Y., Rich, F. J., et al. (2007). The Magnetosphere under Weak Solar Wind Forcing. *Ann. Geophys.* 25 (1), 191–205. doi:10.5194/angeo-25-191-2007

Glassmeier, K.-H., and Heppner, C. (1992). Traveling Magnetospheric Convection Twin Vortices: Another Case Study, Global Characteristics, and a Model. *J. Geophys. Res.* 97 (A4), 3977–3992. doi:10.1029/91JA02464

Gordeev, E., Sergeev, V., Tsyganenko, N., Kuznetsova, M., Rastäetter, L., Raeder, J., et al. (2017). The Substorm Cycle as Reproduced by Global MHD Models. *Space Weather.* 15, 131–149. doi:10.1002/2016SW001495

Hoffmeister, C. (1943). Physikalische Untersuchungen an Kometen. I. Die Beziehungen des primären Schweifstrahls zum Radiusvektor. *Z Astrophys.* 22, 265.

Holzer, R. E., McPherron, R. L., and Hardy, D. A. (1986). A Quantitative Empirical Model of the Magnetospheric Flux Transfer Process. *J. Geophys. Res.* 91 (A3), 3287–3293. doi:10.1029/ja091ia03p03287

Hosokawa, K., Kullen, A., Milan, S., Reidy, J., Zou, Y., Frey, H. U., et al. (2020). Aurora in the Polar Cap: A Review. *Space Sci. Rev.* 216, 15. doi:10.1007/s11214-020-0637-3

Hubert, B., Milan, S. E., Grocott, A., Blockx, C., Cowley, S. W. H., and Gérard, J.-C. (2006b). Dayside and Nightside Reconnection Rates Inferred from IMAGE FUV and Super Dual Auroral Radar Network Data. *J. Geophys. Res.* 111, A03217. doi:10.1029/2005JA011140

Hubert, B., Palmroth, M., Laitinen, T. V., Janhunen, P., Milan, S. E., Grocott, A., et al. (2006a). Compression of the Earth's Magnetotail by Interplanetary Shocks Directly Drives Transient Magnetic Flux Closure. *Geophys. Res. Lett.* 33, a–n. doi:10.1029/2006GL026008

Imber, S. M., Milan, S. E., and Hubert, B. (2006). The Auroral and Ionospheric Flow Signatures of Dual Lobe Reconnection. *Ann. Geophys.* 24 (11), 3115–3129. doi:10.5194/angeo-24-3115-2006

Karlsson, S. B. P., Opgenoorth, H. J., Eglitis, P., Kauristie, K., Syrjäsuo, M., Pulkkinen, T., et al. (2000). Solar Wind Control of Magnetospheric Energy Content: Substorm Quenching and Multiple Onsets. *J. Geophys. Res.* 105, 5335–5356. doi:10.1029/1999JA900297

King, J. H., and Papitashvili, N. E. (2005). Solar Wind Spatial Scales in and Comparisons of Hourly Wind and ACE Plasma and Magnetic Field Data. *J. Geophys. Res.* 110, A02104. doi:10.1029/2004JA010649

Kokubun, S., McPherron, R. L., and Russell, C. T. (1977). Triggering of Substorms by Solar Wind Discontinuities. *J. Geophys. Res.* 82 (1), 74–86. doi:10.1029/ja082i001p00074

Lee, D.-Y., Lyons, L. R., and Yumoto, K. (2004). Sawtooth Oscillations Directly Driven by Solar Wind Dynamic Pressure Enhancements. *J. Geophys. Res.* 109, A04202. doi:10.1029/2003JA010246

Lin, R. L., Zhang, X. X., Liu, S. Q., Wang, Y. L., and Gong, J. C. (2010). A Three-Dimensional Asymmetric Magnetopause Model. *J. Geophys. Res.* 115, a–n. doi:10.1029/2009JA014235

Liu, Z. Q., Lu, J. Y., Wang, C., Kabin, K., Zhao, J. S., Wang, M., et al. (2015). A Three-dimensional High Mach Number Asymmetric Magnetopause Model from Global MHD Simulation. *J. Geophys. Res. Space Phys.* 120, 5645–5666. doi:10.1002/2014JA020961

Lockwood, M., Bentley, S. N., Owens, M. J., Barnard, L. A., Scott, C. J., Watt, C. E., et al. (2019b). The Development of a Space Climatology: 1. Solar Wind Magnetosphere Coupling as a Function of Timescale and the Effect of Data Gaps. *Space Weather.* 17, 133–156. doi:10.1029/2018SW001856

Lockwood, M., Chambodut, A., Finch, I. D., Barnard, L. A., Owens, M. J., and Haines, C. (2019a). Time-of-day/time-of-year Response Functions of Planetary Geomagnetic Indices. *J. Space Weather Space Clim.* 9, A20. doi:10.1051/swsc/2019017

Lockwood, M., and Cowley, S. W. H. (1992). "Ionospheric Convection and the Substorm Cycle in "Substorms 1," in *Proceedings of the First International Conference on Substorms, ICS-1. ESA-SP-335*. Editor C. Mattock (Nordvijk, Netherlands: European Space Agency Publications), 99–109. Available at: http://www.personal.reading.ac.uk/~ym901336/pdfs/95_lockwood_ICS1.pdf.

Lockwood, M. (2019). Does Adding Solar Wind Poynting Flux Improve the Optimum Solar Wind-Magnetosphere Coupling Function? *JGR Space Phys.* 124 (7), 5498–5515. doi:10.1029/2019JA026639

Lockwood, M., Haines, C., Barnard, L. A., Owens, M. J., Scott, C. J., Chambodut, A., et al. (2021). Semi-annual, Annual and Universal Time Variations in the Magnetosphere and in Geomagnetic Activity: 4. Polar Cap Motions and Origins of the Universal Time Effect. *J. Space Weather Space Clim.* 11, 15. doi:10.1051/swsc/2020077

Lockwood, M., Hairston, M., Finch, I., and Rouillard, A. (2009). Transpolar Voltage and Polar Cap Flux during the Substorm Cycle and Steady Convection Events. *J. Geophys. Res.* 114, a–n. doi:10.1029/2008JA013697

Lockwood, M., LanchesterLanchester, B. S. B. S., Morley, S. K., Throp, K., Milan, S. E., Lester, M., et al. (2006). Modeling the Observed Proton Aurora and Ionospheric Convection Responses to Changes in the IMF Clock Angle: 2. Persistence of Ionospheric Convection. *J. Geophys. Res.* 111, A02306. doi:10.1029/2003JA010307

Lockwood, M., and McWilliams, K. A. (2021a). A Survey of 25 years' Transpolar Voltage Data from the SuperDARN Radar Network and the Expanding-Contracting Polar Cap Model. *JGR Space Phys.* 126, e2021JA029554. doi:10.1029/2021JA029554

Lockwood, M., and McWilliams, K. A. (2021b). On Optimum Solar Wind-Magnetosphere Coupling Functions for Transpolar Voltage and Planetary Geomagnetic Activity. *JGR Space Phys.* 126, e2021JA029946. doi:10.1029/2021JA029946

Lockwood, M., McWilliams, K. A., Owens, M. J., Barnard, L. A., Watt, C. E., Scott, C. J., et al. (2020b). Semi-annual, Annual and Universal Time Variations in the Magnetosphere and in Geomagnetic Activity: 2. Response to Solar Wind Power Input and Relationships with Solar Wind Dynamic Pressure and Magnetospheric Flux Transport. *J. Space Weather Space Clim.* 10, 30. doi:10.1051/swsc/2020033

Lockwood, M. (1993). Modelling High-Latitude Ionosphere for Time-Varying Plasma Convection. *IEE Proc. H. Microw. Antennas Propag. U. K.* 140, 91. doi:10.1049/ip-h-2.1993.0015

Lockwood, M., and Moen, J. (1999). Reconfiguration and Closure of Lobe Flux by Reconnection during Northward IMF: Possible Evidence for Signatures in Cusp/cleft Auroral Emissions. *Ann. Geophys.* 17, 996–1011. doi:10.1007/s00585-999-0996-2

Lockwood, M., and Morley, S. K. (2004). A Numerical Model of the Ionospheric Signatures of Time-Varying Magneticreconnection: I.

Ionospheric Convection. *Ann. Geophys.* 22, 73–91. doi:10.5194/angeo-22-73-2004

Lockwood, M., Owens, M. J., Barnard, L. A., Haines, C., Scott, C. J., McWilliams, K. A., et al. (2020a). Semi-annual, Annual and Universal Time Variations in the Magnetosphere and in Geomagnetic Activity: 1. Geomagnetic Data. *J. Space Weather Space Clim.* 10, 23. doi:10.1051/swsc/2020023

Lockwood, M., Owens, M. J., Barnard, L. A., Watt, C. E., Scott, C. J., Coxon, J. C., et al. (2020c). Semi-annual, Annual and Universal Time Variations in the Magnetosphere and in Geomagnetic Activity: 3. Modelling. *J. Space Weather Space Clim.* 10, 61. doi:10.1051/swsc/2020062

Lockwood, M. (20132013). Reconstruction and Prediction of Variations in the Open Solar Magnetic Flux and Interplanetary Conditions. *Living Rev. Sol. Phys.* 10 (4). doi:10.12942/lrsp-2013-4

Lockwood, M. (2022a). Solar Wind-Magnetosphere Coupling Functions: Pitfalls, Limitations, and Applications. *Space Weather.* 20 (2), e2021SW002989. doi:10.1029/2021SW002989

Lockwood, M. (2022b). The Joined-Up Magnetosphere. *Front. Astron. Space Sci.* 9, 856188. doi:10.3389/fspas.2022.856188

Lu, G., Holzer, T. E., Lummerzheim, D., Ruohoniemi, J. M., Stauning, P., Troshichev, O., et al. (2002). Ionospheric Response to the Interplanetary Magnetic Field Southward Turning: Fast Onset and Slow Reconfiguration. *J. Geophys. Res.* 107 (A8), 2–1. doi:10.1029/2001JA000324

Lühr, H., Sandholt, M. P. E., and Moretto, T. L. T. (1996). Multi-instrument Ground-Based Observations of a Travelling Convection Vortices Event. *Ann. Geophys.* 14, 162–181. doi:10.1007/s00585-996-0162-z

Lukianova, R. (2003). Magnetospheric Response to Sudden Changes in Solar Wind Dynamic Pressure Inferred from Polar Cap Index. *J. Geophys. Res.* 108 (A12), 1428. doi:10.1029/2002JA009790

Lyon, J. G., Fedder, J. A., and Mobarry, C. M. (2004). The Lyon-Fedder-Mobarry (LFM) Global MHD Magnetospheric Simulation Code. *J. Atmos. Solar-Terrestrial Phys.* 66, 1333–1350. doi:10.1016/j.jastp.2004.03.020

Marklund, G., and Lindqvist, P. A. (2021). Cluster Multi-Probing of the Aurora during Two Decades. *JGR Space Phys.* 126, e2021JA029497. doi:10.1029/2021JA029497

Mayaud, P. N. (1980). Derivation, Meaning, and Use of Geomagnetic Indices. *Geophys. Monogr. Ser.* 22, 154. doi:10.1029/GM022

McPherron, R. L., Angelopoulos, V., Baker, D. N., and Hones, E. W., Jr. (1993). Is There a Near-Earth Neutral Line? *Adv. Space Res.* 13 (4), 173–186. doi:10.1016/0273-1177(93)90331-5

McPherron, R. L., Hsu, T.-S., and Chu, X. (2015). An Optimum Solar Wind Coupling Function for the *AL* Index. *J. Geophys. Res. Space Phys.* 120, 2494–2515. doi:10.1002/2014JA020619

McPherron, R. L. (1979). Magnetospheric Substorms. *Rev. Geophys.* 17 (4), 657–681. doi:10.1029/RG017i004p00657

Milan, S. E., Boakes, P. D., and Hubert, B. (2008). Response of the Expanding/contracting Polar Cap to Weak and Strong Solar Wind Driving: Implications for Substorm Onset. *J. Geophys. Res.* 113, a–n. doi:10.1029/2008JA013340

Milan, S. E., Carter, J. A., Bower, G. E., Imber, S. M., Paxton, L. J., Anderson, B. J., et al. (2020). Dual-Lobe Reconnection and Horse-Collar Auroras. *J. Geophys. Res. Space Phys.* 125, e2020JA028567. doi:10.1029/2020JA028567

Milan, S. E., Carter, J. A., Sangha, H., Bower, G. E., and Anderson, B. J. (2021). Magnetospheric Flux Throughput in the Dungey Cycle: Identification of Convection State during 2010. *J. Geophys. Res. Space Phys.* 126, e2020JA028437. doi:10.1029/2020JA028437

Milan, S. E. (2004). Dayside and Nightside Contributions to the Cross Polar Cap Potential: Placing an Upper Limit on a Viscous-like Interaction. *Ann. Geophys.* 22, 3771–3777. doi:10.5194/angeo-22-3771-2004

Milan, S. E., Gosling, J. S., and Hubert, B. (2012). Relationship between Interplanetary Parameters and the Magnetopause Reconnection Rate Quantified from Observations of the Expanding Polar Cap. *J. Geophys. Res.* 117, a–n. doi:10.1029/2011JA017082

Milan, S. E., Grocott, A., Forsyth, C., Imber, S. M., Boakes, P. D., and Hubert, B. (2009b). A Superposed Epoch Analysis of Auroral Evolution during Substorm Growth, Onset and Recovery: Open Magnetic Flux Control of Substorm Intensity. *Ann. Geophys.* 27 (2), 659–668. doi:10.5194/angeo-27-659-2009

Milan, S. E., Imber, S. M., Carter, J. A., Walach, M. T., and Hubert, B. (2016). What Controls the Local Time Extent of Flux Transfer Events? *J. Geophys. Res. Space Phys.* 121, 1391–1401. doi:10.1002/2015JA022012

Milan, S. E., Lester, M., Cowley, S. W. H., Oksavik, K., Brittnacher, M., Greenwald, R. A., et al. (2003). Variations in the Polar Cap Area during Two Substorm Cycles. *Ann. Geophys.* 21, 1121–1140. doi:10.5194/angeo-21-1121-2003

Milan, S. E., Lester, M., Cowley, S. W. H., Oksavik, K., Brittnacher, M., Greenwald, R. A., et al. (2009a). Variations in the Polar Cap Area during Two Substorm Cycles. *Ann. Geophys.* 21 (5), 1121–1140. doi:10.5194/angeo-21-1121-2003

Milan, S. E., Provan, G., and Hubert, B. (2007). Magnetic Flux Transport in the Dungey Cycle: A Survey of Dayside and Nightside Reconnection Rates. *J. Geophys. Res.* 112, a–n. doi:10.1029/2006JA011642

Mooney, M. K., Forsyth, C., Rae, I. J., Chisham, G., Coxon, J. C., Marsh, M. S., et al. (2020). Examining Local Time Variations in the Gains and Losses of Open Magnetic Flux during Substorms. *J. Geophys. Res. Space Phys.* 125, e2019JA027369. doi:10.1029/2019JA027369

Мишин, В., Mishin, V., Караваев, Ю., and Karavaev, Y. (2017). Saturation of the Magnetosphere during Superstorms: New Results from the Magnetogram Inversion Technique. *Solar-Terrestrial Phys.* 3 (3), 28–36. doi:10.12737/stp-33201704

Nakamura, R., Kokubun, S., Mukai, T., and Yamamoto, T. (1997). Changes in the Distant Tail Configuration during Geomagnetic Storms. *J. Geophys. Res.* 102 (A5), 9587–9601. doi:10.1029/97JA00095

Newell, P. T., and Gjerloev, J. W. (2011). Evaluation of SuperMAG Auroral Electrojet Indices as Indicators of Substorms and Auroral Power. *J. Geophys. Res.* 116, a–n. doi:10.1029/2011JA016779

Newell, P. T., and Gjerloev, J. W. (2012). SuperMAG-based Partial Ring Current Indices. *J. Geophys. Res.* 117, a–n. doi:10.1029/2012JA017586

Ober, D. M., Wilson, G. R., Maynard, N. C., Burke, W. J., and Siebert, K. D. (2006). MHD Simulation of the Transpolar Potential after a Solar-Wind Density Pulse. *Geophys. Res. Lett.* 33 (33), L04106. doi:10.1029/2005GL024655

Palmroth, M., Pulkkinen, T. I., Janhunen, P., McComas, D. J., Smith, C. W., and Koskinen, H. E. J. (2004). Role of Solar Wind Dynamic Pressure in Driving Ionospheric Joule Heating. *J. Geophys. Res.* 109, A11302. doi:10.1029/2004JA010529

Parker, E. N. (2001). A History of Early Work on the Heliospheric Magnetic Field. *J. Geophys. Res.* 106 (A8), 15797–15801. doi:10.1029/2000ja000100

Parker, E. N. (1958). Dynamics of the Interplanetary Gas and Magnetic Fields. *ApJ* 128, 664. doi:10.1086/146579

Provan, G., Yeoman, T. K., Milan, S. E., Ruohoniemi, J. M., and Barnes, R. (2002). An Assessment of the "Map-Potential" and "Beam-Swinging" Techniques for Measuring the Ionospheric Convection Pattern Using Data from the SuperDARN Radars. *Ann. Geophys.* 20, 191–202. doi:10.5194/angeo-20-191-2002

Raeder, J., McPherron, R. L., Frank, L. A., Kokubun, S., Lu, G., Mukai, T., et al. (2001). Global Simulation of the Geospace Environment Modeling Substorm Challenge Event. *J. Geophys. Res.* 106 (A1), 381–395. doi:10.1029/2000JA000605

Ridley, A. J., Hansen, K. C., Tóth, G., De Zeeuw, D. L., Gombosi, T. I., and Powell, K. G. (2002). University of Michigan MHD Results of the Geospace Global Circulation Model Metrics Challenge. *J. Geophys. Res.* 107 (A10), 1290. doi:10.1029/2001JA000253

Ruohoniemi, J. M., and Baker, K. B. (1998). Large-scale Imaging of High-Latitude Convection with Super Dual Auroral Radar Network HF Radar Observations. *J. Geophys. Res.* 103, 20797–20811. doi:10.1029/98ja01288

Russell, C. T., and McPherron, R. L. (1973). Semiannual Variation of Geomagnetic Activity. *J. Geophys. Res.* 78, 92–108. doi:10.1029/JA078i001p00092

Russell, C. T. (1989). The Universal Time Variation of Geomagnetic Activity. *Geophys. Res. Lett.* 16 (6), 555–558. doi:10.1029/GL016i006p00555

Schieldge, J. P., and Siscoe, G. L. (1970). A Correlation of the Occurrence of Simultaneous Sudden Magnetospheric Compressions and Geomagnetic Bay Onsets with Selected Geophysical Indices. *J. Atmos. Terr. Phys.* 32 (11), 1819–1830. doi:10.1016/0021-9169(70)90139-x

Scurry, L., and Russell, C. T. (1991). Proxy Studies of Energy Transfer to the Magnetosphere. *J. Geophys. Res.* 96 (A6), 9541–9548. doi:10.1029/91JA00569

Sibeck, D. G., and Lin, R.-Q. (2014). Size and Shape of the Distant Magnetotail. *J. Geophys. Res. Space Phys.* 119, 1028–1043. doi:10.1002/2013JA019471

Siscoe, G. L., and Huang, T. S. (1985). Polar Cap Inflation and Deflation. *J. Geophys. Res.* 90 (A1), 543–547. doi:10.1029/ja090ia01p00543

Slavin, J. A., Tsurutani, B. T., Smith, E. J., Jones, D. E., and Sibeck, D. G. (1983). Average Configuration of the Distant (<220 Re) Magnetotail: Initial ISEE-3 Magnetic Field Results. *Geophys. Res. Lett.* 10, 973–976. doi:10.1029/GL010i010p00973

Smith, M. F., and Lockwood, M. (1996). Earth's Magnetospheric Cusps. *Rev. Geophys.* 34 (2), 233–260. doi:10.1029/96RG00893

Sotirelis, T., Keller, M. R., Liou, K., Smith, D., Barnes, R. J., Talaat, E., et al. (2017). Testing the Expanding-contracting Polar Cap Paradigm. *J. Geophys. Res. Space Phys.* 122, 7077–7086. doi:10.1002/2017JA024238

Southwood, D. J. (1987). The Ionospheric Signature of Flux Transfer Events. *J. Geophys. Res.* 92 (A4), 3207–3213. doi:10.1029/JA092iA04p03207

Stauning, P. (2022). The Polar Cap (PC) Index: PCS Version Based on Dome-C Data. *Space Weather*. 20, e2021SW002941. doi:10.1029/2021SW002941

Stauning, P., and Troshichev, O. A. (2008). Polar Cap Convection and PC Index during Sudden Changes in Solar Wind Dynamic Pressure. *J. Geophys. Res.* 113, a–n. doi:10.1029/2007JA012783

Stern, D. P. (1975a). The Motion of a Proton in the Equatorial Magnetosphere. *J. Geophys. Res.* 80 (4), 595–599. doi:10.1029/JA080i004p00595

Stern, D. P. (1975b). *The Source of the Electric Field in the Nightside Magnetosphere*. Greenbelt, MD: NASA Goddard Space Flight Center. Technical report, N-75-28596; NASA-TM-X-70837; X-602-75-17, OSTI Identifier: 7338032.

Throp, K., Lockwood, M., Lanchester, B. S., Morley, S. K., and Frey, H. U. (2005). Modeling the Observed Proton Aurora and Ionospheric Convection Responses to Changes in the IMF Clock Angle: 1. Persistence of Cusp Proton Aurora. *J. Geophys. Res.* 110, A12311. doi:10.1029/2003JA010306

Tsyganenko, N. A. (2013). Data-based Modelling of the Earth's Dynamic Magnetosphere: a Review. *Ann. Geophys.* 31 (10), 1745–1772. doi:10.5194/angeo-31-1745-2013

Vasyliunas, V. M., Kan, J. R., Siscoe, G. L., and Akasofu, S.-I. (1982). Scaling Relations Governing Magnetospheric Energy Transfer. *Planet. Space Sci.* 30 (4), 359–365. doi:10.1016/0032-0633(82)90041-1

Volland, H. (1973). A Semiempirical Model of Large-Scale Magnetospheric Electric Fields. *J. Geophys. Res.* 78 (1), 171–180. doi:10.1029/JA078i001p00171

Walsh, B. M., Bhakyapaibul, T., and Zou, Y. (2019). Quantifying the Uncertainty of Using Solar Wind Measurements for Geospace Inputs. *J. Geophys. Res. Space Phys.* 124, 3291–3302. doi:10.1029/2019JA026507

Wang, X.–Y., Zhang, Q.–H., Wang, C., Zhang, Y.–L., Tang, B.–B., Xing, Z.–Y., et al. (2022). A Small and Nearly Fully Closed Earth's Magnetosphere for Strongly Northward Interplanetary Magnetic Field. *Geophys. Res. Lett.* submitted.

Watt, C. E. J., Rankin, R., Rae, I. J., and Wright, D. M. (2005). Self-consistent Electron Acceleration Due to Inertial Alfvén Wave Pulses. *J. Geophys. Res.* 110, A10S07. doi:10.1029/2004JA010877

Wiltberger, M., Wang, W., Burns, A. G., Solomon, S. C., Lyon, J. G., and Goodrich, C. C. (2004). Initial Results from the Coupled Magnetosphere Ionosphere Thermosphere Model: Magnetospheric and Ionospheric Responses. *J. Atmos. Solar-Terrestrial Phys.* 66, 1411–1423. doi:10.1016/j.jastp.2004.03.026

Wygant, J. R., Torbert, R. B., and Mozer, F. S. (1983). Comparison of S3-3 Polar Cap Potential Drops with the Interplanetary Magnetic Field and Models of Magnetopause Reconnection. *J. Geophys. Res.* 88 (A7), 5727–5735. doi:10.1029/JA088iA07p05727

Yue, C., Zong, Q. G., Zhang, H., Wang, Y. F., Yuan, C. J., Pu, Z. Y., et al. (2010). Geomagnetic Activity Triggered by Interplanetary Shocks. *J. Geophys. Res.* 115, a–n. doi:10.1029/2010JA015356

Zhang, Q. H., Lockwood, M., Foster, J. C., Zhang, S. R., Zhang, B. C., McCrea, I. W., et al. (2015). Direct Observations of the Full Dungey Convection Cycle in the Polar Ionosphere for Southward Interplanetary Magnetic Field Conditions. *J. Geophys. Res. Space Phys.* 120, 4519–4530. doi:10.1002/2015JA021172

Conflict of Interest: The authors declare that the research was conducted in the absence of any commercial or financial relationships that could be construed as a potential conflict of interest.

Publisher's Note: All claims expressed in this article are solely those of the authors and do not necessarily represent those of their affiliated organizations, or those of the publisher, the editors and the reviewers. Any product that may be evaluated in this article, or claim that may be made by its manufacturer, is not guaranteed or endorsed by the publisher.

frontiers | Frontiers in Astronomy and Space Sciences

ORIGINAL RESEARCH
published: 26 July 2022
doi: 10.3389/fspas.2022.923396

Appearance and Precipitation Characteristics of High-Latitude Pulsating Aurora

Noora Partamies[1,2]*, *Fasil Tesema*[3] *and Emma Bland*[1]

[1]The University Centre in Svalbard (UNIS), Longyearbyen, Norway, [2]Birkeland Centre for Space Science, University of Bergen, Bergen, Norway, [3]Department of Physics, University of Helsinki, Helsinki, Finland

Characteristics of pulsating aurora (PsA) at the equatorward part of the auroral oval have been well described in the literature by previous studies. We extend our knowledge on high-latitude PsA observations by analysing 68 PsA events from the optical observatory on Svalbard, at 75° magnetic latitude. We found that the pulsating emission structures are particularly large and transient, they do not experience drift motion, or their drift motion cannot be traced. Our results show that the high-latitude PsA events relate to lower geomagnetic activity and weaker solar wind driving than the lower latitude PsA. The high-latitude PsA events also occur less frequently, which is in agreement with their association to lower-than-average geomagnetic activity. We further show that the ionospheric electron density values during high-latitude PsA events are low compared to the lower latitude PsA. This, together with the non-traceable nature of the pulsating emission structures, suggests that these events are strongly dominated by a sub-type called Amorphous Pulsating Aurora (APA). We therefore conclude that, unlike the lower latitude PsA events, the high-latitude PsA events are not likely to cause direct changes in the chemical composition of the mesosphere.

Keywords: pulsating aurora, particle precipitation, ionosphere, solar wind driving, high-latitude aurora

OPEN ACCESS

Edited by:
Simon Wing,
Johns Hopkins University,
United States

Reviewed by:
Agnit Mukhopadhyay,
National Aeronautics and Space Administration, United States
Jun Liang,
University of Calgary, Canada

***Correspondence:**
Noora Partamies
noora.partamies@unis.no

Specialty section:
This article was submitted to Space Physics, a section of the journal Frontiers in Astronomy and Space Sciences

Received: *19 April 2022*
Accepted: *09 June 2022*
Published: *26 July 2022*

Citation:
Partamies N, Tesema F and Bland E (2022) Appearance and Precipitation Characteristics of High-Latitude Pulsating Aurora. Front. Astron. Space Sci. 9:923396. doi: 10.3389/fspas.2022.923396

1 INTRODUCTION

Pulsating aurora (PsA) consists of irregular shapes of diffuse aurora, which undergo temporal fluctuations between bright and dim states. A thorough review of PsA properties has been recently published by Nishimura et al. (2020). PsA is known to associate with energetic particle precipitation, hard enough to enhance the ionisation of the D region. This further leads to production of odd hydrogen (HO_x, defined as the sum of H, OH, and HO_2 molecules) and odd nitrogen (NO_x, defined as the sum of N, NO, and NO_2 molecules), which in turn catalytically deplete ozone (Turunen et al., 2016; Tesema et al., 2020; Verronen et al., 2021). HO_x species mainly affect the mesospheric ozone, while the NO_x gases have a long enough lifetime to be transported down to the upper stratosphere in the darkness of the polar night. NO_x can thus cause a longer-term reduction in the atmospheric ozone content during the winter season (Verronen et al., 2021).

Based on the visual appearance and temporal behaviour of PsA, Grono & Donovan (2018) categorised auroral pulsations into three sub-classes: patchy aurora (PA), patchy pulsating aurora (PPA) and amorphous pulsating aurora (APA). Both PA and PPA consist of quasi-stable patches of diffuse emission, which experience brightness fluctuations at various extents of the patch area. For both these sub-types the characteristic property is the stability of the patches. They are often trackable in the order of minutes, which includes many periods between stages of dim and bright.

This allows individual patches to be followed, and in fact Grono & Donovan (2018) showed that these patches drift along the ionospheric convection.

The range of electron flux during PsA was studied in more detail by Tesema et al. (2020). They used the Sodankylä Ion and Neutral Chemistry model (Verronen et al., 2005) to investigate the chemical impact of median and extreme flux spectra, which were constructed from spacecraft measurements of precipitating electrons. While the median and upper envelope electron spectra led to significant reduction in mesospheric ozone, no appreciable chemical change was detected during electron precipitation following the lower envelope spectrum of PsA. This led the authors to examine if the PsA type was in any way related to the precipitation energy and flux. In their follow-up study Tesema et al. (2020b) demonstrated that the bulk of PA and PPA is related to higher precipitation energies, while the electron density enhancements during APA are on average milder, and the enhancements are concentrated at higher altitudes in the ionosphere. The tendency for high precipitation energy during PA and PPA is in agreement with the statistical occurrence of these two types. According to Grono & Donovan (2020), PA and PPA occurrence is clustered on the magnetic latitudes of 62–68° and magnetic local time (MLT) of 01–06. The majority of APA type, however, is observed within the same latitude and time region but also extending to pre-midnight MLT, deep into the morning sector (in their dataset up to seven MLT), as well as up to 75°MLAT. The limitations of the observed latitude and time ranges are due to the station locations of the Time History of Events and Macroscale Interactions during Substorms (THEMIS) camera network (Donovan et al., 2006).

The existence of high-latitude PsA is not a new observation but has been confirmed by photometer measurements at high latitudes of both hemispheres (Brekke & Pettersen, 1971; Craven & Burns, 1990; Wu & Rosenberg, 1992). These earlier studies focussed on the occurrence rate, pulsation period and emission intensities of PsA. In the first report on high-latitude PsA, Brekke & Pettersen (1971) investigated photometer measurements collected over two winter seasons at Ny-Ålesund station on Svalbard. They concluded that the peak occurrence of PsA takes place at 8:30–10:30 MLT in the pre-noon sector and that no PsA was observed in the afternoon or night sectors, although the photometer was in operation throughout the day in the polar night. They further noted that the PsA characteristics were not dependent on magnetic activity (measured by Kp index), but commented on PsA being most often seen on the southern part of the sky. Later, Craven & Burns (1990) reported post-noon high-latitude PsA from an Antarctic station at 13–14 MLT. These events typically only lasted for half an hour and had 2–3 times longer pulsation periods (20–30 s) than observations from lower latitudes had suggested (2–10 s). The afternoon PsA events occurred later in MLT during low magnetic activity (Kp index 1–2), while during higher magnetic activity (Kp index ≥3) PsA ended earlier as the station moved into the polar cap earlier in the afternoon. As a comparison, Wu & Rosenberg (1992) also studied PsA activity from South Pole station in Antarctica. They reported a maximum occurrence at magnetic noon for Kp index values 0–1, and a dawnward shift of the occurrence maximum at higher Kp. They further identified an appearance of afternoon occurrence maximum of PsA for higher magnetic activity (Kp index ≥3). Recently, Bland et al. (2021) reported D-region electron density enhancements associated with PsA that extended as far as 80° magnetic latitude over Antarctica. They estimated the instantaneous Energetic Electron Precipitation (EEP) impact area associated with PsA events by measuring 10–12 MHz radiowave attenuation using the Super Dual Auroral Radar Network (SuperDARN). In their set of 76 PsA events, five were accompanied by radiowave attenuation at McMurdo Station (80° magnetic latitude). However, the presence of optical PsA was confirmed only at a lower latitude site (at Syowa at 66.5° magnetic latitude), so it was not known whether the radiowave attenuation observed at McMurdo Station during these events was caused by PsA or another type of EEP occurring simultaneously with the lower-latitude PsA.

What is left unexplored is the precipitation characteristics and type of the high-latitude PsA. In this study, we analyse PsA events observed over Svalbard at 75° magnetic latitude where the polar night allows continuous auroral imaging 3 months a year. Earlier studies on high-latitude PsA were based on data from one or two winter season, while we investigate a decade's worth of auroral image data, which makes the results less biased by the level of solar or geomagnetic activity for any individual winter season. Using image data allows the examination of the two-dimensional structures of PsA. As the previous studies have reported significant atmospheric chemical responses due to PsA electron precipitation at lower latitudes, we want to characterise the high-latitude PsA in order to conclude if this PsA population is likely to contribute to the atmospheric forcing as well.

2 DATA AND EVENTS

To detect the PsA events we have primarily used auroral all-sky camera quicklook data, i.e. keograms, from a DSLR all-sky camera (ASC) at the Kjell Henriksen Observatory (KHO) on Svalbard. The keograms consist of north–south slices of individual images (see samples in **Figure 2**), which are assembled together in time order. PsA appears as thin green and dark vertical stripes in the keograms as the diffuse aurora structures turn on and off (see the keogram part below the white curve in **Figure 1**). As a result of visually viewing all keograms of the colour DSLR data since 2010, we gathered 68 PsA events in total. We followed the event selection criteria of Partamies et al. (2017) in that the pulsations were required to reach the local zenith, and that no events shorter than 30 min were considered. While the lifetime limit is mainly determined by what is reliably detectable in keograms, the minimum PsA duration in our event set is about an hour. The requirement of PsA reaching the local zenith is implemented to allow comparisons with zenith and field aligned pointing European Incoherent Scatter (EISCAT) radar experiments.

We also selected a reference set of events during which PsA signatures are observed on the southern part of the field-of-view without them reaching all the way to the local zenith. This

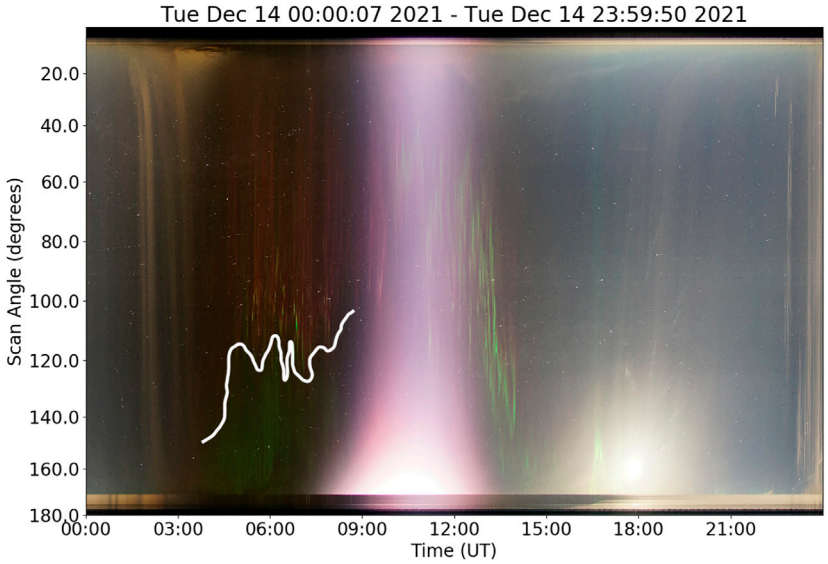

FIGURE 1 | An example keogram on 14 December 2012. Scan angle 0° is towards magnetic north and 180° is towards magnetic south. The orange glow at two to three UT is light pollution illuminated thin clouds. The white curve between three and nine UT and scan angles of 100°–150° approximately separates the red-dominated morning sector aurora over the zenith from the green pulsating aurora over the southern part of the sky. The red/purple glow between about 9 and 13 UT is daylight, during which some red and green auroral structures can be seen. Green aurora continues until about 15 UT. The bright object on the southern sky at 17–18 UT is the moon. At Svalbard the magnetic local time (MLT) is about UT + 3 h.

TABLE 1 | Median values of basic characteristics as well as solar wind and magnetic parameters during PsA at low and high latitudes. The last column includes a set of events where PsA is seen on the souther part of the sky but does not reach the zenith. The numbers in parentheses under each median value describe the median value confidence intervals based on bootstrapping.

Parameter	Low-Latitude PsA	High-Latitude PsA	South of High-Latitude Zenith
1. Number of events	395	68	57
2. Years	1996–2007	2010–2021	2010–2021
3. Duration (h)	1.4	2	2
4. Start time in MLT	4–5	8–10	7–10
5. Magnetic latitude (CGM)	64–66	75	75
6. Solar wind speed (km/s)	500	390	390
	(480–520)	(360–410)	(360–420)
7. IMF magnitude (nT)	7.0	4.5	5.0
	(6.5–7.5)	(4.0–5.3)	(3.9–5.8)
8. Dst index (nT)	−28	−1.0	−9.0
	(−31 to−25)	(−5.5– +6.0)	(−13– +4.5)
9. SML index (nT)	−220	−29	−54
	(−240 to −200)	(−39 to −25)	(−62 to −33)
10. Kp index	3.33	0.67	1.33
	(3.33–3.67)	(0.33–0.67)	(1.00–1.67)

consists of 57 events from the same years as our primary PsA, in 2010–2021, but different days. These PsA periods can be used to assess the role of the solar wind and magnetic activity driving in latitude extent of PsA.

Figure 1 shows an example of the colour ASC daily quicklook data we have used to initially identify PsA events. At 03–09 UT the white curve separates the red-dominated dayside auroral structures at and poleward of the zenith from the green PsA further equatorward. The green PsA consists of diffuse emission with thin vertical stripes that appear as the auroral structures turn on and off over time. This example PsA event did not reach the local zenith (scan angle 90°), but was selected to the reference set of events where PsA only appears equatorward of local zenith (fourth column in **Table 1**).

For further sub-categorising the high-latitude PsA types we have examined individual images in addition to the keograms. These full-colour images are captured at a cadence of about 12 s. Following the PsA sub-categorisation of the earlier work by Grono & Donovan (2018) and Tesema et al. (2020b), the keograms of the high-latitude PsA show no convection-driven

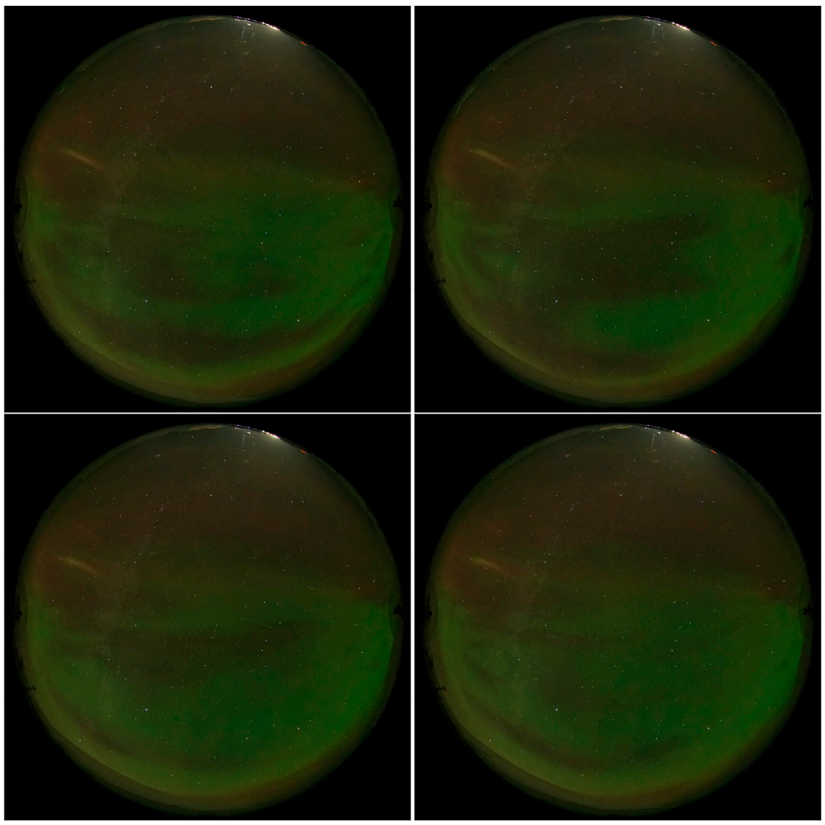

FIGURE 2 | Four consecutive images from the KHO colour all-sky camera during a pulsating aurora event on 16 January 2021. The images are taken at 06:13:15 (top left), 06:13:27 (top right), 06:13:38 (bottom left), and 06:13:50 UT (bottom right). North is to the top and east to the left in the images. An animation of the whole PsA event from 05:50 UT until 07:30 UT is included as supplementary material.

"streamlines" of quasi-stable patches but rather only thin stripes. The finding is confirmed by viewing individual images, which are dominated by large transient regions of diffuse emission, as shown by a sequence of images in **Figure 2**. These regions do not drift, or their drift is not traceable. It is therefore not applicable to talk about pulsation periods in connection with these PsA events. These observations refer to Amorphous Pulsating Aurora (APA) type. In our high-latitude PsA event set and the reference set of PsA events, we found only one case where patches with little pulsations appeared. This Patchy Aurora (PA) region was surrounded by APA type transient structures. An eastward drift of some individual patches was apparent during most of the event. An animation of this example event as well as an animation of the more typical event in **Figure 2** are uploaded as **Supplementary Material**.

To determine the solar wind driving conditions we used the OMNIWeb data for solar wind speed and Interplanetary Magnetic Field (IMF). These data are propagated to the magnetopause and have a temporal resolution of 1 minute. We also used the Dst index to assess the geomagnetic activity conditions. These index data were downloaded from the World Data Centre in Kyoto in 1 hour time resolution. We further used the lower envelope curve of the SuperMAG auroral electrojet index, SML (Gjerloev, 2012) to assess the global electrojet activity level, as well as Kp index (Matzka et al., 2021), which scales with the size of the auroral oval (Sigernes et al., 2011).

EISCAT Svalbard Radar (Wannberg et al., 1997) is located about 1 km away from KHO, thus providing ionospheric measurements within the ASC zenith region. The data consist of height profiles of electron density, electron and ion temperature and ion velocity as a standard set of parameters along the radar beam with a temporal resolution of 1 minute. In this study, we only analyse the electron density profiles collected during PsA events that reached the radar field-of-view. EISCAT data were available for 20 PsA events. The radar experiments[1] range from arc_slice and manda with altitude resolutions of 0.9 km and 0.5–1.0 km respectively, to tau7, ipy, beata, folke and taro with altitude resolutions of 3–4 km at the bottom part of the ionosphere. For all the experiments during the PsA events we only use data from the non-steerable parabolic antenna (a diameter of 42 m). These data are analysed for the electron density values at the height range of 80–110 km, divided into three 10 km thick layers. Each height layer then includes two to

[1]For experiment descriptions see: https://eiscat.se/scientist/document/experiments/

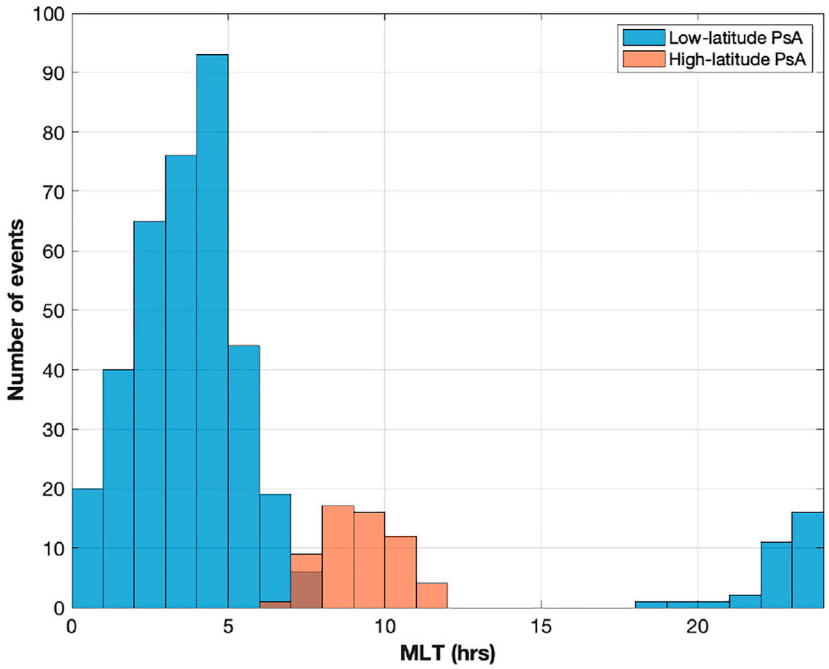

FIGURE 3 | The MLT distribution of low-latitude PsA (blue) and high-latitude PsA (salmon). We have used the start time of the PsA event to compile these histograms. The MLT is estimated as UT+2.5 h for the low-latitude events and as UT+3 h for the high-latitude events.

three electron density values per profile, except for the high-resolution experiments arc_slice and manda where 10–20 electron density values are resolved in each 10 km layer.

3 RESULTS

3.1 Duration and Local Time for PsA

As a low-latitude reference of PsA events we use the list of about 400 PsA events by Partamies et al. (2017), which is based on a decade long time series of ASC images from five camera stations in the Fennoscandian Lapland. This region sees mainly the equatorward part of the auroral oval, and thus the particle precipitation region from the outer radiation belt. It is worth noting that this reference set of PsA events is seven times larger than the list of our high-latitude PsA events, and covers a different time period that is equally long but does not overlap (see **Table 1**). Nonetheless, the comparison is valid for typical values of solar wind driving conditions and the underlying level of magnetic activity during PsA.

Key parameters characterising the PsA events are collected in **Table 1**. The difference in the number of PsA events for the two equally long time periods is striking. While the local cloudiness may affect the number of high-latitude events, which are detected from one station data rather than multiple, this is unlikely to be the only reason for such a big difference. Furthermore, the time span of high-latitude events has been magnetically quieter than that of the low-latitude events, which should be favourable for high-latitude PsA. This kind of an effect is not seen.

The median duration of 1.4 h was reported for the low-latitude events by Partamies et al. (2017) and 2 h by Tesema et al. (2020). The authors also noted, however, that their value was conservative and often limited by the end of the imaging at sunrise. The duration of the high-latitude events (parameter three in **Table 1**) is about 0.5 h longer. A more recent radar study on PsA showed that indeed the median lifetime of PsA is likely to be over 2 hours (Bland et al., 2019), while also taking into account events lasting for less than 30 min. Our high-latitude PsA events also last for about 2 hours, and they also often become undetectable due to the increasing daylight (as can be seen in **Figure 1**). In the Svalbard winter the daylight period is short so this is considered as a minor limitation. On the other hand, other precipitation regions often dominate the camera field-of-view around noon.

The start time of the PsA period in MLT (parameter four in **Table 1**) is consistently 3–4 h earlier for the low-latitude events as compared to the high-latitude events. Although Partamies et al. (2017) showed an event where pulsations continued over Svalbard as soon as the patches disappeared from the Lapland FoV, this scenario is clearly not the average case. There are much fewer PsA events observed at high latitudes and their occurrence in MLT does not often continue seamlessly from the low-latitude PsA activity. The high-latitude PsA typically starts between 7 and 11 MLT, as shown in **Figure 3**. With the duration of about 1–3 h about half of these events last past the MLT noon.

3.2 Solar Wind and Geomagnetic Activity Conditions for PsA

Solar wind speed and IMF magnitude median values are listed in **Table 1** (parameters 6 and 7) for PsA from the two latitude

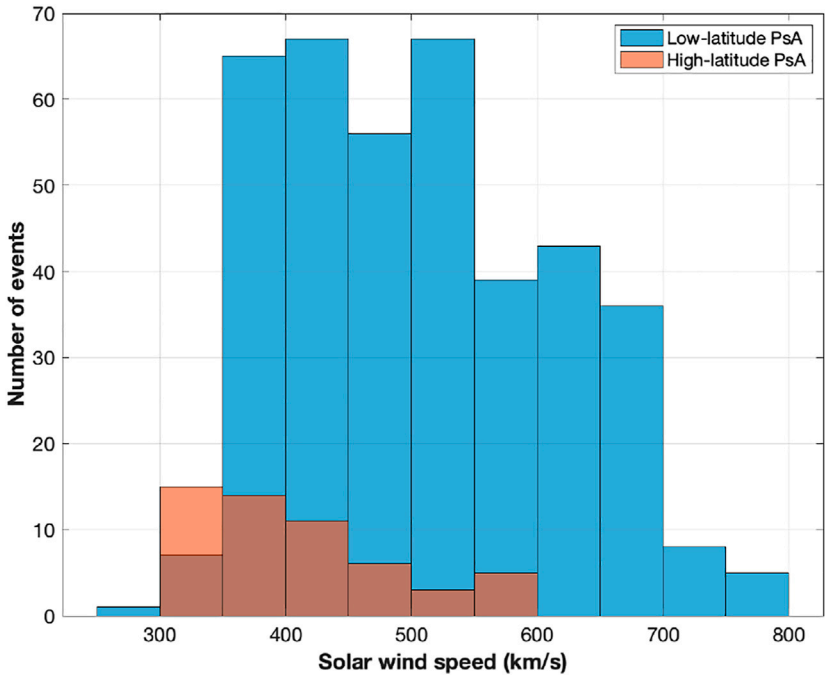

FIGURE 4 | The solar wind speed distribution during the low-latitude PsA (blue) and high-latitude PsA (salmon). We have plotted the median solar wind speed during the individual PsA periods.

ranges. While the median solar wind speed for the low-latitude PsA of 500 km/s exceeds the average speed, the wind speed during the high-latitude events is about 390 km/s, which is at the level of average solar wind speed or below. The difference in the solar wind speed for the two PsA populations is illustrated by the histograms in **Figure 4**. The solar wind speed distribution for the low-latitude events extends up to 800 km/s (blue histogram), while no solar wind speed values above 600 km/s have been observed during the high-latitude PsA events (salmon histogram). Due to the large difference between the number of events in the two PsA populations, we used the bootstrapping method to estimate the confidence interval of the median values. The low-latitude PsA distributions were resampled with replacement 500 times and the high-latitude PsA distributions 100 times. The resulting confidence intervals for the median values are given in the parentheses under the median values in **Table 1**. Even with the relatively small sample sizes in this study, the median values of the two PsA populations clearly differ from each other.

The IMF magnitude values (parameter seven in **Table 1**) for the two PsA populations reveal a similar behaviour: the solar wind driving is stronger during the low-latitude PsA events than it is during the high-latitude PsA events. Both Dst, SML and Kp index values (parameters 8–10 in **Table 1**) also suggest stronger activity during the low-latitude PsA than during the high-latitude PsA. The bootstrapped confidence intervals of the median values for the two PsA populations are clearly separated. This suggests that the low-latitude PsA events take place during substorm recovery phases, while the high-latitude PsA does not have a direct relationship to the global magnetic activity. Instead, the high-latitude events occupy a globally quiet auroral oval, where the "quiet" is not just a time sector difference from the midnight but occurs during the time when the midnight oval is also quiet.

The fourth column of **Table 1** contains the same solar wind and magnetic activity parameters for our reference set of high-latitude PsA events. For this event set we have chosen PsA periods that are observed in the Svalbard ASC data but which only occupy the southern part of the sky without ever reaching the local zenith. These "south of high-latitude zenith" events do not have overlap with the high-latitude PsA events but are a completely separate PsA population. With this additional event set we hope to determine the main driver that brings the PsA poleward. Judging by the median values in the table, PsA stays equatorward of the Svalbard zenith when the global electrojet activity is elevated during the late morning MLT hours. SML and Kp index median values for this reference event set are about twice that for the high-latitude PsA, while none of the other parameters listed in the table shows a significant difference.

3.3 Particle Precipitation During PsA

All available EISCAT Svalbard Radar electron density profiles measured during PsA have been analysed to outline the electron density behaviour in the ionosphere at 80–110 km. As these data have been collected by radar runs with eight different experiments and variable altitude resolutions, we bin all electron density values into three height layers: 80–90 km, 90–100 km and 100–110 km. Additional time averaging is not done but all measured electron density profiles within the PsA periods have been included individually in the height averaging. This procedure is comparable to that by Tesema et al. (2020b). The temporal

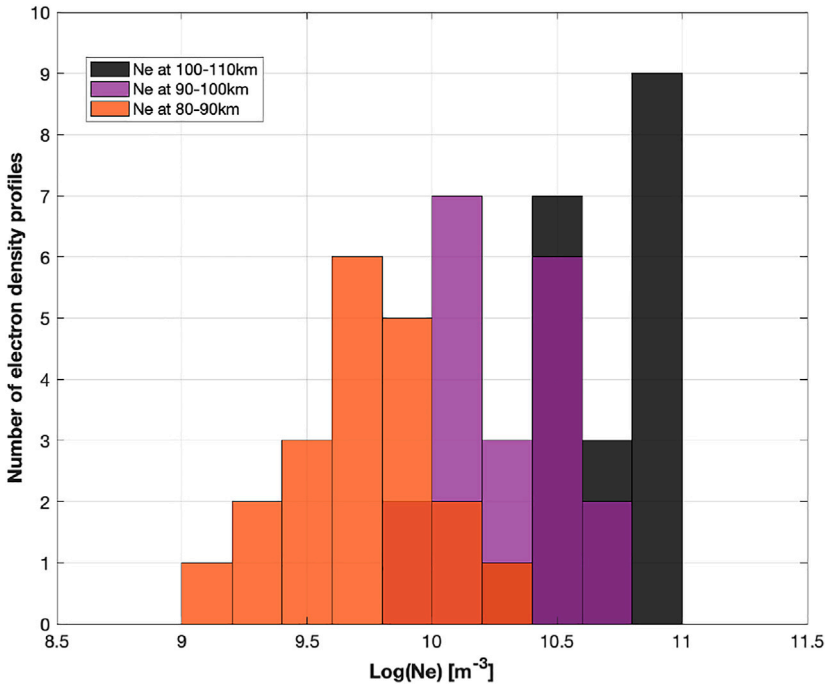

FIGURE 5 | All available electron density (N_e) profiles during PsA events have been averaged over three height regions: 80–90 km (orange), 90–100 km (purple) and 100–110 km (black). The bars here are transparent to show the height of the bars behind. The bin width is 0.2.

resolution of analysed EISCAT data is ~1 min. Most of the 20 PsA events, for which EISCAT data were available, were covered over the full lifetime of the events. Seven PsA events started before the radar experiment did but only four of them lack more than 30 min of data coverage at the beginning. In total 2457 individual electron density profiles were collected during the PsA events.

The results in **Figure 5** show that the logarithm of the electron densities in m^{-3} decreases with decreasing height. Above 100 km, log (N_e) varies from 10.5 to 11 (black histogram). At 90–100 km the logarithm ranges from 9.8 to 10.8 (purple histogram). The widest distribution of electron densities is found at the height of 80–90 km, where log (N_e) peaks at 9.7 but ranges from 9 to 10.4 (orange histogram).

In the results by Tesema et al. (2020b), the logarithm of the electron densities for all PsA types peaked in the range of 11–11.5 at the height of 100–110 km. Percentile values of 10%, 50% and 90% for APA at that height range were 10.8, 11.2, and 11.5 respectively. At 90–100 km, their APA related electron density log values for 10% and 90% percentiles were 10.2 and 11.3 with a median of 10.8. And at 80–90 km, the log (N_e) observed during APA events had 10% and 90% percentiles of 9.4 and 10.6 with a median value of 10.1. Our results overlap with the lower range of their N_e distributions, as apart from two values the high-latitude electron densities are below the median values observed during low latitude APA events. While our results mainly overlap with the low value tails of the electron density distributions collected during APA type PsA of Tesema et al. (2020b), it is worth noting that both PA and PPA also have the tail of the distribution towards the low electron density values.

4 DISCUSSION

To the best of our knowledge this is the first large-scale report and characterisation of high-latitude PsA. Svalbard image data provide a unique opportunity to examine the occurrence and properties of high-latitude PsA. While ASC stations within the main auroral oval region will never experience dark skies during the day, the Svalbard camera data allows us to study the occurrence and the appearance of PsA at any time of the day during the polar night from November until February. The decade of images analysed here does not include a single PsA event at any other time of the day than the pre-noon sector, at 3–10 UT or 6–13 MLT. About half of these events extend across the MLT noon. This is in agreement with the early report on high-latitude pulsating aurora by Brekke & Pettersen (1971), who found high-latitude PsA exclusively in the pre-noon hours. The agreement of these studies suggests that the lack of afternoon PsA in the early study was not due to a solar activity bias as our study covers a full solar cycle.

PsA studies by Partamies et al. (2017) and Tesema et al. (2020) investigated events at the equatorward part of the auroral, which is considered more typical latitude region for PsA occurrence. Compared to their results, our high-latitude PsA events have a lower occurrence rate, and they are related to milder magnetic activity and weaker solar wind driving as well as less energetic electron precipitation. Our results further show that the milder magnetic activity is not only due to the PsA event times being temporally farther away from the midnight sector substorm activity, but that the magnetic activity is globally less severe during the high-latitude PsA as compared to earlier reports of

PsA at the equatorward part of the oval. It is particularly interesting that our PsA observations show electron densities towards the tail of the electron density distributions measured at lower latitudes (Tesema et al., 2020b). PsA has been shown to have a significant effect on the atmospheric chemistry and a significant role in the precipitation energy deposition in the morning sector MLT (Hosokawa & Ogawa, 2015; Tesema et al., 2020; Verronen et al., 2021; Partamies et al., 2022). However, all studies on atmospheric impact have been based on PsA at the equatorward part of the oval with an MLT span from midnight until about six MLT. Our findings suggest that these high-latitude PsA events do not significantly contribute to the changing mesospheric chemistry as the bulk part of the precipitation energy is deposited higher up in the atmosphere. In fact, the high-latitude PsA events more likely resemble the lower envelope energy-flux spectrum of PsA, which has been shown to cause no HO_x production and no O_3 depletion (Tesema et al., 2020).

The quiet electrojet conditions observed during high-latitude PsA suggest an anti-correlation between latitudes of PsA occurrence and geomagnetic activity. The higher the geomagnetic activity the lower latitudes the PsA occupy as the auroral oval expands. This idea is verified by employing a reference PsA event set where PsA is observed in the Svalbard image data but does not reach the local zenith (**Table 1**). In these reference set cases Kp index exceeds unity, while during our zenith-reaching events Kp stays below unity. The fact that Kp is only required to exceed one for PsA not reaching the zenith over Svalbard may also explain why so few high-latitude PsA events were detected over a decade. In the time span of our PsA events (2010–2021) Kp index was below one only for 30% of the time in total. Just like in the early report by Brekke & Pettersen (1971), the occurrence time of our PsA events does not show correlation with the magnetic activity. The meridional extent of PsA, however, does seem to correlate with the magnetic activity.

The statistical occurrence of different PsA types by Grono & Donovan (2020) does not cover our high-latitude region, nor the local magnetic noon. What they do suggest, however, is that APA type reaches furthest poleward and closest to noon. Bland et al. (2019) observed PsA activity extending to magnetic noon at Syowa Station (66.5° magnetic latitude). The five PsA-related events at McMurdo station (80° magnetic latitude) reported by Bland et al. (2021) were classified as APA and one as PPA. The classification was done for Syowa Station where optical data were available, while the rest of the PsA observations were based on HF attenuation of the SuperDARN radar signal and noise. It is worth noting, however, that the whole set of southern hemispheric events was heavily biased by APA (over 70%). Nonetheless, their PsA observations give an indication towards high-latitude PsA being primarily APA. These PsA-related HF attenuation events took place during the late afternoon to pre-midnight MLT hours with Kp index at 2–3. This may indicate that the EEP was related to high-latitude substorm precipitation rather than PsA at McMurdo. However, as mentioned by Grono & Donovan (2018), APA type PsA tend to occur earlier than the other PsA types. APA type has been observed pre-midnight and within substorm aurora, and may thus contribute to substorm-related particle precipitation as well.

In particular our visual sub-categorisation but also the fact that our PsA events were associated with relatively low electron densities, strongly supports the conclusion that the high-latitude PsA events are nearly exclusively APA type events. While our comparison of ionospheric electron densities between low and high latitude PsA events does not take into account a possible difference between the ambient ionospheric conditions of the two station locations, both electron density studies are performed for local time hours leading to the daylight. As we further only conclude that the high-latitude electron density values are low (below the median value) compared to the range of electron densities reported by (Tesema et al., 2020b) during APA type PsA, we anticipate that our conclusion is robust enough to support the visual PsA categorisation of this study. In agreement with earlier studies, our findings indicate that APA tends to be the PsA type carrying the least energy into the atmosphere. It is thus not likely to cause direct chemical changes in the mesosphere but would rather represent the lower envelope energy-flux spectrum of PsA. It is important to note, however, that even without the ionisation reaching the mesosphere, a significant indirect chemical impact may take place through thermospheric ionisation, NO_x production and consequent downward transport inside the winter polar vortex (Verronen et al., 2021).

While our PsA population that occurs south of the high latitude zenith (rightmost column in **Table 1**) may be related to earlier substorm activity in the midnight sector with dawnward drifting energetic electrons, the high-latitude PsA are less dependent on geomagnetic activity and more persistent during quiet conditions. This is in agreement with high-latitude chorus wave observations, which peak in the noon sector and persist through the magnetically quiet time (Spasojevic & Inan, 2010). Due to the quiet conditions the fluxes of the high-energy source electron population may be lower, which can explain the dominance of low-energy APA in the dayside PsA observations. As discussed by Liang et al. (2021), while patchy pulsating aurora is commonly related to cold plasma structuring at the equatorial region, the APA type PsA does not necessarily have the same source region. They further noted a possibility that the APA type would be associated with depletions rather than enhancements in the cold plasma. This would lead to lower fluxes of energetic electrons available for wave-particle interaction and thus, lower fluxes of precipitation. However, there are still unanswered questions about the structuring and the source region of the APA type PsA. Resolving the remaining questions will require coordinated ground and space-based measurements during the different PsA types.

5 CONCLUSION

We have analysed a decade of high-latitude auroral image data for signatures of pulsating aurora (PsA). In total, we identified 68 PsA events, which is a low number compared to the length of the data series. The occurrence of these PsA events is focussed on the pre-noon magnetic local time (MLT) sector, between about 5 and 11 MLT. About half of our PsA events lasted into the post-noon sector,

but no late afternoon or nighttime PsA were found. Our results show that these PsA events are related to lower geomagnetic activity and lower solar wind driving compared to PsA at lower latitudes. Electron density measurements during our PsA events also show lower values at ionospheric heights of 80–110 km compared to the PsA events at lower latitudes. Both the low ionisation rate and the transient and non-traceable appearance of these PsA events suggest that they are of sub-type called Amorphous Pulsating Aurora (APA). Due to their low ionisation rate these PsA events are not likely to lead to any direct changes in the mesospheric chemical composition, but will rather contribute to the indirect chemical changes during the winter months.

DATA AVAILABILITY STATEMENT

The original contributions presented in the study are included in the article/**Supplementary Material**, further inquiries can be directed to the corresponding author.

AUTHOR CONTRIBUTIONS

All authors listed have made a substantial, direct, and intellectual contribution to the work and approved it for publication.

FUNDING

The work by NP is supported by the Norwegian Research Council (NRC) under CoE contract 223252. FT is funded by Finnish Centre of Excellence in Research of Sustainable Space (Academy of Finland grant number 312351). The work by EB is supported by NRC under the contract 287427.

ACKNOWLEDGMENTS

The authors thank Claudia Buck from FH Aachen in Germany for exploring the topic of high-latitude PsA events for her Bachelor thesis. Without those conversations this work would still be undone. The authors also thank the KHO team and PI Dag Lorentzen for maintenance of the auroral colour camera. We gratefully acknowledge the SuperMAG collaborators (https://supermag.jhuapl.edu/info/?page=acknowledgement).

SUPPLEMENTARY MATERIAL

The Supplementary Material for this article can be found online at: https://www.frontiersin.org/articles/10.3389/fspas.2022.923396/full#supplementary-material

REFERENCES

Bland, E. C., Partamies, N., Heino, E., Yukimatu, A. S., and Miyaoka, H. (2019). Energetic Electron Precipitation Occurrence Rates Determined Using the Syowa East SuperDARN Radar. *JGR Space Phys.* 124, 6253–6265. doi:10.1029/2018JA026437

Bland, E., Tesema, F., and Partamies, N. (2021). D-region Impact Area of Energetic Electron Precipitation during Pulsating Aurora. *Ann. Geophys.* 39, 135–149. doi:10.5194/angeo-39-135-2021

Brekke, A., and Pettersen, H. (1971). Some Observations of Pulsating Aurora at Spitzbergen. *Planet. Space Sci.* 19, 536–540. doi:10.1016/0032-0633(71)90171-1

Craven, M., and Burns, G. B. (1990). High Latitude Pulsating Aurorae. *Geophys. Res. Lett.* 17, 1251–1254. doi:10.1029/GL017i009p01251

Donovan, E., Mende, S., Jackel, B., Frey, H., Syrjäsuo, M., Voronkov, I., et al. (2006). The THEMIS All-Sky Imaging Array-System Design and Initial Results from the Prototype Imager. *J. Atmos. Solar-Terrestrial Phys.* 68, 1472–1487. doi:10.1016/j.jastp.2005.03.027

Gjerloev, J. W. (2012). The SuperMAG Data Processing Technique. *J. Geophys. Res.* 117, a–n. doi:10.1029/2012JA017683

Grono, E., and Donovan, E. (2018). Differentiating Diffuse Auroras Based on Phenomenology. *Ann. Geophys.* 36, 891–898. doi:10.5194/angeo-36-891-2018

Grono, E., and Donovan, E. (2020). Surveying Pulsating Auroras. *Ann. Geophys.* 38, 1–8. doi:10.5194/angeo-38-1-2020

Hosokawa, K., and Ogawa, Y. (2015). Ionospheric Variation during Pulsating Aurora. *J. Geophys. Res. Space Phys.* 120, 5943–5957. doi:10.1002/2015JA021401

Liang, J., Nishimura, Y., Donovan, E., Yang, B., and Angelopoulos, V. (2021). Potential Association between the Low-Energy Plasma Structure and the Patchy Pulsating Aurora. *Front. Astron. Space Sci.* 8, 792653. doi:10.3389/fspas.2021.792653

Matzka, J., Stolle, C., Yamazaki, Y., Bronkalla, O., and Morschhauser, A. (2021). The Geomagnetic Kp Index and Derived Indices of Geomagnetic Activity. *Space weather.* 19. doi:10.1029/2020SW002641

Nishimura, Y., Lessard, M. R., Katoh, Y., Miyoshi, Y., Grono, E., Partamies, N., et al. (2020). Diffuse and Pulsating Aurora. *Space Sci. Rev.* 216 (4). doi:10.1007/s11214-019-0629-3

Partamies, N., Whiter, D., Kadokura, A., Kauristie, K., Nesse Tyssøy, H., Massetti, S., et al. (2017). Occurrence and Average Behavior of Pulsating Aurora. *J. Geophys. Res. Space Phys.* 122, 5606–5618. doi:10.1002/2017JA024039

Partamies, N., Whiter, D., Kauristie, K., and Massetti, S. (2022). Local Time Dependence of Auroral Peak Emission Height and Morphology. *Ann. Geophys. Discuss.* doi:10.5194/angeo-2022-6

Sigernes, F., Dyrland, M., Brekke, P., Chernouss, S., Lorentzen, D. A., Oksavik, K., et al. (2011). Two Methods to Forecast Auroral Displays. *J. Space Weather Space Clim.* 1, A03. doi:10.1051/swsc/2011003

Spasojevic, M., and Inan, U. S. (2010). Drivers of Chorus in the Outer Dayside Magnetosphere. *J. Geophys. Res.* 115, a–n. doi:10.1029/2009JA014452

Tesema, F., Partamies, N., Nesse Tyssøy, H., and McKay, D. (2020b). Observations of Precipitation Energies during Different Types of Pulsating Aurora. *Ann. Geophys.* 38, 1191–1202. doi:10.5194/angeo-38-1191-2020

Tesema, F., Partamies, N., Tyssøy, H. N., Kero, A., and Smith-Johnsen, C. (2020). Observations of Electron Precipitation during Pulsating Aurora and its Chemical Impact. *JGR Space Phys.* 125. doi:10.1029/2019JA027713

Turunen, E., Kero, A., Verronen, P. T., Miyoshi, Y., Oyama, S. I., and Saito, S. (2016). Mesospheric Ozone Destruction by High-energy Electron Precipitation Associated with Pulsating Aurora. *JGR Atmos.* 121, 11852–11861. doi:10.1002/2016JD025015

Verronen, P. T., Kero, A., Partamies, N., Szeląg, M. E., Oyama, S.-I., Miyoshi, Y., et al. (2021). Simulated Seasonal Impact on Middle Atmospheric Ozone from High-Energy Electron Precipitation Related to Pulsating Aurorae. *Ann. Geophys.* 39, 883–897. doi:10.5194/angeo-39-883-2021

Verronen, P. T., Seppälä, A., Clilverd, M. A., Rodger, C. J., Kyrölä, E., Enell, C.-F., et al. (2005). Diurnal Variation of Ozone Depletion during the October-November 2003 Solar Proton Events. *J. Geophys. Res.* 110. doi:10.1029/2004JA010932

Wannberg, G., Wolf, I., Vanhainen, L.-G., Koskenniemi, K., Röttger, J., Postila, M., et al. (1997). The EISCAT Svalbard Radar: A Case Study in Modern

Incoherent Scatter Radar System Design. *Radio Sci.* 32, 2283–2307. doi:10.1029/97RS01803

Wu, Q., and Rosenberg, T. J. (1992). High Latitude Pulsating Aurorae Revisited. *Geophys. Res. Lett.* 19, 69–72. doi:10.1029/91GL02781

Conflict of Interest: The authors declare that the research was conducted in the absence of any commercial or financial relationships that could be construed as a potential conflict of interest.

Publisher's Note: All claims expressed in this article are solely those of the authors and do not necessarily represent those of their affiliated organizations, or those of the publisher, the editors and the reviewers. Any product that may be evaluated in this article, or claim that may be made by its manufacturer, is not guaranteed or endorsed by the publisher.

frontiers | Frontiers in Physics

TYPE Original Research
PUBLISHED 05 August 2022
DOI 10.3389/fphy.2022.942486

OPEN ACCESS

EDITED BY
Francesco Malara,
University of Calabria, Italy

REVIEWED BY
Sampad Kumar Panda,
K L University, India
Adriana Settino,
Institute für Weltraumforschung, Austria

*CORRESPONDENCE
C. J. Farrugia,
charlie.farrugia@unh.edu

SPECIALTY SECTION
This article was submitted to Space Physics, a section of the journal Frontiers in Physics

RECEIVED 12 May 2022
ACCEPTED 11 July 2022
PUBLISHED 05 August 2022

CITATION
Farrugia CJ, Lugaz N, Wing S, Wilson LB, Sibeck DJ, Cowley SWH, Torbert RB, Vasquez BJ and Berchem J (2022), Effects from dayside magnetosphere to distant tail unleashed by a bifurcated, non-reconnecting interplanetary current sheet.
Front. Phys. 10:942486.
doi: 10.3389/fphy.2022.942486

Effects from dayside magnetosphere to distant tail unleashed by a bifurcated, non-reconnecting interplanetary current sheet

C. J. Farrugia[1]*, N. Lugaz[1], S. Wing[2], L. B. Wilson III[3], D. J. Sibeck[3], S. W. H. Cowley[4], R. B. Torbert[1], B. J. Vasquez[1] and J. Berchem[5]

[1]Space Science Center, University of New Hampshire, Durham, NH, United States, [2]The Johns Hopkins University Applied Physics Laboratory, Laurel, MD, United States, [3]NASA/Goddard Space Flight Center, Greenbelt, MD, United States, [4]Department of Physics & Astronomy, University of Leicester, Leicester, United Kingdom, [5]Department of Earth, Planetary and Space Sciences, University of California, Los Angeles, Los Angeles, CA, United States

Global magnetospheric effects resulting from the passage at Earth of large-scale structures have been well studied. The effects of common and short-term features, such as discontinuities and current sheets (CSs), have not been studied in the same depth. Herein we show how a seemingly unremarkable interplanetary feature can cause widespread effects in the magnetosheath-magnetosphere system. The feature was observed by Advanced Composition Explorer inside an interplanetary coronal mass ejection on 10 January 2004. It contained 1) a magnetic field dip bounded by directional discontinuities in field and flows, occurring together with 2) a density peak in what we identify as a bifurcated, non-reconnecting current sheet. Data from an array of spacecraft in key regions of the magnetosheath/magnetosphere (*Geotail, Cluster, Polar, and Defense Meteorological Satellite Program*) provide context for *Wind's* observations of flapping of the distant (R ~ −226 R_E) magnetotail. In particular, just before the flapping began, *Wind* observed a hot and tenuous plasma in a magnetic field structure with enhanced field strength, with the *By* and *Bz* components rotating in a fast tailward flow burst. Closer inspection reveals a large flux rope (plasmoid) containing lobe plasma in a tail strongly deflected and twisted by interplanetary non-radial flows and magnetic field *By*. We try to identify the origin of this 'precursor to flapping' by looking at data from the various spacecraft. Working back towards the dayside, we discover a chain of effects which we argue were set in motion by the interplanetary CS and its interaction with the bow shock. These effects include 1) a compression and dilation of the magnetosphere, 2) a local deformation of the postnoon magnetopause, and, 3) at the poleward edge of the oval in an otherwise quiet polar cap flow, a strong (3 km/s) sunward flow burst in a double vortex-like structure flanked by two sets of field-aligned currents. Clearly, an intertwined set of phenomena was occurring at the same time. We learn that multi-spacecraft analysis can give us great insight into the magnetospheric response to transient changes in the solar wind.

KEYWORDS

reconnection, perturbation chain from L1 to far tail, current sheet embedded in an ICME, its imprint seen in the far tail, a strong sunward flow burst in a double-vortex structure flanked by FACs

Introduction

The terrestrial magnetosphere constitutes an obstacle to the continuous flow of magnetized plasma from the Sun, i.e., the solar wind, and its dynamics derive in large measure from its interactions with this stream. The solar wind flowing past the magnetosphere changes over various timescales. From a geoeffectiveness perspective, variations on long time scales have attracted most attention, specifically those associated with interplanetary coronal mass ejections (ICMEs) and, in particular, their subset magnetic clouds (MCs [1]). In these large (fraction of an AU) solar eruptions, important parameters, such as the North-South component of the magnetic field, *Bz*, change slowly and can reach extreme values not otherwise sampled and which are maintained for several hours, even days. This continued forcing of the magnetosphere gives rise to geomagnetic storms of a wide range of intensities (e.g., [2,3]), and repetitive substorm activity [4,5], such as sawtooth events (e.g., [6]).

The solar wind also changes in a discontinuous fashion. Such transient changes can occur, for example, at tangential (TDs) and rotational (RDs) discontinuities [7–9], and shocks. Studies of the impact that these directional discontinuities (DDs) have on the coupled magnetosphere-ionosphere (M-I) system have been by nature more eclectic and, in some sense, more interesting. There are various reasons for this. Among them are: 1) while impulsive at source, they can set in motion a chain of interlinked responses mediated by field-aligned currents (FACs) which couple momentum and energy from the magnetosphere to the ionosphere; 2) waves that typically accompany a strong disturbance of a magnetoplasma propagate and spread out, transmitting the effects and, importantly, 3) DDs are very frequent in the solar wind. Further, the impulsive changes may involve more than one parameter. Even for DDs involving just the magnetic field vector, one has to take into account the different background plasma and field conditions they occur in (e.g., a North-South deflection of a strong magnetic field in a tenuous plasma). Also, shocks may be isolated or may be driven by CMEs and high-speed streams in corotating interaction regions (CIRs), or may be propagating inside a CME. In the last case, for example, the disturbances of magnetospheric plasmas and fields can be very strong: thus, in two studied cases they emptied the outer radiation belt of energetic electrons (see e.g., [10,11]).

Although of short duration at source, the effects of DDs on magnetospheric plasmas and fields can be spread out in time. Intuitively, the strength of the response should depend on the amplitude of the impulsive change, at least until saturation, if there is any, sets in. Combinations of simultaneous impulsive changes introduce additional features in the magnetospheric response. For example, sharp velocity deflections accompanying the magnetic changes at a TD usher in a vortex sheet element and the latter results in tangential stresses being exerted on the magnetopause (see, e.g., [12]). A TD at which there is a sharp rise/drop in density will undergo a change as it interacts with the bow shock. Thus, for a density rise a fast magnetosonic wave carrying part of the density jump precedes the modified TD and perturbs the magnetopause first [13,14]. This was realized in a prescient study by [15] (see also [16]), and shown observationally by [17] and [18]. In addition, a pressure rise at a TD which is oriented such that the motive electric field points towards it from at least one side can excite hot flow anomalies (HFA) at the bow shock which may lead to a distortion of the magnetopause in the form of a local protrusion [19–21] and large-amplitude motions. HFAs illustrate the point that while transient changes in the interplanetary (IP) medium may seem fairly innocuous, they may yet trigger considerable disturbances in the magnetospheric plasmas and fields.

In what follows we shall examine such a case. Our focus is on a short-duration (~1/2 h) variation in the interplanetary plasma and magnetic field parameters which we identify as a current sheet (CS). Absence of accelerated flows indicates it is non-reconnecting. Through a very good deployment of spacecraft we can monitor its effects on the magnetosheath/magnetosphere, from dayside to the far tail (~−230 Re). Its effects are found to be clear and large. In particular, a large flux rope structure was ejected down the distant tail at great speed before a tail flapping episode began. Interestingly, the IP feature is embedded in a long (~1 day) ICME which provides the ambient medium our feature occurs in. This ambient medium is marked by large non-radial flows and strong fields whose effects on the dayside, duskside magnetosheath and in the far tail (windsock-type deflection and twisting) are clearly seen.

We make use of the following data sets. From the Advanced Composition Explorer (ACE) we analyze magnetic field data from the Magnetic Field Experiment (MAG [22]) and proton data from the Solar Wind Electron Proton Alpha Monitor (SWEPAM [23]) at 16 s (occasionally, 1 s) and 64 s resolution, respectively. Data from *Wind* are provided by the Magnetic Fields Instrument (MFI [24]) and the 3DP instrument (3DP [25]). Typically, we use data at 3 s resolution from both. The *Wind* 3DP instrument consists of six different sensors. There are two electron (EESA) and two ion (PESA) electrostatic analyzers with different geometrical factors and field-of-views covering the energy range from 3 eV to 30 keV. More details can be found in [26], who also review 20 years of discoveries

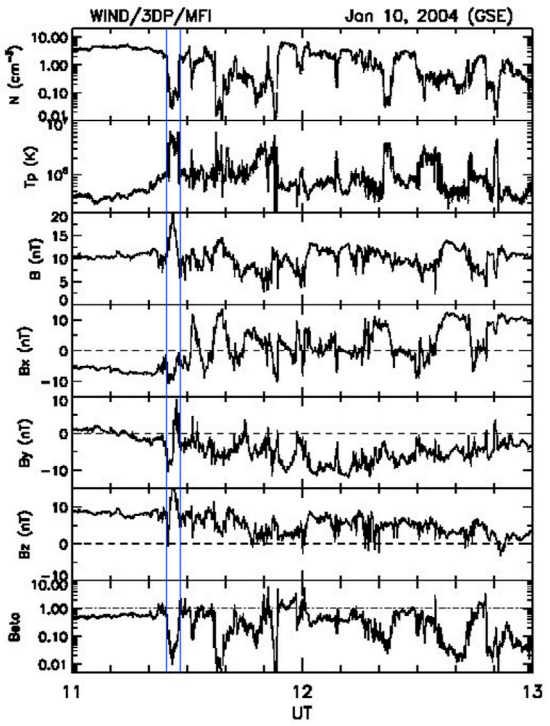

FIGURE 1
Proton and magnetic field data from spacecraft *Wind* during 11–13 UT, 10 January 2004. From top to bottom: the proton density, temperature, total field and its GSE components, and the proton beta.

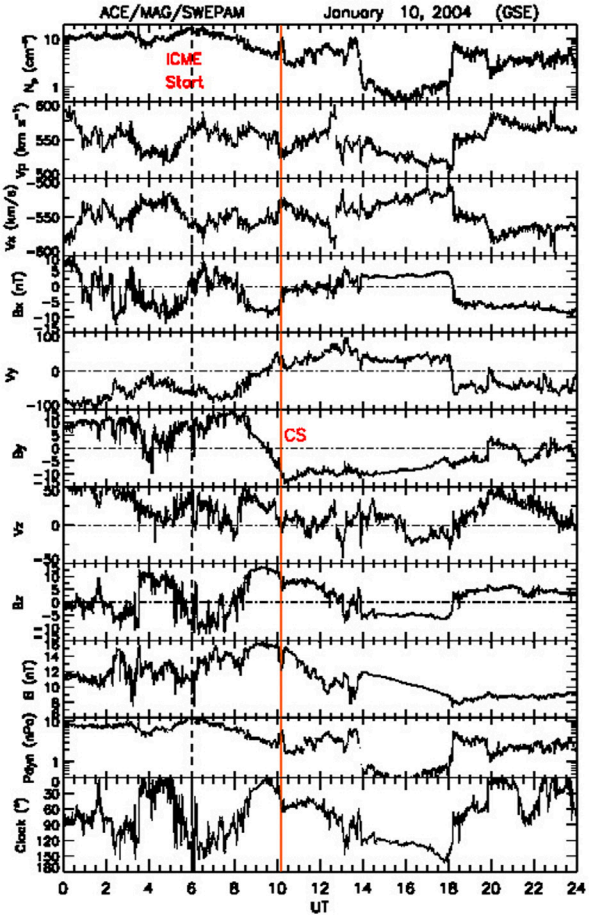

FIGURE 2
ACE observations on 10 January 2004. From top to bottom: the proton density, bulk speed, (pairwise) components of flow and magnetic field, the dynamic pressure in nPa, and the IMF clock angle, i.e., the polar angle in the GSM *YZ* plane. The dynamic pressure includes the alpha-particle contribution. The vertical red line shows the time of the current sheet which we discuss here.

made by *Wind*. Geotail magnetic and plasma data are from the MGF [27] and LEP [28] instruments, respectively, at a resolution of 3 s (MGF) and 12 s (LEP). Cluster magnetic field data are from the Cluster Magnetic Field investigation (MGF [29]), and the plasma data are from the Cluster Ion Spectrometry experiment (CIS [30]). Polar magnetic field data are from the Magnetic Fields Experiment (MFE [31]) and plasma data are from the hot plasma Analyzer (HYDRA [32]). Key parameters at 1 min and 6 s resolution are employed. Defense Meteorological Satellite Program (DMSP) satellites are Sun-synchronous satellites in nearly circular polar orbit at an altitude of roughly 835 km and an orbital period of approximately 101 min. The SSJ instrument package included on all recent DMSP flights uses curved plate electrostatic analyzers to measure ions and electrons from 30 eV to 30 keV in logarithmically spaced steps [33]. Because of its upward pointing and limited pitch angle resolution, DMSP SSJ measures only highly field-aligned precipitating particles. The DMSP magnetic field experiments (SSM) consist of triaxial fluxgate magnetometers with a range of ± 65,535 nT and one-bit resolution of 2 nT [34]. The time resolution of SSJ and SSM data is 1 s. The DMSP magnetic field data can provide estimates of the large-scale structure of FACs (e.g., [35–37]).

Interplanetary and far tail observations

Interplanetary observations are from spacecraft ACE in orbit around the L1 point. Before we describe them, we present an overview of the effect in the far tail which motivated this investigation. It was observed by the spacecraft *Wind* which was sampling the distant tail near the ecliptic plane on the duskside.

Figure 1 shows *Wind* plasma and magnetic field observations over a 2-h interval from 11 to 13 UT on 10 January 2004. During this interval *Wind* was near the Earth-Sun L2 point in the geomagnetic tail at an average position vector $\boldsymbol{R}$ = (−227, 34, −9) R_E (GSE), i.e., on the duskside and slightly south of the ecliptic. From ~11:30 to ~11:55 UT, the Earth-Sun *Bx*

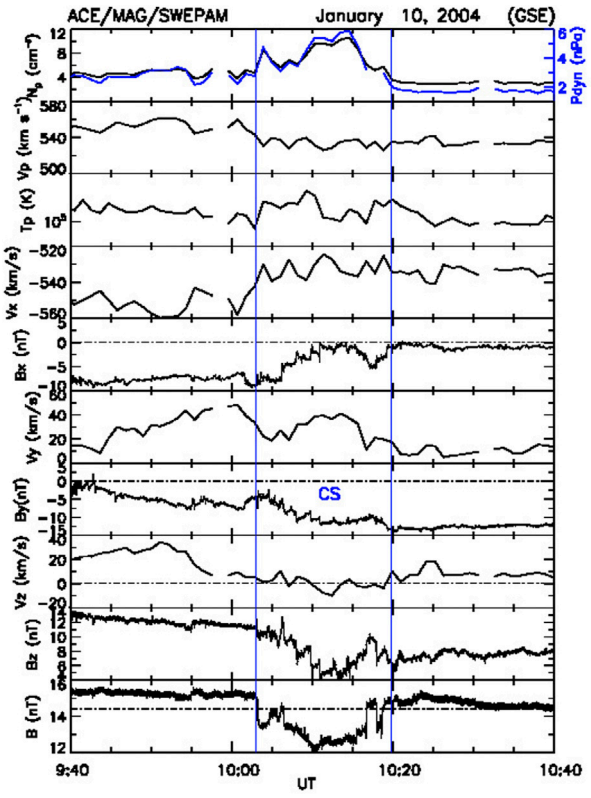

FIGURE 3
A zoom-in of the interval 9:40–10:40 UT. The ACE field data are now at a resolution of 1 s. The vertical blue lines bracket the CS. Overlaid on the density in the top panel is the dynamic pressure (in blue, with scale on the right). Note that the minimum in *B* (bottom panel) occurs ~5 min before the density reaches its peak value.

component repeatedly changed polarity (panel 4), i.e., the tail was flapping. But before the flapping, there is a different structure, a "precursor", shown between vertical guidelines. Here the density is low, and the temperature is high. The total magnetic field, *B,* is enhanced, and the field components rotate through a large angle. As shown later, the field change is embedded in a plasma flow which is strongly tailward. This feature is the focus of our paper: What gave rise to it and what perturbations did it excite in the magnetosphere?

We have not yet included plasma velocities. This is because the bulk velocities from the PESA Low instrument are not trustworthy during this period. They follow the proper trends but are not to be trusted in absolute values. We shall return to this qualification when later we use moments from the analysis of the full 3D velocity distribution functions (VDFs) from PESA High, as we discuss *Wind* observations in more detail.

We return to ACE observations. Figure 2 shows 1 day of data. This is a tabulated, fast ICME lasting from six UT, January 10 to 5 UT, 11 Jan 2004 [38]. Some relevant features are as follows:

1) There are strong non-radial flows, particularly in *Vy*. This is unusual for ICMEs (see [39]). In accordance with the windsock effect, we expect a deflected tail [40–43].
2) Close to the red vertical guideline at ~10:10 UT, there are clear field and flow gradient discontinuities near maximum *B*. These give the temporal profiles of the field and flow a "kink-like" structure. (In this context, by "kink" we mean a place where there is a discontinuous change in the temporal gradients of B and V.) This is our focus. There is a strong *By* component, whose gradient changes at the red line. A short time earlier the *Vy* component transitions from negative to positive values. Torques are being applied to the tail which twist it [20,44,45].
3) At this structure, there is a peak in the density concomitant with a decrease of 20% of a strong *B*. This will serve as a good tracer when we look at observations from other widely-spread spacecraft.
4) The structure lies in a ~4-hour-long region of strong and positive GSM *Bz*. During this, the clock angle (i.e., the polar angle in the GSM *YZ* plane; last panel) is less than 60°.

In summary, while compared to the larger ICME structure these features look innocuous enough, their effects are significant. In addition, we shall also show that they are related to the precursor at *Wind*.

A shorter interval is plotted in Figure 3. The resolution of the magnetic field data is now 1 s. The feature lasts for ~17 min. The dynamic pressure (top panel, blue trace) shows a 2-pronged profile: it rises (from 2 to 4.8 nPa), drops (to 3.2 nPa), rises again (to 6 nPa) and then decreases to ambient values (2 nPa). This will cause the magnetopause to bounce. We performed a minimum variance analysis on the 1-s magnetic field data in the interval 10:00–10:25 UT. The routine returned a normal, $\boldsymbol{N}$ = (0.77, 0.50, 0.38) (GSE). The intermediate-to-minimum eigenvalue ratio = 3.3. We thus have a CS. There was a normal field component, $\boldsymbol{B}_N$ = −4.52 ± 0.59 nT. The CS is bifurcated, with sharp changes at the edges, and a plateau in between. There is no plasma jetting, so that it is a non-reconnecting CS. There is indication that minimum *B* precedes the strongest rise in *Np* by about 5 min.

Figure 4 shows the positions of the spacecraft, with on the left the *XY* GSE plane and on the right the *ZX* plane. The top panel shows ACE at the L1 point (red) and *Wind* (blue) at the L2 point in the distant tail. The spacecraft separation in *X* is ~480 R_E. The bottom panel shows the positions of Geotail (blue), Cluster 1 (red) and Polar (purple). Geotail is in the ecliptic plane at dawn magnetic local times (MLTs). Cluster 1 and Polar are at dusk South of ecliptic. Cluster 1 is near the bow shock and Polar is initially inside the magnetosphere. We thus have satellites providing simultaneous observations from all important regions: unperturbed solar wind, near the magnetopause, just below the magnetopause, and at the distant tail.

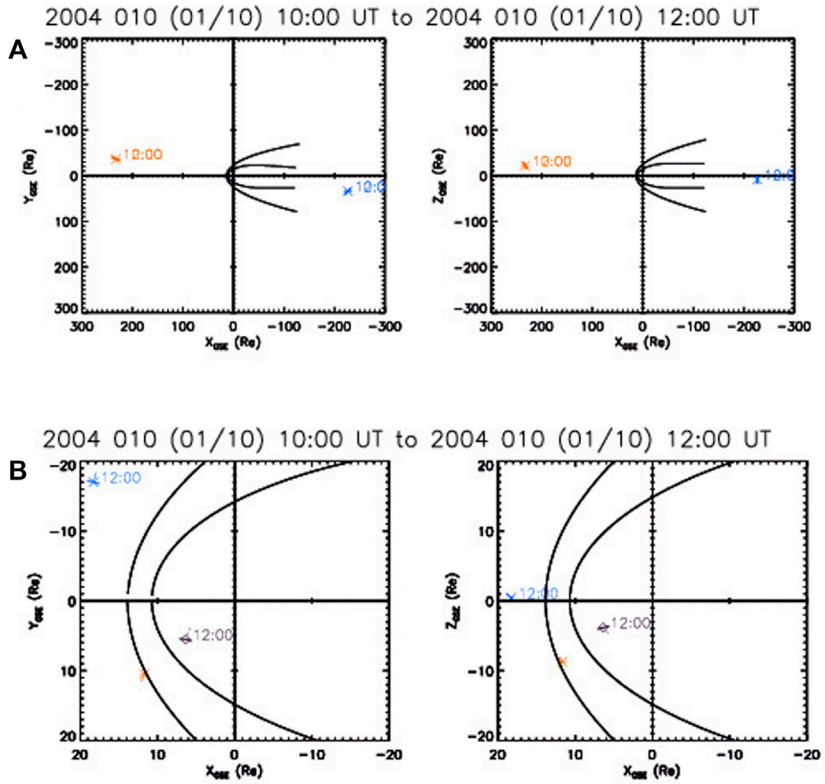

FIGURE 4
The positions of the spacecraft at 11 UT. **(A)** (top): ACE (red) upstream of Earth near the L1 point and Wind (blue) in the distant tail. **(B)** (bottom): The near-magnetopause spacecraft: blue: Geotail, red: Cluster 1, purple: Polar. The left-hand panels show the *XY* GSE plane while those on the right hand show the *XZ* GSE plane. The curves show model bow shock and magnetopause

Observations near the dayside magnetopause and bow shock

We discuss observations near the dayside magnetopause and bow shock made by Geotail, Cluster 1 and Polar. Figure 5 shows an overlay of ACE (black trace) and Geotail (blue trace) magnetic field data at 16 and 3 s resolution, respectively. The CS arrives at Geotail at ~10:50 UT. The agreement is very good when the ACE data are shifted forward in time by 46 min. Correlation coefficients are: 0.93 (*Bx*), 0.98 (*By*), and 0.92 (*Bz*). We conclude that Geotail remained in the solar wind all the time. The remarkable agreement implies that the CS is not evolving much while traveling in the solar wind from ACE to GT, which are separated by 217.0 R_E, mostly in the *X*-direction.

Next, we turn to Cluster 1. We recall that Cluster 1 was expected to be in the Southern hemisphere near the bow shock (Figure 4). Figure 6A gives an overlay of ACE (black trace) and Cluster 1 (red) data for the 10-h interval 6 to 16 UT. Delaying ACE data by 47 min results in very good agreement when Cluster 1 is in the solar wind (up to ~11:10 UT), similar to that between ACE and Geotail. Thus, the CS arrives at Cluster 1 and Geotail practically simultaneously. Performing a minimum variance

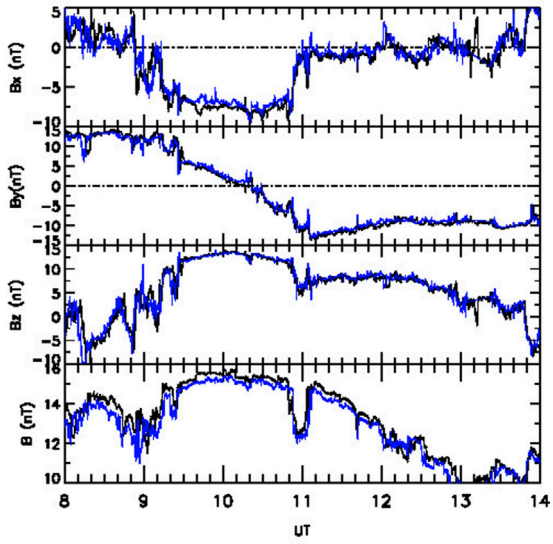

FIGURE 5
An overlay of ACE (black) and Geotail (blue) magnetic field data. ACE data are delayed by 46 min.

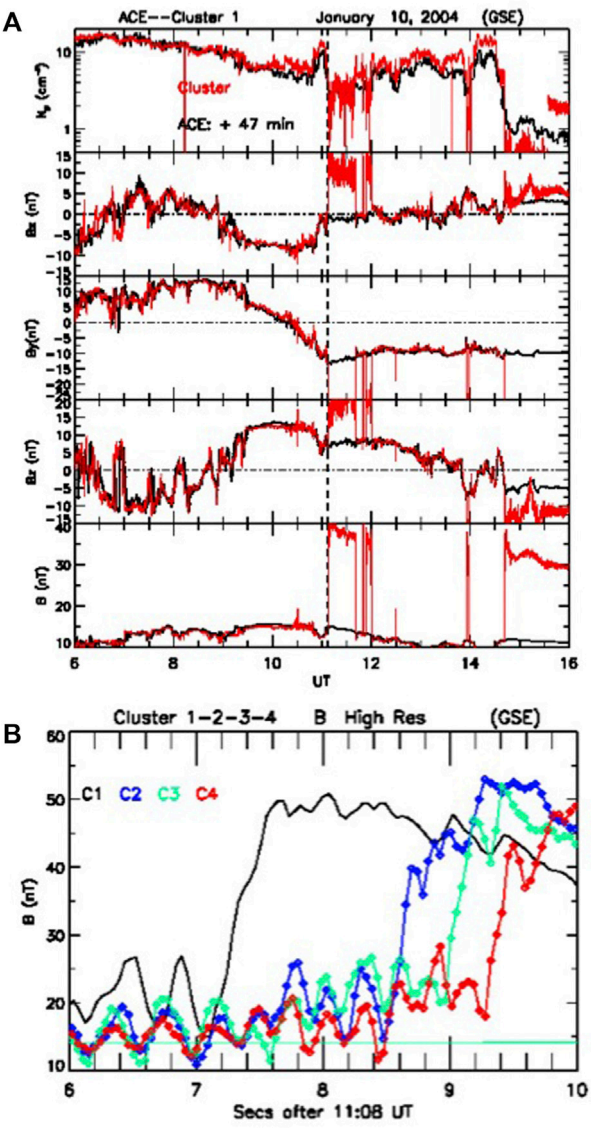

FIGURE 6
(A) (top). Overlay of ACE (black) and Cluster 1 (red) data for the interval 6 to 16 UT. ACE data have been delayed by 47 min. **(B)** (bottom): The crossing of the bow shock by the four Cluster spacecraft.

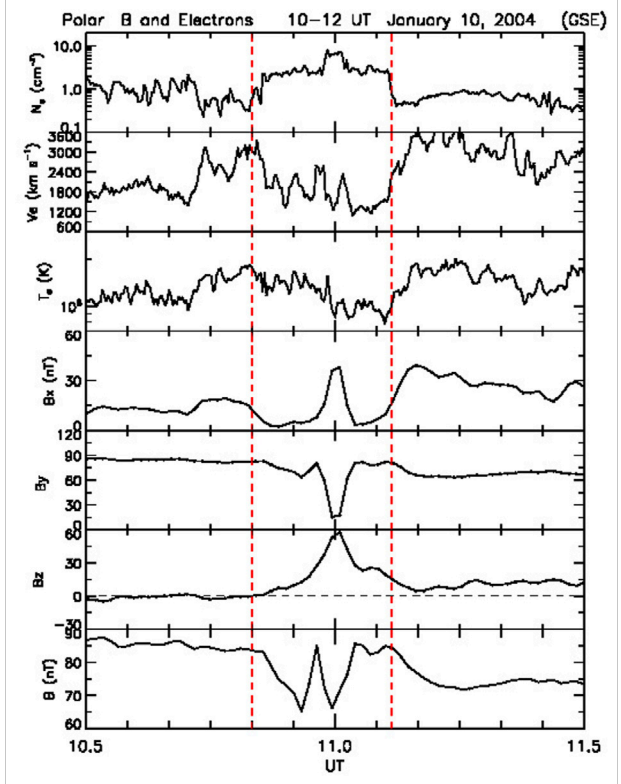

FIGURE 7
Data from the MFE and HYDRA instruments on Polar. Electron data: density, bulk speed and temperature. Magnetic field: Components in GSE coordinates and total field. The vertical guidelines bracket the interval where the clear changes in all these parameters suggest that Polar is sampling the CS-structure observed about 48 min earlier by ACE.

analysis on the Geotail magnetic field data in the interval 10: 40–11:20 UT, we obtain a normal (GSE) $\boldsymbol{N}$ = (0.75, 0.29, 0.60) (eigenvalue ratio = 8.6). Thus, the CS will arrive at the duskside magnetopause first.

As the dynamic pressure decreases just after the *B*-drop at the CS, Cluster 1 crosses the sunward—moving bow shock into the magnetosheath. The outward motion of the bow shock can be studied by timing its passage over the Cluster configuration. The four spacecraft enter the magnetosheath in the order C1-C2-C3-C4. Shown in Figure 6B is a clear rise in *B* observed by all the spacecraft just after 11:08 UT. We triangulate this feature using the technique of [46], [47]. Four-spacecraft timing gives a bow shock velocity along its normal of $\boldsymbol{V}$ = 98.6*(0.9, 0.2, −0.3) km/s, i.e., sunward, duskward and southward.

We now consider Polar observations. At 11 UT, the spacecraft was at (6.1, 4.8, -4.2) R_E (GSE), i.e., on the duskside south of the ecliptic. Figure 7 shows magnetic field and electron data. (Proton data from HYDRA are not available.) From top to bottom, the figure shows the electron density, bulk speed and temperature at 14 s temporal resolution, the magnetic field components in GSE coordinates, and the total magnetic field. The resolution of the magnetic field data is 0.92 min. For the 17-min interval 10: 51 to 11:08 UT (between vertical guidelines), the temporal profile of *Ne* closely resembles that at Cluster 1 and ACE. Timing the arrival of the density peak, we find a delay ACE-Polar of ~48 min. The high-density structure is associated with a decrease in electron flow velocity, and reduced temperatures. There is a 2-pronged drop in the magnetic field strength, the second of which coincides with the density rise.

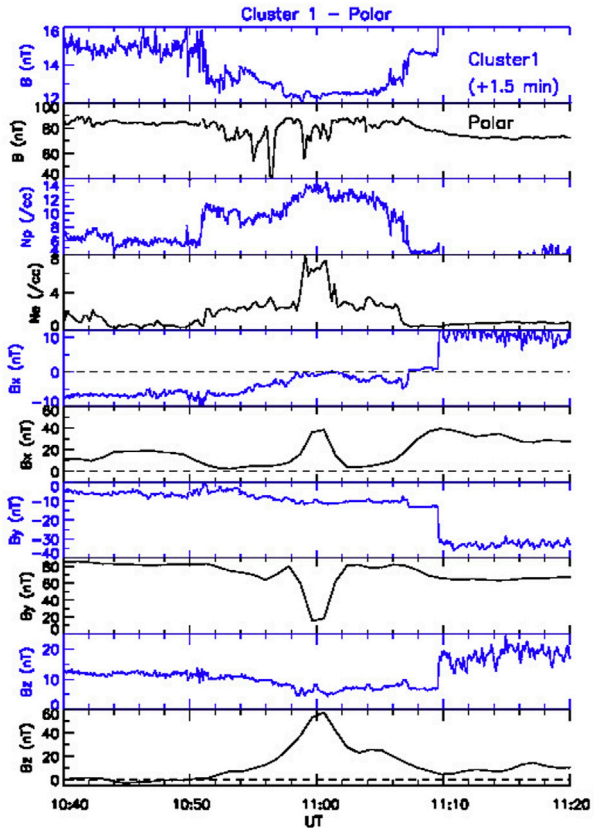

FIGURE 8
Polar (black traces) and Cluster 1 (blue) for the interval 10:40—11:20 UT. Cluster 1 data have been time-shifted by 1.5 min to align the peaks of the density profiles in panels 3 and 4.

To better understand what Polar is seeing, we consider the effect of the CS when it is near the duskside magnetopause. Recall that Cluster 1 and Polar are on the duskside at a distance of 9.4 R_E and on opposite sides of the magnetosheath (Figure 4), so the effect on the immediate neighborhood of Polar can be monitored well. Shown in Figure 8 are the data from Polar and Cluster 1 (in blue) around the time when the CS reached Cluster 1, whose data have been shifted by 1.5 min to align the peaks of the density profiles.

Clearly, the two spacecraft see very different magnetic field profiles. Because the CS is also associated with (large) changes in the velocity, there is a vortex sheet element involved, and the structure will exert tangential stresses in addition to normal ones (see [12]). These will distort the magnetopause. We now show that the tangential stresses are comparable to the normal ones by considering the pressure tensor.

The total pressure tensor (total momentum flux tensor) is given by

$$\Pi_{ab} = \left(p + B^2/2\mu_0\right)\delta_{ab} + \rho V_a V_b - B_a B_b/\mu_0$$

where *a, b* are running indices over the (i, j, k) coordinates resulting from MVAB, *p* is the thermal plasma pressure, and ρ is

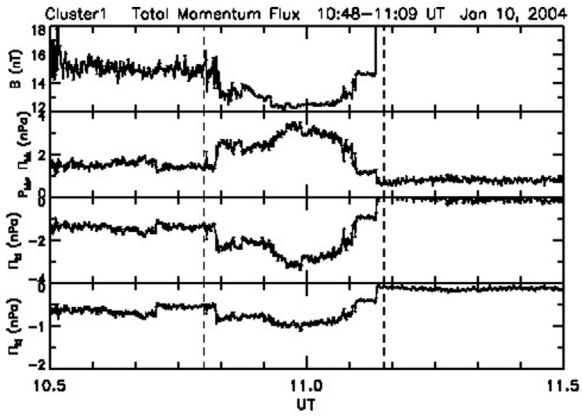

FIGURE 9
The pressure tensor based on Cluster 1 spacecraft data. From top to bottom, the total field for reference, the total pressure in the direction perpendicular to the CS at Cluster 1, $\prod_{kk}$, and the tangential stresses in the ith ($\prod_{ki}$) and jth directions ($\prod_{kj}$).

the mass density. MVAB analysis on the Cluster 1 data for the interval 10:48 to 11:08 UT gave the following eigenvalues i = (−0.58, 0.81, −0.11), j = (−0.24, −0.046, 0.97), and k = (0.78, 0.59, 0.22). The intermediate-to-minimum eigenvalue ratio = 13.0, so the result is robust. The result is shown in Figure 9. The tangential stresses (third and fourth panels) are even somewhat larger than the normal ones (panel 2). Thus, on transmission through the bow shock, we expect a strong local deformation of the magnetopause and perturbations in the magnetosheath [17,48].

Indeed, in Figure 8, around 11 UT when Polar sees a density enhancement, *By* goes from ~90 to ~0 nT and *Bz* goes from 0 to 60 nT. These values are different from those recorded by the spacecraft while in the magnetosphere at the beginning and end of the interval plotted. Thus, Polar is probably crossing briefly into the magnetosheath, which is strongly disturbed and deformed by the forces exerted on it by the CS, which resulted in this field rotation.

Figure 10 shows differential energy fluxes of electrons and ions. From 10:50 to 11:06 UT there is a clear enhancement in both, when Polar is sampling the passage of the density peak in the CS structure. A 2-dip structure in *B* (Figure 7) is seen due to the 2-dip profile of Pdyn at ACE (Figure 3).

Observations from low-altitude spacecraft

We next consider observations from the low-altitude spacecraft F16 and F13, which were following dawn-to-dusk trajectories in the Southern hemisphere, rising to about 80° MLAT. Figure 11 shows, from top to bottom, the energy

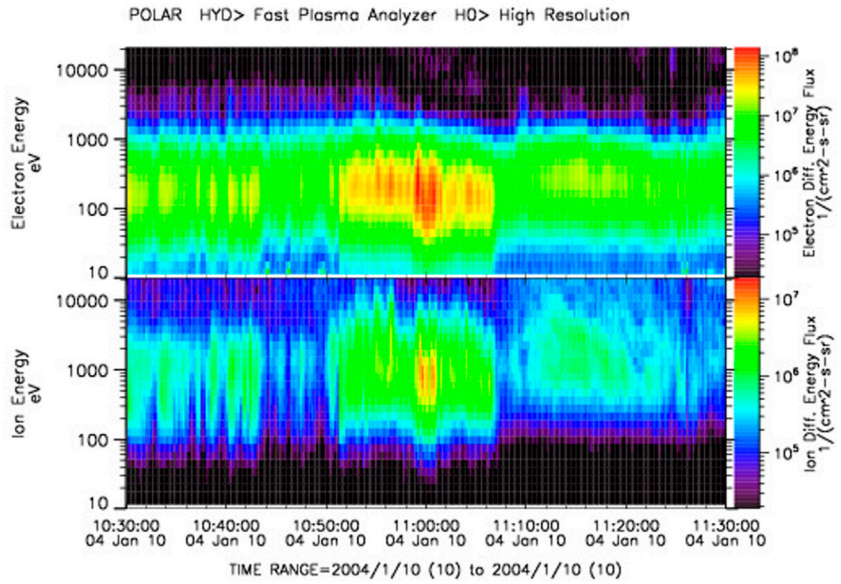

FIGURE 10
Polar/HYDRA differential energy fluxes, with electrons at the top and ions at the bottom. At 11 UT Polar is sampling the SC-structure while located at the distorted magnetosphere/magnetosheath boundary.

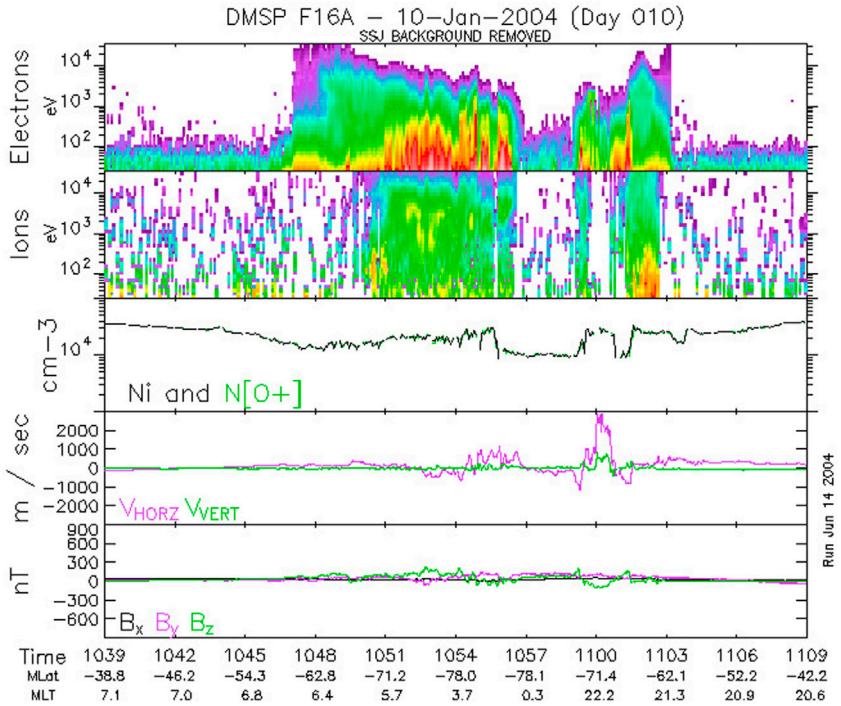

FIGURE 11
Satellite F16 field and plasma data collected on a dawn-dusk pass reaching to high MLATs in the Southern hemisphere. The focus is on the sunward-directed, 3 km/s flow burst at around 11 UT (panel 4). For further details, see text.

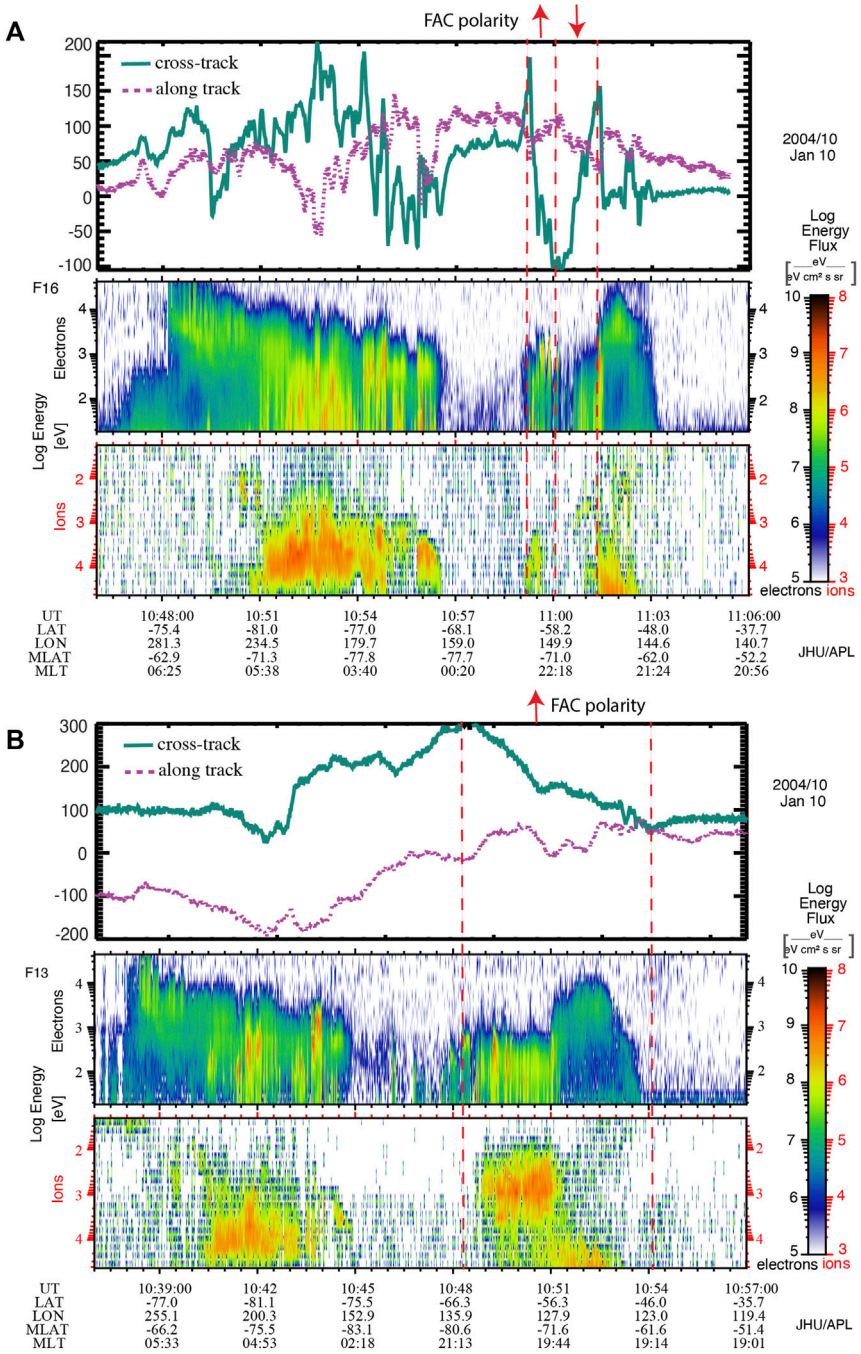

FIGURE 12
(A) (top) A zoom-in of F16 data showing the magnetic field perturbations and associated FAC pair, and the precipitation electrons and ions they occur in. **(B)** (bottom) Similar observations made by F13 in the southern hemisphere in approximately the same region as F16 but about 1–2 h MLT earlier. It is included to put the F16 observations into context.

fluxes of electrons and ions, the density, the velocity and the magnetic field perturbations seen by F16 from 10:39 to 11:09 UT. We supplement this with the top part of Figure 12 (Figure 12A), which shows the magnetic field, and the electron and ion spectrograms. The MLAT and MLT are given at bottom. Around 10:59:02 UT (similar time to Polar) during the bouncing motion of the magnetopause and when F16 was at the poleward edge of the oval, the spacecraft sees a strong (~3 km/s) sunward flow burst in a double vortex-like structure (Figure 11, fourth panel). From Figure 12A, which plots more

clearly the cross-track (green solid line) and along-track (magenta dotted line) perturbations in the magnetic field, this flow structure is flanked by two (up and down) field-aligned currents (FACs), which change polarity at ~11 UT.

In the poleward region of the oval at pre-midnight local times (MLT = 21:48–22:47), the FAC is upward a few min before 11:00 UT and then downward a few min after 11:00 UT. In the upward FAC region, mono-energetic and broadband electrons can be found [49,50]. As discussed next, the equatorward portion of the oval at pre-midnight (MLT ~21:48–21:22 and MLAT ~ −67.0° to −61.4°) is sampled at 11:01:23–11:03:11 UT and the precipitation looks more typical, suggesting that closer to Earth, near the isotropy earthward boundary, the behavior of plasma and magnetic field is more typical. At post-midnight (00:30–05:00 MLT), at the poleward region of the oval, there is evidence of broadband electron acceleration which can be attributed to Alfvén wave activities (e.g., [49]).

Figure 12B, which shows the magnetic field and spectrograms from F13, is included for context. F13 crosses almost the same region as F16 but about 10 min earlier and 1–2 h earlier in MLT. This gives us an idea what the region looked like before the disturbance. Prior to 11:00 UT, the postmidnight-dawn auroral oval looks very similar in F13 and F16 and exhibits typical, moderately active plasma sheet and plasma sheet boundary layer (PSBL) electron and ion precipitation (e.g., [51]; [52]). F13 crosses the premidnight oval from 10:47:44 to 10:53:48 UT, prior to the arrival of the disturbance, and also observes typical moderately active plasma sheet precipitation. The first panel in Figure 12B shows that F13 also observes region-1 (R1) upward FAC (e.g., [37]). However, when F16 crosses the pre-midnight oval about 10 min later the characteristics of the oval had changed, particularly the poleward portion of the auroral oval where the spacecraft observes up and down FAC regions and reduced electron and ion precipitation energy fluxes, as described above. On the other hand, the equatorward portion of the oval at 11:01:23—11:03:11 UT (MLAT = −67.01° to −61.41°) looks similar to that observed by F13.

Far tail observations

We now return to the prime concern which kicked off this investigation: *Wind*'s observation of a precursor to tail flapping (Figure 1). A close view of this "precursor" is given in Figure 13. For the 10-min interval 11:20 to 11:30 UT, this plot shows the proton density, temperature and flow components in GSE coordinates, the total field and its GSE components, and the proton ß. Since, as noted earlier, the absolute values of the velocity moments derived from the onboard moments of the PESA Low instrument are not to be trusted, we use PESA High, at a resolution of ~90 s. Analysis of the 3D VDFs from PESA High

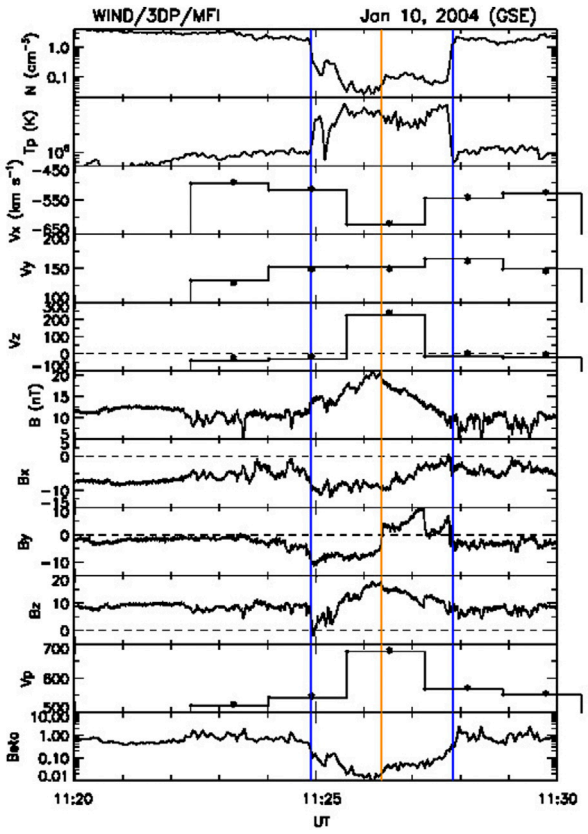

FIGURE 13
A zoom−in of the structure (bracketed by blue guidelines) in the far tail seen by *Wind* before the tail started to flap: A low-density, hot plasma is being ejected down the tail in a flux rope structure. The velocity moments are obtained from the PESA-HIGH instrument. See text for further details.

gives the values shown. The interval over which each data point is valid (~90 s) is also shown.

At the start and end of the interval (outside the time span bracketed by vertical *blue* guidelines), *Wind* is in the magnetosheath: hot and dense plasma moving antisunward at ~540 km/s. Starting at around 11:25 UT *Wind* enters a large blob of lobe (low-ß) plasma in a flux rope-type structure which was being ejected at higher speeds (~680 km/s) down the tail. The low density and high temperature are obtained from the PESA High spectrograms. The flux rope configuration is inferred from the enhanced *B*, peaking at the center, and the coherent rotations in the other field components. Taking the duration (2.9 min) and multiplying it by the plasma velocity (678 km/s) yields a scale size of the plasmoid of 18.4 R_E. Minimum variance analysis [53] gives an orientation for the flux rope axis of (−0.19, −0.24, 0.95) GSE, i.e., pointing strongly North. This would be a strange orientation in the tail if there were no twisting. (See discussion below where the effect of interplanetary *By* < 0 is taken into account.)

The magnetosheath flow has a significant positive *Vy* component (~150 km/s), implying that the tail is deflected towards dusk. The tail axis makes an angle with the Sun-Earth line of ~17°. This is evidence of the windsock effect, which results from the positive East-West flow component, *Vy*, seen by ACE at the CS (Figure 2; [40,42,54]).

How are the fast tailward-moving plasmoid at *Wind* and the fast sunward-moving twin-vortex pattern at F16 related? We suggest the following interpretation. The *Wind* and F16 observations point to the formation of an X line in the near-Earth tail region earthward of *Wind*. *Wind* observes the large plasmoid while F16 observes a fast sunward-flowing, rather large bursty bulk flow (BBF)-like structure (width of about 1 h in MLT).

The velocity shear between the BBF-like structure and the ambient plasma may lead to a vortex-like flow and a pair of upward-downward FACs ([55], their Figure 19) as they sweep aside the field lines, similar to Kelvin-Helmholtz vortices forming at the magnetopause boundary due to velocity shear [56,57]. However, the pair of FACs seen by F16 is in reverse order (the upward FAC is Westward rather than Eastward of the downward FAC), which may be attributed to the twisting of the tail produced by the torque exerted by IMF *By*.

Wind observes a tailward-flowing plasmoid at the distant tail in the lobe on open field lines. DMSP F16 observes fast vortex-like structures flowing sunward, just Earthward of the open-closed boundary (reconnection line; see Figure 11, fourth panel). Moreover, the F16 satellite also observes an upward and downward FAC near the open-closed field line boundary (Figure 12A, top panel), which would be consistent with the fast flow. In the upward FAC region, at −73.6° to −70.6° MLAT, F16 observes mono-energetic electrons, which is suggestive of the presence of a quasi-static upward electric field that accelerates the electrons downward and retards ion precipitation. This may partly explain the low ion energy fluxes in the F16 spectrogram. However, in the downward FAC region in Figure 12A from MLAT = −70.6° to −67.0°, the F16 ion energy fluxes remain low despite there being no evidence of mono-energetic electrons and, hence, of a significant upward electric field. The low ion and electron fluxes observed by F16 are quite noticeable when compared to those in the pre-midnight oval near the open-closed boundary observed by F13 (Figure 12B). F13 observes an upward FAC and there is some evidence of monoenergetic and broadband electrons, which can limit some ion precipitation. Yet, in spite of this, the ion energy fluxes in F13 observations are still higher than those in the downward FAC region in the F16 observations. The F16 electron energy fluxes also appear to be lower than their counterpart in the F13 observations.

Low ion and electron energy fluxes would be consistent with the scenario where the fast flow structure has depleted pressure and flux tube entropy (e.g., [58,59]). In Figure 12A, equatorward of the downward FAC region, the F16 ion and electron energy fluxes appear typical and are comparable to their counterpart in the F13 observations (Figure 12B). This would be expected because this region is not part of the fast flow region.

Additionally, we perform a very crude calculation of the timing when *Wind* and DMSP observe the disturbance. *Wind*, located ~227 Re downtail, observes the plasmoid around 11: 25–11:28 UT. The plasmoid moving at −621 km/s from the X-line around X ~ −25 Re would reach *Wind* in about 34 min, assuming a constant plasmoid speed from the X-line to the *Wind* location. DMSP observes the fast flow structure around 11:00 UT. Assuming fast flow speed of 300 km/s, the timing would suggest an X-line forming in the ballpark of 10: 51–10:54 UT

Summary and discussion

In this work, we analyzed an interlinked chain of effects in the M-I system elicited by a short (~1/2 h) interplanetary non-reconnecting, bifurcated current sheet. The interplanetary structure was observed by ACE, ~237 R_E upstream of Earth. Its signatures included a discontinuity in the gradients of the ***B*** and ***V*** profiles and concomitant *Np*-rise and *B*-dip near peak magnetic field strength. This structure was observed inside an ICME and its magnetic field was dominated by the East-West component, *By*, while strong non-radial flows (*Vy* and *Vz*) were reversing their polarity.

The magnetospheric response included: 1) in-out motions of the magnetopause and bow shock, 2) a local deformation of the magnetopause in the postnoon sector; 3) a 3 km/s sunward flow of a twin vortex pattern at the edge of the auroral oval, which was flanked by two sets of FACs, and associated with low ion and electron energy flux/pressure/flux tube entropy, having a large spatial scale (within 1 h in MLT), and 4) in the distant (~−230 R_E) tail, a fast (~−680 km/s) and large ejection of lobe-like plasma in a magnetic flux rope structure, which preceded observations of tail flapping. Using a reliable timer assured us that these phenomena are inter-related. The circumstances in which the IP feature occurs, in particular a strongly kinked, negative *By* (~−15 nT) and a flow component *Vy* which had just transitioned from negative to positive, strongly twisted and deflected the tail from the Sun-Earth direction. It was possible to monitor the effects over such a long distance because of a good arrangement of spacecraft in the unperturbed solar wind, near the magnetopause, just below the magnetopause, and in the distant tail. The work thus illustrates how observations from an array of spacecraft spread throughout the magnetosphere can provide insight into, and whet our appetite for, magnetospheric dynamics.

Regarding the persistence of the density pulse, it is likely a structural feature of the current sheet related to its total internal pressure balance. The density change is not sharp like at a tangential discontinuity (TD) and does not induce new waves.

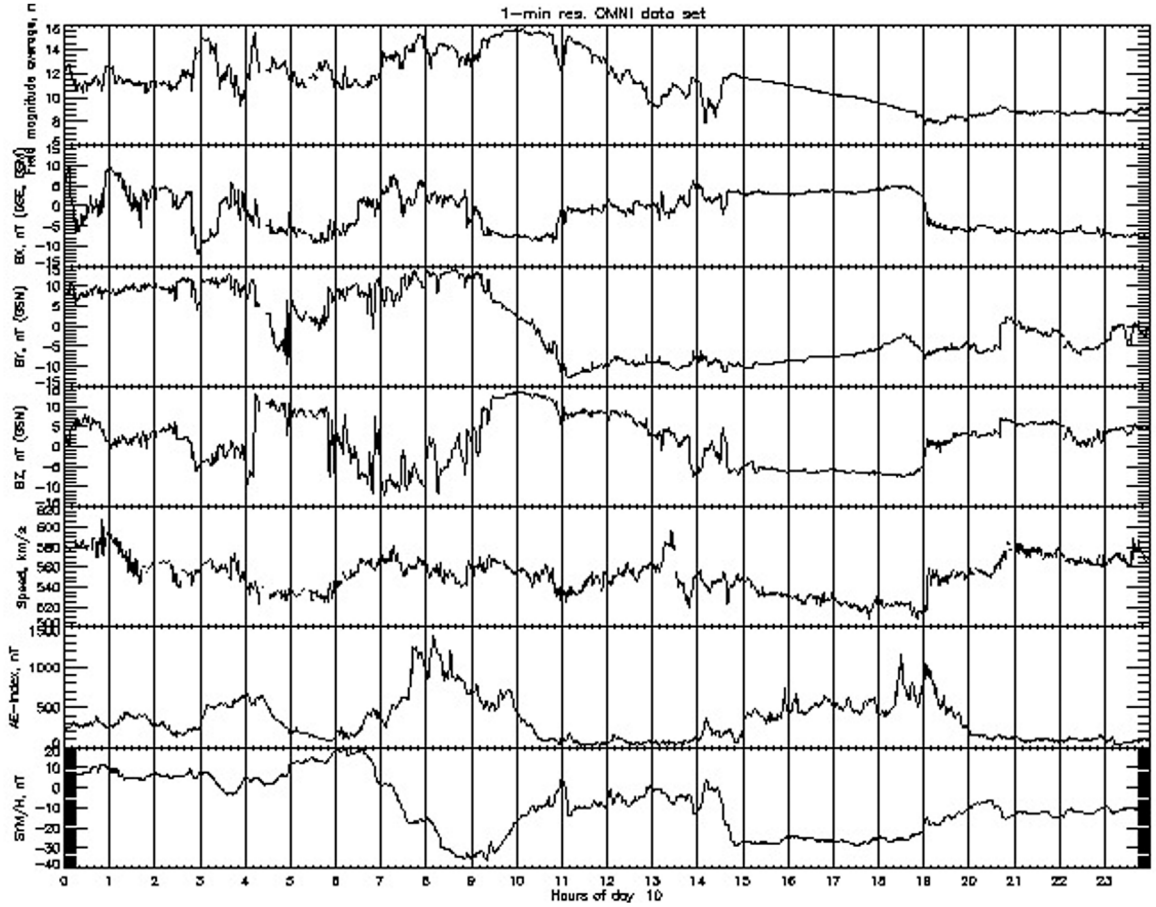

FIGURE 14
Data from the NASA OMNI website showing features of the interplanetary field and flow, and, in the bottom two panels, the substorm auroral electojet (AE) index and the storm-time Sym-H index. Interplanetary data are delayed to the magnetopause. At 11 UT, the time of arrival of the CS structure, both geomagnetic indices indicate very quiet conditions. Substorms appear a few hours before and after 11 UT.

Interestingly, the event took place in otherwise very quiet geomagnetic conditions. As shown in Figure 14 (last 2 panels) the AE index was ~0 nT and Sym-H ~ −10 nT. The kink structure was embedded in a 5-to-6-h period (9-~15 UT), starting in the recovery phase of a substorm and a (weak) storm, and finishing at the start of the growth phase of another substorm and an intensification of the ring current. As seen in the top panels (IP data are time-shifted to the magnetopause), this covered a period in the ICME around a maximum in *B*, positive *Bz* and a bipolar variation in *By*.

With the strong interplanetary *By* (~−15 nT), one would expect the geomagnetic tail to twist. We would expect the tail neutral sheet (NS) to be strongly twisted so that its normal would point towards–Y (GSE, West). Can this effect be seen in the *in situ* data at *Wind*? There are at least two indications. 1) Above, we derived the axis orientation of the flux rope at *Wind*, and found it to be mainly in the + z GSE direction. With the imposed twist this would be mainly along the *Y*-direction, which is an orientation more in line with what one would expect; 2) A further confirmation of the tail twist comes from the FAC polarities seen at F16 (Figure 12A). If we accept the hypothesis of a BBF-like origin, then the FAC polarity is in reverse order. From (55, their schematic Figure 19), the inward FAC (i.e., into ionosphere) is more towards dawn than the outward FAC. Here, however, the inward FAC occurs at 21 MLT and the outward at 22 MLT, i.e., the inward one is more toward the dusk than the outward one. However, a large enough twist would invert the location of the FACs in the dawn-dusk direction and restore agreement.

The IP medium had also a significant *Vy* component, which had turned positive shortly before our event (see Figures 2, 3). Interplanetary *Vy* is at the origin of the tail windsock effect [40,42,54], i.e., a deflection of the aberrated geomagnetic tail to align its axis along the solar wind flow. In our case the tail would be dragged toward dusk (i.e., tilted toward the + *Y* direction, where *Wind* was). This was also observed.

The North-South interplanetary component of the flow *Vz* varies over a significant range. Directional changes in this component have been argued to be the cause of the flapping of the tail [60–62]. Flapping consists of an up-down perturbation of the tail neutral sheet, advancing in the East-West direction and approaching the flanks [63]. From this we conclude that *Vz* is the major source of the tail flapping seen by *Wind* after the "precursor."

We identified a nice "timer", i.e., a rise in *Np* and a simultaneous drop in *B*, as an imprint of this event. Did we see this imprint in the *Wind* spacecraft observations? Taking a longer interval, we obtain a second peak in *Np* simultaneous with a minimum in *B* (Supplementary Figure S2, red traces) at 11: 49 UT, i.e., 99 min after they were seen at ACE. From [64] we get an estimate of this delay if we divide the ACE-*Wind* separation by the solar wind speed (540 km/s). This estimate gives 92 min, which is in reasonable agreement. The CS lags behind the arrival of precursor (~11:25 UT) by ~24 min. This delay is expected since, as argued above, the CS triggers reconnection and the accelerated flows produced there travel inside the tail and outrun the SC, which travels in the solar wind [65].

Though multi-faceted, the effects in the M-I system do not indicate a system-wide response. Consider the F13 and F15 observations. F15 (Supplementary Figure S1 in the Supplementary Material S1), for example, observes the dusk auroral oval (not nightside) and observes signatures of Kelvin-Helmholtz instability near the open-closed boundary, which would be consistent with the high solar wind speed (~540 km/s) observed during this event [56,57].

To conclude, in this paper we have focused on a clear interplanetary magnetic field and plasma structure. This feature consisted of a simultaneous drop in B and a rise in N which were accompanied by strong magnetic field and plasma flow changes. It was embedded in a—much larger—ICME, so that it would hardly have drawn any attention by itself had not a fortuitous deployment of spacecraft allowed us to monitor the multi-faceted response it elicited in the magnetosphere-ionosphere-magnetotail system over a radial distance of more than 400 Re.

Data availability statement

The original contributions presented in the study are included in the article/Supplementary Material, further inquiries can be directed to the corresponding author.

Author contributions

CF, SF, LW, DS, and SC, Develop idea, write manuscript and analyze data NL, RT, and JB: Contribute to interpretation.

Funding

CJF would like to acknowledge support from NASA Grants 80NSSC20K0197 and 80NSSC19K1293. SW acknowledges support of NASA grants 80NSSC20K0704, 80NSSC20K0188, 80NSSC22K0515, 80NSSC19K0843, 80NSSC21K1678. BJV is supported by the NASA Solar and Heliospheric Physics grant 80NSSC19K0832.

Acknowledgments

We are grateful to F. T. Gratton and N. V. Erkaev for helpful discussions.

Conflict of interest

The authors declare that the research was conducted in the absence of any commercial or financial relationships that could be construed as a potential conflict of interest.

Publisher's note

Supplementary material

The Supplementary Material for this article can be found online at: https://www.frontiersin.org/articles/10.3389/fphy.2022.942486/full#supplementary-material

References

1. Burlaga L., Sittler E., Mariani F., Schwenn R. Magnetic loop behind an interplanetary shock: Voyager, Helios, and IMP 8 observations. *J Geophys Res* (1981) 86:6673. doi:10.1029/ja086ia08p06673

2. Gonzalez W. D., Tsurutani B. T. Criteria of interplanetary parameters causing intense magnetic storms (Dst<– 100 nT). *Planey Space Sce* (1987) 35(9):1101–9. doi:10.1016/0032-0633(87)90015-8

3. Farrugia C. J., Burlaga L. F., Lepping R. P. Magnetic clouds and the quiet/storm effect at Earth: A review, in magnetic storms. In: T. B. Tsurutani, W. D. Gonzalez, Y. Kamide, J. K. Arballo, editors. *Geophysical monogr. Ser*, vol. 98. Washington, D. C.: AGU (1997). p. 91.

4. Farrugia C. J., Freeman M. P., Burlaga L. F., Lepping R. P., Takahashi K. The Earth's magnetosphere under continued forcing: Substorm activity during the

passage of an interplanetary magnetic cloud. *J Geophys Res* (1993) 98:7657–71. doi:10.1029/92ja02351

5. Huang C.-S., Reeves G. D., Borovsky J. E., Skoug R. M., Pu Z. Y., Le G. Periodic magnetospheric substorms and their relationship with solar wind variations. *J Geophys Res* (2003) 100:1255. doi:10.1029/2002JA009704

6. Henderson M. G., Skoug R., Donovan E., Thomsen M. F., Reeves G. D., Denton M. H., et al. Substorms during the 10-11 August 2000 sawtooth event. *J Geophys Res* (2006) 111:A06206. doi:10.1029/2005JA011366

7. Neugebauer M., Clay D. R., Goldstein B. E., Tsurutani B. T., Zwickl R. D. A reexamination of rotational and tangential discontinuities in the solar wind. *J Geophys Res* (1984) 89:5395. doi:10.1029/ja089ia07p05395

8. Neugebauer M. The structure of rotational discontinuities. *Geophys Res Lett* (1989) 16(11):1261–4. doi:10.1029/gl016i011p01261

9. Neugebauer M. Comment on the abundances of rotational and tangential discontinuities in the solar wind. *J Geophys Res* (2006) 111:A04103. doi:10.1029/2005JA011497

10. Liu Y. D., Luhmann J. G., Kajdiz P., Kilpua E. K. J., Lugaz N., Nitta N. V., et al. Observations of an extreme storm in interplanetary space caused by successive coronal mass ejections. *Nat Commun* (2014) 5:3481. doi:10.1038/ncomms4481

11. Lugaz N., Farrugia C. J., Huang C.-L., Spence H. E. Extreme geomagnetic disturbances due to shocks within CMEs. *Geophys Res Lett* (2015) 42:4694–701. doi:10.1002/2015gl064530

12. Farrugia C. J., Gratton F. T., Lund E. J., Sandholt P. E., Cowley S. W. H., Torbert R. B., et al. Two-stage oscillatory response of the magnetopause to a tangential discontinuity/vortex sheet followed by northward IMF: Cluster observations. *J Geophys Res* (2008) 113:A03208. doi:10.1029/2007JA012800

13. Völk H. J., Auer R. D. Motions of the bow shock induced by interplanetary disturbances. *J Geophys Res* (1974) 79:40–8. doi:10.1029/ja079i001p00040

14. Wu B. H., Mandt M. E., Lee L. C., Chao J. K. Magnetospheric response to solar wind dynamic pressure variations: Interaction of interplanetary tangential discontinuities with the bow shock. *l Geophyl Re: Space Phys* (1993) 98:21297. doi:10.1029/93JA01013

15. Kaufmann R. L., Konradi A. Explorer 12 magnetopause observations: Large-scale nonuniform motion. *J Geophys Res* (1969) 74:3609–27. doi:10.1029/ja074i014p03609

16. Sibeck D. G. A model for the transient magnetospheric response to sudden solar wind dynamic pressure variations. *J Geophys Res* (1990) 95:3755. doi:10.1029/ja095ia04p03755

17. Fairfield D. H., Farrugia C. J., Mukai T., Nagai T., Fedorov A. Motion of the dusk flank boundary layer caused by solar wind pressure changes and the kelvin-helmholtz instability: 10–11 january 1997. *Geophy. Re.* (2003) 108:A121460. doi:10.1029/2003JA010134

18. Maynard N. C., Farrugia C. J., Ober D. M., Burke W. J., Dunlop M., Mozer F. S., et al. Cluster observations of fast shocks in the magnetosheath launched as a tangential discontinuity with a pressure increase crossed the bow shock. *J Geophys Res* (2008) 113:A10212. doi:10.1029/2008JA013121

19. Thomsen M. F., Thomas V. A., Winske D., Gosling J. T., Farris M. H., Russell C. T., et al. Observational test of hot flow anomaly formation by the interaction of a magnetic discontinuity with the bow shock. *J Geophys Res* (1993) 98:15319. doi:10.1029/93ja00792

20. Sibeck D. G., Borodkova N. L., Schwartz S. J., Owen C. J., Kessel R. Comprehensive study of the magnetospheric response to a hot flow anomaly. *J Geophys Res* (1999) 104(A3):4577–93. doi:10.1029/1998ja900021

21. Schwartz S. J., Paschmann G., Sckopke N., Bauer T. M., Dunlop M., Fazakerly A. N., et al. *Geophy. Re.* (2000) 105(12):639650–12.

22. Smith C. W., L'heureux J., Ness N. F., Acuna M. H., Burlaga L. F., Scheifele J. The ACE magnetic fields experiment. *Space Sc. Re.* (1998) 86:613–32.

23. McComas D. J., Bame S. J., Barker P., Feldman W., Phillips J., Riley P., et al. Solar wind electron proton alpha monitor (SWEPAM) for the advanced composition explorer. *Space Sc. Re.* (1998) 86:563–612. doi:10.1023/A:1005040232597

24. Lepping R. P., Acuna MH, Burlaga LF, Farrell WM, Slavin JA, Schatten KH, et al. The wind magnetic field investigation. *Space Sci Rev* (1995) 71:207–29. doi:10.1007/bf00751330

25. Lin R. P., Anderson KA, Ashford S, Carlson C, Curtis D, Ergun R, et al. A three-dimensional plasma and energetic particle investigation for the wind spacecraft. *Space Sci Rev* (1995) 71:125–53. doi:10.1007/bf00751328

26. Wilson L. B., Brosius A. L., Gopalswamy N., Nieves-Chinchilla T., Szabo A., Hurley K., et al. A quarter century of *Wind* spacecraft discoveries. *Res Geophys* (2021) 59:e2020RG000714. doi:10.1029/2020RG000714

27. Kokubun S., Yamamoto T., Acuna M. H., Hayashi K., Shiokawa K., Kawano H. The geotail magnetic field experiment . *Geoma. Geoelect.* (1994) 46:7–21. doi:10.5636/jgg.46.7

28. Mukai T., Machida S., Saito Y., Hirahara M., Terasawa T., Kaya N., et al. The low energy particle (LEP) experlment onboard the GEOTAIL satellite. *JGgeomagnGeoelec* (1994) 46:669–92. doi:10.5636/jgg.46.669

29. Balogh A., Carr CM, Acuna MH, Dunlop MW, Beek TJ, Brown P, et al. The Cluster magnetic field investigation: Overview of inflight performance and initial results. *Ann Geophys* (2001) 19:1207–17. doi:10.5194/angeo-19-1207-2001

30. Rème H., Aoustin C, Bosqued JM, Dandouras I, Lavraud B, Sauvaud JA, et al. First multispacecraft ion measurements in and near the Earth's magnetosphere with the identical Cluster ion spectrometry (CIS) experiment. *Ann Geophys* (2001) 19:1303–54. doi:10.5194/angeo-19-1303-2001

31. Russell C. T., Snare R. C., Means J. D., Pierce D, Dearborn D, Larson M, et al. The GGS/POLAR magnetic fields investigation. *Space Sci Rev* (1995) 71:563–82. doi:10.1007/BF00751341

32. Scudder J., Hunsacker F., Miller G., Lobell J, Zawistowski T, Ogilvie K, et al. Hydra — a 3-dimensional electron and ion hot plasma instrument for the polar spacecraft of the ggs mission. *Space Sci Rev* (1995) 71:459–95. doi:10.1007/bf00751338

33. Hardy D. A., Schmitt L. K., Gussenhoven M. S., Marshall F. J., Yeh H. C, Shumaker T. L., et al. *Precipitating electron and ion detectors (SSJ/4) for the block 5D/flights 6-10 DMSP satellites: Calibration and data presentation, rep. AFGL-TR-84-0317, air force geophys*. Mass: Lab., Hanscom Air Force Base (1984).

34. Rich F. J., Hardy D. A., Gussenhoven M. S. Enhanced ionosphere-magnetosphere data from the DMSP satellites. *Eos Trans AGU* (1985) 66:513. doi:10.1029/eo066i026p00513

35. Wing S., Johnson J. R. Theory and observations of upward field-aligned currents at the magnetopause boundary layer. *Geophys Res Lett* (2015) 42:9149–55. doi:10.1002/2015GL065464

36. Johnson J. R., Wing S. The dependence of the strength and thickness of field-aligned currents on solar wind and ionospheric parameters. *J Geophys Res Space Phys* (2015) 120:3987–4008. doi:10.1002/2014JA020312

37. Wing S., Ohtani S. I., Newell P. T., Higuchi T., Ueno G., Weygand J. M., et al. Dayside field-aligned current source regions. *J Geophys Res* (2010) 115:A12215. doi:10.1029/2010JA015837

38. Richardson I.G., Cane H.V. Near-earth interplanetary coronal mass ejections during solar cycle 23 (1996 – 2009): Catalog and summary of properties. *Sol Phys* (2010) 264:189–237. doi:10.1007/s11207-010-9568-6

39. Al-Haddad N., Galvin A. B., Lugaz N., Farrugia C. J., Yu W. Investigating the cross-section of coronal mass ejections through the study of non-radial flows with STEREO/PLASTIC.*Astrophysical J* (2021) 927(1):68.

40. Shodhan S., Siscoe G. L., Frank L. A., Ackerson K. L., Paterson W. R. Boundary oscillations at Geotail: Windsock, breathing, and wrenching. *J Geophys Res* (1996) 101(A2):2577–86. doi:10.1029/95ja03379

41. Shang W. S., Tang B. B., Shi Q. Q., Tian A. M., Zhou X. Y., Yao Z. H., et al. Unusual location of the geotail magnetopause near lunar orbit: A case study. *J Geophys Res Space Phys* (2019) 125(4):e2019JA027401. doi:10.1029/2019ja027401

42. Borovsky J. E. The effect of sudden wind shear on the Earth's magnetosphere: Statistics of wind shear events and CCMC simulations of magnetotail disconnections. *J Geophys Res* (2012) 117(A6). doi:10.1029/2012ja017623

43. Borovsky J.E. Looking for evidence of wind-shear disconnections of the earth's magnetotail: GEOTAIL measurements and LFM MHD simulations. *J Geophys Res Space Phys* (2018) 123(7):5538–60. doi:10.1029/2018ja025456

44. Cowley S. W. H. Magnetospheric asymmetries associated with the Y-component of the IMF. *Planet Space Sci* (1981) 29:79–96. doi:10.1016/0032-0633(81)90141-0

45. Wing S., Newell P. T., Sibeck D. G., Baker K. B. A large statistical study of the entry of interplanetary magnetic field Y-component into the magnetosphere. *Geophys Res Lett* (1995) 22:2083–6. doi:10.1029/95GL02261

46. Russell C. T., Melliot M. M., Smith E. J., King J. H. Multiple spacecraft observations of interplanetary shocks: Four spacecraft determinations of shock normals. . *Geophy. Re.* (1983) 88:4739–5408.

47. Knetter T., Neubauer F. M., Horbury T., Balogh A. Four-point discontinuity observations cluster magnetic field data: A statistical survey. *JGgeomagnGeoelec* (2004) 109:A06102. doi:10.5636/jgg.46.7

48. Farrugia C. J., Cohen I. J., Vasquez B. J., Lugaz N., Alm L., Torbert R. B., et al. Effects in the near-magnetopause magnetosheath elicited by large-amplitude Alfvénic fluctuations terminating in a field and flow discontinuity. *J Geophys Res Space Phys* (2018) 123(11):8983–9004. doi:10.1029/2018ja025724

49. Wing S., Gkioulidou M., Johnson J. R., Newell P. T., Wang C.-P. Auroral particle precipitation characterized by the substorm cycle. *J Geophys Res Space Phys* (2013) 118:1022–39. doi:10.1002/jgra.50160

50. Newell P. T., Sotirelis T., Wing S. Diffuse, monoenergetic, and broadband aurora: The global precipitation budget. *J Geophys Res* (2009) 114:A09207. doi:10.1029/2009JA014326

51. Wing S., Newell P. T. Central plasma sheet ion properties as inferred from ionospheric observations. *J Geophys Res* (1998) 103(A4):6785–800. doi:10.1029/97JA02994

52. Wing S., Newell P. T. 2D plasma sheet ion density and temperature profiles for northward and southward IMF. *Geophys Res Lett* (2002) 29(9):21. doi:10.1029/2001GL013950

53. Sönnerup B. U. Ö., Scheible M. Minimum andmaximum variance analysis. In: G. Paschmann P. W. Daly, editors. *Analysis methods for multi-spacecraft data*. Bern, Switzerland: International Space Science Institute (1998). p. 185–220.

54. Grygorov K., Přech L., Šafránková J., Němeček Z., Goncharov O. The far magnetotail response to an interplanetary shock arrival. *Planey Space Sce* (2014) 103:228–37. doi:10.1016/j.pss.2014.07.016

55. Birn J., Raeder J., Wang Y. L., Wolf R. A., Hesse M., On the propagation of bubbles in the geomagnetic tail. *Ann Geophys* (2004) 22(5): 1773–86. Copernicus GmbH. doi:10.5194/angeo-22-1773-2004

56. Johnson J. R., Wing S., Delamere P., Petrinec S., Kavosi S. Field-aligned currents in auroral vortices. *J Geophys Res Space Phys* (2021) 126:e2020JA028583. doi:10.1029/2020JA028583

57. Petrinec S. M., Wing S., Johnson J. R., Zhang Y. Multi-spacecraft observations of fluctuations occurring along the dusk flank magnetopause, and testing the connection to an observed ionospheric bead. *Front Astron Space Sci* (2022) 9: 827612. doi:10.3389/fspas.2022.827612

58. Pontius D. H., Wolf R. A. Transient flux tubes in the terrestrial magnetosphere. *Geophys Res Lett* (1990) 17(1):49–52. doi:10.1029/gl017i001p00049

59. Wing S., Johnson J. R., Chaston C. C., Echim M., Escoubet C. P., Lavraud B., et al. Review of solar wind entry into and transport within the plasma sheet. *Space Sci Rev* (2014) 184:33–86. doi:10.1007/s11214-014-0108-9

60. Runov A., Angelopoulos V., Sergeev V. A., Glassmeier K. H., Auster U., McFadden J., et al. Global properties of magnetotail current sheet flapping: THEMIS perspectives. *Ann Geophys* (2009) 27:319–28. doi:10.5194/angeo-27-319-2009

61. Sergeev V. A., Tsyganenko N. A., Angelopoulos V. Dynamical response of the magnetotail to changes of the solar wind direc-tion: An MHD modeling perspective. *Ann Geophys* (2008) 26:2395–402. doi:10.5194/angeo-26-2395-2008

62. Farrugia C. J., Rogers A. J., Torbert R. B., Genestreti K. J., Nakamura T. K. M, Lavraud B., et al. An encounter with the ion and electron diffusion regions at a flapping and twisted tail current sheet. *JGR Space Phys* (2021) 126:e2020JA028903. doi:10.1029/2020JA028903

63. Sergeev V. A., Runov A., Baumjohann M., Nakamura R., Zhang T. L., Volwerk M., et al. Current sheet flapping motion and structure observed by cluster. *Geophys Res Lett* (2003) 30:1327. doi:10.1029/2002GL016500

64. Kaymaz Z., Petschek H. E., Siscoe G. L., Frank L. A., Ackerson K. L., Paterson W. R., et al. Disturbance propagation times to the far tail. *J Geophys Res* (1995) 100(A12):23743. doi:10.1029/95ja02855

65. Sugiura M., Skillman T. L., Ledley B. G., Heppner J. P. Propagation of the sudden commencement of July 8, 1966, to the magnetotail. *J Geophys Res* (1968) 73(21):6699–709. doi:10.1029/ja073i021p06699

frontiers | Frontiers in Astronomy and Space Sciences

TYPE Original Research
PUBLISHED 30 August 2022
DOI 10.3389/fspas.2022.977801

OPEN ACCESS

EDITED BY
Olga Khabarova,
Institute of Terrestrial Magnetism Ionosphere and Radio Wave Propagation (RAS), Russia

REVIEWED BY
Xiaochen Shen,
Boston University, United States
Kyung-Chan Kim,
Chungbuk National University, South Korea

*CORRESPONDENCE
Dmitri Kondrashov,
dkondras@atmos.ucla.edu

SPECIALTY SECTION
This article was submitted to Space Physics,
a section of the journal
Frontiers in Astronomy and Space Sciences

RECEIVED 24 June 2022
ACCEPTED 08 August 2022
PUBLISHED 30 August 2022

CITATION
Kondrashov D, Drozdov AY, Vech D and Malaspina DM (2022), Prediction of plasmaspheric hiss spectral classes. *Front. Astron. Space Sci.* 9:977801. doi: 10.3389/fspas.2022.977801

Prediction of plasmaspheric hiss spectral classes

Dmitri Kondrashov[1]*, Alexander Y. Drozdov[2], Daniel Vech[3] and David M. Malaspina[3,4]

[1]Department of Atmospheric and Oceanic Sciences, University of California, Los Angeles, Los Angeles, CA, United States, [2]Department of Earth, Planetary and Space Sciences, University of California, Los Angeles, Los Angeles, CO, United States, [3]Laboratory for Atmospheric and Space Physics, University of Colorado Boulder, Boulder, CO, United States, [4]Department of Astrophysical and Planetary Sciences, University of Colorado Boulder, Boulder, CO, United States

We present a random forests machine learning model for prediction of plasmaspheric hiss spectral classes from the Van Allen Probes dataset. The random forests model provides accurate prediction of plasmaspheric hiss spectral classes obtained by the self organizing map (SOM) unsupervised machine learning classification technique. The high predictive skill of the random forests model is largely determined by the distinct and different locations of a given spectral class ("no hiss", "regular hiss", and "low-frequency hiss") in (MLAT, MLT, L) coordinate space, which are the main predictors of the simplest and most accurate base model. Adding to such a base model any other single predictor among different magnetospheric, geomagnetic, and solar wind conditions provides only minor and similarly incremental improvements in predictive skill, which is comparable to the one obtained when including all possible predictors, and thus confirming major role of spatial location for accurate prediction.

KEYWORDS

hiss waves, machine learning, random forests, radiation belts, plasmasphere

Introduction

The plasmasphere is a region of the Earth's inner magnetosphere consisting of low-energy (cool) plasma and is filled with a plasma wave mode called hiss: a broadband superposition of whistler-mode waves (Thorne et al., 1973). Hiss efficiently scatters electrons, facilitating their loss to the atmosphere and thereby playing a significant role in shaping inner magnetospheric electron populations, including the radiation belts. For this reason, predictive understanding of hiss waves is a critical component of inner magnetosphere research (e.g., Millan and Thorne, 2007; Ripoll et al., 2020).

The Van Allen Probes mission has greatly expanded our understanding of hiss. Li et al. (2015) showed that Van Allen Probes provided capability of measurement's of the low-frequency part of hiss waves (starting from 20 Hz). The previous hiss waves model was based on the CRESS measurements and was limited by the low frequency cut off being at ≈ 100Hz. However, realistic hiss wave frequency spectra are critical in evaluating pitch angle scattering rates inside the Earth's plasmasphere and plumes.

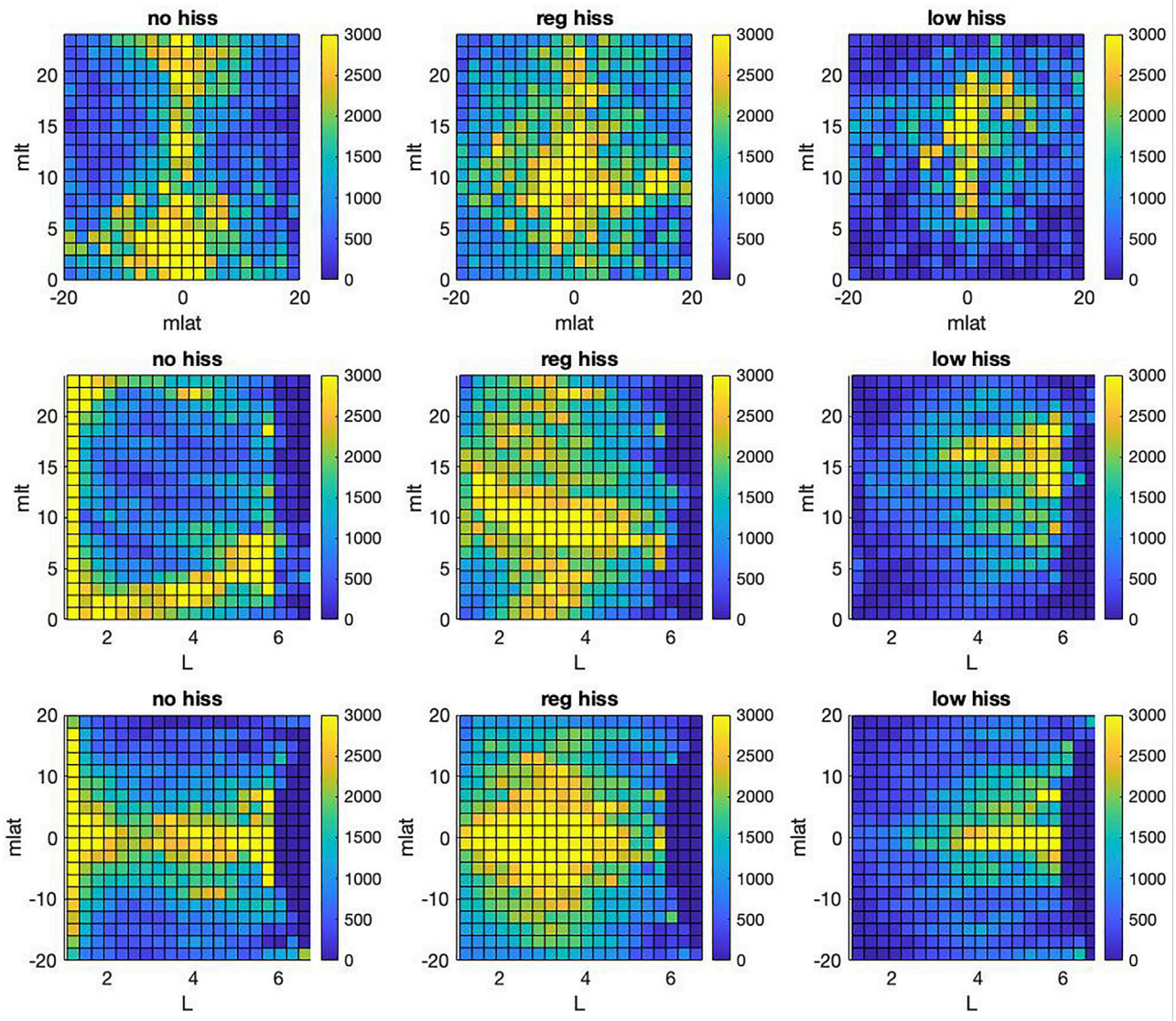

FIGURE 1
Distribution of spectral hiss classes: left column - "no hiss"; center column—"regular hiss"; right column - "low frequency hiss"; top row—(MLT, MLAT); middle row - (MLT, L); bottom row - (MLAT, L); color bar corresponds to class membership (number count of spectral shapes) in a given bin.

Indeed accounting for the low-frequency part of the hiss spectrum decreases the decay time scale by a factor of two for the multi-MeV electrons (Li et al., 2015). Additionally, accounting of the low-frequency hiss improves the numerical simulation of radiation belt electrons (Saikin et al., 2022).

The traditional approach for studying plasmaspheric hiss is based on calculating spatial averages of the magnetic field power spectra (Meredith et al., 2018). This technique has a disadvantage since it does not take into account the different shapes of power spectra that occur in a given L-shell vs MLT bin. Malaspina et al. (2017) showed that low-frequency hiss is a very distinct wave population in comparison to the hiss in the "regular" frequency range (> 150 Hz). In this study we show that low- and regular-frequency hiss have different spatial distributions, which is in agreement with results from Malaspina et al. (2017).

Vech et al. (2022) used an unsupervised machine learning technique of self organizing maps (SOM) for identification of plasma waves (Vech and Malaspina, 2021) to categorize plasmaspheric hiss power spectra, namely "no-hiss', "low-frequency" and "regular". Random forests (RF) is a well established machine learning technique for both regression and classification problems that found wide use is geosciences, such as in climate research (Kondrashov et al., 2007) and more

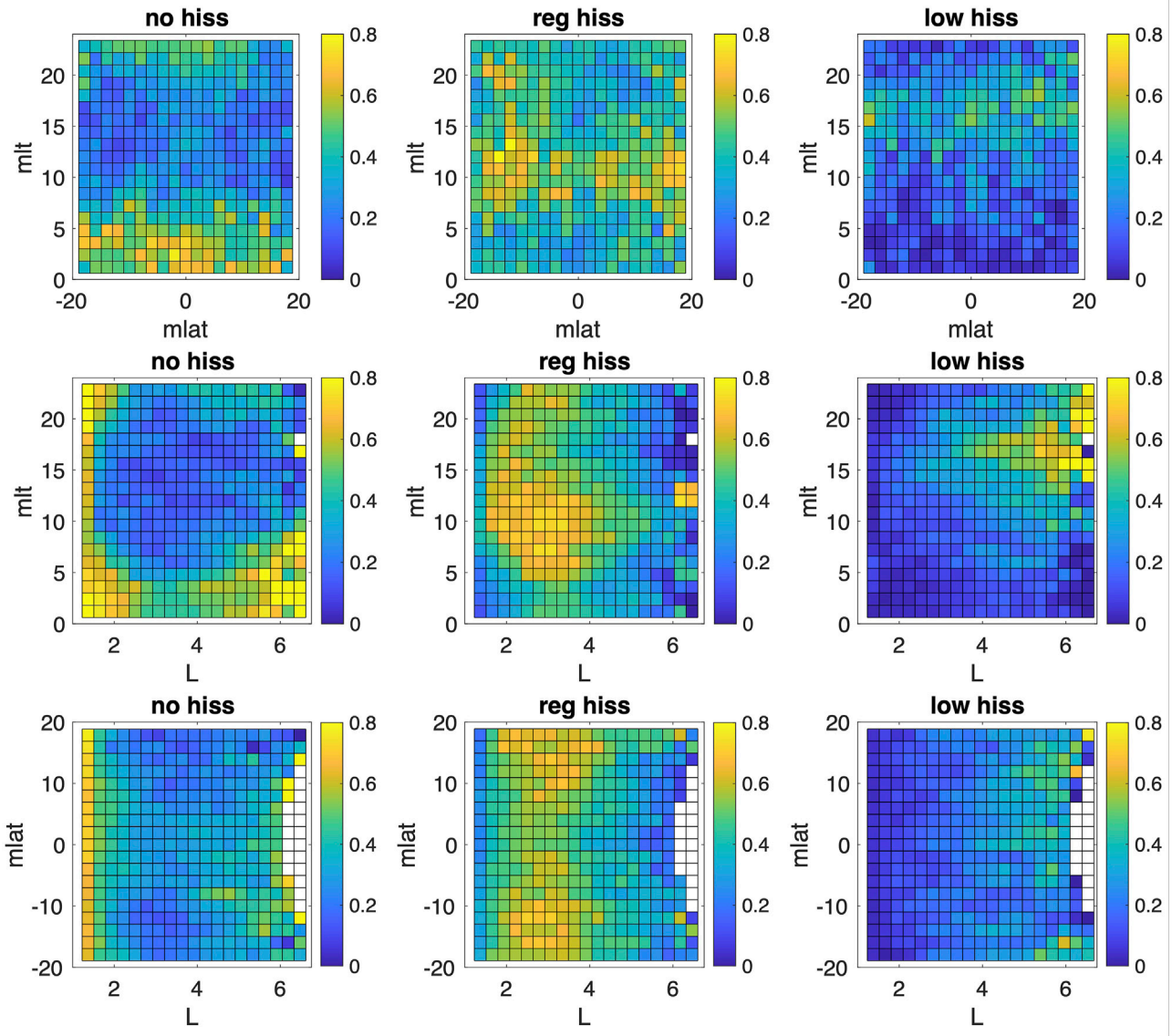

FIGURE 2
Same as in Figure 1 but normalized by the total number of spectral shapes for all three classes combined in each bin; white color corresponds to no data in the bin.

recently in space physics (Engell et al., 2017; Smith et al., 2020; Reep and Barnes, 2021; Zewdie et al., 2021; Bristow et al., 2022; Kasapis et al., 2022). In this work, we use RF to predict plasmaspheric hiss spectral classes by considering multiple magnetospheric, geomagnetic, and solar wind predictors, including information on the plasmapause that has been previously shown to be important in characterizing plasmaspheric hiss (Malaspina et al., 2017). Our predictive RF model can be used to enable additional statistical studies of distinct populations of the hiss waves.

Data and methods

Data

For this study we use the Van Allen Probes datasets of measurements from the Electric Fields and Waves (EFW) instrument (Wygant et al., 2013) and the Electric and Magnetic Field Instrument Suite and Integrated Science (EMFISIS) instrument suite (Kletzing et al., 2013). We used the same methodology of the hiss waves identification as in Malaspina et al. (2017), but with a different definition of the

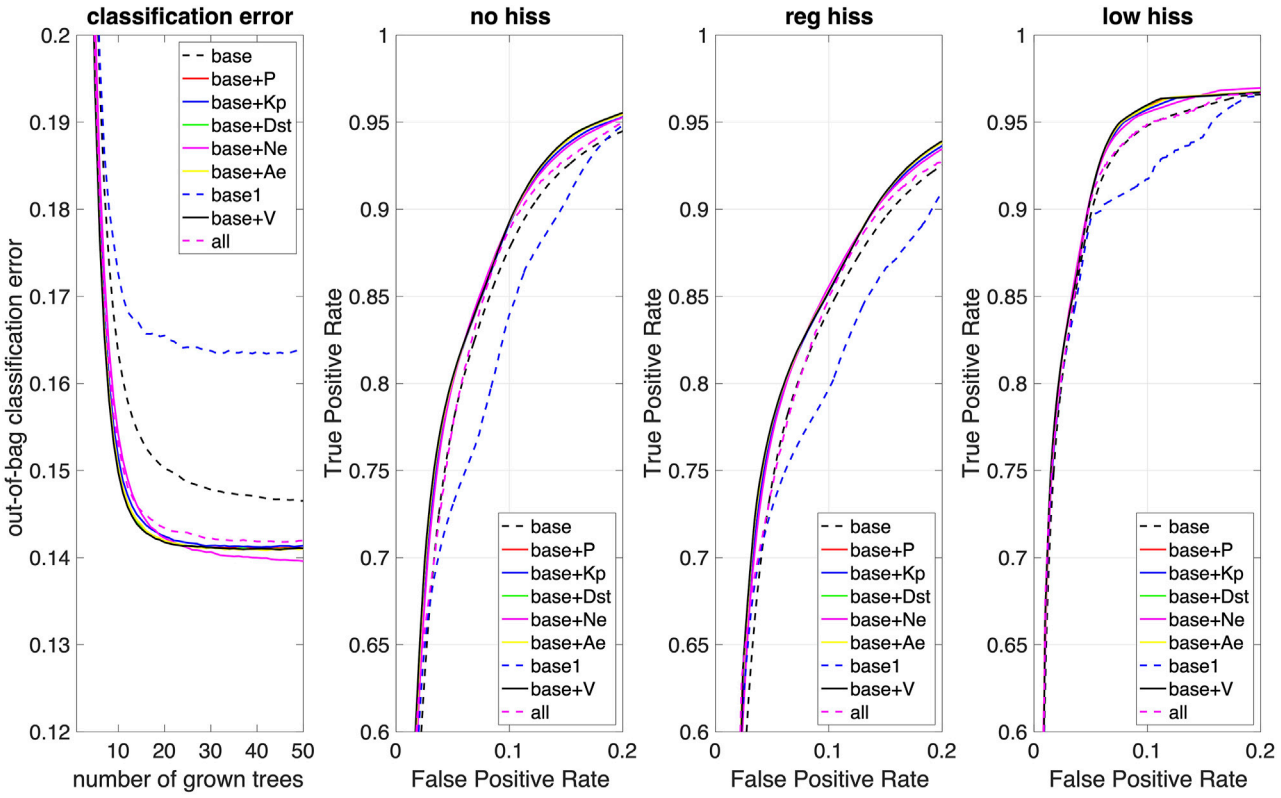

FIGURE 3
Overall classification error and receiver operating characteristic (ROC) curves (zoomed in) for predicting specific spectral classes of plasmaspheric hiss by random forest models using different predictors; "base" model—(MLAT, MLT, L); "base1" model — (MLAT, MLT, Lpp, dL) predictors; "all" model - all predictors.

plasmapause location. Data outside the plasmasphere ($Ne < 50\ cm^{-3}$) and data recorded during spacecraft charging events, eclipses, thruster firings, or EFW bias sweeps were excluded from our analysis (see (Malaspina et al., 2017) for details of the data cleaning). This Van Allen Probes data was used to classify spectral hiss classes with the self-organizing maps technique (see Vech et al. (2022) for details) and is briefly summarized next.

Plasmaspheric hiss spectral signatures classification using self-organizing maps

SOM is applied to identify plasmaspheric hiss power spectra that have "similar" shapes and without averaging together vastly different spectral shapes. SOM consists of a two-dimensional grid of nodes where the number of nodes is typically between a few dozen and a few hundred; in this study, we use 100 nodes. The goal of the training process is to assign each input vector (i.e., power spectra as a function of frequency at one time slice) to a node while ensuring that "similar" input vectors are assigned to the same or neighbouring nodes, while "dissimilar" input vectors are assigned to nodes far from each other. The dataset in this study is based on 1.76M normalized electric field power spectra measured by Van Allen Probes. The dataset was limited to approximately 250 days which were randomly selected from Probe A due to computationally expensive processing of SOM. After excluding data points contaminated by magnetosonic waves we are left with dataset containing 1.51M power spectra (see Vech et al. (2022) for details). We then categorized the power spectra by SOM as "regular hiss," with 38 nodes and 0.65 million spectra; "low frequency hiss," with 26 nodes and 0.33 million spectra; and "no hiss," with 36 nodes and 0.53 million spectra. The "no hiss" class has no wave activity in the range of 20–2000 Hz; and the "regular hiss" has a peak in the power spectra in the range of 150–2000 Hz, while the "low-frequency hiss" has additional wave activity that extends below 150 Hz (see Figure 1 in Vech et al. (2022)).

Figure 1 shows binned distribution of resulting plasmaspheric hiss spectral classes in different 2D planes of (MLAT, MLT, L) coordinates, where MLAT is magnetic latitude, MLT is magnetic local time, and L is spatial location

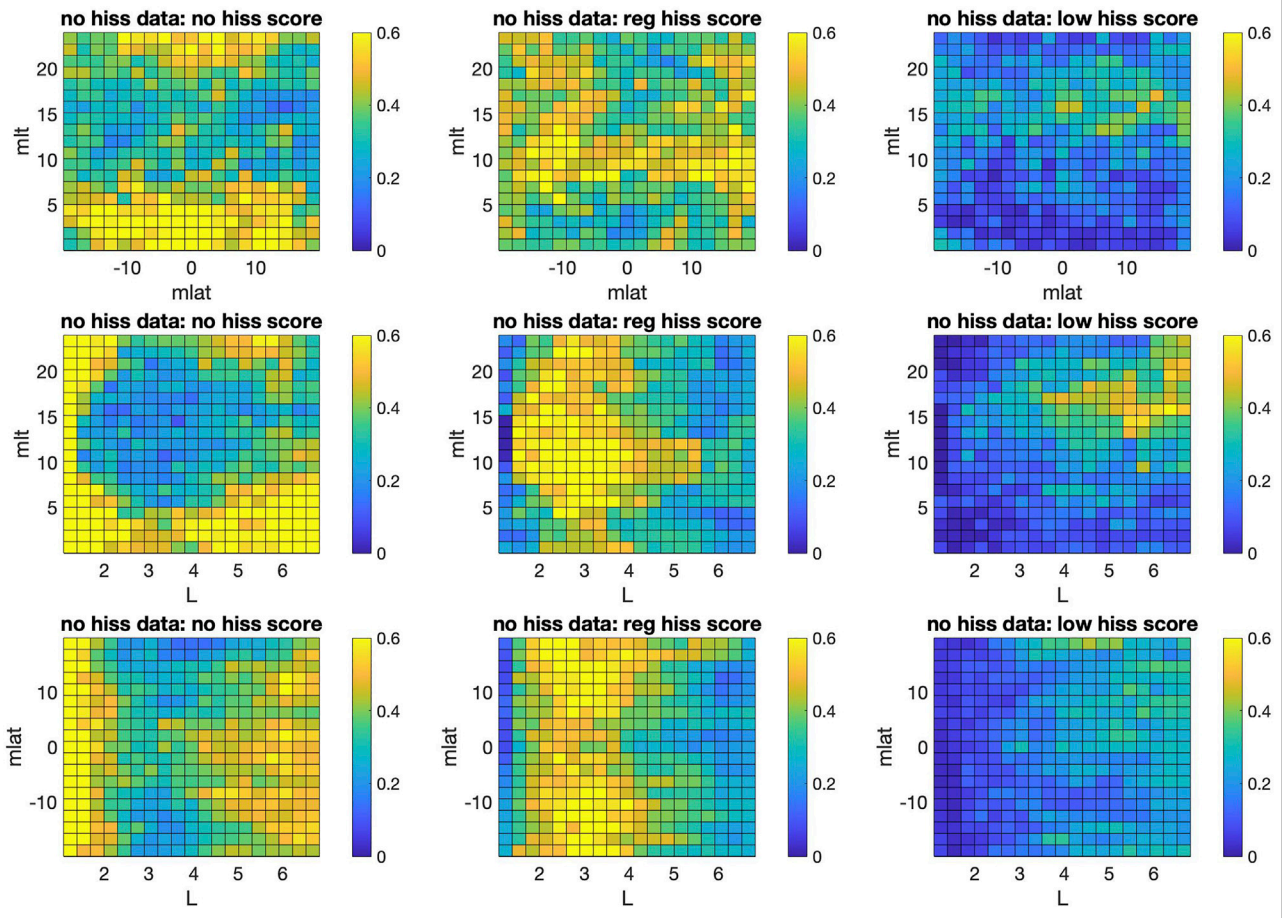

FIGURE 4
Partial dependence (Eq. 2) computed on the"no hiss" data points; color bar corresponds to the score of RF model.

(L-shell) in Earth radii. The spectral classes occupy distinct and different regions that are largely separated from each other, especially in the (MLT, L) plane. Figure 2 shows occurrence rate obtained by normalizing distribution in Figure 1 by normalizing to the total samples of all three spectral classes in each bin. Furthermore, different classes tend to occur in separate sectors of (MLAT, MLT, L) space, in agreement with Figures 1, 2 indicates that low-frequency hiss occurs more frequently from noon to dusk sector and at a larger L ($\gtrsim$ 5), which is generally similar to results of Shi et al. (2017). On the other hand, regular hiss is more dominant around noon sector. He et al. (2020, 2021) have also studied distribution of hiss, reporting a larger coverage in MLT. However, direct comparison with these studies is complicated due to details and differences in definitions of hiss wave measurements, including that our spectral classification does not consider the wave amplitude but only the shape of the wave spectra, as well as various geomagnetic activity levels (such as AE index).

Random forests model

Random forests (RF) is an advanced classification procedure that generalizes classification and regression trees (CART); it is described in greater detail in Breiman (2001). The key idea is to assign a given data point to a class based on information contained in a set of predictors in an ensemble of regression or classification trees, or bag of trees. It is important to note that for RF the split into training and test dataset is done intrinsically during construction of the model. Each tree in the RF is constructed from a random sample of the training data, using sampling with replacement, and is then used to "predict" the class of each observation held out in the replacement when that tree was grown. The final classification of each observation is determined by a majority vote over all such tree-by-tree classifications. In our case, there are three classes of response variables, classified as "no hiss," "regular hiss," and "low-frequency hiss" event.

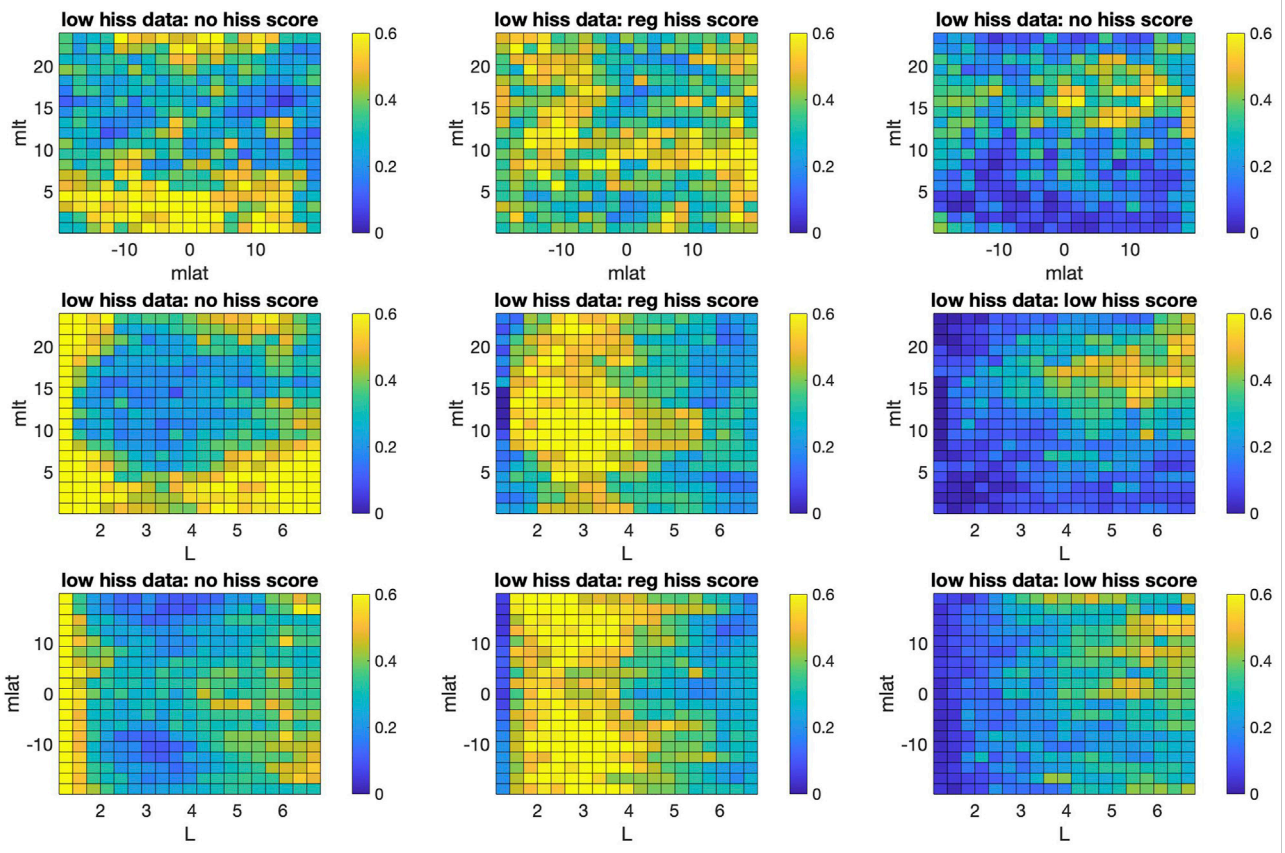

FIGURE 5
Partial dependence (Eq. 2) computed on "low-frequency hiss" data points; color bar corresponds to the score of RF model.

The most credible measures of RF model performance discussed in Sect. 3, such as classification errors, partial dependence scores, and receiver operating characteristics, are also derived from the held-out data. In addition, when each potential partitioning of the data is considered, only a random sample (without replacement) of predictors are candidates to define the split; this restriction helps one to take into account highly specialized predictors that fit only a few observations.

RF have several features that make the algorithm attractive for our purposes, among other machine learning methods. First, for the kinds of highly nonlinear and noisy relationships analyzed in this paper, there are no classifiers to date that consistently classify and forecast more accurately (Breiman, 2001). Second, it has been proven (Breiman, 2001) that RF does not overfit, which implies that the results will generalize well to new random samples from the same population. Third, because key performance measures are computed from the observations not used in tree construction, they are honest indicators of classification skill. Fourth, random forests provides informative plots of the relationships between inputs and outputs (i.e., predictors and predicted scores of spectral classes).

Results

For each data point, the RF classification model outputs a score in the [0, one] range for each of the three spectral classes, and the highest score determines the predicted class. Figure 3 shows the resulting overall classification error (fraction of misclassified observations) independent of the number of grown trees for RF models using different predictors. In addition to MLAT, MLT, and L-shell predictors, we have considered Kp, AE, and Dst geomagnetic indices, cold plasma density *Ne*, as well as solar wind V and solar wind dynamic pressure P. Recently, Malaspina et al. (2018) showed that plasmaspheric hiss waves power strongly depends on the plasmaspheric density and the location of the plasmapause. Hence, we additionally consider the location of plasmapause Lpp and distance from the plasmapause dL = L-Lpp as a RF predictor.

The overall classification error of the "base" RF model using only MLAT, MLT, and L-shell predictors reaches the minimum and saturates at ≈ 0.15, meaning that $\approx 85\%$ of data points are classified correctly. The classification error for given spectral class

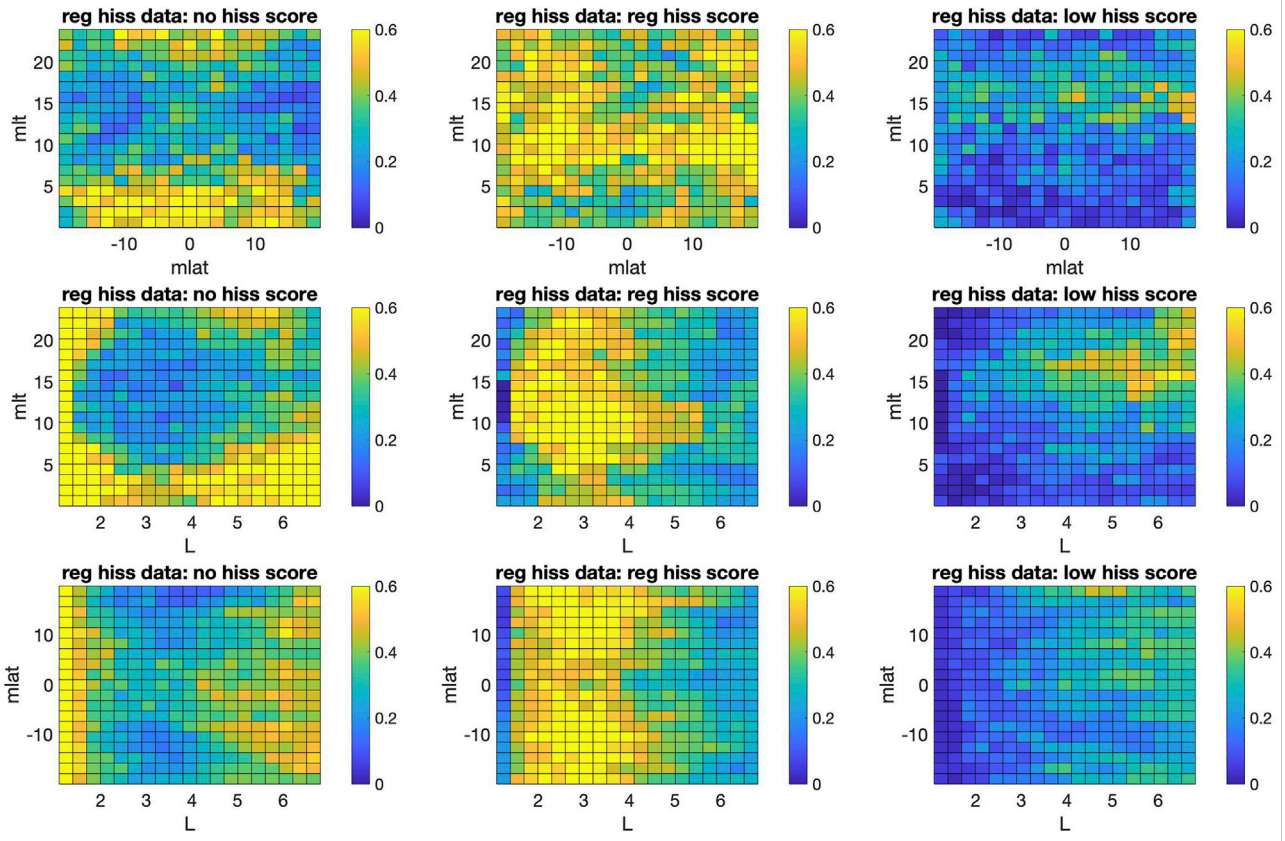

FIGURE 6
Partial dependence (Eq. 2) computed on "regular hiss" data points; color bar corresponds to the score of RF model.

is also at ≈ 0.15. On the other hand, the classification error of the "base1" model that utilizes information on the plasmapause location with (MLAT, MLT, Lpp, dL) predictors is a bit higher at 0.165. Adding to the "base" model, any other single predictor from the list of considered predictors, provides only a minor improvement in classification error to 0.14, and it is comparable to the one obtained when including all possible predictors in the "all" model.

A Receiver Operating Characteristic (ROC) curve informs on the quality of classifiers (such as RF) over a range of trade-offs between true positive and false positive error rates by applying threshold values across the interval [0,1] to classifier results. For a given threshold value and particular class i, true positive ratio (TPR) is the number of outputs whose actual and predicted class is class i, divided by the total number of outputs whose predicted class is class i, thus including also wrongfully made predictions. Similarly, false positive ratio (FPR) is the number of outputs whose actual class is not class i, but the predicted class is class i, divided by the number of outputs whose predicted class is not class i. Obtained ROC's are presented in Figure 3 separately for each of spectral classes and different RF models, as well zoomed into the area of high TPR and small FPR, which both vary in [0 one] range. The larger area under the curve (AUC) values indicates a better classifier performance, and the perfect classifier would have the maximum AUC equal to 1, that is TPR being equal to one when FPR is zero. Resulting AUCs are very high, such as with a "base" RF model: ≈ 0.95 for "no hiss" class, ≈ 0.94 for "regular hiss" class, and ≈ 0.97 for "low-frequency hiss" class, confirming overall very good predictive skill of RF.

Discussion

To help with interpretation of our RF results and understand the origin of such high predictive skill for our base model with MLAT, MLT and L predictors, we use partial dependence which quantifies the relationship between the subset of selected predictor variables X^S and predicted responses (scores of classes) by averaging remaining predictors X^C. A predicted response (in our case it is the score of three classes in the [0, one] range) $f(X)$ depends on all MLAT, MLT and L predictor variables:

$$f(X) = f(X^S, X^C). \quad (1)$$

The highest score among three classes determines the predicted class by RF model. The partial dependence is then estimated as:

$$f^S(X^S) = \sum_{i=1}^{N} f(X^S, X_i^C), \quad (2)$$

where N is the number of observations and $X_i = (X_i^S, X_i^C)$ is the ith data point. We compute partial dependence in 2-D planes of (MLT, MLAT, L) coordinates; for example, X^S=(MLT, MLAT) and X^C = L, etc. Furthermore, we compute partial dependence of scores for each class and separately on the three subsets of our full dataset associated with three spectral classes: "no hiss", "low-frequency hiss," and "regular hiss," shown in Figures 4–6, respectively. As can be seen from the 2-D partial dependence plots, the highest scores for the subset of data associated with a given spectral class, largely match the spatial distribution of that class on Figure 1, as well as exceeding scores of the other two classes. This model feature is most pronounced in MLT-L and is common for all partial dependence plots in Figures 4– 6. For example, the maximum of "low frequency hiss" class occurrence is roughly at $4 < L < 6$ and $10 < MLT < 24$ (Figure 1), same as for the one for 2-D partial dependence computed on the subset of 'low frequency hiss" class (Figure 5). Similarly, the maximums of "no hiss" class occurrence and associated partial dependence are at narrow regions $L < 1$ or $MLT < 10$ (Figure 1 and Figure 4), while for the "regular hiss" these maximums are at $2 < L < 5$ and $7 < MLT < 15$. In other words, the RF model picks up the distinct spatial location of a given spectral class and yields the highest score with respect to other classes in that location. This feature explains a high predictive skill of RF model by using only these location-based predictors.

Conclusion

We have developed the RF model for prediction of plasmaspheric hiss spectral classes obtained by SOM classification of the Van Allen Probes dataset. The RF model provides accurate prediction that is largely determined by distinct and different locations of a given spectral class in (MLAT, MLT, L) coordinate spaces, which are main predictors of the simplest RF base model. Adding any other single predictor among different magnetospheric, geomagnetic, and solar wind conditions provides only minor and similar incremental improvement in predictive skill, which is comparable to the one obtained when including all possible predictors.

A somewhat unexpected result is that adding predictors informing on the plasmapause location did not lead to a higher predictive skill. Because the SOM classification of plasmaspheric hiss spectral classes does not take into account the wave power, and considers spectral shape only, low-hiss class does not exclude the presence of regular hiss. If the classification model also were to take into account wave power, we might expect greater significance of plasmapause location, but this is beyond the scope of this study and is left for future research.

Data availability statement

The original contributions presented in the study are included in the article/supplementary material further inquiries can be directed to the corresponding author.

Author contributions

DK led the work, performed the RF analyses, and wrote the paper. AD advised on the interpretation and wrote the paper. DV developed SOM model. DM conceptualized the study and processed the observational data set that was used by DV in the SOM model.

Funding

This work was supported by NASA 80NSSC18K1034 award.

Acknowledgments

We thank Sharon Uy for proofreading this manuscript. We also thank two reviewers for helpful and constructive comments.

Conflict of interest

The authors declare that the research was conducted in the absence of any commercial or financial relationships that could be construed as a potential conflict of interest.

Publisher's note

References

Breiman, L. (2001). Random forests. *Mach. Learn.* 1, 5–32.

Bristow, W. A., Topliff, C. A., and Cohen, M. B. (2022). Development of a high-latitude convection model by application of machine learning to SuperDARN observations. *Space Weather* 20, e2021SW002920. doi:10.1029/2021SW002920

Engell, A. J., Falconer, D. A., Schuh, M., Loomis, J., and Bissett, D. (2017). Sprints: A framework for solar-driven event forecasting and research. *Space Weather* 15, 1321–1346. doi:10.1002/2017SW001660

He, Z., Yu, J., Chen, L., Xia, Z., Wang, W., Li, K., et al. (2020). Statistical study on locally generated high-frequency plasmaspheric hiss and its effect on suprathermal electrons: Van allen probes observation and quasi-linear simulation. *J. Geophys. Res. Space Phys.* 125, e2020JA028526. doi:10.1029/2020JA028526

He, Z., Yu, J., Li, K., Liu, N., Chen, Z., and Cui, J. (2021). A comparative study on the distributions of incoherent and coherent plasmaspheric hiss. *Geophys. Res. Lett.* 48, e2021GL092902. doi:10.1029/2021GL092902

Kasapis, S., Zhao, L., Chen, Y., Wang, X., Bobra, M., and Gombosi, T. (2022). Interpretable machine learning to forecast SEP events for solar cycle 23. *Space Weather* 20, e2021SW002842. doi:10.1029/2021sw002842

Kletzing, C. A., Kurth, W. S., Acuna, M., MacDowall, R. J., Torbert, R. B., Averkamp, T., et al. (2013). The electric and magnetic field instrument suite and integrated science (EMFISIS) on RBSP. *Space Sci. Rev.* 179, 127–181. doi:10.1007/s11214-013-9993-6

Kondrashov, D., Shen, J., Berk, R., D'Andrea, F., and Ghil, M. (2007). Predicting weather regime transitions in Northern Hemisphere datasets. *Clim. Dyn.* 29, 535–551. doi:10.1007/s00382-007-0293-2

Li, W., Ma, Q., Thorne, R. M., Bortnik, J., Kletzing, C. A., Kurth, W. S., et al. (2015). Statistical properties of plasmaspheric hiss derived from van allen probes data and their effects on radiation belt electron dynamics. *JGR. Space Phys.* 120, 3393–3405. doi:10.1002/2015JA021048

Malaspina, D. M., Jaynes, A. N., Hospodarsky, G., Bortnik, J., Ergun, R. E., and Wygant, J. (2017). Statistical properties of low-frequency plasmaspheric hiss. *JGR. Space Phys.* 122, 8340–8352. doi:10.1002/2017JA024328

Malaspina, D. M., Ripoll, J.-F., Chu, X., Hospodarsky, G., and Wygant, J. (2018). Variation in plasmaspheric hiss wave power with plasma density. *Geophys. Res. Lett.* 45, 9417–9426. doi:10.1029/2018GL078564

Meredith, N. P., Horne, R. B., Kersten, T., Li, W., Bortnik, J., Sicard, A., et al. (2018). Global model of plasmaspheric hiss from multiple satellite observations. *JGR. Space Phys.* 123, 4526–4541. doi:10.1029/2018JA025226

Millan, R. M., and Thorne, R. M. (2007). Review of radiation belt relativistic electron losses. *J. Atmos. Sol. Terr. Phys.* 69, 362–377. doi:10.1016/j.jastp.2006.06.019

Reep, J. W., and Barnes, W. T. (2021). Forecasting the remaining duration of an ongoing solar flare. *Space Weather* 19, e2021SW002754. doi:10.1029/2021sw002754

Ripoll, J.-F., Claudepierre, S. G., Ukhorskiy, A. Y., Colpitts, C., Li, X., Fennell, J. F., et al. (2020). Particle dynamics in the earth's radiation belts: Review of current research and open questions. *J. Geophys. Res. Space Phys.* 125, 1. doi:10.1029/2019ja026735

Saikin, A., Drozdov, A., Malaspina, D. M., and Zhu, H. (2022). *Low frequency plasmaspheric hiss wave activity parametrized by plasmapause location: Models and simulations.* ESSOAr. doi:10.1002/essoar.10511948.1

Shi, R., Li, W., Ma, Q., Reeves, G. D., Kletzing, C. A., Kurth, W. S., et al. (2017). Systematic evaluation of low-frequency hiss and energetic electron injections. *JGR. Space Phys.* 122, 10, 263–310, 274. doi:10.1002/2017JA024571

Smith, A. W., Rae, I. J., Forsyth, C., Oliveira, D. M., Freeman, M. P., and Jackson, D. R. (2020). Probabilistic forecasts of storm sudden commencements from interplanetary shocks using machine learning. *Space Weather* 18, e2020SW002603. doi:10.1029/2020SW002603

Thorne, R. M., Smith, E. J., Burton, R. K., and Holzer, R. E. (1973). Plasmaspheric hiss. *J. Geophys. Res.* 78, 1581–1596. doi:10.1029/ja078i010p01581

Vech, D., and Malaspina, D. M. (2021). A novel machine learning technique to identify and categorize plasma waves in spacecraft measurements. *JGR. Space Phys.* 126, e2021JA029567. doi:10.1029/2021JA029567

Vech, D., Malaspina, D. M., Drozdov, A., and Saikin, A. (2022). *Correlation between bandwidth and frequency of plasmaspheric hiss uncovered with unsupervised machine learning.* arXiv. doi:10.48550/ARXIV.2207.10505

Wygant, J. R., Bonnell, J. W., Goetz, K., Ergun, R. E., Mozer, F. S., Bale, S. D., et al. (2013). The electric field and waves instruments on the radiation belt storm probes mission. *Space Sci. Rev.* 179, 183–220. doi:10.1007/s11214-013-0013-7

Zewdie, G. K., Valladares, C., Cohen, M. B., Lary, D. J., Ramani, D., and Tsidu, G. M. (2021). Data-driven forecasting of low-latitude ionospheric total electron content using the random forest and LSTM machine learning methods. *Space Weather* 19, e2020SW002639. doi:10.1029/2020SW002639

frontiers | Frontiers in Astronomy and Space Sciences

TYPE Original Research
PUBLISHED 06 September 2022
DOI 10.3389/fspas.2022.978371

OPEN ACCESS

EDITED BY
Lauri Holappa,
University of Oulu, Finland

REVIEWED BY
Binbin Ni,
Wuhan University, China
Nickolay Ivchenko,
Royal Institute of Technology, Sweden

*CORRESPONDENCE
Emma Bland,
emmab@unis.no

SPECIALTY SECTION
This article was submitted to Space Physics,
a section of the journal
Frontiers in Astronomy and Space Sciences

RECEIVED 25 June 2022
ACCEPTED 12 August 2022
PUBLISHED 06 September 2022

CITATION
Bland E, Bozóki T and Partamies N (2022), Spatial extent of the energetic electron precipitation region during substorms.
Front. Astron. Space Sci. 9:978371.
doi: 10.3389/fspas.2022.978371

Spatial extent of the energetic electron precipitation region during substorms

Emma Bland[1]*, Tamás Bozóki[2,3] and Noora Partamies[1,4]

[1]Department of Arctic Geophysics, University Centre in Svalbard, Longyearbyen, Norway, [2]Institute of Earth Physics and Space Science (ELKH EPSS), Sopron, Hungary, [3]Department of Optics and Quantum Electronics, University of Szeged, Szeged, Hungary, [4]Birkeland Centre for Space Science, University of Bergen, Bergen, Norway

The spatial coverage of the energetic electron precipitation (EEP) region during three substorms has been determined using a combination of ground-based instruments in North America. The primary datasets used to determine the presence or absence of EEP are riometer measurements of cosmic noise absorption (CNA); attenuation of the 10–11 MHz atmospheric noise in the D-region ionosphere determined using the Super Dual Auroral Radar Network (SuperDARN); amplitude variations in subionospheric very low frequency (VLF) propagation observed using the Antarctic-Arctic Radiation-belt (Dynamic) Deposition VLF Atmospheric Research Konsortium (AARDDVARK) VLF receivers, and total electron content measurements derived from global navigation satellite systems. Our results show that substorm EEP during moderate geomagnetic conditions can extend considerably equatorward or poleward of the average latitude limits reported in a previous statistical study of substorm EEP and an EEP model. This evidence is provided by the SuperDARN radars and the radar signature is not always accompanied by cosmic noise absorption measured by the riometers. Further work is required to determine which EEP energies and fluxes the SuperDARN radars are sensitive to, but we can conclude that EEP with sufficient flux to attenuate 10–11 MHz radiowaves by ~5 dB reaches latitudes well equatorward of the statistical EEP latitude limits previously modelled for >30 keV electrons.

KEYWORDS

particle precipitation, substorm, ionosphere, riometer, superdarn

1 Introduction

Substorms are one of the key processes that facilitate energy transfer from the Earth's magnetotail into the ionosphere through energetic electron precipitation (EEP). At the substorm onset, there is an injection of energetic electrons from the plasma sheet into a narrow spatial region of the auroral zone ionosphere, which then rapidly expands azimuthally and poleward (e.g., Berkey et al., 1974; Gjerloev et al., 2007; Spanswick et al., 2009). The particle injection is often observed as a sharp increase in cosmic noise absorption (CNA), and this decays gradually throughout the expansion and recovery

phases (e.g., Spanswick et al., 2007; Partamies et al., 2021). The peak CNA is associated with precipitating electron energies of about 40–60 keV (Kellerman et al., 2015), which impact the atmosphere at about 90 km altitude (Fang et al., 2008).

Precipitating electrons that reach altitudes below about 120 km are known to affect the atmospheric chemistry through the production of odd-nitrogen (NO_X = N,NO,NO_2) and odd-hydrogen (HO_X = H,OH,HO_2) chemical species, which are catalysts in ozone depletion reactions (Sinnhuber et al., 2012). HO_X species are produced mainly in the mesosphere due to medium-energy electron precipitation (tens of keV), while NO_X species are produced mainly in the thermosphere due to auroral electron precipitation with energies of ~1–10 keV. The short chemical lifetime of HO_X species limits their atmospheric impact to the mesosphere. In contrast, NO_X species have a long chemical lifetime in the dark and can be transported downwards in the polar vortex, leading to ozone depletion in the mesosphere and stratosphere. These atmospheric chemical effects have been identified during individual EEP events (e.g., Daae et al., 2012; Turunen et al., 2016; Smith-Johnsen et al., 2018) and as a contributor to natural climate variability (e.g., Randall et al., 2007; Seppälä et al., 2007; Seppälä et al., 2014). To help quantify these contributions, substantial effort has gone into developing realistic statistical descriptions of the EEP forcing for climate modelling applications. This includes the van de Kamp et al. (2016), van de Kamp et al. (2018) models of > 30 keV electron flux, which are derived from long-term electron flux measurements from the Polar Orbiting Environmental Satellites (POES) and parametrised by the geomagnetic indices *Ap* and *Dst*. Geomagnetic indices provide the long time series of geomagnetic activity that is necessary for long-term modelling of the Earth's climate, but one should be aware that this approach systematically excludes some components of the EEP forcing. For example, a very common feature of the substorm recovery phase is pulsating aurora, which is associated with the high-energy tail of the auroral precipitation spectrum and persists for several hours after the magnetic signature has recovered (Partamies et al., 2017). This type of aurora has occurrence rates exceeding 40% in the early morning sector (Jones et al., 2011; Bland et al., 2019) and is known to cause ozone depletion in the auroral oval (Turunen et al., 2016; Tesema et al., 2020; Verronen et al., 2021). It is therefore likely that the *Ap* and *Dst* parametrisations of EEP do not properly capture the energy input associated with pulsating aurora during substorm recovery phases.

Global geomagnetic indices with time resolutions of hours or days are also unable to capture the variability in the EEP energy spectrum, spatial extent, and temporal evolution of EEP from event to event. The *Ap* index, for example, provides only a daily average of geomagnetic activity and could therefore underestimate or overestimate the energy input from substorm EEP. The 3-h time resolution of the *ap* (or *Kp*) index is comparable to the typical substorm duration of 2–4 h, so this may still be insufficient to describe the EEP input. Recently, Sergeev et al. (2020) developed a semi-empirical model that characterises the recurring spatial and temporal features of auroral absorption during substorms. This model is driven by the recently-developed midlatitude positive bay index, which captures the field-aligned current enhancement from the substorm current wedge (McPherron and Chu, 2018). Although accounting for this variability may be unnecessary for climate modelling, it is important in space weather applications because the amount of auroral absorption depends strongly on the current state and time history of the magnetosphere–ionosphere system. Chemical changes in the middle atmosphere due to EEP also depend heavily on the strength and duration of the forcing (Tesema et al., 2020), so long-term average particle energy spectra may not be sufficient for describing the short-term atmospheric response.

To work towards a more complete description of the variability in EEP during substorms, we use a combination of ground-based instruments to study the spatial and temporal evolution of the EEP impact area for three substorms that occurred during moderate geomagnetic conditions ($10 \leq Ap \leq 25$). We use the Go-Canada riometer network (Spanswick et al., 2007), the Super Dual Auroral Radar Network (SuperDARN) (Greenwald et al., 1995; Chisham et al., 2007; Nishitani et al., 2019), the network of very low frequency (VLF) receivers that comprise the Antarctic-Arctic Radiation-belt (Dynamic) Deposition VLF Atmospheric Research Konsortium (AARDDVARK) (Clilverd et al., 2009), and vertical total electron content measurements derived from global navigation satellite systems (Rideout and Coster, 2006). The spatial extent of the EEP region for each substorm is then compared with the van de Kamp et al. (2018) model prediction, and an earlier statistical study of the latitudinal extent of substorm EEP performed using satellite measurements of particle energy spectra (Cresswell-Moorcock et al., 2013). These results provide some insight into how well the geomagnetic index *Ap* captures the spatial coverage of substorm EEP, and how well the average latitude limits of > 30 keV electron flux determined by Cresswell-Moorcock et al. (2013) match the substorm EEP region determined from the ground-based instruments. Our results provide a detailed picture of the two-dimensional spatial evolution of substorm EEP at the energy ranges that are associated with auroral absorption and ozone depletion.

2 Instrumentation

The locations and fields of view of the main instruments used in this study are shown in Table 1 and Figure 1. Dashed lines in Figure 1 indicate altitude-adjusted corrected geomagnetic (AACGM) coordinates (Shepherd, 2014) projected to a height of 100 km. The Go-Canada riometer network consists of 14 wide-beam (60°) riometers that measure the absorption of 30 MHz cosmic radio noise.

TABLE 1 Station codes and locations of the riometers, SuperDARN radars, and VLF transmitters and receivers used in this study. AACGM = Altitude-Adjusted Corrected Geomagnetic. MLT = magnetic local time.

Station code	Name	Geodetic latitude	Geodetic longitude	AACGM latitude	AACGM longitude	L Value	MLT at 00UT
Riometers							
CHUR	Churchill	58.76	−94.08	67.57	−24.49	6.9	17.6
DAWS	Dawson	64.05	−139.11	65.92	−83.39	6.0	13.7
FSIM	Fort Simpson	61.76	−121.23	66.97	−62.99	6.5	15.1
FSMI	Fort Smith	60.02	−111.95	66.86	−50.57	6.5	15.9
GILL	Gillam	56.38	−94.64	65.31	−25.04	5.7	17.6
ISLL	Island Lake	53.86	−94.66	62.94	−24.81	4.8	17.6
MCMU	Fort McMurray	56.66	−111.21	63.76	−48.54	5.1	16.0
PGEO	Prince George	53.81	−122.83	58.93	−61.92	3.8	15.1
PINA	Pinawa	50.02	−96.04	59.21	−26.47	3.8	17.5
RABB	Rabbit Lake	58.22	−103.68	66.27	−38.62	6.2	16.7
RANK	Rankin Inlet	62.82	−92.11	71.42	−21.99	9.8	17.8
TALO	Taloyoak	69.54	−93.55	77.49	−26.05	21.3	17.5
SuperDARN Radars							
CLY	Clyde River	70.49	−68.50	77.41	17.36	21.0	20.4
GBR	Goose Bay	53.32	−60.46	59.49	23.13	3.9	20.8
INV	Inuvik	68.41	−133.77	71.18	−81.04	9.6	13.9
KAP	Kapuskasing	49.39	−82.32	58.72	−6.58	3.7	18.8
PGR	Prince George	53.98	−122.59	59.15	−61.69	3.8	15.1
RKN	Rankin Inlet	62.83	−92.11	71.43	−22.00	9.9	17.8
SAS	Saskatoon	52.16	−106.53	60.13	−41.29	4.0	16.5
VLF transmitters							
NDK		46.37	−98.34	55.38	−29.38	3.1	17.3
NLK		48.20	−121.92	53.45	−59.34	2.8	15.3
VLF receivers							
CHU	Churchill	58.73	−94.05	67.48	−24.43	6.8	17.6
NYA	Ny Ålesund	78.92	11.93	76.65	106.47	18.8	2.4
REY	Reykjavík	64.13	−21.93	64.19	64.38	5.3	23.6
SEA	Seattle	47.95	−124.38	52.70	−62.02	2.7	15.1

The locations of the riometers used in this study are shown as grey circles in Figure 1. The symbol size is the same for all riometers and indicates the approximate field of view projected to 90 km height. The cosmic noise absorption (CNA) is measured relative to a 'quiet day curve' (QDC) that characterises the background sidereal variation of the cosmic noise strength during undisturbed conditions. Deviations from the QDC are attributed to absorption of the cosmic noise through collisions between neutrals and free electrons, so an increase in the electron density due to EEP can be identified as an increase in CNA. The ionospheric electron density and the electron-neutral collision frequency are typically most favourable for attenuating HF radiowaves at about 90 km altitude (e.g., Rodger et al., 2012), so changes in CNA are associated with EEP energies exceeding 30 keV.

To extend the spatial coverage provided by the riometers, we use raw power measurements from several SuperDARN radars in North America (Super Dual Auroral Radar Network, 2021; Super Dual Auroral Radar Network, 2022). The near-range fields of view of the SuperDARN radars used in this study are represented by the blue fan-shaped symbols in Figure 1. SuperDARN radars are phased-array high frequency (HF) radar systems consisting of a linear array of log-periodic or twin-terminated folded dipole antennas. The standard SuperDARN field of view extends to over 3,500 km in range, but in this study we consider only the very near-range field of view that covers the D-region ionosphere (e.g., Bland et al., 2021). The field of view is divided into 16 azimuthal beams that are sampled in succession. For this study we use data only from the beam that is shaded dark blue in the figure, which is

FIGURE 1
Locations and fields of view of the riometers, SuperDARN radars, and VLF transmitters and receivers used in this study. For the SuperDARN radars, only the near-range field of view is shown, and the shading indicates the beam direction that was used (see text for details). The propagation paths between selected VLF transmitter–receiver pairs are shown in the inset.

beam 12 for the GBR radar and beam 5 for all other radars. Building on results from our earlier work (Bland et al., 2018; Bland et al., 2019), we use a riometry-like approach to estimate the attenuation of the 10–11 MHz radio noise at each SuperDARN radar site. At this frequency range, radio noise arises primarily from radio emissions associated with lightning activity (atmospheric noise), as well as anthropogenic sources such as radio emissions from electrical equipment and interference from other HF transmitters (Ponomarenko et al., 2022). These noise sources are therefore distinct from the cosmic noise that riometers are sensitive to. To distinguish these measurements from the 30 MHz CNA, we refer to the attenuation of the 10–11 MHz noise measured by the SuperDARN radars as *atmospheric noise attenuation* (ANA). Our earlier work shows that the SuperDARN radars have sufficient sensitivity to detect ANA associated with relatively low-flux EEP during pulsating aurora (Bland et al., 2019; Bland et al., 2021), so this method is also appropriate for detecting substorm EEP.

Also shown in Figure 1 are four VLF receivers from the AARDDVARK network and the powerful VLF communication transmitters NDK and NLK. The propagation paths between selected transmitter and receiver sites are shown in the figure inset. AARDDVARK measures amplitude and phase variations of the narrowband VLF radiowaves along these paths. VLF waves propagate within the Earth–ionosphere waveguide, and any change in the height of the D-region ionospheric boundary caused by EEP can be observed by a VLF receiver as a decrease in amplitude (increase in phase) (Clilverd et al., 2008). At night time the reflection height for the VLF propagation is expected to be about 85 km, so the VLF data provide information about a higher energy range of precipitating electrons compared to the riometer and radar observations, from about 50 keV to over 200 keV (Rodger et al., 2012).

In addition to the instruments shown in Figure 1, we also use vertically-integrated total electron content (vTEC) measurements derived from the World-wide Global Navigation Satellite Systems Receiver Network to validate the EEP impact area determined from the radio instruments described above. The high density and wide spatial coverage of the vTEC dataset complements the relatively sparse measurements from the other radio instruments. The processed vTEC dataset (Coster, 2019) is binned in a 1° geographic latitude by 1° longitude grid. Although the vTEC measurements do not provide any height or energy information about the EEP, a comparison between vTEC and CNA measurements during two substorms by Watson et al. (2011) showed that 1 dB of CNA is associated with an increase in vTEC of about 2–4 TECu, whereas lower-energy EEP impacting the F-region ionosphere produce much larger changes up to 15 TECu (Mendillo, 2006).

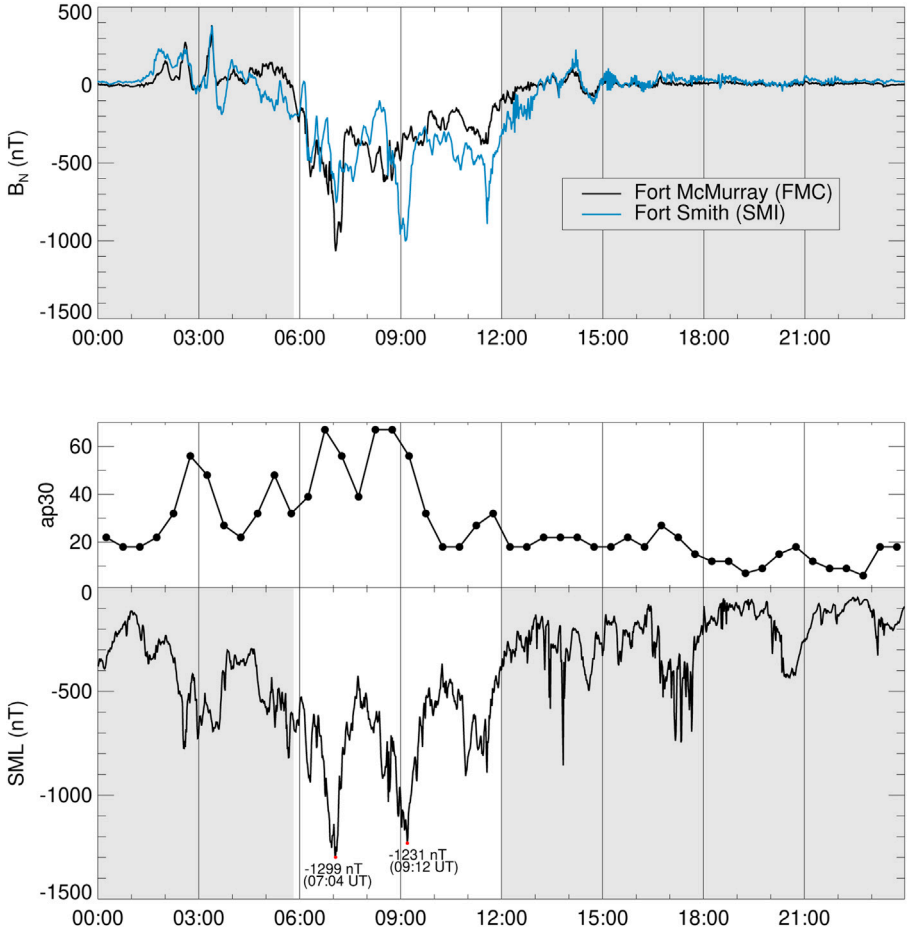

FIGURE 2
Magnetic field disturbances and selected geomagnetic indices for 25 October 2019. The top panel shows the magnetic field disturbance in the local magnetic north direction, B_N measured by the Fort McMurray (FMC) and Fort Smith (SMI) magnetometers. The centre and bottom panels show the ap30 and SML indices respectively.

To obtain an overview of the ground magnetic field disturbance during the substorms, we use the gridded magnetic field data product from SuperMAG (Gjerloev, 2012), which provides ground magnetic field vectors on an equal area magnetic coordinate grid. We also use the data from two individual magnetometers at Fort McMurray and Fort Smith, which are part of the CARISMA magnetometer network (Mann et al., 2008). Several geomagnetic indices are also used to describe the substorm evolution. These are: the lower component of the auroral electrojet index derived from SuperMAG, known as *SML* (Newell and Gjerloev, 2011); the daily geomagnetic index *Ap*, which is the daily average of the eight 3-h *ap* indices (Matzka et al., 2021a; Matzka et al., 2021b); and *ap*30, which is like the *ap* index but provided with a time resolution of 30 min (Matzka et al., 2022; Yamazaki et al., 2022).

3 Substorm on 25 October 2019

Our main substorm case study event occurred on 25 October 2019. The top panel of Figure 2 shows the magnetic field disturbance in the local magnetic north direction, B_N, measured by the Fort McMurray (FMC) and Fort Smith (SMI) magnetometers. These instruments are co-located with the MCMU and FSMI riometers (see Table 1). We identify the substorm onset by the sudden decrease in B_N at FMC at 05:49 UT. The substorm consists of three intensifications with local B_N minima at 07:04 UT (FMC), 09:12 UT (SMI) and 11:36 UT (SMI), and the recovery phase ends at approximately 12:00 UT. In the lower panels of Figure 2 we show the *ap*30 index and the *SML* index. Both *ap*30 and *SML* capture the main features of the magnetic field disturbance detected by the individual FMC and SMI magnetometers.

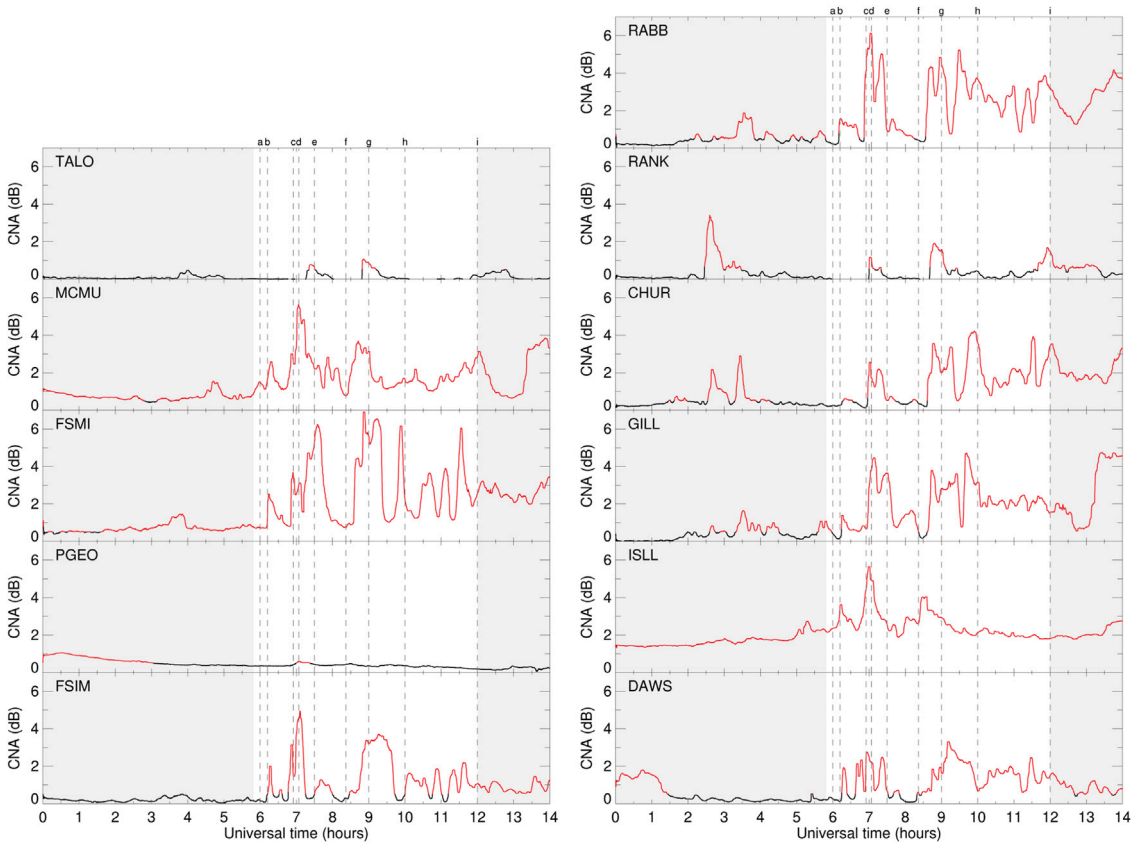

FIGURE 3
30 MHz cosmic noise absorption (CNA) measurements from the Go-Canada riometer network on 25 October 2019. CNA measurements below the threshold value of 0.5 dB are coloured black. The vertical dashed lines correspond to the time intervals shown in Figure 7.

3.1 Cosmic noise absorption

The CNA measurements from the Go-Canada riometer network are shown in Figure 3. We determined the QDC for each riometer using the raw voltage measurements obtained during the 21-day period centered on the substorm event day (15 October to 4 November 2019). The most active days during this time interval are the event day and the day after (25–26 October), and there were no major solar flares or solar proton events. To construct the QDC for each riometer, the raw data were organised into 30 min bins of sidereal time, and then the 90th percentile value in each bin was selected as the quiet day voltage. This percentile-based method appears to accurately characterise the quiet-time voltage measurements within the 21-days interval without being significantly impacted by the data from more active days. We then calculated the CNA relative to the QDC as

$$\mathrm{CNA\,(dB)} = \log_{10}\left(\frac{V_0}{V}\right) \quad (1)$$

where V is the measured voltage from the riometer and V_0 is the value of the quiet day curve in the corresponding sidereal time bin. The resulting CNA estimates for each riometer are shown in Figure 3. To remove short-duration fluctuations, we also smoothed the data using a boxcar filter of width 1 h. The line colour is red when the CNA exceeds 0.5 dB, which we have determined to be the threshold amount of CNA that can be reliably measured using this dataset. CNA estimates below this threshold are shown in black. Note that there is a 1.3 dB offset in the ISLL data that is probably caused by an instrumental artifact and will be corrected manually later. The vertical dashed lines correspond to specific time intervals during the substorm that will be discussed later. The left column shows the data from the north-south chain of riometers, and the data from the other riometers are shown in the right column in order of east (top) to west (bottom). Most riometers detect a CNA enhancement at around 07:00 UT, which corresponds to the first intensification measured by the magnetometers (Figure 2). The CNA enhancement occurs about 30 min later at TALO, indicating a poleward expansion of the EEP region. A second CNA enhancement is observed by most riometers at around 08:30–09:00 UT, which coincides with the second intensification when the SML index reaches a local minimum at 09:12 UT. After

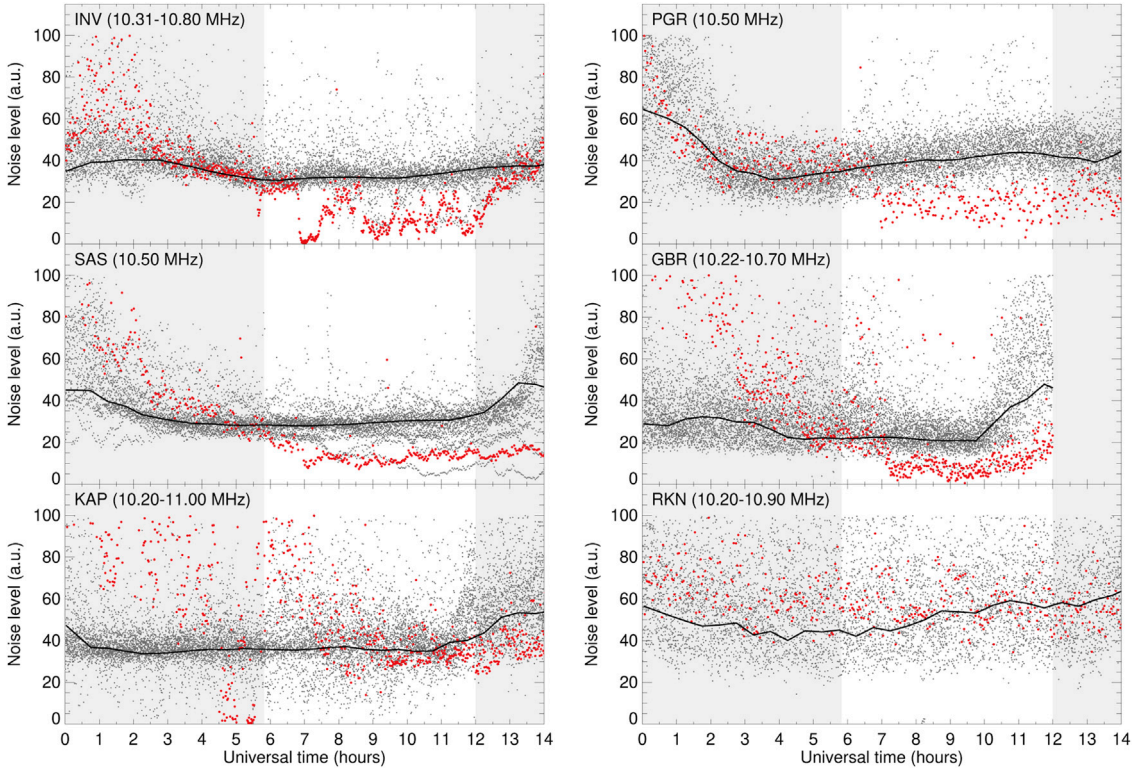

FIGURE 4
HF radio noise measurements from six SuperDARN radars in North America. The grey dots show noise measurements for the 21-day period 15 October to 4 November 2019, and the solid black line shows the quiet day curve derived from these data. The red dots show the noise measurements for the event day (25 October 2019). Grey shading indicates time periods before and after the substorm event.

the second intensification, the CNA data become more complicated and there is no obvious relationship between the CNA enhancements at each station.

3.2 Atmospheric noise attenuation

Estimates of the atmospheric noise attenuation (ANA) derived from the SuperDARN radars have been used to complement the CNA measurements from Figure 3. Like the CNA, the ANA has been calculated relative to a quiet day curve determined from the noise measurements obtained during the 21-days interval centred on the substorm event date. The 10–11 MHz noise measurements from the six SuperDARN radars in North America that had data available during this period are shown in Figure 4 as a function of universal time. The noise measurements from the entire 21-days interval are shown as grey dots, and the noise measurements from the event date are shown as red dots. The radar data analysis software estimates the noise level as the mean of the 10 lowest power measurements along the beam, and then a correction for the effective number of noise samples is applied (Ponomarenko et al., 2022). The resulting noise estimates have arbitrary units that vary widely from radar-to-radar, so the data shown in Figure 4 have been scaled to the range 0–100 a.u. to simplify the presentation of the results.

To determine the QDC for each radar, we first divided the noise measurements into 30min bins of universal time. In each time bin we calculated a probability distribution function (PDF) of the noise, and the noise level corresponding to the maximum of that PDF was selected as the quiet day value in that time bin. The quiet day values were then smoothed in time using a boxcar filter of width 2-h to obtain the final QDC, which is the solid black line shown in Figure 4. Although each radar samples in 16 different directions, for simplicity we have used data from only a single beam from each radar in this study. During the period 15 October to 4 November, many of the radars operated with a reduced number of beams in order to sample at a higher time resolution. Therefore, we used the beam with the largest amount of available data during the 21-days reference period, which was beam 12 for the GBR radar and beam 5 for all other radars. To avoid biasing the quiet day curve towards the dates with high time resolution measurements, all data were downsampled to a time resolution of 1 min before determining the QDC. No usable

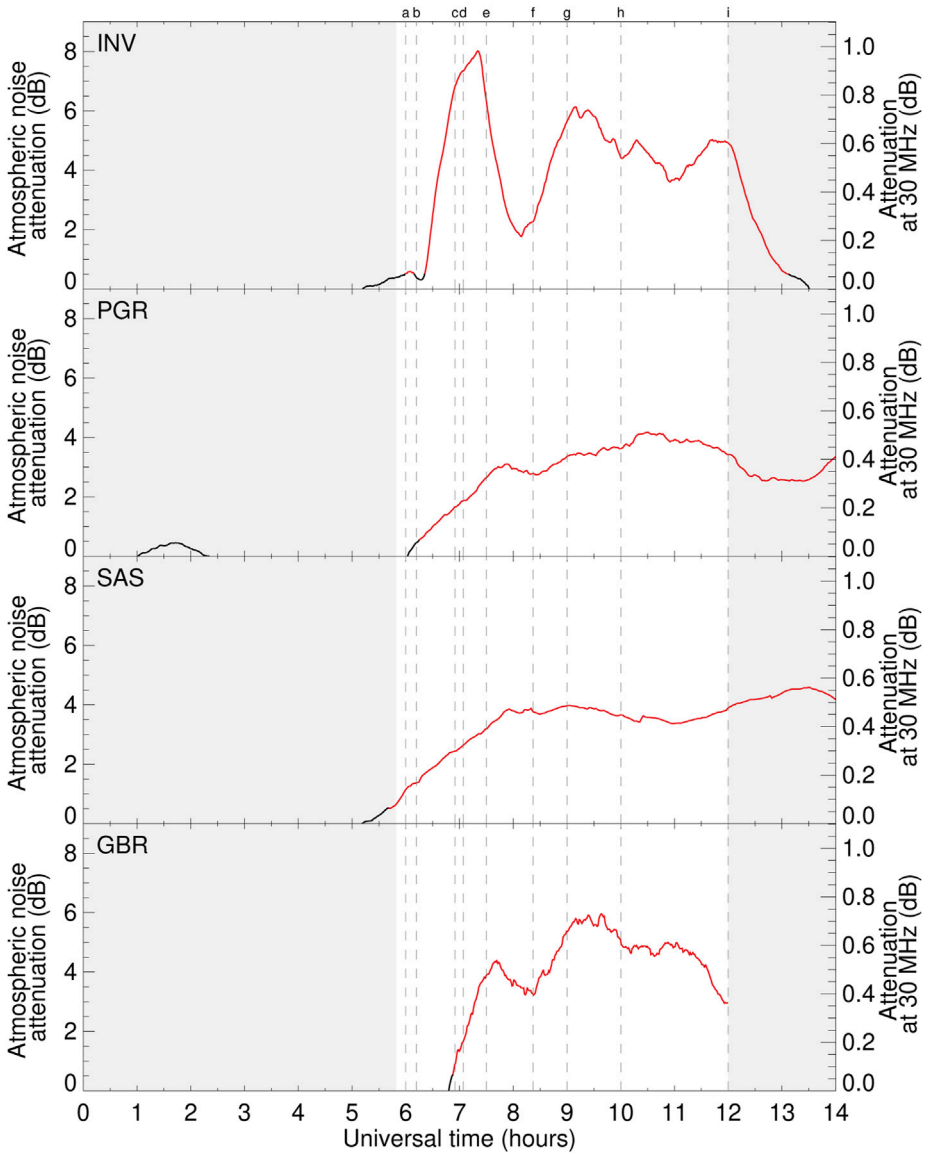

FIGURE 5
Atmospheric noise attenuation (ANA) estimates for the Inuvik (INV), Prince George (PGR), Saskatoon (SAS) and Goose Bay (GBR) SuperDARN radars on 25 October 2019. The left axis shows the ANA values at the native radar operating frequency. The right axis shows the equivalent attenuation at 30 MHz (see text for details). The vertical dashed lines correspond to the time intervals shown in Figure 7.

data were available from the GBR radar after 12:00 UT, since the radar switched to a different operating frequency at that time each day.

The grey shading in Figure 4 indicates the time periods before and after the substorm on 25 October 2019. For all radars except KAP and RKN, the noise measurements during the substorm are much lower than the reference level (QDC), indicating that the 10–11 MHz radio noise was attenuated during the event. This is especially clear for the INV radar, where the noise level decreases sharply just before 07:00 UT. In all six panels, there are times when the noise values on the event day are much higher than the QDC, which may be evidence of interference from other HF emitters. For example, the noise levels on the event day (red dots) at INV and GBR clearly exceed the quiet day values from about 00:00–03:00 UT, making the data unreliable at this time. We also note that the KAP and RKN datasets appear to be dominated by external interference. For KAP, the noise measurements from the event day are distributed well above the quiet day curve from 00:00–07:30 UT. For RKN, the noise data have large variability for the entire 21-day period, including the event day. We conclude that the KAP

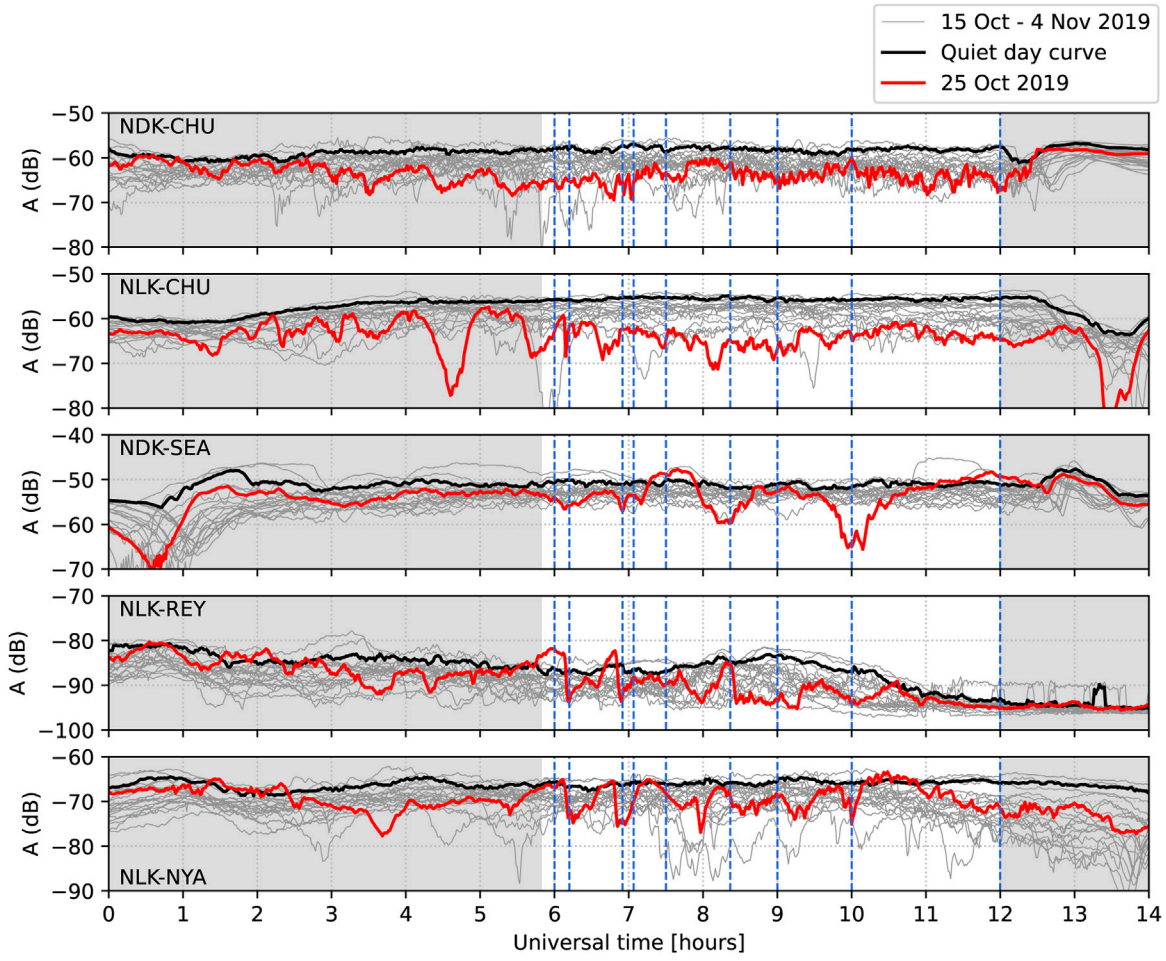

FIGURE 6
Amplitude variation of narrowband VLF observations corresponding to the NDK–Churchill (CHU), NLK–Churchill, NPM–Churchill, NLK–Reykjavík (REY) and NLK–Ny Ålesund (NYA) propagation paths. The red line shows the data from the event day (25 October 2019) and the grey lines show data from the 21-day period 15 October to 4 November 2019. The quiet day curve is shown in black. The white shading indicates the substorm event. The blue dashed lines correspond to the time instants shown in Figure 7.

and RKN data cannot be used to obtain a reliable estimate of the ANA during this time period and we exclude these data from further analysis.

ANA estimates at 10–11 MHz for the INV, PGR, SAS and GBR radars on 25 October 2019 are shown in Figure 5. These values were calculated relative to each radar's QDC using Eq. 1 and then smoothed using a boxcar filter of width 1 h. Following the format of Figure 3, ANA values above our chosen threshold value of 0.5 dB are coloured red. We also show the equivalent attenuation at the riometer operating frequency at 30 MHz using the right vertical axis. This was determined by assuming an inverse square relationship between frequency and attenuation (e.g., Milan et al., 2008). However, it is clear from Figures 3, 5 that this scaling procedure does not produce comparable CNA/ANA magnitudes, and the time evolution of the CNA and ANA datasets is also very different. In particular, only the INV radar observes distinct ANA peaks at 07:00 UT and 09:00 UT, in contrast to the CNA which includes clearly discernible peaks at these times at most riometer stations. The PGR, SAS and GBR radars observe a steady increase in ANA that does not recover during the time interval shown. The co-located PGR radar and PGEO riometer also observe very different responses to the EEP. While the radar measured a clear increase in ANA at the beginning of the event that persisted to the end of the recovery phase, the PGEO riometer did not detect any CNA above the threshold level except for a brief enhancement at 07:00 UT. These results indicate that the SuperDARN radars may be sensitive to lower EEP fluxes than the riometers, or they may be sensitive to different parts of the precipitating energy spectrum.

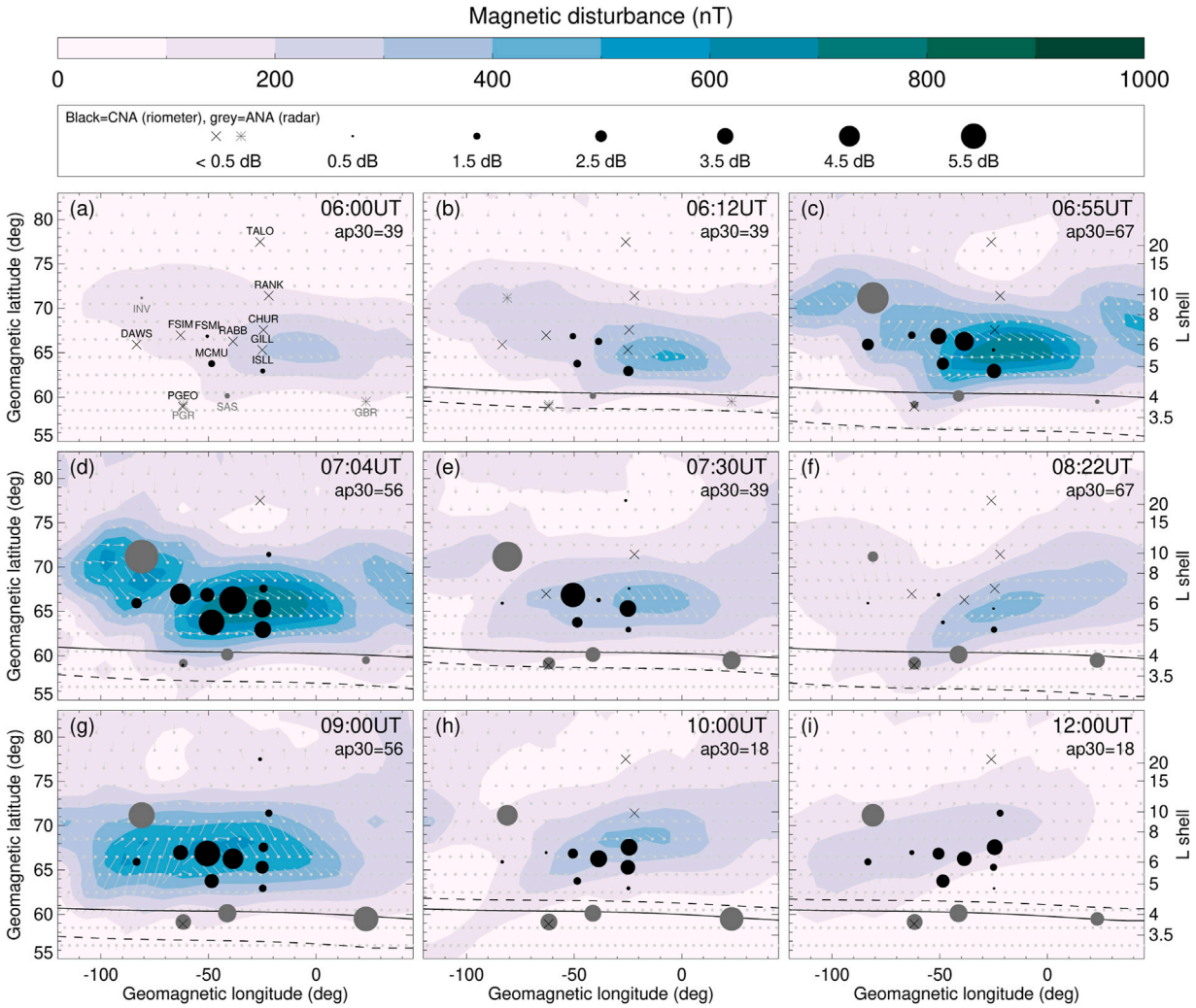

FIGURE 7
Spatial evolution of the magnetic field disturbance, 30 MHz cosmic noise absorption and 10–11 MHz atmospheric noise attenuation during the substorm on 25 October 2019. The solid black line near L = 4 indicates the lower-latitude boundary of > 30 keV electron flux from the van de Kamp et al. (2018) energetic electron precipitation model for Ap = 25, and the dashed line is the same boundary estimated from the ap30 index given in each panel (see text for details).

3.3 Sub-ionospheric very low frequency propagation

Figure 6 shows the amplitude variations for the five VLF transmitter–receiver paths that were shown in the inset of Figure 1. The thin grey lines show the amplitude measurements for the reference period 15 October to 4 November 2019, and the upper envelope (90th percentile) of these data is used as the quiet day curve (black line). The VLF amplitudes during the reference period exhibit substantial day-to-day variability, reflecting the reduced stability of the lower ionosphere on the nightside (Thomson et al., 2007). The data for the substorm event day are shown in red. Substorm EEP causes decreases in the VLF amplitude (increase in phase) (Clilverd et al., 2008), and several such amplitude decreases can be identified in Figure 6 relative to the QDC. The NLK–CHU, NLK–REY and NLK–NYA pairs all detect a sharp amplitude decrease near the substorm onset at ~06:10 UT. A more gradual amplitude decrease is observed by the NDK–SEA pair at the substorm onset. In all cases the amplitude recovers well before the maximum magnetic field disturbance at 07:04 UT. Just before 07:00 UT, another amplitude decrease is observed by the NLK–REY and NLK–NYA pairs, which both recover within about 15–20 min. Amplitude decreases are also observed by all station pairs during the second expansion phase (07:45–09:12 UT). A final amplitude decrease occurs at around 10:00 UT at

NDK–SEA, NLK–REY and NLK–NYA, indicating an enhancement in the ~50–200 keV electron flux well into the second recovery phase when the magnetic indices have already recovered.

3.4 Energetic electron precipitation spatial extent

Now that we have determined the responses of the ground-based instruments to the substorm EEP, we can visualise the spatial coverage and evolution of the EEP impact area. We focus initially on the CNA and ANA responses, and then return to the VLF dataset. Figure 7 shows the CNA, ANA and horizontal magnetic field disturbance at nine time intervals during the substorm. The filled contours show the magnitude of the total horizontal magnetic field disturbance, and the grey vectors indicate the direction of the ionospheric equivalent current obtained by rotating the horizontal magnetic field perturbation direction clockwise by 90°. The filled circles in each panel show the CNA (black) and ANA (grey) measured by the riometers and radars respectively. Cross/star symbols are used when the CNA/ANA is below the threshold value of 0.5 dB. The CNA and ANA measurements have been averaged over a 6-min time window centered on the time stamp shown on each panel. To remove the effect of the apparent offset in the ISLL riometer data, 1.3 dB has been subtracted from all ISLL measurements shown in the figure. In addition, we completely exclude the KAP and RKN radar observations since we have concluded they are unreliable. All other observations shown match the time series data presented in Figures 3, 5. Due to the different operating frequencies of the riometers and SuperDARN radars, it is not appropriate to compare the CNA and ANA magnitudes.

The results in panels (a) and (b) show that the initial CNA enhancement associated with the substorm injection is confined to a narrow region between approximately 63° and 67° CGM latitude. At 06:55 UT (panel c), the magnetic disturbance increases and CNA/ANA enhancements are measured over a wider longitudinal and latitudinal area, reaching a maximum spatial coverage and magnitude at 07:04 (panel d). The TALO riometer was the only instrument that did not detect any EEP signature at 07:04 UT, indicating that the EEP impact area was confined to latitudes below 77° CGM at this time. However, the TALO riometer detected a brief CNA enhancement shortly afterwards, which is evident in panel (e) and also in Figure 3.

Panels (e) and (f) show the response of each instrument during the first recovery phase. As expected, the CNA/ANA gradually decrease across most of the observable area as the magnetic field disturbance weakens. The three SuperDARN radars at the equatorward edge of the observable area (~58–60° CGM latitude) continue to detect ANA above the threshold level at 08:22 UT, and the INV radar measures about 2 dB ANA at ~ 70° CGM latitude. At the same time, all CNA measurements are close to or below the threshold value.

Panel (g) shows the CNA/ANA response during the second intensification of the substorm. The magnetic field disturbance is accompanied by a CNA/ANA enhancement across the entire observable area. The PGEO riometer did not detect CNA above the threshold level, but there is a clear ANA response from the co-located SuperDARN radar (PGR). The enhanced CNA/ANA continues into the substorm recovery phase (panels h–i) at all sites except the highest-latitude riometer (TALO). We note that a substantially higher CNA response was measured during the final recovery phase (panels h–i) compared to the first recovery phase (panel f), even though the magnetic field intensifications preceding them had similar magnitudes. Although not shown in Figure 7, it is evident from Figures 3, 5 that the CNA/ANA enhancements at some sites continue until 14:00 UT, which is 2 h after the end of the final recovery phase and more than 8 h after the substorm onset.

To determine whether the observations presented in Figure 7 provide a reasonable estimate of the EEP impact area, we compare the CNA/ANA results with the vertical total electron content (vTEC) dataset. Figure 8 shows the vTEC data for the same time instants as in Figure 7, with some small differences in timing due to the 5 min resolution of the vTEC dataset. The midlatitude ionospheric trough can be identified in each panel as the electron density depression with wide longitudinal extent that is located equatorward of the riometers. The poleward boundary of the midlatitude trough is associated with the equatorward edge of the auroral oval, and can therefore be used to identify the lower latitude limit of substorm EEP (e.g., Zou et al., 2011). There is a clear vTEC increase of 2–4 TECu in the northwest at the first intensification (panels c–d) that extends to the approximate locations of the PGR and SAS radars. This matches well with the CNA and ANA enhancements near DAWS and INV, and also the magnetic field enhancement in the equivalent panels of Figure 7. South of the PGR, SAS and GBR radar sites the vTEC is close to zero, indicating that the equatorward edge of the EEP impact area for this event is close to the radar locations. Similarly, the vTEC enhancement extends about as far north as the RANK riometer during the first intensification (panel d), and then further north to TALO during the second intensification (panel g), which matches the CNA observations from these two riometers. Based on this comparison, we conclude that our CNA/ANA measurements provide a reasonable estimate of the latitudinal extent of the EEP impact area for this substorm. The enhanced vTEC over Alaska indicates the EEP impact area may extend much further westward of the area observable by the riometers and radars.

The green lines in Figure 8 show the propagation paths between the VLF transmitter–receiver pairs. A solid line is used if the amplitude A_{VLF} meets the criterion $A_{VLF} < A_{QDC} - 2A_{\sigma}$, where A_{QDC} is the value of the QDC and A_{σ} is the standard deviation of the amplitude measurements over the 21-days

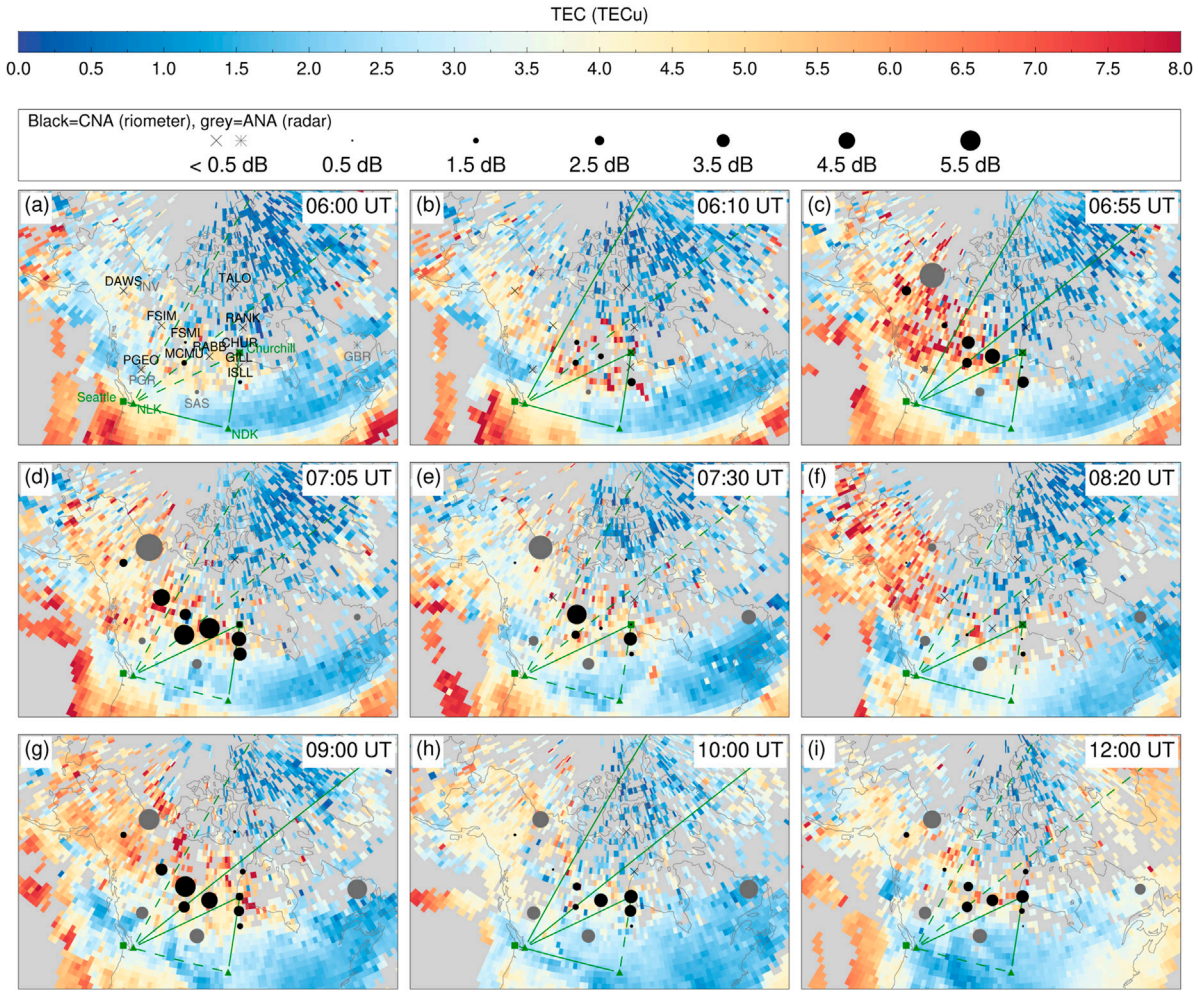

FIGURE 8
Spatial evolution of the vertical total electron content (vTEC), 30 MHz cosmic noise absorption, and 10–11 MHz atmospheric noise attenuation during the substorm on 25 October 2019. The solid green lines show the VLF propagation paths with a significant amplitude change relative to the reference period, and the dashed green lines indicate VLF propagation paths with no significant amplitude change (see text for details). VLF = very low frequency.

reference period at the corresponding universal time. A dashed line is used if that criterion is not met. All station pairs meet the criterion at 06:55 UT (panel c) when the vTEC enhancements along the propagation paths reach a maximum. The NLK–Churchill pair also meets the criterion from panel b onwards. An important observation is that the amplitude enhancements detected by the low-latitude pair NDK–Seattle coincide with vTEC enhancements closer to the receiver station (Seattle), and that there are no vTEC enhancements near the NDK transmitter at any of the times shown. However, it is unclear whether the vTEC enhancement near Seattle is actually related to the substorm EEP, since the Seattle VLF receiver is located equatorward of the midlatitude ionospheric trough identified in the vTEC dataset throughout the event.

Existing statistical descriptions of EEP flux can be used to put the spatial extent of the EEP during this substorm into a broader context, in particular the latitudinal extent of the EEP. Cresswell-Moorcock et al. (2013) showed that equatorward edge of the EEP flux above 30 keV during an average substorm occurs at L = 4.6 ± 0.2, and at L = 4.1 ± 0.1 for the strongest 25% of substorms in their dataset, where the strength of an event was defined by the EEP flux. Their latitudinal extent results were similar to the earlier statistical study of >0.3 dB CNA during substorms by Berkey et al. (1974). For our case study, the SuperDARN radars detected evidence of EEP at L = 3.7–4.0, indicating that the EEP impact area extended *at least* this far equatorward and possibly further. No satellite EEP flux measurements were available for our case study event, but the moderate geomagnetic conditions ($18 \leq ap30 \leq 67$) suggest that the EEP fluxes could easily be

within the upper quartile range of the Cresswell-Moorcock et al. (2013) event list.

The Ap-dependent EEP flux model by van de Kamp et al. (2018) provides another helpful comparison with our case study. This model provides median electron fluxes above 30 keV as a function of the daily geomagnetic index *Ap*, the L-value, and the magnetic local time (MLT). The van de Kamp et al. (2018) model includes all EEP flux above 30 keV, including from non-substorm activity, but we expect that most of the EEP is associated with substorm processes (Nesse Tyssøy et al., 2021). We have estimated the latitude limits of the EEP as the L-value at which the modelled > 30 keV electron flux falls below 2000 cm^{-2} s^{-1} sr^{-1} using the equations for the MLT-dependent model described in Section 3.2 of van de Kamp et al. (2018). The modelled EEP flux decays sharply at the lower latitude limit, so the lower latitude limit of the EEP is not overly sensitive to our choice of flux threshold. In contrast, the EEP flux decays more gradually at the poleward edge of the EEP impact area, so it is more difficult to choose a specific L-value as the poleward extent of the EEP. Therefore, we focus only on the lower latitude limit when comparing our results to the van de Kamp et al. (2018) model. The solid black line near L = 4 in Figure 7 shows the equatorward boundary of the EEP predicted by the model, with *Ap* = 25 for 25 October 2019. As mentioned already, the SuperDARN radars at L = 3.7–4 detect a clear ANA response throughout the substorm, indicating the EEP boundary extends at least as far equatorward as L = 3.7–4, and probably further. Noting that the *Ap* index represents only a daily average of the geomagnetic activity, it is not surprising that the observed EEP impact area extends further equatorward than predicted by the model, since *ap*30 is well above the daily average during the actual event (up to *ap*30 = 67). The dashed lines in Figure 7 show the modelled position of the equatorward EEP boundary determined using the 30 min *ap*30 index rather than the daily *Ap*. With the *ap*30 model input, the equatorward EEP boundaries in panels c–g are positioned equatorward of the ANA response and therefore consistent with the observations. In the final recovery phase when *ap*30 decreases to below the daily average (panels h–i), using *ap*30 as the model input shifts the EEP boundary to higher latitudes. This further underestimates the size of the EEP impact area during the substorm recovery phase compared to the *Ap* model input (solid lines).

4 Two additional substorms

To further investigate the extent to which the *Ap* and *ap*30 indices capture the EEP spatial extent, we present two further examples of substorms that occurred during lower geomagnetic activity conditions. The riometer and radar data were processed in the same manner as the previous example, using the 21-days window centred on each event date to determine the quiet day curve.

4.1 18 June 2018

Maps of the CNA/ANA at nine time instants for a substorm that occurred on 18 June 2018 are shown in Figure 9. This substorm consists of a single expansion–recovery phase pair and the maximum magnetic disturbance of ≲450 nT is considerably weaker than the event already presented. For this event, data from the Pinawa (PINA) riometer and the Clyde River (CLY) and Kapuskasing (KAP) SuperDARN radars were also available, which extends the observable area towards the northeast and the south. Throughout the event, the CNA did not exceed 2 dB, and the CNA gradually decreased to below the threshold value of 0.5 dB during the recovery phase (panels g–i). No CNA enhancement was observed by the PGEO or PINA riometers near L = 4, however we note that CNA up to 0.4 dB was measured at PINA (not shown), which is only slightly below the threshold value. In contrast, ANA enhancements were detected by all four SuperDARN radars near L = 4 (PGR, SAS, KAP and GBR), which commenced near the event onset (panel b) and were still present at the end of the substorm recovery phase (panel i). The *Ap* index for 18 June 2018 is 16, which places the equatorward edge of the > 30 keV electron flux at about L = 4.3–4.7 based on the van de Kamp et al. (2018) model. This is shown by the solid black line in each panel of Figure 9. This model prediction is consistent with the absence of CNA at L = 4, but the SuperDARN measurements indicate that some type of EEP is present at lower latitudes. When *ap*30 is used as the model input, the low latitude EEP boundary (dashed line) is still poleward of the ANA enhancement measured by the SuperDARN radars. Therefore, neither the *Ap* or *ap*30 model inputs capture the spatial extent of the EEP observed near L = 4 for this substorm.

4.2 10 December 2018

Our final case study, presented in Figure 10, shows the EEP spatial coverage during a substorm on 10 December 2018 (*Ap* = 10). Like the 18 June 2018 event, this substorm consists of a single expansion–recovery phase pair. Throughout the event, the CNA and ANA enhancements are confined to L ≥5. This agrees with the van de Kamp et al. (2018) model, which places the EEP impact area at $L \geq 5$ for *Ap* = 10 (black solid line). There is a small ANA enhancement at PGR in panels (d)–(e), but no other instruments near L = 4 detected any EEP signatures above the threshold level. Based on these observations, it appears that the van de Kamp et al. (2018) model with the *Ap* index input provides a good estimate of the low latitude boundary of the EEP for this substorm. The modelled boundary determined from the *ap*30 index is further equatorward (dashed line), and the observations do not suggest that the EEP extends that far equatorward.

Also apparent in Figure 10 is a clear ANA enhancement at the poleward edge of the observable area. This is observed by the

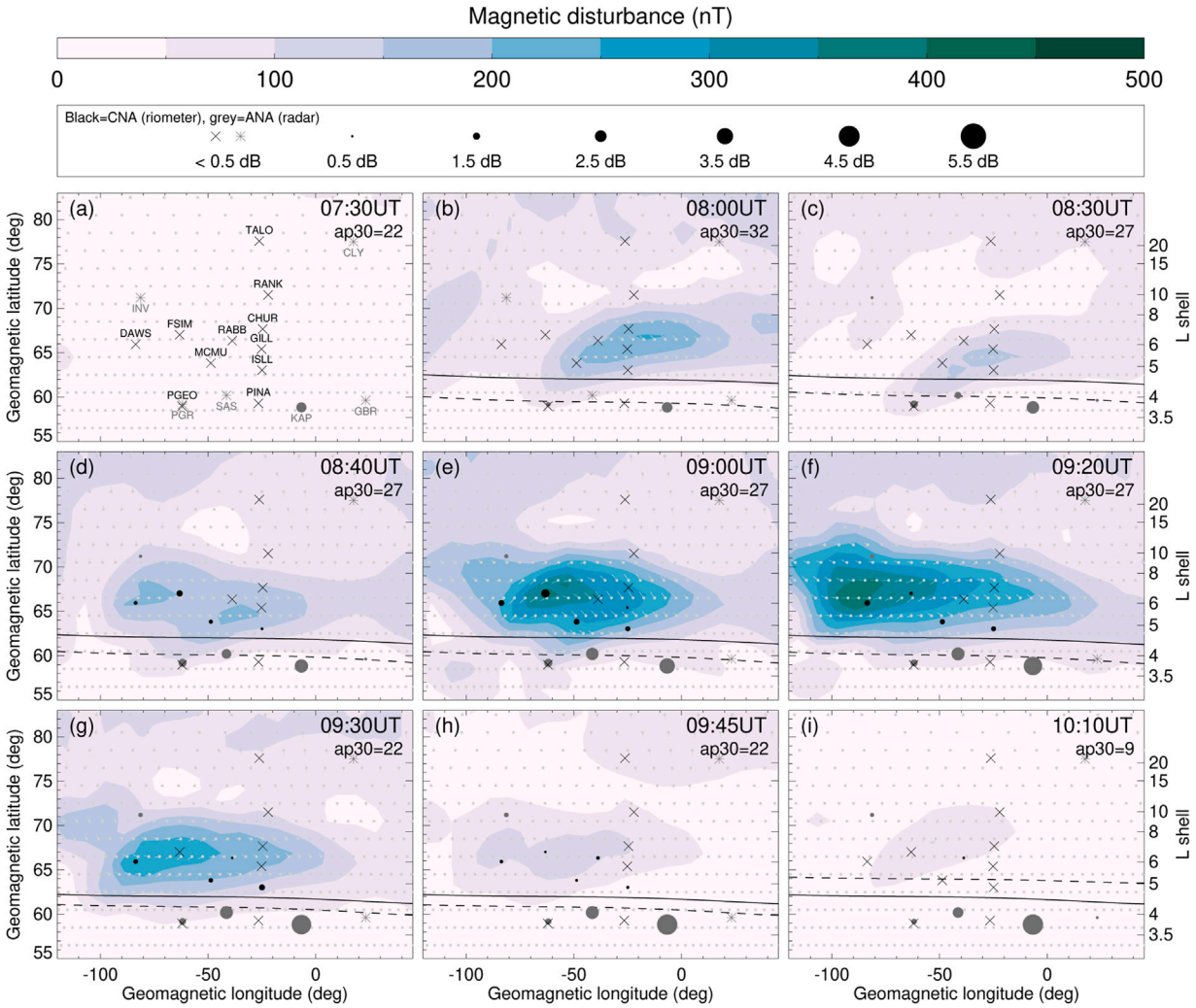

FIGURE 9
Spatial evolution of the magnetic field disturbance, 30 MHz cosmic noise absorption and 10–11 MHz atmospheric noise attenuation during the substorm event on 18 June 2018.

INV radar commencing at 08:27 UT (panel c) and continuing until just after 10:00 UT (panels h–i). Similar behaviour in the CNA is measured by the RANK riometer further to the east. This CNA enhancement does not extend as far north as TALO, but there is an ANA enhancement even further east at CLY from 08:48 UT (panel d) onwards at the northeast edge of the observable area. This is considerably poleward of the EEP boundary of L = 14.5 ± 2 reported by Cresswell-Moorcock et al. (2013) for an average-type substorm.

5 Discussion

In this study we have combined several types of ground-based instruments to estimate the EEP impact area during three substorms that occurred during low to moderate geomagnetic conditions. The case studies demonstrate that substorm EEP can extend considerably equatorward or poleward of the average latitude limits determined in two earlier studies, Cresswell-Moorcock et al. (2013) and van de Kamp et al. (2018). The evidence for this extended latitude range comes from the atmospheric noise attenuation (ANA) estimates from the SuperDARN radars, and the position of the low-latitude EEP boundary is also supported by the vTEC and VLF amplitude observations. We have also shown that the riometers and radars may detect CNA and ANA enhancements throughout the substorm recovery phases. It is likely that these EEP signatures are caused by pulsating aurora (PsA), which are a very common feature of the substorm recovery phase. The latitudinal extent of the recovery phase EEP is well within the

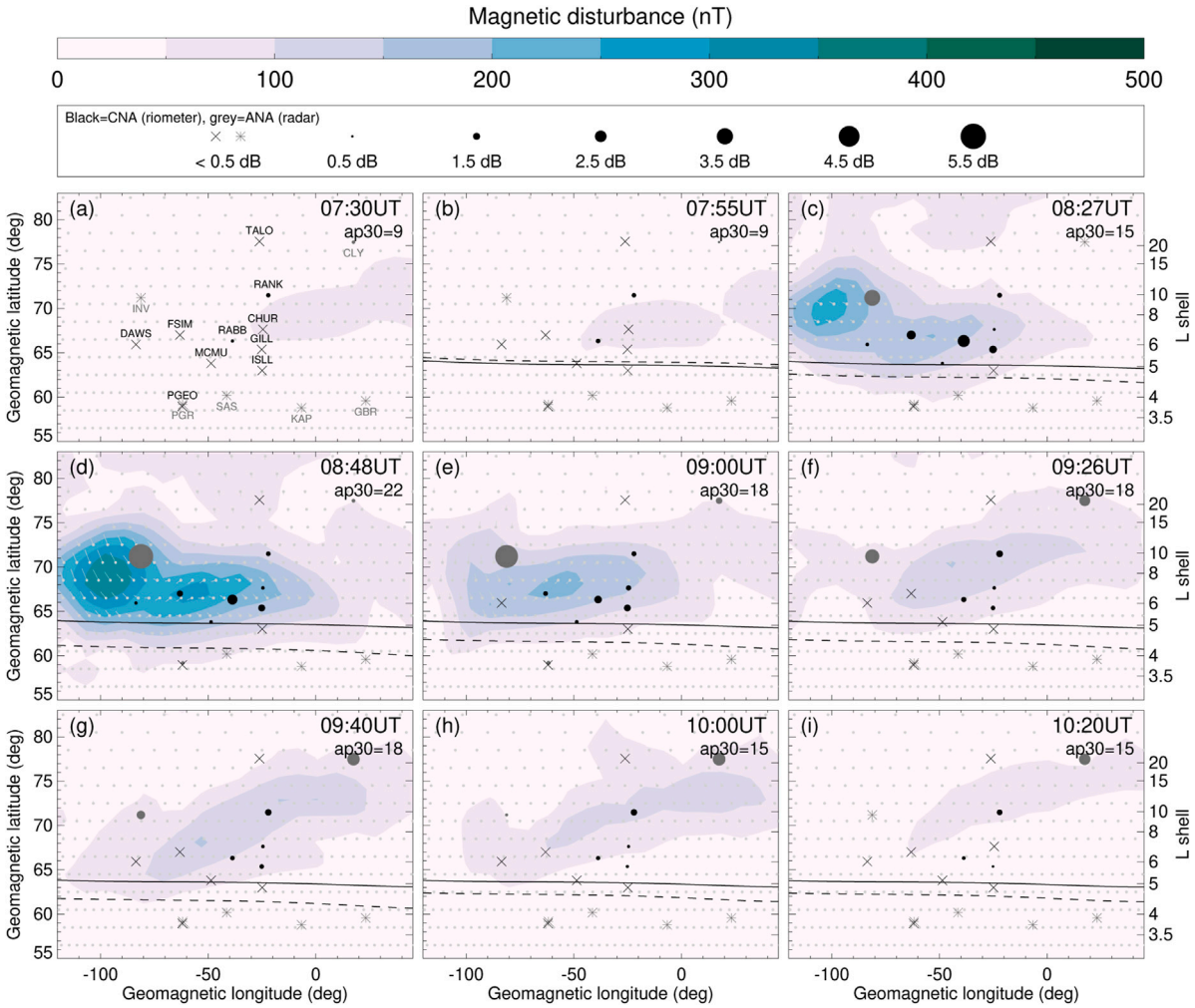

FIGURE 10
Spatial evolution of the magnetic field disturbance, 30 MHz cosmic noise absorption and 10–11 MHz atmospheric noise attenuation during the substorm event on 10 December 2018.

latitude limits reported in our earlier SuperDARN study of ANA during pulsating aurorae (PsA) (Bland et al., 2021). That study showed that the spatial extent of ANA during PsA in the southern hemisphere regularly extends equatorward of 59° CGM latitude and occasionally equatorward of 40° CGM latitude. It is important to note that the recovery phase EEP signatures observed in the CNA, ANA, VLF amplitude and vTEC data are not captured by the magnetometer data or the geomagnetic indices due to the decay of the substorm current systems during this time. This means that geomagnetic indices are not a suitable proxy for EEP during substorm recovery phases.

Another key result from this study is that the ANA enhancements at L = 3.7–4 were not accompanied by clear CNA responses from the riometers at similar latitudes. For the substorms on 25 October 2019 (Figure 7) and 18 June 2018 (Figure 9), these ANA enhancements commenced at the event onset and persisted to the end of the last recovery phase. The ANA was well above the 0.5 dB threshold and therefore represents a significant attenuation of the 10–11 MHz radio noise compared to the 21-days reference period. Without the radar data, one would conclude from Figure 9 that the EEP impact area never extended as far equatorward as PINA (L = 3.8) or as far poleward as CHUR (L = 6.9). The radar observations, however, show that the latitudinal range of the EEP during the 18 June 2018 event extended from *at least* L = 3.7 (KAP) to *at least* L = 9.6 (INV). It is possible that the EEP fluxes are too low during these events for many of the riometers to detect any significant amount of CNA, where we have defined 'significant' as CNA > 0.5 dB. The lower operating frequency and the different antenna properties of the SuperDARN radars may make them more sensitive to low-flux EEP compared to the riometers.

In this study we have estimated the minimum spatial extent of substorm EEP based on the response measured by several ground-based radio instruments. The presence or absence of EEP at each instrument site was essentially determined by the instrument sensitivity, rather than a fixed >30 keV electron flux threshold, for example. Since CNA and ANA are both height-integrated quantities, the same absorption response measured from the ground could be attributed to many different EEP energy spectra. While there have been some studies examining the relationship between >30 keV flux and CNA (e.g., Rodger et al., 2013), a clear correlation between >30 keV flux and CNA was identified only for relatively high electron fluxes of at least 10^6 cm^{-2} s^{-1} sr^{-1}, which corresponds to about 1 dB of CNA. Our results show that the EEP spatial extent can be much larger than the region in which >1 dB of CNA was measured, so it is difficult to estimate what EEP fluxes might be occurring at the equatorward edge of the EEP impact area where the SuperDARN radars detected significant ANA.

Our estimates of the latitude limits of the EEP impact area rely heavily on a novel EEP detection method (ANA from SuperDARN radars). It is therefore necessary to discuss the uncertainties in the ANA observations and the instrumental differences between the riometers and radars that may contribute to this result. Our earlier work demonstrates that SuperDARN radars can detect ANA associated with energetic proton precipitation (Bland et al., 2018) as well as low-flux EEP associated with pulsating aurora (Bland et al., 2019; Bland et al., 2021), which represent two spectral extremes of energetic particle precipitation. However, the sensitivity of the SuperDARN radars to different EEP spectra has not yet been studied in detail. We expect that the amount of attenuation depends on the electron density and electron-neutral collision frequency, so that the height of maximum attenuation should be the same for radars and riometers. The radars and riometers would therefore be sensitive to the same EEP energies. However, the minimum electron fluxes required to produce a measurable amount of absorption is likely to be different for riometers and radars. As mentioned above, the lower operating frequency of the SuperDARN radars compared to the riometers may make them more sensitive to lower EEP fluxes, which would account for the different instrument responses to the EEP. The width and oblique orientation of the radar beams, and the presence of backlobes and sidelobes in the beam patterns, may also contribute to the differences observed between the radar and riometer datasets. All of these factors require further investigation to make it possible to perform quantitative comparisons between the radar and riometer datasets.

Another important aspect of the radar dataset is the difficulty in assigning geomagnetic coordinates to the ANA measurements. In Figure 7 we have used the radar site as the location of the ANA, but in reality the D-region sampled by each radar is about 2–3° poleward of the radar site (see radar fields of view in Figure 1). We have chosen to display the ANA measurements at the actual radar locations because the phased-array design of SuperDARN radars results in a large backlobe in the beam pattern, effectively creating a second field of view behind the radar (Milan et al., 1997). The noise measurements from the radars are therefore a superposition of the noise measured in the front and rear fields of view. The vTEC data presented in Figure 8 indicate that the poleward edge of the midlatitude ionospheric trough is very close to the PGR and SAS radar sites, which suggests that the EEP region is likely to be poleward of the radar site for the 25 October 2019 substorm. This means that the ANA measured at these two sites can probably be attributed to the front fields of view shown in Figure 1.

Although more work is required to properly understand what EEP energies and fluxes the SuperDARN radars are sensitive to, our results indicate that EEP with sufficient flux to attenuate 10–11 MHz radiowaves by ~5 dB reaches latitudes well equatorward of the model predictions for >30 keV electron flux. This is an important consideration for studying auroral absorption for space weather applications, where the detailed spatial and temporal evolution of the EEP provides important information to HF radio communicators. The long-term atmospheric chemical response to EEP is probably less sensitive to an underestimated EEP impact area because the ozone depletion associated with NO_X catalysts is confined to the polar vortex (Verronen et al., 2021). Based on this, we expect that the EEP near L = 4 would contribute to NO_X-related ozone depletion only when the polar vortex is present at these latitudes. Short-term mesospheric ozone depletion caused by HO_X catalysts occurs independently of the polar vortex location, so accurate knowledge of the EEP impact area would still be required to properly determine the atmospheric response.

6 Conclusion

The spatial coverage of the EEP impact area during three substorms has been determined using a combination of riometers, SuperDARN radars, VLF receivers and vTEC measurements in North America. Our results show that substorm EEP can extend considerably equatorward and poleward of the average latitude limits reported in previous studies. Evidence of this extended latitude range was provided by atmospheric noise attenuation (ANA) estimates from SuperDARN radars and from amplitude variations measured by the VLF receivers, which extended the total observable area provided by the riometer network. For our main case study, these datasets indicated that the lower latitude limit of EEP extended at least as far equatorward as L = 3.7–4, but this was not accompanied by a CNA enhancement from the riometer at the same latitude (PGEO). This result reveals a limitation of using 30 MHz CNA measurements to estimate auroral absorption, since the riometers and radars respond differently to the substorm EEP. Further work is required to determine what

EEP energies and fluxes the SuperDARN radars are sensitive to at 10–11 MHz, and to determine how the SuperDARN ANA measurements can be quantitatively compared to the 30 MHz CNA. The wider latitude limits of EEP reported in this study are unlikely to have significant consequences for modelling the long-term atmospheric response to EEP, since the polar vortex already sets a stricter limit on the spatial extent of the NO_X-related atmospheric response. However, accurate knowledge of the EEP spatial extent would be necessary for modelling the short-term atmospheric response to EEP and for studying auroral absorption. We therefore highlight the potential of the SuperDARN, AARDDVARK and vTEC datasets to help refine our understanding of EEP by extending the area over which EEP can be detected from the ground.

Data availability statement

Publicly available datasets were analyzed in this study. This data can be found here: The raw data from the Canadian riometers are available from the University of Calgary Space Physics Data portal (https://data-portal.phys.ucalgary.ca/go_rio). SuperDARN data are published in the Federated Research Data Repository (https://www.frdr-dfdr.ca/repo/collection/superdarn). The total electron content data are available at https://w3id.org/cedar?experiment_list=experiments4/2019/gps/25oct19&file_list=gps191025g.002.hdf5. The VLF data are available at the British Antarctic Survey Polar Data Centre (http://psddb.nerc-bas.ac.uk/data/access/coverage.php?menu=1,7&class=232&bc=1). The SuperMAG MLT-Mlat gridded magnetic field data are available at https://supermag.jhuapl.edu/mag and the SML indices are available at https://supermag.jhuapl.edu/indices. The ap30 and ap indices are available at https://doi.org/10.5880/Hpo.0002 and https://doi.org/10.5880/Kp.0001 respectively.

Author contributions

EB performed the riometer and radar data analysis. TB analysed the VLF data. NP assisted with selecting the case study events. EB wrote the first draft of the manuscript, and all authors contributed to the manuscript revision and approved the submitted version.

Funding

EB is supported by the Norwegian Research Council (NRC) under contract 287427. NP is supported by the NRC under CoE contract 223252.

Acknowledgments

The authors gratefully acknowledge the SuperMAG collaborators (https://supermag.jhuapl.edu/info/?page=acknowledgement). The authors acknowledge the use of SuperDARN data. SuperDARN is a collection of radars funded by the national scientific funding agencies of Australia, Canada, China, France, Japan, Norway, South Africa, United Kingdom, and United States. TB wishes to thank Mark Clilverd and Péter Steinbach for the helpful discussions related to narrowband VLF measurements and all operators of the AARDDVARK for maintaining the network. The Go-Canada riometer array is operated by the University of Calgary with financial support from the Canadian Space Agency.

Conflict of interest

The authors declare that the research was conducted in the absence of any commercial or financial relationships that could be construed as a potential conflict of interest.

Publisher's note

References

Berkey, F. T., Driatskiy, V. M., Henriksen, K., Hultqvist, B., Jelly, D. H., Shchuka, T. I., et al. (1974). A synoptic investigation of particle precipitation dynamics for 60 substorms in IQSY (1964–1965) and IASY (1969). *Planet. Space Sci.* 22, 255–307. doi:10.1016/0032-0633(74)90028-2

Bland, E. C., Heino, E., Kosch, M. J., and Partamies, N. (2018). SuperDARN radar-derived HF radio attenuation during the September 2017 solar proton events. *Space* 16, 1455–1469. doi:10.1029/2018SW001916

Bland, E., Tesema, F., and Partamies, N. (2021). D-region impact area of energetic electron precipitation during pulsating aurora. *Ann. Geophys.* 39, 135–149. doi:10.5194/angeo-39-135-2021

Bland, E. C., Partamies, N., Heino, E., Yukimatu, A. S., and Miyaoka, H. (2019). Energetic electron precipitation occurrence rates determined using the Syowa East SuperDARN radar. *JGR. Space Phys.* 124, 6253–6265. doi:10.1029/2018JA026437

Chisham, G., Lester, M., Milan, S. E., Freeman, M. P., Bristow, W. A., Grocott, A., et al. (2007). A decade of the super dual auroral radar network (SuperDARN): Scientific achievements, new techniques and future directions. *Surv. Geophys.* 28, 33–109. doi:10.1007/s10712-007-9017-8

Clilverd, M. A., Rodger, C. J., Brundell, J., Bähr, J., Cobbett, N., Moffat-Griffin, T., et al. (2008). Energetic electron precipitation during substorm injection events: High-latitude fluxes and an unexpected midlatitude signature. *J. Geophys. Res.* 113, A10311. doi:10.1029/2008JA013220

Clilverd, M. A., Rodger, C. J., Thomson, N. R., Brundell, J. B., Ulich, T., Lichtenberger, J., et al. (2009). Remote sensing space weather events: Antarctic-arctic radiation-belt (dynamic) deposition-vlf atmospheric research konsortium network. *Space* 7, S04001. doi:10.1029/2008SW000412

[Dataset] Coster, A. (2019). Data from the cedar madrigal database. MIT/Haystack Observatory.

Cresswell-Moorcock, K., Rodger, C. J., Kero, A., Collier, A. B., Clilverd, M. A., Häggström, I., et al. (2013). A reexamination of latitudinal limits of substorm-produced energetic electron precipitation. *J. Geophys. Res. Space Phys.* 118, 6694–6705. doi:10.1002/jgra.50598

Daae, M., Espy, P., Nesse Tyssøy, H., Newnham, D., Stadsnes, J., and Søraas, F. (2012). The effect of energetic electron precipitation on middle mesospheric night-time ozone during and after a moderate geomagnetic storm. *Geophys. Res. Lett.* 39, L21811. doi:10.1029/2012GL053787

Fang, X., Randall, C. E., Lummerzheim, D., Solomon, S. C., Mills, M. J., Marsh, D. R., et al. (2008). Electron impact ionization: A new parameterization for 100 eV to 1 MeV electrons. *J. Geophys. Res.* 113, A09311. doi:10.1029/2008JA013384

Gjerloev, J. W., Hoffman, R. A., Sigwarth, J. B., and Frank, L. A. (2007). Statistical description of the bulge-type auroral substorm in the far ultraviolet. *J. Geophys. Res.* 112, A07213. doi:10.1029/2006JA012189

Gjerloev, J. W. (2012). The SuperMAG data processing technique. *J. Geophys. Res.* 117, A09213. doi:10.1029/2012JA017683

Greenwald, R. A., Baker, K. B., Dudeney, J. R., Pinnock, M., Jones, T. B., Thomas, E. C., et al. (1995). DARN/SuperDARN: A global view of the dynamics of high-latitude convection. *Space Sci. Rev.* 71, 761–796. doi:10.1007/BF00751350

Jones, S. L., Lessard, M. R., Rychert, K., Spanswick, E., and Donovan, E. (2011). Large-scale aspects and temporal evolution of pulsating aurora. *J. Geophys. Res.* 116, A03214. doi:10.1029/2010JA015840

Kellerman, A. C., Shprits, Y. Y., Makarevich, R. A., Spanswick, E., Donovan, E., and Reeves, G. (2015). Characterization of the energy-dependent response of riometer absorption. *J. Geophys. Res. Space Phys.* 120, 615–631. doi:10.1002/2014JA020027

Mann, I. R., Milling, D. K., Rae, I. J., Ozeke, L. G., Kale, A., Kale, Z. C., et al. (2008). The upgraded CARISMA magnetometer array in the THEMIS era. *Space Sci. Rev.* 141, 413–451. doi:10.1007/s11214-008-9457-6

[Dataset] Matzka, J., Bronkalla, O., Kervalishvili, G., Rauberg, J., and Yamazaki, Y. (2022). Geomagnetic hpo index. v. 2.0. GFZ Data Services. doi:10.5880/Hpo.0002

[Dataset] Matzka, J., Bronkalla, O., Tornow, K., Elger, K., and Stolle, C. (2021a). Geomagnetic kp index. v. 1.0. doi:10.5880/Kp.0001

Matzka, J., Stolle, C., Yamazaki, Y., Bronkalla, O., and Morschhauser, A. (2021b). The geomagnetic kp index and derived indices of geomagnetic activity. *Space* 19, e2020SW002641. doi:10.1029/2020SW002641

McPherron, R. L., and Chu, X. (2018). The midlatitude positive bay index and the statistics of substorm occurrence. *JGR. Space Phys.* 123, 2831–2850. doi:10.1002/2017JA024766

Mendillo, M. (2006). Storms in the ionosphere: Patterns and processes for total electron content. *Rev. Geophys.* 44, RG4001. doi:10.1029/2005RG000193

Milan, S. E., Hosokawa, K., Lester, M., Sato, N., Yamagishi, H., and Honary, F. (2008). D region HF radar echoes associated with energetic particle precipitation and pulsating aurora. *Ann. Geophys.* 26, 1897–1904. doi:10.5194/angeo-26-1897-2008

Milan, S. E., Jones, T. B., Robinson, T. R., Thomas, E. C., and Yeoman, T. K. (1997). Interferometric evidence for the observation of ground backscatter originating behind the CUTLASS coherent HF radars. *Ann. Geophys.* 15, 29–39. doi:10.1007/s00585-997-0029-y

Newell, P. T., and Gjerloev, J. W. (2011). Evaluation of SuperMAG auroral electrojet indices as indicators of substorms and auroral power. *J. Geophys. Res.* 116, 12211. doi:10.1029/2011ja016779

Nesse Tyssøy, H., Partamies, N., Babu, E. M., Smith-Johnsen, C., and Salice, J. A. (2021). The predictive capabilities of the auroral electrojet index for medium energy electron precipitation. *Front. Astron. Space Sci.* 8. doi:10.3389/fspas.2021.714146

Nishitani, N., Ruohoniemi, J. M., Lester, M., Baker, J. B. H., Koustov, A. V., Shepherd, S. G., et al. (2019). Review of the accomplishments of mid-latitude super dual auroral radar network (SuperDARN) HF radars. *Prog. Earth Planet. Sci.* 6, 27–57. doi:10.1186/s40645-019-0270-5

Partamies, N., Tesema, F., Bland, E., Heino, E., Nesse Tyssøy, H., and Kallelid, E. (2021). Electron precipitation characteristics during isolated, compound, and multi-night substorm events. *Ann. Geophys.* 39, 69–83. doi:10.5194/angeo-39-69-2021

Partamies, N., Whiter, D., Kadokura, A., Kauristie, K., Nesse Tyssøy, H., Massetti, S., et al. (2017). Occurrence and average behavior of pulsating aurora. *J. Geophys. Res. Space Phys.* 122, 5606–5618. doi:10.1002/2017JA024039

Ponomarenko, P. V., Bland, E. C., McWilliams, K. A., and Nishitani, N. (2022). On the noise estimation in super dual auroral radar network data. *Radio Sci.* 57, e2022RS007449. doi:10.1029/2022rs007449

Randall, C. E., Harvey, V. L., Singleton, C. S., Bailey, S. M., Bernath, P. F., Codrescu, M., et al. (2007). Energetic particle precipitation effects on the southern hemisphere stratosphere in 1992–2005. *J. Geophys. Res.* 112, D08308. doi:10.1029/2006jd007696

Rideout, W., and Coster, A. (2006). Automated GPS processing for global total electron content data. *GPS Solut.* 10, 219–228. doi:10.1007/s10291-006-0029-5

Rodger, C. J., Clilverd, M. A., Kavanagh, A. J., Watt, C. E. J., Verronen, P. T., and Raita, T. (2012). Contrasting the responses of three different ground-based instruments to energetic electron precipitation. *Radio Sci.* 47, 1–13. doi:10.1029/2011RS004971

Rodger, C. J., Kavanagh, A. J., Clilverd, M. A., and Marple, S. R. (2013). Comparison between POES energetic electron precipitation observations and riometer absorptions: Implications for determining true precipitation fluxes. *J. Geophys. Res. Space Phys.* 118, 7810–7821. doi:10.1002/2013JA019439

Seppälä, A., Matthes, K., Randall, C. E., and Mironova, I. A. (2014). What is the solar influence on climate? Overview of activities during CAWSES-II. *Prog. Earth Planet. Sci.* 1, 24. doi:10.1186/s40645-014-0024-3

Seppälä, A., Verronen, P. T., Clilverd, M. A., Randall, C. E., Tamminen, J., Sofieva, V., et al. (2007). Arctic and Antarctic polar winter $NO_x$and energetic particle precipitation in 2002–2006. *Geophys. Res. Lett.* 34, L12810. doi:10.1029/2007gl029733

Sergeev, V. A., Shukhtina, M. A., Stepanov, N. A., Rogov, D. D., Nikolaev, A. V., Spanswick, E., et al. (2020). Toward the reconstruction of substorm-related dynamical pattern of the radiowave auroral absorption. *Space* 18, e2019SW002385. doi:10.1029/2019SW002385

Shepherd, S. G. (2014). Altitude-adjusted corrected geomagnetic coordinates: Definition and functional approximations. *J. Geophys. Res. Space Phys.* 119, 7501–7521. doi:10.1002/2014ja020264

Sinnhuber, M., Nieder, H., and Wieters, N. (2012). Energetic particle precipitation and the chemistry of the mesosphere/lower thermosphere. *Surv. Geophys.* 33, 1281–1334. doi:10.1007/s10712-012-9201-3

Smith-Johnsen, C., Marsh, D. R., Orsolini, Y., Nesse Tyssøy, H., Hendrickx, K., Sandanger, M. I., et al. (2018). Nitric oxide response to the april 2010 electron precipitation event—Using WACCM and WACCM-D with and without medium energy electrons. *J. Geophys. Res. Space Phys.* 123, 5232–5245. doi:10.1029/2018JA025418

Spanswick, E., Donovan, E., Friedel, R., and Korth, A. (2007). Ground based identification of dispersionless electron injections. *Geophys. Res. Lett.* 34, L03101. doi:10.1029/2006GL028329

Spanswick, E., Donovan, E., Liu, W., Liang, J., Blake, J. B., Reeves, G., et al. (2009). Global observations of substorm injection region evolution: 27 august 2001. *Ann. Geophys.* 27, 2019–2025. doi:10.5194/angeo-27-2019-2009

[Dataset] Super Dual Auroral Radar Network (2021). SuperDARN 2018 RAWACF. doi:10.20383/101.0290

[Dataset] Super Dual Auroral Radar Network (2022). SuperDARN 2019 RAWACF. doi:10.20383/102.0558

Tesema, F., Partamies, N., Nesse Tyssøy, H., Kero, A., and Smith-Johnsen, C. (2020). Observations of electron precipitation during pulsating aurora and its chemical impact. *JGR. Space Phys.* 125, e2019JA027713. doi:10.1029/2019JA027713

Thomson, N. R., Clilverd, M. A., and McRae, W. M. (2007). Nighttime

ionospheric D region parameters from VLF phase and amplitude. *J. Geophys. Res.* 112, A07304. doi:10.1029/2007JA012271

Turunen, E., Kero, A., Verronen, P. T., Miyoshi, Y., Oyama, S.-I., and Saito, S. (2016). Mesospheric ozone destruction by high-energy electron precipitation associated with pulsating aurora. *JGR. Atmos.* 121, 11,852–11,861. doi:10.1002/2016JD025015

van de Kamp, M., Rodger, C. J., Seppälä, A., Clilverd, M. A., and Verronen, P. T. (2018). An updated model providing long-term data sets of energetic electron precipitation, including zonal dependence. *J. Geophys. Res. Atmos.* 123, 9891–9915. doi:10.1029/2017JD028253

van de Kamp, M., Seppälä, A., Clilverd, M. A., Rodger, C. J., Verronen, P. T., and Whittaker, I. C. (2016). A model providing long-term data sets of energetic electron precipitation during geomagnetic storms. *J. Geophys. Res. Atmos.* 121, 12, 520–540. doi:10.1002/2015JD024212

Verronen, P. T., Kero, A., Partamies, N., Szelag, M. E., Oyama, S.-I., Miyoshi, Y., et al. (2021). Simulated seasonal impact on middle atmospheric ozone from high-energy electron precipitation related to pulsating aurorae. *Ann. Geophys.* 39, 883–897. doi:10.5194/angeo-39-883-2021

Watson, C., Jayachandran, P. T., Spanswick, E., Donovan, E. F., and Danskin, D. W. (2011). GPS TEC technique for observation of the evolution of substorm particle precipitation. *J. Geophys. Res.* 116. doi:10.1029/2010JA015732

Yamazaki, Y., Matzka, J., Stolle, C., Kervalishvili, G., Rauberg, J., Bronkalla, O., et al. (2022). Geomagnetic activity index hpo. *Geophys. Res. Lett.* 49, e2022GL098860. doi:10.1029/2022gl098860

Zou, S., Moldwin, M. B., Coster, A., Lyons, L. R., and Nicolls, M. J. (2011). Gps tec observations of dynamics of the mid-latitude trough during substorms. *Geophys. Res. Lett.* 38, L14109. doi:10.1029/2011GL048178

frontiers | Frontiers in Astronomy and Space Sciences

TYPE Original Research
PUBLISHED 08 September 2022
DOI 10.3389/fspas.2022.973276

OPEN ACCESS

EDITED BY
Marian Lazar,
Ruhr University Bochum, Germany

REVIEWED BY
Weijie Sun,
University of Michigan, United States
Elizabeth Mitchell,
JHUAPL, United States

*CORRESPONDENCE
Jone Peter Reistad,
jone.reistad@uib.no

SPECIALTY SECTION
This article was submitted to Space Physics,
a section of the journal
Frontiers in Astronomy and Space Sciences

RECEIVED 20 June 2022
ACCEPTED 15 August 2022
PUBLISHED 08 September 2022

CITATION
Reistad JP, Holappa L, Ohma A, Gabrielse C, Sur D, Asikainen T and DeJong A (2022), Dependence of the global dayside reconnection rate on interplanetary magnetic field B_y and the earth's dipole tilt.
Front. Astron. Space Sci. 9:973276.
doi: 10.3389/fspas.2022.973276

Dependence of the global dayside reconnection rate on interplanetary magnetic field B_y and the earth's dipole tilt

Jone Peter Reistad[1]*, Lauri Holappa[2], Anders Ohma[1], Christine Gabrielse[3], Dibyendu Sur[4,5], Timo Asikainen[2] and Anna DeJong[6,7]

[1]Birkeland Centre for Space Science, University of Bergen, Bergen, Norway, [2]Space Physics and Astronomy Research Unit, University of Oulu, Oulu, Finland, [3]The Aerospace Corporation, El Segundo, CA, United States, [4]CIRES, University of Colorado Boulder, Boulder, CO, United States, [5]Narula Institute of Technology, Kolkata, India, [6]Howard Community College, Columbia, MD, United States, [7]NASA Goddard Space Flight Center, Greenbelt, MD, United States

In the recent years, significant attention has been given to the combined effect of Interplanetary Magnetic Field (IMF) duskward component (B_y) and dipole tilt on the global magnetosphere-ionosphere system response. Numerous studies have pointed out that when the Earth's magnetic dipole is tilted away from the Sun (negative dipole tilt during northern winter), and IMF has a positive B_y component, the effects on ionospheric currents, particle precipitation, ionospheric convection, and average size of the auroral oval, is significantly more enhanced, compared to when IMF B_y is negative. Furthermore, this IMF B_y polarity effect reverses when Earth's dipole is tilted in the opposite direction. The underlying cause has remained unclear. Our analysis shows that substorms tend to be stronger during the same IMF B_y and dipole tilt polarity combination. Taken together with earlier results showing also more frequent substorms during the same conditions, our observations suggests that when IMF B_y and dipole tilt have opposite signs, there is a more efficient global dayside reconnection rate. We also show analysis of the occurrence frequency of periods of Steady Magnetospheric Convection, substorm onset latitude, and the isotropic boundary of proton precipitation, that are all consistent with our conclusion that the combination of IMF B_y and dipole tilt polarity affect the global dayside reconnection rate.

KEYWORDS

explicit by, dayside reconnection, global reconnection, asymmetry, substorm strength, SMC, onset latitude

1 Introduction

Understanding the mechanisms that cause the range of different near-Earth space phenomena is often a difficult task. The system is highly coupled, from the thermosphere/ionosphere to the solar wind. It can therefore be challenging to determine the underlying cause of observed phenomena, as multiple processes occurring in different regions, alone or in combination, may produce very similar observational signatures.

This paper addresses why we observe a different behaviour of the magnetosphere-ionosphere system when the B_y component of the Interplanetary Magnetic Field (IMF) is positive vs negative during periods when the Earth's magnetic axis is tilted towards or away from the Sun. Although first mentioned by Friis-Christensen and Wilhjelm (1975), it was not until recently that this topic has been revisited and further characterized. Friis-Christensen and Wilhjelm noted that during northern hemisphere winter (negative dipole tilt angle, Ψ), the westward electrojet was significantly stronger for positive compared to negative IMF B_y during otherwise similar IMF B_z conditions. Holappa and Mursula (2018) revisited this effect on the westward electrojet and established that these differences were not due to the Russell-McPherron effect (Russell and McPherron, 1973). They called this the *explicit B_y effect* to differentiate it from the Russell-McPherron effect, which is essentially due to seasonally varying correlation between IMF B_y and the geoeffective B_z component (IMF B_y not directly causing the Russell-McPherron effect). Holappa and Mursula (2018) quantified the difference in electrojet strength to be about 50 percent during winter conditions. During summer conditions, the IMF B_y dependence reverses as the westward electrojet is stronger for negative compared to positive IMF B_y, but the effect on the westward electrojet is minor compared to the difference during winter conditions (Holappa and Mursula, 2018; Holappa et al., 2021b).

The large IMF B_y and seasonal related asymmetries in the westward electrojet sparked the interest for investigating other aspects of the coupled system for similar behavior. Reistad et al. (2020) reported similar asymmetries in the average size of the polar cap. During negative dipole tilt, they found larger polar caps in both hemispheres when IMF B_y is positive compared to negative. The $\pm B_y$ asymmetry reversed when the dipole was tilted in the opposite direction. Since the same behaviour was seen in both the winter and summer hemisphere for a specific IMF B_y polarity, ionospheric effects related to season could not alone explain the observations. They suggested that in addition, one or both of the following scenarios must be the case: A) The global dayside reconnection rate depends on IMF B_y polarity when Earth's dipole is tilted, allowing for a stronger Dungey cycle and more energy input to the system when IMF B_y and Ψ have opposite signs; or B) When Earth's dipole is tilted, IMF B_y has an influence on the amount of magnetic flux the magentotail lobes typically can support, for a given dayside reconnection rate. While the results reported by Reistad et al. (2020) indicate a global difference in the magnetospheric response, the minor effect on the westward electrojet in the summer hemisphere compared to the winter hemisphere suggests that the influence on the ionospheric currents are more complex than what can be explained by type A and B mechanisms.

Other aspects of the solar wind - magnetosphere coupling has also been investigated in this regard. Holappa et al. (2020) and Holappa and Buzulukova (2022) found that fluxes of precipitating energetic electrons and protons in both hemispheres show a very similar asymmetry, namely that the precipitation is more intense when IMF B_y and Ψ have opposite signs, compared to when they have the same sign, during otherwise similar IMF B_z conditions. Holappa and Buzulukova (2022) showed that the growth rate of the ring current (measured by the Dst index) also exhibits a similar B_y-dependence. Ohma et al. (2021) investigated the occurrence frequency of magnetospheric substorms during periods of either positive or negative IMF B_y. Based on several independent lists of identified substorms, they concluded that substorms are more frequent when the sign of IMF B_y and Ψ are opposite, compared to when IMF B_y has the same sign as the dipole tilt. These findings further indicate that the explicit B_y-effect is a global phenomenon, which is likely related to a type A or B mechanism (or both) as mentioned above. Since dayside and nightside reconnection are the processes that allow for opening and closure of magnetic flux; the steady state, in which we interpret the long-term averages to represent (Laundal et al., 2020), must represent a balance of the two. The observed changes of the steady state open flux content depending on IMF B_y/Ψ polarity must therefore either be due to a type A or B mechanism (or both). These spatially separated processes (A: dayside and B: tail) are nevertheless highly coupled, as the dayside loading affects the conditions in the magnetotail, making the interpretation of the data analysis highly challenging, as will be elaborated on in more detail in the following.

Reistad et al. (2021) studied ionospheric convection on the basis of Doppler-shift from ground based HF radar echoes. They presented climatological patterns of the high latitude convection pattern during IMF B_y dominated periods, for various dipole tilt intervals. By normalizing the observed convection to the present size of the polar cap as inferred from simultaneous observations from the Active Magnetosphere and Planetary Electrodynamics Response Experiment (AMPERE), they were able to distinguish the contribution from lobe reconnection on the global convection pattern, which were found to be more efficient during local summer. This allowed the authors to quantify the part of the convection associated with dayside (and nightside) reconnection. Their results indicated that when IMF B_y and dipole tilt had opposite polarity, the Dungey cycle was slightly enhanced ($\sim 10\%$).

The results presented above demonstrate that the global magnetospheric response to positive and negative IMF B_y is

different when Ψ is nonzero: The westward electrojet is stronger, particle precipitation is more intense, substorms are more frequent, the polar cap is larger, and the ring current increases more rapidly when the signs of IMF B_y and Ψ are opposite. Previous studies have not identified whether this is mainly due to differences in the dayside coupling (type A) or mainly due to differences in how the tail responds to the same flux loading, influencing the amount of magnetic flux the lobes typically sustain (type B). However, there are key differences in how the magnetosphere and ionosphere are expected to respond between the type A and type B mechanisms, enabling new insights to be obtained about their relative importance.

If the observed explicit B_y effects are solely a result of mechanism B, the flux throughput in the (tilted) magnetosphere should be the same for both polarities of IMF B_y, if all other solar wind parameters are equal. Since substorms are more frequent for opposite signs of IMF B_y and Ψ, the substorms must either be stronger (closing more flux) or the flux must be transported by another process when IMF B_y and Ψ have the same sign. In addition to substorms, the magnetosphere can respond to solar wind forcing by entering into steady magnetospheric convection (SMC) periods (e.g., Sergeev et al., 1996; Kissinger et al., 2012). Hence, a type B process would imply weaker substorms and/or less frequent SMC events for opposite signs of IMF B_y and Ψ. On the other hand, mechanism A demands the flux throughput to be greater in the magnetospheric system for positive B_y during Northern Hemisphere (NH) winter and for negative B_y during NH summer. If the occurrence frequency of SMCs and the strength of substorms follow the same dependence as the other observed phenomena (stronger for opposite signs of IMF B_y and Ψ), it would suggest the influence of a type A mechanism in producing the observed explicit B_y effects.

In this paper, we present new analyses to demonstrate how IMF B_y and Ψ in combination affects the response of the magnetosphere-ionosphere system. The goal is to address whether mechanisms A or B are the main contributor to the explicit B_y effects. We will address how the occurrence frequency of SMC events are modulated and use various proxies to assess the global substorm strength. In the following section we will present our new analysis contributing to the investigation of the origin of the explicit B_y effect. The methodology used in the presented analysis is outlined as the results are presented. Our new results are discussed together with the existing knowledge on the topic in section 3. Our main conclusions are explicitly stated in the concluding section.

2 Results

When comparing the magnetosphere responses to intervals of positive and negative IMF B_y and dipole tilt, it is important that we compare instances with similar dayside forcing. This is largely controlled by the IMF B_z component. In all our analyses, we use the dayside coupling function presented by Milan et al. (2012), which is set out to quantify the global dayside reconnection rate, Φ_D [Wb/s], in response to the upstream IMF and solar wind, given by the formula

$$\Phi_D = \Lambda V_x^{4/3} B_{yz} \sin^{9/2}(\theta/2). \quad (1)$$

Here, $\Lambda = 3.3 \cdot 10^5$ $m^{2/3}s^{1/3}$ is a scaling constant related to the length of the dayside X-line, V_x is the solar wind velocity in the anti-sunward direction, B_{yz} is the magnitude of the IMF vector perpendicular to the Sun-Earth line, and θ is the IMF clock angle. When SI units are used, Φ_D gets the units of Wb/s = Volt, representing the rate of conversion of magnetic flux from a closed to open topology on the dayside.

As noted by Holappa et al. (2021a), the particular choice of coupling function is typically not crucial for this kind of analyses, yet they provide a convenient way to select periods of similar forcing for comparison. In all plots, the dayside coupling value is normalized to its mean value from the entire analysis period. This normalized coupling parameter we denote $\Phi_D/\langle\Phi_D\rangle$. We use IMF data time shifted to the bow shock of the Earth from the OMNI database (King and Papitashvili, 2005).

2.1 Occurrence of steady magnetospheric convection intervals: Interplanetary magnetic field B_y and dipole tilt dependence

The magnetosphere can enter different "modes" of response to the energy input from the interplanetary medium. The perhaps most common situation is the so-called loading/unloading cycle in which the magnetospheric substorm plays a central role. The typical sequence of events is a growth phase (dayside loading dominates) (McPherron, 1970), followed by the onset of a rapid expansion phase coinciding with the initiation of intense tail reconnection. In a typical "isolated" substorm, the magnetosphere transitions into a so-called recovery phase, characterized by the return to a quiet geomagnetic level (Ohtani and Gjerloev, 2020). However, if the IMF remain southward, the system may transition into a situation where the nightside and dayside merging rates are approximately balanced, marking the onset of a *Steady Magnetospheric Convection* (SMC) period (Sergeev et al., 1996). Milan et al. (2021) did a manual classification of the convection state of the magnetosphere system during the year 2010. He referred to the SMC intervals as a *driven* phase, and found it to occur during 18% of the time, in contrast to the traditional substorm phases occurring 23% of the time during that year. Hence, it seems likely that a significant amount of the magnetic flux throughput may

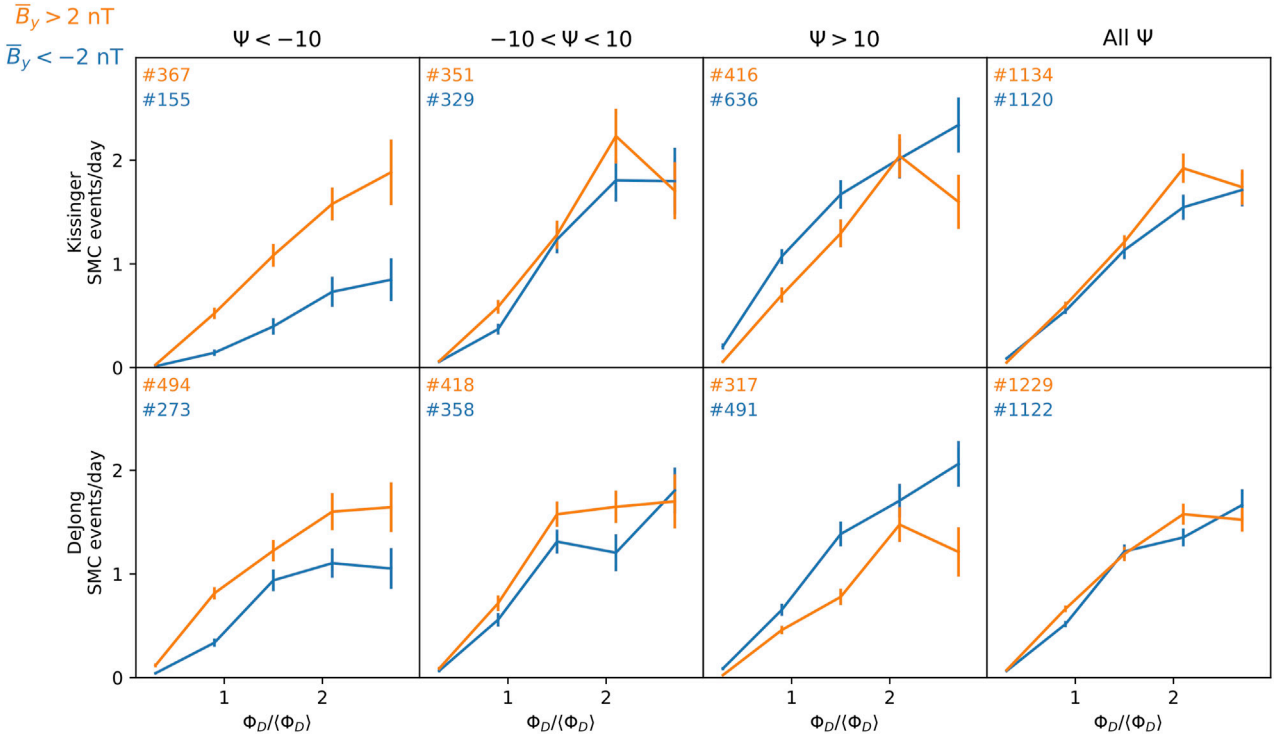

FIGURE 1
Average occurrence rates of SMC intervals (number per day on y-axis) versus increasing levels of dayside reconnection rate. Top row: SMC list described by Kissinger et al. (2012). Bottom row: SMC list described by Dejong (2014). An explicit B_y dependence in the SMC occurence rates are seen in both lists: Opposite B_y/tilt polarity also lead to more frequent SMC intervals.

take place during periods of SMC. Similar to looking at the occurrence rate and strength of substorms, it is thus relevant to look at how the combination of IMF B_y and dipole tilt affect the occurrence of SMC events, as they also represent information about the external forcing and how the magnetosphere responds to the forcing.

To investigate how the occurrence frequency of SMC events are modulated by IMF B_y and dipole tilt conditions, we use two different lists of identified SMC intervals. The *Kissinger* list contain 3444 SMC intervals with a minimum duration of 90 min, from the time period 1997–2013. The list is described in (Kissinger et al., 2011, 2012) and has been compiled by a combination of selection criteria based on the Auroral Electrojet index and manual inspection, and made publicly available recently (Kissinger et al., 2022). We also make use of the SMC list described by Dejong (2014) that goes from 1997 to 2015. Their list requires steadiness in the AL-index of at least 3 h and uses a seasonal cutoff in activity in AE-index as described in McWilliams et al. (2008). We use an extended version of the list described, where the extended part (2008–2015) only differ from their published list by not having applied the manual inspection of possible particle injection signatures at geosynchronous orbit (such events was removed in the published list). Common for both SMC lists is that steadiness in magnetospheric activity is the core selection criteria, which is quantified by how rapid the AL index is allowed to change in a sliding window [20 min in Dejong (2014) and 30 min in Kissinger et al. (2011)]. We group the SMC events into two groups based on the mean IMF B_y in the hour preceding each event ($B_y < -2$ nT and $B_y > 2$ nT). The main reason for considering the hour proceeding the event is that we are interested in whether our selection parameters may influence the initiation of the SMC. We further associate each SMC interval with the rate of dayside reconnection during the hour preceding the SMC onset using the Φ_D parameter normalized to the mean of all the 60 min Φ_D values during the entire time period of each list, referred to as $\langle\Phi_D\rangle$.

In Figure 1, the number of SMC events within the indicated Ψ (different columns) and $\Phi_D/\langle\Phi_D\rangle$ intervals (x-axis) are normalized to the amount of time the selection conditions was fulfilled in the period of the SMC lists. If one group (shown as a data point in Figure 1) has in total 100 SMC events, and the conditions of that specific group is met for a cumulative total of 100 days during the span of the list, the occurrence frequency will be one per day. This represent our measure of SMC events per day (y-axis), which is computed separately for the positive (orange) and negative (blue) IMF B_y

conditions. The number of SMC events in each group is indicated with its respective color in each panel. Similar to Ohma et al. (2021), the uncertainty is estimated by re-sampling with replacement (bootstrapping), leading to a distribution of SMC events per day that is normal, from which its ± 1 standard deviation is interpreted as the uncertainty in Figure 1.

Similar to the occurrence rates of substorms (Ohma et al., 2021), the SMC occurrences in Figure 1 exhibit a so-called explicit B_y-dependence. Namely, for a given orientation of the dipole tilt, Ψ, SMC intervals take place more frequently when Ψ and IMF B_y have opposite signs compared to when they have the same sign. This is consistently seen for both SMC lists investigated. In the Kissinger list, the explicit B_y effect is more pronounced during negative dipole tilt. The total number of SMC events (irrespective if IMF B_y) in the Kissinger list is also higher for positive than negative dipole tilt. This difference is likely related to the seasonal cut off criteria McWilliams et al. (2008) used only in the DeJong list, that aims to compensate for the elevated AL levels during the more sunlit conditions. This may explain why the IMF B_y polarity difference in DeJong's list is approximately as strong during positive and negative dipole tilts. Nevertheless, the IMF B_y polarity difference remain in both lists.

2.2 Substorm strength: Mid-latitude positive bay index

The strength of substorms can be routinely quantified from their ground-based magnetic signatures. In NH, substorms produce southward perturbations (negative bays) on the ground in high latitudes and northward perturbations (positive bays) in mid-latitudes. Ohma et al. (2021) showed that substorms identified from high-latitude negative bays have a more pronounced magnetic response (producing stronger *AL*/*SML* index in the NH) when the signs of the dipole tilt and IMF B_y are opposite. However, similar to Holappa and Mursula (2018), they found that this explicit B_y-dependence is very weak in the summer hemisphere, indicating that local ionospheric conditions strongly modulate the ground disturbances of substorms at high latitudes. Hence, addressing the strength of a substorm in a global sense (i.e., in terms of magnetic flux closure in the tail) is a very challenging task. As pointed out by Ohma et al. (2021), the local ionospheric conditions are much influenced by the degree of sunlight, and the geometry of the ionospheric current systems depend strongly on IMF B_y, in opposite sense in the two hemispheres. Hence, Ohma et al. (2021) suggested that a metric not associated with such local high latitude phenomenon should be used in assessing the global strength of substorms across various magnitude and polarities of dipole tilt and IMF B_y. Ideally, such a substorm strength metric should be based on observations distributed equally between the two hemispheres. Although Ohma et al. (2021) did not find a statistical significant difference in substorm strength for the different combinations of IMF B_y and dipole tilt, we will show how choices made in the statistical analysis may alter their conclusions.

We here repeat the analysis of substorm strength for different dipole tilt and IMF B_y polarities, as shown in Figure 7 in Ohma et al. (2021). Similar to Ohma et al. (2021), we focus on substorms identified with an algorithm applied to the Mid-latitude Positive Bay (MPB) index developed by Chu et al. (2015) to assess the substorm strength, for the above mentioned reasons. This list includes 57,558 substorms observed in 1982–2012. The list contains the onset times as well as the peak values and area (time-integral of the squared perturbation) of the identified MPB pulses, quantifying the strength of the events. An advantage of the McPherron and Chu list over widely used substorm lists based on the *SML* index (Newell and Gjerloev, 2011) (using only NH measurements) is that it uses magnetometers observations from both hemispheres, and from mid-latitudes only ($20^\circ <$ | magnetic latitude| $< 52^\circ$), potentially reducing the hemispheric bias. However, due to inherent geographical limitations, there are sill more stations in NH than SH. The MPB signature is interpreted as a direct signature of the Birkeland currents associated with the substorm (Chu et al., 2015). This is different from magnetic perturbations observed at high latitudes, that are blind to Birkeland and Pedersen currents, i.e., the curl-free component of the 3D ionospheric current system [Fukushima theorem, see e.g., Fukushima (1994)].

Figure 2 shows the median MPB area for negative ($< -10^\circ$) and positive ($> 10^\circ$) dipole tilts (Ψ) as a function $\Phi_D/\langle\Phi_D\rangle$ averaged over 6 h prior the substorm onset. The 6 h window is chosen to allow the magnetosphere system to adjust to the upstream forcing. In this way, any potential B_y-dependence in the upstream forcing (from a type A mechanism) is expected to be exaggerated. The choice of averaging window is also discussed more in detail in the next subsection. The error bars indicate ± one-sigma errors of the median derived by bootstrap resampling (with replacement) applied 1,000 times. The MPB area is clearly greater for $B_y >$ 2 nT during negative dipole tilt and for $B_y < -$ 2 nT during positive dipole tilt. Interestingly, the explicit B_y-dependence is about equally strong during negative tilt (NH winter) than during positive tilt (NH summer). We also find very similar results (not shown) for the peak MPB amplitude also given in the McPherron and Chu list. Thus, we interpret the results in Figure 2 as an effect of IMF B_y modulating the global substorm strength during both local summer and winter conditions.

The explicit B_y-dependence in Figure 2 is clearer than in the similar analysis of Ohma et al. (2021), which is due to three differences between the analyses. First, the present analysis sorts data by Φ_D instead of the clock angle. Second, instead of the mean we are using the median of the MPB strength, making the analysis less prone to extremes of the distribution. Third, using a long (6-h) averaging window will more efficiently average out noise in the relation between coupling function Φ_D and the response.

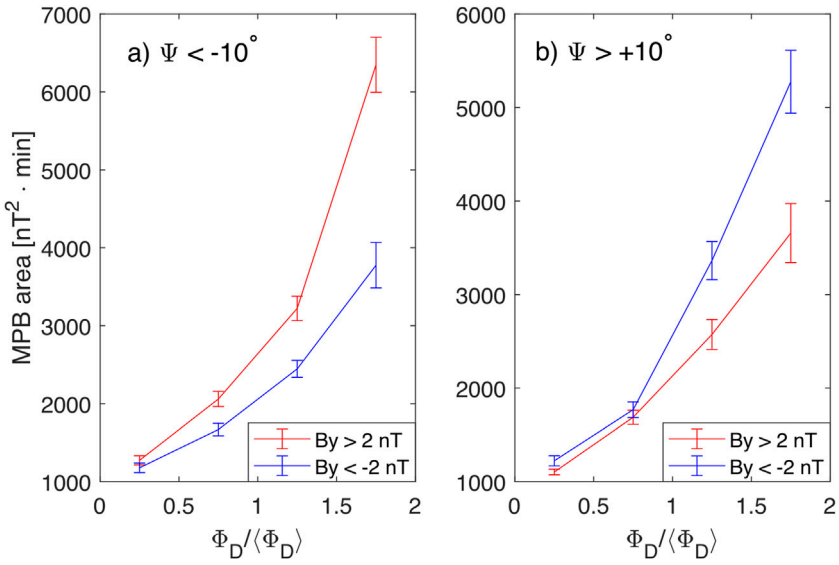

FIGURE 2
The MPB pulse area as a function of the normalized Φ_D parameter separately for $B_y > 2$ nT and $B_y < -2$ nT.The error bars indicate ± one standard deviation of the median. Left: Negative dipole tilt. Right: Positive dipole tilt.

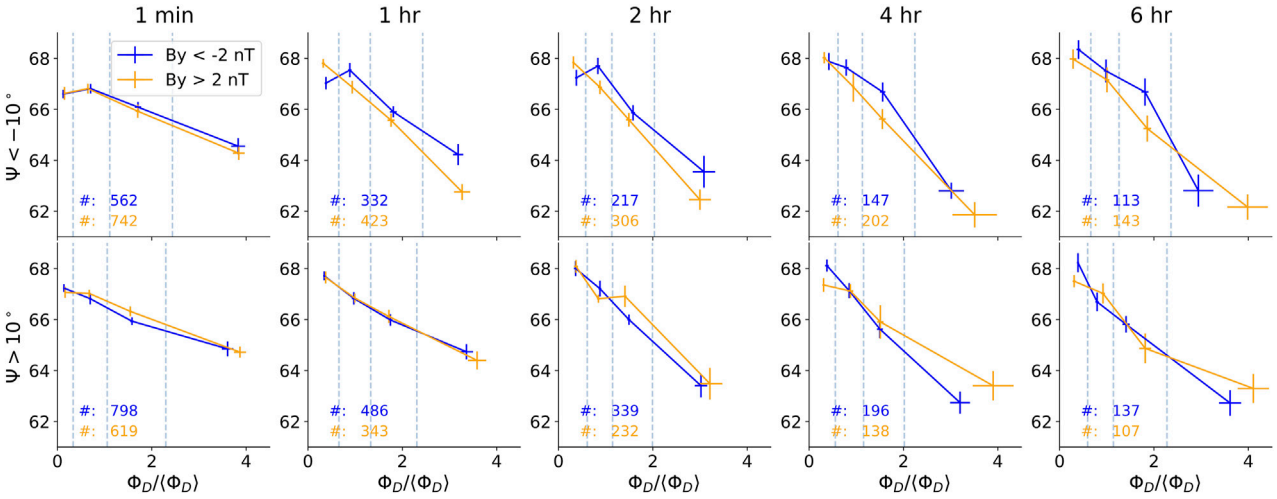

FIGURE 3
Median onset latitude from IMAGE + Polar onset lists. Top row: Negative dipole tilt. Bottom row: Positive dipole tilt. The two lines indicate different IMF B_y regimes. Columns represent size of averaging window applied to IMF B_y and Φ_D parameter. Φ_D bins are indicated with vertical dashed lines. Total number of substorms in each IMF B_y group satisfying the IMF stability criteria is also printed in each panel.

2.3 Substorm strength: Onset latitude

The substorm onset latitude is a direct measure of the size of the open magnetosphere at time of onset, which has a dependence on the degree of dayside loading during the time before the substorm [e.g., Milan et al. (2008)]. Figure 3 shows the median substorm onset latitude, as determined from the lists of substorm onsets from global Far Ultraviolet imaging presented by Frey et al. (2004) and Liou (2010). This combined list contain substorms from both hemispheres (71% from NH) from which

the onset latitude most often can be placed with confidence within ± 1°. Common for both the Frey et al. (2004) and Liou (2010) substorm lists is that the substorm onset is identified as a sudden localized auroral brightening in the nightside oval, experiencing a poleward and zonal expansion. The binning into positive (orange) and negative (blue) IMF B_y substorms are done similarly as described above. The bins of the normalized dayside coupling parameter $\Phi_D/\langle\Phi_D\rangle$ is determined such that each of the four bins contain the same number of substorms. These bins are indicated with the vertical dashed lines. The median value of the onset latitude (y-axis) and the normalized loading parameter (x-axis) with its associated ± one-sigma bootstrap error are indicated with crosses. The size of the averaging window used to compute IMF B_y and $\Phi_D/\langle\Phi_D\rangle$ prior to binning is varied. From left, the columns in Figure 3 represent window sizes of 1 min (no averaging), 1 hr, 2 hr, 4 hr, and 6 hr. To further constrain the IMF B_y polarity within the averaging window used, we require the circular variance of the IMF clock angle (the angle of the IMF vector projected in the GSM YZ plane) to be < 0.1 based on minute resolution data. In this way, the positive and negative IMF B_y intervals (defined by the mean IMF B_y > 2 nT or < -2 nT during the averaging window) are clearly separated. Due to the constraint on the circular variance of the IMF clock angle, fewer substorms meet the criteria for larger window sizes.

We clearly observe the median onset latitude to have greater dependence on Φ_D for larger window sizes, as expected. On the other hand, we observe no clear explicit B_y dependence on the onset latitude. For window sizes of two or more hrs, Figure 3 may indicate a trend toward lower latitude onsets when IMF B_y and Ψ has opposite signs during the two highest Φ_D intervals, but the difference is not significant. Hence, from the presented evidence, we must conclude that the net effect on onset latitude by the sign of IMF B_y must be small, if any, during times of significant dipole tilt. On the other hand, this means that we also can conclude that there is no evidence suggesting that the more frequent substorms for one IMF B_y polarity are associated with higher latitude onsets, which could be an indication of weaker substorms. These results, together with the MPB analysis of substorm strength, are further discussed in section 3.

2.4 Interplanetary magnetic field B_y dependence of isotropic boundary

The proton isotropic boundary marks the equatorward boundary of proton precipitation. The isotropic boundary (IB) is assumed to be located on a field line on which the radius of curvature is comparable to the proton gyroradius (Sergeev et al., 1993). Poleward of the IB latitude the proton loss cone is efficiently filled by pitch-angle scattering, whereas protons are mainly trapped equatorward of the IB latitude (Newell et al., 1998). The IB latitude can be routinely monitored using the Polar Operational Environmental Satellites (POES) measurements of energetic protons made with the The Medium Energy Proton and Electron Detector (MEPED) instruments. Asikainen et al. (2010) used corrected and calibrated MEPED proton measurements of 80–250 keV energy to determine the isotropic boundary latitude. Instead of 80–250 keV energy we use here proton fluxes between 120 and 250 keV, which have been obtained by interpolating the MEPED measurements at the nominal energy channels. Asikainen and Mursula (2011) showed that as the MEPED proton instruments degrade in time the effective energies they measure increase. They also showed that the lowest proton energy channel could not be reliably corrected if the degradation has been large enough. Asikainen et al. (2012) showed that the lowest energy one can use to get a homogeneous series of proton fluxes from 1979 to present is 120 keV. Therefore, we here use the proton measurements between 120 and 250 keV to determine the isotropic boundary. The IB latitude on each orbit is found by the most equatorward corrected geomagnetic latitude where the fluxes of the two orthogonal MEPED telescopes (I_0 and I_{90}) fulfill the condition

$$\frac{|I_0 - I_{90}|}{I_0 + I_{90}} < 0.3 \tag{2}$$

In addition to this the determined L-value of the IB location must be > 2.5 and the count rates of the telescopes must exceed 500 cts/(cm^2 sr s). As shown by Asikainen et al. (2010) the IB latitudes display a systematic MLT dependence. We followed their approach to estimate and subtract the MLT dependence from the IB latitudes. This procedure yields the so called MT index (magnetotail index) separately for both hemispheres. Because the MT indices (IB latitude identifications) are irregularly sampled in time we calculated the hourly averages from all those MT index values, which are located within the hour. In the following, our mentions of IB latitude is in fact referring to this MLT-normalized version, the MT index. We also restrict our analysis to the 18–06 MLT nightside region.

As shown by Meurant et al. (2007), the IB latitude at substorm onset is very similar to the onset latitude. As pointed out by Newell et al. (2007), the IB latitude has its best correlation with solar wind driving when averaging over the previous 6 h. Hence, the IB latitude represents a diagnostic tool of the state of the inner magnetosphere, which depends on the magnitude of dayside loading from at least the previous 6 h. The main advantage of considering the IB latitude for our purposes, in contrast to the onset latitude, is that we do not have to restrict ourselves to the onset of a substorm to get a datapoint indicating the extent of the stretched magnetosphere. The full POES database of high latitude crossings can thus be utilized for this purpose, similar as what was done by Holappa et al. (2021a).

Figure 4 shows the median IB latitude for positive (red) and negative (blue) IMF B_y conditions. Similar to the previous figures, the observations are also binned according to the normalized dayside coupling value (x-axis) over 6 h preceding the measurement. The analysis is shown from both hemispheres (northern hemisphere in

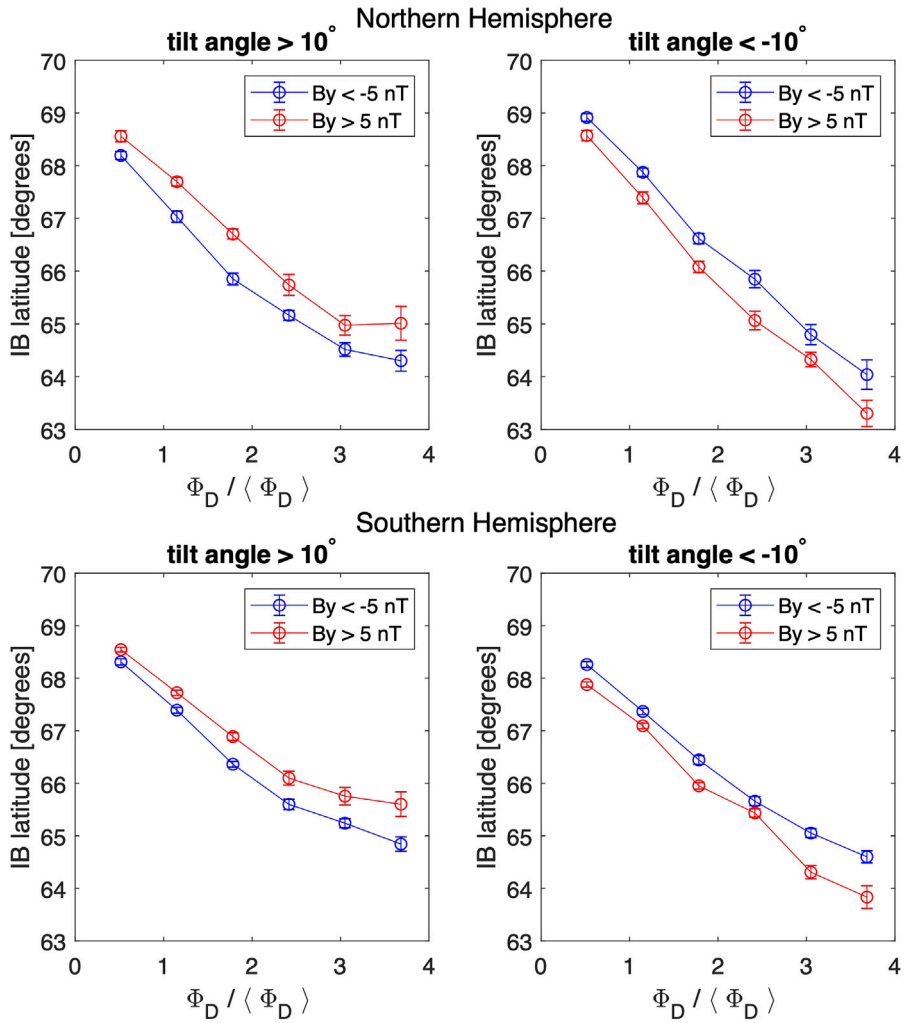

FIGURE 4
Median IB latitude determined from NOAA15-19 satellites in the nightside (18–6 MLT) as a function of the normalized Φ_D parameter separately for $B_y > 5$ nT and $B_y < -5$ nT. The error bars indicate ± one standard deviation of the median.

top row, south in bottom row) during positive and negative dipole tilt intervals. Note that the same tilt interval represents opposite local season in the two hemispheres. It is evident from Figure 4 that the explicit B_y effect on IB latitude is a pronounced and significant feature. The latitudinal difference between the two IMF B_y polarities are on the order of 1° latitude, similar to what was reported by Reistad et al. (2020) using the field-aligned current estimates of the size of the auroral oval from AMPERE.

3 Discussion

In recent years, a growing body of evidence (see introduction) has demonstrated how various aspects of the solar wind—magnetosphere—ionosphere interactions depend on the combination of the polarities of IMF B_y and dipole tilt, often referred to as an *explicit B_y effect*. That is, for a given, nonzero tilt angle Ψ, the system responds differently to positive and negative IMF B_y. In this paper we provide further observational evidence of this effect, aiming to provide observational constraints on the source of the explicit B_y behaviour of the system. Two types of mechanisms have been suggested to explain the explicit B_y effect:

A) The combination of the polarity of IMF B_y and dipole tilt affects the global dayside reconnection rate, with higher flux throughput when the two has opposite polarity compared to equal polarity.
B) The combination of the polarity of IMF B_y and dipole tilt influence the amount of magnetic flux the magnetotail lobes

typically support, for a given dayside reconnection rate. The magnetosphere thus responds differently to similar magnetic flux throughput.

Observations consistent with a type B mechanism have been reported on earlier (Holappa et al., 2021a). However, can this type of process, confined to the magnetotail, be the sole explanation for the presented observations? This is the core question we address in this article. Evidence on the existence of a type A mechanism has not been presented to date (to our knowledge). There is an ongoing debate whether the dipole tilt angle modulates the dayside reconnection rate (Cliver et al., 2000; Russell et al., 2003; Lockwood et al., 2020). However, these studies have not addressed the combined action of the dipole tilt and IMF By (which are both included in the type A mechanism). Previous studies focusing on the *explicit B_y effect* have not been able to make definite conclusions about the relative importance of A versus B type of mechanisms. However, a critical test for the above hypotheses is to determine whether or not the magnetic flux throughput of the system (the strength of the Dungey cycle) is stronger for the opposite signs of Ψ and IMF B_y. This is predicted by mechanism A, but not by mechanism B. By combining the results presented in this study with earlier observations, we can now address how the flux throughput is modulated by IMF B_y and Ψ.

Milan et al. (2008) investigated how the magnetosphere responds to weak and strong solar wind forcing, and showed that enhanced magnetic flux input (Φ_D) lead to both stronger and more frequent substorms. It has also been shown that the substorm occurrence frequency is higher when IMF B_y and Ψ have opposite compared to equal polarity (Ohma et al., 2021). The global substorm strength shown in Figure 2 demonstrates that the strength of substorms is also greater, therefore closing more magnetic flux per substorm (Milan et al., 2009), on average, when signs of IMF B_y and tilt angle are opposite compared to equal. Taken together, these results strongly suggests that the IMF B_y/Ψ polarity combination affect the magnetic flux throughput, hence supporting a type A mechanism.

The IB latitude analysis presented in Figure 4, which can be interpreted as the transition region from dipolar to stretched field lines, is systematically displaced based on IMF B_y and dipole tilt polarity, highlighting the profound influence by these parameters. This region of the magnetotail is known to depend upon the previous magnetospheric activity (and hence solar wind - magnetosphere coupling) with a significant memory. Newell et al. (2007) found the IB latitude to show the best correlation with a 6 h long averaging window of the upstream forcing. It is therefore highly expected that a type A mechanism would lead to the observed differences in Figure 4. The observed shift in IB latitude is remarkably similar to the corresponding shift in polar cap radius during similar conditions, as reported by Reistad et al. (2020). However, as Reistad et al. (2020) pointed out, we can not exclude a type B mechanism influencing these results, when interpreting this analysis alone. However, when interpreting these results in light of our findings regarding the substorm strength as discussed above, the we find that a type A mechanism is the most plausible scenario to explain also the IMF B_y polarity effect on IB latitude.

Interpreting the onset latitude as a metric of the strength of the substorm in terms of flux closure (Milan et al., 2009), the similar onset latitude for ± B_y (Figure 3) combined with their more frequent occurrence (Ohma et al., 2021) suggests a larger flux throughput when IMF B_y and Ψ has opposite polarity, in agreement with a type A mechanism. We find no direct evidence that the substorm onset shifts to higher latitudes for opposite IMF B_y and tilt polarity compared to same polarity, as would be indicative of a type B mechanism (the more frequent substorms closing less flux each, hence taking place at a higher latitude [e.g., Milan et al. (2009)] to accommodate the same flux throughput). This analysis is therefore consistent with the conclusions above, namely that a type A mechanism is likely to exist during these conditions. One may argue that if the global dayside reconnection rate is affected (type A mechanism) as suggested, a lower onset latitude would be expected for opposite B_y and Ψ polarity, contrary to what we see (the weak trend in the suggested direction is below the level of statistical significance). One possibility is that both a type A and B mechanism may be present, since their influence on onset latitude is expected to be opposite. If so, the presence of a type B mechanism indicates inherent limitations of addressing the strength of a substorm only through its onset latitude. Nevertheless, our main conclusion remains, namely, that a type B mechanism alone can not explain the results, and that the global dayside reconnection rate has an explicit B_y dependence during periods of significant dipole tilt.

As mentioned in the introduction, more frequent SMC intervals during the IMF B_y/tilt polarity associated with more frequent substorms would be indicative of a type A mechanism. This is indeed what we see in Figure 1. It is nevertheless relevant to mention the study by Milan et al. (2019) in this regard, showing that the substorm onset latitude is an important parameter in determining whether the magnetotail develop into a period of SMC if the IMF remains southward after a substorm. They found that substorms taking place in an extended oval (below 65° MLAT) was less likely to develop into an SMC interval, and suggested this was due to the atmosphere invoking friction on the ionosphere-magnetosphere system, since lower latitude substorms are typically stronger. From Figure 2 we have seen that the more frequent substorms observed for opposite B_y/tilt polarity (Ohma et al., 2021) are associated with stronger substorms. The fact that we also observe more frequent SMC intervals when IMF B_y and the dipole tilt have opposite signs suggests that the effect reported on by Milan et al. (2019) is less relevant for the more typical substorms considered here. In fact, the quartile binning used in Figure 3 shows that three of four bins (75% of the onsets) have a median onset latitude above 65°, which was the limit for "convection breaking" used by Milan et al. (2019).

For opposite compared to equal polarity of IMF B_y and tilt angle, observations show stronger substorms, more frequent substorms and

more frequent SMCs. Furthermore, the average IB latitude and polar cap radius indicate a larger oval, which means that the average flux content is also greater for opposite IMF B_y and Ψ. In addition, Reistad et al. (2021) found 10% stronger flux throughput during the same conditions. Taken together, we conclude that the body of evidence presented is pointing towards mechanism A being the main source of the observed explicit B_y behaviour of the system. However, we can not exclude that a type B mechanism take place at the same time, but taken alone, a type B mechanism is insufficient to explain the observed behavior.

The results from this paper suggests that an explicit B_y effect should be included in future global dayside reconnection rate coupling functions, which is expected to enhance the predictive abilities of geospace activity. When taking this contribution into account, it would likely be easier to make further constraints on the importance of mechanism B type of processes.

Although we suggest that an explicit B_y effect is present on the global dayside reconnection rate, we have at present no good understanding of why. As suggested earlier by Reistad et al. (2020) and Ohma et al. (2021), the many dawn-dusk asymmetries upstream of the magnetopause (Walsh et al., 2014) may introduce dawn-dusk asymmetries in the local dayside reconnection rate. How this combine with a tilted dipole will be a very interesting topic to explore with 3D global kinetic models such as the Vlasiator model (Palmroth et al., 2018).

4 Conclusion

Based on the new analysis presented in section 2, together with recent advances in describing the geospace response during these conditions (Holappa and Mursula, 2018; Holappa et al., 2020; Reistad et al., 2020; Holappa et al., 2021b; Ohma et al., 2021), we conclude that the global dayside reconnection rate is likely to be enhanced when IMF B_y and the dipole tilt have opposite signs (± and −/+), compared to when they have the same signs (−/− and +/+). This is referred to as a type A mechanism. We have also discussed the possible contribution from a type B mechanism, where the magnetotail response may depend on IMF B_y and the dipole tilt, affecting the amount of magnetic flux the magnetotail lobes typically can support. While we can not neglect that a type B mechanism has a significant contribution to the observed response, we find it insufficient to explain our analysis alone, pointing toward the existence of a type A mechanism taking place at the dayside of the magnetosphere. The detailed physical mechanism of such an effect should be further investigated.

Data availability statement

We acknowledge the use of NASA/GSFC Space Physics Data Facility http://omniweb.gsfc.nasa.gov for OMNI data. The Kissinger SMC list is available at https://doi.org/10.5281/zenodo.6147689. The DeJong SMC list is published along with its description in Dejong (2014). The FUV substorm lists can be downloaded from https://supermag.jhuapl.edu/substorms/. The MPB substorm list is available from their publication McPherron and chu (2018). The dipole tilt angle is computed based on the International Geomagnetic Reference Field dipole coefficients using the klaundal/dipole library, available on GitHub. All the original POES/MEPED energetic particle data used here are archived in the NOAA/NGDC dataserver http://www.ngdc.noaa.gov/stp/satellite/poes/index.html.

Author contributions

This paper is a result of a team effort emerging from a breakout group initiated during the initial workshop of the Center for Unified Studies of Interhemispheric Asymmetries (CUSIA). JR did the substorm onset latitude data analysis, organized regular online meetings, and was the lead writer of the manuscript. LH did the MPB and IB latitude data analysis, AO did the SMC data analysis, and both played an active role in shaping the manuscrupt and discussion throughout the entire processs. CG and DS also actively participated in the discussions shaping the paper throughout the entire process, in addition to participating in the writing process. TA has been involved in consulting the IB latitude analysis, as well as writing relevant parts of that section, and providing comments on the manuscript. AD was consulted in the SMC analysis, assisted writing the respective section, and commented on the manuscript.

Funding

JR were funded by the Norwegian Research Council (NRC) through grant 300844/F50. LH was funded by the Academy of Finland postdoctoral project 322459. AO were funded by the Norwegian Research Council (NRC) through grant 223252/F50. DS was supported by NASA LWS 80NSSC17K0718. TA was supported by the Academy of Finland (PROSPECT project 24303278). This work was also supported by the Center for the Unified Study of Interhemispheric Asymmetries (CUSIA), NASA Award 80NSSC20K0606.

Acknowledgments

We thank the Centre for Unified Studies on Interhemispheric Asymmetries for hosting interesting discussions and meeting venues where the collaboration for this work was initiated. We also thank all data vendors

across the community contributing to the higher level data products we use, see data availability statement.

Conflict of interest

The authors declare that the research was conducted in the absence of any commercial or financial relationships that could be construed as a potential conflict of interest.

Publisher's note

References

Asikainen, T., Maliniemi, V., and Mursula, K. (2010). Modeling the contributions of ring, tail, and magnetopause currents to the corrected *Dst* index. *J. Geophys. Res.* 115, A12203. doi:10.1029/2010JA015774

Asikainen, T., and Mursula, K. (2011). *J. Atmos. Sol. Terr. Phys.* 73, 335–347. doi:10.1016/j.jastp.2009.12.011

Asikainen, T., Mursula, K., and Maliniemi, V. (2012). Correction of detector noise and recalibration of noaa/meped energetic proton fluxes. *J. Geophys. Res.* 117. doi:10.1029/2012ja017593

Chu, X., McPherron, R. L., Hsu, T. S., and Angelopoulos, V. (2015). Solar cycle dependence of substorm occurrence and duration: Implications for onset. *JGR. Space Phys.* 120, 2808–2818. doi:10.1002/2015JA021104

Cliver, E., Kamide, Y., and Ling, A. (2000). Mountains versus valleys: Semiannual variation of geomagnetic activity. *J. Geophys. Res.* 105, 2413–2424. doi:10.1029/1999ja900439

Dejong, A. D. (2014). Steady magnetospheric convection events: How much does steadiness matter? *J. Geophys. Res. Space Phys.* 119, 4389–4399. doi:10.1002/2013JA019220

Frey, H. U., Mende, S. B., Angelopoulos, V., and Donovan, E. F. (2004). Substorm onset observations by image-fuv. *J. Geophys. Res.* 109, A10304. doi:10.1029/2004JA010607

Friis-Christensen, E., and Wilhjelm, J. (1975). Polar cap currents for different directions of the interplanetary magnetic field in the y-z plane. *J. Geophys. Res.* 80, 1248–1260. doi:10.1029/JA080i010p01248

Fukushima, N. (1994). Some topics and historical episodes in geomagnetism and aeronomy. *J. Geophys. Res.* 99, 19113–19142. doi:10.1029/94ja00102

Holappa, L., Asikainen, T., and Mursula, K. (2020). Explicit IMF dependence in geomagnetic activity: Modulation of precipitating electrons. *Geophys. Res. Lett.* 47, 1–7. doi:10.1029/2019gl086676

Holappa, L., and Buzulukova, N. (2022). Explicit IMF By-dependence of energetic protons and the ring current. *Geophys. Res. Lett.* 49, e2022GL098031. doi:10.1029/2022GL098031

Holappa, L., and Mursula, K. (2018). Explicit IMF B_y dependence in high-latitude geomagnetic activity. *J. Geophys. Res. Space Phys.* 4728, 4728–4740. doi:10.1029/2018JA025517

Holappa, L., Reistad, J. P., Ohma, A., Gabrielse, C., and Sur, D. (2021a). The magnitude of IMF b_y-influences the magnetotail response to solar wind forcing. *JGR. Space Phys.* 126. doi:10.1029/2021JA029752

Holappa, L., Robinson, R., Pulkkinen, A., Asikainen, T., and Mursula, K. (2021b). Explicit IMF b_y-dependence in geomagnetic activity: Quantifying ionospheric electrodynamics. *JGR. Space Phys.* 126, e2021JA029202. doi:10.1029/2021ja029202

King, J. H., and Papitashvili, N. E. (2005). Solar wind spatial scales in and comparisons of hourly wind and ace plasma and magnetic field data. *J. Geophys. Res.* 110, A02104. doi:10.1029/2004JA010649

Kissinger, J., McPherron, R. L., Hsu, T.-S., and Angelopoulos, V. D. (2022). Dataset of steady magnetospheric convection events in earth's magnetosphere from 1997 to 2013. *Zenodo*. doi:10.5281/zenodo.6147689

Kissinger, J., McPherron, R. L., Hsu, T. S., and Angelopoulos, V. (2012). Diversion of plasma due to high pressure in the inner magnetosphere during steady magnetospheric convection. *J. Geophys. Res.* 117. doi:10.1029/2012JA017579

Kissinger, J., McPherron, R. L., Hsu, T. S., and Angelopoulos, V. (2011). Steady magnetospheric convection and stream interfaces: Relationship over a solar cycle. *J. Geophys. Res.* 116. doi:10.1029/2010JA015763

Laundal, K. M., Reistad, J. P., Hatch, S. M., Moretto, T., Ohma, A., Østgaard, N., et al. (2020). Time-scale dependence of solar wind-based regression models of ionospheric electrodynamics. *Sci. Rep.* 1, 16406. doi:10.1038/s41598-020-73532-z

Liou, K. (2010). Polar ultraviolet imager observation of auroral breakup. *J. Geophys. Res.* 115, 1–7. doi:10.1029/2010JA015578

Lockwood, M., Owens, M. J., Barnard, L. A., Watt, C. E., Scott, C. J., Coxon, J. C., et al. (2020). Semi-annual, annual and universal time variations in the magnetosphere and in geomagnetic activity: 3. Modelling. *J. Space Weather Space Clim.* 10, 61. doi:10.1051/swsc/2020062

McPherron, R. L., and Chu, X. (2018). The midlatitude positive bay index and the statistics of substorm occurrence. *JGR. Space Phys.* 123, 2831–2850. doi:10.1002/2017ja024766

McPherron, R. L. (1970). Growth phase of magnetospheric substorms. *J. Geophys. Res.* 75, 5592–5599. doi:10.1029/ja075i028p05592

McWilliams, K. A., Pfeifer, J. B., and McPherron, R. L. (2008). Steady magnetospheric convection selection criteria: Implications of global superdarn convection measurements. *Geophys. Res. Lett.* 35, L09102. doi:10.1029/2008GL033671

Meurant, M., Gérard, J. C., Blockx, C., Spanswick, E., Donovan, E. F., Hubert, B., et al. (2007). El - a possible indicator to monitor the magnetic field stretching at global scale during substorm expansive phase: Statistical study. *J. Geophys. Res.* 112. doi:10.1029/2006ja012126

Milan, S. E., Boakes, P. D., and Hubert, B. (2008). Response of the expanding/contracting polar cap to weak and strong solar wind driving: Implications for substorm onset. *J. Geophys. Res.* 113, 1–11. doi:10.1029/2008JA013340

Milan, S. E., Carter, J. A., Sangha, H., Bower, G. E., and Anderson, B. J. (2021). Magnetospheric flux throughput in the dungey cycle: Identification of convection state during 2010. *J. Geophys. Res. Space Phys.* 126. doi:10.1029/2020JA028437

Milan, S. E., Gosling, J. S., and Hubert, B. (2012). Relationship between interplanetary parameters and the magnetopause reconnection rate quantified from observations of the expanding polar cap. *J. Geophys. Res.* 117, A03226. doi:10.1029/2011JA017082

Milan, S. E., Grocott, A., Forsyth, C., Imber, S. M., Boakes, P. D., and Hubert, B. (2009). A superposed epoch analysis of auroral evolution during substorm growth, onset and recovery: Open magnetic flux control of substorm intensity. *Ann. Geophys.* 27, 659–668. doi:10.5194/angeo-27-659-2009

Milan, S. E., Walach, M. T., Carter, J. A., Sangha, H., and Anderson, B. J. (2019). Substorm onset latitude and the steadiness of magnetospheric convection. *J. Geophys. Res. Space Phys.* 124, 1738–1752. doi:10.1029/2018JA025969

Newell, P. T., and Gjerloev, J. W. (2011). Substorm and magnetosphere characteristic scales inferred from the supermag auroral electrojet indices. *J. Geophys. Res.* 116, A12232. doi:10.1029/2011JA016936

Newell, P. T., Sergeev, V. A., Bikkuzina, G. R., and Wing, S. (1998). Characterizing the state of the magnetosphere: Testing the ion precipitation maxima latitude (b2i) and the ion isotropy boundary. *J. Geophys. Res.* 103, 4739–4745. doi:10.1029/97JA03622

Newell, P. T., Sotirelis, T., Liou, K., Meng, C.-I., and Rich, F. J. (2007). A nearly universal solar wind-magnetosphere coupling function inferred from 10 magnetospheric state variables. *J. Geophys. Res.* 112, 1–16. doi:10.1029/2006JA012015

Ohma, A., Reistad, J. P., and Hatch, S. M. (2021). Modulation of magnetospheric substorm frequency: Dipole tilt and IMF B_y effects. *JGR. Space Phys.* 126. doi:10.1029/2020JA028856

Ohtani, S., and Gjerloev, J. W. (2020). Is the substorm current wedge an ensemble of wedgelets?: Revisit to midlatitude positive bays. *JGR. Space Phys.* 125. doi:10.1029/2020JA027902

Palmroth, M., Ganse, U., Pfau-Kempf, Y., Battarbee, M., Turc, L., Brito, T., et al. (2018). Vlasov methods in space physics and astrophysics. *Living Rev. comput. Astrophys.* 4, 1. doi:10.1007/s41115-018-0003-2

Reistad, J. P., Laundal, K. M., Ohma, A., Moretto, T., and Milan, S. E. (2020). An explicit IMF B dependence on solar wind-magnetosphere coupling. *Geophys. Res. Lett.* 47. doi:10.1029/2019GL086062

Reistad, J. P., Laundal, K. M., Østgaard, N., Ohma, A., Burrell, A. G., Hatch, S. M., et al. (2021). Quantifying the lobe reconnection rate during dominant IMF B_y periods and different dipole tilt orientations. *JGR. Space Phys.* 126. doi:10.1029/2021JA029742

Russell, C. T., and McPherron, R. L. (1973). Semiannual variation of geomagnetic activity. *J. Geophys. Res.* 78, 92–108. doi:10.1029/JA078i001p00092

Russell, C., Wang, Y., and Raeder, J. (2003). Possible dipole tilt dependence of dayside magnetopause reconnection. *Geophys. Res. Lett.* 30. doi:10.1029/2003gl017725

Sergeev, V. A., Malkov, M., and Mursula, K. (1993). Testing the isotropic boundary algorithm method to evaluate the magnetic field configuration in the tail. *J. Geophys. Res.* 98, 7609–7620. doi:10.1029/92JA02587

Sergeev, V., Pellinen, R. J., and Pulkkinen, T. (1996). Steady magnetospheric convection: A review of recent results. *Space Sci. Rev.* 75, 551–604. doi:10.1007/bf00833344

Walsh, A. P., Haaland, S., Forsyth, C., Keesee, A. M., Kissinger, J., Li, K., et al. (2014). Dawn-dusk asymmetries in the coupled solar wind-magnetosphere-ionosphere system: A review. *Ann. Geophys.* 32, 705–737. doi:10.5194/angeo-32-705-2014

frontiers | Frontiers in Astronomy and Space Sciences

TYPE Original Research
PUBLISHED 20 September 2022
DOI 10.3389/fspas.2022.990789

OPEN ACCESS

EDITED BY
Georgios Balasis,
National Observatory of Athens, Greece

REVIEWED BY
Caitriona Jackman,
Dublin Institute for Advanced Studies (DIAS), Ireland
Brandon Burkholder,
University of Maryland, Baltimore County, United States
Mikhail Sitnov,
Johns Hopkins University, United States

*CORRESPONDENCE
Joseph E. Borovsky,
jborovsky@spacescience.org

SPECIALTY SECTION
This article was submitted to Space Physics,
a section of the journal
Frontiers in Astronomy and Space Sciences

RECEIVED 10 July 2022
ACCEPTED 31 August 2022
PUBLISHED 20 September 2022

CITATION
Borovsky JE (2022), Noise and solar-wind/magnetosphere coupling studies: Data.
Front. Astron. Space Sci. 9:990789.
doi: 10.3389/fspas.2022.990789

Noise and solar-wind/magnetosphere coupling studies: Data

Joseph E. Borovsky*

Center for Space Plasma Physics, Space Science Institute, Boulder, CO, United States

Using artificial data sets it was earlier demonstrated that noise in solar-wind variables alters the functional form of best-fit solar-wind driver functions (coupling functions) of geomagnetic activity. Using real solar-wind data that noise effect is further explored here with an aim at obtaining better best-fit formulas by removing noise in the real solar-wind data. Trends in the changes to best-fit solar-wind formulas are examined when Gaussian random noise is added to the solar-wind variables in a controlled fashion. Extrapolating those trends backward toward lower noise makes predictions for improved solar-wind driver formulas. Some of the error (noise) in solar-wind data comes from using distant L1 monitors for measuring the solar wind at Earth. An attempt is made to confirm the improvements in the solar-wind driver formulas by comparing results of best-fit formulas using L1 spacecraft measurements with best-fit formulas obtained from near-Earth spacecraft measurements from the IMP-8 spacecraft. However, testing this methodology fails owing to observed large variations in the best-fit-formula parameters from year-to-year and spacecraft-to-spacecraft, with these variations probably overwhelming the noise-correction variations. As an alternative to adding Gaussian random noise to the solar-wind variables, replacing a fraction of the values of the variables with other values was explored, yielding essentially the same noise trends as adding Gaussian noise.

KEYWORDS

magnetosphere, solar wind, geomagnetic activity, geomagnetic indices, solar wind magnetosphere coupling, space weather borovsky: noise solar-wind/magnetosphere coupling

1 Introduction

Correlative-type data studies comparing the behavior of the magnetosphere-ionosphere system to the behavior of the solar wind are performed 1) to determine the solar-wind variables that control magnetospheric activity and 2) to determine or confirm the physics of solar-wind/magnetosphere coupling. Often a goal is to find the most accurate solar-wind driver function (coupling function) to describe magnetospheric activity in terms of solar-wind parameters [e.g., Newell et al., 2007; 2008; Borovsky, 2014; McPherron et al., 2015; Lockwood and McWilliams, 2021]. There is hope that this best driver function describes the physics of solar-wind/magnetosphere coupling, but see the

discussion in Borovsky (2021). It is known that noise in the data reduces the quality of a fit of one data set to another data set (Spearman, 1904; Bock and Petersen, 1975; Liu, 1988; Hutcheon et al., 2010). This is true for the magnetospheric and solar-wind data sets (Sivadas and Sibeck, 2022). Using artificial data sets Borovsky (2022a) demonstrated that noise (error) in the solar-wind measurements can also change the functional form of best-fit solar-wind driver functions when fitting solar-wind data to geomagnetic indices. Note that Borovsky (2022a) found that adding noise to geomagnetic indices does not change the best-fit formula for the solar-wind driving of that index, the added noise just reduces the solar-wind/magnetosphere correlation coefficient.

We know that the real solar-wind data used for such coupling studies has noise (errors), mostly owed to the use of solar-wind monitors located far from the Earth at L1 (Sandahl et al., 1996; Ashour-Abdalla et al., 2008; Walsh et al., 2019; Burkholder et al., 2020; Borovsky, 2020a, 2022b; Lockwood, 2022; Sivadas and Sibeck, 2022). The basic error is incorrect values caused by the fact that the solar wind that hits an L1 monitor is typically not the solar wind that hits the Earth (Walsh et al., 2019; Burkholder et al., 2020; Borovsky, 2020a, 2022b). The error this causes is incorrect values, not propagation-time errors. If that measurement noise could be removed, more-valuable best-fit driver functions, in the sense that they may better describe the physics of coupling, could be obtained.

In this report the effects of noise in the real solar-wind data will be explored. Controlled noise will be added to the solar-wind data and the effect of that noise on best-fit solar-wind drivers will be analyzed. To explore the effects of noise, noise will be added to the solar-wind data in two simple, controlled fashions: 1) random values extracted from Gaussian distributions will b added to all values in the solar-wind time series or 2) a fraction of the time-series values will be completely replace with other values. Arguments extrapolating backward to remove noise in the solar-wind data will be made and data from the years in which the near-Earth solar-wind monitor IMP-8 operated will be explored.

2 Data sets

A commonly used solar-wind driver function that was obtained as a best fit to geomagnetic data is the "Newell function" $v_{sw}^{4/3}B_{\perp}^{2/3}\sin^{8/3}(\theta_{clock}/2)$ (Newell et al., 2007), where v_{sw} is the solar-wind speed, $B_{\perp}$ is the magnitude of the component of the solar-wind magnetic field that is perpendicular to the Sun-Earth line, and $\theta_{clock} = \text{Arccos}(B_z/(B_y^2+B_z^2)^{1/2})$ is the (GSM) clock angle of the solar-wind magnetic field relative to the Earth's magnetic dipole. Here we will form best-fit driver functions $D = v_{sw}^{a}B_{sw}^{b}\sin^{c}(\theta_{clock}/2)$ where the exponents a, b, and c are optimized so that D has the largest Pearson linear correlation coefficient with various time-lagged geomagnetic indices. For the solar-wind data 1-h averages in the OMNI2 data set (King and Papitashvili, 2005) for the years 1995–2018 are used. In making hourly averaged values of $\sin(\theta_{clock}/2)$, hourly averaged values of B_y and B_z from OMNI2 are used: Lockwood and McWilliams (2021) and Lockwood (2022) point out that creating high-time-resolution values of $\sin(\theta_{clock}/2)$ and then making an hourly average of those $\sin(\theta_{clock}/2)$ values (combine-then-average) would be a superior method. Statistically comparing the results of the two methods finds that the distribution of θ_{clock} values obtained have very similar mean values, but the calculate from high-resolution and then average yields a distribution with many fewer occurrences near 0° clock angle and many fewer occurrences near 180° clock angle. Thus for a given functional form of a driver function, the combine-then-average method yields far fewer cases of extremely weak driving and far fewer cases of extremely strong driving (as measured by the magnitude of the driver function) than does the calculating from averaged values of B_y and B_z (average-then-combine).

In the data analysis each of the three solar-wind variables v_{sw}, B_{sw}, and $\sin(\theta_{clock}/2)$ is "standardized" by first subtracting the mean value from every value and then by dividing every value by the standard deviation of the distribution of values. Each standardized solar-wind variable has a mean value of zero and a standard deviation of unity. Then Gaussian noise (Gaussianly distributed random numbers) is added to the standardized solar-wind variables in a number of ways: adding noise to only one solar-wind variable or adding noise to all three solar-wind variables. The amplitude of the noise is varied. When the amplitude of the noise is "1" the noise has the same standard deviation as the variable.

The years 1995–2018 are chosen for two reasons. First, we will be using at times the Hp60 index, which is only available since 1995. Hp60 is a 60-min-resolution version of the 3-hr-resolution Kp index, available at ftp://ftp.gfz-potsdam.de/pub/home/obs/Hpo. Second, as part of this project we want to compare the results from using solar-wind data at L1 with solar wind measurements closer to the Earth from the IMP-8 spacecraft (Feldman et al., 1978; Butler, 1980): the OMNI2 data beginning in 1995 is almost exclusively from L1 with the WIND spacecraft launched in 1995 and the ACE spacecraft launched in 1998.

The geomagnetic indices that will be used are the following, all at 1-h time resolution. The time lags given to each index comes from optimal lags found in prior solar-wind-coupling studies. The auroral-electrojet indices AE, AL, and AU (and their SuperMag equivalents SME, SML, and SMU) measure the peak intensity of high-latitude ionospheric current in the auroral electrojet: they are considered to be an indicator of the intensity of auroral activity (Goertz et al., 1993) and total Joule dissipation in the ionosphere (Baumjohann, 1986). They are utilized with a 1-h time lag from the OMNI solar wind data. The polar-cap index PC is a measure of the intensity of

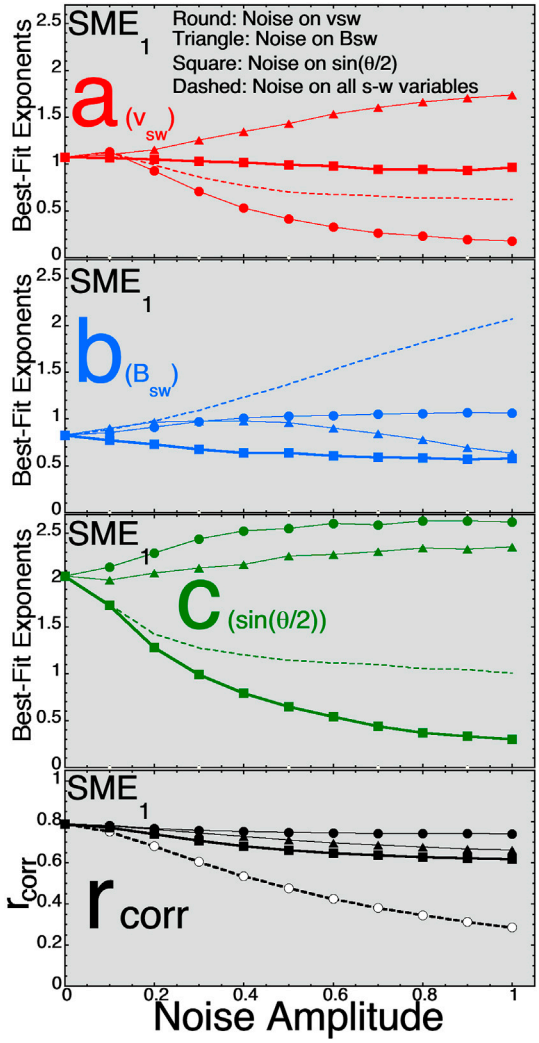

FIGURE 1
For best fits to the 1-hr-lagged SME_1 index the three exponents **(A)** (red, top panel), **(B)** (blue, second panel), and **(C)** (green, third panel) are plotted as functions of the amplitude of the Gaussian noise added to the three solar-wind variables. In the bottom panel the Pearson linear correlation coefficient between $D = v_{sw}{}^a B_{sw}{}^b \sin^c(\theta_{clock}/2)$ and SME_1 is plotted as a function of the amplitude of the added noise.

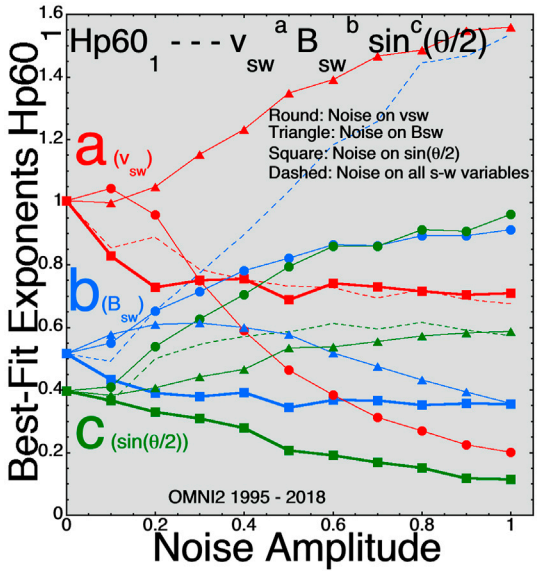

FIGURE 2
For best fits to the 1-hr-lagged $Hp60_1$ index the three exponents **(A)** (red), **(B)** (blue), and **(C)** (green) are plotted as functions of the amplitude of the Gaussian noise added to the three solar-wind variables.

ionospheric current flowing across the northern polar cap: it is related to the intensity of polar-cap anti-Sunward convection (Stauning, 2013) and the cross-polar-cap potential (Ridley and Kihn, 2004). It is utilized with a 0-h time lag from the OMNI solar wind data. The Kp, Hp60, and Ap60 indices measure the strength of mid-latitude ionospheric currents around the Earth: they are a measure of the strength of magnetospheric convection (Thomsen, 2004). They are utilized with a 1-h time lag from the OMNI solar wind data. The Dst current measures an equatorial magnetic-field perturbation: that perturbation is related to the plasma pressure in the dipolar portions of the magnetosphere (Dessler and Parker, 1959; Sckopke, 1966; Liemohn et al., 2001), but it is also perturbed by the Chapman-Ferraro current at the dayside magnetosphere (Su and Konradi, 1975; Siscoe et al., 2005) and by the cross-tail current in the magnetotail (Ohtani et al., 2001; Borovsky and Denton, 2010). It is utilized with a 2-h time lag from the OMNI solar wind data.

3 The data studies

In Figure 1 the 1-hr-lagged (from the solar wind) SuperMAG auroral electrojet index SME_1 is studied. SME measures high-latitude auroral-zone ionospheric currents using 80-or-more ground-based magnetometers [the SuperMAG network (Bergin et al., 2020)], wheras the older AE index makes the same measurement using ~12 magnetometers. In the top three panels the values of the three exponents a, b, and c of $D = v_{sw}{}^a B_{sw}{}^b \sin^c(\theta_{clock}/2)$ are plotted vertically as a function of the amplitude of the added noise horizontally: a (v_{sw}) is plotted in red, b (B_{sw}) is plotted in blue, and c [$\sin(\theta_{clock}/2)$] is plotted in green. For the solid curves with round points noise is added only to v_{sw}, for the solid curves with triangle points noise is added only to B_{sw}, for the thick solid curves with square points noise is added only to $\sin(\theta_{clock}/2)$, and for the dashed curves noise is added to all three of the solar-wind variables. In the bottom panel of Figure 1 the Pearson linear correlation coefficient between

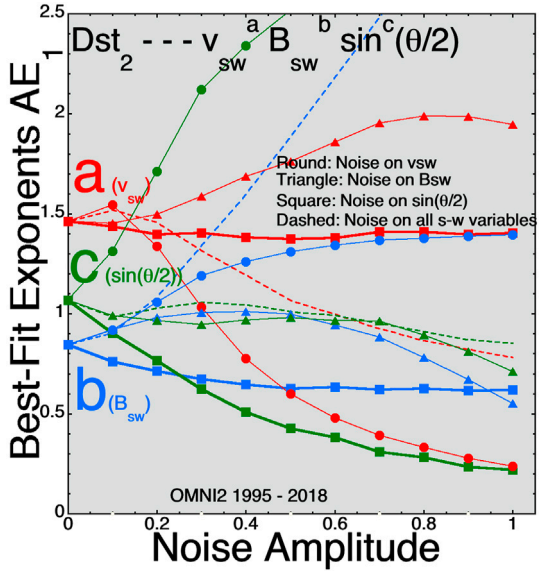

FIGURE 3
For best fits to the 2-hr-lagged Dst_2 index the three exponents **(A)** (red), **(B)** (blue), and **(C)** (green) are plotted as functions of the amplitude of the Gaussian noise added to the three solar-wind variables.

D and SME_1 is plotted as a function of the amplitude of the added noise.

Note that Newell et al., 2007 used $B_\perp = (B_y^2+B_z^2)^{1/2}$ and used multiple hours of solar-wind data in the fitting: here we are using $B_{sw} = (B_x^2+B_y^2+B_z^2)^{1/2}$ and using only a single hour of solar-wind data in the fitting.

SME is a "high-latitude" index measuring the strength of high-latitude magnetosphere-ionosphere currents. In creating plots similar to Figure 1 for other high-latitude indices (AE, AU, AL, and PCI, and the SuperMAG versions of the AL and AU indices called SML and SMU) one finds very similar trends on the plots, with the exponent c on $\sin(\theta_{clock}/2)$ being the largest of the three exponents.

Figure 2 plots the best-fit exponents a, b, and c for $D = v_{sw}^a B_{sw}^b \sin^c(\theta_{clock}/2)$ for the 1-hr-lagged $Hp60_1$ index. Hp60 is a convection-strength index (as is Kp, Ap, and MBI) (Thomsen, 2004) reacting to the strength of magnetospheric convection. These convection indices do not focus on the rapidly changing clock angle of the solar wind $\sin(\theta_{clock}/2)$ and so the c exponent for $\sin(\theta_{clock}/2)$ is small for these convective indices.

Figure 3 plots the best fit exponents a, b, and c for $D = v_{sw}^a B_{sw}^b \sin^c(\theta_{clock}/2)$ for the 2-hr-lagged Dst index. Dst measures mostly the pressure (diamagnetic currents) of plasma in the inner magnetosphere. The 2-h lag was chosen because that was found to be optimal in prior solar-wind/magnetosphere coupling studies using 1-h averaged data [e.g. Borovsky,

TABLE 1 An increase (↑) or a decrease (↓) to the three exponents a, b, and c of $D = v_{sw}^a B_{sw}^b \sin^c(\theta_{clock}/2)$ are noted as Gaussian random noise is added to the OMNI2 solar-wind variables for the years 1995–2018.

Increasing Noise on Variable	a	b	c
AE_1: Noise on v_{sw}	↓	↑	↑
AE_1: Noise on B_{sw}	↑	↑↓	↑
AE_1: Noise on sin(θ/2)	↓	↓	↓
AE_1: Noise on all 3	↓	↑	↓
SME_1: Noise on v_{sw}	↑↓	↑	↑
SME_1: Noise on B_{sw}	↑	↑↓	↑
SME_1: Noise on sin(θ/2)	↓	↓	↓
SME_1: Noise on all 3	↓	↑	↓
AL_1: Noise on v_{sw}	↓	↑	↑
AL_1: Noise on B_{sw}	↑	↑↓	—
AL_1: Noise on sin(θ/2)	↓	↓	↓
AL_1: Noise on all 3	↓	↑	↓
SML_1: Noise on v_{sw}	↑↓	↑	↑
SML_1: Noise on B_{sw}	↑	↑↓	↑
SML_1: Noise on sin(θ/2)	↓	↓	↓
SML_1: Noise on all 3	↑↓	↑	↓
AU_1: Noise on v_{sw}	↓	↑	↑
AU_1: Noise on B_{sw}	↑	↑↓	↑
AU_1: Noise on sin(θ/2)	↓	↓	↓
AU_1: Noise on all 3	↓	↑	↓
SMU_1: Noise on v_{sw}	↑↓	↑	↑
SMU_1: Noise on B_{sw}	↑	↑↓	↓↑
SMU_1: Noise on sin(θ/2)	—	↓	↓
SMU_1: Noise on all 3	↑↓	↑	↓
PCN_0: Noise on v_{sw}	↑	↑	↑
PCN_0: Noise on B_{sw}	↑	↑↓	—
PCN_0: Noise on sin(θ/2)	—	↓	↓
PCN_0: Noise on all 3	↓	↑	↓
Kp_1: Noise on v_{sw}	↑↓	↑	↑
Kp_1: Noise on B_{sw}	↑	↑↓	↑
Kp_1: Noise on sin(θ/2)	↓	↓	↓
Kp_1: Noise on all 3	↓	↑	↑
$Hp60_1$: Noise on v_{sw}	↑↓	↑	↑
$Hp60_1$: Noise on B_{sw}	↑	↑↓	↑
$Hp60_1$: Noise on sin(θ/2)	↓	↓	↓
$Hp60_1$: Noise on all 3	↓	↑	↑
$Ap60_1$: Noise on v_{sw}	↑↓	↑	↑
$Ap60_1$: Noise on B_{sw}	↑	↑↓	↓↑
$Ap60_1$: Noise on sin(θ/2)	—	↓	↓
$Ap60_1$: Noise on all 3	↓	↑	↓
Dst_2: Noise on v_{sw}	↑↓	↑	↑
Dst_2: Noise on B_{sw}	↑	↑↓	↑
Dst_2: Noise on sin(θ/2)	—	↓	↓
Dst_2: Noise on all 3	↑↓	↑	↓

2020b]. Like the convection indices, the exponent c of $\sin(\theta_{clock}/2)$ is weak.

Examining a number of these plots for various geomagnetic indices some trends can be seen. 1) Increasing the noise on v_{sw} reduces the magnitude of the exponent a on v_{sw}. 2) Increasing the noise on $\sin(\theta_{clock}/2)$ reduces the magnitude of the exponent c on $\sin(\theta_{clock}/2)$. 3) Increasing the noise on B_{sw} at first increases the magnitude of the exponent b on B_{sw} and then as the noise amplitude becomes large it decreases the magnitude of the exponent b. 4) Increasing the noise on v_{sw} tends to raise the magnitudes of the exponents b and c on B_{sw} and $\sin(\theta_{clock}/2)$. 5) Increasing the noise on B_{sw} tends to raise the magnitudes of the exponents a and c on v_{sw} and $\sin(\theta_{clock}/2)$. 6) Increasing the noise on $\sin(\theta_{clock}/2)$ tends to lower the magnitude of all three exponents a, b, and c. Note that there are exceptions to these trends.

Examining plots similar to those of Figures 1–3 for a number of geomagnetic indices, the trend in each of the exponents a, b, and c are noted in Table 1 as noise is added to the OMNI2 solar-wind variables v_{sw}, B_{sw}, and $\sin(\theta_{clock}/2)$. An upward arrow in Table 1 indicates that the value of the exponent increases with increasing noise amplitude and a downward arrow indicates that the value of the exponent decreases with increasing noise amplitude.

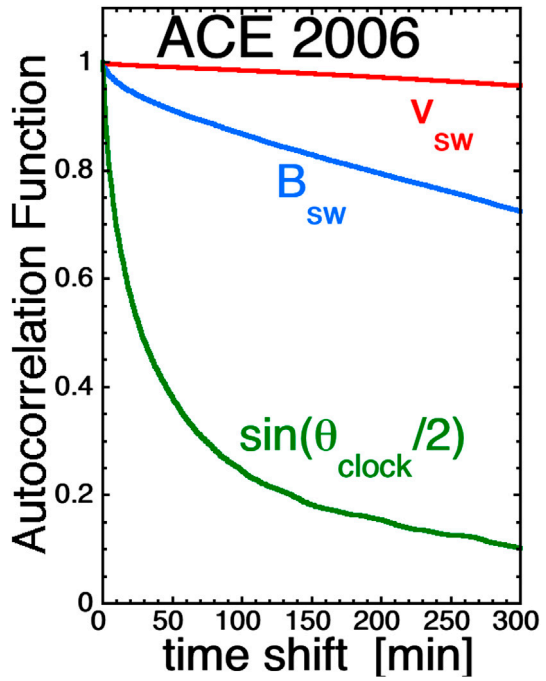

FIGURE 4
Autocorrelation functions for the three solar-wind variables v_{sw} (red), B_{sw} (blue), and $\sin(\theta_{clock}/2)$ (green) calculated using 64-s measurements from ACE for the year 2006.

4 Extrapolating backward to remove or reduce the solar-wind noise

Looking at the trends in the changes of the a, b, and c exponents of $D = v_{sw}{}^a B_{sw}{}^b \sin^c(\theta_{clock}/2)$ with increasing added noise, one might guess that extrapolating the curves in the plots of Figures 1–3 back to values of noise < 0 might represent the better values of the exponents a, b, and c in the presence of less solar-wind noise (less error). Figure 4 plots the temporal autocorrelation functions of the three variables v_{sw} (red curve), B_{sw} (blue curve), and $\sin(\theta_{clock}/2)$ (green curve) obtained from 64-s-resolution data from ACE SWEPAM (McComas et al., 1998) and ACE MAG (Smith et al., 1998) for the year 2006. (The year 2006 is in the late declining phase with mild high-speed streams and with a nice mix of solar-wind plasma types [cf. Xu and Borovsky, 2015].) The autocorrelation times (using the 1/e method) in Figure 4 are about 43.9 h for v_{sw}, 15.3 h for B_{sw}, and 53 min for $\sin(\theta_{clock}/2)$. The temporal autocorrelation function represents the spatial structure of the solar-wind plasma and magnetic field advected past the measuring spacecraft. The spatial structure of the variable $\sin(\theta_{clock}/2)$ in the solar wind is much smaller than the spatial structure of the variables B_{sw} and v_{sw}, hence the much shorter autocorrelation time for $\sin(\theta_{clock}/2)$ [See also Lockwood and McWilliams (2021)]. One problem with a solar-wind monitor for Earth at L1 is that the solar wind that hits the L1 monitor is not the same solar wind that hits the Earth (Sandahl et al., 1996; Ashour-Abdalla et al., 2008; Walsh et al., 2019; Burkholder et al., 2020; Borovsky, 2020a): the monitored solar-wind streamline often misses the Earth by 10s of R_E typically passing on the duskward side of the magnetosphere (Borovsky, 2022b). Contributing factors for this miss are 1) the solar-wind flow is not radial [the direction fluctuates by about ±5° plus there is a systematic dawn-dusk offset to the average flow vector (Nemecek et a., 2020a)] 2) there is a duskward aberration to the flow caused by the Earth's motion around the Sun (Fairfield, 1993), and 3) the solar-wind structure moves away from the Sun faster than the plasma wind with a velocity vector relative to the plasma that is in the Parker-spiral direction (Borovsky, 2020c; Nemecek et al., 2020b). This L1 error is much more critical for the smaller-structured $\sin(\theta_{clock}/2)$ than it is for v_{sw} or B_{sw}. Hence the thick solid curves with the square points in Figures 1–3 that add noise only to $\sin(\theta_{clock}/2)$ are the most important to think about and extrapolate backward.

For the high-latitude-current indices AE, AU, AL, SME, SMU, SML, and PCI the exponent c on $\sin(\theta_{clock}/2)$ is the largest of the three exponents and also undergoes the most-significant change (reduction) as noise is added to the $\sin(\theta_{clock}/2)$ values in the data set (cf. Figure 1). Extrapolating to negative values of noise in the thick solid curves of Figures 1–3 would increase the magnitude of the c exponent: the extrapolation would not change a (for v_{sw}) or b (for B_{sw}) significantly. For

TABLE 2 For five different geomagnetic indices the best-fit exponents a, b, and c of the solar-wind driver $D = v_{sw}^{a} B_{sw}^{b} \sin^{c}(\theta_{clock}/2)$ are listed for the 1995–2018 OMNI2 solar-wind data and for the OMNI2 data that utilized measurements from IMP-8. The expected change in the a, b, and c exponents if there were a reduction of noise on $\sin(\theta_{clock}/2)$ and the observed change in the exponents a, b, and c (from Table 1) are listed.

	a	b	c	r_{corr}
AE_1 1995–2018	1.071	0.711	2.025	0.772
AE_1 IMP8	1.227	0.596	2.159	0.762
AE_1 Expected	increase	increase	increase	
AE_1 Observed	increase	decrease	increase	
AL_1 1995–2018	1.206	0.703	2.406	0.749
AL_1 IMP8	1.390	0.572	2.434	0.737
AL_1 Expected	increase	increase	increase	
AL_1 Observed	increase	decrease	increase	
AU_1 1995–2018	0.779	0.706	1.310	0.678
AU_1 IMP8	0.859	0.640	1.599	0.649
AU_1 Expected	increase	increase	increase	
AU_1 Observed	increase	decrease	increase	
Kp_1 1995–2018	1.148	0.437	0.337	0.728
Kp_1 IMP8	1.198	0.441	0.368	0.714
Kp_1 Expected	increase	increase	decrease	
Kp_1 Observed	increase	none	increase	
PC_0 1995–2018	1.054	0.735	1.908	0.730
PC_0 IMP8	1.228	0.613	1.886	0.716
PC_0 Expected	none	increase	increase	
PC_0 Observed	increase	decrease	decrease	

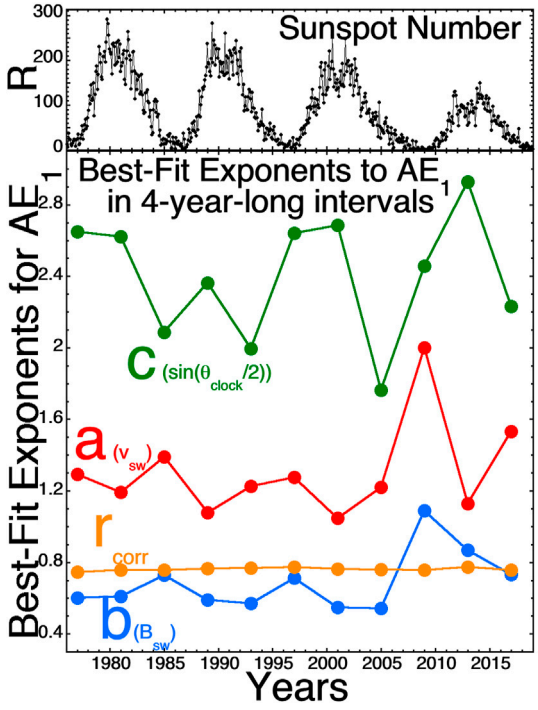

FIGURE 5
(top panel) For the years 1995–2008 the 27-days-averaged sunspot number is plotted. (bottom panel) The best-fit **(A)** (red), **(B)** (blue), and **(C)** (green) exponents for AE_1 are calculated in four-year blocks of OMNI2 solar-wind data from 1995–2018. For each four-year data block the Pearson linear correlation coefficient between D and AE_1 is plotted in orange.

the magnetospheric convection index $Hp60_1$ extrapolating backward to noise values less than zero on $\sin(\theta_{clock}/2)$ in Figure 2 (thick curve with square points) would increase the a exponent (on v_{sw}) the most and also increase the b (on B_{sw}) and c [on $\sin(\theta_{clock}/2)$] exponents.

One might guess that by using the times when the nearer-to-Earth solar-wind monitor IMP-8 (Feldman et al., 1978; Butler, 1980) was used in the OMNI2 data set, these extrapolations to lower noise could be confirmed. Unfortunately, it will be seen that this is not the case. In Table 2 the best-fit values for the exponents a, b, and c for five geomagnetic indices are listed for the hours when IMP-8 solar-wind measurements were incorporated into OMNI2 (with most of the IMP-8 data incorporated in the years 1975–1994). The best-fit values of a, b, and c are also listed in Table 2 for the 1995–2018 OMNI2 data. The changes in a, b, and c predicted by extrapolation of the 1995–2018 data (cf. Table 1) are noted, and the observed changes in a, b, and c from the 1995–2018 data to the IMP-8 data are noted in Table 2. (Note that these expected changes are opposite to the arrows in Table 1: the arrows are the direction when noise is added and the "expected" change is the expectation for reduction of noise.) As can be seen in Table 2, the changes observed by using IMP-8 are in poor agreement with the extrapolation-predicted changes from the 1995–2018 added-noise calculations: eight times there is agreement and seven times there is disagreement. Note that the change in the exponent b on B_{sw} is wrong for all five cases.

The bottom panel of Figure 5 plots the best-fit a, b, and c exponents to AE_1 in four-year blocks of OMNI2 solar-wind data from 1995–2018. As can be seen, the values of these best-fit exponents change from data subset to data subset. In the top panel of Figure 5 the 27-days-averaged sunspot number R is plotted. The temporal changes in the exponents seen in the bottom panel might be owed to solar-cycle-type variations in the solar-wind properties and/or to solar-wind spacecraft differences from year to year. As a comparison for Figure 5, Figure 6 looks at the best-fit a, b, and c exponents for AE_1 when the 1995–2018 OMNI2 data is randomized in time and binned into 10 subsets, each containing data from the full years 1995–2018. When the data is mixed in time (Figure 6) it results in much smaller variations in the best-fit exponents a, b, and c from data subset to data subset, supporting the idea that there are variances caused by spacecraft differences and by year-by-year solar-cycle differences in the wind. The variances in a, b, and c in

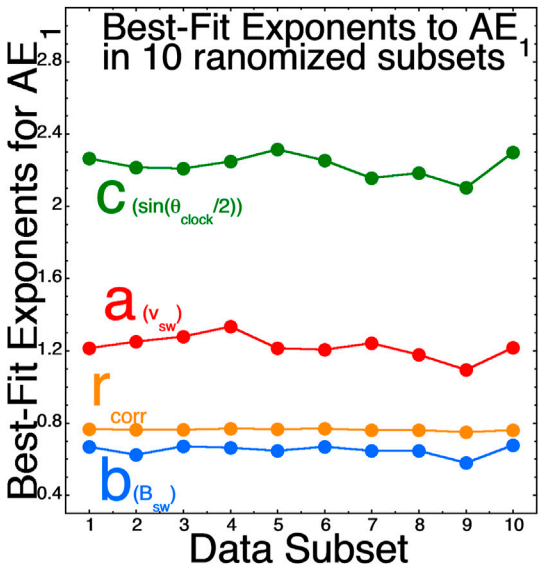

FIGURE 6
The best-fit **(A)** (red), **(B)** (blue), and **(C)** (green) exponents for AE_1 are plotted when the 1995–2018 OMNI2 data is randomized in time and binned into 10 subsets, each of which containing data from the full years 1995–2018. The Pearson linear correlation coefficient for each subset is plotted in orange.

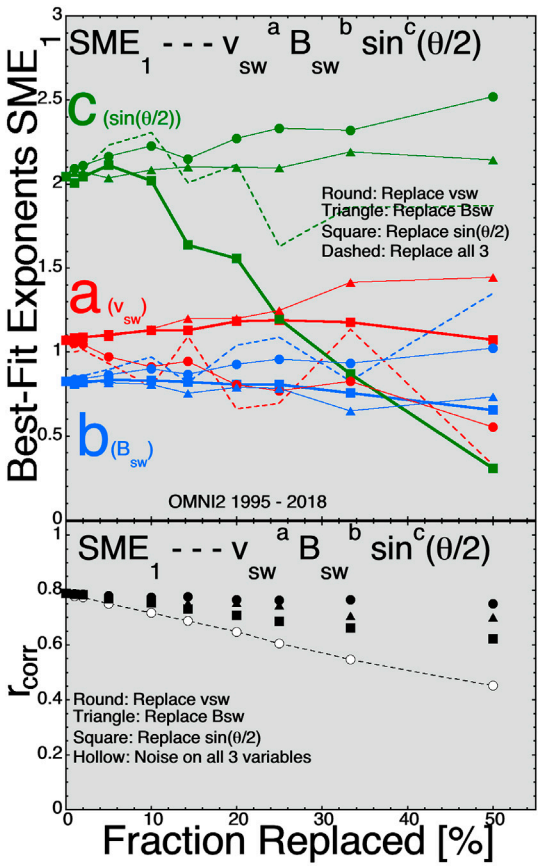

FIGURE 7
For best fits to the 1-hr-lagged SME_1 index the three exponents **(A)** (red), **(B)** (blue), and **(C)** (green) are plotted in the top panel as functions of the fraction of time-series values replaced for three solar-wind variables. In the bottom panel the Pearson linear correlation coefficient between D and SME_1 is plotted as a function of the fraction replaced.

Figure 5 are large, and so the choosing of IMP-8 data in a finite set of years could result in variations of a, b, and c that are more-significant than the noise-reduction changes. Hence the hope that using IMP-8 to reduce the noise and improve the a, b, and c values is not so straightforward: moving to IMP-8 from the 1995–2018 data set does not always move the a, b, and c values in the expected direction and changing eras (years) and spacecraft results in changes to the behavior of the a, b, and c values. A question is which of these year-to-year changes in a, b, and c (e.g. Figure 5) are better and which are worse in terms of finding a driver function that describes the physics of the solar wind coupling to the Earth; as discussed in Borovsky (2021) there are math-versus-physics reasons why a driver function has a good correlation with the Earth.

5 Discussion

This report explored expectations for solar-wind noise reduction by looking at the trends that resulted from adding Gaussian noise to solar-wind data. Extrapolating those added-noise trends backward yielded predictions for noise-reduction changes to the exponents a, b, and c of best-fit connections between the solar-wind driver function $D = v_{sw}{}^a B_{sw}{}^b \sin^c(\theta_{clock}/2)$ and various geomagnetic indices. Going from L1 solar-wind data to near-Earth IMP-8 solar-wind data, the observed changes in the exponents a, b, and c of the best-fit formula $D = v_{sw}{}^a B_{sw}{}^b \sin^c(\theta_{clock}/2)$ did not show good agreement with the expected noise-reduction changes. Looking at year-to-year changes in the a, b, and c exponents for the best-fit formula found that these year-to-year changes were large: hence different parts of the solar cycle and/or using different spacecraft to monitor the solar wind results in large changes that may overwhelm observation of the desired noise-reduction changes.

One issue with the methodology used here is the addition of Gaussian noise (random numbers with Gaussian distributions) to the OMNI2 solar-wind variables. The main error with solar-wind monitors at L1 is that the solar wind that hits a monitoring spacecraft at L1 is not the solar wind that hits the Earth. Hence the real error in the solar-wind data for Earth is not random noise on all solar-wind values, rather that some of the values are completely wrong. Adding noise, for instance, by replacing a fraction of the $\sin(\theta_{clock}/2)$

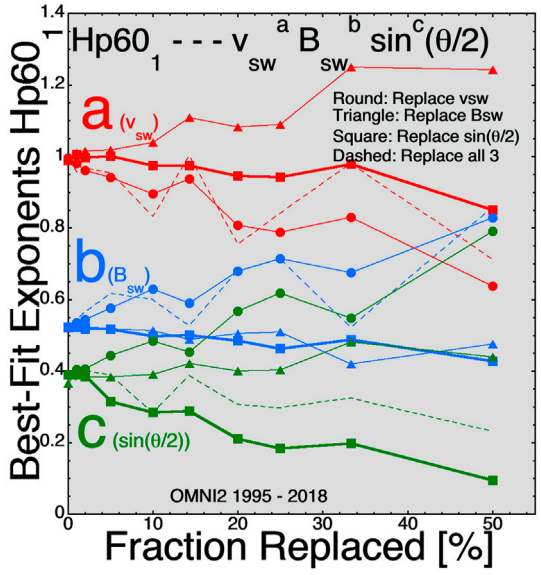

FIGURE 8
For best fits to the 1-hr-lagged $Hp60_1$ index the three exponents **(A)** (red), **(B)** (blue), and **(C)** (green) are plotted as functions of the fraction of time-series values replaced for three solar-wind variables.

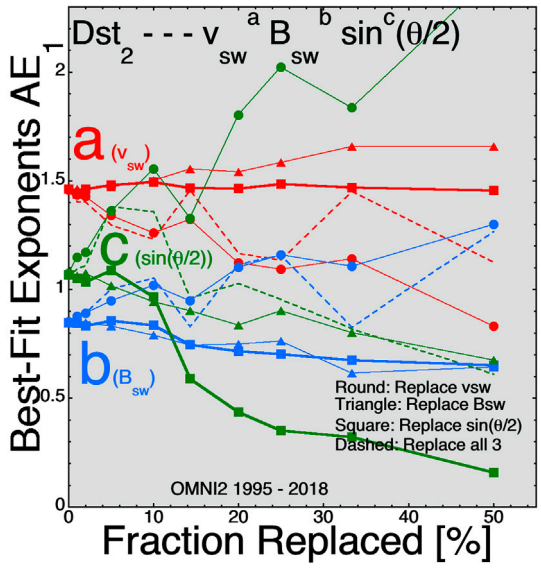

FIGURE 9
For best fits to the 2-hr-lagged Dst_2 index the three exponents **(A)** (red), **(B)** (blue), and **(C)** (green) are plotted as functions of the fraction of time-series values replaced for three solar-wind variables.

values in the time series with completely different values of $\sin(\theta_{clock}/2)$ may be a more-realistic way to emulate the L1 errors in the solar-wind measurements. This is explored in Figures 7–9 where the best-fit exponents a, b, and c are plotted as a function of the fraction of the solar-wind time-series values that are replaced with different values. Comparing Figure 7 with Figure 1 (fits to SuperMAG SME_1), Figure 8 with Figure 2 (Fits to $Hp60_1$), and Figure 9 with Figure 3 (fits to Dst_2), it is seen that the trends in the changes of the exponents a, b, and c with increasing noise (either increasing the amplitude of added Gaussian noise or increasing the fraction of time-series values replaced) are quite similar. Between these three pairs of plots there are no contradictions where one method leads to an increase in an exponent and the other leads to a decrease in that exponent. There are a few cases where the Gaussian-noise method leads to an increase or a decrease of an exponent while the replacement method shows no change in that exponent.

For 1-hour-averaged data, the L1 error most likely does not result in the whole hour being incorrect, but just part of the hour being incorrect. A hybrid methodology to add noise might try adding random noise (for the fraction of the hour being wrong) to only some of the hourly solar-wind data points. Since the two methods 1) adding noise to all solar-wind data points and 2) replacing a fraction of the data points both yielded similar results, one might guess that adding noise to a fraction of the data points will also yield similar results.

The analysis of this study using IMP-8 data found difficulty in demonstrating that near-Earth monitoring yields more-accurate solar-wind measurements for Earth, although there have been several studies estimating of the solar-wind errors between L1 and Earth (Crooker et al., 1982; Ridley, 2000; Weimer et al., 2002; Mailyan et al., 2008; Case and Wild, 2012). That is not to say that this study does not recommend fielding near-Earth solar-wind monitors in future. It is an intellectual certainty that better solar-wind-monitor measurements with truer values of what is hitting the Earth will result in better future data studies of solar-wind/magnetosphere interactions. A study to optimize monitors for solar-wind/magnetosphere interaction science is needed. One possibility is multiple spacecraft in IMP-type circular orbits ($r \sim 30\ R_E$) (Feldman et al., 1978; Butler, 1980) where at least one spacecraft would always be in the near-Earth upstream solar wind.

Data availability statement

Publicly available datasets were analyzed in this study. This data can be found here: https://omniweb.gsfc.nasa.gov.

Author contributions

The author confirms being the sole contributor of this work and has approved it for publication.

Funding

JB was supported at the Space Science Institute by the NSF GEM Program *via* grant AGS-2027569 and by the NASA HERMES Interdisciplinary Science Program *via* grant 80NSSC21K1406.

Acknowledgments

The author thanks Mike Lockwood and Nithin Sivadas for useful conversations. The author also acknowledges GFZ Potsdam for the Hp60 index, which is available at ftp://ftp.gfz-potsdam.de/pub/home/obs/Hpo, and the author acknowledges the SuperMAG team, where the SuperMAG auroral-electrojet indices are available at http://supermag.jhuapl.edu/indices.

Conflict of interest

The authors declare that the research was conducted in the absence of any commercial or financial relationships that could be construed as a potential conflict of interest.

Publisher's note

References

Ashour-Abdalla, M., Walker, R. J., Peroomian, V., and El-Alaoui, M. (2008). On the importance of accurate solar wind measurements for studying magnetospheric dynamics. *J. Geophys. Res.* 113, A08204. doi:10.1029/2007ja012785

Baumjohann, W. (1986). Merits and limitations of the use of geomagnetic indices in solar wind-magnetosphere coupling studies, in *Solar wind-magnetosphere coupling*, Y. Kamide and J. A. Slavin (eds.), p. 3, Terra Scientific, Tokyo.

Bergin, A., Chapman, S. C., and Gjerloev, J. W. (2020). $A\ E$, D_{ST} , and their SuperMAG counterparts: The effect of improved spatial resolution in geomagnetic indices. *J. Geophys. Res. Space Phys.* 125, e2020JA027828. doi:10.1029/2020ja027828

Bock, R. D., and Petersen, A. C. (1975). A multivariate correction for attenuation. *Biometrika* 62, 673–678. doi:10.1093/biomet/62.3.673

Borovsky, J. E. (2020b). A survey of geomagnetic and plasma time lags in the solar-wind-driven magnetosphere of Earth. *J. Atmos. Sol. Terr. Phys.* 208, 105376. doi:10.1016/j.jastp.2020.105376

Borovsky, J. E. (2014). Canonical correlation analysis of the combined solar-wind and geomagnetic-index data sets. *J. Geophys. Res. Space Phys.* 119, 5364–5381. doi:10.1002/2013ja019607

Borovsky, J. E., and Denton, M. H. (2010). The magnetic field at geosynchronous orbit during high-speed-stream-driven storms: Connections to the solar wind, the plasma sheet, and the outer electron radiation belt. *J. Geophys. Res.* 2010, 115A08217. doi:10.1029/2009JA015116

Borovsky, J. E. (2022a). Noise, regression dilution bias, and solar-wind/magnetosphere coupling studies. *Front. Astron. Space Sci.* 9, 867282. doi:10.3389/fspas.2022.867282

Borovsky, J. E. (2020c). On the motion of the heliospheric magnetic structure through the solar wind plasma. *J. Geophys. Res. Space Phys.* 125, e2019JA027377. doi:10.1029/2019JA027377

Borovsky, J. E. (2021). Perspective: Is our understanding of solar-wind/magnetosphere coupling satisfactory? *Front. Astron. Space Sci.* 8, 634073. doi:10.3389/fspas.2021.634073

Borovsky, J. E. (2022b). The triple dusk-dawn aberration of the solar wind at Earth. *Front. Astron. Space Sci.* 9, 917163. doi:10.3389/fspas.2022.917163

Borovsky, J. E. (2020a). What magnetospheric and ionospheric researchers should know about the solar wind. *J. Atmos. Sol. Terr. Phys.* 204, 105271. doi:10.1016/j.jastp.2020.105271

Burkholder, B. L., Nykyri, K., and Ma, X. (2020). Use of the L1 constellation as a multispacecraft solar wind monitor. *JGR. Space Phys.* 125, e2020JA027978. doi:10.1029/2020ja027978

Butler, P. (1980). "Interplanetary Monitoring Platform engineering history and acievements," in *Nasa TM-80758* (Greenbelt Maryland USA: Goddard Space Flight Center).

Case, N. A., and Wild, J. A. (2012). A statistical comparison of solar wind propagation delays derived from multispacecraft techniques. *J. Geophys. Res.* 117, A02101. doi:10.1029/2011ja016946

Crooker, N. U., Siscoe, G. L., Russell, C. T., and Smith, E. J. (1982). Factors controlling degree of correlation between ISEE 1 and ISEE 3 interplanetary magnetic field measurements. *J. Geophys. Res.* 87, 2224–2230. doi:10.1029/ja087ia04p02224

Dessler, A. J., and Parker, E. N. (1959). Hydromagnetic theory of geomagnetic storms. *J. Geophys. Res.* 64, 2239–2252. doi:10.1029/jz064i012p02239

Fairfield, D. H. (1993). Solar wind control of the distant magnetotail: Isee 3. *J. Geophys. Res.* 98, 21265–21276. doi:10.1029/93ja01847

Feldman, W. C., Asbridge, J. R., Bame, S. J., and Gosling, J. T. (1978). Long-term variations of selected solar wind properties: Imp 6, 7, and 8 results. *J. Geophys. Res.* 83, 2177. doi:10.1029/ja083ia05p02177

Goertz, C. K., Shan, L.-H., and Smith, R. A. (1993). Prediction of geomagnetic activity. *J. Geophys. Res.* 98, 7673–7684. doi:10.1029/92ja01193

Hutcheon, J. A., Chiolero, A., and Hanley, J. A. (2010). Random measurement error and regression dilution bias. *BMJ* 340, c2289–1406. doi:10.1136/bmj.c2289

King, J. H., and Papitashvili, N. E. (2005). Solar wind spatial scales in and comparisons of hourly Wind and ACE plasma and magnetic field data. *J. Geophys. Res.* 110, A02104. doi:10.1029/2004ja010649

Liemohn, M. W., Kozyra, J. U., Thomsen, M. F., Roeder, J. L., Lu, G., Borovsky, J. E., et al. (2001). Dominant role of the asymmetric ring current in producing the stormtime Dst. *J. Geophys. Res.* 106, 10883–10904. doi:10.1029/2000ja000326

Liu, K. (1988). Measurement error and its impact on partial correlation and multiple linear regression analysis. *Am. J. Epidemiol.* 127, 864–874. doi:10.1093/oxfordjournals.aje.a114870

Lockwood, M., and McWilliams, K. A. (2021). On optimum solar wind-magnetosphere coupling functions for transpolar voltage and planetary geomagnetic activity. *JGR. Space Phys.* 126, e2021JA029946. doi:10.1029/2021ja029946

Lockwood, M. (2022). Solar wind--magnetosphere coupling functions: Pitfalls, limitations, and applications. *Space weather.* 20, e2121SW002989. doi:10.1029/2021sw002989

Mailyan, B., Munteanu, C., and Haaland, S. (2008). What is the best method to calculate the solar wind propagation delay? *Ann. Geophys.* 26, 2383–2394. doi:10.5194/angeo-26-2383-2008

McComas, D. J., Blame, S. J., Barker, P., Feldman, W. C., Phillips, J. L., Riley, P., et al. (1998). Solar wind electron proton alpha monitor (SWEPAM) for the advanced composition explorer. *Space Sci. Rev.* 86, 563.

McPherron, R. L., Hsu, T.-S., and Chu, X. (2015). An optimum solar wind coupling function for the AL index. *JGR. Space Phys.* 120, 2494–2515. doi:10.1002/2014ja020619

Nemecek, Z., Durovcova, T., Safrankova, J., Nemec, F., Matteini, L., Stansby, D., et al. (2020b). What is the solar wind frame of reference? *Astrophys. J.* 889, 163. doi:10.3847/1538-4357/ab65f7

Nemecek, Z., Durovcova, T., Safrankova, J., Richardson, J. D., Simunek, J., and Stevens, M. L. (2020a). Non)radial solar wind propagation through the heliosphere. *Astrophys. J.* 897, L39. doi:10.3847/2041-8213/ab9ff7

Newell, P. T., Sotirelis, T., Liou, K., Meng, C. I., and Rich, F. J. (2007). A nearly universal solar wind-magnetosphere coupling function inferred from 10 magnetospheric state variables. *J. Geophys. Res.* 112, A01206. doi:10.1029/2006ja012015

Ohtani, S., Nose, M., Rostoker, G., Singer, H., Lui, A. T. Y., and Kakamura, M. (2001). Storm-substorm relationship: Contribution of the tail current to Dst. *J. Geophys. Res.* 106, 21199–21209. doi:10.1029/2000ja000400

Ridley, A. J. (2000). Estimations of the uncertainty in timing the relationship between magnetospheric and solar wind processes. *J. Atmos. Sol. Terr. Phys.* 62, 757–771. doi:10.1016/s1364-6826(00)00057-2

Ridley, A. J., and Kihn, E. A. (2004). Polar cap index comparisons with AMIE cross polar cap potential, electric field, and polar cap area. *Geophys. Res. Lett.* 31, L07801. doi:10.1029/2003gl019113

Sandahl, I., Lundstedt, H., Koskinen, H., and Glassmeir, K.-H. (1996). On the need for solar wind monitoring close to the magnetosphere. *Asp. Conf. Ser.* 95, 300.

Sckopke, N. (1966). A general relation between the energy of trapped particles and the disturbance field near the Earth. *J. Geophys. Res.* 71, 3125–3130. doi:10.1029/jz071i013p03125

Siscoe, G. L., McPherron, R. L., and Jordanova, V. K. (2005). Diminished contribution of ram pressure to Dst during magnetic storms. *J. Geophys. Res.* 110, A12227. doi:10.1029/2005ja011120

Sivadas, N., and Sibeck, D. G. (2022). Regression bias in using solar wind measurements. *Front. Astron. Space Sci.* 9, 924976.

Smith, C. W., Acuna, M. H., Burlaga, L. F., L'Heureux, J., Ness, N. F., and Scheifele, J. (1998). The ACE magnetic fields experiment space. *Space Sci. Rev.* 86, 613–632. doi:10.1023/a:1005092216668

Spearman, C. (1904). The proof and measurement of association between two things. *Am. J. Psychol.* 15, 72. doi:10.2307/1412159

Stauning, P. (2013). The polar cap index: A critical review of methods and a new approach. *J. Geophys. Res. Space Phys.* 118, 5021–5038. doi:10.1002/jgra.50462

Su, S.-Y., and Konradi, A. (1975). Magnetic field depression at the Earth's surface calculated from the relationship between the size of the magnetosphere and the Dst values. *J. Geophys. Res.* 80, 195–199. doi:10.1029/ja080i001p00195

Thomsen, M. F. (2004). Why Kp is such a good measure of magnetospheric convection. *Space weather.* 2, S11004. doi:10.1029/2004sw000089

Walsh, B. M., Bhakyapaibul, T., and Zou, Y. (2019). Quantifying the uncertainty of using solar wind measurements for geospace inputs. *JGR. Space Phys.* 124, 3291–3302. doi:10.1029/2019ja026507

Weimer, D. R., Ober, D. M., Maynard, N. C., Burke, W. J., Collier, M. R., McComas, D. J., et al. (2002). Variable time delays in the propagation of the interplanetary magnetic field. *J. Geophys. Res.* 107, SMP 29-3 1–SMP 29-15. doi:10.1029/2001ja009102

Xu, F., and Borovsky, J. E. (2015). A new four-plasma categorization scheme for the solar wind. *J. Geophys. Res. Space Phys.* 120, 70–100. doi:10.1002/2014ja020412

frontiers | Frontiers in Astronomy and Space Sciences

TYPE Original Research
PUBLISHED 29 September 2022
DOI 10.3389/fspas.2022.972150

OPEN ACCESS

EDITED BY
Joseph E. Borovsky,
Space Science Institute, United States

REVIEWED BY
Gian Luca Delzanno,
Los Alamos National Laboratory (DOE), United States
Michael Wiltberger,
National Center for Atmospheric Research (UCAR), United States

*CORRESPONDENCE
Tuija I. Pulkkinen,
tuija@umich.edu

SPECIALTY SECTION
This article was submitted to Space Physics,
a section of the journal
Frontiers in Astronomy and Space Sciences

RECEIVED 17 June 2022
ACCEPTED 22 August 2022
PUBLISHED 29 September 2022

CITATION
Pulkkinen TI, Brenner A, Al Shidi Q and Toth G (2022), Statistics of geomagnetic storms: Global simulations perspective. *Front. Astron. Space Sci.* 9:972150. doi: 10.3389/fspas.2022.972150

Statistics of geomagnetic storms: Global simulations perspective

Tuija I. Pulkkinen[1]*, Austin Brenner[1,2], Qusai Al Shidi[1] and Gabor Toth[1]

[1]Department of Climate and Space Sciences and Engineering, University of Michigan, Ann Arbor, MI, United States, [2]Department of Aerospace Engineering, University of Michigan, Ann Arbor, MI, United States

We present results of 131 geomagnetic storm simulations using the University of Michigan Space Weather Modeling Framework Geospace configuration. We compare the geomagnetic indices derived from the simulation with those observed, and use 2D cuts in the noon-midnight planes to compare the magnetopause locations with empirical models. We identify the location of the current sheet center and look at the plasma parameters to deduce tail dynamics. We show that the simulation produces geomagnetic index distributions similar to those observed, and that their relationship to the solar wind driver is similar to that observed. While the magnitudes of the Dst and polar cap potentials are close to those observed, the simulated AL index is consistently underestimated. Analysis of the magnetopause position reveals that the subsolar position agrees well with an empirical model, but that the tail flaring in the simulation is much smaller than that in the empirical model. The magnetotail and ring currents are closely correlated with the Dst index, and reveal a strong contribution of the tail current beyond 8 R_E to the Dst index during the storm main phase.

KEYWORDS

MHD simulations, magnetosphere-ionophere coupling, magnetopause, ring current, tail current, geomagnetic index and solar conditions, solar wind

Introduction

Geomagnetic storms are a class of major disturbances in the Earth's space environment driven by solar wind structures containing either strong southward interplanetary magnetic field (IMF), large solar wind speed or both (Gonzalez et al., 1994). The storm intensity is measured by the Dst index, and storms are often classified to minor storms causing a magnetic depression of the Earth's field by more than −50 nT and major storms with Dst peak below −100 nT (Burton et al., 1975). Other indicators of stormtime activity include an enhanced cross-polar cap potential (CPCP) and strong auroral electrojet currents causing large signals in the AL index (Davis and Sugiura, 1966).

The relationship between the solar wind driver and the consequent geomagnetic activity is complex, and often expressed in terms of coupling functions that relate interplanetary parameters with the geomagnetic indices. Coupling functions have been widely used and much studied (see e.g., Borovsky and Birn, (2014) and Lockwood, (2019, 2022)). On one hand, the coupling functions describe different

attributes of the driver such as the solar wind electric field (Burton et al., 1975), the incident Poynting flux (Akasofu, 1981) or the reconnected magnetic flux (Newell et al., 2007) at the magnetopause. On the other hand, they have been optimized to different geomagnetic indices like Dst (Akasofu, 1981), the AL index (McPherron et al., 2015), or cross-polar cap potential (Lockwood and McWilliams, 2021). The coupling functions are typically derived using theoretical considerations together with correlations between the solar wind parameters and geomagnetic indices.

The lack of global observations either in space or on ground brings inherent limitations to correlation studies between the interplanetary parameters and geomagnetic indices. Scatter sources include but are not limited to errors in measurements and transit time of the solar wind and IMF (Papitashvili et al., 2014), dynamics occurring at the bow shock and within the magnetosheath (Pulkkinen et al., 2016), and lack of station coverage and signals in ground magnetic recordings caused by ground conductivity structure and other effects not related to the solar wind driving (Tanskanen et al., 2001; Häkkinen et al., 2002). Furthermore, the magnetospheric response to the solar wind driver is neither instantaneous nor independent of the state of the magnetosphere (Pulkkinen et al., 2006b; Brenner et al., 2021).

Global MHD simulations can model the solar wind–magnetosphere coupling covering the entire magnetosphere out to cislunar distances (e.g., Janhunen et al., 2012; Tóth et al., 2012). Such simulations have been shown to give an accurate representation of the large-scale evolution of the magnetosphere-ionosphere system (Liemohn M. W. et al., 2018), while allowing us to quantitatively assess the plasma and energy flow from the solar wind into the magnetosphere (Palmroth et al., 2003), and thereby assess the parameters controlling the coupling.

Using methods developed in Palmroth et al. (2003), Pulkkinen et al. (2008) examined the energy input from the solar wind into the magnetosphere-ionosphere system under a variety of driving conditions (northward and southward IMF, high and low solar wind density and speed) in the GUMICS-4 global MHD simulation (Janhunen et al., 2012). They showed that the reconnection efficiency is higher for high solar wind speed, and that the optimal energy coupling function scaled as the electric field parallel to the large-scale X-line at the magnetopause (i.e., proportional to $\sin\theta$ rather than the often-used $\sin\theta/2$). Furthermore, the response of the magnetopause energy transfer depends on the past history with energy input being larger for periods with large preceding energy input (Palmroth et al., 2006; Pulkkinen et al., 2006a). Using similar methodology, Wang et al. (2014) examined the energy transfer through the magnetopause in the Hu et al. (2005) simulation. They arrived at a new coupling function proportional to the energy incident at the magnetopause, which gave better correlations with geomagnetic indices than the Akasofu (1981) epsilon function. Both of these studies suffer from the limitation of using pure MHD plasma description, which does not allow for development of a high-energy ring current in the inner magnetosphere that is a major characteristic of a magnetic storm evolution.

The cross-polar cap potential is a measure of the coupling between the ionosphere and the solar wind: The rate at which magnetic flux reconnects at the magnetopause is equal to a voltage drop along the reconnection X-line. This potential maps to the ionosphere along the magnetic field lines, and can be measured as the cross-polar cap potential (Crooker, 1988; Siscoe et al., 2002). However, this direct relationship is

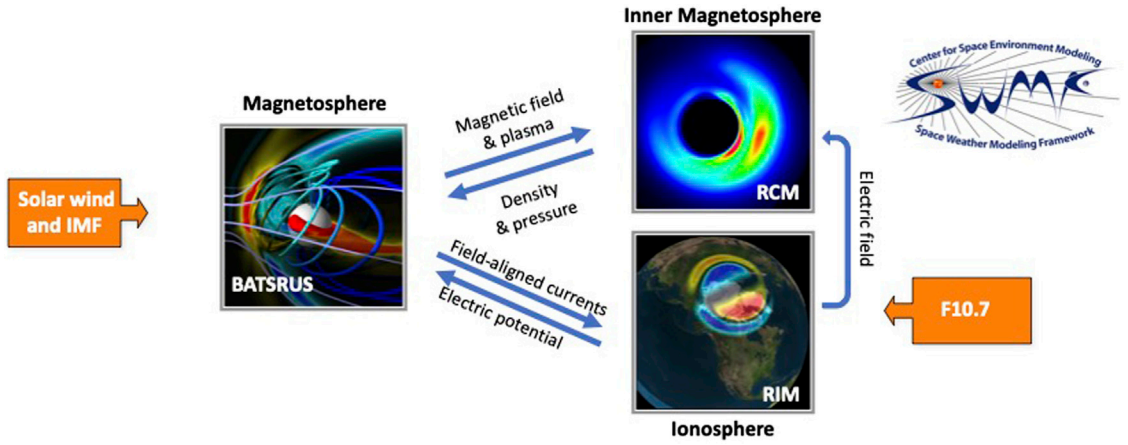

FIGURE 1
The SWMF Geospace model setup. The arrays indicate the one-way or two-way couplings between the modules (see text). The orange boxes indicate model input parameters.

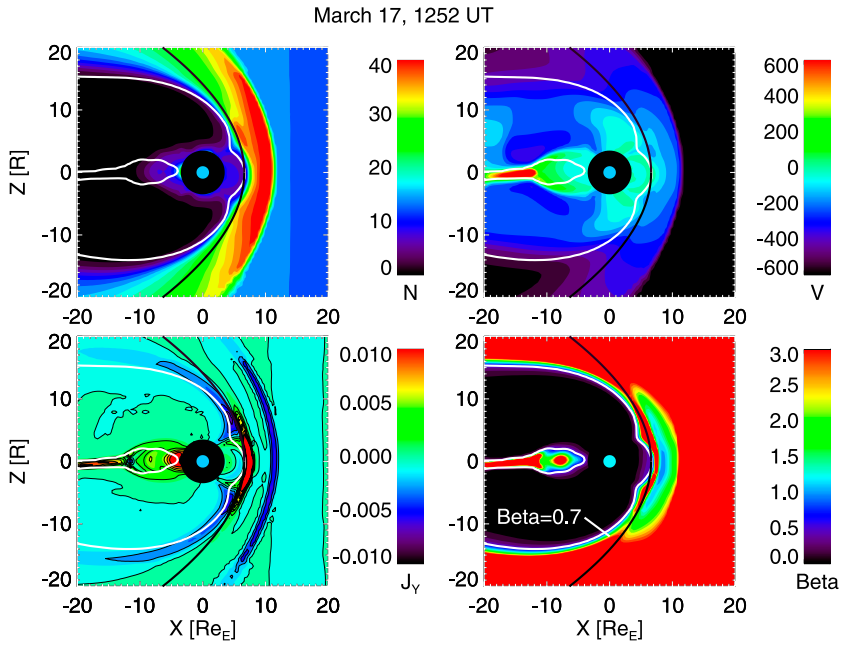

FIGURE 2
Noon-midnight meridian cuts from the simulation. (Top left) Plasma density in cm^{-3}; (Top right) Plasma velocity V_X component in km/s; (Bottom left) Current density in $\mu A/m^2$; and (Bottom right) β^* parameter (see text). The white lines show the $\beta^* = 0.7$ contours, which are used to define the simulation magnetopause location. The black thick curve shows the Shue magnetopause model (see text).

altered as other factors contribute to the CPCP. A residual potential exists even if the dayside reconnection is completely shut off (Axford and Hines, 1961), and the potential saturates at high levels of driving (Russell et al., 2001). The saturation potential value varies from study to study, but several authors have linked the process to low Mach number conditions in the solar wind (Lopez et al., 2010; Myllys et al., 2017; Lakka et al., 2018), typical of Interplanetary Coronal Mass Ejections (ICME) that are key drivers of geomagnetic storms (Kilpua et al., 2017).

In this paper, we return to the analysis of geomagnetic storms and their drivers using the SWMF Geospace model. Improving on the simulation studies referenced above, we include the ring current formation, which requires coupling the MHD code with a model for the drift physics processes in the inner magnetosphere (De Zeeuw et al., 2004), and which is critical in getting a realistic representation of the storm evolution (Liemohn et al., 2018).

We examine a statistical dataset of geomagnetic storm simulations. We compare and contrast the simulated values with those observed in order to discuss the performance of the coupling parameters and the dynamics of the solar wind–magnetosphere coupling. We first introduce the model, then present the simulation dataset, discuss the model performance, and compare the model with observed coupling functions. We then compare the model magnetotail configuration and magnetopause position with empirical formulations. We conclude with discussion.

Space weather modeling framework

The Space Weather Modeling Framework (SWMF) comprises a set numerical models to simulate plasma processes from the Sun to Earth's upper atmosphere and/or the outer heliosphere (Tóth et al., 2012; Gombosi et al., 2021). The simulation core is the Block-Adaptive-Tree-Solarwind-Roe-Upwind-Scheme (BATSRUS), which solves the 3-dimensional extended magnetohydrodynamic (MHD) equations in various forms (Powell et al., 1999). In the Geospace configuration (see Figure 1) BATSRUS is coupled to the Ridley Ionosphere electrodynamics Model (RIM, (Ridley et al., 2004)) as well as to the Rice Convection Model (RCM), a drift physics model for the inner magnetosphere ring current (Wolf et al., 1983). The Geospace configuration used in this study is similar to the one operationally used at the NOAA Space Weather Prediction Center (SWPC), and has been extensively tested and validated for numerical stability and robustness (Kwagala et al., 2020).

BATSRUS, configured to solve the semi-relativistic MHD equations, models the solar wind and the magnetosphere with an adaptive grid resolution ranging from 0.125 R_E in the near-Earth region to $8R_E$ in the distant tail. The simulation box covers the region from 32 R_E to −224 R_E in the X direction and ±128 R_E in the Y and Z directions in Geocentric Solar Magnetospheric (GSM) coordinates. The inner boundary is a spherical surface

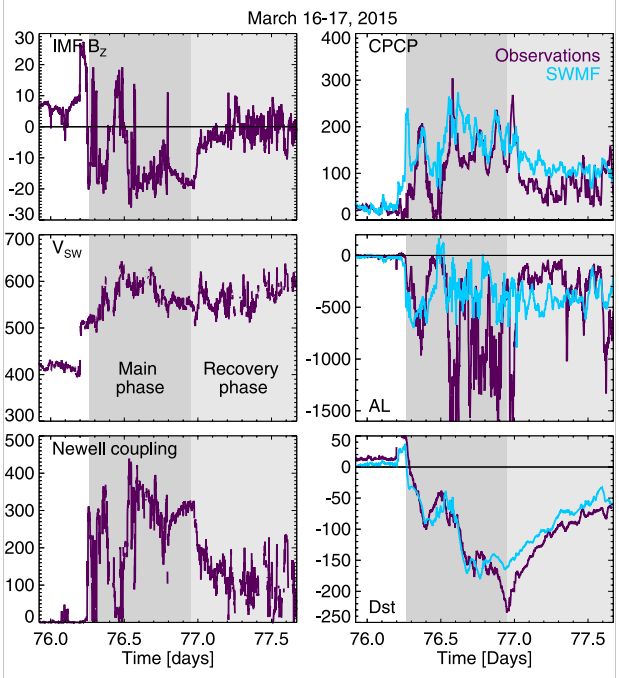

FIGURE 3
(Left panel) Solar wind driver parameters: (Top) IMF B_Z in nT; (Middle) solar wind speed in km/s; and (Bottom) Newell coupling function (arbitrary units, see text). (Right panel) Geomagnetic index response: (Top) Cross-polar cap potential in kV; (Middle) Auroral electrojet AL index in nT; and (Bottom) Storm Dst index in nT. The observed valueas are shown in dark blue, the SWMF simulation values in light blue. Storm main phase (from start of Dst decrease to peak Dst) and recovery phase (from peak Dst to storm end) are shown with darker and lighter gray shading, respectively.

at radial distance $R = 2.5\ R_E$. The Geospace setup uses the ideal MHD equations to describe the large-scale plasma dynamics in the solar wind and magnetosphere. The adaptive grid is fixed in time, selected to focus the highest resolution to close to the dayside boundaries and to the magnetotail where many of the smaller scale dynamic processes take place.

The Ridley Ionosphere electrodynamics Model (RIM) solves the Poisson equation for the electrostatic potential on a two-dimensional height-integrated ionospheric surface (Ridley et al., 2004). BATSRUS passes field-aligned currents from the simulation inner boundary to RIM, which uses them to derive the ionospheric conductance distribution in combination with the background conductances from the solar illumination characterized with the F10.7 index. RIM solves the Vasyliunas equation (Vasyliunas and McCormack, 1970) for the electric potential, and feeds the electric field back to BATSRUS to drive the inner boundary condition for the plasma velocity. RIM and BATSRUS are coupled at every 5 s.

The non-Maxwellian plasmas in the inner magnetosphere are modeled by the Rice Convection Model (RCM) that solves the bounce- and pitch-angle-averaged phase space densities for protons, singly charged oxygen, and electrons (Toffoletto et al., 2003). BATSRUS feeds the outer boundary condition and magnetic field configuration and RIM feeds the **E**×**B** drift speed to RCM. The RCM plasma density and pressure values are returned to BATSRUS, which relaxes MHD values towards the RCM values with a 20 s relaxation time (De Zeeuw et al., 2004). The 2-way coupling of BATSRUS with RCM and the one-way coupling of RIM to RCM are performed every 10 s.

This configuration can represent the dynamic response of the magnetosphere and ionosphere to the strong solar wind driving during geomagnetic storms. The RCM facilitates development of strong ring current (Liemohn M. W. et al., 2018), and the ground magnetic disturbances can be computed by Biot-Savart integration of the currents external to the Earth, using both the MHD and RIM domains (Yu and Ridley, 2008).

The Geospace model takes the solar wind plasma parameters (density, temperature, velocity, magnetic field), the F10.7 radio flux, and the dipole orientation as function of time as input and boundary conditions, and develops the magnetosphere from an empty dipole subjected to the observed solar wind which is fed in to the Sunward boundary of the simulation box.

The SWMF and the Geospace configuration numerical schemes are described in detail in (Tóth et al., 2012; Pulkkinen et al., 2013; Gombosi et al., 2021).

Statistical analysis of geomagnetic storms

We study a set of 131 geomagnetic storms with Dst minima below −50 nT identified from the time period 2010–2019 (Al Shidi et al., 2022, see Table 1). Each of the storms was run with the SWMF Geospace model described above, using the same model setup apart from the initial and boundary conditions given by the solar wind parameters and the F10.7 solar flux. The model outputs comprised the geomagnetic indices as well as noon-midnight and equatorial plane cuts of the 3D magnetosphere domain. Each of the storms was run from 6 h prior to onset for 54 h. While the ionospheric and geomagnetic index data was stored at 1-min intervals, the 2D magnetospheric output was saved at 15-min cadence.

Figures 2–4 show results from a sample storm that took place on March 16–17, 2015, and introduce the type of simulation results used in the following analysis. Figure 2 shows simulation results in the noon-midnight meridian plane with magnetopause identifications overlaid (see below).

Figure 3 shows the observed solar wind and IMF parameters as well as the geomagnetic indices compared with the simulation results shown in light blue. The storm main and recovery phases are indicated by the darker and lighter gray shading, respectively. The storm main phase is driven by strongly southward IMF as well as high-speed solar wind. The polar cap potential was of the order of 150 kV

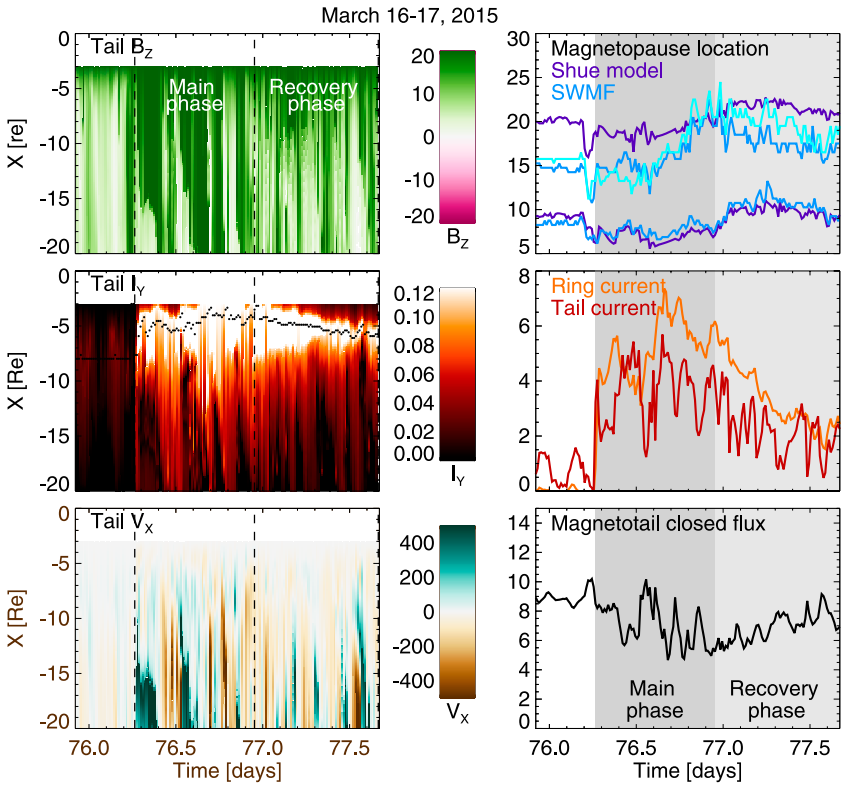

FIGURE 4
(Left panel) Simulation results along the magnetotail current sheet at the midnight meridian in a keogram format (see text for definition of the current sheet surface): (Top) Tail B_Z in nT; (Middle) Z-integrated current intensity (arbitrary units, see text) with current peak intensity location shown with the black dotted line; (Bottom) Plasma velocity V_X component in km/s. The storm main phase and recovery phases are defined by the dotted lines. (Right panel) Characteristic numbers for the magnetospheric state: (Top) Magnetopause nose at $Y = Z = 0$ and magnetopause distance from the X-axis at $Y = 0$, $X = -10R_E$. The Shue model is shown in dark blue, the SWMF Geospace values are shown in lighter blue. The southern lobe simulation value is shown with the lightest shade of blue; the Shue model is symmetric and gives the same value for northern and southern lobes. (Middle) Total ring current (orange) and tail current (dark red) integrated along the tail length in MA (see text); (Bottom) Closed magnetic flux through the magnetotail at midnight meridian (arbitrary units, see text). Storm main phase (from onset to peak Dst) and recovery phase (from peak Dst to storm end) are shown with darker and lighter gray shading, respectively.

during the main phase, and the observed AL index reached below −1500 nT. Characteristically to the SWMF Geospace simulation, the simulation AL does not reach such low values. However, the bottom panel shows the Dst index, which is highly correlated with that derived from the simulation.

The left panels of Figure 4 show the magnetospheric tail magnetic field, electric current, and plasma velocity along the tail current sheet center in the midnight meridian in a keogram format. The higher values of the magnetic field in the magnetotail are characteristics of tail field dipolarizations. The strong current in the inner tail represents the intensifying ring current during the storm main phase. The flow speed shows both tailward and Earthward flow periods–here it is especially important to remember that the noon-midnight meridian represents only one location in the tail, while the flows are highly structured in the cross-tail dimension.

The right panels show the magnetopause locations, ring and tail current intensities, and the integrated magnetotail flux. Note the compression of the magnetospheric size during the storm main phase, and the high level of correlation between the tail and ring currents. More detailed description of each of the parameters will be provided in later sections.

For each storm, we identified onset time as the time when the Dst index starts to decrease (i.e., not necessarily the time of impact of an interplanetary coronal mass ejection or ICME), a storm peak as the time of the Dst minimum, and an end indicating recovery of the Dst index, a second major depression of the Dst index indicating another period of main phase -like activity, or end of simulation period. Note that while we wish to exclude main phase -like behavior from the analysis of recovery phase phenomena, we recognize that individual storms can have complex structure with multiple activations. Note also that many of the simulations do not reach to the end of the

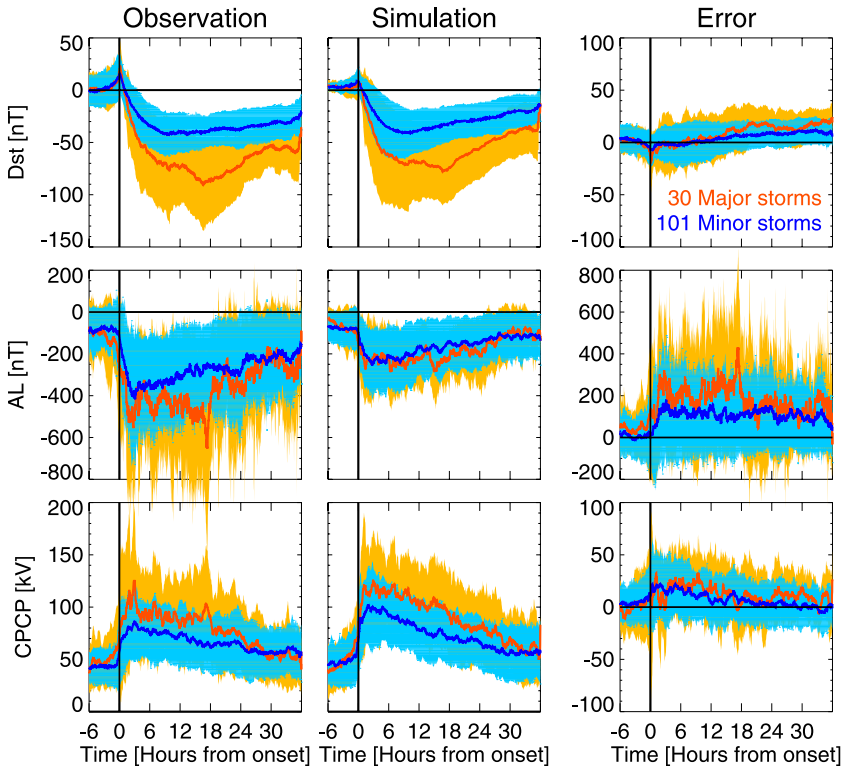

FIGURE 5
(Top row) Dst; (Middle row) AL; and (Bottom row) CPCP from (Left column) Observations; (Middle column) Simulation; and (Right column) Error (simulation−observation) for minor (blue, peak Dst > −100 nT) and major (red, peak Dst < −100 nT) storms. The thick solid lines show the superposed epoch curve (1-min temporal resolution), the shadings indicate the standard deviation.

observed recovery phase. Furthermore, storms were categorized into two groups, "major storms" with peak Dst below −100 nT and "minor storms" with Dst peak between −50 and −100 nT, following often-used convention.

The full set of storms is represented in the form of a superposed epoch analysis. Figure 5 shows superposed epoch curves for the major (in red) and minor (in blue) storms with the standard deviation (orange/light blue shading) indicating the variability in each category. The superposition was done aligning the onset times, but time is not scaled to account for the main phase duration. The top row shows the ring current (Dst) index, the middle row the auroral electrojet (AL) index, and the bottom row shows the cross-polar cap potential (CPCP) from the northern hemisphere. The left column shows the observed indices extracted from the OMNI database (htpps://omniweb.nasa.gov); the CPCP values are computed using the formulation from (Ridley et al., 2004) as a function of the polar cap index (PCI) measured in the northern polar cap (Thule station) and season as

$$CPCP = 29.28 - 3.31\sin(T + 1.49) + 17.81PCI \qquad (1)$$

where the time of year is scaled as $T = 2\pi(N_{MONTH}/12)$ and the numbering of months starts from zero (Jan = 0). The middle column shows the simulated values, while the right column show the difference between the simulated and observed values, i.e., the model error and its variance.

The simulations of the major and minor storms give quite good prediction of the Dst index, with relatively moderate errors between the model and observed values. The errors are closest to zero during the storm start and main phase, while they systematically increase (more for the major storms) during the recovery phase. This indicates that the Geospace model has a tendency to predict smaller Dst disturbance during the recovery phase, i.e., recover faster than the observed Dst.

The AL index has large variability in observations, while the values and the variability are much smaller in the simulation. Consequently, the errors are large with no systematic trend during the storm for minor storms, but a tendency for larger errors during the storm main phase than during the recovery phase for major storms. For strong AL activity, the Geospace model AL indices are substantially weaker than the observed ones. Furthermore, as accurate modeling of individual substorms still poses a major challenge to the simulations, the timing differences in the substorm evolution cause large instantaneous errors in the observed and model values.

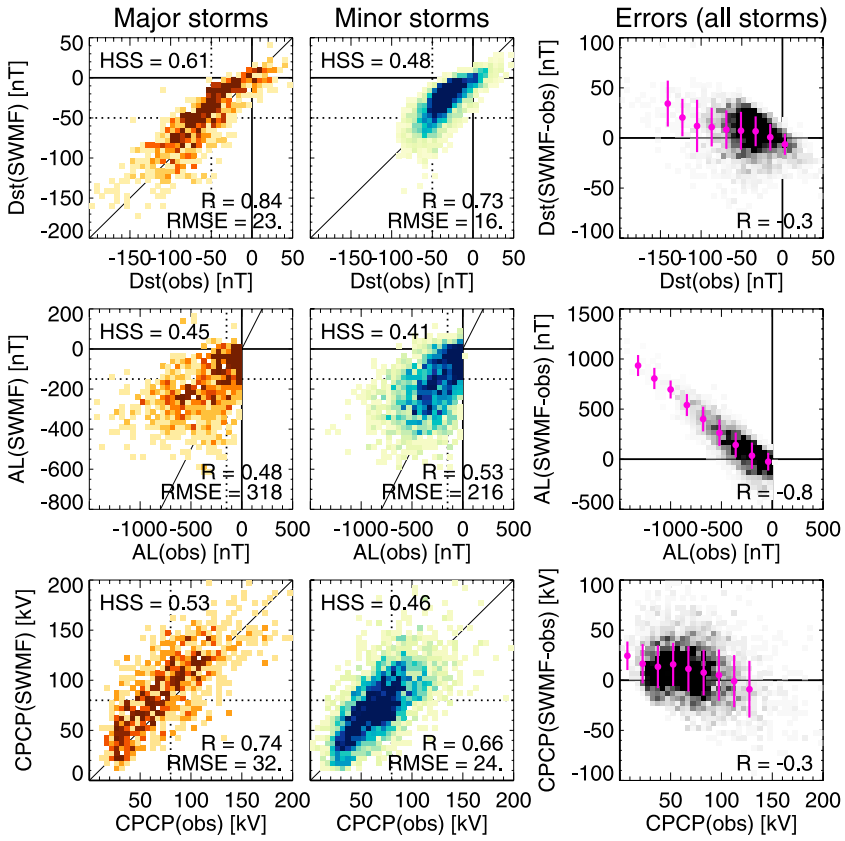

FIGURE 6
Heat map plots showing hourly values of (Top row) Dst; (Middle row) AL; and (Bottom row) the CPCP observed vs. simulated values, for (Right column) major storms and(Center column) minor storms. The unity line is shown in thin solid line, the dotted linesshow the threshold values used in the Heidke Skill Score (HSS) calculation (see text).The heat maps indicate the share of points falling in each bin. (Right column) Errors(simulated – observed value) as function of the observed values. The magenta dotsshow bin averages, and the vertical thin lines indicate the standard deviation in eachbin.

The simulated polar cap potentials are somewhat larger than those obtained from the empirical model, and furthermore show a larger difference between the averages of the major and minor storms. The errors are largest during the main phase, while close to zero during the recovery phase. This means that the simulation predicts larger polar cap potentials than the empirical model, indicative of either stronger dayside merging or weaker tail reconnection during the storm main phase.

Model performance

The model performance can be assessed by computing skill scores for the geomagnetic index predictions. The Heidke skill score (Heidke, 1926) is one often used performance measure for geomagnetic index predictions, and is defined as

$$\mathrm{HSS} = \frac{2(H \cdot N - M \cdot F)}{(H+M)(M+N)+(H+F)(F+N)}, \qquad (2)$$

where H = hit, M = miss, F = false positive, and N = true negative, which are evaluated based on the observation and prediction values being above or below the selected thresholds. The HSS maximum value for no misses and no false positives is 1, value of zero indicates no skill, and negative values indicate skill worse than chance coincidence.

Figure 6 shows heat map plots of hourly averaged index values for Dst, AL, and the polar cap potential, as well as the errors as function of the observed index values (right column). The left and middle column show the major and minor storms separately. The dotted lines indicate the chosen "event" values for the Heidke skill score calculation (−50 nT for Dst, − 150 nT for AL, and 80 kV for the CPCP). While changing the selected "event" values somewhat changes the skill scores, our conclusions are independent of the exact values of the limits.

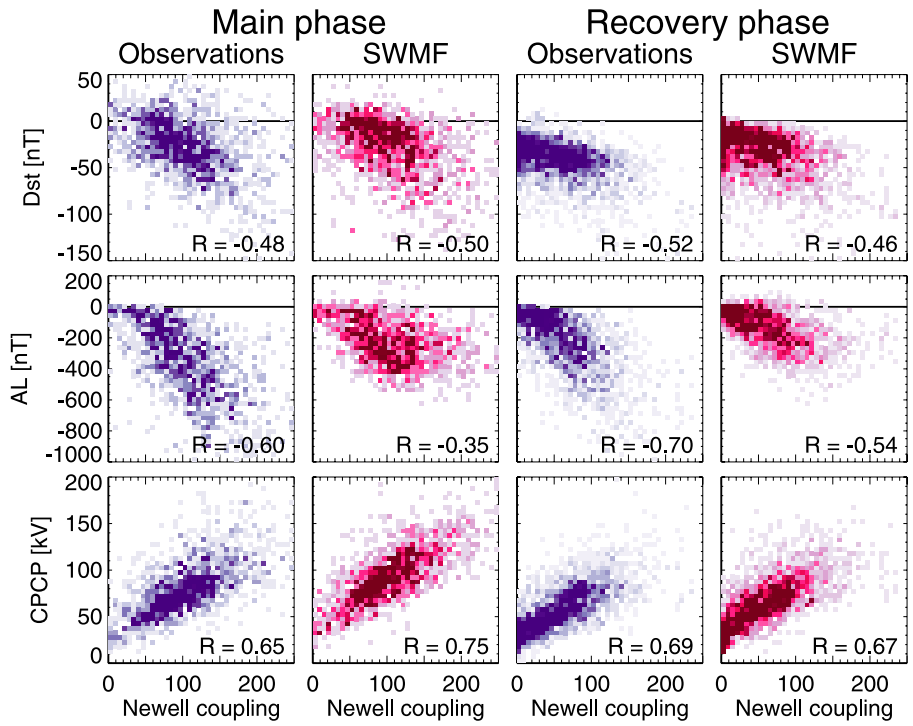

FIGURE 7
(Top row) Dst; (Middle row) AL; and (Bottom row) CPCP during (Left two columns) the storm main phase and (Right two columns) recovery phase as function of the Newellcoupling function (in arbitrary units) using 1-hour averaged data for observations (darkpurple) and simulations (dark red). The heat maps indicate the share of points falling ineach bin.

The Heidke skill score for the major storms is HSS = 0.61, which is somewhat better than the value 0.57 obtained by (Liemohn M. W. et al., 2018), who computed skill scores for a 3-month period including both storm and nonstorm times. The skill for the smaller storms is lower (0.48). Furthermore, the skill scores for the AL and the CPCP are lower, showing similar difference between major and minor storms. Comparison between minor and major storms and with the Liemohn et al. (2018) results indicate that the Heidke skill scores are larger for data sets that contain sufficient number of data points in the "hit" quadrant.

The plots also indicate the values of the commonly used Pearson linear correlation coefficient defined as the ratio of the covariance and the product of the standard deviations of each set (o = observation, m = model:

$$R = \frac{\sigma_{mo}}{\sigma_m \sigma_o} \tag{3}$$

where the covariance is given by $\sum_i (m_i - < m >)(o_i - < o >)/(N-1)$ and the variance (square of the standard deviation) is given by $\sum_i (x_i - < x >)^2/(N-1)$, and $< x > = \sum_i x_i/N$ denotes the mean for $x = m, o$.

The right column shows the errors (simulation–observation) as function of the observed values. All errors show a tendency to increase with increasing level of activity, but for Dst and CPCP, the effect is relatively minor. On the other hand, the error in AL is strongly and almost linearly dependent on the intensity of the AL index throughout the higher values of the observed AL. This indicates that the simulation value is smaller than the predicted value by a factor dependent on the intensity of the (observed) activity. While the scatter in the values is still large, the model predictive performance could be improved by accounting for this persistent behavior.

Solar wind driver

Most geomagnetic activity predictions rely on empirical relationship between the driving solar wind and interplanetary magnetic field and the resulting geomagnetic activity. The Newell coupling function (Newell et al., 2007), representing the rate of change of magnetic flux at the nose of the magnetopause, is given by

$$\frac{d\Phi_{MP}}{dt} = \alpha \left[V^2 B_T \sin^4\left(\frac{\theta}{2}\right) \right]^{2/3} \tag{4}$$

where $\theta = \tan^{-1}(B_Y/B_Z)$ is the IMF clock angle and $B_T = (B_Y^2 + B_Z^2)^{1/2}$ denotes the transverse component of the

TABLE 1 Storm onset dates for events used in this study. For more detailed documentation see (Al Shidi et al., 2022) and the data availability statement.

20100214	20120312	20130705	20150512	20160402	20181104
20100405	20120315	20130705	20150518	20160407	20190316
20100411	20120315	20130709	20150607	20160412	20190510
20100501	20120327	20130713	20150621	20160416	20190513
20100527	20120404	20131001	20150622	20160507	20190804
20100803	20120422	20131008	20150704	20160604	20190830
20101010	20120602	20131030	20150722	20160801	20190926
20110204	20120610	20131106	20150815	20160823	
20110214	20120616	20131108	20150815	20161012	
20110301	20120708	20131110	20150825	20161221	
20110309	20120714	20131207	20150907	20170301	
20110406	20120901	20140218	20150908	20170326	
20110411	20120930	20140223	20150919	20170527	
20110528	20121007	20140227	20151003	20170716	
20110805	20121012	20140410	20151006	20170830	
20110909	20130116	20140507	20151018	20170906	
20110916	20130125	20140607	20151102	20170927	
20110925	20130228	20140826	20151106	20171106	
20110926	20130317	20140912	20151130	20180318	
20111024	20130320	20150107	20151219	20180419	
20120121	20130430	20150216	20160215	20180505	
20120124	20130517	20150316	20160216	20180531	
20120218	20130524	20150409	20160305	20180825	
20120306	20130606	20150409	20160306	20180910	
20120308	20130627	20150414	20160314	20181007	

magnetic field perpendicular to the Sun-Earth line. While a normalizing factor $\alpha \sim 10^3$ is needed to get the coupling function in units of Wb/s, here we show the coupling intensity as unnormalized ($\alpha = 1$) and thus in arbitrary units.

Figure 7 shows the geomagnetic indices as function of the Newell coupling function separately for the main phase and recovery phases for all storms. The data are averaged to 1-h bins, which should remove most scatter associated with timing errors of the arrival time of the solar wind front at the subsolar bow shock. Correlations are shown both for observations (dark purple) and simulation results (magenta). The correlations don't show significant differences between the main and recovery phases, but the scatter during the recovery phase is somewhat smaller.

Essentially, the distribution of points for the observations and the simulation look similar. This indicates that the simulation is doing as good a job in the prediction as the observations. On the other hand, despite the simulation being deterministic, it does not provide better correlations. This fact emphasizes that better observations will not lead to improved correlations (as the simulation can use data from any point), and that improving the predictions requires better coupling functions (with inclusion of time history of the solar wind driver and magnetospheric state).

Magnetotail configuration

Using two-dimensional cuts in the simulation saved at 15-min cadence, we examine the properties at the center of the current sheet along the midnight meridian. The current sheet center is defined as the point with minimum B_X between the lobes for each X-value along the tail, which in a simple geometry coincides with the peak of the current intensity. At times, the current sheet is bifurcated tailward of a large-scale neutral line. In such cases, the algorithm chooses one or the other branches and uses those values as the current sheet center. This choice does not significantly impact our results that focus on the inner magnetosphere.

For each storm and each time step, we identify the current sheet center location Z_{CS} along the midnight meridian, plasma velocity V_X, magnetic field B_Z, and current j_Y at the current sheet center, and integrate the total current ($J_Y(X) = \int j_Y dZ$) across the current sheet thickness. We extend the analysis out to $X = -20R_E$.

Furthermore, we identify the location of the innermost X-line, X_{NL}, from a B_Z sign change, and calculate the amount of closed magnetic flux through the tail from

$$\Phi_C = \int_{X_{NL}}^{-3R_E} B_Z dX \tag{5}$$

where the limit at $-3R_E$ is close to the inner boundary of the simulation domain. As the analysis is limited to $X > -20R_E$, for situations where the X-line is further than that, we set $X_{NL} = -20R_E$ (the flux crossing the equatorial plane beyond that distance is small and would not cause significant changes to the results). Furthermore, as the magnetic flux is generally defined as magnetic field through an area, and we are limited here to the two-dimensional noon-midnight plane (i.e. flux per unit cross-tail width), we show the closed flux in arbitrary units focusing on time variations rather than absolute values.

While the distinction between tail and ring current is arbitrary as well in observations as in the simulation, we denote the current inside of 8 R_E as the "ring current" and the current tailward of 8 R_E as "tail current". Similarly to the magnetic flux, we integrate the total ring and tail currents crossing the midnight meridian as

$$I_{RING} = \int_{-8R_E}^{-3R_E} J_Y(X) dX \tag{6}$$

$$I_{TAIL} = \int_{-20R_E}^{-8R_E} J_Y(X) dX. \tag{7}$$

Figure 8 shows the relationship of the ring current, tail current, and closed flux with the Dst index and the cross-polar cap potential. The good correlation between the ring

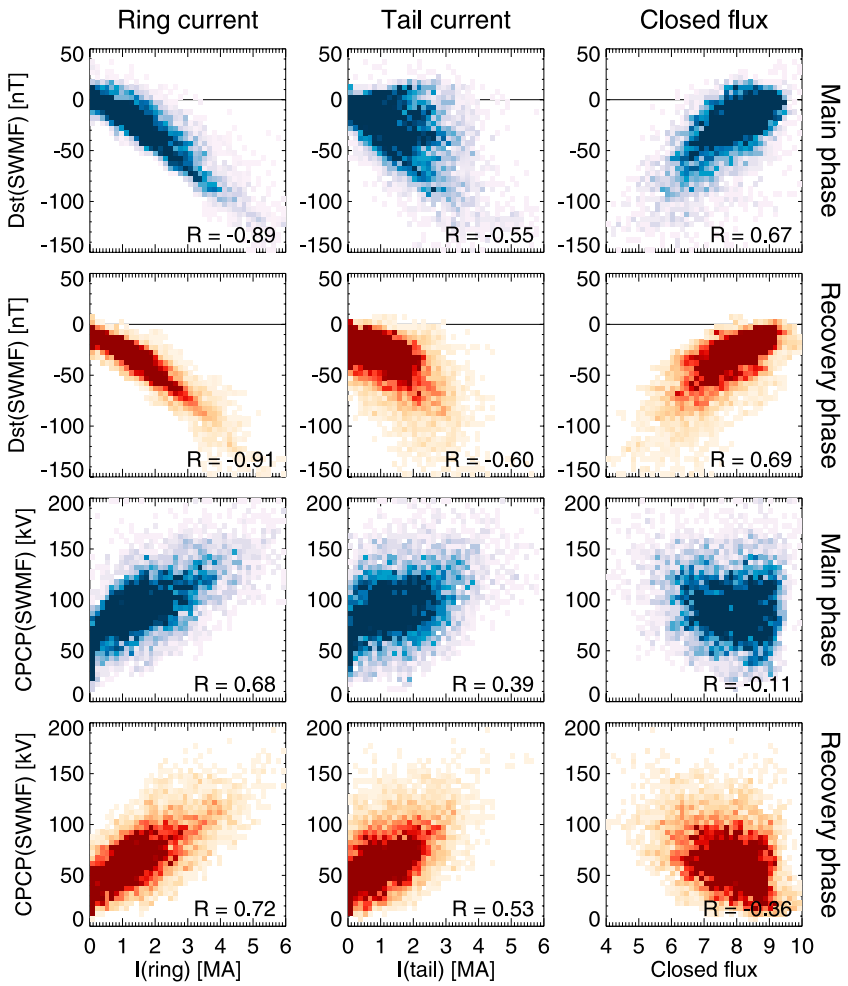

FIGURE 8
(Top two rows) Dst and (Bottom two rows) CPCP from the SWMF simulation as function of (Left column) total ring current; (Middle column) total tail current; and (Right column) Closed magnetic flux in the tail (see definitions given in the text). The storm main phase (blue) and recovery phase (orange) are shown separately. The data are snapshotstaken at 15-min cadence in the magnetotail, tagged with the 30-min smoothed values ofthe indices. The heat maps indicate the share of points falling in each bin.

current and the Dst index shows that, indeed, the Dst index is a good (albeit not strictly linear) measure of the ring current. The ring current intensity for the same value of Dst is higher during the main phase than during the recovery phase, which likely comes from the positive contribution to Dst from the dayside compression, which is often larger during the main phase than during the recovery phase. The amount of closed flux along the midnight meridian is likewise well correlated with Dst, linking the decrease of tail magnetic flux to the intensification of the ring (and tail) currents.

The tail current shows a larger variability, but still clear correlation with the Dst index, indicating that the currents even beyond $-8R_E$ contribute to the index in a significant way.

As the polar cap potential is quite directly driven by the changing solar wind driver, correlations with the CPCP indicate directly driven processes. It is evident that the ring current is more directly driven (i.e. has better correlation with the CPCP than the tail current, or the closed magnetic flux, that shows very low if any correlation with the polar cap potential).

Figure 9 shows the ring current and the Dst index from the simulation as functions of the Newell coupling parameter. The coupling parameter was smoothed by a 30-min filter before tagging the values to the simulation values. If the coupling parameter were a perfect indicator of the state of the magnetosphere, one would expect a very high correlation, as the simulation itself is a self-consistent, fully deterministic system. If the coupling function is not a perfect

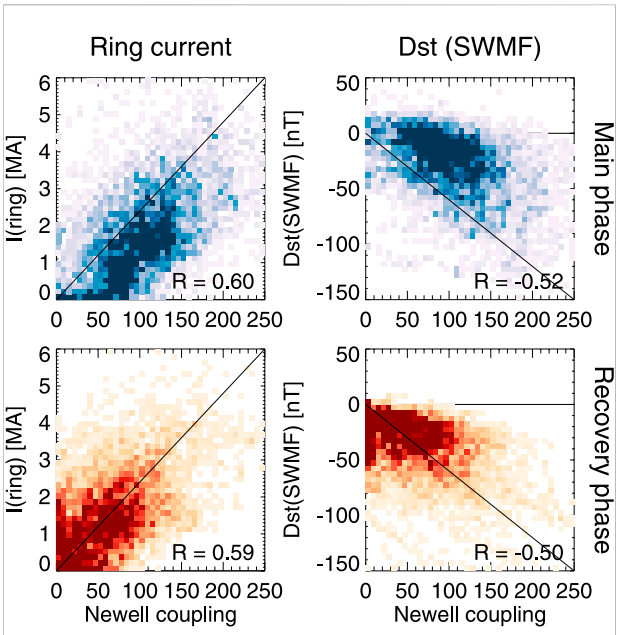

FIGURE 9
(Left) Total ring current and (Right) the simulation Dst during the main phase (top row) and recovery phase (bottom row) as function of Newell coupling function (in arbitrary units). The data are snapshots taken at 15-min cadence in the magnetotail, tagged with the 30-min smoothed values of the driver intensity. The heat maps indicate the share ofpoints falling in each bin.

predictor of the ring current, there are other factors than those included in the coupling function that affect the state of the ring current. As can be seen in the figure, the scatter in these parameters is large, indicative of the complexity of the processes and the significance of prior history both of the driver and of the magnetospheric dynamics not included in a point-by-point correlations. This complexity of course reflects on the scatter between the driver function and the geomagnetic indices discussed above. This conclusion remains valid even if we acknowledge that the simulation is not a perfect model of the true magnetospheric plasma system.

The coupling function comparison between the storm main and recovery phases is an indicator of the effects of time history to the correlations. The ring current intensity for similar level of driving is slightly higher for the recovery phase (likely indicating a higher preceding values of the current). Comparing to the Dst index, the difference is even more significant, highlighting the effects of the dayside processes on the Dst index. For the closed flux and cross-polar potential there is no difference in the distributions during storm main and recovery phases (not shown).

Dayside boundary locations

The size of the magnetosphere is often characterized by the subsolar magnetopause location, which together with the flaring

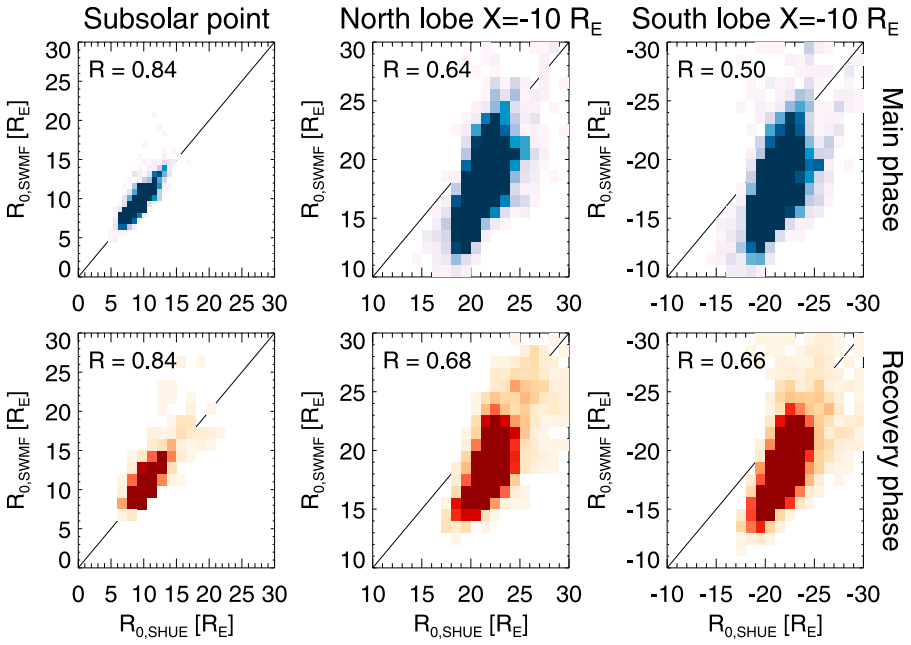

FIGURE 10
SWMF magnetopause location vs. the Shue model. (Left) Magnetopause subsolarposition *X*-value for *Y = Z = 0*. (Middle) North lobe magnetopause position *Z*-value at *Y = 0, X = -10 R_E*. (Right) South lobe magnetopause position *Z*-value at *Y = 0, X=-10 R_E*. (Top row) storm main phase, (Bottom row) storm recovery phase. The heat maps indicate the share of points falling in each bin.

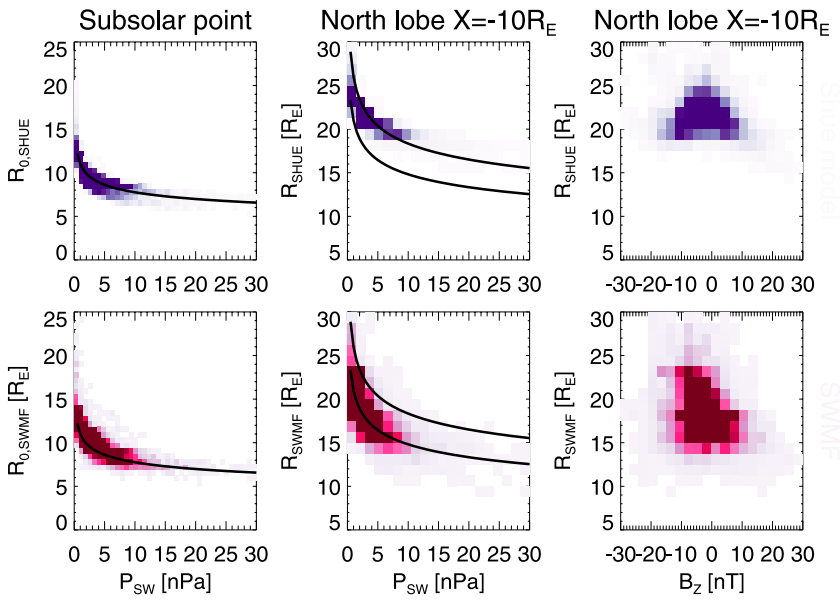

FIGURE 11
Magnetopause location vs solar wind driver parameters during the storm main phase. (Left) Magnetopause subsolar position X-value for $Y = Z = 0$ as function of solar wind dynamic pressure. (Middle) North lobe magnetopause position Z-value at $Y = 0$, $X = -10\ R_E$ as function of solar wind dynamic pressure. (Right) North lobe magnetopause position Z-value at $Y = 0$, $X = -10\ R_E$ as function of IMF B_Z. (Top row) The Shue model values are shown in blue, (Bottom row) the SWMF values are shown in red. The black lines show the Shue model functional dependence on dynamic pressure ($P^{(-1/6.6)}$) using arbitrary scaling.

angle describes the shape of the boundary in the downwind direction. Statistical analyses yielded an empirical relationship (Shue et al., 1997), revised for extreme periods (Shue et al., 1998) to the form

$$R = R_0\left[\frac{2}{1+cos(\theta)}\right]^{\alpha}, \tag{8}$$

$$R_0 = [10.22 + 1.29\tanh(0.184(B_Z + 8.14))]P^{-1/6.6}, \tag{9}$$

$$\alpha = (0.58 - 0.007B_Z)[1 + 0.24\ln(P)]. \tag{10}$$

The subsolar magnetopause nose distance from the Earth R_0 is given in R_E when the IMF B_Z is given in nT and the solar wind pressure P in nPa. The model assumes cylindrical symmetry, and produces a flaring magnetotail with the degree of flaring controlled by the factor α dependent on both IMF B_Z and dynamic pressure P.

We determined the magnetopause location from the 2D simulation cuts in the noon-midnight meridian plane using the open-closed field line boundary (in the dayside) and a parameter $\beta^* = 2\mu_0(P_{th} + P)/B^2$, which on the nightside shows a clear boundary between the dense magnetosheath with high $\beta^* > 1$ and the low-density, high-field magnetotail lobe with low $\beta^* \ll 1$ (see bottom left panel of Figure 2; Brenner et al., 2021). In determining the boundary location, we used a limit value of $\beta^* = 0.7$, but changing the limit value causes minimal changes to the outcome. Figure 2 shows the magnetopause definition overlaid with other parameters. This definition agrees with a velocity shear region at the high latitude tail magnetopause as well as follows closely the peak magnetopause currents.

Figure 2 also shows how the two magnetopause definitions agree during the storm main phase: The subsolar locations are close to each other, but the Shue model flares much more than the magnetopause defined using the β^* parameter in the simulation. This is true more generally beyond the individual time step shown here: Figure 4 shows time series for the subsolar point location as well as two individual points at $X = -10R_E$ at the northern and southern tail lobes. While the subsolar locations agree for most of the time, the magnetotail size in the SWMF is smaller than that predicted by the Shue model throughout the storm with the exception of a short interval near the end of the main phase of the storm. Note also that the simulation magnetopause has a lot of small-scale variability, which is not always symmetric between the northern and southern lobes, indicating that the internal magnetospheric dynamics and the changing dipole tilt angle also contribute to the shape of the magnetopause.

Figure 10 shows a statistical comparison of the subsolar and high-latitude ($Y = 0$, $X = -10R_E$) tail magnetopause locations identified from the Geospace simulation and obtained from the Shue model using the formulation above. While there is a general correlation, there are clear deviations between the models.

For the subsolar point, the models agree very well. However, generally the SWMF magnetopause values are slightly larger than the Shue model values. There are a few isolated occurrences where the SWMF values are considerably higher than those predicted by the Shue model. All of those occur during periods of very low solar wind density and moderate solar wind speed combined with negative IMF B_Z, and low Alfvén Mach numbers (< 4).

The center and right panels show the magnetopause position at $Y = 0$, $X = -10R_E$. At the high-latitude magnetotail, the magnetopause in SWMF is typically much closer to the Sun-Earth line than the Shue model for strongly driven conditions (smallest sizes of the magnetosphere). For more average driving conditions (and during the storm recovery phase), the difference diminishes, but the majority of Shue model values still fall below the Geospace ones.

Lastly we examine the magnetopause location dependence on the IMF driver parameters. Figure 11 shows the subsolar and north tail lobe locations as function of solar wind dynamic pressure and IMF B_Z component. The black curves show the functional dependence of the Shue model (proportional to $P^{-1/6.6}$) to guide the eye (not a fit to the points). It is clear that the functional dependence for the subsolar location is similar for both the Shue model and the SWMF Geospace results, as the distributions almost completely overlap. However, for the tail lobe location, the functional form seems to still be valid for the SWMF results (with large scatter), but the flaring angle formula, which also includes dynamic pressure, changes that for the Shue model. Thus, the solar wind dynamic pressure response of the simulation differs from that given by the Shue formulation, leading to less flaring tail and smaller tail lobe cross-sectional area.

The right panel of Figure 11 showing the tail lobe magnetopause dependence on the IMF B_Z documents that the magnetopause dependence on that parameter is at best weak. The largest magnetopause distances (largest flaring) is obtained when B_Z is close to zero, while both highly negative and highly positive IMF B_Z lead to compressed magnetosphere–much more so for the SWMF than for the Shue model.

Discussion and conclusion

In this paper, we show results from the first large-scale statistical set of geomagnetic storm simulations developed by Al Shidi et al. (2022). We focus especially on comparing the geomagnetic indices with observed values as well as their dependence on the solar wind driver functions. While we did not have sufficient storage space to store all 3D simulation data, we focus on the 2D noon-midnight plane cuts and examine the magnetotail parameters along the tail current sheet center as well as the magnetopause locations at the dayside and in the magnetotail.

The statistical results can be used to infer the characteristic behavior of the SWMF Geospace simulation in a quantitative manner. All the examined indices (Dst, AL, CPCP) show behavior that is different during the storm main phase and recovery phase: For Dst, the error (simulated–observed value) is smallest during the main phase and increases systematically toward the recovery phase, while the opposite is true for the AL and CPCP. Thus, the model Dst index recovers faster than the observed one, indicating that further modeling or parametrization of the ring current decay processes could improve the model performance. Such processes could either be related to charge exchange and Coulomb collisions (Dessler and Parker, 1959; Fok et al., 1995) the wave-particle interactions scattering the ions away from the ring current (Jordanova et al., 2001; Yue et al., 2019), multi-ion physics (Daglis, 2006) or ion outflow from the ionosphere (Glocer et al., 2012). Regarding model performance metrics, the results in this paper, focusing solely on storm periods, are slightly better in terms of the HSS than those obtained by (Liemohn M. et al., 2018), who used 3 months of real-time simulation containing both quiet and storm periods, but dominated by quiet periods.

The AL index shows a consistent offset from the observed value, which calls for further investigation of the auroral electrodynamics and magnetosphere–ionosphere coupling processes, including the acceleration region processes (Liemohn et al., 2002; Connor et al., 2016). Especially, the model has poor capability to reproduce the largest AL values, with the simulated values mostly limited to above −800 nT; the same is true for comparison with local magnetic perturbations (Al Shidi et al., 2022). Furthermore, the instantaneous values of the AL index are critically dependent on timing of the substorm onsets and hence magnetotail dynamic processes, which still are difficult to reproduce to high accuracy in location and timing (Newell et al., 2016; Maimaiti et al., 2019).

The auroral conductances regulate the closure of the field-aligned currents through the Hall and Pedersen currents in the ionosphere (Iijima and Potemra, 1976; Ridley et al., 2004). In general, auroral conductance arises from the solar EUV radiation in the dayside and from energetic particle precipitation to the auroral oval region especially in the nightside (Fuller-Rowell and Evans, 1987; Newell et al., 2009). In the SWMF simulation, the auroral conductances are derived from a simple empirical parametrization, which may in part lead to weaker coupling of the magnetotail currents into the ionosphere. Mukhopadhyay et al. (2020) examined the conductance effects on the coupling, and propose a new model for the auroral conductances, which has been coupled to the SWMF simulation. The CMEE model for auroral conductances allows for a larger range of values, which lead to lower cross-polar potential values (as a result of currents closing between R1 and R2 currents), and larger ground magnetic perturbation values (Mukhopadhyay et al., 2020). However, accurate modeling of both the diffuse and discrete sources and inclusion of their ionospheric impacts into the global simulations is still work in progress (Mukhopadhyay et al., 2022).

The polar cap potential is a central parameter describing the balance between dayside and nightside energy conversion processes, but observationally we are limited to radar (model-based) estimates of the convection (Koustov et al., 2009; Gao, 2012), low-Earth orbit satellite electric field measurements (Hairston et al., 1998), or empirical models based on the polar cap index (Troshichev et al., 1996; Ridley et al., 2004). The Ridley epirical model (Ridley et al., 2004) has quite high correlation with the simulated polar cap potential time series, with the simulation producing slightly higher potentials especially during the storm main phase. The Ridley model based on the PCI is quite directly driven by the solar wind and IMF parameters, as is the simulation polar cap potential. Better global observations of the CPCP evolution are needed to fully understand the role of the detailed magnetospheric processes on the polar cap potential evolution.

The anticorrelation of the errors between the polar cap potential and the AL index indicates that the current closure processes between the ionosphere and the magnetosphere could be further optimized in the simulation. It seems that sometimes the magnetotail reconnection is not sufficiently strong to balance the dayside energy input, leading to weaker auroral currents (and hence AL) and stronger polar cap potential (larger lobe flux) (Milan et al., 2003; Lockwood et al., 2009).

An important part of empirical predictions of the magnetospheric and ionospheric states is the use of coupling functions that tie the solar wind parameters to their geomagnetic response. For example, assuming that a solar wind coupling function is able to predict the ring current intensity, a deterministic simulation should always yield a good correlation. On the other hand, data contain many uncertainties: the solar wind input from L1 may be different than that impacting the Earth, and the Dst index is an indirect measure of the true ring current and may miss localized signatures. Therefore, even for a perfect coupling parameter, one would expect to have scatter in the results. Our results show that the distributions of the deterministic model and the observations are similar. This indicates that the scatter in the results arises largely from the inability of the simple coupling parameter to represent the complex solar wind–magnetosphere coupling and its time history, and that their predictive power cannot be further increased with a denser observational network. The magnetospheric processes as well as the time history of the system have quite strong effects on the system response, which yield high level of scatter in the correlation figures (see Figure 7, (Tsyganenko and Sitnov, 2005)). It also points out to the usefulness of a physics-based model over a prediction based on solar wind input only.

Analysis of the nightside ring current and tail current intensities shows that the ring current is highly correlated with the Dst index, but that there is a difference between the storm main and recovery phases. This likely stems from the dayside positive contribution to the Dst index, which is higher during the main phase. It is also noteworthy that the tail current and ring current intensities are highly correlated, and that they are of almost equal magnitude during the storm main phase, while the ring current starts to dominate during later phases of the storm, consistent with earlier observational and empirical model studies (Ganushkina et al., 2005; Kalegaev and Makarenkov, 2008). In our study, the "ring current" was arbitrarily defined as the current inside 8 R_E, which is the domain covered by the RCM drift physics model, while the "tail current" was taken to be everything tailward of that. The results are not sensitive to the exact separation distance.

The subsolar distance to the magnetopause is largely determined by the solar wind dynamic pressure, but the orientation and magnitude of the IMF, the time history of the solar wind, as well as internal state of the magnetosphere cause substantial scatter to the results. The Geospace model gives quite good agreement with the empirical (Shue et al., 1998) model developed using a statistical database of magnetopause crossings, but the results along the magnetopause flank vary quite a bit from the empirical paraboloid shape. Especially during highly compressed situations (high dynamic pressure), the Geospace simulation gives significantly smaller distances from the Sun-Earth line to the lobe boundary than the empirical model.

Shukhtina et al. (2004) derived the magnetopause location using both solar wind parameters and tail magnetic flux derived from the Geoatail measurements, parametrizing the tail flaring angle. They demonstrate the strong dependence of the size of the magnetosphere on the internal state of the magnetosphere, by examining quiet periods, periods close to substorm onset, and periods of steady magnetospheric convection, which are characterized by enhanced, steady-state convection in the magnetotail, an expanded polar cap and enhanced lobe magnetic flux content (Sergeev et al., 1996).

Gordeev et al. (2015) performed an extensive comparison of global MHD simulations of the Earth's space environment using the Community Coordinated Modeling Center (CCMC) resources and four different MHD simulations, including BATSRUS, the MHD simulation core of the SWMF Geospace model used in this study. When comparing the results in that paper with our results, two things must be pointed out: (1) the Gordeev et al. (2015) study used the MHD simulations without coupling to an inner magnetosphere model, which significantly alters the "memory" of the magnetosphere, when the ring current response is not included, and (2) the comparison was made using an artificially created solar wind time series including constant solar wind and a constant IMF that flipped from B_Z northward to B_Z southward after 2 h of northward IMF. In our case, we have simulated real events, which involve all the complexities of true solar wind driver characteristics. The Gordeev et al. (2015) study shows that the pure BATSRUS gives a subsolar location that is very highly correlated with the Shue et al. (1998) model, with even higher correlation coefficient (0.95) than that found in this study, and BATSRUS was the best-performing simulation of the four examined in that metric. They also showed that BATSRUS produces good agreement with the Lin et al. (2010) model of the high-latitude magnetotail boundary. That model provides a more detailed

description of the tail boundary including effects of the dipole tilt angle in addition to the solar wind and IMF parameters.

In conclusion, we show results from a first large statistical study of storm simulations using the SWMF Geospace model. The results help assess the usability of the geomagnetic indices, the solar wind driver functions, and point further to magnetotail parameters that could be used to define the state of the magnetosphere.

Data availability statement

The datasets analyzed for this study can be found in the University of Michigan Deep Blue repository under: Al Shidi et al. (2022). Space Weather Modeling Framework simulations of ground magnetometer data [Data set], University of Michigan - Deep Blue Data. DOI: https://doi.org/10.7302/dkjd-1j05 under Creative Commons license http://creativecommons.org/licenses/by/4.0/.

Author contributions

TP did the analysis and wrote majority of the analysis. AB developed the methods and helped analyze the 2D data. QA developed methods and helped analyze the geomagnetic index data. GT advised on the use of the Geospace simulation.

Funding

NSF grant 2033563 supported analysis of the storm simulation results on solar wind entry into the magnetosphere and developing the analysis methodology. NASA grant 80NSSC21K1753 supported running the simulations and analysis of the results.

Conflict of interest

The authors declare that the research was conducted in the absence of any commercial or financial relationships that could be construed as a potential conflict of interest.

Publisher's note

All claims expressed in this article are solely those of the authors and do not necessarily represent those of their affiliated organizations, or those of the publisher, the editors and the reviewers. Any product that may be evaluated in this article, or claim that may be made by its manufacturer, is not guaranteed or endorsed by the publisher.

References

Akasofu, S.-I. (1981). Energy coupling between the solar wind and the magnetosphere. *Space Sci. Rev.* 28, 121–190. doi:10.1007/bf00218810

Al Shidi, Q., Pulkkinen, T. I., Brenner, A., Toth, G., and Gjerloev, J. (2022). Can simulations predict ground magnetic perturbations? *Space Weather.* submitted.

Axford, W. I., and Hines, C. O. (1961). A unifying theory of high-latitude geophysical phenomena and geomagnetic storms. *Can. J. Phys.* 39, 1433–1464. doi:10.1139/p61-172

Borovsky, J. E., and Birn, J. (2014). The solar wind electric field does not control the dayside reconnection rate. *J. Geophys. Res. Space Phys.* 119, 751–760. doi:10.1002/2013JA019193

Brenner, A., Pulkkinen, T. I., Al Shidi, Q., and Toth, G. (2021). Stormtime energetics: Energy transport across the magnetopause in a global MHD simulation. *Front. Astron. Space Sci.* 8, 180. doi:10.3389/fspas.2021.756732

Burton, R. K., McPherron, R. L., and Russell, C. T. (1975). An empirical relationship between interplanetary conditions and Dst. *J. Geophys. Res.* 80, 4204–4214. doi:10.1029/ja080i031p04204

Connor, H. K., Zesta, E., Fedrizzi, M., Shi, Y., Raeder, J., Codrescu, M. V., et al. (2016). Modeling the ionosphere-thermosphere response to a geomagnetic storm using physics-based magnetospheric energy input: OpenGGCM-CTIM results. *J. Space Weather Space Clim.* 6, A25. doi:10.1051/swsc/2016019

Crooker, N. U. (1988). Mapping the merging potential from the magnetopause to the ionosphere through the dayside cusp. *J. Geophys. Res.* 93, 7338–7344. doi:10.1029/JA093iA07p07338

Daglis, I. A. (2006). Ring current dynamics. *Space Sci. Rev.* 124, 183–202. doi:10.1007/s11214-006-9104-z

Davis, T. N., and Sugiura, M. (1966). Auroral electrojet activity index AE and its universal time variations. *J. Geophys. Res.* 71, 785–801. doi:10.1029/JZ071i003p00785

De Zeeuw, D., Sazykin, S., Wolf, R., Gombosi, T., Ridley, A., and Tóth, G. (2004). Coupling of a global MHD code and an inner magnetospheric model: Initial results. *J. Geophys. Res.* 109, A12219. doi:10.1029/2003JA010366

Dessler, A. J., and Parker, E. N. (1959). Hydromagnetic theory of geomagnetic storms. *J. Geophys. Res.* 64, 2239–2252. doi:10.1029/jz064i012p02239

Fok, M., Moore, T. E., Kozyra, J. U., Ho, G. C., and Hamilton, D. C. (1995). Three-dimensional ring current decay model. *J. Geophys. Res.* 100, 9619. doi:10.1029/94ja03029

Fuller-Rowell, T. J., and Evans, D. S. (1987). Height-integrated Pedersen and Hall conductivity patterns inferred from the TIROS-NOAA satellite data. *J. Geophys. Res.* 92, 7606–7618. doi:10.1029/ja092ia07p07606

Ganushkina, N. Y., Pulkkinen, T. I., and Fritz, T. (2005). Role of substorm-associated impulsive electric fields in the ring current development during storms. *Ann. Geophys.* 23, 579–591. doi:10.5194/angeo-23-579-2005

Gao, Y. (2012). Comparing the cross polar cap potentials measured by SuperDARN and AMIE during saturation intervals. *J. Geophys. Res.* 117, A08325. doi:10.1029/2012JA017690

Glocer, A., Kitamura, N., Tóth, G., and Gombosi, T. (2012). Modeling solar zenith angle effects on the polar wind. *J. Geophys. Res.* 117. doi:10.1029/2011JA017136

Gombosi, T. I., Chen, Y., Glocer, A., Huang, Z., Jia, X., Liemohn, M. W., et al. (2021). What sustained multi-disciplinary research can achieve: The space weather modeling framework. *J. Space Weather Space Clim.* 11, 42. doi:10.1051/swsc/2021020

Gonzalez, W. D., Joselyn, J. A., Kamide, Y., Kroehl, H. W., Rostoker, G., Tsurutani, B. T., et al. (1994). What is a geomagnetic storm? *J. Geophys. Res.* 99, 5771–5792. doi:10.1029/93ja02867

Gordeev, E., Sergeev, V., Honkonen, I., Kuznetsova, M., Rastätter, L., Palmroth, M., et al. (2015). Assessing the performance of community-available global mhd models using key system parameters and empirical relationships. *Space Weather.* 13, 868–884. doi:10.1002/2015sw001307

Hairston, M. R., Weimer, D. R., Heelis, R. A., and Rich, F. (1998). Analysis of the ionospheric cross polar cap potential drop and electrostatic potential distribution patterns during the January 1997 CME event using DMSP data. *J. Atmos. Sol. Terr. Phys.* 61, 195–206. doi:10.1016/s1364-6826(98)00128-x

Häkkinen, L. V. T., Pulkkinen, T. I., Nevanlinna, H., Pirjola, R. J., and Tanskanen, E. I. (2002). Effects of induced currents on dst and on magnetic variations at midlatitude stations. *J. Geophys. Res.* 107, 1014–SMP 7–8. doi:10.1029/2001JA900130

Heidke, P. (1926). Berechnung des erfolges und der gute der windstarkevorhersagen im sturmwarnungsdienst. *Geogr. Ann.* 8, 301–349. doi:10.2307/519729

Hu, Y.-Q., Guo, X.-C., Li, G.-Q., Wang, C., and Huang, Z.-H. (2005). Oscillation of quasi-steady Earth's magnetosphere. *Chin. Phys. Lett.* 22, 2723–2726. doi:10.1088/0256-307X/22/10/073

Iijima, T., and Potemra, T. A. (1976). The amplitude distribution of field-aligned currents at northern high latitudes observed by Triad. *J. Geophys. Res.* 81, 2165–2174. doi:10.1029/ja081i013p02165

Janhunen, P., Palmroth, M., Laitinen, T., Honkonen, I., Juusola, L., Facskó, G., et al. (2012). The GUMICS-4 global MHD magnetosphere-ionosphere coupling simulation. *J. Atmos. Solar-Terrest. Phys.* 80, 48–59. doi:10.1016/j.jastp.2012.03.006

Jordanova, V. K., Farrugia, C. J., Thorne, R. M., Khazanov, G. V., Reeves, G. D., and Thomsen, M. F. (2001). Modeling ring current proton precipitation by electromagnetic ion cyclotron waves during the may 14–16, 1997, storm. *J. Geophys. Res.* 106, 7–22. doi:10.1029/2000JA002008

Kalegaev, V. V., and Makarenkov, E. V. (2008). Relative importance of ring and tail currents to Dst under extremely disturbed conditions. *J. Atmos. Solar-Terrest. Phys.* 70, 519–525. doi:10.1016/j.jastp.2007.08.029

Kilpua, E., Koskinen, H. E. J., and Pulkkinen, T. I. (2017). Coronal mass ejections and their sheath regions in interplanetary space. *Living Rev. Sol. Phys.* 14, 5. doi:10.1007/s41116-017-0009-6

Koustov, A. V., Khachikjan, G. Y., Makarevich, R. A., and Bryant, C. (2009). On the SuperDARN cross polar cap potential saturation effect. *Ann. Geophys.* 27, 3755–3764. doi:10.5194/angeo-27-3755-2009

Kwagala, N. K., Hesse, M., Moretto, T., Tenfjord, P., Norgren, C., Tóth, G., et al. (2020). Validating the space weather modeling framework (SWMF) for applications in northern europe. Ground magnetic perturbation validation. *J. Space Weather Space Clim.* 10, 33. doi:10.1051/swsc/2020034

Lakka, A., Pulkkinen, T. I., Dimmock, A. P., Myllys, M., Honkonen, I., and Palmroth, M. (2018). The cross-polar cap saturation in GUMICS-4 during high solar wind driving. *J. Geophys. Res. Space Phys.* 123, 3320–3332. doi:10.1002/2017JA025054

Liemohn, M. W., Kozyra, J. U., Clauer, C. R., Khazanov, G. V., and Thomsen, M. F. (2002). Adiabatic energization in the ring current and its relation to other source and loss terms. *J. Geophys. Res.* 107, 1045. doi:10.1029/2001JA000243

Liemohn, M., Ganushkina, N., De Zeeuw, D., Rastaetter, L., Kuznetsova, M., Welling, D., et al. (2018). Real-time swmf at ccmc: assessing the dst output from continuous operational simulations. *Space Weather.* 16, 1583–1603. doi:10.1029/2018SW001953

Liemohn, M. W., McCollough, J. P., Jordanova, V. K., Ngwira, C. M., Morley, S. K., Cid, C., et al. (2018). Model evaluation guidelines for geomagnetic index predictions. *Space Weather.* 16, 2079–2102. doi:10.1029/2018SW002067

Lin, R. L., Zhang, X. X., Liu, S. Q., Wang, Y. L., and Gong, J. C. (2010). A three-dimensional asymmetric magnetopause model. *J. Geophys. Res.* 115. doi:10.1029/2009JA014235

Lockwood, M., and McWilliams, K. A. (2021). On optimum solar wind-magnetosphere coupling functions for transpolar voltage and planetary geomagnetic activity. *JGR. Space Phys.* 126, e2021JA029946. doi:10.1029/2021ja029946

Lockwood, M., Hairston, M., Finch, I., and Rouillard, A. (2009). Transpolar voltage and polar cap flux during the substorm cycle and steady convection events. *J. Geophys. Res.* 114, A01210. doi:10.1029/2008JA013697

Lockwood, M. (2019). Does adding solar wind poynting flux improve the optimum solar wind-magnetosphere coupling function? *JGR. Space Phys.* 124, 5498–5515. doi:10.1029/2019JA026639

Lockwood, M. (2022). Solar wind—Magnetosphere coupling functions: Pitfalls, limitations, and applications. *Space Weather.* 20, e2021SW002989. doi:10.1029/2021sw002989

Lopez, R. E., Bruntz, R., Mitchell, E. J., Wiltberger, M., Lyon, J. G., and Merkin, V. G. (2010). Role of magnetosheath force balance in regulating the dayside reconnection potential. *J. Geophys. Res.* 115, 216. doi:10.1029/2009JA014597

Maimaiti, M., Kunduri, B., Ruohoniemi, J. M., Baker, J. B. H., and House, L. L. (2019). A deep learning-based approach to forecast the onset of magnetic substorms. *Space Weather.* 17, 1534–1552. doi:10.1029/2019SW002251

McPherron, R. L., Hsu, T.-S., and Chu, X. (2015). An optimum solar wind coupling function for the al index. *JGR. Space Phys.* 120, 2494–2515. doi:10.1002/2014JA020619

Milan, S. E., Lester, M., Cowley, S. W. H., Oksavik, K., Brittnacher, M., Greenwald, R. A., et al. (2003). Variations in the polar cap area during two substorm cycles. *Ann. Geophys.* 21, 1121–1140. doi:10.5194/angeo-21-1121-2003

Mukhopadhyay, A., Welling, D. T., Liemohn, M. W., Ridley, A. J., Chakraborty, S., and Anderson, B. J. (2020). Conductance model for extreme events: Impact of auroral conductance on space weather forecasts. *Space Weather.* 18, e2020SW002551. doi:10.1029/2020sw002551

Mukhopadhyay, A., Welling, D., Liemohn, M., Ridley, A., Burleigh, M., Wu, C., et al. (2022). Global driving of auroral precipitation: 1. Balance of sources. *JGR. Space Phys.* 127, e2022JA030323. doi:10.1029/2022ja030323

Myllys, M., Kilpua, E. K. J., and Lavraud, B. (2017). Interplay of solar wind parameters and physical mechanisms producing the saturation of the cross polar cap potential. *Geophys. Res. Lett.* 44, 3019–3027. doi:10.1002/2017GL072676

Newell, P. T., Sotirelis, T., Liou, K., Meng, C. I., and Rich, F. J. (2007). A nearly universal solar wind-magnetosphere coupling function inferred from 10 magnetospheric state variables. *J. Geophys. Res.* 112, 01206. doi:10.1029/2006ja012015

Newell, P. T., Sotirelis, T., and Wing, S. (2009). Diffuse, monoenergetic, and broadband aurora: The global precipitation budget. *J. Geophys. Res.* 114, A09207. doi:10.1029/2009JA014326

Newell, P., Liou, K., Gjerloev, J., Sotirelis, T., Wing, S., and Mitchell, E. (2016). Substorm probabilities are best predicted from solar wind speed. *J. Atmos. Solar-Terrestrial Phys.* 146, 28–37. doi:10.1016/j.jastp.2016.04.019

Palmroth, M., Pulkkinen, T. I., Janhunen, P., and Wu, C.-C. (2003). Stormtime energy transfer in global MHD simulation. *J. Geophys. Res.* 108, 1048. doi:10.1029/2002ja009446

Palmroth, M., Laitinen, T., and Pulkkinen, T. I. (2006). Magnetopause energy and mass transfer: results from a global MHD simulation. *Ann. Geophys.* 24, 3467–3480. doi:10.5194/angeo-24-3467-2006

Papitashvili, N., Bilitza, D., and King, J. (2014). "OMNI: A description of near-earth solar wind environment," in 40th COSPAR Scientific Assembly, Moscow, Russia. C0.1–12–14.40.

Powell, K. G., Roe, P. L., Linde, T. J., Gombosi, T. I., and De Zeeuw, D. L. (1999). A solution-adaptive upwind scheme for ideal magnetohydrodynamics. *J. Comput. Phys.* 154, 284–309. doi:10.1006/jcph.1999.6299

Pulkkinen, T. I., Ganushkina, N. Y., Tanskanen, E. I., Kubyshkina, M., Reeves, G. D., Thomsen, M. F., et al. (2006). Magnetospheric current systems during stormtime sawtooth events. *J. Geophys. Res.* 111, A11S17. doi:10.1029/2006ja011627

Pulkkinen, T. I., Palmroth, M., Tanskanen, E. I., Janhunen, P., Koskinen, H. E. J., and Laitinen, T. V. (2006). New interpretation of magnetospheric energy circulation. *Geophys. Res. Lett.* 33, L07101. doi:10.1029/2005gl025457

Pulkkinen, T., Palmroth, M., and Laitinen, T. (2008). Energy as a tracer of magnetospheric processes: GUMICS-4 global MHD results and observations compared. *J. Atmos. Solar-Terrest. Phys.* 70, 687–707. doi:10.1016/j.jastp.2007.10.011

Pulkkinen, A., Rastatter, L., Kuznetova, M., Singer, H., Balch, C., Weimer, D., et al. (2013). Community-wide validation of geospace model ground magnetic field perturbation predictions to support model transition to operations. *Space Weather.* 11, 369–385. doi:10.1002/swe.20056

Pulkkinen, T. I., Dimmock, A. P., Lakka, A., Osmane, A., Kilpua, E., Myllys, M., et al. (2016). Magnetosheath control of solar wind-magnetosphere coupling efficiency. *J. Geophys. Res. Space Phys.* 121, 8728–8739. doi:10.1002/2016JA023011

Ridley, A., Gombosi, T., and De Zeeuw, D. L. (2004). Ionospheric control of the magnetosphere: conductance. *Ann. Geophys.* 22, 567–584. doi:10.5194/angeo-22-567-2004

Russell, C., Luhmann, J., and Lu, G. (2001). Nonlinear response of the polar ionosphere to large values of the interplanetary electric field. *J. Geophys. Res.* 106, 18, 495–518, 504. doi:10.1029/2001ja900053

Sergeev, V., Pellinen, R. J., and Pulkkinen, T. I. (1996). Steady magnetospheric convection: A review of recent results. *Space Sci. Rev.* 75, 551–604. doi:10.1007/bf00833344

Shue, J.-H., Chao, J. K., Fu, H. C., Russell, C. T., Song, P., Khurana, K. K., et al. (1997). A new functional form to study the solar wind control of the magnetopause size and shape. *J. Geophys. Res.* 102, 9497–9511. doi:10.1029/97ja00196

Shue, J.-H., Chao, J. K., Fu, H. C., Russell, C. T., Song, P., Khurana, K. K., et al. (1998). Magnetopause location under extreme solar wind conditions. *J. Geophys. Res.* 103, 17691–17700. doi:10.1029/98JA01103

Shukhtina, M. A., Dmitrieva, N. P., and Sergeev, V. A. (2004). Quantitative magnetotail characteristics of different magnetospheric states. *Ann. Geophys.* 22, 1019–1032. doi:10.5194/angeo-22-1019-2004

Siscoe, G. L., Erickson, G. M., Sonnerup, B. U. Ö., Maynard, N. C., Schoendorf, J. A., Siebert, K. D., et al. (2002). Hill model of transpolar potential saturation: Comparisons with MHD simulations. *J. Geophys. Res.* 107, 1075. doi:10.1029/2001JA000109

Tanskanen, E. I., Viljanen, A., Pulkkinen, T. I., Pirjola, R., Häkkinen, L., Pulkkinen, A., et al. (2001). At substorm onset, 40% of al comes from underground. *J. Geophys. Res.* 106, 13119–13134. doi:10.1029/2000JA900135

Toffoletto, F., Sazykin, S., Spiro, R., and Wolf, R. (2003). Inner magnetospheric modeling with the Rice convection model. *Space Sci. Rev.* 107, 175–196. doi:10.1023/A:1025532008047

Tóth, G., van der Holst, B., Sokolov, I. V., De Zeeuw, D. L., Gombosi, T. I., Fang, F., et al. (2012). Adaptive numerical algorithms in space weather modeling. *J. Comput. Phys.* 231, 870–903. doi:10.1016/j.jcp.2011.02.006

Troshichev, O., Shishkina, E., Meng, C.-I., and Newell, P. (1996). Identification of the poleward boundary of the auroral oval using characteristics of ion precipitation. *J. Geophys. Res.* 101, 5035–5046. doi:10.1029/95ja03634

Tsyganenko, N. A., and Sitnov, M. I. (2005). Modeling the dynamics of the inner magnetosphere during strong geomagnetic storms. *J. Geophys. Res.* 110, A03208. doi:10.1029/2004JA010798

Vasyliunas, V. M. (1970). "Mathematical models of magnetospheric convection and its coupling to the ionosphere," in *Particles and fields in the magnetosphere*. Editor B. M. McCormack (Dordrecht, Holland: D. Reidel Publishing), 60–71.

Wang, C., Han, J. P., Li, H., Peng, Z., and Richardson, J. D. (2014). Solar wind-magnetosphere energy coupling function fitting: Results from a global mhd simulation. *J. Geophys. Res. Space Phys.* 119, 6199–6212. doi:10.1002/2014JA019834

Wolf, R. A. (1983). "The quasi-static (slow-flow) region of the magnetosphere," in *Solar terrestrial physics*. Editors R. L. Carovillano, and J. M. Forbes (Hingham, MA: D. Reidel Publishing), 303–368.

Yu, Y., and Ridley, A. (2008). Validation of the space weather modeling framework using ground-based magnetometers. *Space Weather.* 6. doi:10.1029/2007SW000345

Yue, C., Jun, C.-W., Bortnik, J., An, X., Ma, Q., Reeves, G. D., et al. (2019). The relationship between emic wave properties and proton distributions based on van allen probes observations. *Geophys. Res. Lett.* 46, 4070–4078. doi:10.1029/2019GL082633

frontiers | Frontiers in Astronomy and Space Sciences

TYPE Original Research
PUBLISHED 21 October 2022
DOI 10.3389/fspas.2022.952486

OPEN ACCESS

EDITED BY
Joseph E. Borovsky,
Space Science Institute, United States

REVIEWED BY
Richard Boynton,
The University of Sheffield,
United Kingdom
Chongjing Yuan,
Institute of Geology and Geophysics (CAS), China

*CORRESPONDENCE
Sneha A. Gokani,
gokanisneha@gmail.com

SPECIALTY SECTION
This article was submitted to Space Physics, a section of the journal Frontiers in Astronomy and Space Sciences

RECEIVED 25 May 2022
ACCEPTED 07 October 2022
PUBLISHED 21 October 2022

CITATION
Gokani SA, Han D-S, Selvakumaran R and Pant TK (2022), Dependence of radiation belt flux depletions at geostationary orbit on different solar drivers during intense geomagnetic storms.
Front. Astron. Space Sci. 9:952486.
doi: 10.3389/fspas.2022.952486

Dependence of radiation belt flux depletions at geostationary orbit on different solar drivers during intense geomagnetic storms

Sneha A. Gokani[1,2]*, De-Sheng Han[1], R. Selvakumaran[1,2] and Tarun Kumar Pant[2]

[1]State Key Laboratory of Marine Geology, School of Ocean and Earth Science, Tongji University, Shanghai, China, [2]Space Physics Laboratory, Vikram Sarabhai Space Centre, Thiruvananthapuram, India

The loss of electron flux of the outer radiation belt has been widely studied in terms of the mechanism that brings in these losses. There are a few studies which have attempted to explain the interplanetary conditions that favor the depletions. As the Sun is the prime cause of any change happening in the magnetosphere, it is important to look at the solar drivers that bring in such changes. In this study, we attempt to understand the effect of solar structures and substructures on the loss of radiation belt high-energy electrons during intense geomagnetic storms. The superposed epoch analysis is used to observe any peculiar changes in GOES electron flux data during the storms that are associated with solar structures such as CME and CIR, ICME substructures such as the magnetic cloud, magnetic cloud with sheath, ejecta, ejecta with sheath, and only sheath. The long-term data also give an opportunity to compare the flux decrease during solar cycles 23 and 24. It has been observed that 1) CIR-associated storms cause a comparatively higher flux decrease than CME-associated storms, 2) sheath-related storms bring out a higher flux decrease, and 3) there is no significant change in flux for the storms of both the solar cycles. The flux decrease in intense storms at the geostationary orbit is essentially triggered by the "Dst effect." Apart from this, the minimum IMF Bz and northward IMF Bz before turning southward add to the flux decrease. These results hold true for the electron depletions occurring only during intense geomagnetic storms and may alter otherwise.

KEYWORDS

radiation belt, solar wind, solar drivers, geomagnetic storms, electron flux depletion

Introduction

The outer radiation belts are very much vibrant in the sense that they undergo many dynamic processes such as particle acceleration (Summers et al., 1998; Friedel et al., 2002; Elkington et al., 2003; Meredith et al., 2003; Horne et al., 2005; Reeves et al., 2013), transport (Lyons & Thorne, 1973; Baker et al., 2007), and loss (Iles et al., 2002; Onsager

et al., 2002; Reeves et al., 2003; Bortnik et al., 2006; Millan & Thorne, 2007; Baker et al., 2016). Among these processes, the true loss of radiation belt particles is of prime concern because they can cause significant spacecraft operational anomalies (Baker et al., 1987; Allen, 2002; Baker et al., 2004), sometimes causing permanent damage to space systems (Baker et al., 2018) and posing a threat to the climate through instances of highly energetic electron precipitation into the atmosphere (Clilverd et al., 2016; Tsurutani et al., 2016; Baker et al., 2018). These reasons make it necessary to thoroughly study the outer belt particle losses, especially of the highly energetic electrons.

Many researchers have given special attention to understand the mechanism behind the true loss of these electrons. The observed loss of electron flux is attributed to adiabatic losses (McIlwain, 1966; Kim and Chan, 1997) or real losses either by magnetopause shadowing (Shprits et al., 2006; Baker et al., 2016; Herrera et al., 2016; Zhang et al., 2016) or precipitation into the atmosphere (Thorne & Kennel, 1971; Green et al., 2004; Turner et al., 2014; Shprits et al., 2016; Tsurutani et al., 2016; Pham et al., 2017) by resonant wave–particle interaction. Li et al. (1997) used multi-satellite observations during geomagnetic storms to suggest adiabatic losses in the inner part of the belt, whereas nonadiabatic losses in the outer part. Later, Onsager et al. (2002) also came to a similar conclusion by using multi-spacecraft observations. Bortnik et al. (2006) suggested that at high L-shells ($L > 5$), the dropout is independent of energy and caused due to magnetopause shadowing in addition to radial diffusion, whereas at $L < 5$, the dropout is strongly energy dependent and caused due to electromagnetic ion cyclotron (EMIC)–driven pitch angle scattering. Contradicting results have been obtained by Xiang et al. (2017), suggesting the importance of μ and K dependence of electron phase space density (PSD) in understanding the dropout mechanism.

Very few studies have focused on the influence of different interplanetary parameters on the loss of radiation belt electrons. Borovsky and Denton (2010) studied the solar wind effect on electron flux dropouts during geomagnetic storms, using superposed epoch analysis. Similar studies have been undertaken by Meredith et al. (2011) for high-speed solar wind (HSS)–driven storms and by Yuan and Zong (2013). They concluded that the southward interplanetary magnetic field (IMF) and high pressure led to the strongest dropouts. Gao et al. (2015) also came to a similar conclusion by studying the dropouts occurring during both storm and non-storm periods for >2 MeV electrons. Boynton et al. (2016, 2017) carried out an error reduction ratio analysis to explore the nonlinear relationship between electron dropouts and solar wind, as well as other geomagnetic indices. Ni et al. (2016) from their study of the dynamic response of the Earth's radiation belts during periods of solar wind dynamic pressure pulse based on normalized superposed epoch analysis suggested that deeper earthward magnetopause erosion provides favorable conditions for the prompt occurrence of dropout at lower L-shells ($L < 5$). Pinto et al. (2018) by using GOES 8 and 10 electron flux data of energy >2 Mev studied the role of interplanetary parameters on the relativistic flux enhancements and persistent depletion events. These studies have established the role of solar wind conditions in favoring the radiation belt electron losses. From their study on the interplanetary shock properties and preconditions, Yue and Zong (2011) concluded that the perpendicular shock can produce more intense geomagnetic disturbance under the same IMF precondition. They also suggested that the interplanetary shocks can intensify the southward IMF precondition by a factor of 3–6. This study suggests that the orientation of the shocks and preconditioning are also important while considering their impact on the magnetosphere. As the Sun is the ultimate source of any change seen in the interplanetary medium, it thereby causes the magnetosphere to alter. This fact highlights the importance of studying the effect of various solar drivers on the radiation belt electron flux decrease. There are very few studies which have attempted to understand the effect of different solar structures on the radiation belt electron fluxes. Benacquista et al. (2018) studied the impact of two different solar structures, that is, the corotating interaction region (CIR) and interplanetary coronal mass ejection (ICME), on the variations of radiation belt electron fluxes. Their study revealed that the ICMEs are effective at all L-shells, whereas the CIRs have much less access to the innermost parts of the belts. Recently, Turner et al. (2019) showed that storms driven by coronal mass ejection (CME) sheaths or CME ejecta only are capable of producing prolonged depletions of multi-MeV electrons throughout the outer belt. By contrast, storms driven by full CMEs and stream interaction regions are prone to enhance MeV electrons. All these studies suggest the complexity and diversity of the radiation belt response to a space weather event at a given point of time. There has been ample research on the loss mechanism of the outer belt energetic electrons and also on the solar wind conditions which favor these losses. But, there are very few studies which have established a link between the solar structures and outer radiation belt response. Different heliospheric structures interact with the magnetosphere differently through variable forcing (Kilpua et al., 2009). All these in turn affect the response of the radiation belt electron flux. Not only the conditions within these structures are important but also in a broader way, the impacts these structures have can be different. There are still few open questions that need to be answered: 1) how differently do solar structures affect the energetic electron population of the outer radiation belt? 2) Why do two similar solar structures have different impacts on the magnetosphere? 3) Can we anticipate the response of the radiation belt if we know a particular solar structure is heading towards the Earth? 4) Is there any variation in the radiation belt flux from one solar cycle to another? In the present study, we try to investigate the response of the energetic electrons in terms of flux depletion to different solar structures. The long-term data set also provides an opportunity

10.3389/fspas.2022.952486

TABLE 1 List of events considered in this study along with the GOES spacecraft, the energy channel used, and the type of solar structure associated.

Sr. No.	Date	Spacecraft	Energy channel	Type of solar structure
1	23 October 1996	GOES 8	>0.6 MeV	CIR
2	21 April 1997	GOES 8	>0.6 MeV	MC
3	15 May 1997	GOES 8	>0.6 MeV	MC
4	11 October 1997	GOES 8	>0.6 MeV	MC
5	07 November 1997	GOES 8	>0.6 MeV	EJ-S
6	23 November 1997	GOES 8	>0.6 MeV	MC
7	18 February 1998	GOES 8	>0.6 MeV	MC
8	10 March 1998	GOES 8	>0.6 MeV	CIR
9	04 May 1998	GOES 8	>0.6 MeV	S
10	26 June 1998	GOES 8	>0.6 MeV	EJ
11	06 August 1998	GOES 8	>0.6 MeV	EJ
12	27 August 1998	GOES 8	>0.6 MeV	EJ
13	25 September 1998	GOES 8	>0.6 MeV	EJ
14	19 October 1998	GOES 8	>0.6 MeV	MC
15	08 November 1998	GOES 8	>0.6 MeV	EJ
16	09 November 1998	GOES 8	>0.6 MeV	S
17	13 November 1998	GOES 8	>0.6 MeV	MC
18	13 January 1999	GOES 8	>0.6 MeV	MC
19	18 February 1999	GOES 8	>0.6 MeV	EJ
20	22 September 1999	GOES 8	>0.6 MeV	EJ
21	22 October 1999	GOES 8	>0.6 MeV	EJ-S
22	13 November 1999	GOES 8	>0.6 MeV	MC
23	12 February 2000	GOES 8	>0.6 MeV	S
24	07 April 2000	GOES 8	>0.6 MeV	EJ-S
25	24 May 2000	GOES 8	>0.6 MeV	EJ
26	16 July 2000	GOES 8	>0.6 MeV	MC-S
27	11 August 2000	GOES 8	>0.6 MeV	EJ
28	12 August 2000	GOES 8	>0.6 MeV	MC
29	17 September 2000	GOES 8	>0.6 MeV	MC-S
30	05 October 2000	GOES 8	>0.6 MeV	EJ
31	14 October 2000	GOES 8	>0.6 MeV	MC
32	29 October 2000	GOES 8	>0.6 MeV	MC
33	06 November 2000	GOES 8	>0.6 MeV	MC
34	29 November 2000	GOES 8	>0.6 MeV	EJ
35	20 March 2001	GOES 8	>0.6 MeV	MC
36	31 March 2001	GOES 8	>0.6 MeV	MC-S
37	11 April 2001	GOES 8	>0.6 MeV	EJ
38	18 April 2001	GOES 8	>0.6 MeV	MC
39	22 April 2001	GOES 8	>0.6 MeV	MC-S
40	17 August 2001	GOES 8	>0.6 MeV	EJ
41	26 September 2001	GOES 8	>0.6 MeV	EJ
42	01 October 2001	GOES 8	>0.6 MeV	MC
43	03 October 2001	GOES 8	>0.6 MeV	MC
44	21 October 2001	GOES 8	>0.6 MeV	EJ
45	28 October 2001	GOES 8	>0.6 MeV	EJ
46	06 November 2001	GOES 8	>0.6 MeV	EJ
47	24 November 2001	GOES 8	>0.6 MeV	MC-S

(Continued on following page)

10.3389/fspas.2022.952486

TABLE 1 (*Continued*) List of events considered in this study along with the GOES spacecraft, the energy channel used, and the type of solar structure associated.

Sr. No.	Date	Spacecraft	Energy channel	Type of solar structure
48	24 March 2002	GOES 8	>0.6 MeV	MC
49	20 April 2002	GOES 8	>0.6 MeV	MC
50	11 May 2002	GOES 8	>0.6 MeV	EJ
51	23 May 2002	GOES 8	>0.6 MeV	MC
52	02 August 2002	GOES 8	>0.6 MeV	MC
53	21 August 2002	GOES 8	>0.6 MeV	EJ
54	04 September 2002	GOES 8	>0.6 MeV	CIR
55	08 September 2002	GOES 8	>0.6 MeV	EJ
56	01 October 2002	GOES 8	>0.6 MeV	MC
57	04 October 2002	GOES 8	>0.6 MeV	EJ
58	07 October 2002	GOES 8	>0.6 MeV	CIR
59	14 October 2002	GOES 8	>0.6 MeV	CIR
60	21 November 2002	GOES 8	>0.6 MeV	CIR
61	30 May 2003	GOES 8	>0.6 MeV	EJ
62	18 June 2003	GOES 10	>0.6 MeV	S
63	12 July 2003	GOES 10	>0.6 MeV	CIR
64	18 August 2003	GOES 10	>0.6 MeV	MC
65	30 October 2003	GOES 10	>0.6 MeV	MC
66	30 October 2003	GOES 10	>0.6 MeV	MC
67	20 November 2003	GOES 10	>0.6 MeV	MC
68	22 January 2004	GOES 10	>0.6 MeV	EJ
69	04 April 2004	GOES 10	>0.6 MeV	MC
70	25 July 2004	GOES 10	>0.6 MeV	MC
71	27 July 2004	GOES 10	>0.6 MeV	EJ
72	30 August 2004	GOES 10	>0.6 MeV	MC
73	08 November 2004	GOES 10	>0.6 MeV	MC
74	18 January 2005	GOES 10	>0.6 MeV	EJ
75	15 May 2005	GOES 10	>0.6 MeV	MC
76	30 May 2005	GOES 10	>0.6 MeV	EJ
77	13 June 2005	GOES 10	>0.6 MeV	MC
78	24 August 2005	GOES 10	>0.6 MeV	S
79	31 August 2005	GOES 10	>0.6 MeV	CIR
80	11 September 2005	GOES 10	>0.6 MeV	EJ
81	15 December 2006	GOES 10	>0.6 MeV	MC
82	06 August 2011	GOES 15	>0.8 MeV	EJ
83	26 September 2011	GOES 15	>0.8 MeV	EJ-S
84	25 October 2011	GOES 15	>0.8 MeV	MC
85	09 March 2012	GOES 15	>0.8 MeV	MC
86	24 April 2012	GOES 15	>0.8 MeV	MC
87	15 July 2012	GOES 15	>0.8 MeV	EJ
88	01 October 2012	GOES 15	>0.8 MeV	MC-S
89	09 October 2012	GOES 15	>0.8 MeV	MC
90	14 November 2012	GOES 15	>0.8 MeV	MC
91	17 March 2013	GOES 15	>0.8 MeV	MC-S
92	01 June 2013	GOES 15	>0.8 MeV	MC-S
93	29 June 2013	GOES 15	>0.8 MeV	S

(Continued on following page)

TABLE 1 (*Continued*) List of events considered in this study along with the GOES spacecraft, the energy channel used, and the type of solar structure associated.

Sr. No.	Date	Spacecraft	Energy channel	Type of solar structure
94	19 February 2014	GOES 15	>0.8 MeV	EJ-S
95	17 March 2015	GOES 15	>0.8 MeV	MC-S
96	23 June 2015	GOES 15	>0.8 MeV	MC
97	07 October 2015	GOES 15	>0.8 MeV	CIR
98	20 December 2015	GOES 15	>0.8 MeV	MC
99	01 January 2016	GOES 15	>0.8 MeV	MC
100	13 October 2016	GOES 15	>0.8 MeV	MC
101	28 May 2017	GOES 15	>0.8 MeV	MC
102	08 September 2017	GOES 15	>0.8 MeV	MC
103	26 August 2018	GOES 15	>0.8 MeV	MC

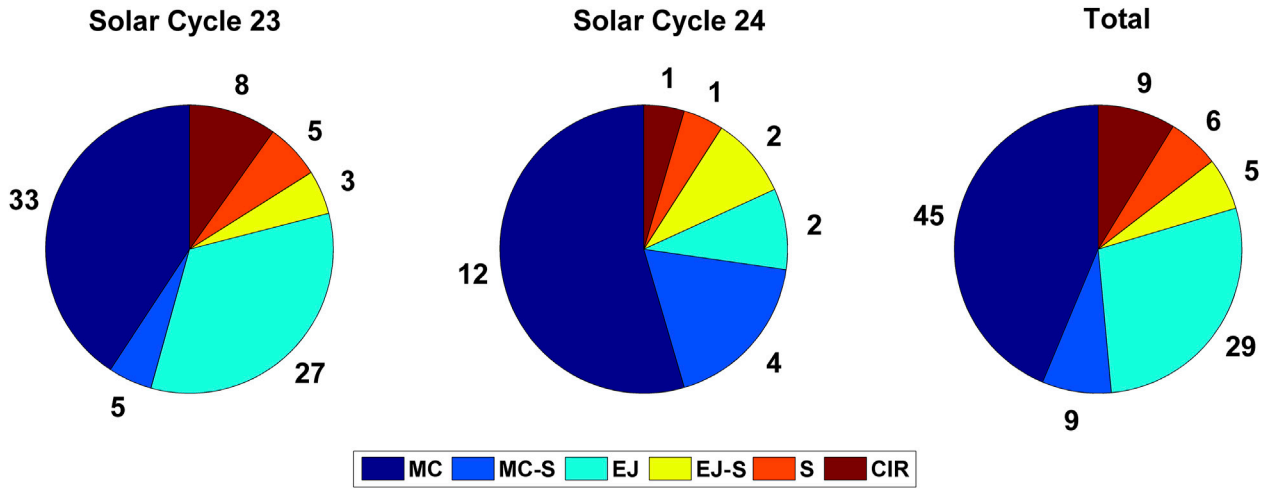

FIGURE 1
Number of storms that occurred due to different structures and substructures during solar cycles 23 and 24 (first and middle panels). A total of 103 storms are considered in this study, divided according to the solar drivers (last panel).

to compare this response over two solar cycles. We identified the flux depletions of electrons having energies >0.6 MeV and >0.8 MeV at the geostationary orbit during 103 intense geomagnetic storms that occurred between 1996 and 2019, which comprises solar cycles 23 and 24. We performed the epoch analysis to understand the contribution of different solar wind and interplanetary conditions. We have divided the events as per the solar structure which drives the changes in the magnetosphere. Firstly, the solar structures are characterized as CME or CIR. When it is CME, then depending on the ICME structure, they are further divided into magnetic cloud (MC), ejecta (EJ), sheath (S), magnetic cloud with sheath (MC-S), and ejecta with sheath (EJ-S).

Materials and methods

The intense geomagnetic storms (Dst ≤ −100 nT) that have occurred during solar cycles 23 and 24 were identified from the World Data Center (http://wdc.kugi.kyoto-u.ac.jp/dst_final/index.html). A total of 103 intense geomagnetic storms had been identified from 1996 to 2019. In order to check the electron depletions during all the selected events, the electron flux data of energy >0.6 MeV was obtained from the Geostationary Operational Environmental Satellite (GOES) 8 and 10 till 2006. From 2011 onward, we have made use of >0.8 MeV channel from GOES 15 spacecraft. The list of the energy channels and spacecraft used is given in Table 1.

These data can be found at https://www.ngdc.noaa.gov/stp/satellite/goes/dataaccess.html. We made use of the OMNIWeb data (https://omniweb.gsfc.nasa.gov/form/dx1.html) to identify solar structures and substructures. The same set of data was used to examine the interplanetary conditions during the flux depletion events. Figure 1 shows the number of geomagnetic storms that occurred during solar cycles 23 and 24, which are further divided into solar structures such as CME and CIR. A total of 81 intense geomagnetic storms occurred during solar cycle 23, out of which 73 were associated with CME and 8 were associated with CIR. As we all know, solar cycle 24 was mild. It consisted of only 22 intense geomagnetic storms, out of which 21 were associated with CME and only 1 was associated with CIR. The CMEs were further divided into ICME substructures such as MC, MC-S, EJ, EJ-S, and S.

The identification of CMEs that occurred in solar cycle 23 was done using the catalog by Gopalswamy et al. (2010) along with the list provided by Richardson and Cane (2010). The identification of CMEs that occurred in solar cycle 24 was done by running movies of coronagraph images available at https://cdaweb.gsfc.nasa.gov. Few of the CMEs were identified using the list provided by Richardson and Cane (2010). The storms which were not associated with CME were checked for any CIR association. Such storms were identified using WIND and ACE observations. Furthermore, the substructures of CMEs were identified by their signatures in interplanetary data. The magnetic clouds (MC) were thought to have one or more of the following signatures: 1) strong magnetic field, 2) smooth latitudinal rotation of the field, and 3) low proton temperature or plasma β (Selvakumaran et al., 2016). Whereas, ejecta (EJ) had 1) a comparatively weaker magnetic field, 2) higher proton temperature or higher plasma β, 3) no clear rotation in the magnetic field, and 4) an enhanced N_α/Np ratio (Gopalswamy et al., 2010). During sheaths, no particular change was observed in plasma β, and there was no smooth rotation of the magnetic field. Major events were taken from the MC list provided by Gopalswamy et al. (2015). Other events were identified by ourselves. The respective number of storms in each category is presented in Figure 1. The storms that occurred due to MC are dominant in both solar cycles, making 45 out of a total of 103 storms, followed by 29, 9, 6, and 5 storms associated with EJ, MC-S, S, and EJ-S, respectively.

Epoch analysis was carried out to understand the effect of different solar drivers on the relativistic electron flux decrease at a geostationary orbit. The time of minimum Dst was taken as the epoch. The flux decrease (ΔF) was calculated by subtracting the minimum flux from the pre-depletion value. To do this, the flux was normalized by the pre-depleted flux value. For easy understanding, we present these values in terms of the order of magnitude. We took care of the flux depletions that occurred on the same day but not during the storm period, that is, we strictly chose the depletions that occurred during the main phase of the geomagnetic storm.

Observations and results

A total of 103 intense geomagnetic storms were considered in this study that had occurred from 1996 to 2019, comprising two solar cycles. The reason behind choosing only intense storms is that not all storms produce electron flux depletions (Reeves et al., 2003). The main motive of this study was to check the dependence of electron flux decrease on different solar drivers. We calculated the level of flux decrease for each of the storms after performing superposed epoch analysis and tried to find any relationship that it may have with different solar drivers.

Epoch analysis

With the time of minimum Dst as an epoch, the epoch analysis was performed on various interplanetary conditions for different solar drivers. The magnetopause standoff distance was also considered in the analysis, which was calculated by using the model given by Shue et al. (1997). We chose a time window of 1 day before and after the epoch to examine full depletion till its recovery. Figure 2 represents the mean value of A) IMF Bz (nT); B) solar wind speed, Vsw (km/h); C) solar wind density, Np (n/cc); D) solar wind dynamic pressure, Pdy (nPa); E) electric field (V/m); F) Sym-H (nT); G) magnetopause stand-off distance, R_0 (R_E); and H) GOES >0.6 MeV electron flux (e cm^{-2} s^{-1} sr^{-1}) for the different abovementioned ICME structures, shown using different colors. From the figure, it can be seen that the level of electron flux decrease is independent of the Sym-H values. This analysis reveals that the storms which are associated with sheath (MC-S, EJ-S, and S) show more flux decrease (ΔF) than non-sheath drivers (MC and EJ). The highest flux decrease (in the order of magnitude) of ~3.0 ± 0.6 was seen for the storms associated with sheath, followed by ~2.7 ± 0.6 for EJ-S, ~2.4 ± 0.55 for MC-S, ~1.9 ± 0.4 for MC, and ~1.6 ± 0.35 for EJ. At none of the times was the magnetopause pushed beyond 6.2 R_E.

Figures 3A–H are in a similar format as Figures 2A–H, but for solar structures such as CME and CIR. From the figure, it can be seen that the flux decrease is more, with $\Delta F \approx 2.2 \pm 0.35$ order of magnitude for the storms that are associated with CIR. The storms associated with CME show comparatively lesser flux decrease with $\Delta F \approx 1.7 \pm 0.41$ order of magnitude, even though the Sym-H is high for CME-related storms.

A similar analysis was carried out for the storms that occurred during solar cycles 23 and 24, as shown in Figures 4A–H. It is in the same format as Figures 2, 3. Though the number of intense storms had decreased drastically, almost by ~57% in solar cycle 24 when compared to solar cycle 23, no difference is seen in the level of electron flux decrease (Figure 4H). It is ~1.69 ± 0.35 for solar cycle 23 and ~1.77 ± 0.4 for solar cycle 24. However, it can be noticed that the overall flux level is significantly lower for the storms that occurred in solar cycle 24 than for those that occurred in solar cycle 23.

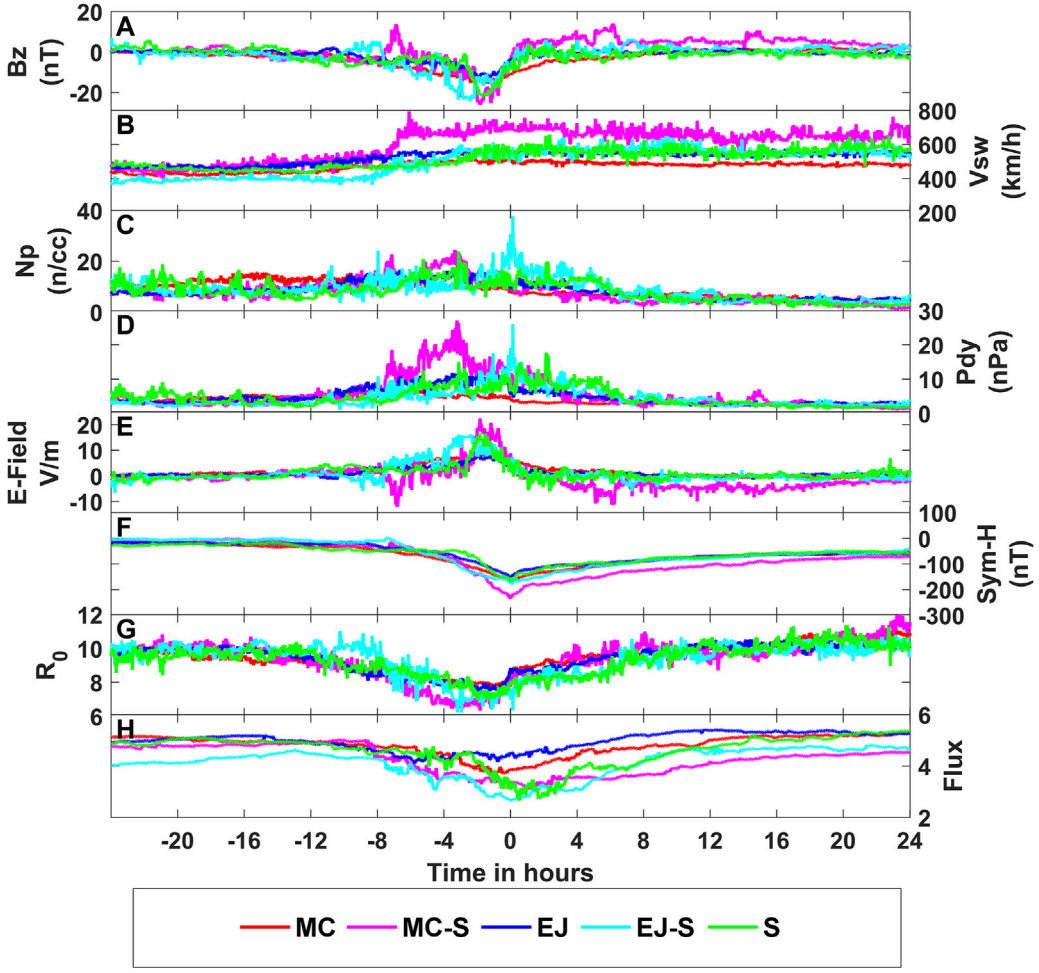

FIGURE 2
Superposed epoch analysis performed on the various interplanetary conditions: **(A)** IMF Bz (nT), **(B)** solar wind speed, Vsw (km/h), **(C)** solar wind density, Np (n/cc), **(D)** solar wind dynamic pressure, Pdy (nPa), **(E)** electric field (V/m), **(F)** Sym-H (nT), **(G)** magnetopause stand-off distance, R_0 (R_E), and **(H)** GOES >0.6 MeV electron flux (e cm^{-2} s^{-1} sr^{-1}) for different solar substructures such as magnetic cloud (MC), magnetic cloud with sheath (MC-S), ejecta (EJ), ejecta with sheath (EJ-S), and sheath (S) represented by different colors.

Effect of solar wind parameters

Some differences in maximum values of interplanetary conditions such as solar wind speed, pressure, density, and electric field are seen for different solar structures and substructures after performing epoch analysis, as seen in Figures 2, 3, respectively. Some previous studies had also examined the role of IMF Bz and solar wind dynamic pressure on radiation belt electron flux (Borovsky and Denton, 2010; Meredith et al., 2011; Yuan and Zong, 2013; Gao et al., 2015). Boynton et al. (2016)had carried out an error reduction ratio analysis and concluded that the solar wind dynamic pressure coupled with solar wind density are the main driving factors for the loss of electrons at energies 128 ≤ E ≤ 925 keV and the solar wind dynamic pressure coupled with southward IMF at energies 1.3 ≤ E ≤ 2 MeV at the geostationary orbits. We also tried to look at the role of solar wind dynamic pressure, speed, density, and electric field on flux depletions. The effect of IMF Bz is studied separately in the next section. We used maximum values of solar wind dynamic pressure, speed, density, and electric field obtained after epoch analysis to check its influence on the level of flux decrease described in terms of the order of magnitude, as shown in Figure 5 for different solar structures and substructures. Seen superimposed on it is an IMF Bz, which is divided into two groups, *viz.*, IMF Bz < −20 nT (big circles) and IMF Bz > −20 nT (small circles). From the figure, it is evident that most of the flux depletion is accompanied by strong southward IMF Bz. All the CIR-related storms are produced by IMF Bz > −20 nT. It

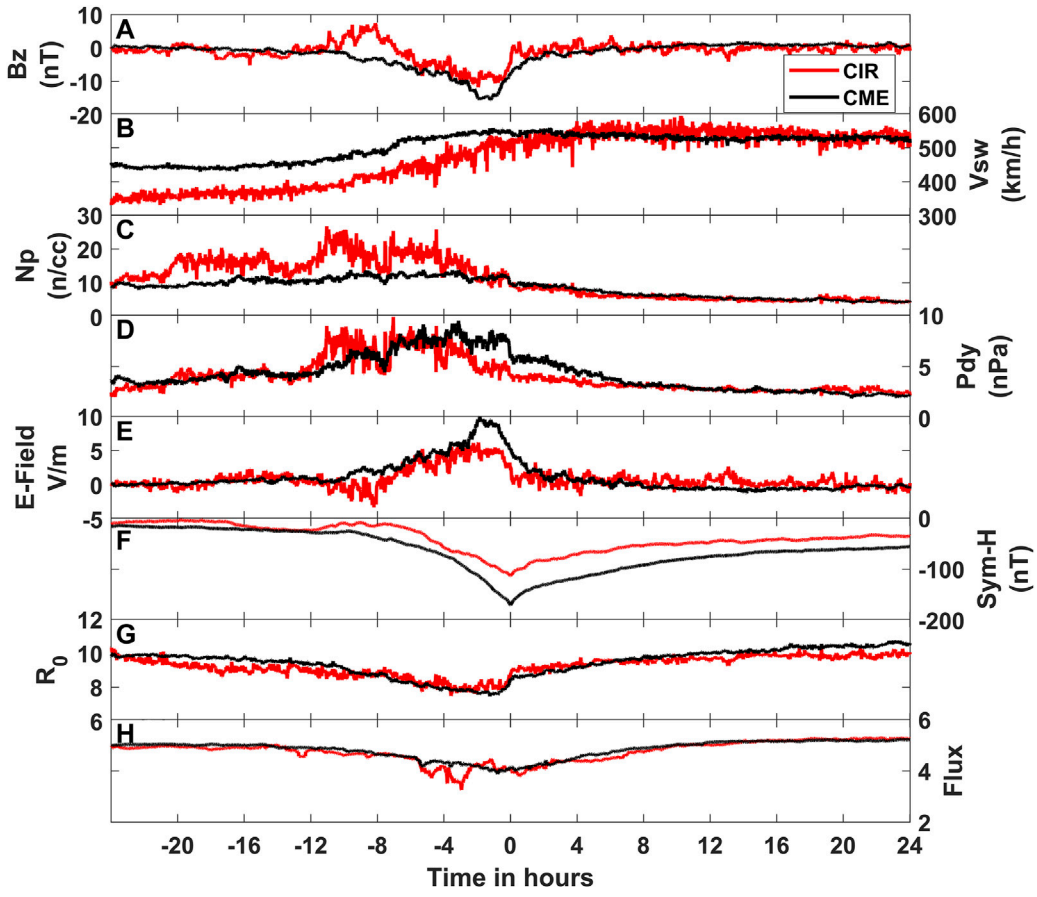

FIGURE 3
Superposed epoch analysis performed on the various interplanetary conditions: **(A)** IMF Bz (nT), **(B)** solar wind speed, Vsw (km/h), **(C)** solar wind density, Np (n/cc), **(D)** solar wind dynamic pressure, Pdy (nPa), **(E)** electric field (V/m), **(F)** Sym-H (nT), **(G)** magnetopause stand-off distance, R_0 (R_E), and **(H)** GOES >0.6 MeV electron flux (e cm^{-2} s^{-1} sr^{-1}) for different solar structures such as CME (black curve) and CIR (red curve).

can also be seen that there is no significant difference in the values of Vmax, Nmax, Pmax, and Emax for the storms associated with different solar drivers. The average values of Vmax, Nmax, Pmax, and Emax along with flux decrease (ΔF) for different solar drivers are given in Table 2. Figure 6 is similar to Figure 5, with R_0 superimposed instead of IMF Bz. Here, R_0 is categorized in two groups, *viz.*, $R_0 < 6$ (small circles) and $R_0 \geq 6$ (big circles). From the figure, it can be seen that in most of the cases, the magnetopause did not move inward beyond the geostationary orbit. This suggests that essentially, the flux decrease is governed by the 'Dst effect' (McIlwain, 1966). Having said that, one cannot neglect the effects of wave–particle interactions during such events. Table 3 shows the number of events for $R_0 < 6$ R_E and $R_0 \geq 6$ R_E. It can be seen that during the storms that are associated with sheaths (MC-S, EJ-S, and S), mostly the magnetopause is pushed inward with $R_0 < 6$. During such cases, the magnetopause shadowing effect may dominate. The sheath passages also favor ULF waves to grow and therefore deplete the particles under the influence of pitch angle scattering.

Dependence of IMF Bz

Apart from solar wind parameters, IMF Bz has been observed to show peculiar features during electron flux depletions. Gao et al. (2015) have shown that the strong southward IMF Bz is solely capable of significant relativistic electron depletions. Figure 2 shows that in some cases, IMF Bz is seen to turn northward before turning southward during the course of flux decrease. To check the effect in detail, we plotted ΔF against IMF Bz for A) MC, B) MC-S, C) EJ, D) EJ-S, and E) S, as shown in Figure 7. The IMF Bz and flux values are of 1 min resolution and are mean values taken after performing epoch analysis during the course of flux depletion. From the figure, it can be noted that the storms that are associated with MC-S, EJ-S, and S show more positive IMF Bz values (fourth quadrant), for which the flux

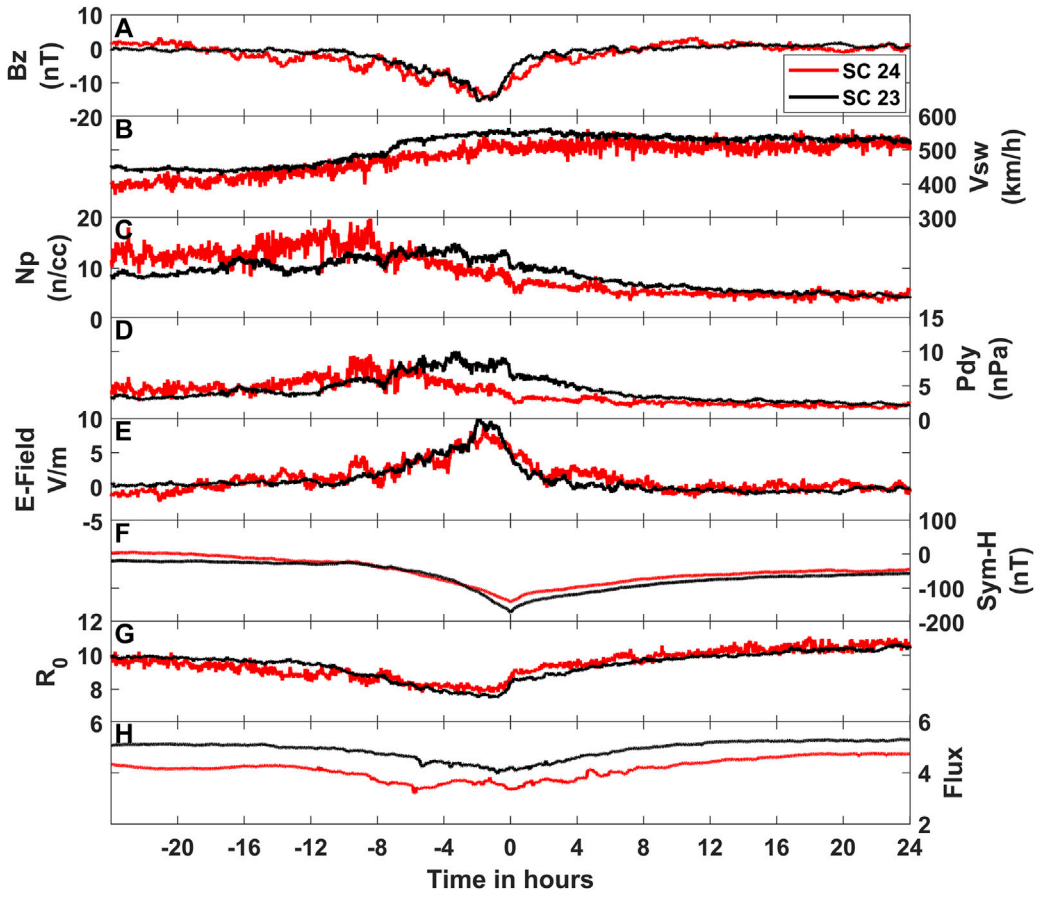

FIGURE 4
Superposed epoch analysis performed on the various interplanetary conditions: **(A)** IMF Bz (nT), **(B)** solar wind speed, Vsw (km/h), **(C)** solar wind density, Np (n/cc), **(D)** solar wind dynamic pressure, Pdy (nPa), **(E)** electric field (V/m), **(F)** Sym-H (nT), **(G)** magnetopause stand-off distance, R_0 (R_E), and **(H)** GOES >0.6 MeV electron flux (e cm^{-2} s^{-1} sr^{-1}) for the storms those occurred during solar cycle 23 (black curve) and solar cycle 24 (red curve).

decrease is seen to be comparatively high. Also, we can see that the storms associated with these drivers have a minimum Bz exceeding −20 nT, whereas the storms associated with the other two categories have a minimum Bz < −15 nT. A similar trend is observed for storms triggered by CIR when compared to CME, as shown in Figure 8. Here also, the fourth quadrant for CIR-related storms is dominant, highlighting the importance of northward IMF Bz before turning southward. A similar analysis is carried out for the storms of both solar cycles (Figure 9). However, no difference is seen either for positive IMF Bz values or minimum IMF Bz between the two, which may have led to no significant change in the level of flux decrease.

Discussion

By performing epoch analysis on the interplanetary conditions and GOES electron flux data, we tried to examine the effect of different solar drivers on the loss of radiation belt electron flux at geostationary orbit during intense geomagnetic storms. Reeves et al. (2003) analyzed the response of relativistic electrons to 276 moderate and intense (Dst < −50 nT) geomagnetic storms. They observed that 56% of the storms showed an overall increase in the trapped flux, only 19% exhibited a decrease, while there was no flux change during 28% of the storms. This suggests the complexity in the response of relativistic electron flux to geomagnetic storms, and it is a delicate balance between acceleration and loss of the particles. As our focus was to analyze only the flux depletion and its dependence on various solar drivers, we chose the days of intense geomagnetic storms, which guaranteed only flux decrease. A total of 103 intense (Dst ≤ −100 nT) geomagnetic storms occurred during 1996–2019, which are considered in the present study, and the change in relativistic electron flux for E > 0.6 and > 0.8 MeV at geostationary orbit is observed using GOES electron flux measurements. A decrease of more than one order

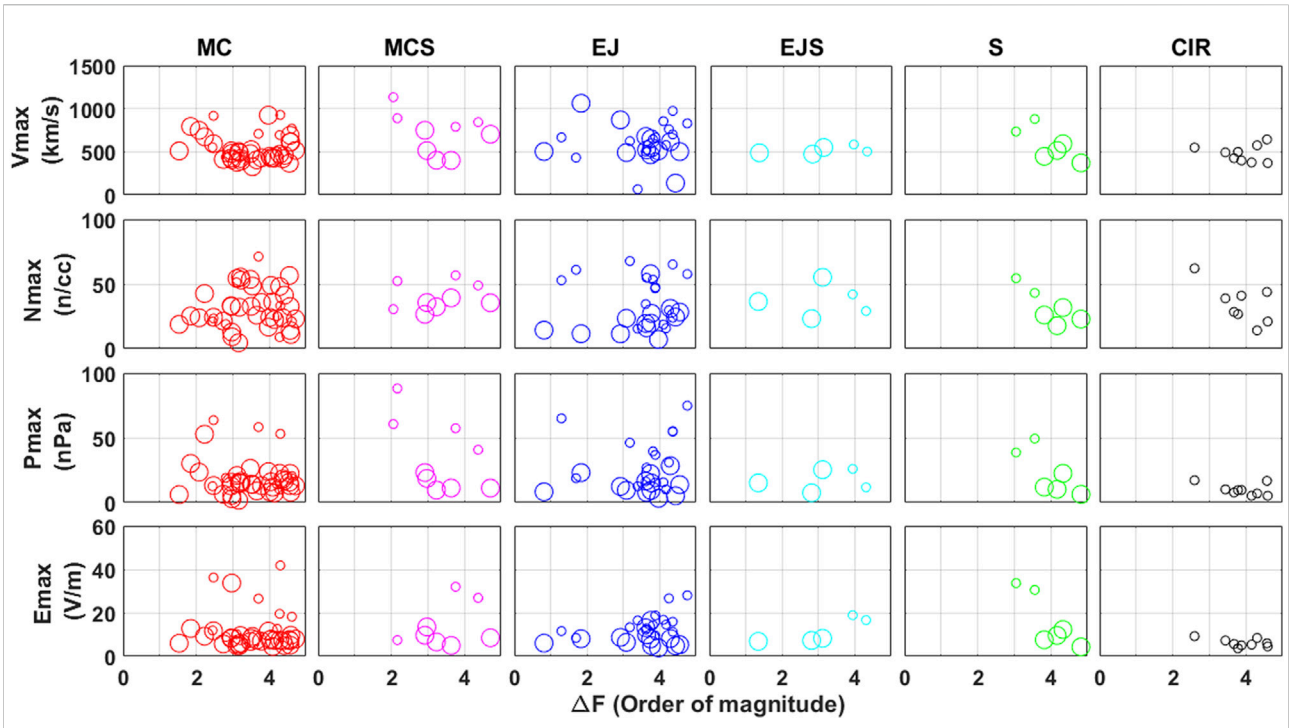

FIGURE 5
Variation of decrease in the electron flux (ΔF in orders of magnitude) with maximum solar wind speed (Vmax in km/s), density (Nmax in n/cc), pressure (Pmax in nPa), and electric field (Emax in V/m) for different solar drivers. Superimposed on that is the IMF Bz in two groups: IMF Bz > −20 nT (small circles) and IMF Bz < −20 nT (big circles).

TABLE 2 Average values of maximum solar wind speed (Vmax in km/s), density (Nmax in n/cc), dynamic pressure (Pmax in nPa), electric field (Emax in V/m), and electron flux decrease (ΔF in the order of magnitude) for different solar drivers after performing epoch analysis.

Type	Vmax (Km/s)	Nmax (n/cc)	Pmax (nPa)	Emax (V/m)	ΔF (ord. of mag.)
MC	521.7	15.53	7.306	9.113	1.2727
MC-S	793.6	24.46	27.1	22.48	1.8726
EJ	577.2	16.62	11.67	7.996	1.0932
EJ-S	640.4	37.82	26.09	15.97	1.5395
S	656.5	23.8	17.71	16.56	2.2656
CIR	593.7	26.67	9.818	6.19	1.5901

of magnitude is seen in the electron flux for all the events. The flux decrease is observed to start with the main phase of the geomagnetic storm. Many different mechanisms, right from the adiabatic process ("Dst effect"), magnetopause shadowing, and scattering of electrons into the loss cone by resonant wave–particle interaction, either alone or in combination act on these particles. There are numerous studies to find the exact mechanism behind electron flux depletion (Bortnik et al., 2006; Shprits et al., 2006; Kim et al., 2010; Turner et al., 2012; Turner et al., 2014; Yuan and Zong, 2013; Baker et al., 2016; Tsurutani et al., 2016; and references given in Millan and Thorne, 2007); however, very few studies have focused on the solar drivers and interplanetary conditions on facilitating electron depletions. In this study, we exclusively focus on the role of different solar structures, such as CME and CIR, and different substructures, such as magnetic cloud, magnetic cloud with sheath, ejecta, ejecta with sheath, and only sheath, in favoring the depletions. The space weather depends mainly on the condition of the Sun and its emissions that hit the Earth, thereby making it necessary to analyze any effect/process happening in the magnetosphere due to changes in solar drivers. As the radiation belt electron flux response is different for shocks, sheaths, and MCs, it is necessary to understand their short- and long-term effects along with their occurrence (Kilpua E. et al., 2017). We make use of superposed

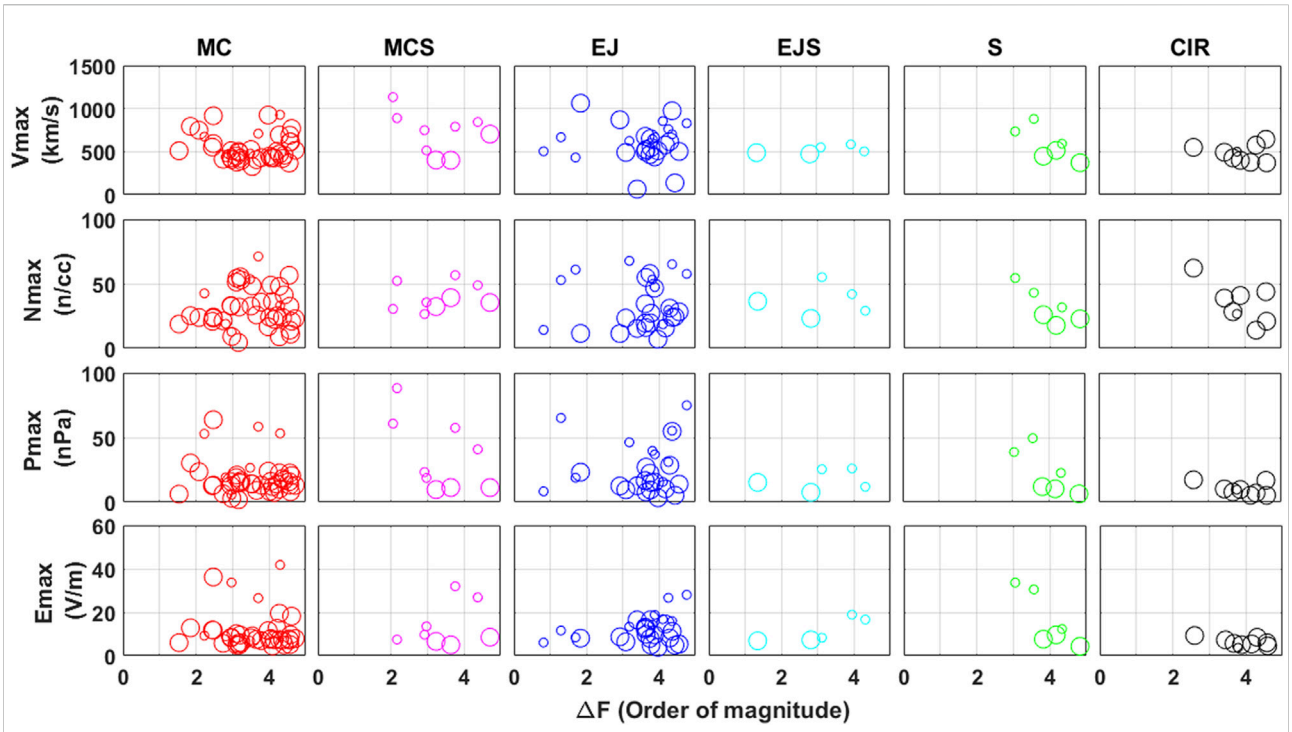

FIGURE 6
Variation of decrease in the electron flux (ΔF in orders of magnitude) with maximum solar wind speed (Vmax in km/s), density (Nmax in n/cc), pressure (Pmax in nPa), and electric field (Emax in V/m) for different solar drivers. Superimposed on that is the R_0 in two groups, $R_0 < 6\ R_E$ (small circles) and $R_0 \geq 6\ R_E$ (big circles).

TABLE 3 Number of events with $R_0 < 6$ and $R_0 \geq 6$ for different solar drivers.

Type	$R_0 < 6$	$R_0 \geq 6$	Total
MC	6	39	45
MC-S	6	3	9
EJ	10	19	29
EJ-S	3	2	5
S	3	3	6
CIR	1	8	9

epoch analysis to see the effect of the aforementioned solar drivers on the radiation belt electron loss. Gopalswamy et al. (2010) found that the CMEs with magnetic cloud (MC) structure are more geoeffective than the ejecta (EJ). We also found a higher degree of flux depletion for MC-related storms than for those related to EJ. We observed (from Figure 2) more flux depletion in the case of storms that are related to sheaths (MC-S, EJ-S, and S) than for the ones which are not (MC and EJ). Yermolaev et al. (2010) found that the geoeffectiveness of MC with sheath was the highest at 61%, that for EJ with sheath was 21%, and for the one without sheath had the lowest geoeffectiveness—only about 8%. The remaining contribution comes from only sheath and CIR-related storms. The sheath properties, which include high dynamic pressure (Palmroth et al., 2007; Myllys et al., 2016), enhanced ULF wave power in turn enhancing the viscous interactions at the magnetosphere (Borovsky and Funsten, 2003), and also stronger compression of the plasma and field caused by high Alfven Mach numbers (Borovsky and Brin, 2014; Myllys et al., 2016) all positively contribute toward the solar wind–magnetosphere coupling (Klipua et al., 2017b). However, the total energy input into the magnetosphere is larger during ICMEs without sheath due to their long encounters. The strong depleting tendency of the sheath-associated storms are presented in Figure 2 that may come from the pitch angle scattering and radial diffusion in combination with the highly compressed dayside magnetopause, due to enhanced ULF power and high dynamic pressure.

Though the storms associated with CME have been observed to be more geoeffective than the storms associated with CIR, we found that the radiation belt electron depletion is more in the latter case (Figure 3). Turner et al. (2019) observed enhancements of MeV electrons at higher L-shells ($L > 4.5$) after the initial depletion during the main phase of the storm. They also observed higher flux depletions for CME-related storms. However, our results

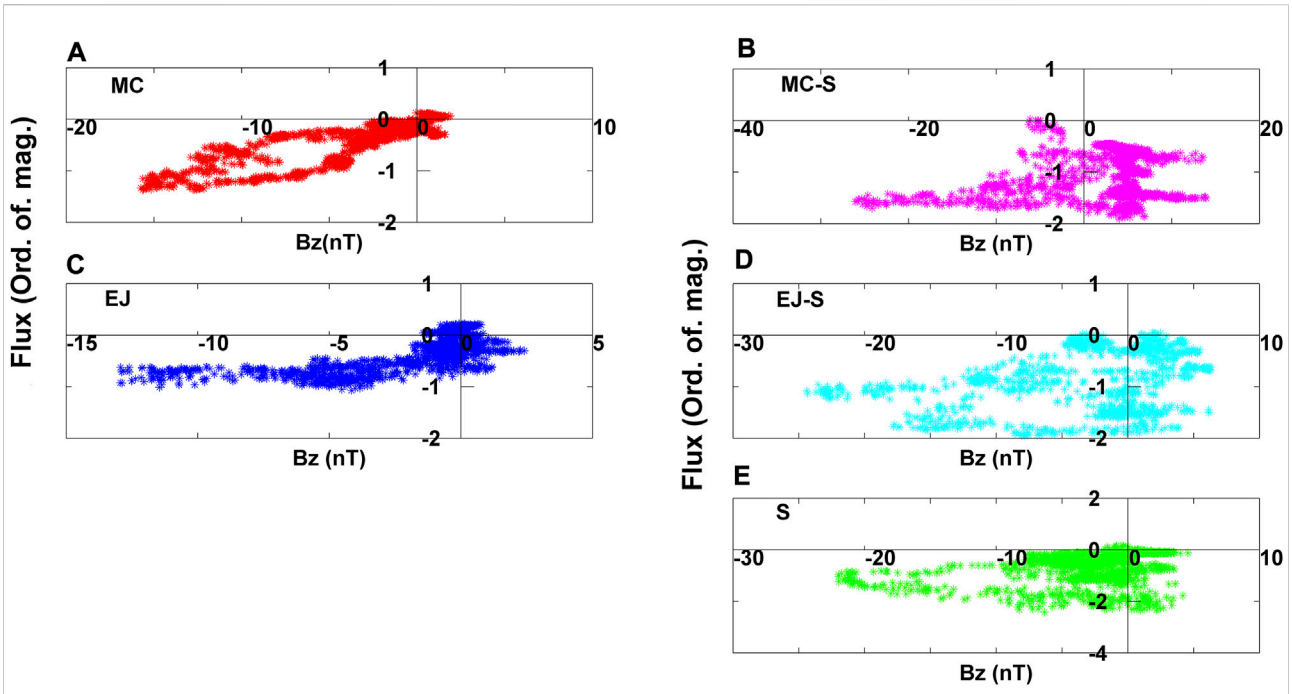

FIGURE 7
Variation of ΔF (in the order of magnitude) with IMF Bz (nT) for storms associated with **(A)** MC, **(B)** MC-S, **(C)** EJ, **(D)** EJ-S, and **(E)** S.

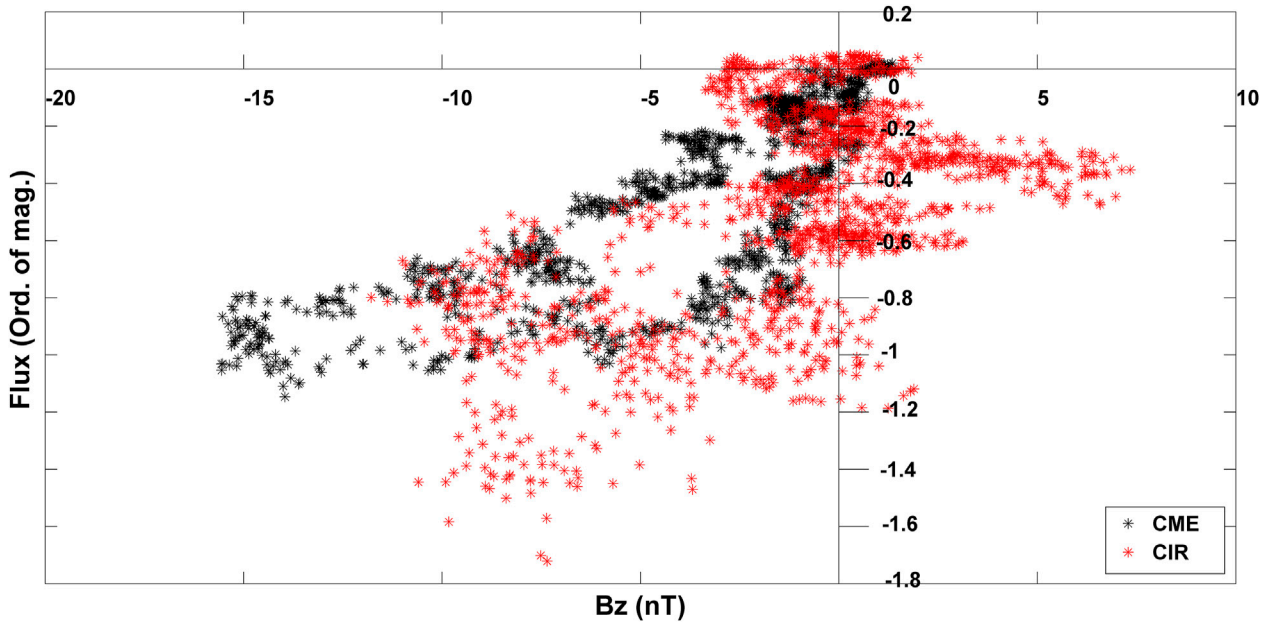

FIGURE 8
Variation of ΔF (in the order of magnitude) with IMF Bz (nT) for storms associated with CME (black) and CIR (red).

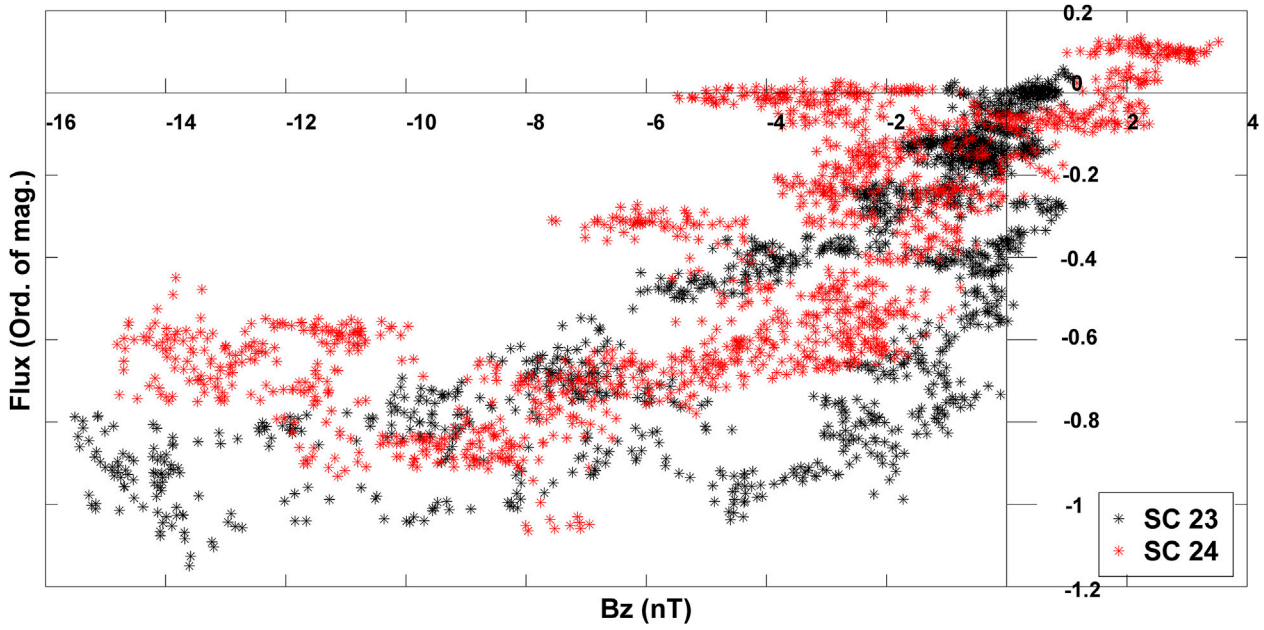

FIGURE 9
Variation of ΔF (in the order of magnitude) with IMF Bz (nT) for storms that occurred during solar cycle 23 (black) and solar cycle 24 (red).

contradict both these observations. We see a comparatively higher flux decrease for CIR-related storms. Also, we do not observe any flux enhancements after the initial depletion. Miyoshi and Kataoka (2005), after applying the superposed epoch analysis, also found that the CIRs tend to cause a much higher increase in the flux than ICMEs at the geosynchronous orbits. Benacquista et al. (2018) also supported the idea of flux increase on a large range of L* and decrease by only a limited number of CIR storms. Koskinen and Kilpua (2022) supported the idea of relativistic flux decrease during SIRs. The observations shown here are strictly during intense geomagnetic storms. Our results urge a reinvestigation of the comparison of flux decrease during CME- and CIR-driven intense geomagnetic storms.

We did not find any significant change in the level of flux decrease for the storms that occurred during the two solar cycles 23 and 24 (Figure 4), although the occurrence of intense geomagnetic storms had drastically decreased in solar cycle 24 (Figure 1). Selvakumaran et al. (2016) from their study on the comparison of moderate geomagnetic storms during solar cycles 23 and 24 observed a reduced magnetospheric energy transfer during solar cycle 24. Gopalswamy et al. (2015) from their study on the properties and geoeffectiveness of magnetic clouds during solar cycles 23 and 24 concluded that the geoeffectiveness was comparatively reduced during solar cycle 24 because of the anomalous CME expansion through its course in the interplanetary medium. Our results from Figure 4 show that the reduced geoefficiency or reduced magnetospheric energy transfer in solar cycle 24 has very less or no impact on the dynamics of radiation belt electron flux depletions.

The interplanetary and solar wind conditions also play an important role in causing radiation belt energetic electron flux decrease. We tried to understand the variations in the degree of flux decrease with different interplanetary properties such as solar wind pressure, speed, density, and electric field as shown in Figure 5 (which includes IMF Bz) and Figure 6 (which includes magnetopause distance). The high flux decrease is seen for the events when IMF Bz is < −20 nT. In most of the cases, the magnetopause did not cross the geostationary orbit, eliminating the possibility of magnetopause shadowing. For CIR-related storms, the influence of IMF Bz being comparatively less and $R_0 \geq 6$ suggest the importance of wave–particle interaction-driven pitch angle scattering as a cause for the flux decrease. As mentioned earlier, here the magnetopause distance is calculated using Shue et al. (1997) model. This model is widely and effectively used by many researchers like Turner et al. (2012), Gao et al. (2015), and Herrera et al. (2016). But, it should be kept in mind that the model values can have uncertainties and can vary from the actual values. Recently, Staples et al. (2020) constructed a database of ~20,000 spacecraft crossings of the dayside magnetopause and concluded that when the magnetopause is compressed below 8 R_E, the average measured location is >1 R_E inside the magnetopause. They also suggested that even extreme magnetopause events rarely reach the outer radiation belt. Our result that the magnetopause does not move beyond the geostationary orbit (~6 R_E) is in-line with the conclusions drawn by Staples et al. (2020). The solar wind pressure and speed seem to have an almost similar effect on the flux decrease.

Previous studies have only focused on the role of solar wind dynamic pressure, IMF Bz, and, up to some extent, solar wind speed. From their study on the correlation between relativistic electrons at GEO and properties of solar wind drivers during the solar minimum period, Blake et al. (1997) found that solar wind speed and density increase along with the southward turning of IMF leading to the enhancement of relativistic electrons. Many other studies have also found a positive correlation between the relativistic flux and solar wind speed (Baker et al., 1979; Paulika and Blake, 1979). Li et al. (2001) found solar wind speed to be the most important factor in their prediction model of electron fluxes at geostationary orbits. Some other studies have favored the role of high solar wind dynamic pressure and southward IMF Bz in reducing the relativistic electrons in the outer radiation belt (Borovsky and Denton, 2010; Meredith et al., 2011; Yuan and Zong, 2013; Gao et al., 2015).

The role of IMF Bz in the depletion of electron flux is analyzed separately as can be seen from Figures 7, 8, 9. We found two distinct features: 1) the flux decrease is more when there are more positive IMF Bz values and 2) the flux decrease is also more when the minimum negative Bz value is comparatively lesser. These two features are true for the cases of MC-S, EJ-S, S (Figures 7B,D,E), and CIR (Figure 8). Both of the features are absent in the case of comparison between solar cycles 23 and 24 where we do not observe much difference between the level of the flux. Gao et al. (2015), by analyzing the electron flux dropout events during storm and non-storm periods, found that when IMF Bz was southward, both the flux of precipitating electrons and the ratio between the precipitating electrons and trapped electrons were much larger. Our results show that the northward turning of IMF Bz before southward contributes positively toward more flux decrease. This can be visualized in the following way: during the course of positive Bz, the magnetosphere gets compressed and triggers the diffusion of the electrons to higher L-shells. Once the Bz turns southward, the magnetopause becomes eroded significantly due to enhanced magnetic reconnection. Souza et al. (2017) have studied the recovery of the relativistic radiation belt electrons and argue that the whistler mode chorus wave power is enhanced when IMF Bz is negative, on average, which in addition to amplification of magnetic integrated power in the ULF range accelerates the outer radiation belt electrons. Our study deals with the depletion of the electrons and suggests that the flux decrease is strengthened when IMF Bz turns southward after a significant positive course. Gao et al. (2015) suggested that the more stretched magnetic field during large solar wind dynamic pressure or southward IMF Bz intensifies the ring current. Then, the relativistic electrons are scattered as a result of deviation of the first adiabatic invariant. Our study not only stresses the importance of southward IMF Bz but also gives insight into the northward turning of IMF Bz before turning southward during a geomagnetic storm. We also suggest that the lesser negative Bz minimum leads to more flux decrease which can be attributed to maximum energy transfer during lesser southward IMF Bz (Selvakumaran et al., 2016).

By studying the depleting effects of ICME-driven sheath regions on the outer electron radiation belt, Hietela et al. (2014) suggested that under magnetospheric compression, the sheaths increase the radial diffusion that enhances the chances of magnetopause shadowing effects producing higher flux decrease. It is also believed that the fluctuating IMF Bz can launch magnetosonic waves, which propagate into the magnetosphere and can scatter the electrons into the loss cone by virtue of the resonant wave–particle interaction. Kilpua E. et al. (2017) has also claimed the dominating tendency of sheath passages in depleting the electrons. The results presented in this study suggest the importance of considering solar driver properties while anticipating the electron flux changes in the radiation belts. The detailed analysis of electron flux decrease at different L-shells using long-term data will be pursued in the future to add to the knowledge gained.

Summary and conclusion

A superposed epoch analysis is performed to investigate the effect of different solar structures and substructures on the depletion of relativistic electron flux at the geostationary orbit during the cases of intense geomagnetic storms. Our analysis found some interesting results:

1) Sheath-related storms (MC-S, EJ-S, and S) produce more flux decrease than the non-sheath ones (MC and EJ).
2) The increase in the solar wind pressure and speed increases the flux decrease.
3) Either northward IMF Bz before turning southward or rapidly fluctuating IMF Bz causes a higher flux decrease.

As the main aim of space weather studies is to know what, when, and how it will happen, our results presented here may provide a positive input to radiation belt modeling studies, while predicting the dynamics under particular solar and solar wind conditions.

Data availability statement

Publicly available data sets were analyzed in this study. These data can be found at OMNIWeb (https://omniweb.gsfc.nasa.gov/form/dx1.html), World Data Center, Kyoto (https://wdc.kugi.kyoto-u.ac.jp/dst_final/index.html), GOES (https://www.ngdc.noaa.gov/stp/satellite/goes/dataaccess.html), and CDAWeb (https://cdaweb.gsfc.nasa.gov).

Author contributions

SG, the first author has conceptualized the idea, carried out the analysis, written the manuscript, and contributed towards the physical interpretation of the results. DH has contributed towards interpreting the results and also provided the basic infrastructure to carry out the research. RS has identified the solar structures and substructures and

contributed in interpreting the results. TP has contributed towards interpreting the results.

Funding

This work is partly supported by the National Natural Science Foundation of China (42050410313, 42030101, and 41974185). SG carried out this work using the research grant from the Science and Engineering Research Board, Department of Science and Technology, India (2020/RJF/000125). RS acknowledges the support from the research grant from the Science and Engineering Research Board, Department of Science and Technology, India (PDF/2021/002226).

Acknowledgments

The authors thank the head of the School of Ocean and Earth Sciences for supporting the research work. They also thank SPL and VSSC for encouraging the research activities toward this work and the OMNIWeb (https://omniweb.gsfc.nasa.gov/form/dx1.html) team for providing solar wind data. They also thank the World Data Center, Kyoto, for providing Dst values (https://wdc.kugi.kyoto-u.ac.jp/dst_final/index.html), GOES (https://www.ngdc.noaa.gov/stp/satellite/goes/dataaccess.html) team, and CDAWeb (https://cdaweb.gsfc.nasa.gov).

Conflict of interest

The authors declare that the research was conducted in the absence of any commercial or financial relationships that could be construed as a potential conflict of interest.

Publisher's note

All claims expressed in this article are solely those of the authors and do not necessarily represent those of their affiliated organizations, or those of the publisher, editors, and reviewers. Any product that may be evaluated in this article, or claim that may be made by its manufacturer, is not guaranteed or endorsed by the publisher.

References

Allen, J. H. (2002). "Historical and recent solar activity and geomagnetic storms affecting spacecraft operations," in *Proceedings of the government* Microcircuit and applications conference (Monterey, CA: GOMAC'02).

Baker, D. N., Belian, R. D., Higbie, P. R., Klebesadel, R. W., and Blake, J. B. (1987). Deep dielectric charging effects due to high-energy electrons in Earth's outer magnetosphere. *J. Electrost.* 20 (1), 3–19. doi:10.1016/0304-3886(87)90082-9

Baker, D. N., Erickson, P. J., Fennell, J. F., Foster, J. C., Jaynes, A. N., and Verronen, P. T. (2018). Space weather effects in the Earth's radiation belts. *Space Sci. Rev.* 214 (1), 17–60. doi:10.1007/s11214-017-0452-7

Baker, D. N., Higbie, P. R., Belian, R. D., and Hones, E. W., Jr (1979). Do Jovian electrons influence the terrestrial outer radiation zone? *Geophys. Res. Lett.* 6 (6), 531–534. doi:10.1029/gl006i006p00531

Baker, D. N., Jaynes, A. N., Kanekal, S. G., Foster, J. C., Erickson, P. J., Fennell, J. F., et al. (2016). Highly relativistic radiation belt electron acceleration, transport, and loss: Large solar storm events of March and June 2015. *JGR. Space Phys.* 121 (7), 6647–6660. doi:10.1002/2016ja022502

Baker, D. N., Kanekal, S. G., and Blake, J. B. (2004). Characterizing the Earth's outer Van Allen zone using a radiation belt content index. *Space weather.* 2 (2). doi:10.1029/2003sw000026

Baker, D. N., Kanekal, S. G., Horne, R. B., Meredith, N. P., and Glauert, S. A. (2007). Low-altitude measurements of 2–6 MeV electron trapping lifetimes at 1.5≤ L≤ 2.5. *Geophys. Res. Lett.* 34 (20), L20110. doi:10.1029/2007gl031007

Benacquista, R., Boscher, D., Rochel, S., and Maget, V. (2018). Variations of the electron fluxes in the terrestrial radiation belts due to the impact of corotating interaction regions and interplanetary coronal mass ejections. *J. Geophys. Res. Space Phys.* 123 (2), 1191–1199. doi:10.1002/2017ja024796

Blake, J. B., Baker, D. N., Turner, N., Ogilvie, K. W., and Lepping, R. P. (1997). Correlation of changes in the outer-zone relativistic-electron population with upstream solar wind and magnetic field measurements. *Geophys. Res. Lett.* 24 (8), 927–929. doi:10.1029/97gl00859

Borovsky, J. E., and Birn, J. (2014). The solar wind electric field does not control the dayside reconnection rate. *J. Geophys. Res. Space Phys.* 119 (2), 751–760. doi:10.1002/2013ja019193

Borovsky, J. E., and Denton, M. H. (2010). Magnetic field at geosynchronous orbit during high-speed stream-driven storms: Connections to the solar wind, the plasma sheet, and the outer electron radiation belt. *J. Geophys. Res.* 115 (A8). doi:10.1029/2009ja015116

Borovsky, J. E., and Funsten, H. O. (2003). MHD turbulence in the Earth's plasma sheet: Dynamics, dissipation, and driving. *J. Geophys. Res.* 108 (A7), 1284. doi:10.1029/2002ja009625

Bortnik, J., Thorne, R. M., O'Brien, T. P., Green, J. C., Strangeway, R. J., Shprits, Y. Y., et al. (2006). Observation of two distinct, rapid loss mechanisms during the 20 November 2003 radiation belt dropout event. *J. Geophys. Res.* 111 (A12), A12216. doi:10.1029/2006ja011802

Boynton, R. J., Mourenas, D., and Balikhin, M. A. (2016). Electron flux dropouts at Geostationary Earth Orbit: Occurrences, magnitudes, and main driving factors. *J. Geophys. Res. Space Phys.* 121 (9), 8448–8461. doi:10.1002/2016ja022916

Boynton, R. J., Mourenas, D., and Balikhin, M. A. (2017). Electron flux dropouts at L~ 4.2 from global positioning system satellites: Occurrences, magnitudes, and main driving factors. *J. Geophys. Res. Space Phys.* 122 (11), 11–428. doi:10.1002/2017ja024523

Clilverd, M. A., Rodger, C. J., Andersson, M. E., Seppala, A., and Verronen, P. T. (2016). "Linkages between the radiation belts, polar atmosphere and climate: Electron precipitation through wave particle interactions," in *Waves particles and storms in geospace* (Oxford: Oxford University Press), 354–376.

Elkington, S. R., Hudson, M. K., and Chan, A. A. (2003). Resonant acceleration and diffusion of outer zone electrons in an asymmetric geomagnetic field. *J. Geophys. Res.* 108 (A3), 1116. doi:10.1029/2001ja009202

Friedel, R. H. W., Reeves, G. D., and Obara, T. (2002). Relativistic electron dynamics in the inner magnetosphere—a review. *J. Atmos. Solar-Terrestrial Phys.* 64 (2), 265–282. doi:10.1016/s1364-6826(01)00088-8

Gao, X., Li, W., Bortnik, J., Thorne, R. M., Lu, Q., Ma, Q., et al. (2015). The effect of different solar wind parameters upon significant relativistic electron flux dropouts in the magnetosphere. *JGR. Space Phys.* 120 (6), 4324–4337. doi:10.1002/2015ja021182

Gopalswamy, N., Yashiro, S., Michalek, G., Xie, H., Mäkelä, P., Vourlidas, A., et al. (2010). A catalog of halo coronal mass ejections from SOHO. *Sun Geosph.* 5 (1), 7–16.

Gopalswamy, N., Yashiro, S., Xie, H., Akiyama, S., and Mäkelä, P. (2015). Properties and geoeffectiveness of magnetic clouds during solar cycles 23 and 24. *JGR. Space Phys.* 120 (11), 9221–9245. doi:10.1002/2015ja021446

Green, J. C., Onsager, T. G., O'Brien, T. P., and Baker, D. N. (2004). Testing loss mechanisms capable of rapidly depleting relativistic electron flux in the Earth's outer radiation belt. *J. Geophys. Res.* 109 (A12), A12211. doi:10.1029/2004ja010579

Herrera, D., Maget, V. F., and Sicard Piet, A. (2016). Characterizing magnetopause shadowing effects in the outer electron radiation belt during geomagnetic storms. *JGR. Space Phys.* 121 (10), 9517–9530. doi:10.1002/2016ja022825

Hietala, H., Kilpua, E. K. J., Turner, D. L., and Angelopoulos, V. (2014). Depleting effects of ICME-driven sheath regions on the outer electron radiation belt. *Geophys. Res. Lett.* 41 (7), 2258–2265. doi:10.1002/2014gl059551

Horne, R. B., Thorne, R. M., Glauert, S. A., Albert, J. M., Meredith, N. P., and Anderson, R. R. (2005). Timescale for radiation belt electron acceleration by whistler mode chorus waves. *J. Geophys. Res.* 110 (A3), A03225. doi:10.1029/2004ja010811

Iles, R. H. A., Fazakerley, A. N., Johnstone, A. D., Meredith, N. P., and Bühler, P. (2002). The relativistic electron response in the outer radiation belt during magnetic storms. *Ann. Geophys.* 20, 957–965. doi:10.5194/angeo-20-957-2002

Kilpua, E. K. J., Balogh, A., Von Steiger, R., and Liu, Y. D. (2017b). Geoeffective properties of solar transients and stream interaction regions. *Space Sci. Rev.* 212 (3), 1271–1314. doi:10.1007/s11214-017-0411-3

Kilpua, E. K. J., Hietala, H., Turner, D. L., Koskinen, H. E. J., Pulkkinen, T. I., Rodriguez, J. V., et al. (2015). Unraveling the drivers of the storm time radiation belt response. *Geophys. Res. Lett.* 42 (9), 3076–3084. doi:10.1002/2015gl063542

Kilpua, E., Koskinen, H. E., and Pulkkinen, T. I. (2017a). Coronal mass ejections and their sheath regions in interplanetary space. *Living Rev. Sol. Phys.* 14 (1), 5–83. doi:10.1007/s41116-017-0009-6

Kim, H. J., and Chan, A. A. (1997). Fully adiabatic changes in storm time relativistic electron fluxes. *J. Geophys. Res.* 102 (A10), 22107–22116. doi:10.1029/97ja01814

Kim, K. C., Lee, D. Y., Kim, H. J., Lee, E. S., and Choi, C. R. (2010). Numerical estimates of drift loss and Dst effect for outer radiation belt relativistic electrons with arbitrary pitch angle. *J. Geophys. Res.* 115 (A3). doi:10.1029/2009ja014523

Koskinen, H. E., and Kilpua, E. K. (2022). *Physics of Earth's radiation belts: Theory and observations*. Springer Nature, 272.

Li, X., Baker, D. N., Temerin, M., Cayton, T. E., Reeves, E. G. D., Christensen, R. A., et al. (1997). Multisatellite observations of the outer zone electron variation during the November 3–4, 1993, magnetic storm. *J. Geophys. Res.* 102 (A7), 14123–14140. doi:10.1029/97ja01101

Li, X., Temerin, M., Baker, D. N., Reeves, G. D., and Larson, D. (2001). Quantitative prediction of radiation belt electrons at geostationary orbit based on solar wind measurements. *Geophys. Res. Lett.* 28 (9), 1887–1890. doi:10.1029/2000gl012681

Lyons, L. R., and Thorne, R. M. (1973). Equilibrium structure of radiation belt electrons. *J. Geophys. Res.* 78 (13), 2142–2149. doi:10.1029/ja078i013p02142

McIlwain, C. E. (1966). Ring current effects on trapped particles. *J. Geophys. Res.* 71 (15), 3623–3628. doi:10.1029/jz071i015p03623

Meredith, N. P., Cain, M., Horne, R. B., Thorne, R. M., Summers, D., and Anderson, R. R. (2003). Evidence for chorus-driven electron acceleration to relativistic energies from a survey of geomagnetically disturbed periods. *J. Geophys. Res.* 108 (A6), 1248. doi:10.1029/2002ja009764

Meredith, N. P., Horne, R. B., Lam, M. M., Denton, M. H., Borovsky, J. E., and Green, J. C. (2011). Energetic electron precipitation during high-speed solar wind stream driven storms. *J. Geophys. Res.* 116 (A5). doi:10.1029/2010ja016293

Millan, R. M., and Thorne, R. (2007). Review of radiation belt relativistic electron losses. *J. Atmos. Solar-Terrestrial Phys.* 69 (3), 362–377. doi:10.1016/j.jastp.2006.06.019

Miyoshi, Y., and Kataoka, R. (2005). Ring current ions and radiation belt electrons during geomagnetic storms driven by coronal mass ejections and corotating interaction regions. *Geophys. Res. Lett.* 32 (21), L21105. doi:10.1029/2005gl024590

Myllys, M., Kilpua, E. K. J., Lavraud, B., and Pulkkinen, T. I. (2016). Solar wind-magnetosphere coupling efficiency during ejecta and sheath-driven geomagnetic storms. *J. Geophys. Res. Space Phys.* 121 (5), 4378–4396. doi:10.1002/2016ja022407

Ni, B., Xiang, Z., Gu, X., Shprits, Y. Y., Zhou, C., Zhao, Z., et al. (2016). Dynamic responses of the Earth's radiation belts during periods of solar wind dynamic pressure pulse based on normalized superposed epoch analysis. *J. Geophys. Res. Space Phys.* 121 (9), 8523–8536. doi:10.1002/2016ja023067

Onsager, T. G., Rostoker, G., Kim, H. J., Reeves, G. D., Obara, T., Singer, H. J., et al. (2002). Radiation belt electron flux dropouts: Local time, radial, and particle-energy dependence. *J. Geophys. Res.* 107 (A11), 138221. doi:10.1029/2001ja000187

Palmroth, M., Partamies, N., Polvi, J., Pulkkinen, T. I., McComas, D. J., Barnes, R. J., et al. (2007). Solar wind–magnetosphere coupling efficiency for solar wind pressure impulses. *Geophys. Res. Lett.* 34 (11), L11101. doi:10.1029/2006gl029059

Paulikas, G. A., and Blake, J. B. (1979). Effects of the solar wind on magnetospheric dynamics: Energetic electrons at the synchronous orbit. *Quantitative Model. Magnetos. Process. Geophys. Monogr. Ser* 21, 180–202.

Pham, K. H., Tu, W., and Xiang, Z. (2017). Quantifying the precipitation loss of radiation belt electrons during a rapid dropout event. *JGR. Space Phys.* 122 (10), 10–287. doi:10.1002/2017ja024519

Pinto, V. A., Kim, H. J., Lyons, L. R., and Bortnik, J. (2018). Interplanetary parameters leading to relativistic electron enhancement and persistent depletion events at geosynchronous orbit and potential for prediction. *JGR. Space Phys.* 123 (2), 1134–1145. doi:10.1002/2017ja024902

Reeves, G. D., McAdams, K. L., Friedel, R. H. W., and O'brien, T. P. (2003). Acceleration and loss of relativistic electrons during geomagnetic storms. *Geophys. Res. Lett.* 30 (10). doi:10.1029/2002gl016513

Reeves, G. D., Spence, H. E., Henderson, M. G., Morley, S. K., Friedel, R. H. W., Funsten, H. O., et al. (2013). Electron acceleration in the heart of the Van Allen radiation belts. *Science* 341 (6149), 991–994. doi:10.1126/science.1237743

Richardson, I. G., and Cane, H. V. (2010). Near-Earth interplanetary coronal mass ejections during solar cycle 23 (1996–2009): Catalog and summary of properties. *Sol. Phys.* 264 (1), 189–237. doi:10.1007/s11207-010-9568-6

Selvakumaran, R., Veenadhari, B., Akiyama, S., Pandya, M., Gopalswamy, N., Yashiro, S., et al. (2016). On the reduced geoeffectiveness of solar cycle 24: A moderate storm perspective. *J. Geophys. Res. Space Phys.* 121 (9), 8188–8202. doi:10.1002/2016ja022885

Shprits, Y. Y., Drozdov, A. Y., Spasojevic, M., Kellerman, A. C., Usanova, M. E., Engebretson, M. J., et al. (2016). Wave-induced loss of ultra-relativistic electrons in the Van Allen radiation belts. *Nat. Commun.* 7 (1), 12883–12887. doi:10.1038/ncomms12883

Shprits, Y. Y., Thorne, R. M., Friedel, R., Reeves, G. D., Fennell, J., Baker, D. N., et al. (2006). Outward radial diffusion driven by losses at magnetopause. *J. Geophys. Res.* 111 (A11), A11214. doi:10.1029/2006ja011657

Shue, J. H., Chao, J. K., Fu, H. C., Russell, C. T., Song, P., Khurana, K. K., et al. (1997). A new functional form to study the solar wind control of the magnetopause size and shape. *J. Geophys. Res.* 102 (A5), 9497–9511. doi:10.1029/97ja00196

Souza, V. M., Lopez, R. E., Jauer, P. R., Sibeck, D. G., Pham, K., Da Silva, L. A., et al. (2017). Acceleration of radiation belt electrons and the role of the average interplanetary magnetic field Bz component in high-speed streams. *J. Geophys. Res. Space Phys.* 122 (10), 10–084.

Staples, F. A., Rae, I. J., Forsyth, C., Smith, A. R. A., Murphy, K. R., Raymer, K. M., et al. (2020). Do statistical models capture the dynamics of the magnetopause during sudden magnetospheric compressions? *J. Geophys. Res. Space Phys.* 125 (4), e2019JA027289. doi:10.1029/2019ja027289

Summers, D., Thorne, R. M., and Xiao, F. (1998). Relativistic theory of wave-particle resonant diffusion with application to electron acceleration in the magnetosphere. *J. Geophys. Res.* 103 (A9), 20487–20500. doi:10.1029/98ja01740

Thorne, R. M., and Kennel, C. (1971). Relativistic electron precipitation during magnetic storm main phase. *J. Geophys. Res.* 76 (19), 4446–4453. doi:10.1029/ja076i019p04446

Tsurutani, B. T., Hajra, R., Tanimori, T., Takada, A., Remya, B., Mannucci, A. J., et al. (2016). Heliospheric plasma sheet (HPS) impingement onto the magnetosphere as a cause of relativistic electron dropouts (REDs) via coherent EMIC wave scattering with possible consequences for climate change mechanisms. *J. Geophys. Res. Space Phys.* 121 (10), 10–130. doi:10.1002/2016ja022499

Turner, D. L., Angelopoulos, V., Li, W., Bortnik, J., Ni, B., Ma, Q., et al. (2014). Competing source and loss mechanisms due to wave-particle interactions in Earth's outer radiation belt during the 30 September to 3 October 2012 geomagnetic storm. *JGR. Space Phys.* 119 (3), 1960–1979. doi:10.1002/2014ja019770

Turner, D. L., Kilpua, E. K. J., Hietala, H., Claudepierre, S. G., O'Brien, T. P., Fennell, J. F., et al. (2019). The response of Earth's electron radiation belts to geomagnetic storms: Statistics from the Van Allen Probes era including effects from different storm drivers. *JGR. Space Phys.* 124 (2), 1013–1034. doi:10.1029/2018ja026066

Turner, D. L., Shprits, Y., Hartinger, M., and Angelopoulos, V. (2012). Explaining sudden losses of outer radiation belt electrons during geomagnetic storms. *Nat. Phys.* 8 (3), 208–212. doi:10.1038/nphys2185

Xiang, Z., Tu, W., Li, X., Ni, B., Morley, S. K., and Baker, D. N. (2017). Understanding the mechanisms of radiation belt dropouts observed by Van Allen Probes. *JGR. Space Phys.* 122 (10), 9858–9879. doi:10.1002/2017ja024487

Yermolaev, Y. I., Nikolaeva, N. S., Lodkina, I. G., and Yermolaev, M. Y. (2010). Specific interplanetary conditions for CIR-Sheath-and ICME-induced geomagnetic storms obtained by double superposed epoch analysis. *Ann. Geophys.* 28, 2177–2186. doi:10.5194/angeo-28-2177-2010

Yuan, C., and Zong, Q. (2013). Relativistic electron fluxes dropout in the outer radiation belt under different solar wind conditions. *J. Geophys. Res. Space Phys.* 118 (12), 7545–7556. doi:10.1002/2013ja019066

Yue, C., and Zong, Q. (2011). Solar wind parameters and geomagnetic indices for four different interplanetary shock/ICME structures. *J. Geophys. Res.* 116 (A12). doi:10.1029/2011ja017013

Zhang, X. J., Li, W., Thorne, R. M., Angelopoulos, V., Ma, Q., Li, J., et al. (2016). Physical mechanism causing rapid changes in ultrarelativistic electron pitch angle distributions right after a shock arrival: Evaluation of an electron dropout event. *JGR. Space Phys.* 121 (9), 8300–8316. doi:10.1002/2016ja022517

frontiers | Frontiers in Astronomy and Space Sciences

TYPE Original Research
PUBLISHED 05 January 2023
DOI 10.3389/fspas.2022.975135

OPEN ACCESS

EDITED BY
Georgios Balasis,
National Observatory of Athens, Greece

REVIEWED BY
Lauri Holappa,
University of Oulu, Finland
David Gary Sibeck,
Goddard Space Flight Center, National Aeronautics and Space Administration, United States
Matteo Faganello,
UMR7345 Physique des interactions ioniques et moléculaires (P2IM), France

*CORRESPONDENCE
Joseph E. Borovsky,
jborovsky@spacescience.org

SPECIALTY SECTION
This article was submitted to Space Physics, a section of the journal Frontiers in Astronomy and Space Sciences

RECEIVED 21 June 2022
ACCEPTED 16 December 2022
PUBLISHED 05 January 2023

CITATION
Borovsky JE (2023), Further investigation of the effect of upstream solar-wind fluctuations on solar-wind/magnetosphere coupling: Is the effect real?
Front. Astron. Space Sci. 9:975135.
doi: 10.3389/fspas.2022.975135

Further investigation of the effect of upstream solar-wind fluctuations on solar-wind/magnetosphere coupling: Is the effect real?

Joseph E. Borovsky*

Center for Space Plasma Physics, Space Science Institute, Boulder, CO, United States

There is a general consensus that fluctuations in the solar wind magnetic field and/or the Alfvenicity of the solar wind drive a solar wind-magnetosphere interaction. 11 years of hourly-averaged solar wind and magnetospheric geomagnetic indices are used to further examine this hypothesis in detail, confirming that geomagnetic activity statistically increases with the amplitude of upstream fluctuations and with the Alfvénicity, even when solar-wind reconnection driver functions are weak and reconnection on the dayside magnetopause should vanish. A comparison finds that the fluctuation-amplitude effect appears to be stronger than the Alfvénicity effect. In contradiction to the generally accepted hypothesis of driving an interaction, it is also demonstrated that many solar wind parameters are correlated with the fluctuation amplitude and the Alfvénicity. As a result, we caution against immediately concluding that the latter two parameters physically drive the overall solar-wind/magnetosphere interaction: the fluctuation amplitude and Alfvénicity could be acting as proxies for other more-relevant variables. More decisive studies are needed, perhaps focusing on the roles of ubiquitous solar-wind strong current sheets and velocity shears, which drive the measured amplitudes and Alfvénicities of the upstream solar-wind fluctuations.

KEYWORDS

magnetosphere, solar wind, geomagnetic activity, reconnection, viscous interaction, turbulence, Alfvenicity

1 Introduction

The impact of upstream solar-wind fluctuations on the driving of the Earth's magnetosphere has been of interest for decades [*cf.* the recent review by D'Amicis et al., (2020)]. Early interest was on the association between low-frequency Alfvénic magnetic-field fluctuations in high-speed-stream solar wind with high-speed-stream-driven geomagnetic activity, so-called "HILDCAA" events (Tsurutani and Gonzalez, 1987; Tsurutani et al., 1995; Tsurutani et al., 1999; Gonzalez et al., 1999; Diego et al., 2005). During the high-speed streams coordinated few-hour periodicities are seen in the

properties of the solar-wind fluctuations and in the behavior of geomagnetic indices (e.g., Tsurutani and Gonzalez, 1987; Diego et al., 2005). For these high-speed-stream driving events the underlying physical mechanism driving the Earth was hypothesized to be enhanced dayside reconnection during the southward–IMF portions of the low-frequency magnetic fluctuations (Gonzalez et al., 1999; Tsurutani et al., 1999). This hypothesis is consistent with the observed Russell-McPherron-effect variation of magnetospheric activity during high-speed stream driving (Borovsky and Steinberg, 2006a; McPherron et al., 2009). Voros et al., (2002) proposed a further hypothesis that the fluctuating direction of the solar-wind magnetic field gives rise to patchy reconnection on the dayside magnetosphere.

Jankovicova et al., (2008a), Jankovicova et al., (2008b) focused their solar-wind/magnetosphere data-analysis research on the correlations between geomagnetic activity and 1) the solar-wind fluctuation kurtosis and 2) the solar wind "Shebalin angle" θ. The Shebalin angle is directly related to the normalized fluctuation amplitude ΔB/B of the solar wind fluctuations, where ΔB is the vector fluctuation amplitude of the magnetic-field vector $\Delta B = < (\mathbf{B} - < \mathbf{B} >)^2 >^{1/2}$ where <> denotes averaging over an hour of measurements and where $B = < |\mathbf{B}| >$: the Shebalin angle θ (in degrees) is approximately 85–23.6ΔB/B, which is a linear-regression fit to expression (2) of Jankovicova et al., (2008b) with parameters m = 0.4 and c = 0.01. Jankovicova et al., (2008a), Jankovicova et al., (2008b) suggested that turbulent fluctuations in the solar wind created an increase in favorable reconnection geometries on the dayside magnetopause.

Beyond reconnection driving of the magnetosphere, evidence has been found of an enhanced driving associated with the amplitude of solar-wind upstream magnetic-field fluctuations (Borovsky and Funsten, 2003; Borovsky and Steinberg, 2006b; Borovsky, 2006; Borovsky, 2013), even during intervals of strongly northward IMF when dayside reconnection should not be occurring (Borovsky and Funsten, 2003; Borovsky and Steinberg, 2006b; Osmane et al., 2015). The increase in the amplitude of the solar-wind fluctuations was correlated with about a 100-nT increase in the AE index. In analogy with the "freestream turbulence effect" in wind tunnels (Kwok and Melborne, 1980; Sullerey and Sayeed Khan, 1983; Blair, 1983a; Blair, 1983b; Hoffmann, 1991; Hoffmann and Mohammadi, 1991; Wu and Faeth, 1994; Volino, 1998; Pal, 1985; Thole and Bogard, 1996; Volino et al., 2003), Borovsky and Funsten (2003) hypothesized that the beyond-reconnection driving mechanism was an enhanced eddy viscosity in the solar wind plasma associated with the enhanced fluctuations [see Figure 1 of Borovsky (2006)]: the enhanced eddy viscosity would more-efficiently transfer momentum from the solar wind to the magnetosphere. A specific freestream-turbulence driver function was derived for the supersonic solar wind (*cf.* Section 2).

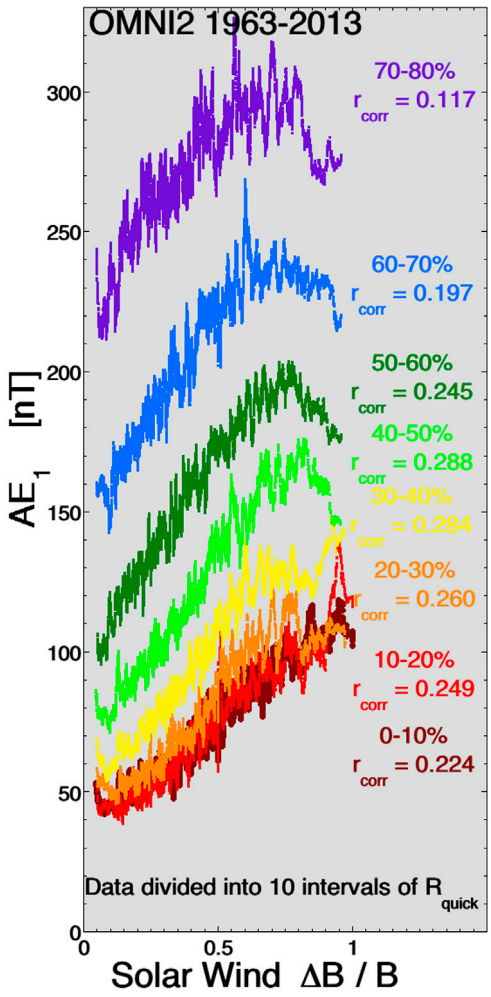

FIGURE 1
For times when the value of R_{quick} is in 10-percent intervals, 300-point running averages of the one-hour-lagged AE index is plotted as a function of the amplitude ΔB/B of the upstream solar-wind turbulence.

D'Amicis et al., (2007), D'Amicis et al., (2009), D'Amicis et al., (2010) focused their solar-wind/magnetosphere data analysis on the driving of the Earth's magnetosphere by highly Alfvénic fluctuations during high-speed streams, finding clear evidence of the relationship between Alfvénic fluctuations in the solar wind and elevated values of the AE index activity.

Osmane et al., (2015) examined the relation between the occurrence distributions of AL-index values as functions of the mean spectral power of solar-wind B_z fluctuations for both average southward and average northward IMF. That study found effects of the magnetic-field fluctuations impacting the AL index at levels up to 200 nT.

An important question is whether this enhanced (beyond reconnection) driving of the Earth's magnetosphere correlated

TABLE 1 Correlation coefficients between relevant variables and $\Delta B = \langle (\underline{B} - \langle \underline{B} \rangle)^2 \rangle^{1/2}$, $\Delta B/B$, and Alfvénicity $|A|$. The Alfvénicity is calculated using the ACE data in the years 1998–2008, other correlations use the OMNI2 dat in the years 1998–2012.

Variable	rcorr with ΔB	rcorr with $\Delta B/B$	rcorr with $\|A\|$
v_{sw}	+0.31	+0.22	+0.35
N	+0.30	+0.08	−0.30
T_p	+0.46	+0.26	+0.24
B_{mag}	+0.55	−0.16	−0.01
ΔB	+1.00	+0.62	+0.14
$\Delta B/B$	+0.62	+1.00	+0.19
Alfvénicity $\|A\|$	+0.14	+0.19	+1.00
M_A	−0.20	+0.31	−0.20
Newell driver	+0.26	−0.05	+0.05
R_{quick} driver	+0.41	−0.01	+0.07
$S_{(1)(9b)}$	+0.42	+0.09	+0.05
AE_1	+0.36	+0.07	+0.10
Kp_1	+0.54	+0.18	+0.16
Dst_2	−0.25	+0.02	−0.08
$E_{(1)(9a)}$	+0.42	+0.12	+0.04

with solar-wind fluctuations is real in the sense that the solar-wind fluctuations are physically doing something to the Earth's magnetosphere. An alternative is that the properties of the solar-wind fluctuations are acting as a proxy for other solar-wind variables that are in fact causally affecting the rate of driving. Determining cause and effect has been difficult in solar-wind/magnetosphere data studies for a number of reasons: 1) the solar wind that hits an upstream monitor at L1 is not the solar wind that hits the Earth leading to errors in the solar-wind variables (Borovsky, 2018a; Borovsky, 2022a; Walsh et al., 2019; Burkholder et al., 2020; Sivadas and Sibeck, 2022), 2) geomagnetic indices are imperfect measures of solar-wind driving 3) there are strong intercorrelations of all pertinent solar-wind variables (Borovsky, 2018b; Borovsky, 2020a), 4) noise in the measurement values change the best-data-fit answers for solar-wind driver functions (Borovsky, 2022b; Borovsky, 2022c), and 5) there is a math-versus-physics dilemma in fitting solar wind data to magnetospheric data (Borovsky, 2021a).

Table 1 lists some of the variables that the fluctuation amplitudes ΔB and $\Delta B/B$ and the Alfvénicity $|A|$ are correlated with. Most relevant, ΔB, $\Delta B/B$, and $|A|$ are all positively correlated with the solar-wind speed v_{sw}, which is known to be a strong driver variable of the magnetosphere. Also relevant is the fact that ΔB is strongly correlated with the solar-wind magnetic-field strength B, another strong driving variable for the magnetosphere.

Three key questions are as follows. 1) Is the fluctuation effect on geomagnetic activity real? 2) If it is real, by what mechanisms do the fluctuations affect the coupling of the solar wind to the magnetosphere? 3) Or, is the fluctuation amplitude a proxy for something else in the solar wind that affects the coupling? Prior publications on the fluctuation effect largely did not consider these three issues.

This paper is organized as follows. Section 2 contains new and improved data analysis of the connections between upstream fluctuation amplitudes, Alfvénicity, and geomagnetic activity. Section 3 summarizes the new statistical findings and draws conclusions. Section 4 discusses (a) the potential role of solar-wind current sheets and velocity shears, (b) the fluctuation effect in the different major types of solar-wind plasma, (c) a reconnection-clock-angle effect, and (d) a connection between the solar-wind driving of the magnetosphere and the standard model for MHD turbulence in the solar wind. Section 5 suggests needed future work to discern whether or not the upstream-fluctuation effect is real.

2 Solar-wind/magnetosphere data analysis

Figure 1 uses 1-hr-averaged OMNI2 data (King and Papitashvili, 2005) to demonstrate the suspected effect of upstream solar-wind fluctuations on the magnetosphere independent of the rate of dayside reconnection. Here the 1-hr-lagged (from the solar wind) AE index (AE_1) is plotted as a function of the fluctuation amplitude $\Delta B/B$ in the upstream solar wind. $\Delta B/B$ is effectively the rms wiggle angle (in radians) of the magnetic-field direction averaged for that hour of solar-wind data. To gauge the magnitude of the dayside reconnection rate the function R_{quick} is used, where

$$R_{quick} = 6.9\, m_p^{1/2} n_{sw}^{1/2} v_{sw}^{2} \sin^{2}(\theta_{clock}/2) M_A^{-1.35} \left[1 + 680 M_A^{-3.30}\right]^{-1/4} \quad (1)$$

(e.g., Borovsky and Birn, 2014; Borovsky and Yakymenko, 2017), where n_{sw} is the solar-wind number density, m_p is the proton mass, θ_{clock} is the (GSM) clock angle $\theta_{clock} = \arccos(B_z/(B_y^2+B_z^2)^{1/2})$, and M_A is the solar-wind Alfvén Mach number. R_{quick} was derived to be the solar-wind controlling factor for the reconnection rate at the nose of the dayside magnetopause. Each of the curves plotted in different colors in Figure 1 pertains to a subset of 10% of the data categorized into the subsets according to the magnitude of R_{quick} in each hour of data. For example, the dark-red curve at the bottom of the plot is for the times when the value of R_{quick} is in the lowest 10% of its values, the red curve is for the second lowest 10% of the R_{quick} values, the orange curve is

for the third lowest 10% of the R_{quick} values, etc. Only the first six of the 10 intervals are plotted: the two highest-R_{quick} intervals have a trend that reverses in the plot. As the R_{quick} values increase from subset to subset in Figure 1, the dayside reconnection rate increases and the curves shift to higher values of AE_1. In Figure 1 the individual hourly values of AE_1 are not plotted, rather for each subset of data a 300-point running average of AE_1 versus $\Delta B/B$ is plotted to show the underlying trend in the scatter of points. The Pearson linear correlation coefficient r_{corr} between AE_1 and $\Delta B/B$ is indicated on the plot for each data subset: this r_{corr} value pertains to the individual hourly data points not to the running averages. In each data subset there are about 27,000 hourly data points so r_{corr} values that are $|r_{corr}| > 0.012$ are statistically significant (i.e., inconsistent with random). As can be seen in Figure 1, AE_1 increases systematically with increasing amplitudes $\Delta B/B$ of upstream solar-wind fluctuations, whether or not dayside reconnection is expected on the basis of solar-wind conditions.

Figure 1 is similar to Figure 6 of Borovsky and Steinberg (2006b) where the solar-wind driver function $v_{sw}B_z$ was used to sort the data: R_{quick} used in Figure 1 is a superior variable to use for sorting the data according to the expected dayside reconnection rate.

The reversal of the $\Delta B/B$ correlation with AE_1 for strong values of R_{quick} can be seen in the red curve with circular points in Figure 2 where correlation coefficients r_{corr} between several solar-wind variables and AE_1 are plotted for each of the 10 bins of R_{quick}, with low values of R_{quick} to the left in the plot and large values of R_{quick} to the right. In Figure 2 attention should be paid to the R_{quick} bins to the left where the $\Delta B/B$ effect is not overwhelmed by the R_{quick} reconnection driving. Note that with this R_{quick} sorting there are other solar-wind variables that have higher correlation coefficients with AE_1 than $\Delta B/B$ does: in particular nv^2 (green curve) and v_{sw} (dark-red curve). In constructing viscous-interaction driver functions that act in addition to dayside-reconnection driving, these two variables are prominent (Borovsky, 2013), including when an "eddy-viscosity" driver function is derived (*cf.* expression (2a) below). As can be seen in expressions (2a), (2b), and (2c) below, this derived eddy-viscosity driver function depends linearly on the amplitude of the solar-wind magnetic-field fluctuations ΔB, and also on various powers of the solar-wind number density and the solar-wind velocity and it depends on algebraic functions of the solar-wind Mach number and the angle between the solar-wind magnetic field and the Sun-Earth line.

As stated above, for very large values of R_{quick} the AE-versus-$\Delta B/B$ trend reverses. For strong R_{quick}, the $\Delta B/B$ effect is a small fraction of the total driving and difficult to analyze: any effect that causes the strong reconnection rate to vary could dominate over the $\Delta B/B$ effect. Without specifically studying these cases, one can only speculate. The decrease at strong R_{quick} might be owed to the fact that the strong-driving cases sometimes involve

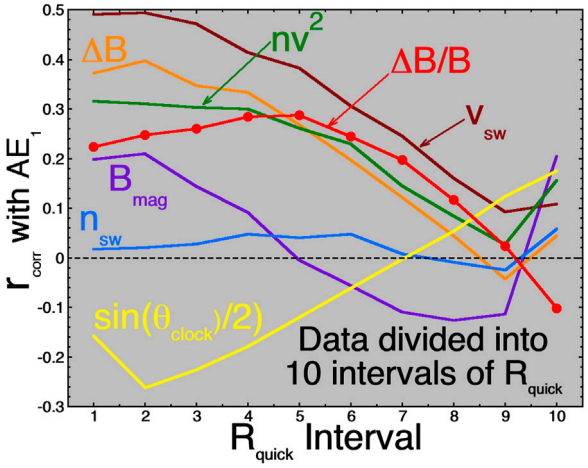

FIGURE 2
Correlation coefficients r_{corr} between several solar-wind variables and AE_1 are plotted for each of the 10 bins of R_{quick} (binned as in Figure 1).

magnetic clouds (often the strongest-driving times) and $\Delta B/B$ is small in clouds (e.g., Richardson and Cane, 2010): the selection of small $\Delta B/B$ in that case is then picking out strong driving by clouds.

The two panels of Figure 3 repeat the process of Figure 1, but sort on two other solar-wind variables besides R_{quick}. The left panel sorts the data into 10 bins of v_{sw} values and the right panel sorts the data into 10 bins of ram pressure nv^2 values. In both panels the relationship between $\Delta B/B$ and AE is much weakened from Figure 1 with correlation coefficients r_{corr} that are in general a small fraction of those in Figure 1 where R_{quick} sorting was used. This validates the interpretation of Figure 1 that the $\Delta B/B$ affect is in addition to the reconnection driving described by R_{quick}.

Figure 4 is similar to the plots of Figure 1, but a composite "Earth index" is used rather than a single geomagnetic index. The composite index $E_{(1)(9a)}$ is given by eq. (9a) of Borovsky and Denton (2014) and it is comprised from nine measures of magnetospheric activity: the standard geomagnetic indices AE, AU, AL, PCI, Kp, and Dst, plus a 1-hr-resolution midnight boundary index MBI (Gussenhoven et al., 1983), plus two ULF indices S_{grd} and S_{geo} (Borovsky and Denton, 2014). The mathematical method used to derive the composite index $E_{(1)(9a)}$ is canonical correlation analysis (CCA) and the method also derives a solar-wind driver function $S_{(1)(9b)}$ that corresponds to $E_{(1)(9a)}$. To make Figure 4, only times when the driver function $S_{(1)(9b)}$ is in its first (lowest) ten percentiles are used. The first 10% choice is for simplicity and is meant to sort for times when dayside reconnection is low. Then, for those times, a running average of $E_{(1)(9a)}$ as a function of $\Delta B/B$ is plotted. As can be seen, there is a clear trend where the Earth index $E_{(1)(9a)}$ systematically increases as the amplitude of the solar-wind fluctuations increases. For the

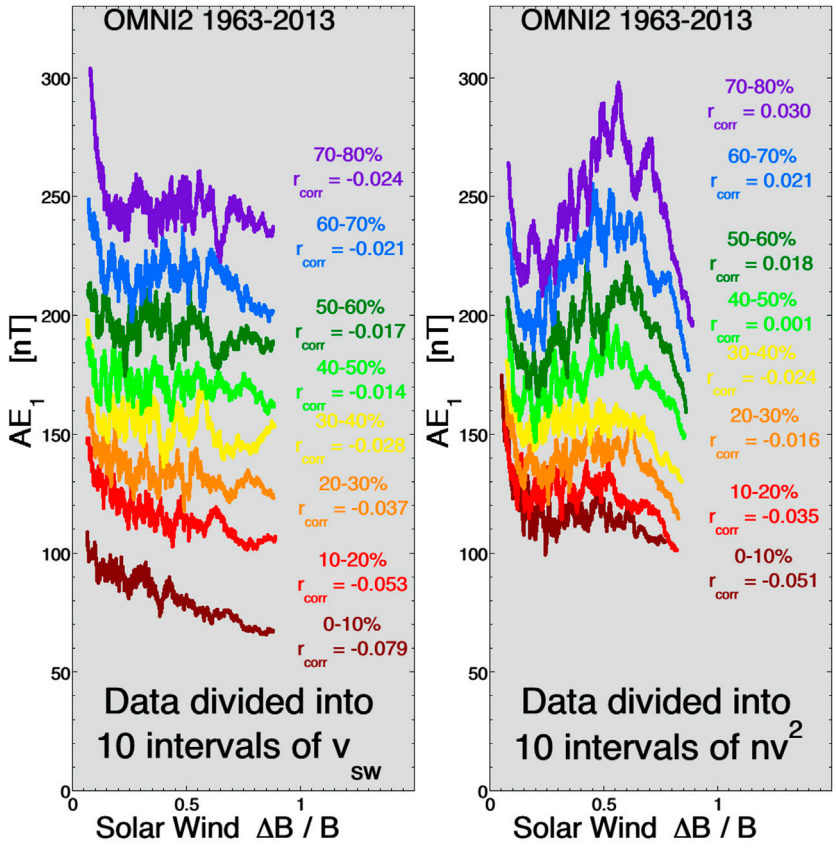

FIGURE 3
(left panel) For times when the value of v_{sw} is in 10-percent intervals, 300-point running averages of the one-hour-lagged AE index is plotted as a function of the amplitude ΔB/B of the upstream solar-wind turbulence. (right panel) For times when the value of the solar wind ram pressure nv^2 is in 10-percent intervals, 300-point running averages of the one-hour-lagged AE index is plotted as a function of the amplitude ΔB/B of the upstream solar-wind turbulence.

hourly points used in Figure 4 (not the running average), the Pearson linear correlation coefficient r_{corr} between $E_{(1)(9a)}$ and ΔB/B is $r_{corr} = 0.16$, again a definite correlation.

Figure 5 is similar to Figure 1 but it uses only the lowest 10% of the R_{quick} values and it examines geomagnetic activity as functions of other non-reconnection solar-wind drivers. Again, the choice of the first 10% is for simplicity and is meant to sort for times when dayside reconnection is low. The blue curves replot AE_1 [panel (a)] and $Hp60_1$ [panel (b)] as a function of ΔB/B for the upstream solar-wind fluctuations. (Hp60 is a 60-minute-resolution version of the Kp index now available at ftp://ftp.gfz-potsdam.de/pub/home/obs/Hpo; $Hp60_1$ is the Hp index lagged by 1 h from the solar-wind-at-Earth measurements.) Again running averages of the individual hourly points are plotted. The red curves in both panels of Figure 5 plot geomagnetic activity as a function of v_{sw} for the times with the lowest 10% of R_{quick} values, with v_{sw} intercorrelated with ΔB/B (*cf.* Table 1). The green curves in both panels of Figure 5 plot geomagnetic activity as a function of the Mach-number-dependent theoretical eddy-viscosity-based coupling coefficient F for the super-sonic solar wind [*cf.* Eqs. 4d, (61), and (63) of Borovsky (2013)]

$$\mathcal{F} = n_{sw}^{1/2} v_{sw}^{11/6} \Delta B^{1/2} C^{-1} G \tag{2a}$$

$$G = C^{2/3}(1+C)^{1/4}\left[1 - 0.5\left(1 - C^{-2}\right)\sin^2(\theta_{Bn})\right]^{1/4} \tag{2b}$$

$$C = \left\{2.44 \times 10^{-4} + \left[1 + 1.38\log_e(M_A)\right]^{-6}\right\}^{-1/6} \tag{2c}$$

where n_{sw} is the solar-wind number density, v_{sw} is the solar-wind speed, $\Delta B = < (\mathbf{B} - < \mathbf{B} >)^2 >^{1/2}$ is that amplitude of vector fluctuations of the solar wind magnetic field, C is the compression ratio of the bow shock, M_A is the solar-wind Alfvén Mach number, and θ_{Bn} is taken to be a nominal Parker-spiral angle of 45°. The black curves in Figure 5 plot geomagnetic activity as a function of a Mach-number-dependent Bohm-diffusion viscous-coupling coefficient B for the super-

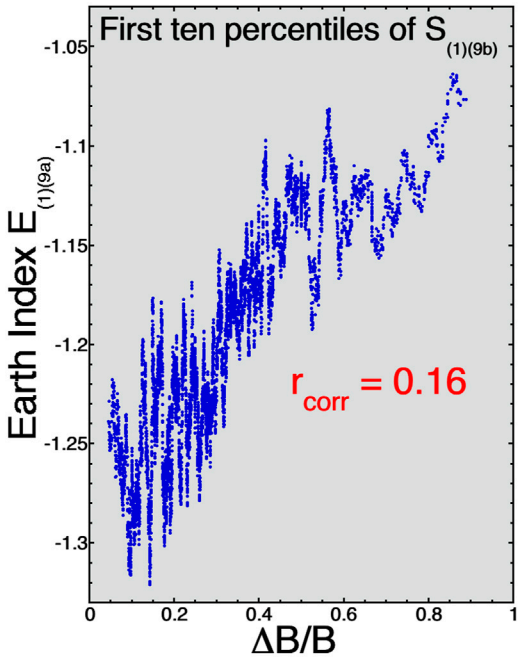

FIGURE 4
For times when the solar-wind composite driver function $S_{(1)(9b)}$ is in its lowest 10% of values, a 101-point running average of the Earth index $E_{(1)(9a)}$ is plotted as a function the upstream fluctuation amplitude ΔB/B.

sonic solar wind (*cf.* Eqs. 4d, (33), and (39) of Borovsky (2013) and eq. (7) of Borovsky (2008a))

$$\mathcal{B} = n_{sw}^{1/2} v_{sw}^{5/2} C^{-1/2} W^{1/2} \quad (3a)$$

$$W = \beta_s C^{-1/2} (1 + 0.5 M_A^{-2})^{1/2} (1 + \beta_s)^{-1/2} \quad (3b)$$

$$\beta_s = (M_A/6)^{1.92} \quad (3c)$$

where β_s is the plasma-beta value of the magnetosheath plasma at the nose of the magnetopause. Simpler non-Mach-number dependent Bohm viscosity coefficients for non-super-sonic solar wind have been derived by Eviatar and Wolf (1968) and by Vasyliunas et al., (1982). Again, for F and B only the running averages are plotted in Figure 5. Note that the horizontal axis of Figure 5 has been approximately "normalized" for all variables ΔB/B, v_{sw}, F, and B so that the running-average curves each extend from ~0 to ~1 for easy visual intercomparison. Figure 5 shows systematic increases in AE_1 [panel (a)] and $Hp60_1$ [panel (b)] for increasing values of each of the drivers. Pearson linear correlation coefficients r_{corr} are also indicated for the hourly points in Figure 5. The significance levels for the correlation coefficients (with ~15,600 hourly data points for each variable) is $|r_{corr}| > 0.016$. Recall that the data points used for Figure 5 were only the times when the R_{quick} values were in the lowest 10 percentiles, i.e., during weak dayside reconnection.

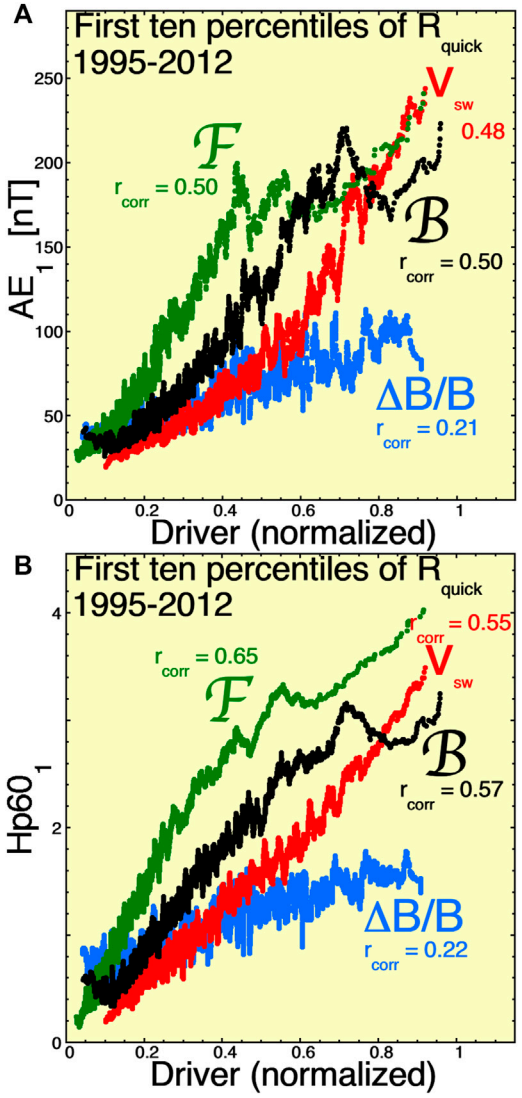

FIGURE 5
For times when the value of R_{quick} is in its lowest 10%, 101-point running averages of AE_1 [panel **(A)**] and $Hp60_1$ [panel **(B)**] are plotted as functions of four "drivers": ΔB/B (blue), v_{sw} (red), F (green), and B (black).

Whereas in Figure 5 the variation of ΔB/B corresponds to an increase in AE_1 of about 75 nT and to an increase of $Hp60_1$ of about 1, the other driver variables seem to account for much larger increases, about 200 nT in AE_1 and up to 3.5 values of $Hp60_1$. The values of AE_1 increase seem reasonable, but the values of $Hp60_1$ increase seem large if this is a "subtle" as-yet-unconfirmed driving mechanism. The Hp601 changes in Figure 5 are from ~0.5 to ~4; note that Hp60 is a logarithmic index so changes of Hp at small values of Hp involve smaller changes in activity than do changes of Hp at large values of Hp.

The effect of the solar-wind Alfvénicity is explored in Figures 6–10. The Alfvénicity |A| of the solar wind is

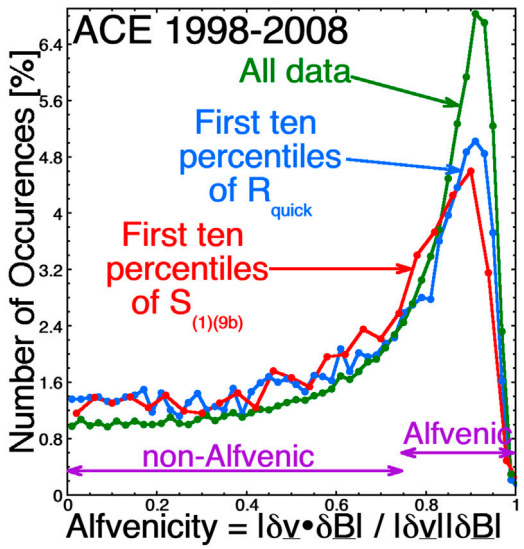

FIGURE 6
Occurrence distributions of the Alfvénicity |A| are plotted for all times (green), for times when the value of R_{quick} is in the lowest 10% of its values (blue), and for time when the value of $S_{(1)(9a)}$ is in the lowest 10% of its values.

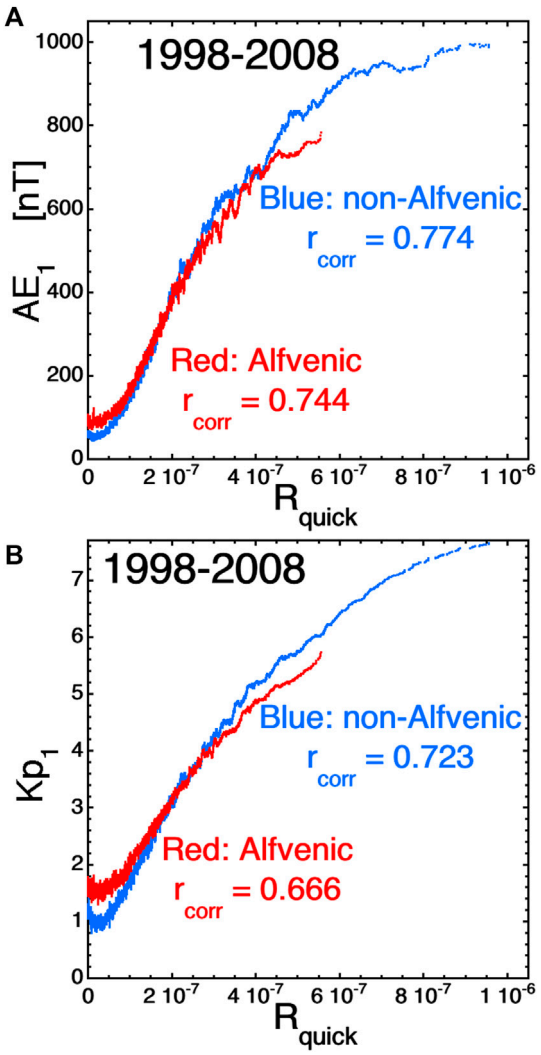

FIGURE 7
201-point running averages of AE_1 [panel **(A)**] and of Kp_1 [panel **(B)**] are plotted as functions of the solar-wind driver R_{quick} separately for times when the solar wind was non-Alfvénic (blue, |A| < 0.75) and for times when the solar wind was Alfvénic (red, |A| > 0.75).

calculated using measurements from the ACE spacecraft at L1 with 64-s averaged values from the Magnetic Field Instrument (MFI) (Smith et al., 1998) and proton flow measurements with 64-s time resolution from the Solar Wind Electron Proton Alpha Monitor (SWEPAM) (McComas et al., 1998), both data sets from the "Merged IMF and Solar Wind 64-s Averages" (available from the ACE Science Center at http://www.srl.caltech.edu/ACE/ASC/level2/index.html). The |A| value of the fluctuations for each hour of data at 128-s is calculated, where

$$|A| = |\delta \underline{v} \bullet \delta \underline{B}| / |\delta \underline{v}||\delta \underline{B}| \quad (4)$$

with $\delta \underline{v}(t) = \underline{v}(t + 64s) - \underline{v}(t - 64s)$ and $\delta \underline{B}(t) = \underline{B}(t + 64s) - \underline{B}(t - 64s)$. As described in Borovsky et al., (2019), calculations of the solar-wind Alfvénicity are contained in the Level 3 "ACE Hourly Data Parameters for Magnetospheric Driving" data set available at http://www.ssg.sr.unh.edu/mag/ace/HourlyParms/HourlyParms.html in the ACE Science Data Center. The downloadable data file THA.out contains a fluctuation analysis for each 1-h interval of the ACE for the years 1998–2008.

Three occurrence distributions for the Alfvénicity |A| are plotted in Figure 6: for all times (green curve), for times when the R_{quick} values are low (the first ten percentiles) (blue curve), and for times when the solar-wind driver function $S_{(1)(9b)}$ is low (the first ten percentiles) (red curve). High Alfvénicity is high velocity-field correlation, so Alfvénic wind in Figure 6 will be taken as |A| > 0.75 and non-Alfvénic wind will be taken to be |A| < 0.75. As can be discerned by the distribution shapes of Figure 6, the Alfvenicity tends to be high (>75%) or modest (<75%). The Alfvenicity is rarely unity. The flat-shaped distribution of Alfvenicity values in Figure 6 (which should extend from |A| = 0 to |A| = 1) is consistent with uncorrelated (random, non-Alfvenic) values of $\delta \underline{B}$ and $\delta \underline{v}$ changes, i.e., non-Alfvenic regions of solar wind [*cf.* Figure 11B of Borovsky et al., (2019)].

In the two panels of Figure 7 the relation of Alfvénic wind (red curves) *versus* non-Alfvénic wind (blue curves) to geomagnetic activity as measured by the AE index [panel (a)] and by the Kp index [panel (b)] is explored. Data for all

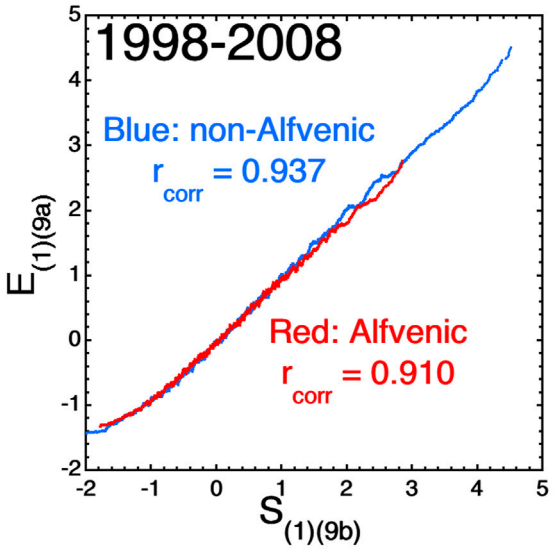

FIGURE 8
201-point running averages of the Earth index $E_{(1)(9a)}$ are plotted as functions of the solar-wind composite driver $S_{(1)(9b)}$ separately for times whe n the solar wind was non-Alfvénic (blue, |A| < 0.75) and for times when the solar wind was Alfvénic (red, |A| > 0.75).

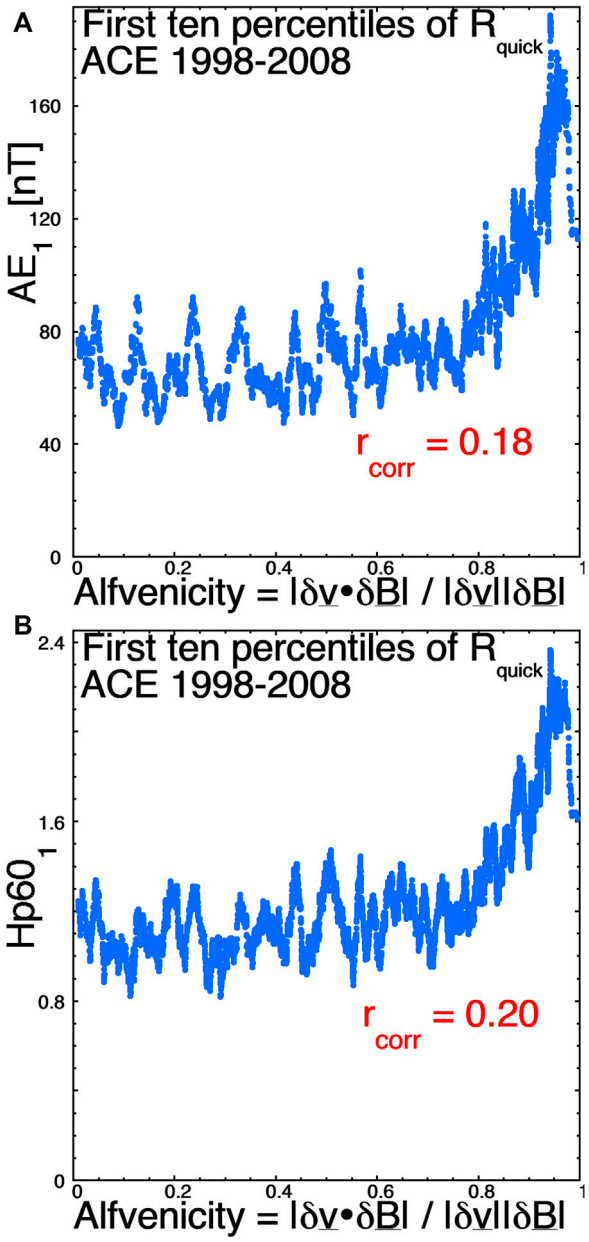

FIGURE 9
For times when the solar-wind driver R_{quick} is in its lowest 10% of values, 101-point running averages of AE_1 [panel **(A)**] and of $Hp60_1$ [panel **(B)**] are plotted as functions of the Alfvénicity |A|.

times in 1998–2008 is used. The individual hourly data points are not plotted: instead 201-point running averages of the individual hourly points are plotted to show the trends underlying the scatter of points. Pearson linear correlation coefficients r_{corr} for the hourly data points (not the running averages) are indicated on the plots. Both panels of Figure 7 indicate a change in the geomagnetic activity for weak driving (low R_{quick} values) between Alfvénic wind (red) and non-Alfvénic wind (blue), with elevated geomagnetic activity in the Alfvénic wind. A "relationship" between Alfvénicity and geomagnetic activity is seen, but an important question focuses on whether or not the relationship is cause and effect? One might worry because the Alfvénicity |A| of the solar wind is correlated with several other variables and a "correlative" relationship could be created by |A| acting as a proxy for a more-causal variable. In Table 1 some Pearson linear correlation coefficients between the Alfvénicity |A| and other solar-wind and magnetospheric variables are collected. Note in the solar wind a somewhat robust correlation of |A| with v_{sw} (+0.35) and weaker correlations of |A| with ΔB and ΔB/B (+0.14 and +0.19). These positive correlations in part are probably associated with the high Alfvenicity of coronal-hole-origin plasma, which has tends to have high velocities [*cf.* Figures 8, 11 of Borovsky et al., (2019)].

In Figure 8 the relation of Alfvénic wind (red curve) versus non-Alfvénic wind (blue curve) to geomagnetic activity as measured by the $E_{(1)(9a)}$ composite magnetospheric-activity index is explored. As in the prior figures, the individual hourly data points are not plotted: instead a 201-point running average of the individual hourly $E_{(1)(9a)}$ values are plotted to show the trends underlying the scatter of points. Pearson linear correlation coefficients r_{corr} for the hourly data points (not the running averages) are indicated on the plot. Contrary to AE and Kp in Figure 7, there is very little systematic difference between the values of $E_{(1)(9a)}$ for

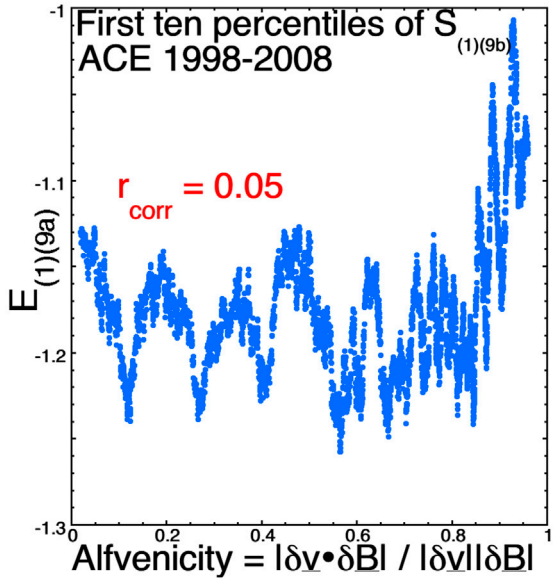

FIGURE 10
For times when the solar-wind composite driver $S_{(1)(9b)}$ is in its lowest 10% of values, 101-point running averages of the Earth index $E_{(1)(9a)}$ is plotted as a function of the Alfvénicity |A|.

Alfvénic versus non-Alfvénic solar wind. At this point, no explanation for the reduced effect on $E_{(1)(9a)}$ is available: two inconclusive research efforts intersect on this point. 1) In the present research the effect of solar-wind fluctuations is being examined and 2) in other active research efforts (e.g., Borovsky and Denton, 2018; Borovsky and Osmane, 2019; Borovsky, 2021b) the properties of the composite index are being examined, with no full understanding on either issue.

Figure 9 is similar to Figure 5 using the lowest 10% of the R_{quick} values, examining geomagnetic activity as measured by AE [panel (a)] and Hp60 [panel (b)] as functions of the value of the Alfvénicity |A| for the weak R_{quick} driving of the magnetosphere. Again running averages of the individual hourly points are plotted. Both panels of Figure 8 indicate increases in geomagnetic activity associate with Alfvénic wind (|A| > 0.75), with almost 100 nT of AE increase and about half a unit of Hp60 increase. For the times when the R_{quick} value is in the lowest 10%, the Pearson linear correlation coefficient r_{corr} between |A| and the two geomagnetic indices are indicted on the two plots of Figure 9.

Figure 10 is similar to Figure 9, but it looks at the effect of the solar-wind Alfvénicity |A| on the composite magnetospheric-activity index $E_{(1)(9a)}$ when the magnetospheric driving by the solar-wind variable $S_{(1)(9b)}$ is at its lowest 10% of values. A distinct relation is seen in Figure 10 between Alfvénic wind (|A| > 0.75) and an increase in $E_{(1)(9a)}$, but compared with the vertical range of values of $E_{(1)(9a)}$ seen in Figure 8, the ~0.15 increase in $E_{(1)(9a)}$ is quite small. The correlation between |A| and $E_{(1)(9a)}$ for the lowest 10% of $S_{(1)(9b)}$ driving is also quite weak (+0.05).

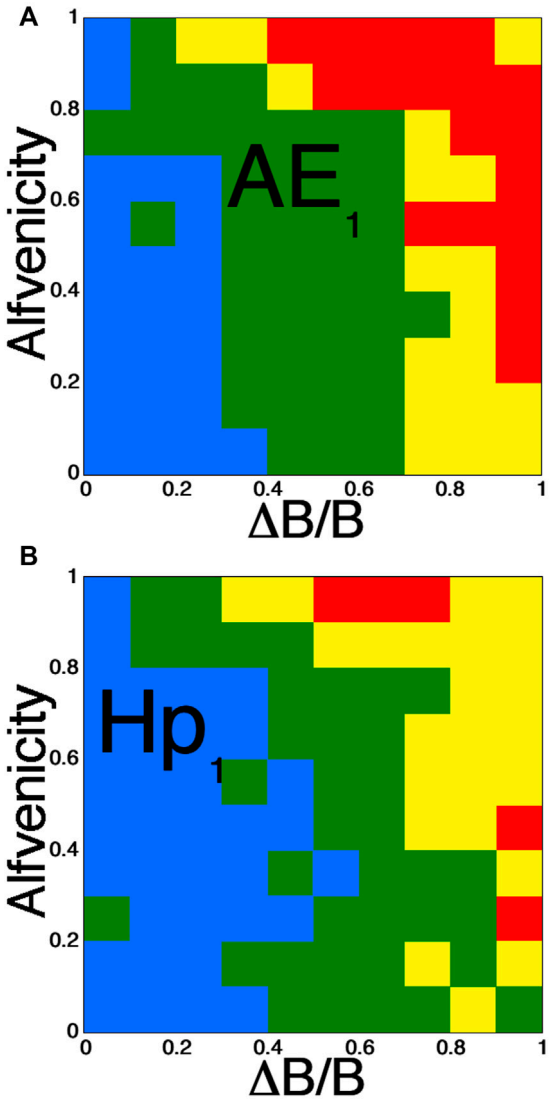

FIGURE 11
For times when R_{quick} is in the lowest 20% of its values, the AE index and the Hp60 index are binned according to the values of ΔB/B and the Alfvénicity |A|. Panel **(A)** denotes the mean value of AE_1 in each bin: red (AE_1 > 100 nT), yellow (75 < AE_1 < 100) green (50 < AE_1 < 75), and blue (AE_1 < 50 nT). Panel **(B)** denotes the m an value of $Hp60_1$ in each bin: red ($Hp60_1$ > 2), yellow (1.5 < $Hp60_1$ < 2), green (1 < $Hp60_1$ < 1.5), and blue ($Hp60_1$ < 1).

Figure 11 explores the combined effects of ΔB/B and Alfvénicity |A|. For times when the value of R_{quick} is in the lowest 20% of its values, the 1-h lagged AE_1 index and the 1-h-lagged $Hp60_1$ index are binned according to the values of ΔB/B and the Alfvénicity |A| in each hour of data. Figure 11A denotes the mean value of AE_1 in each bin: red (AE_1 > 100 nT), yellow (75 < AE_1 < 100), green (50 < AE_1 < 75), and blue (AE_1 < 50 nT).

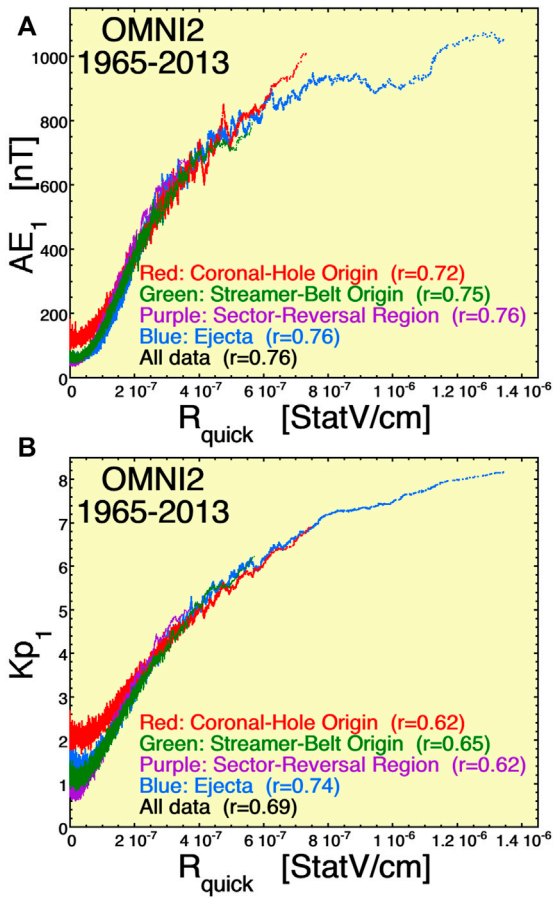

FIGURE 12
Geomagnetic activity is plotted as a function the reconnection driver function R_{quick} separately for the four types of solar-wind plasma. Panel **(A)** plote AE_1 and panel **(B)** plots Kp_1. Only running averages of the individual hourly data points are plotted.

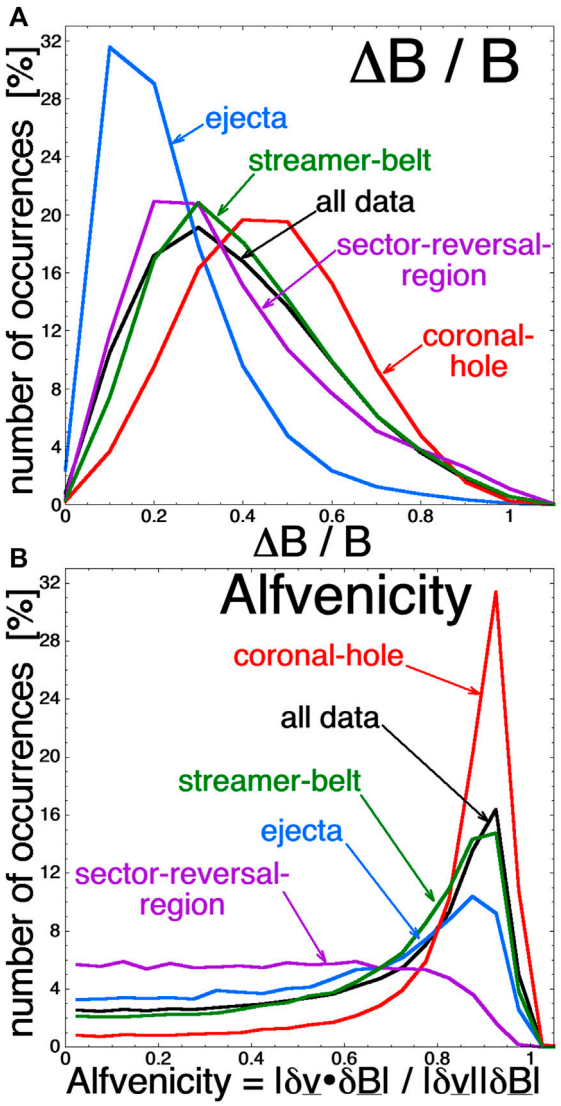

FIGURE 13
The occurrence distribution of ΔB/B [panel **(A)**] and Alfvénicity |A| [panel **(B)**] are plotted for the four types of solar-wind plasma.

Figure 11B denotes the mean value of $Hp60_1$ in each bin: red ($Hp60_1 > 2$), yellow ($1.5 < Hp60_1 < 2$), green ($1 < Hp60_1 < 1.5$), and blue ($Hp60_1 < 1$). Both large ΔB/B and strong |A| seem geoeffective: the highest activity levels are approximately in the upper-right corners of the plots where ΔB/B and |A| are largest. The two plots seem to indicate that stronger geomagnetic activity can occur for strong ΔB/B, even if |A| is weak. However, the opposite is not true: if ΔB/B is weak there is no strong activity if |A| is weak. The interpretation of Figure 11 is not definitive, but it seems to indicate that ΔB/B is more important than Alfvénicity for driving geomagnetic activity.

3 Summary and conclusions

There are three key questions. 1) Is the fluctuation effect on geomagnetic activity real? 2) If it is real, by what mechanisms do the fluctuations affect the coupling of the solar wind to the magnetosphere? 3) Or, is the fluctuation amplitude a proxy for something else in the solar wind that affects the coupling? Related to question 2) are two further questions: (A) do the solar-wind fluctuations change the dayside reconnection rate? or (B) do the solar-wind fluctuations create or enhance a viscous coupling of the solar wind to the magnetosphere?

In this report statistical data-analysis evidence is gathered that is consistent with an effect of the amplitude of solar-wind magnetic-field fluctuations on geomagnetic activity, supporting a number of prior studies. This report also gathers statistical data-analysis evidence consistent with a connection between the

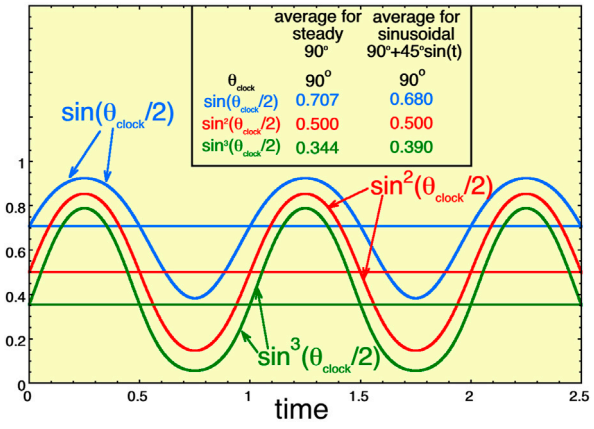

FIGURE 14
The functions $\sin(\theta_{clock}/2)$ (green), $\sin^2(\theta_{clock}/2)$ (red), and $\sin^3(\theta_{clock}/2)$ (blue) are plotted as functions of time for the steady 90° clock angle and for the sinusoidally oscillating clock angle 90° + 45°sin(t). The table in the figure lists the average values for the steady 90° clock angle and for the sinusoidal 90° + 45°sin(t) clock angle.

Alfvénicity of solar-wind fluctuations and geomagnetic activity, supporting prior studies. Evidence that argues against a change-in-dayside-reconnection-rate effect is 1) an effect of the amplitude of fluctuations on geomagnetic activity for strongly northward IMF in the studies of Borovsky and Funsten (2003), Borovsky and Steinberg (2006b), Borovsky (2006), and Osmane et al., (2015) and 2) the effect of the amplitude of fluctuations on geomagnetic activity for very weak values of R_{quick} throughout the present study. On this second issue (R_{quick} being weak) there are two worries. First, R_{quick} is not a perfect description of the control of geomagnetic activity by the solar wind. For instance, in Figure 7A the linear correlations between R_{quick} and AE_1 are r_{corr} ~ 0.75, so the amount of variation of AE_1 not described by a knowledge of the R_{quick} value is 1 - r_{corr}^2 = 44%. Second, R_{quick} can change quickly mostly owing to frequent clock-angle changes and there is persistence to geomagnetic activity (*cf.* Lockwood, 2022), so an hour of weak R_{quick} could have been preceded by an hour of strong R_{quick} and the geomagnetic activity from that prior hour of driving could still persist. When ΔB/B is larger, temporal changes in R_{quick} are likely to be larger (Note that the analysis of Figure 5 of Borovsky and Steinberg (2006b) attempted to guard against this persistence phenomenon and when persistence was eliminated the relationship between ΔB/B on geomagnetic activity was lessened.).

The Bohm-viscosity driver function B without direct information about the fluctuation amplitudes ΔB does about as good a job as does the freestream-turbulence driver function F that contains information about ΔB, as seen by comparing the black and green curves in each of the two panels of Figure 5. This might be an indication of a proxy effect for ΔB/B.

In the present data analysis the effect of the fluctuation amplitudes ΔB/B on the composite whole-magnetosphere activity index $E_{(1)(9a)}$ is found to be small compared to the effect of ΔB/B on AE or Kp. There is no idea as to why. The driver function $S_{(1)(9b)}$ used in the present data-analysis study does not have direct information in it about ΔB (*cf.* eq. (9b) of Borovsky and Denton (2014)). Note that in other constructions of composite solar-wind driving functions using the CCA methodology, if the ΔB variable is offered to the process it will be accepted into the solar-wind driving function $S_{(1)}$; examples are eq. (14) of Borovsky (2014) and Eq. 1b of Borovsky and Osmane (2019). Interpreting the CCA process, the acceptance of the ΔB variable indicates that it may carry unique information that is needed to better describe geomagnetic activity in terms of solar-wind variables.

In summary, evidence is found that supports definitive relationships 1) between the solar wind ΔB/B and geomagnetic activity and 2) between solar-wind Alfvénicity and geomagnetic activity. The ΔB/B relationship seems to be stronger than the Alfvénicity relationship. No clear evidence is found that precludes these relationships from being physical cause-and-effect, although that is still an outstanding question. Needed future work is discussed in Section 5: meanwhile researchers should be cautious.

4 Discussion

The potential roles of solar-wind current sheets, the coupling in different types of solar-wind plasma, and the role of averaging of solar-wind magnetic clock angles are discussed.

4.1 Solar-wind current sheets and velocity shears

The amplitude measure ΔB of the magnetic-field fluctuations in the upstream solar wind is dominated by the ubiquitous strong current sheets (discontinuities) in the solar-wind plasma (Siscoe et al., 1968; Borovsky, 2010); the amplitude measure ΔB does not represent randomly-phased waves (or eddies) at diverse wavelengths (Borovsky, 2022b). The magnetic-field Fourier power spectral density (amplitude and shape) of the solar wind reflects the properties (sizes, occurrence distribution, thickness, and thickness profile) of the solar-wind current sheets [*cf.* Table 1 of Borovsky and Burkholder (2020)]. The strong current sheets have thicknesses of about 1,000 km (Vasquez et al., 2013) and pass the Earth at a rate of several per hour (Borovsky, 2008b); their orientations are such that the normals to the current sheets tend to be perpendicular to the Parker-spiral direction (Borovsky, 2008b). If the current sheets are not time resolved in the time series, the time series still contains the information about the jump sizes in vector-B across

the current sheets and about the temporal occurrence distribution of the current sheets. In Figure 3 of Borovsky (2010) it is demonstrated that the Fourier power (amplitude) of the solar wind at frequencies lower than the time resolution is captured by using only 64-s information about the properties (size and occurrence distribution) of the current sheets seen in the ACE 64-s data for 9 years of measurements. This is the amplitude of ΔB that OMNI2 contains in its ΔB values, which are the fluctuation amplitudes for every UT hour measured with a time resolution that is a small fraction of an hour. Hence, OMNI2 contains a proper measurement of the amplitude of solar-wind fluctuations driven by the solar-wind current sheets. If the current sheets are fully time resolved in the measurements, then the Fourier power above the first high-frequency Fourier breakpoint is captured, in addition to the lower-frequency Fourier amplitude in the inertial range. This capture of high-frequency power when current sheets are resolved is demonstrated in Figures 7, 8 of Borovsky and Podesta (2015) and in Figure 11 of Borovsky and Burkholder (2020).

It is worth speculating whether the passages of the strong current sheets have an impact on the net driving of the Earth's magnetosphere by the solar wind. It is well known that some solar-wind current sheets can produce dayside transients as the current sheets encounter the Earth's bow shock [e.g., Sibeck et al., 1999; Sibeck et al., 2000; Zesta and Sibeck, 2004]. The passage of a strong current sheet represents a sudden strong change in the orientation of the solar-wind magnetic-field vector: this produces a temporal "on-off" driving of the magnetosphere *via* dayside reconnection. A question is: does the on-off driving produce a stronger overall coupling than does steady driving? The change in the reconnecting IMF can produce a twist to the magnetosphere requiring a re-orientation of some magnetospheric current systems. A second question is: does the suddenness of the changes between on-off driving result in enhanced overall coupling? The sudden change of the magnetic-field orientation across a current sheet also produces a sudden change in the IMF clock angle θ_{clock} and a shift in the level of driving *via* dayside reconnection and probably a change in the location of the reconnection site on the dayside magnetopause. A third question is whether jumps in the location of the dayside reconnection site somehow results in enhanced overall coupling? Arguments against these three speculations lie in the fact that the ΔB/B effect persists under strongly northward IMF when there should be little reconnection between the solar wind and the magnetosphere.

Solar-wind strong current sheets (which drive the amplitude of the measured solar-wind magnetic-field fluctuations) are often accompanied by intense abrupt velocity shears, particularly in the "Alfvénic" solar wind. The Alfvénicity measure of the solar wind $|A| = |\delta\underline{v}\bullet\delta\underline{B}/|\delta\underline{v}||\delta\underline{B}|$ is also dominated by the strong current sheets ("discontinuities") of the solar wind and their co-located strong velocity shears [*cf.* Figure 12 of Borovsky and Denton (2010)]. The impacts of intense velocity shears on the magnetosphere have been investigated by Borovsky (2012a), Borovsky (2018c) *via* data analysis and global MHD computer simulations. A common feature seen in the global simulations are comet-like disconnections of the Earth's magnetotail, although these are not likely to produce an enhanced coupling as seen in geomagnetic indices. Other effects seen in the global simulations (Borovsky, 2012a) are temporary enhancements or decreases in the cross-polar-cap potential, the production of ULF waves interior to the magnetosphere, and abrupt changes in the wind-sock orientation of the magnetosphere.

In general $\mathbf{\Delta v}$ is strongly correlated with ΔB in the solar wind [e.g., Figure 14 of Borovsky (2012b)] and particularly in the Alfvénic coronal-hole-origin plasma $\Delta v/v_A$ (where v_A is the Alfvén speed of the solar wind) is highly correlated with ΔB/B [e.g., Figure 13B of Borovsky and Denton (2010)]. Hence, it is undoubtedly true that geomagnetic activity is correlated with Δv and $\Delta v/v_A$ of the solar wind. Future studies should explore the connection between the solar-wind velocity-fluctuation amplitude and geomagnetic activity.

4.2 Different types of solar wind

Xu and Borovsky (2015) developed a categorization scheme at one AU that separates the solar wind at 1AU into four types, depending on the regions of the solar surface from which the different plasma types originate. The four types are coronal-hole-origin plasma, streamer-belt-origin plasma, sector-reversal-region plasma, and ejecta. The four types of solar wind have systematically different properties, including the properties of the magnetic-field and velocity fluctuations in the plasmas (Xu and Borovsky, 2015; Borovsky et al., 2019). Figure 12 plots geomagnetic activity as a function of the reconnection driver function R_{quick} as given by expression 1): in panel (a) geomagnetic activity is measured with the 1-h-lagged AE index and in panel (b) geomagnetic activity is measured with the 1-h lagged Kp index. For the plots of Figure 12, the 1-hr-resolution OMNI2 data was separated into the four categories of solar-wind plasma and a 101-point running averages of the data for each type is plotted. Both panels of Figure 12 show a trend that for weak reconnection driving (low values of R_{quick}) coronal-hole-origin plasma (red curves) exhibits higher levels of geomagnetic activity than do the other types of plasma. The four types of plasma have systematically different properties: as noted in Table 5 of Xu and Borovsky (2015) and Table 1 of Borovsky et al., (2019): coronal-hole-origin plasma tends to have higher values of the solar-wind speed v_{sw}, lower values of the solar-wind number density n_{sw}, higher values of the magnetic-field-vector fluctuation amplitude ΔB/B, higher values of the flow-vector fluctuation amplitude $\Delta v/v_A$, and higher values of the Alfvénicity |A|. The occurrence distributions of ΔB/B [panel (a)]

and Alfvénicity |A| [panel (b)] are shown in Figure 13 separately for the four types of solar-wind plasma: the elevated values of ΔB/B and |A| for coronal-hole-origin plasma (red curves) are clearly seen. In Figure 12A at low driving (low R_{quick} values), the mean AE_1 values of the coronal-hole-origin plasma are about 60 nT larger than they are for the three other plasma types. In Figure 13A, the median ΔB/B value of coronal-hole-origin plasma is 0.443 and for all other plasma types combined the median value is 0.315, meaning that ΔB/B is increased by about 0.128 for coronal-hole-origin plasma. In Figure 1 for weak driving (lower curves), an increase of ΔB/B by about 0.13 would correspond to an increase of AE by only about 10 nT. This sheds doubt on the increase of AE (and Kp) for low driving in the two panels of Figure 12 being caused by a systematic increase in the fluctuation amplitude in coronal-hole-origin plasma. If one zooms in on the low-driving portions of the plots in the two panels of Figure 12 one finds that geomagnetic activity, as measured by both AE and Kp, increases systematically from sector-reversal-region plasma (purple), to streamer-belt-origin plasma (green), to ejecta (blue), to coronal-hole-origin plasma (red): one solar-wind variable that systematically increases in that order from plasma type to plasma type is the solar-wind speed v_{sw} (*cf.* Figure 8C of Xu and Borovsky (2015) and Figure 2A of Borovsky et al., (2019) with the same color scheme). As noted in Table 1, ΔB/B is positively correlated with v_{sw} and the correlation of geomagnetic activity with ΔB/B could be a proxy for a cause-and-effect correlation between v_{sw} and geomagnetic activity in addition to the driving described by R_{quick}, which is itself a function of v_{sw}. Here, the use of information transfer (*cf.* Section 5) may be able to discern causal versus correlative connections between the two solar-wind variables ΔB/B and v_{sw} versus geomagnetic activity.

4.3 The reconnection-clock-angle effect

The dayside reconnection rate is thought to vary as $\sin^a(\theta_{clock}/2)$ where the exponent a = 2 in the R_{quick} driver function (Borovsky and Birn, 2014) and a = 8/3 in the Newell driver function (Newell et al., 2007). For various geomagnetic indices the optimal value of the exponent a varies (Borovsky, 2022c). A question is: does the time-variable clock angle θ_{clock} produce a stronger overall coupling than does steady driving? This is examined in Figure 14, where steady driving with a steady clock angle of 90° (Parker-spiral orientation at the solstice) is compared with a sinusoidally varying clock angle that varies with time t as 90° + 45°sin(t). In Figure 14 $\sin(\theta_{clock}/2)$, $\sin^2(\theta_{clock}/2)$, and $\sin^3(\theta_{clock}/2)$ are each plotted as a function of time for the steady 90° clock angle (flat lines) and for the sinusoidally oscillating clock angle. In the black-font table in Figure 14 the time averages of these quantities is listed. As can be seen in Figure 14 the average value of the clock angle θ_{clock} is the same for the steady 90° angle as it is for the sinusoidally varying angle. As can be seen in Figure 14 (and the table within) the average value of $\sin(\theta_{clock}/2)$ (blue curves) is lower for the sinusoidally varying clock angle than it is for the steady clock angle. For $\sin^2(\theta_{clock}/2)$ (red curves in Figure 14) the time-averaged value is the same for the steady and the varying clock angle. For $\sin^3(\theta_{clock}/2)$ (green curves in Figure 14) the time-varying clock angle yields a larger mean value than does the steady clock angle. Hence, if the physical reconnection driver function has a dependence $\sin^a(\theta_{clock}/2)$ with exponent a >2, then one could expect the fluctuations in the solar-wind clock angle to produce an enhanced solar-wind reconnection coupling than would a steady clock angle, giving one possible explanation to the observed statistical increase of coupling with an increase in the amplitude of upstream solar-wind magnetic fluctuations. In this case the enhanced coupling driven by the solar-wind fluctuations would be an enhanced average dayside reconnection rate. The Newell coupling function has $\sin^{8/3}(\theta_{clock}/2)$, which would result in an enhance coupling with fluctuations; the R_{quick} coupling functions has $\sin^2(\theta_{clock}/2)$ which would not result in an enhanced coupling with fluctuations.

When considering this clock-angle effect, it must be kept in mind that the amplitude of the ΔB/B effect persists under strongly northward IMF [e.g., Figure 4 of Borovsky and Funsten (2003) or Figure 5 of Borovsky and Steinberg (2006a), Borovsky and Steinberg (2006b)] where dayside reconnection should be a very weak effect and modulating it should not produce much geomagnetic-activity change. The fact that the baseline level of geomagnetic activity is low when R_{quick} is low (*cf.* the dark-red, red, and orange curves in Figure 1) confirms that there is very little reconnection driving when $\theta_{clock} \sim 0^\circ$ (strongly northward).

4.4 The "freestream turbulence" effect

In previous publications this is enhanced-geomagnetic-activity affect was referred to as a "turbulence" effect (e.g., Borovsky and Funsten, 2003; Borovsky and Steinberg, 2006b; Borovsky, 2006; Jankovicova et al., 2008a; Jankovicova et al., 2008b; D'Amicis et al., 2007; D'Amicis et al., 2009; D'Amicis et al., 2010; D'Amicis et al., 2020). As noted in Section 4.1 the measured amplitudes of ΔB in the solar wind are primarily owed to strong current sheets in the solar wind, with several sheets passing a spacecraft per hour. The origin of those current sheets is not understood (Neugebauer and Giacalone, 2010; Neugebauer and Giacalone, 2015; Li and Qin, 2011; Owens et al., 2011; Tu et al., 2016; Telloni et al., 2016; Viall and Borovsky, 2020): some could be associated with active turbulence (Greco et al., 2009; Zhdankin et al., 2012; Vasquez et al., 2013) but it is known that some are fossils from the corona (Borovsky, 2020b; Borovsky, 2021c; Borovsky and Raines, 2022). In this report the author chose to focus on the term "fluctuations" rather than "turbulence".

If the fluctuations in the solar wind are purely turbulence, then the ΔB/B effect analyzed here would have an interesting interpretation. The "standard model" for MHD turbulence in the solar wind (based on the shape of the magnetic power spectral density plot for the solar wind) is that energy in large scale-scale passive structures feeds the turbulence cascade (Matthaeus et al., 1994; Matthaeus et al., 2015). The magnetic power spectral density of the solar wind typically has a mild breakpoint at a frequency of about 1 h (Tu and Marsch, 1995; Bruno et al., 2019). In the standard model lower-frequency power (1 h and longer) is attributed to the passive "energy-containing" scales and higher frequency power (1 h and shorter) is denoted as the "inertial range" of active turbulence. When hourly averaging the solar wind data, the hourly-averaged data describes the energy-containing structure: when looking at ΔB/B measured during 1 h one is looking at the inertial range fluctuations. Hence, from a turbulence point of view, an interpretation of the ΔB/B effect is that the R_{quick} driving is a driving of the Earth by the energy-containing structures in the solar wind and the additional ΔB/B geomagnetic activity represents driving of the Earth by active solar-wind turbulent fluctuations. Getting away from a turbulence point of view one could say that the R_{quick} driving is owed to larger-scale structure in the solar wind and that the ΔB/B effect is owed to the ubiquitous strong current sheets within that structure.

5 Future work

A number of mechanisms have been suggested for upstream solar-wind fluctuations to act to increase the coupling of the solar wind to the Earth's magnetosphere: 1) reconnection with the southward-IMF portion of fluctuations (Tsurutani and Gonzalez, 1987; Tsurutani et al., 1999), 2) patchy magnetopause reconnection (Voros et al., 2002), 3) fluctuations increase favorable geometry for dayside reconnection (Jankovicova et al., 2008a; Jankovicova et al., 2008b), 4) fluctuations produce a global-scale eddy viscosity (Borovsky and Funsten, 2003; Borovsky, 2013), 5) current sheets or velocity shears play a role (suggested in Section 4.1), and 6) averaging of fluctuating $\sin^x(\theta_{clock}/2)$ functions suggested in Section 4.3). An alternative explanation is that the fluctuation amplitude acts as a proxy for some other more-relevant solar-wind variable. This presents an outstanding problem for space physics.

Further advancements in computer simulations are needed to help quantify and understand the effect of upstream solar-wind fluctuations on the Earth's magnetosphere. These simulations can be local (focusing on perhaps one region around the magnetopause) or global, encompassing the upstream solar wind, the bow shock and magnetosheath, and the entire magnetosphere and magnetotail. Localized kinetic simulations indicate that the presence of magnetic-field fluctuations can lead to an enhanced growth of Kelvin-Helmholtz waves on the magnetopause (Nakamura et al., 2020), presumably producing a stronger coupling of the solar wind to the Earth's magnetosphere. Adding Alfvénic fluctuations to the upstream solar wind in global MHD simulations of the magnetosphere found that ULF waves could be driven inside the magnetosphere McGregor et al., (2014): certainly if geomagnetic activity were to be measured by a ULF index (e.g., Romanova et al., 2007; Kozyreva et al., 2007; Romanova and Pilipenko, 2009), an increase in geomagnetic activity associated with the added Alfvénic fluctuations would be seen in the simulation. For solar-wind-fluctuation coupling studies, global MHD simulations have good aspects and bad aspects. Two good aspects are that the simulations can analyze the reaction of the global coupled magnetospheric system to the solar wind and that the simulations can correctly account for multiple simultaneous timelags for the diverse reactions. A bad aspect is the fact that MHD simulations can be dominated by high-derivative numerical errors at steep boundaries such as the magnetopause [*cf.* eq. (23) of Raeder (2003) or *cf.* Sect. 37.3 of Raeder et al., (2021)]. and at those critical locations physical conservation laws can be violated. This is not a resolution problem: it happens at the ideal-MHD grid scale whatever that scale is. This numerical-error problem leads to coupling related questions such as: Is the reconnection rate correct in the simulation? Are the viscous mechanisms correct in the simulation? Are the plasma-entry mechanisms correct in the simulation? Another drawback to present-day global MHD simulations is that the spatial resolution in the solar-wind portions of the simulation domain are very coarse so that small-spatial-scale (higher-frequency) solar-wind fluctuations cannot be included in the simulations. The field of solar-wind/magnetosphere coupling research looks forward to higher-Reynolds-number global-MHD simulations and to much-needed advancements in global hybrid and global Vlasov simulation methods.

Going beyond correlation studies with the use of information theory (information transfer, transfer entropy, etc.) is clearly a pathway that needs to be utilized in the future (e.g., March et al., 2005; Materassi et al., 2011; Balasis et al., 2013; Wing et al., 2016; Runge et al., 2018; Wing and Johnson, 2019; Manshour et al., 2021). For the outstanding question of whether or not the observed relationships between the solar-wind fluctuations and geomagnetic activity are cause-and-effect relationships, information theory can provide critical and more-clear evidence than simple correlations do.

As pointed out by D'Amicis et al., (2007), D'Amicis et al., (2009), D'Amicis et al., (2010) in regard to the relationship between solar-wind fluctuations and geomagnetic activity, there are different types of solar-wind fluctuations such as Alfvén waves, convected magnetic structures, MHD

turbulence, etc. The work by D'Amicis et al., (2007), D'Amicis et al., (2009), D'Amicis et al., (2010) (and the work in the present study) of sorting Alfvénic versus non-Alfvénic wind for the coupling studies is a starting point for sorting the solar-wind data according to the type of fluctuations. In future, this sorting could be further progressed by inspection of the solar-wind time series and categorizing individual structures as they pass the solar-wind monitor.

Related to the sorting of the fluctuation type, it is recommended that analysis and thinking be focused on the specific effects of solar-wind current sheets and solar-wind velocity shears on geomagnetic activity. As noted in the discussion of Section 4, 1) the magnetic-field fluctuation-amplitude measure of the solar wind and 2) the Alfvénicity measure of the solar wind are both dominated by the ubiquitous strong current sheets of the solar wind.

A leading candidate mechanism underlying the viscous interaction is the Kelvin-Helmholtz instability on the Earth's magnetopause (Miura, 1997; Nykyri and Otto, 2001; Masson and Nykyri, 2018) transporting magnetosheath momentum into the magnetosphere, transporting magnetosheath plasma into the magnetosphere, and enhancing reconnection between solar-wind magnetic-field lines and magnetospheric field lines. The "effective diffusion coefficient" related to the Kelvin-Helmholtz non-linear phase is able to explain the mass transport in different IMF configurations and taking into account the complex three-dimensional dynamics at the magnetopause (*cf.* Nakamura and Daughton, 2014; Borgogno et al., 2015; Sisti et al., 2019; Nykyri et al., 2021; Nakamura et al., 2022). It has been argued that the growth rate and effectiveness of the Kelvin-Helmholtz instability is enhanced when the level of velocity fluctuations in the magnetosheath is higher (Nykyri et al., 2017), and the level of fluctuations in the magnetosheath may be related to the level in the upstream solar wind. An investigation of the impact of solar-wind current sheets and their abrupt velocity shears on the Kelvin-Helmholtz physics might be fruitful.

Data availability statement

Publicly available datasets were analyzed in this study. This data can be found here: https://omniweb.gsfc.nasa.gov.

Author contributions

JB performed all work for this project and wrote the manuscript.

Acknowledgments

The author thanks Gian Luca Delzanno, Chuck Smith, and Simon Wing for useful conversations. The author also acknowledges GFZ Potsdam for the Hp60 index, which is available at ftp://ftp.gfz-potsdam.de/pub/home/obs/Hpo, and the author acknowledges the SuperMAG team, where the SuperMAG auroral-electrojet indices are available at http://supermag.jhuapl.edu/indices.

Conflict of interest

The author declares that the research was conducted in the absence of any commercial or financial relationships that could be construed as a potential conflict of interest.

Publisher's note

References

Balasis, G., Donner, R. V., Potirakis, S. M., Runge, J., Papadimitriou, C., Daglis, I. A., et al. (2013). Statistical mechanics and information-theoretic perspectives on complexity in the Earth system. *Entropy* 15, 4844. doi:10.3390/e15114844

Blair, M. F. (1983a). Influence of free-stream turbulence on turbulent boundary layer heat transfer and mean profile development part 1: Experimental data. *J. Heat. Transf.* 105, 33.

Blair, M. F. (1983b). Influence of free-stream turbulence on turbulent boundary layer heat transfer and mean profile development, part II, Analysis of results. *J. Heat. Transf.* 105, 41–47. doi:10.1115/1.3245557

Borgogno, D., Califano, F., Faganello, M., and Pegorado, F. (2015). Double-reconnected magnetic structures driven by Kelvin-Helmholtz vortices at the Earth's magnetosphere. *Phys. Plasmas* 22, 032301. doi:10.1063/1.4913578

Borovsky, J. E., and Birn, J. (2014). The solar-wind electric field does not control the dayside reconnection rate. *J. Geophys. Res.* 119, 751–760. doi:10.1002/2013ja019193

Borovsky, J. E., and Burkholder, B. L. (2020). On the Fourier contribution of strong current sheets to the high-frequency magnetic power spectral density of the solar wind. *J. Geophys. Res.* 125, e2019JA027307. doi:10.1029/2019ja027307

Borovsky, J. E. (2014). Canonical correlation analysis of the combined solar-wind and geomagnetic-index data sets. *J. Geophys. Res.* 119, 5364–5381. doi:10.1002/2013ja019607

Borovsky, J. E. (2010). Contribution of strong discontinuities to the power spectrum of the solar wind. *Phys. Rev. Lett.* 105, 111102. doi:10.1103/physrevlett.105.111102

Borovsky, J. E., and Denton, M. H. (2018). Exploration of a composite index to describe magnetospheric activity: Reduction of the magnetospheric state vector to a single scalar. *J. Geophys. Res.* 123, 7384–7412. doi:10.1029/2018ja025430

Borovsky, J. E., and Denton, M. H. (2014). Exploring the cross-correlations and autocorrelations of the ULF indices and incorporating the ULF indices into the

systems science of the solar-wind-driven magnetosphere. *J. Geophys. Res.* 119, 4307–4334. doi:10.1002/2014ja019876

Borovsky, J. E., Denton, M. H., and Smith, C. W. (2019). Solar wind turbulence and shear: A superposed-epoch analysis of corotating interaction regions at 1 AU. *J. Geophys. Res.* 124, 2406. doi:10.1029/2009ja014966

Borovsky, J. E., and Denton, M. H. (2010). Solar-wind turbulence and shear: A superposed-epoch analysis of corotating interaction regions at 1 AU. *J. Geophys. Res.* 115, A10101. doi:10.1029/2009ja014966

Borovsky, J. E. (2006). Eddy viscosity and flow properties of the solar wind: Co-Rotating interaction regions, coronal-mass-ejection sheaths, and solar-wind/magnetosphere coupling. *Phys. Plasmas* 13, 056505. doi:10.1063/1.2200308

Borovsky, J. E., and Funsten, H. O. (2003). Role of solar wind turbulence in the coupling of the solar wind to the Earth's magnetosphere. *J. Geophys. Res.* 108, 1246. doi:10.1029/2002ja009601

Borovsky, J. E. (2018c). Looking for evidence of wind-shear disconnections of the Earth's magnetotail: GEOTAIL measurements and LFM MHD simulations. *J. Geophys. Res.* 123, 5538–5560. doi:10.1029/2018ja025456

Borovsky, J. E. (2022c). Noise and solar-wind/magnetosphere coupling studies: Data, submitted to *Front. Astron. Space Sci.* 9, 990789. doi:10.3389/fspas.2022.990789

Borovsky, J. E. (2022b). Noise, regression dilution bias, and solar-wind/magnetosphere coupling studies. *Front. Astron. Space Sci.* 9, 867282. doi:10.3389/fspas.2022.867282

Borovsky, J. E. (2018b). On the origins of the intercorrelations between solar wind variables. *J. Geophys. Res.* 123, 20–29. doi:10.1002/2017ja024650

Borovsky, J. E. (2021b). On the saturation (or not) of geomagnetic indices. *Front. Astron. Space Sci.* 8, 740811. doi:10.3389/fspas.2021.740811

Borovsky, J. E., and Osmane, A. (2019). Compacting the description of a time-dependent multivariable system and its multivariable driver by reducing the state vectors to aggregate scalars: The Earth's solar-wind-driven magnetosphere. *Nonlin. Process. Geophys.* 26, 429–443. doi:10.5194/npg-26-429-2019

Borovsky, J. E. (2021a). Perspective: Is our understanding of solar-wind/magnetosphere coupling satisfactory? *Front. Astron. Space Sci.* 8, 634073. doi:10.3389/fspas.2021.634073

Borovsky, J. E. (2013). Physics based solar-wind driver functions for the magnetosphere: Combining the reconnection-coupled MHD generator with the viscous interaction. *J. Geophys. Res.* 118, 7119–7150. doi:10.1002/jgra.50557

Borovsky, J. E., and Podesta, J. J. (2015). Exploring the effect of current sheet thickness on the high-frequency Fourier spectrum breakpoint of the solar wind. *J. Geophys. Res.* 120, 9256–9268. doi:10.1002/2015ja021622

Borovsky, J. E., and Raines, J. M. (2022). Heliospheric structure analyzer (hsa): A simple 1-AU mission Concept focusing on large-geometric-factor measurements. *Front. Astron. Space Sci.* 9, 919755. doi:10.3389/fspas.2022.919755

Borovsky, J. E. (2021c). Solar wind structures that are not destroyed by the action of solar-wind turbulence. *Front. Astron. Space Sci.* 8, 721350. doi:10.3389/fspas.2021.721350

Borovsky, J. E., and Steinberg, J. T. (2006a). The "calm before the storm" in CIR/magnetosphere interactions: Occurrence statistics, solar-wind statistics, and magnetospheric preconditioning. *J. Geophys. Res.* 111, A07S10. doi:10.1029/2005ja011397

Borovsky, J. E., and Steinberg, J. T. (2006b). The freestream turbulence effect in solar-wind/magnetosphere coupling: Analysis through the solar cycle and for various types of solar wind. *Geog. Monog. Ser.* 167, 59. doi:10.1029/167GM07

Borovsky, J. E. (2012a). The effect of sudden wind shear on the Earth's magnetosphere: Statistics of wind-shear events and CCMC simulations of magnetotail disconnections. *J. Geophys. Res.* 117, A06224. doi:10.1029/2012ja017623

Borovsky, J. E. (2008b). The flux-tube texture of the solar wind: Strands of the magnetic carpet at 1 AU? *J. Geophys. Res.* 113, A08110. doi:10.1029/2007ja012684

Borovsky, J. E. (2020b). The magnetic structure of the solar wind: Ionic composition and the electron strahl. *Geophys. Res. Lett.* 27, e2019GL084586. doi:10.1029/2019GL084586

Borovsky, J. E. (2008a). The rudiments of a theory of solar-wind/magnetosphere coupling derived from first principles. *J. Geophys. Res.* 113, A08228. doi:10.1029/2007ja012646

Borovsky, J. E. (2018a). The spatial structure of the oncoming solar wind at Earth and the shortcomings of a solar-wind monitor at L1. *J. Atmos. Solar-Terr. Phys.* 177, 2–11. doi:10.1016/j.jastp.2017.03.014

Borovsky, J. E. (2022a). The triple dusk-dawn aberration of the solar wind at Earth. *Front. Astron. Space Sci.* 9, 917163. doi:10.3389/fspas.2022.917163

Borovsky, J. E. (2012b). The velocity and magnetic-field fluctuations of the solar wind at 1 AU: Statistical analysis of Fourier spectra and correlations with plasma properties. *J. Geophys. Res.* 117, A05104. doi:10.1029/2011ja017499

Borovsky, J. E. (2020a). What magnetospheric and ionospheric researchers should know about the solar wind. *J. Atmos. Solar-Terr. Phys.* 204, 105271. doi:10.1016/j.jastp.2020.105271

Borovsky, J. E., and Yakymenko, K. (2017). Substorm occurrence rates, substorm recurrence times, and solar-wind structure. *J. Geophys. Res.* 122, 2973–2998. doi:10.1002/2016ja023625

Bruno, R., Telloni, D., Sorriso-Valvo, L., Marino, R., De Marco, R., and D'Amicis, R. (2019). The low-frequency break observed in the slow solar wind magnetic spectra. *Astron. Astrophys.* 627, A96. doi:10.1051/0004-6361/201935841

Burkholder, B. L., Nykyri, K., and Ma, X. (2020). Use of the L1 constellation as a multispacecraft solar wind monitor. *J. Geophys. Res.* 125, e2020JA027978. doi:10.1029/2020ja027978

D'Amicis, R., Bruno, R., and Bavassano, B. (2009). Alfvénic turbulence in high speed solar wind streams as a driver for auroral activity. *J. Atmos. Sol. Terr. Phys.* 71, 1014–1022. doi:10.1016/j.jastp.2008.05.002

D'Amicis, R., Bruno, R., and Bavassano, B. (2010). Geomagnetic activity driven by solar wind turbulence. *Adv. Space Res.* 46, 514–520. doi:10.1016/j.asr.2009.08.031

D'Amicis, R., Bruno, R., and Bavassano, B. (2007). Is geomagnetic activity driven by solar wind turbulence? *Geophys. Res. Lett.* 34, L05108. doi:10.1029/2006gl028896

D'Amicis, R., Telloni, D., and Bruno, R. (2020). The effect of solar-wind turbulence on magnetospheric activity. *Front. Phys.* 8, 604857. doi:10.3389/fphy.2020.604857

Diego, P., Storini, M., Parisi, M., and Cordaro, E. G. (2005). AE index variability during corotating fast solar wind streams. *J. Geophys. Res.* 110, A06105. doi:10.1029/2004ja010715

Eviatar, A., and Wolf, R. A. (1968). Transfer processes in the magnetopause. *J. Geophys. Res.* 73, 5561–5576. doi:10.1029/ja073i017p05561

Gonzalez, W. D., Tsurutani, B. T., and Clua de Gonzalez, A. L. (1999). Interplanetary origin of geomagnetic storms. *Space Sci. Rev.* 88, 529–562. doi:10.1023/a:1005160129098

Greco, A., Matthaeus, W. H., Servidio, S., Chuychai, P., and Dmitruk, P. (2009). Statistical analysis of discontinuities in solar wind ACE data and comparison with intermittent MHD turbulence. *Astrophys. J.* 691, L111–L114. doi:10.1088/0004-637x/691/2/l111

Gussenhoven, M. S., Hardy, D. A., and Heinemann, N. (1983). Systematics of the equatorward diffuse auroral boundary. *J. Geophys. Res.* 88, 5692. doi:10.1029/ja088ia07p05692

Hoffmann, J. A. (1991). Effects of freestream turbulence on the performance characteristics of an airfoil. *AIAA J.* 29, 1353–1354. doi:10.2514/3.10745

Hoffmann, J. A., and Mohammadi, K. (1991). Velocity profiles for turbulent boundary layers under freestream turbulence. *J. Fluids Engin.* 113, 399–404. doi:10.1115/1.2909509

Jankovicova, D., Voros, Z., and Simkanin, J. (2008b). The effect of upstream turbulence and its anisotropy on the efficiency of solar wind - magnetosphere coupling. *Nonlin. Process. Geophys.* 15, 523–529. doi:10.5194/npg-15-523-2008

Jankovicova, D., Voros, Z., and Simkanin, J. (2008a). The influence of solar wind turbulence on geomagnetic activity. *Nonlin. Process. Geophys.* 15, 53–59. doi:10.5194/npg-15-53-2008

King, J. H., and Papitashvili, N. E. (2005). Solar wind spatial scales in and comparisons of hourly Wind and ACE plasma and magnetic field data. *J. Geophys. Res.* 110, A02104. doi:10.1029/2004ja010649

Kozyreva, O., Pilipenko, V., Engebretson, M. J., Yumoto, K., Watermann, J., and Romanova, N. (2007). In search of a new ULF wave index: Comparison of Pc5 power with dynamics of geostationary relativistic electrons. *Planet. Space Sci.* 55, 755–769. doi:10.1016/j.pss.2006.03.013

Kwok, K. C. S., and Melbourne, W. H. (1980). Freestream turbulence effects on galloping. *ASCE J. Engin. Mech. Div.* 106, 273–288. doi:10.1061/jmcea3.0002584

Li, G., and Qin, G. (2011). A solar wind model with current sheets. *Asp. Conf. Ser.* 444, 117.

Lockwood, M. (2022). Solar wind-magnetosphere coupling functions: Pitfalls, limitations, and applications. *Space Weath* 20, e2021SW002989. doi:10.1029/2021sw002989

Manshour, P., Balasis, G., Consolini, G., Papadimitriou, C., and Paluš, M. (2021). Causality and information transfer between the solar wind and the magnetosphere–ionosphere system. *Entropy* 23, 390. doi:10.3390/e23040390

March, T. K., Chapman, S. C., and Dendy, R. O. (2005). Mutual information between geomagnetic indices and the solar wind as seen by WIND: Implications for propagation time estimates. *Geophys. Res. Lett.* 32, L04101. doi:10.1029/2004gl021677

Masson, A., and Nykyri, K. (2018). Kelvin-Helmholtz instability: Lessons learned and ways forward. *Space Sci. Rev.* 214, 71. doi:10.1007/s11214-018-0505-6

Materassi, M., Ciraolo, L., Consolini, G., and Smith, N. (2011). Predictive Space Weather: An information theory approach. *Adv. Space Res.* 47, 877–885. doi:10.1016/j.asr.2010.10.026

Matthaeus, W. H., Oughton, S., Pontius, D. H., and Zhou, Y. (1994). Evolution of energy-containing turbulent eddies in the solar wind. *J. Geophys. Res.* 99, 19267. doi:10.1029/94ja01233

Matthaeus, W. H., Wan, M., Servidio, S., Greco, A., Osman, K. T., Oughton, S., et al. (2015). Intermittency, nonlinear dynamics and dissipation in the solar wind and astrophysical plasmas. *Phil Trans. Roy. Soc.* A373, 20140154. doi:10.1098/rsta.2014.0154

McComas, D. J., Blame, S. J., Barker, P., Feldman, W. C., Phillips, J. L., Riley, P., et al. (1998). Solar wind electron proton Alpha monitor (SWEPAM) for the advanced composition explorer. *Space Sci. Rev.* 86, 563.

McGregor, S. L., Hudson, M. K., and Hughes, W. J. (2014). Modeling magnetospheric response to synthetic alfvénic fluctuations in the solar wind: ULF wave fields in the magnetosphere. *J. Geophys. Res. Space Phys.* 119, 8801–8812. doi:10.1002/2014ja020000

McPherron, R. L., Baker, D. N., and Crooker, N. U. (2009). Role of the Russell-McPherron effect in the acceleration of relativistic electrons. *J. Atmos. Solar-Terr. Phys.* 71, 1032–1044. doi:10.1016/j.jastp.2008.11.002

Miura, A. (1997). Compressible magnetohydrodynamic Kelvin–Helmholtz instability with vortex pairing in the two-dimensional transverse configuration. *Phys. Plasmas* 4, 2871–2885. doi:10.1063/1.872419

Nakamura, T. K. M., Blasl, K. A., Liu, Y.-H., and Peery, S. A. (2022). Diffusive plasma transport by the magnetopause kelvin-helmholtz instability during southward IMF. *Front. Astron. Space Sci.* 8, 809045. doi:10.3389/fspas.2021.809045

Nakamura, T. K. M., and Daughton, W. (2014). Turbulent plasma transport across the Earth's low-latitude boundary layer. *Geophys. Res. Lett.* 41, 8704–8712. doi:10.1002/2014gl061952

Nakamura, T. K. M., Stawarz, J. E., Hasegawa, H., Narita, Y., Franci, L., Wilder, F. D., et al. (2020). Effects of fluctuating magnetic field on the growth of the Kelvin-Helmholtz instability at the Earth's magnetopause. *J. Geophys. Res.* 125, e2019JA027515. doi:10.1029/2019ja027515

Neugebauer, M., and Giacalone, J. (2010). Progress in the study of interplanetary discontinuities. *AIP Conf. Proc.* 1216, 194.

Neugebauer, M., and Giacalone, J. (2015). Energetic particles, tangential discontinuities, and solar flux tubes. *J. Geophys. Res.* 120, 8281–8287. doi:10.1002/2015ja021632

Newell, P. T., Sotirelis, T., Liou, K., Meng, C. I., and Rich, F. J. (2007). A nearly universal solar wind-magnetosphere coupling function inferred from 10 magnetospheric state variables. *J. Geophys. Res.* 112, A01206. doi:10.1029/2006ja012015

Nykyri, K., Ma, X., Dimmock, A., Foullon, C., Otto, A., and Osmane, A. (2017). Influence of velocity fluctuations on the Kelvin-Helmholtz instability and its associated mass transport. *Geophys. Res. Lett.* 122, 9489–9512. doi:10.1002/2017ja024374

Nykyri, K., Ma, X., and Johnson, J. (2021). *Cross-scale energy transport in space plasmas: Applications to the magnetopause boundary*. Washington, DC: American Geophysical Union. doi:10.1002/9781119815624.ch7

Nykyri, K., and Otto, A. (2001). Plasma transport at the magnetospheric boundary due to reconnection in Kelvin-Helmholtz vortices. *Geophys. Res. Lett.* 28, 3565–3568. doi:10.1029/2001gl013239

Osmane, A., Dimmock, A. P., Naderpour, R., Pulkkinen, T. I., and Nykyri, K. (2015). The impact of solar wind ULF B_z fluctuations on geomagnetic activity for viscous timescales during strongly northward and southward IMF. *J. Geophys. Res.* 120, 9307–9322. doi:10.1002/2015ja021505

Owens, M. J., Wicks, R. T., and Horbury, T. S. (2011). Magnetic discontinuities in the near-Earth solar wind: Evidence of in-transit turbulence or remnants of coronal structure? *Sol. Phys.* 269, 411–420. doi:10.1007/s11207-010-9695-0

Pal, S. (1985). Freestream turbulence effects on wake properties of a flat plate at an incidence. *AIAA J.* 23, 1868–1871. doi:10.2514/3.9189

Raeder, J., Germaschewski, K., Cramer, W. D., and Lyon, J. (2021). Global simulations. *Geophys. Monog. Ser.* 259, 597.

Raeder, J. (2003). Global magnetohydrodynamics - A tutorial. *Lect. Notes Phys.* 615, 212.

Richardson, I. G., and Cane, H. V. (2010). Near-Earth interplanetary coronal mass ejections during solar cycle 23 (1996-2009): Catalog and summary of properties. *Sol. Phys.* 264, 189–237. doi:10.1007/s11207-010-9568-6

Romanova, N., and Pilipenko, V. (2009). ULF wave indices to characterize the solar wind-magnetosphere interaction and relativistic electron dynamics. *Acta geophys.* 57, 158–170. doi:10.2478/s11600-008-0064-4

Romanova, N., Plipenko, V., Crosby, N., and Khabarova, O. (2007). ULF wave index and its possible applications in space physics. *Bulg. J. Phys.* 34, 136.

Runge, J., Balasis, G., Daglis, I. A., Papadimitriou, C., and Donner, R. V. (2018). Common solar wind drivers behind magnetic storm–magnetospheric substorm dependency. *Sci. Rep.* 8, 16987. doi:10.1038/s41598-018-35250-5

Sibeck, D. G., Borodkova, N. L., Schwartz, S. J., Owen, C. J., Kessel, R., Kodubun, S., et al. (1999). Comprehensive study of the magnetospheric response to a hot flow anomaly. *J. Geophys. Res.* 104, 4577–4593. doi:10.1029/1998ja900021

Sibeck, D. G., Kudela, K., Lepping, R. P., Lin, R., Nemecek, Z., Nozdrachev, M. N., et al. (2000). Magnetopause motion driven by interplanetary magnetic field variations. *J. Geophys. Res.* 105, 25155–25169. doi:10.1029/2000ja900109

Siscoe, G. L., Davis, L., Coleman, P. J., Smith, E. J., and Jones, D. E. (1968). Power spectra and discontinuities of the interplanetary magnetic field: Mariner 4. *J. Geophys. Res.* 73, 61–82. doi:10.1029/ja073i001p00061

Sisti, M., Faganello, M., Califano, F., and Lavraud, B. (2019). Satellite data-based 3-D simulation of kelvin-helmholtz instability and induced magnetic reconnection at the Earth's magnetopause. *Geophys. Res. Lett.* 46, 11597–11605. doi:10.1029/2019gl083282

Sivadas, N., and Sibeck, D. G. (2022). Regression bias in using solar wind measurements. *Front. Astron. Space Sci.* 9, 924976. doi:10.3389/fspas.2022.924976

Smith, C. W., Acuna, M. H., Burlaga, L. F., L'Heureux, J., Ness, N. F., and Scheifele, J. (1998). The ACE magnetic fields experiment space. *Sci. Rev.* 86, 613–632. doi:10.1023/a:1005092216668

Sullerey, R. K., and Sayeed Khan, M. A. (1983). Freestream turbulence effects on compressor cascade wake. *J. Aircr.* 20, 733–734. doi:10.2514/3.44936

Telloni, D., Perri, S., Carbone, V., and Bruno, R. (2016). Selective decay and dynamic alignment in the MHD turbulence: The role of the rugged invariants. *AIP Conf. Proc.* 1720, 040015. doi:10.1063/1.4943826

Thole, K. A., and Bogard, D. G. (1996). High freestream turbulence effects on turbulent boundary layers. *J. Fluids Engin.* 118, 276–284. doi:10.1115/1.2817374

Tsurutani, B. T., Gonzalez, W. D., Gonzalez, A. L. C., Tang, F., Arballo, J. K., and Okada, M. (1995). Interplanetary origin of geomagnetic activity in the declining phase of the solar cycle. *J. Geophys. Res.* 100, 21717–21733. doi:10.1029/95ja01476

Tsurutani, B. T., Gonzalez, W. D., Kamide, Y., Ho, C. M., Lakhina, G. S., Arballo, J. K., et al. (1999). The interplanetary causes of magnetic storms, HILDCAAs and viscous interaction. *Phys. Chem. Earth C.* 24, 93–99. doi:10.1016/s1464-1917(98)00014-2

Tsurutani, B. T., and Gonzalez, W. D. (1987). The cause of high-intensity long-duration continuous AE Activity (HILDCAAS): Interplanetary Alfvén wave trains. *Planet. Space Sci.* 35, 405–412. doi:10.1016/0032-0633(87)90097-3

Tu, C.-Y., and Marsch, E. (1995). Comment on "Evolution of energy containing turbulent eddies in the solar wind" by W. H. Matthaeus, S. Oughton, D. H. Pontius Jr., and Y. Zhou. *J. Geophys. Res.* 100, 12323.

Tu, C. Y., Wang, X., He, J., Marsch, E., and Wang, L. (2016). Two cases of convecting structure in the slow solar wind turbulence. *AIP Conf. Proc.* 1720, 040017. doi:10.1063/1.4943828

Vasquez, B. J., Markovskii, S. A., and Smith, C. W. (2013). Solar wind magnetic field discontinuities and turbulence generated current layers. *AIP Conf. Proc.* 1539, 291. doi:10.1063/1.4811045

Vasyliunas, V. M., Kan, J. R., Siscoe, G. L., and Akasofu, S.-I. (1982). Scaling relations governing magnetospheric energy transfer. *Planet. Space Sci.* 30, 359–365. doi:10.1016/0032-0633(82)90041-1

Viall, N. M., and Borovsky, J. E. (2020). Nine outstanding questions of solar wind physics. *J. Geophys. Res.* 125, e2018JA026005. doi:10.1029/2018ja026005

Volino, R. J. (1988). A new model for free-stream turbulence effects on boundary layers. *J. Turbomach.* 120, 613–620. doi:10.1115/1.2841760

Volino, R. J., Schultz, M. P., and Pratt, C. M. (2003). Conditional sampling in a transitional boundary layer under high freestream turbulence conditions. *Trans. ASME.* 125, 28–37. doi:10.1115/1.1521957

Voros, Z., Jankovicova, D., and Kovacs, P. (2002). Scaling and singularity characteristics of solar wind and magnetospheric fluctuations. *Nonl. Proc. Geophys.* 9, 149–162. doi:10.5194/npg-9-149-2002

Walsh, B. M., Bhakapaibul, T., and Zou, Y. (2019). Quantifying the uncertainty of using solar wind measurements for geospace inputs. *J. Geophys. Res.* 124, 3291–3302. doi:10.1029/2019ja026507

Wing, S., and Johnson, J. R. (2019). Applications of information theory in solar and space physics. *Entropy* 21, 140. doi:10.3390/e21020140

Wing, S., Johnson, J. R., Camporeale, E., and Reeves, G. D. (2016). Information theoretical approach to discovering solar wind drivers of the outer radiation belt. *J. Geophys. Res. Space Phys.* 121, 9378–9399. doi:10.1002/2016ja022711

Wu, J.-S., and Faeth, G. M. (1994). Sphere wakes at moderate Reynolds numbers in a turbulent environment. *AIAA J.* 32, 535–541. doi:10.2514/3.12018

Xu, F., and Borovsky, J. E. (2015). A new four-plasma categorization scheme for the solar wind. *J. Geophys. Res.* 120, 70–100. doi:10.1002/2014ja020412

Zesta, E., and Sibeck, D. G. (2004). A detailed description of the solar wind triggers of two dayside transients: Events of 25 July 1997. *J. Geophys. Res.* 109, A01201. doi:10.1029/2003ja009864

Zhdankin, V., Boldyrev, S., Mason, J., and Perez, J. C. (2012). Magnetic discontinuities in magnetohydrodynamic turbulence and in the solar wind. *Phys. Rev. Lett.* 108, 175004. doi:10.1103/physrevlett.108.175004

frontiers | Frontiers in Astronomy and Space Sciences

TYPE Original Research
PUBLISHED 02 February 2023
DOI 10.3389/fspas.2023.1098388

OPEN ACCESS

EDITED BY
Simon Wing,
Johns Hopkins University, United States

REVIEWED BY
Katherine Garcia-Sage,
Goddard Space Flight Center (NASA), United States
Adam Michael,
Applied Physics Laboratory, Johns Hopkins University, United States

*CORRESPONDENCE
Pauline M. Dredger,
pauline.dredger@mavs.uta.edu

SPECIALTY SECTION
This article was submitted to Space Physics, a section of the journal Frontiers in Astronomy and Space Sciences

RECEIVED 14 November 2022
ACCEPTED 18 January 2023
PUBLISHED 02 February 2023

CITATION
Dredger PM, Lopez RE and Hamrin M (2023), A case study in support of closure of bow shock current through the ionosphere utilizing multi-point observations and simulation.
Front. Astron. Space Sci. 10:1098388.
doi: 10.3389/fspas.2023.1098388

A case study in support of closure of bow shock current through the ionosphere utilizing multi-point observations and simulation

Pauline M. Dredger[1]*, Ramon E. Lopez[1] and Maria Hamrin[2]

[1]Department of Physics, University of Texas at Arlington, Arlington, TX, United States, [2]Department of Physics, Umeå University, Umeå, Sweden

On the bow shock in front of Earth's magnetosphere flows a current due to the curl of the interplanetary magnetic field across the shock. The closure of this current remains uncertain; it is unknown whether the bow shock current closes with the Chapman-Ferraro current system on the magnetopause, along magnetic field lines into the ionosphere, through the magnetosheath, or some combination thereof. We present simultaneous observations from Magnetosphere Multiscale (MMS), AMPERE, and Defense Meteorological Satellite Program (DMSP) during a period of strong B_y, weakly negative B_z, and very small B_x. This IMF orientation should lead to a bow shock current flowing mostly south to north on the shock. AMPERE shows a current poleward of the Region 1 and Region 2 Birkeland currents flowing into the northern polar cap and out of the south, the correct polarity for bow shock current to be closing along open field lines. A southern Defense Meteorological Satellite Program F18 flyover confirms that this current is poleward of the convection reversal boundary. Additionally, we investigate the bow shock current closure for the above-mentioned solar wind conditions using an MHD simulation of the event. We compare the magnitude of the modeled bow shock current due to the IMF B_y component to the magnitude of the modeled high-latitude current that corresponds to the real current observed in AMPERE and by Defense Meteorological Satellite Program. In the simulation, the current poleward of the Region 1 currents is about 37% as large as the bow shock I_z in the northern ionosphere and 60% in the south. We conclude that the evidence points to at least a partial closure of the bow shock current through the ionosphere.

KEYWORDS

bow shock current, closure, MMS, LFM, DMSP, FAC

1 Introduction

When the supersonic and super-Alfvénic solar wind encounters the Earth's magnetic field, it abruptly slows and becomes subsonic, creating the bow shock. Both the solar wind plasma and the interplanetary magnetic field are compressed across the shock. This compression of the magnetic field is associated with a curl of $\vec{B}$ and therefore, by Ampere's law, a current flows on the shock.

Because of the difference in density between the solar wind plasma and the plasma in the magnetosheath, a pressure gradient force points away from the bow shock back into the solar wind. This force does work on the incoming solar wind, converting flow energy into thermal energy. The current due to the compression of the IMF also plays a part in extracting energy from the solar wind flow. The bow shock is always a dynamo or generator, meaning that

$\vec{J} \cdot \vec{E} < 0$. Although the direction of the bow shock current clearly depends on the orientation of the incoming IMF, the current is always oriented in such a way relative to electric field in the frame of the shock so that mechanical energy is always extracted from the solar wind and converted into magnetic energy (Lopez et al., 2011).

The bow shock can also at times be the primary location in the system where force is exerted against the solar wind (Siscoe et al., 2002) and energy is extracted from the solar wind flow. As discussed by Lopez et al. (2010), when the magnetosonic Mach number is high, the pressure gradient force dominates and solar wind energy at the shock is primarily converted to thermal energy; on the other hand, when the Mach number is low, the $\vec{J} \times \vec{B}$ force dominates, and the energy extracted from the solar wind flow is dominated by the magnetic energy downstream of the shock. In this low Mach number regime, the $\vec{J} \times \vec{B}$ force exerted on the shocked solar wind in the magnetosheath by the interior portion of the Chapman-Ferraro current on closed field lines is balanced by an oppositely directed force from the exterior Chapman-Ferraro current on open field lines (Lopez and Gonzalez, 2017). Since under such conditions there is no net outward force at the magneotopause, the force on the solar wind must be mainly provided by the $\vec{J} \times \vec{B}$ force associated with the bow shock current (Lopez and Gonzalez, 2017).

The location of the primary force on the solar wind has consequences for energy transfer throughout the geospace system. Magnetopause reconnection and other load processes require energy to proceed. Lopez et al. (2011) found that for conditions of low Mach number and strongly negative B_z the dynamo that can exist at high latitudes near the cusps disappears. Yet reconnection occurs at the magnetopause for strong southward IMF, which is a load. During low Mach number conditions, then, the bow shock is the main dynamo in the system and must be the energy source for magnetospheric processes (Siebert and Siscoe, 2002; Lopez and Gonzalez, 2017). This conclusion is supported by the work of Tang et al. (2012), who found that for strong IMF B_z the high latitude magnetopause current decreased while the bow shock current increased.

Poynting flux associated with the bow shock current carries energy away from the shock, so the closure of this current relates to the system of loads and generators in the magnetosphere (Lopez, 2018). The magnetopause is an obvious place for the bow shock current to close, but various studies have used global MHD simulations to investigate the question and found that the Chapman-Ferraro current is most likely not the only current in the system which can close bow shock current. Lopez et al. (2011) presented evidence that current in the magnetosheath with Region 1 polarity was connected to the bow shock, supporting the argument made by Siscoe et al. (2002) that the Region 1 field-aligned or Birkeland currents are partially closed by the bow shock current, which was first suggested by Fedder et al. (1997). A study by Guo et al. (2008) showed that under strong southward IMF a significant fraction of the Region 1 field-aligned currents (FACs) could originate from the bow shock. Tang et al. (2009) found that the bow shock current could also contribute to the cross-tail current and power nightside reconnection. In addition to these modeling studies, analysis of MMS (Magnetosphere Multiscale) bow shock crossings by Hamrin et al. (2018) presented observational evidence consistent with closure of the bow shock current across the magnetosheath.

Except for Hamrin et al. (2018), there remains a significant lack of observational studies relating to bow shock current closure. Modeling has suggested a connection between current at the bow shock and current in the ionosphere, but the nature of this possible closure path has been virtually unexplored using real data. This paper presents a set of observations consistent with closure of bow shock current into the ionosphere on open field lines, for a single event. MMS crossings of the bow shock provide direct measurement of the shock current itself during a time of strong negative B_y and weakly negative B_z. During this period, AMPERE data show unipolar field-aligned currents, of the right polarity to close the observed bow shock current, while supporting observations from a DMSP flyover in the south pole confirm the existence of Birkeland current poleward of the open-closed boundary. Results from a simulation of the event using the Lyon-Fedder-Mobarry (LFM) global MHD model (Lyon et al., 2004) tell the same story. In the simulation, the unipolar, high-latitude Birkeland current corresponding to the current seen in the AMPERE observations is 37%–60% as large as the current on the modeled bow shock. Taken together, these data and model results give evidence that the bow shock current could be closing through the magnetosheath and also in part through the polar ionosphere.

2 Materials and methods

2.1 Data

The following is a brief description of the datasets used in this study. Solar wind data was compiled from ACE and from THEMIS C (Angelopoulos, 2008). ACE (Advanced Composition Explorer) orbits the first Lagrange point and provides solar wind observations. The ACE IMF data are provided by the Magnetic Field Experiment (MAG), another pair of fluxgate magnetometers (Smith et al., 1998), and the plasma data are from the Solar Wind Electron, Proton, and Alpha Monitor (SWEPAM) (McComas et al., 1998), two electrostatic analyzers measuring ions and electrons separately. THEMIS C is one of the two spacecraft in the ARTEMIS mission and orbits the Moon; magnetic field data are taken by the Fluxgate Magnetometer (FGM) (Auster et al., 2008), while plasma data come from the Electrostatic Analyzer (ESA) instrument (McFadden et al., 2008). Wind is another upstream solar wind monitor and has orbited at the L1 point since 2004; magnetic field data come from the Magnetic Field Instrument (MFI), a pair of fluxgate magnetometers (Lepping et al., 1995), and plasma data from the Solar Wind Experiment (SWE) instrument, an electron ion spectrometer (Ogilvie et al., 1995). We considered the Wind data but did not use it, as described later.

The MMS (Magnetosphere Multiscale) mission is a constellation of four spacecraft on an elliptical orbit around Earth designed to study magnetic reconnection (Burch et al., 2016). MMS magnetic and electric field data were observed by the suite of instruments on the FIELDS investigation (Torbert et al., 2016) and ion moments are from the Fast Plasma Investigation (Pollock et al., 2016). Field-aligned currents are from AMPERE (Active Magnetosphere and Planetary Electrodynamics Response Experiment), a data product from Johns Hopkins University Applied Physics Laboratory that derives ionospheric currents using the magnetic perturbation data from the Iridium communications satellite constellations (Anderson et al., 2014). DMSP (Defense Meteorological Satellite Program) satellites fly on separate polar orbits and provide the Department of Defense with environmental information (Redmann, 1985). This study utilizes data from the plasma driftmeter to determine where the reversal

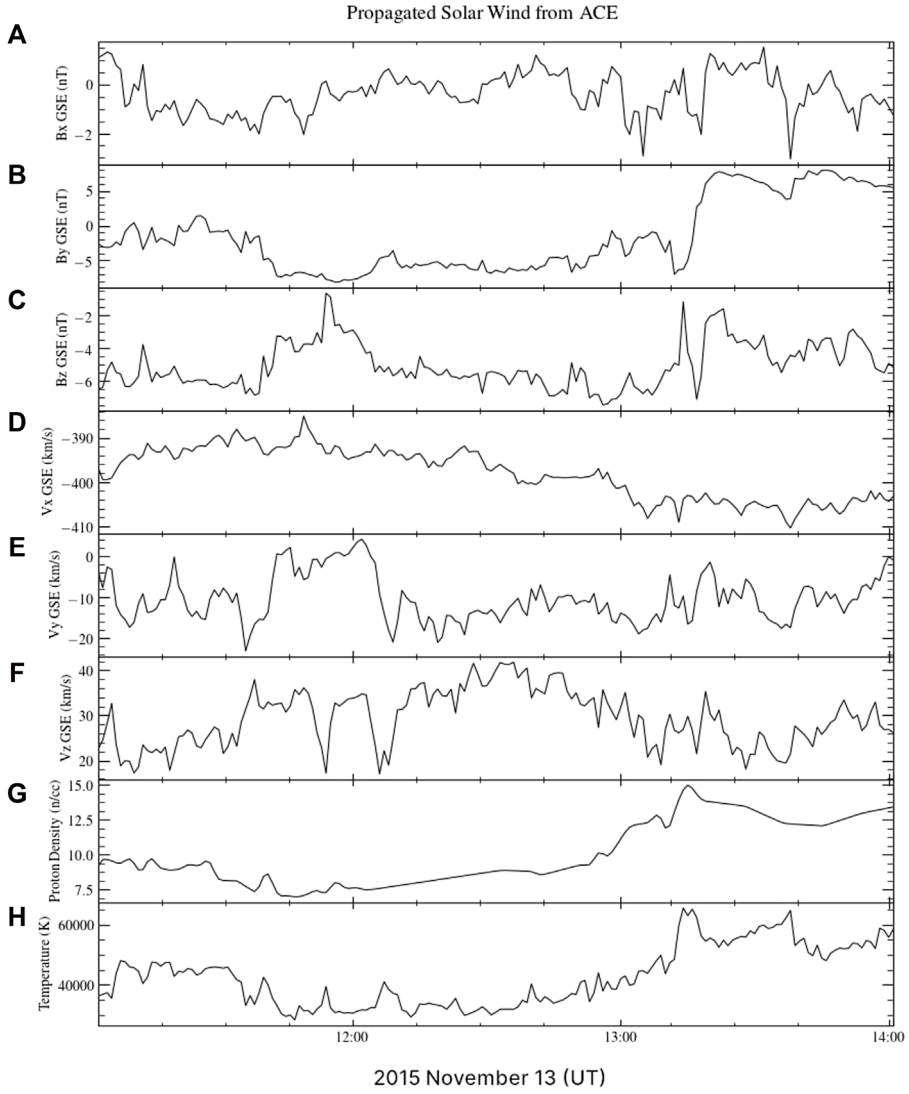

FIGURE 1
Combined ACE and THEMIS C data, propagated forward 62 min to the nominal bow shock. All data shown here are from ACE except the proton densities, which are from THEMIS C and have been time-shifted to correspond with the ACE data. The period of interest is from about 11:45 UT to shortly before 13:00. **(A–C)** show the X, Y, and Z components in GSE coordinates of the IMF. **(D–F)** show the X, Y, and Z components in GSE coordinates of the solar wind bulk velocity. **(G)** shows the solar wind proton density and **(H)** shows the solar wind ion temperature. (Data provided at https://cdaweb.gsfc.nasa.gov/).

of ionospheric convection from sunward to antisunward occurs, magnetometer data to indicate the location of Birkeland currents, and precipitating particle data from the SSJ/4 instrument to determine the location of the open-closed field line boundary. Detailed information about the spacecraft and instruments may be found at the websites for the missions listed in the Acknowledgements where the data sources are specified.

2.2 The Lyon-Fedder-Mobarry model

The MHD model used in this study was the Lyon-Fedder-Mobarry (LFM) global MHD model (Lyon et al., 2004), and the version of LFM used in this study was LFM-MIX (Magnetosphere-Ionosphere Coupler Solver) (Merkin and Lyon, 2010) coupled to the Thermosphere-Ionosphere-Electrodynamics General Circulation Model (TIEGCM). TIEGCM is a first-principles model of the ionosphere-thermosphere system (Dickinson et al., 1981; Roble et al., 1988; Qian et al., 2014). LFM solves the ideal MHD equations on a logically orthogonal, distorted spherical meshed grid. There is a higher density of grid points in areas of special interest, such as where the magnetopause and bow shock are typically located. The grid point separation in these areas is about 0.25 R_E. In the areas of the distant magnetotail and upstream of the bow shock, where the solar wind enters the grid space, the grid separation is about 1.25 R_E. The grid space extends from $-30R_E < X < 350R_E$ (in GSE) and

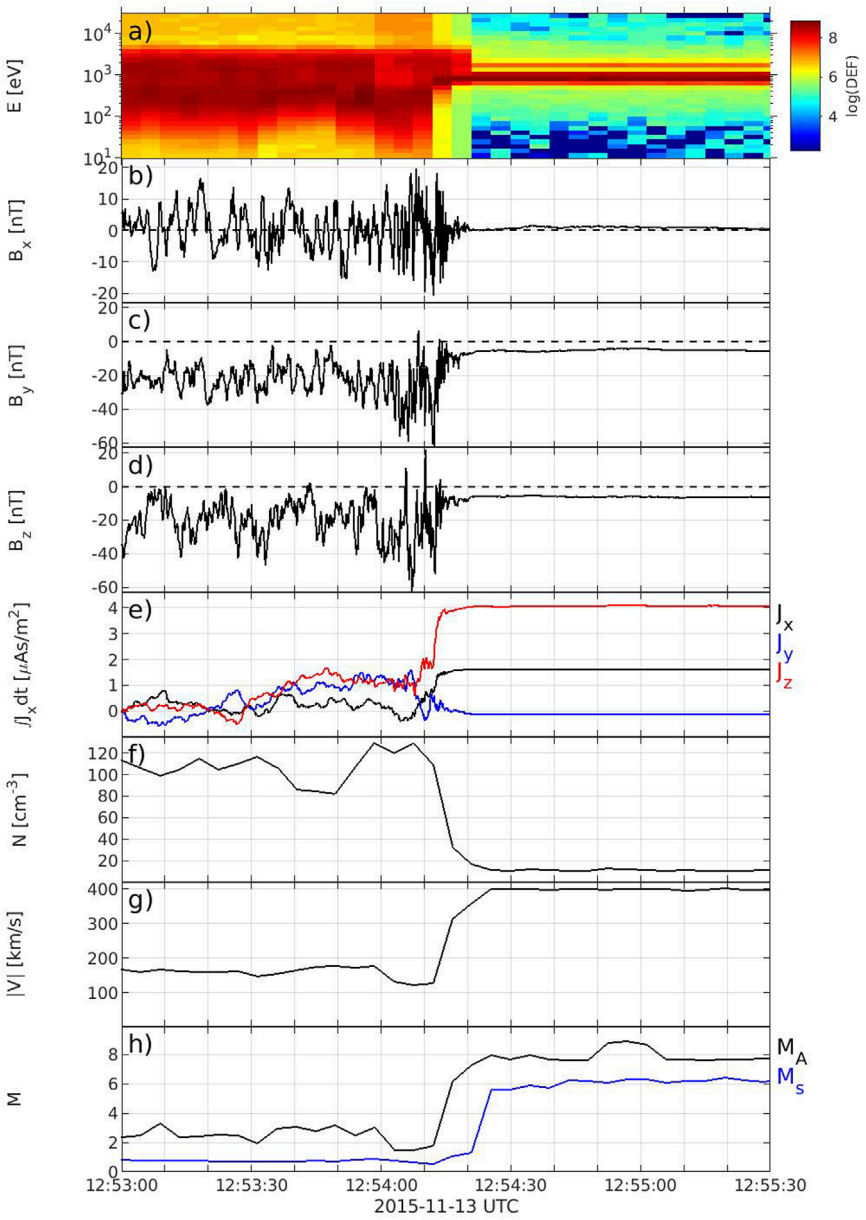

FIGURE 2
MMS observations of the bow shock. The spacecraft encountered the shock between 12:54:10 and 12:54:20 UT. **(A)** Ion energy-time spectrogram, **(B–D)** magnetic field components in GSE coordinates, **(E)** GSE components of J, each integrated with respect to time, **(F)** ion density, **(G)** the magnitude of the ion velocity, and **(H)** the Alvén (M_A) and magnetosonic (M_s) Mach numbers.

is cylindrically wrapped to $Y,Z < 130R_E$. The run in this study had a spatial resolution of 106 × 96 × 128 cells, known as "quad" resolution (e.g., Liu et al., 2021). At the inner boundary, MIX calculates the field-aligned currents from the curl of B and maps them to ionospheric altitudes, where the height-integrated electrostatic equation is solved for the ionospheric potential. The ionospheric electric field is then mapped back to the MHD grid to provide a boundary condition for Faraday's Law and for the perpendicular velocity. The MIX grid for this run is $1° \times 1°$ in magnetic coordinates and the TIEGCM grid is $5° \times 5°$ in latitude and longitude. The simulation run was completed at NASA's Community Coordinated Modeling Center (CCMC).

3 Observations

3.1 Solar wind conditions during the event

The OMNI data in the period of interest, namely, 11:00 UT to 14:00 UT on 13 November 2015, was taken from Wind observations, but these data have significant gaps at important times. For this reason, we considered the event with reference to ACE observations, which were more complete except for a total lack of proton density measurements. ACE and Wind were around 80 R_E apart in X, less than 40 R_E apart in Y, and roughly 8 R_E apart in Z. The exact location of ACE was (236.3, 35.3, 11.6) R_E. THEMIS C was relatively close to the Earth-sun

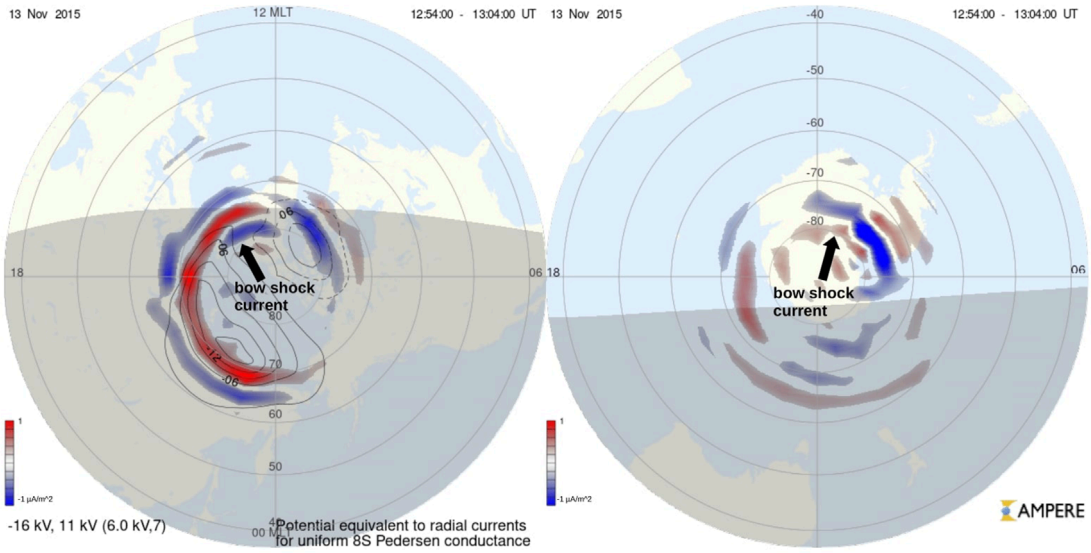

FIGURE 3
AMPERE derived Birkeland currents. The northern hemisphere is on the left and the southern hemisphere is on the right. In both hemispheres, red currents are coming out of the ionosphere and blue currents are going in. The southern hemisphere plot uses a "glass-Earth" projection. We see high latitude unipolar current (indicated) in the afternoon sector in the north and in the morning sector in the south, both with the right polarity to be bow shock current closing into the ionosphere. Potential contours are not available for the southern hemisphere on this day. (Plots from http://ampere.jhuapl.edu/).

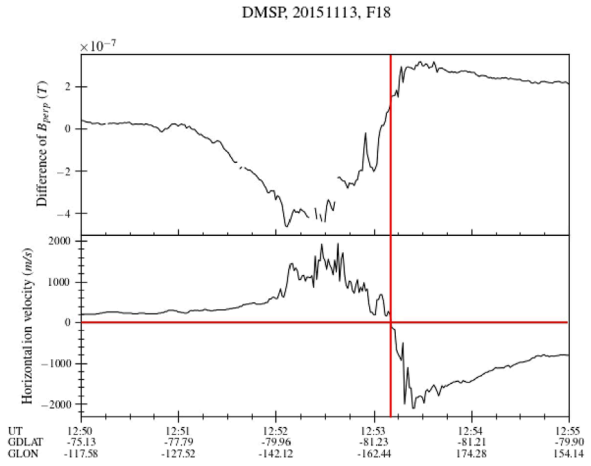

FIGURE 4
F18 observations: difference of B_{perp} and horizontal ion drift velocities. After the ion velocities turn negative shortly after 12:53 UT, marking the convection reversal boundary, we see some magnetic field perturbations, indicative of current flowing on open field lines. F18 is here moving poleward. (Data provided at http://cedar.openmadrigal.org/list/).

line during this period, at (56.6, 18.3, 4.6) R_E. Based on a comparison between ACE and THEMIS magnetic field data, THEMIS C seemed to be seeing the same solar wind that ACE saw but approximately 48 min later. We determined that the delay was 48 min between the two sets of observations using the average solar wind velocity and the distance between the two spacecraft; we then confirmed that initial estimation by comparing plots of the two datasets. We were therefore able to replace the missing ACE densities (between 0950 UT and 1300 UT) with those observed by THEMIS C (time-shifted by 48 min), after which we propagated the combined dataset forward 62 min, to line up with available OMNI data. The resulting combined solar wind data time series is shown in **Figure 1** and this solar wind time series, which was used to drive the LFM simulation at the CCMC, can be replicated using the information provided here and the archived ACE and THEMIS C data.

The coordinates used in this paper for all the spacecraft, with the exception of DMSP-F18, are Geocentric Solar Ecliptic (GSE) coordinates, where the X-axis points from Earth to the Sun, the Y-axis is in the ecliptic plane, and the Z-axis is perpendicular to both, pointing northward. The solar wind conditions for the event are shown in **Figure 1**. Between 11:45 and 13:15 UT on 13 November 2015, IMF B_x was close to zero, while B_z was weakly negative. B_y was between −5 and −8 nT but was overall pretty steady during this period. Solar wind velocities were steady, as were the temperature and pressure. The fact that B_y dominated the IMF during the event means that the bow shock current should have been flowing mostly south to north, as determined by the curl of $\vec{B}$ across the shock.

3.2 MMS observations of the bow shock

Figure 2 shows MMS data from 12:53:00 to 12:55:30 UT, near the end of the period described above. Shortly before 12:51 UT (not shown), the MMS constellation crossed the bow shock into the magnetosheath, where it remained for roughly three and a half minutes before crossing back into the solar wind right after 12:54 UT, as shown. This encounter with the shock occurred at (X, Y, Z) = (9.7, 5.2, −0.9) R_E, relatively close to the nose. The compression of the magnetic field (panels b, c, d), the decrease in the ion density

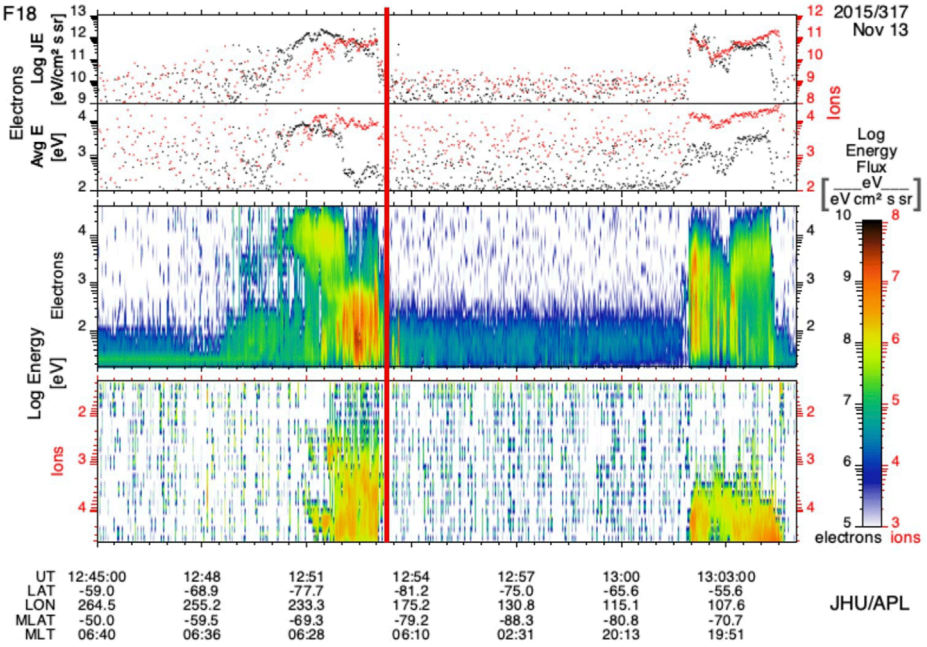

FIGURE 5
F18 particle precipitation data over the southern polar cap. The red line indicates when the spacecraft crossed the convection reversal boundary at 12:53 UT. (Plot from http://sd-www.jhuapl.edu/Aurora/spectrogram/).

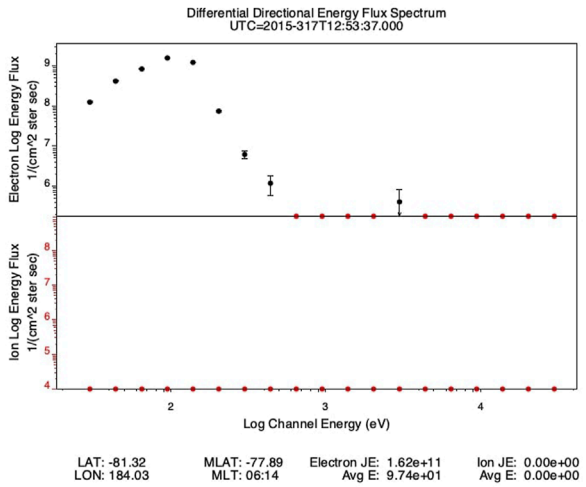

FIGURE 6
Spectrum of the particle precipitation seen at 12:53:37 in figure. The accelerated Maxwellian seen in the electron spectrum indicates electrons being pushed upward in a current. (Plot from http://sd-www.jhuapl.edu/Aurora/spectrogram/).

(panel f), and the increase in the ion velocity (panel g) across the shock are consistent with the data from ACE at the observed magnetosonic Mach number (panel h). This agreement means that the solar wind data we infer from ACE and THEMIS C are indeed the real conditions directly upstream of the bow shock, a fact that becomes crucial when we simulate the event with an MHD model using these data as input. Panel e of **Figure 2** shows the current density components integrated along the spacecraft path; the dominant component is J_z with some contribution from J_y. These currents were calculated using the curlometer; for more information on this technique, see Dunlop et al. (2021). Thus, MMS observed a tilted south to north current as the spacecraft crossed the bow shock.

3.3 AMPERE and DMSP observations of field-aligned currents

The AMPERE-derived Birkeland currents are shown in **Figure 3**; red indicates current coming out of the ionosphere (upward) and blue current is flowing into the ionosphere (downward). The projection is known as "glass-Earth," so that the view in both cases is from the perspective of an observer above the north pole; the southern polar cap view is as if the observer were looking through a transparent Earth. In each view noon is at the top of the figure, dawn to the right, and dusk to the left. We can see the Region 1 current flowing into the ionosphere (blue) in the dawn sector and out (red) in the dusk sector, while at lower latitudes are the Region 2 currents, of opposite polarity to Region 1. The convection pattern is rotated towards the afternoon, consistent with the negative IMF B_y (Heppner and Maynard, 1987). At the time of MMS's encounter with the bow shock, AMPERE data show a unipolar current region poleward of the Region 1 Birkeland current patterns in both northern and southern hemispheres, with the northern hemisphere current primarily in the postnoon sector and the southern hemisphere current in the prenoon sector, again consistent with the overall convection pattern for negative IMF B_y (Heppner and Maynard, 1987). This current flows into the northern polar cap and out of the south at high latitudes. These FACs are of the right polarity—downward (blue) in the north and upward (red)

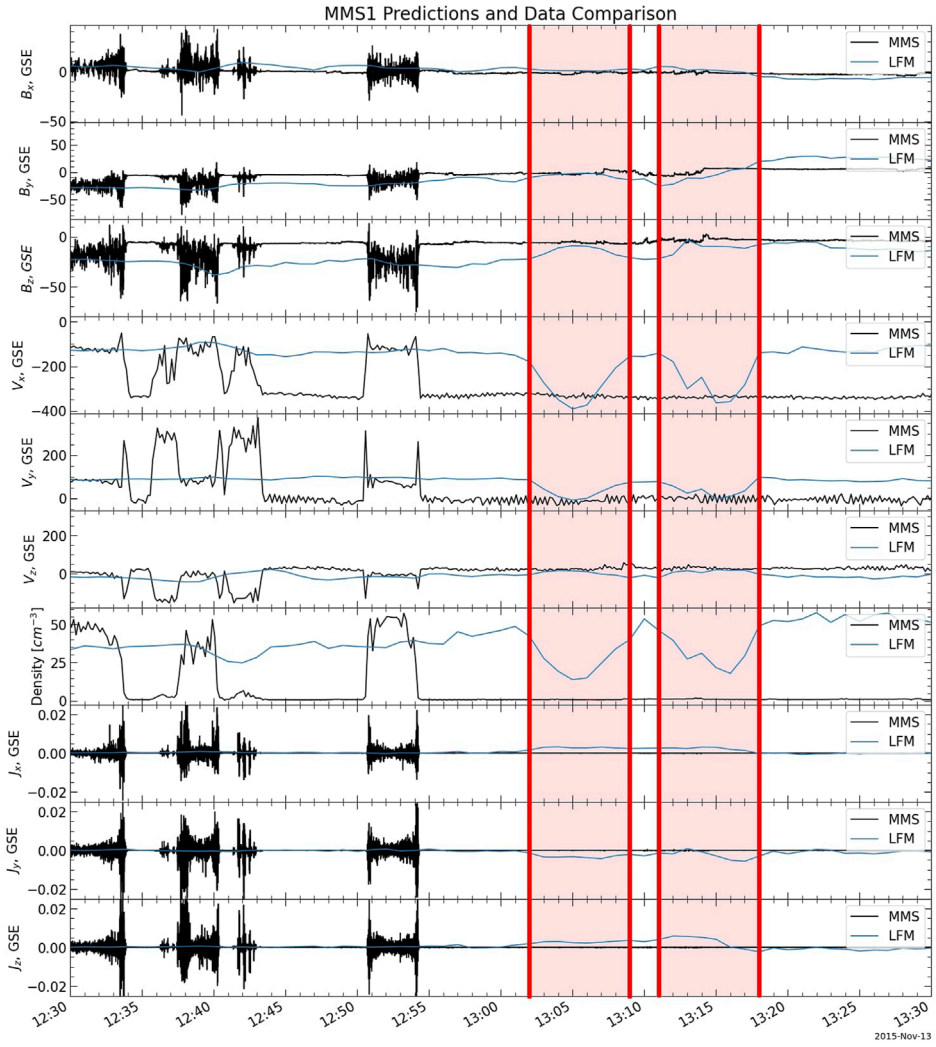

FIGURE 7
MMS1 data (black) and LFM output along the MMS1 track (blue) for the hour around the crossing time on 2015 November 13. Although the modeled satellite did not encounter the bow shock exactly at 12:54 UT or during the earlier crossings shown, the modeled bow shock was near the MMS position, as shown by several predicted encounters with the boundary (marked in red) around 13:05 and 13:15 UT. The periods spent out in the solar wind are shaded red. From the top, the plotted quantities are the magnetic field components B_x, B_y, B_z, proton bulk velocity components V_x, V_y, V_z, the proton number density, and the components of the current J_x, J_y, and J_z. Vector quantities are in GSE coordinates. The current from LFM is in $\frac{\mu A}{m^2}$ and the current from MMS is in $\frac{nA}{m^2} \times 10^{-6}$ (see explanation in text).

in the south—to close the south-north bow shock current observed by MMS, if those currents are on open field lines. It seems likely that if currents originating outside the magnetosphere, like the bow shock current, do connect to the Birkeland currents, they would close along open field lines, which reach out into the magnetosheath, rather than closed field lines. The critical point, then, is to find the position of these Birkeland currents relative to the open-closed field line boundary.

For this event, we can determine the location of the open-closed boundary at least in one hemisphere by means of ion driftmeter data from DMSP. During the period in which MMS crossed the bow shock, F18 was making an overpass of the southern polar cap and flew right through the high latitude upward current seen by AMPERE and discussed above. The top panel of **Figure 4** shows the difference between the observed magnetic field and the International Geomagnetic Reference Field (IGRF) model perpendicular to the flight track of F18, which gives an estimate of the magnetic perturbation resulting from Birkeland currents (Alken et al., 2021). The bottom panel is a plot of the horizontal ion drift velocities, from which we can determine the convection reversal boundary by noting where the plasma velocities turn negative. Negative velocities correspond to open field lines being dragged toward the nightside and the plasma flowing with them, whereas positive velocities are associated with closed field lines and plasma moving toward the dayside, as expected for the magnetospheric convection pattern. By this reasoning, we can say that F18 encountered the open-closed boundary a few seconds after 12:53, flying poleward. From the magnetic field perturbations observed after the satellite passes through the boundary, we infer that part of the upward current through which F18 flew was flowing on open field lines. The particle precipitation data in **Figure 5** shows a clear auroral oval with an open polar cap, consistent with southward IMF. Just after 12:52 we see an

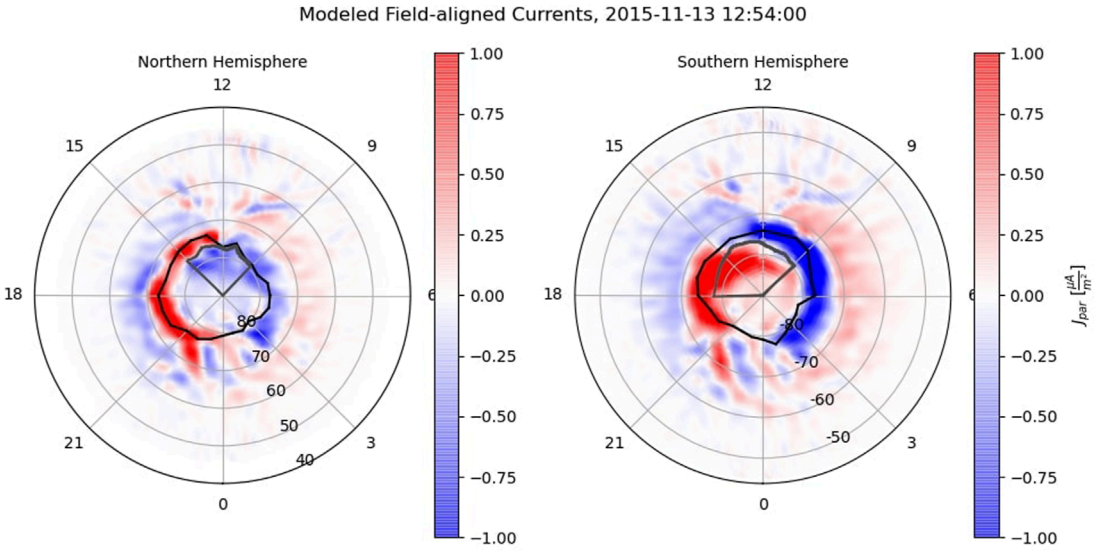

FIGURE 8
MIX currents for the time of the MMS crossing. Red current is flowing out of the ionosphere and blue is flowing in. The southern hemisphere is once again in a "glass-Earth" projection. The black tracings indicate the polar cap boundary and the regions circled in grey contain the currents possibly closing the bow shock. The model broadly reproduces the AMPERE-derived currents.

intense downward flux of low energy electrons that corresponds to an upward Birkeland current. We identify this downward electron flux as an upward current because electrons are the main current carriers for Birkeland currents, since ions are much heavier and therefore slower to respond to electromagnetic forces. Additionally, the particle detectors on DMSP satellites only look upward, so they cannot measure any upward-moving ions that might contribute to a downward current. We do see some precipitating ions, but after F18 crosses the open-closed boundary at 12:53 the ions disappear. Only a distinct electron population remains; the spectrum of this population, shown in **Figure 6**, can be compared to the spectrum shown in **Figure 1** in Newell et al. (1996), which is identified as an accelerated electron distribution. The spectrum shown here is not as sharply peaked as the spectrum in Newell et al. (1996), with much weaker acceleration and therefore much weaker field-aligned potential, but the two spectra have similar characteristics otherwise. This is therefore the signature of electrons carrying an upward current, with a field-aligned potential accelerating the electrons downward to the velocity required to carry the current, which in this case was on open field lines. In short, the DMSP observations confirm that in the southern hemisphere there was current at the location seen by AMPERE and of the same orientation, poleward of the convection reversal boundary and therefore on open field lines.

4 Results from the MHD simulation

As mentioned above, we are confident, because of the MMS observations right outside the bow shock, that the solar wind conditions seen by ACE/THEMIS C, propagated forward to a nominal shock position, accurately represent the real conditions at the bow shock during the event and thus are the correct input to the simulation for the event. We used the propagated ACE/THEMIS C dataset described in **Section 3.1** to drive LFM at quad resolution. The model more or less correctly predicts the location of the bow shock at the time of the crossing by MMS, since the satellite's location during real crossing at 12:54 UT was only about 0.1 R_E from its location during the modeled crossing at 13:01 UT, less than the separation of the grid points in this region. **Figure 7** shows the modeled conditions along the MMS1 track for the hour around the time of the event; the closeness of the MMS constellation, compared to the LFM spatial resolution in the magnetosheath, means that we can choose any of the four spacecraft to compare to the simulation. Although the model output in **Figure 7** is of a lower temporal resolution than the actual data, i.e., every minute as opposed to seconds, we can see that the simulated bow shock passes over the satellite shortly after 13:00 UT; both magnetic field and plasma parameters change rapidly from magnetosheath values to values corresponding to the solar wind input conditions at the time. The predicted B_y and B_z approach the IMF values reported in the OMNI data at that time, while V_x decreases to −400 km/s and V_y, along with V_z, decreases to nearly zero. Correspondingly, the proton density decreases by more than half as the simulated MMS1 satellite encounters the bow shock. The modeled crossing is about 7 min after the real crossing. In addition, before the 12:54 UT crossing MMS encountered the bow shock a handful of times in quick succession, which are not predicted by the model. However, the simulated boundary is near the MMS position at the time of the crossing under consideration, since the modeled satellite measures very similar magnetosheath values to the real MMS observations, except for the current. Any minor discrepancies could be a result of local disturbances on the bow shock, the physics of which are not necessarily included in the MHD simulation. The discrepancies could also be a result of uncertainties in solar wind timing and the spatial resolution of LFM versus the actual thickness of the bow shock. In the magnetosphere domain the temporal resolution of LFM is on the order

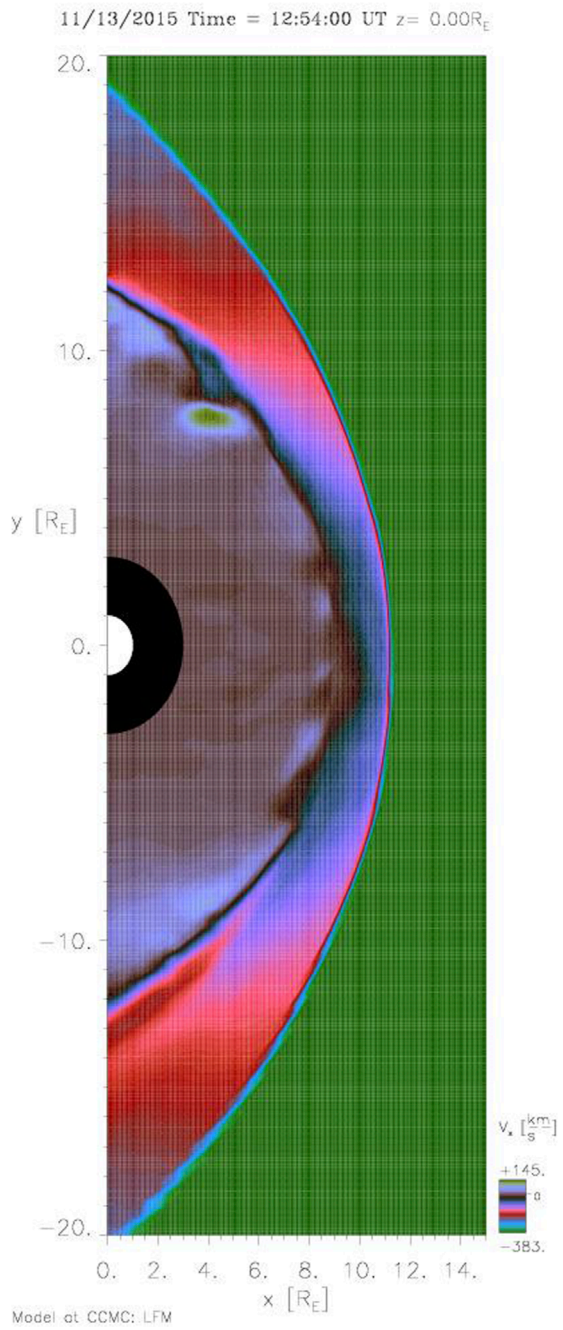

FIGURE 9
The equatorial plane in the LFM simulation at 12:54 UT, colored by the X component of the ion velocity. The bow shock was identified by eye using a plot like this for the integration of the J_z on the bow shock described in **Section 4**. (Plot generated by the CCMC).

of a second, although the code typically writes the MHD variables to a data file with a 1-min cadence. The MMS data used for this study are fast survey mode data, and the resolutions are 16 s^{-1} (magnetic field) and 32 s^{-1} (electric field) (Torbert et al., 2016); ion data are taken at 4.5 s per sample (Pollock et al., 2016). Because of the high temporal resolution of the model, small discrepancies between the data and the model are better attributed to the spatial resolution of the MHD code than to the temporal resolution. Broadly speaking, however, the bow shock was in the right position at the right time in the simulation output.

Although the directly measureable quantities such as $\vec{B}$ and $\vec{V}$ in the simulation match the corresponding MMS quantities reasonably well, the current in LFM is significantly smaller than the current in the MMS dataset. This can be explained by the fact that $\vec{J}$, the current per unit area, is a derived quantity, determined from an approximation of Ampere's law in both MMS data and LFM calculations, which necessarily involves a term like $\frac{\Delta B}{\Delta R}$, where R is the distance between either two spacecraft or two points in the simulation. Because of the much higher spatial resolution in the MMS current calculation than in LFM, MMS $\vec{J}$ is often of much greater magnitude than the simulated $\vec{J}$. However, the total current at the bow shock, which is determined by the compression of the magnetic field across the shock, is very similar for both observations and simulation, as can be seen in **Figures 1**, **2**, **7**. There can also be noise and processes such as physical waves contributing to the measured ΔB that are not actually associated with currents, yet they can contribute to the calculation of $\vec{J}$. The calculation methods additionally assume a linear change in $\vec{B}$ between the two spacecraft, which may not be true. For the very small ΔR in the case of MMS, errors in the estimate of ΔR can have a large impact on the calculation of the current. For these and additional caveats associated with the calculation of $\vec{J}$, the magnitude difference between the MMS current and the LFM current is not surprising and it is more instructive to compare the variations of the two parameters than their magnitudes.

The simulated field-aligned currents from MIX are shown in **Figure 8**; red currents are upward and blue currents are downward (matching AMPERE). Like the AMPERE images, dawn is on the right in both hemispheres. The simulated FACs are generally similar to observations, including the tilt in the patterns due to IMF B_y; in particular, the model produces FACs at high latitude, resembling those seen by AMPERE in **Figure 3**, that are flowing along open field lines. The modeled currents are similar in magnitude, though a bit larger than the AMPERE-derived currents, but it is known that MIX tends to overestimate the cross polar cap potential, which would explain this discrepancy (Wiltberger et al., 2012). The scale sizes of some FAC features are much smaller than the MIX resolution, so the currents in the MIX plots appear smoother than those in the AMPERE plots.

Figure 8 also shows the polar cap boundaries for both hemispheres as calculated by the model. The high latitude upward current in the southern hemisphere on the dawn side, indicated by the arrow in **Figure 3**, is flowing on open field lines, both in DMSP observations and in the simulation results. Moreover, the AMPERE plot for the northern hemisphere includes the potential contours from the MIX model, using real data and run separately from the MHD code; it can be seen that the northern counterpart of the southern hemisphere current discussed above was in a region of antisunward plasma flow, poleward of the convection reversal boundary. Therefore, the global simulation of the event and the observations are in agreement that the high latitude Birkeland current with polarity consistent with bow shock current closure was flowing on open field lines.

To more quantitatively compare the current on open field lines in the ionosphere and the south-north current flowing on the bow shock, we integrated the modeled currents in both locations. If the bow shock current is closing at least partially into the ionosphere, the integrated current on open field lines which we identify as possible

bow shock current should be less than or equal to the integrated Z-component of the current density on the bow shock in the equatorial plane. Identifying the bow shock in the LFM output by eye in a plot of the equatorial plane (e.g., **Figure 9**), using the discontinuity in the solar wind density across the shock, we find that the dayside bow shock current flowing from south to north in the simulation is 2.3 ±0.4 MA. This value was calculated by taking the value of the current per square meter in each grid cell identified as containing the bow shock, for X > 0 R_E in the equatorial plane; these values were multiplied by the area of the X-Y face of the cell and then summed. Since identifying the bow shock by eye introduces some uncertainty, the process was repeated with slightly different selections of cells and the results were averaged. In **Figure 8**, the areas in each polar cap enclosed by the grey contours represent the regions of possible bow shock current, based on overlap with the Region 1/Region 2 current pattern. The integrated current in the northern region is 0.84 ± 0.08 MA and in the southern region 1.4 ± 0.2 MA. In the southern hemisphere, part of the upward current on open field lines was omitted from the calculation as it seemed to belong more properly to the Region 1 FACs, assuming a more or less regular "banana shape" for the Region 1 current, so the southern hemisphere value represents in some sense a lower limit for that calculation. Conversely, the downward current on open field lines is more difficult to separate into Region 1 current and possible bow shock current, so the northern hemisphere value is more of an upper limit. For both cases the identification of possible bow shock current in the ionosphere and, consequently, the calculated values are certainly not exact, yet we have provided them here as estimates. The integration of the current in the northern (southern) hemisphere was performed multiple times, including once with all of the dayside blue (red) current inside the polar cap boundary, and the results were averaged. The uncertainties stated above are the standard deviations for each set of calculations. Regardless of the uncertainties, in both the northern and the southern hemisphere, the integrated currents on open field lines are a fraction of the estimated south-north current on the bow shock.

5 Discussion and conclusion

In this paper, we have presented a set of coordinated observations of the bow shock and low altitude Birkeland currents on 13 November 2015, during a period when the IMF was dominated by the B_y component. The MMS data show the primarily south-to-north current at the bow shock, while DMSP and Ampere show upward Birkeland current in the southern hemisphere at high latitudes in the MMS local time sector. Moreover, the DMSP data show that some of the Birkeland current was flowing in the polar cap on open field lines, and as such would connect to currents in the magnetosheath. These observations are consistent with the hypothesis that, in this case, some of the bow shock current was closing across the magnetosheath into the ionosphere.

The event has been simulated with the LFM global magnetosphere model. The simulation puts the bow shock in the right place at essentially the right time. The Birkeland current pattern in the simulation is generally similar to the pattern derived by AMPERE, particularly with respect to the high latitude Birkeland current that is of the correct polarity to close part of the bow shock current. Moreover, the model results indicate that some of this Birkeland current is on open field lines, poleward of the Region 1 currents. Given observations of the predicted bow shock current, a Birkeland current on open field lines of the correct polarity and magnitude to close the bow shock current at least partially, and support from a global MHD simulation showing the same results, we believe that the evidence is strongly in favor of the closure through the polar cap ionosphere of at least part of the bow shock current.

Many questions remain about bow shock current closure. If the bow shock current is closing in part through the ionosphere with the Birkeland currents, where does it cross the magnetosheath? Does it flow back towards the nightside first, or does it begin to flow along open field lines on or close to the dayside? The relationship of the bow shock current with the Chapman-Ferraro current, and what role the magnetopause plays or does not play in bow shock current closure, should also be investigated. It is probable that the nature of this closure depends largely on prevailing conditions. The IMF clock angle dictates the direction of the bow shock current and thus clearly regulates its closure. The magnetosonic Mach number may be particularly important, since it affects the location of the primary force exerted on the solar wind and the main dynamo in the system. In addition, ionospheric conductance must influence the ability of the bow shock current to close into the polar cap. The fraction of the bow shock current that closes into the ionosphere could also vary, depending on the state of the magnetosphere. Further study is needed to examine the interconnected system of currents, conductance, and solar wind conditions.

Data availability statement

The datasets presented in this study can be found in online repositories. The names of the repository/repositories and accession number(s) can be found below: https://cdaweb.sci.gsfc.nasa.gov/index.html/, http://ampere.jhuapl.edu/, http://sd-www.jhuapl.edu/Aurora/spectrogram/, http://cedar.openmadrigal.org, https://ccmc.gsfc.nasa.gov/results/viewrun.php?domain=GM&runnumber=Pauline_Dredger_080522_4.

Author contributions

MH provided the MMS data and expertise. PD and RL compiled all other observational data and PD ran the MHD simulation. All authors contributed to the analysis of the event studied. PD is the principal author of the text of the paper; the other authors edited and contributed to the text.

Funding

We acknowledge the support of the US National Science Foundation (NSF) under grant 1916604. We also acknowledge the support of the National Aeronautics and Space Administration (NASA) under grants 80NSSC19K1670 and 80NSSC20K0606 [The Center for the Unified Study of Interhemispheric Asymmetries (CUSIA)]. MH was supported by

the Swedish National Space Agency and the Swedish Research Council.

Acknowledgments

Simulation results have been provided by the Community Coordinated Modeling Center at Goddard Space Flight Center through their public Runs on Request system (http://ccmc.gsfc.nasa.gov). The LFM Model was developed by John Lyon et al. at Dartmouth College/NCAR-HAO/JHU-APL/CISM. We thank Patricia Doherty for conversations concerning the DMSP plasma drift and magnetometer data. We also thank Kevin Pham for assistance in running the LFM model.

Conflict of interest

The authors declare that the research was conducted in the absence of any commercial or financial relationships that could be construed as a potential conflict of interest.

Publisher's note

References

Alken, P., Thébault, E., Beggan, C. D., Amit, H., Aubert, J., Baerenzung, J., et al. (2021). International geomagnetic reference field: The thirteenth generation. *Earth, Planets Space* 73, 49. doi:10.1186/s40623-020-01288-x

Anderson, B. J., Korth, H., Waters, C. L., Green, D. L., Merkin, V. G., Barnes, R. J., et al. (2014). Development of large-scale birkeland currents determined from the active magnetosphere and planetary electrodynamics response experiment. *Geophys. Res. Lett.* 41, 3017–3025. doi:10.1002/2014GL059941

Angelopoulos, V. (2008). The themis mission. *Space Sci. Rev.* 141, 5–34. doi:10.1007/s11214-008-9336-1

Auster, H., Glassmeier, K., Magnes, W., Aydogar, O., Baumjohann, W., Constantinescu, O., et al. (2008). The themis fluxgate magnetometer. *Space Sci. Rev.* 141, 235–264. doi:10.1007/s11214-008-9365-9

Burch, J. L., Moore, T. E., Torbert, R. B., and Giles, B. L. (2016). Magnetospheric multiscale overview and science objectives. *Space Sci. Rev.* 199, 5–21. doi:10.1007/s11214-015-0164-9

Dickinson, R. E., Ridley, E. C., and Roble, R. G. (1981). A three-dimensional general circulation model of the thermosphere. *J. Geophys. Res. Space Phys.* 86, 1499–1512. doi:10.1029/JA086iA03p01499

Dunlop, M. W., Dong, X. C., Wang, T. Y., Eastwood, J. P., Robert, P., Haaland, S., et al. (2021). Curlometer technique and applications. *J. Geophys. Res. Space Phys.* 126, e2021JA029538. doi:10.1029/2021ja029538

Fedder, J. A., Slinker, S. P., Lyon, J. G., Russell, C. T., Fenrich, F. R., and Luhmann, J. G. (1997). A first comparison of polar magnetic field measurements and magnetohydrodynamic simulation results for field-aligned currents. *Geophys. Res. Lett.* 24, 2491–2494. doi:10.1029/97GL02608

Guo, X. C., Wang, C., Hu, Y. Q., and Kan, J. R. (2008). Bow shock contributions to region 1 field-aligned current: A new result from global mhd simulations. *Geophys. Res. Lett.* 35, L03108. doi:10.1029/2007GL032713

Hamrin, M., Gunell, H., Lindkvist, J., Lindqvist, P. A., Ergun, R. E., and Giles, B. L. (2018). Bow shock generator current systems: Mms observations of possible current closure. *J. Geophys. Res. Space Phys.* 123, 242–258. doi:10.1002/2017JA024826

Heppner, J., and Maynard, N. (1987). Empirical high-latitude electric field models. *J. Geophys. Res. Space Phys.* 92, 4467–4489. doi:10.1029/ja092ia05p04467

Lepping, R. P., Acũna, M. H., Burlaga, L. F., Farrell, W. M., Slavin, J. A., Schatten, K. H., et al. (1995). The wind magnetic field investigation. *Space Sci. Rev.* 71, 207–229. doi:10.1007/BF00751330

Liu, J., Wang, W., Qian, L., Lotko, W., Burns, A. G., Pham, K., et al. (2021). Solar flare effects in the Earth's magnetosphere. *Nat. Phys.* 17, 807–812. doi:10.1038/s41567-021-01203-5

Lopez, R. E., Bruntz, R., Mitchell, E. J., Wiltberger, M., Lyon, J. G., and Merkin, V. G. (2010). Role of magnetosheath force balance in regulating the dayside reconnection potential. *J. Geophys. Res. Space Phys.* 115, 14597. doi:10.1029/2009JA014597

Lopez, R. E., and Gonzalez, W. D. (2017). Magnetospheric balance of solar wind dynamic pressure. *Geophys. Res. Lett.* 44, 2991–2999. doi:10.1002/2017GL072817

Lopez, R. E., Merkin, V. G., and Lyon, J. G. (2011). The role of the bow shock in solar wind-magnetosphere coupling. *Ann. Geophys.* 29, 1129–1135. doi:10.5194/angeo-29-1129-2011

Lopez, R. E. (2018). *The bow shock current system*. Wiley. doi:10.1002/9781119324522.ch28

Lyon, J., Fedder, J., and Mobarry, C. (2004). The Lyon–Fedder–Mobarry (LFM) global MHD magnetospheric simulation code. *J. Atmos. Solar-Terrestrial Phys.* 66, 1333–1350. doi:10.1016/j.jastp.2004.03.020

McComas, D. J., Bame, S. J., Barker, P., Feldman, W. C., Phillips, J. L., Riley, P., et al. (1998). Solar wind electron proton Alpha monitor (SWEPAM) for the advanced composition explorer. *Space Sci. Rev.* 86, 563–612. doi:10.1023/A:1005040232597

McFadden, J., Carlson, C., Larson, D., Ludlam, M., Abiad, R., Elliott, B., et al. (2008). The themis esa plasma instrument and in-flight calibration. *Space Sci. Rev.* 141, 277–302. doi:10.1007/s11214-008-9440-2

Merkin, V. G., and Lyon, J. G. (2010). Effects of the low-latitude ionospheric boundary condition on the global magnetosphere. *J. Geophys. Res. Space Phys.* 115, 15461. doi:10.1029/2010JA015461

Newell, P. T., Lyons, K. M., and Meng, C. I. (1996). A large survey of electron acceleration events. *J. Geophys. Res. Space Phys.* 101, 2599–2614. doi:10.1029/95JA03147

Ogilvie, K. W., Chornay, D. J., Fritzenreiter, R. J., Hunsaker, F., Keller, J., Lobell, J., et al. (1995). SWE, A comprehensive plasma instrument for the wind spacecraft. *Space Sci. Rev.* 71, 55–77. doi:10.1007/BF00751326

Pollock, C., Moore, T., Jacques, A., Burch, J., Gliese, U., Saito, Y., et al. (2016). Fast plasma investigation for magnetospheric multiscale. *Space Sci. Rev.* 199, 331–406. doi:10.1007/s11214-016-0245-4

Qian, L., Burns, A. G., Emery, B. A., Foster, B., Lu, G., Maute, A., et al. (2014). *The NCAR TIE-GCM*. Wiley. doi:10.1002/9781118704417.ch7

Redmann, J. (1985). "An overview of the mission sensor systems of the dmsp satellites," in *American institute of Aeronautics and astronautics, aerospace Sciences meeting* (Reno, NV: ASM), 240.

Roble, R. G., Ridley, E. C., Richmond, A. D., and Dickinson, R. E. (1988). A coupled thermosphere/ionosphere general circulation model. *Geophys. Res. Lett.* 15, 1325–1328. doi:10.1029/GL015i012p01325

Siebert, K. D., and Siscoe, G. L. (2002). Dynamo circuits for magnetopause reconnection. *J. Geophys. Res. Space Phys.* 107, 1095. doi:10.1029/2001JA000237

Siscoe, G. L., Crooker, N. U., and Siebert, K. D. (2002). Transpolar potential saturation: Roles of region 1 current system and solar wind ram pressure. *J. Geophys. Res. Space Phys.* 107, 1321. doi:10.1029/2001JA009176

Smith, C. W., L'Heureux, J., Ness, N. F., Acuña, M. H., Burlaga, L. F., and Scheifele, J. (1998). The ACE magnetic fields experiment. *Space Sci. Rev.* 86, 613–632. doi:10.1023/A:1005092216668

Tang, B. B., Guo, X. C., Wang, C., Hu, Y. Q., and Kan, J. R. (2009). Bow shock and magnetopause contributions to the cross-tail current from global mhd simulations. *J. Geophys. Res. Space Phys.* 114, 14325. doi:10.1029/2009JA014325

Tang, B. B., Wang, C., and Guo, X. C. (2012). Bow shock and magnetopause contributions to the magnetospheric current system: Hints from the cluster observations. *J. Geophys. Res. Space Phys.* 117, 16681. doi:10.1029/2011JA016681

Torbert, R. B., Russell, C. T., Magnes, W., Ergun, R. E., Lindqvist, P. A., Le Contel, O., et al. (2016). The FIELDS instrument suite on MMS: Scientific objectives, measurements, and data products. *Space Sci. Rev.* 199, 105–135. doi:10.1007/s11214-014-0109-8

Wiltberger, M., Qian, L., Huang, C. L., Wang, W., Lopez, R. E., Burns, A. G., et al. (2012). Cmit study of cr2060 and 2068 comparing l1 and mas solar wind drivers. *J. Atmos. Solar-Terrestrial Phys.* 83, 39–50. doi:10.1016/j.jastp.2012.01.005

frontiers | Frontiers in Astronomy and Space Sciences

TYPE Original Research
PUBLISHED 09 February 2023
DOI 10.3389/fspas.2022.1037096

OPEN ACCESS

EDITED BY
Simon Wing,
Johns Hopkins University, United States

REVIEWED BY
Scott William McIntosh,
National Center for Atmospheric Research (UCAR), United States
Antonio Vecchio,
Radboud University, Netherlands

*CORRESPONDENCE
S. C. Chapman,
S.C.Chapman@warwick.ac.uk

SPECIALTY SECTION
This article was submitted to Space Physics, a section of the journal Frontiers in Astronomy and Space Sciences

RECEIVED 05 September 2022
ACCEPTED 12 December 2022
PUBLISHED 09 February 2023

CITATION
Chapman SC (2023), Charting the solar cycle.
Front. Astron. Space Sci. 9:1037096.
doi: 10.3389/fspas.2022.1037096

Charting the solar cycle

S. C. Chapman[1,2]*

[1]Centre for Fusion, Space and Astrophysics, University of Warwick, Coventry, United Kingdom, [2]Department of Mathematics and Statistics, University of Tromso, Tromso, Norway

Sunspot records reveal that whilst the Sun has an approximately 11 year cycle of activity, no two cycles are of the same duration. Since this activity is a direct driver of space weather at Earth, this presents an operational challenge to quantifying space weather risk. We recently showed that the Hilbert transform of the sunspot record can be used to map the variable cycle length onto a regular "clock" where each cycle has the same duration in Hilbert analytic phase. Extreme geomagnetic storms rarely occur within the quiet part of the cycle which is a fixed interval of analytic phase on the clock; there is a clear active-quiet switch-off and quiet-active switch-on of activity. Here we show how the times of the switch-on/off can be determined directly from the sunspot time-series, without requiring a Hilbert transform. We propose a method-charting-that can be used to combine observations, and reports of societal impacts, to improve our understanding of space weather risk.

KEYWORDS

solar cycle, space weather, geomagnetic storms, Hilbert transform, sunspot record, Gleissberg cycle

1 Introduction

Extreme space weather storms can disrupt power distribution, communication, aviation and satellites. They are directly driven by solar activity, but the severity of the technological and societal impact of a geomagnetic storm depends on many factors, from the amplitude of structure emitted from the corona, to how it propagates from Sun to Earth, how it interacts with the magnetosphere of the Earth (Yermolaev et al., 2013; Hathaway, 2015; Baker and Lanzerotti, 2016), and where geographically the maximum ground induced currents occur (Thomson et al., 2010). The largest events can result in significant societal impact and financial loss (Oughton et al., 2016; Oughton et al., 2017; Hapgood, 2019).

Decision making for mitigating the effects of space weather is supported by 1) *forecasts* of individual events that use modelling to map forwards in time a prediction of how a given space weather event will evolve in time and 2) *risk estimates*, that is, probabilistic estimates of the likelihood of occurrence of events of a given severity. The first of these supports real-time operational decisions, whereas the latter provides guidance on planning and preparedness which necessarily must balance resilience against cost. It is the latter that is the topic of this paper.

Risk estimates for extreme space weather events are usually aggregated over multiple solar cycles, (Siscoe, 1976; Silbergleit, 1996; Silbergleit, 1999; Thomson et al., 2011; Riley, 2012; Riley and Love, 2016; Chapman et al., 2020a), which improves the statistical sample size at the expense of averaging over different levels of solar activity. Risk estimates suggest that geomagnetic storms are more likely in the active phase of the cycle (Tsubouchi and Omura, 2007) and this solar cycle modulation appears to be stronger for the more extreme events (Tsurutani et al., 2006; Chapman et al., 2020b). However, extreme events are rare, so that statistical quantification of the solar cycle variation of their occurrence probability is challenging (Riley and Love, 2016).

Each solar cycle differs in its duration and amplitude [see e.g., (Hathaway, 2015; Russell et al., 2019)] and overall geomagnetic activity tracks this variation both within and between solar cycles (Chapman et al., 2018b; Lockwood et al., 2018; Bergin et al., 2022). Quantifying the solar cycle dependence of the risk of extreme space weather events therefore requires timing the start and end of each 11 year cycle. Sunspot data can be used to time solar cycles [e.g., Owens et al. (2011)] to facilitate comparison of long-term observations across multiple cycles. Cycle terminators (McIntosh et al., 2014; McIntosh and Leamon, 2014; McIntosh et al., 2019) have been identified based on multiple observations of coronal magnetic activity, they coincide with a rapid "switch-on" of activity. Recently Chapman et al. (2020b) used the Hilbert transform of smoothed sunspot number (SSN) to map the non-uniform duration solar cycle onto a uniform interval 2π of analytic phase. This provides a regular clock for the solar cycle which can be used to organise long-term observations of solar and geomagnetic activity. From the solar clock, a clear quiet interval in the solar cycle can be identified, with a switch-on of activity at the terminators, and a switch-off that occurs at an analytic phase $\sim 4\pi/5$ earlier, which would correspond to a duration of the quiet interval of 4.4 years in an exactly 11 year cycle. This switch-on and switch-off can be identified as sharp changes in multiple indicators of solar and geomagnetic activity (Chapman et al., 2020b; Leamon et al., 2022), suggesting that there is a clear demarcation between active and quiet phases of the cycle.

In this paper we will map back from the phase of the solar cycle clock to the time domain. This provides a cycle-by-cycle chart which can be used to integrate heterogeneous information. On the one hand, long-term observations, such as the time-series of geomagnetic indices, can form the basis of statistical quantification of risk (i.e., event return times). On the other hand, information that is partially qualitative, such as reports of technological impacts, historical auroral sightings, and lists of the most severe storms based on a variety of indicators [e.g., Knipp et al. (2021); Cliver and Svalgaard (2004)], contain valuable information about the potential hazard [e.g., Mitchell-Wallace et al. (2017)], of extreme space weather events. Charting provides a method to combine this information.

Extreme events have occurred in quiet conditions so that their risk is never zero (Thomson et al., 2010). There have been several instances where extreme storms have occurred under relatively quiet conditions, that is, not at solar maximum. The most notable of these are the 1903 event (Hayakawa et al., 2020) and the 2012 Carrington class storm that missed the Earth (Baker et al., 2013). We will see that these are examples of events that did not occur during the quiet interval, but that can occur just before/after the switch-off/on of activity.

Quantifying, and potentially predicting, the switch-off and switch-on of activity is thus of key importance to space weather resilience planning. It has the potential to translate an overall awareness of a solar cycle modulation of risk, into a quantitative estimate of the specific time intervals when the risk is high or low. Whilst it is possible to directly extrapolate the analytic phase forwards to make a prediction (Leamon et al., 2020), the well known edge effects of the Hilbert transform [e.g., Boashash (1992)] can introduce subtle systematic errors (Booth, 2021; Leamon et al., 2021). In this paper we show how the switch-on and switch-off can be directly estimated from the SSN time-series, without recourse to a Hilbert transform.

The organization of the paper is as follows. **Section 2** introduces the data and provides a brief summary of how the Sun clock is constructed using Hilbert transform of the sunspot number (SSN) record. **Section 3.1** details how the solar cycle switch-on and switch-off times can be directly read-off the SSN time-series. **Section 3.2** discusses charting as a method to integrate heterogeneous data. This is followed by a summary.

2 Methods

2.1 Data

We will determine the activity switch-on and switch-off times direct from the SILSO SSN version 2.0 record. Monthly sunspot observations are available since 1749 and daily sunspot number are available since 1818; data downloaded to 28 August 2022. To identify active times we will use geomagnetic indices definitive and preliminary data. The *aa* index is available since 1868, downloaded to 28 August 2022 and the *Dst* index is available since 1957, downloaded to 31 December 2021. The *aa* index (units, *nT*) (Mayaud, 1980) is discretized in amplitude (Bubenik and Fraser-Smith, 1977; Chapman et al., 2020a) so that throughout this paper we will consider days within which the *aa* exceeds a given threshold as an activity indicator, rather than the peak *aa* value. Other data and lists of events will be introduced as they are used.

2.2 Solar clock *via* Hilbert transform

A time-series $S(t)$ can be expressed in terms of a time-varying amplitude $A(t)$ and phase $\phi(t)$ by obtaining its analytic signal (Gabor, 1946; Boashash, 1992) $A(t)\exp[i\phi(t)] = S(t) + iH(t)$ where $H(t)$ is the Hilbert transform of $S(t)$. It is routinely used to test for synchronisation [e.g., Chapman et al. (2018a)] and for amplitude-frequency (Palŭs and Notovna, 1999) and mode-mode (Vecchio et al., 2017) relationships. Here it maps the variable duration of each solar cycle into a corresponding uniform 0 to 2π phase interval.

In this paper we will use both daily and monthly sunspot number for $S(t)$. After 1818, we construct the solar cycle clock using daily sunspot number as described in Chapman et al. (2020b), again working with the 180 days smoothed daily sunspot number. Post 1749, we work with the 13 month smoothed monthly sunspot number. For both these time-series we obtain the slow trend by performing a robust local linear regression which down-weights outliers ("rlowess") using a 40 year span (or window). The procedure is shown in **Figure 1** for the monthly sunspot number record. Panel (a) plots the monthly sunspot number (black dots), its 13 month running mean (red line) and the 40 year slow trend (blue). We found previously [Figure 13 of (Chapman et al., 2021)] that this slow trend simply tracks the Gleissberg cycle (Gleissberg, 1967). The results are robust for a reasonable range of the spans over which the running mean and slow trend are obtained, the times of occurrence of the terminators obtained from the monthly sunspot number vary within ±2 months for running mean span in the range 6–25 months and for slow trend span in the range 30–60 years.

For the analytic signal to be meaningful we require an oscillatory, albeit irregular, signal that crosses zero every half cycle as input. We

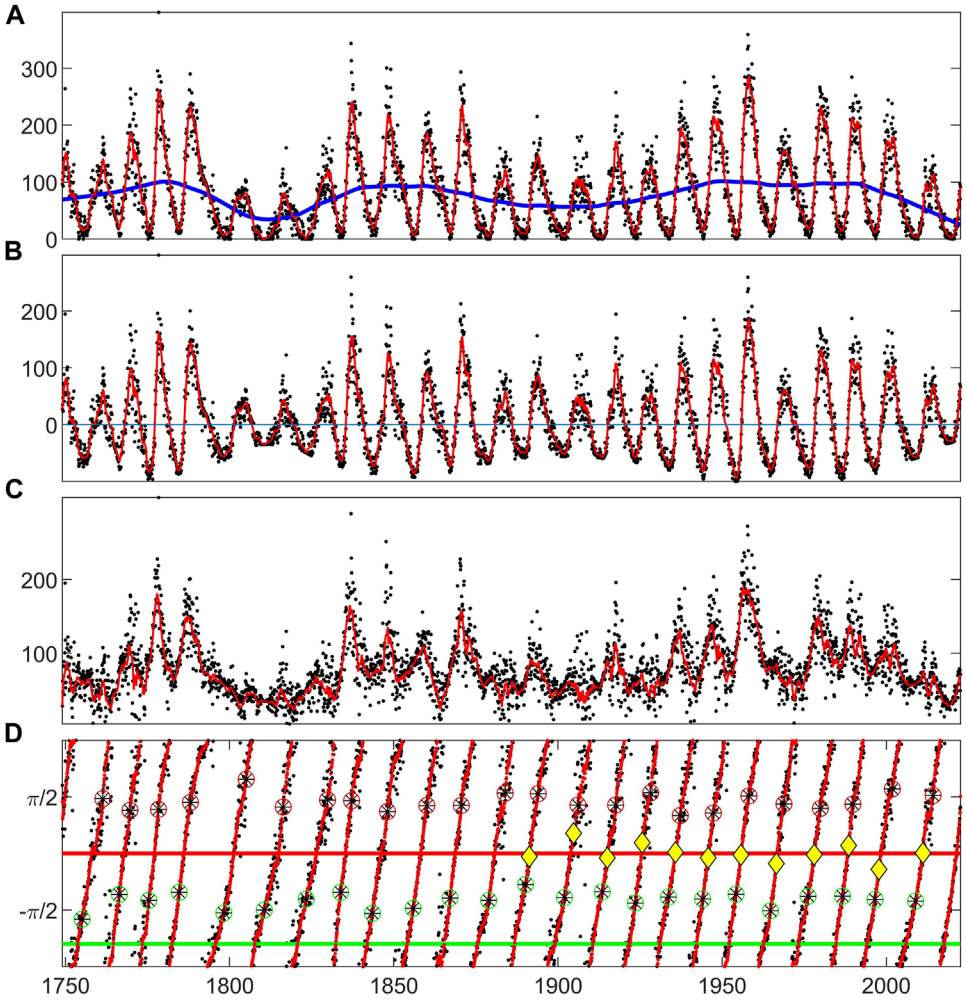

FIGURE 1
Analytic signal of the monthly sunspot record time-series. Monthly sunspot number (black dots) and its 13 month running mean (red) are plotted: **(A)** with the slow trend (blue), the 40 year window local linear regression of monthly sunspot number. **(B)** with the slow trend subtracted. This is Hilbert transformed to obtain the analytic signal with amplitude **(C)** and phase **(D)**. In **(D)**, solar maxima and minima are indicated by the red and green circled asterisks respectively, terminators by yellow diamonds. Zero phase is set at the average of the terminator times from McIntosh et al. (2019). Horizontal lines are at phases zero (terminator, red) and $-4\pi/5$ (pre-terminator, green).

therefore work with the SSN smoothed sufficiently to remove fast fluctuations from which a slow trend is then subtracted [see e.g., Chapman et al. (2018a); Boashash (1992); Chapman et al. (2020b)]. Panel (b) plots the slow trend subtracted 13 month running average smoothed SSN. This is Hilbert transformed and panel (c) and (d) plot the analytic signal amplitude $A(t)$ and phase $\phi(t)$ respectively. We can plot any other quantity on these plots for which we have an occurrence time, here, we plot the solar maxima and minima (red/green circles around black asterisks). The yellow diamonds indicate cycle terminators identified in (McIntosh et al., 2019); we set zero phase at the average of these.

The switch-off (pre-terminators) and switch-on (terminators) [see Chapman et al. (2020b)] are at analytic phases $-4\pi/5$ and zero, indicated by horizontal green and red and lines respectively on Panel (d) of **Figure 1**. These bracket the quiet intervals of each solar cycle. They are identified by inspection of the solar cycle clock as shown here in **Figure 2** [see Chapman et al. (2020b) for a statistical analysis]. The **Figure 2** solar cycle clock summarizes the rationale for these particular values of analytic phase; it is a composite of results presented in (Chapman et al., 2020b) which has also been updated with current data. The clock plots as its angular coordinate the analytic phase with time increasing clockwise. It has been constructed from the daily SSN since 1818 and can overplot observations from the last 18 Schwabe cycles. The maxima and minima of these 18 cycles are shown in red and green circles respectively, along with their average phases (black lines). The terminators, identified for the last 12 cycles by McIntosh et al. (2019) are plotted (blue circles) with their average (red line). The terminator average phase estimates the switch-on of activity.

We plot long-term observations on the clock; binned occurrences of solar flares (6 month binned GOES X-ray flux catalog, four cycles), the F10.7 index time-series [daily solar radio flux at 10.7 cm, six cycles (Tapping, 2013)] (blue dots). Activity in the *aa* index (14 cycles) is indicated by plotting black dots arranged on concentric circles at any day when $aa > 100, 200, 300, 400, 500, 600\ nT$ so that extreme events appear as outward radiating "spokes". We can then

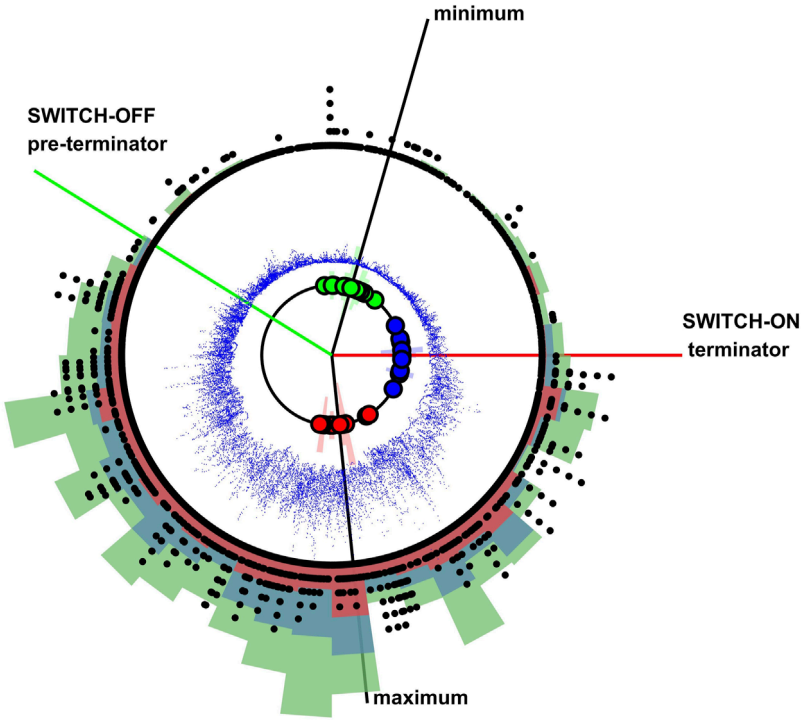

FIGURE 2
Solar cycle clock. Increasing time (analytic phase) is read clockwise. The clock shown is obtained from the daily sunspot number record since 1818. Analytic phases of the maxima and minima of the last 18 solar cycles are indicated by red and green circles respectively and the blue circles indicate terminators for the last 12 solar cycles (McIntosh et al., 2019). Black lines indicate the average analytic phase for the maxima and minima. A red line indicates the average analytic phase of the terminators. The pre-terminator (green line) is at a phase $-4\pi/5$ w.r.t. the terminator. Black dots arranged on concentric circles where increasing radius indicates *aa* values which in any given day exceeded 100, 200, 300, 400, 500, 600 *nT*. Blue dots overplot daily F10.7 and overplotted red, blue and green histograms show counts in non-overlapping (normalized) 3-month long bins for X-class, M-Class and C-class flare occurrence (scaled relative to each other in ratio 75:500:2000).

see that there is an increase (switch-on) in activity just following the terminator. By inspection, activity declines (switch-off) around the pre-terminator (green line) which we simply identified as being $-4\pi/5$ in phase w.r.t the terminator, this locates the switch-off and switch-on at approximately $\pm 2\pi/5$ either side of the average phase of the minimum [see (Chapman et al., 2020b)]. Both the switch-on and switch-off provide approximate markers that bracket the quiet interval of the cycle which we now map back into the time domain.

3 Results

3.1 Activity switch-off/on direct from the sunspot record

The occurrence times of the pre-terminators (switch-off) and terminators (switch-on) are essentially read off Panel (d) of **Figure 1** across the entire monthly sunspot record from 1750. To improve accuracy, the 13 month smoothed SSN was up-sampled by a factor of 10 in time resolution by linear interpolation in determining these occurrence times. The times of the pre-terminators (switch-off) are when the analytic phase crosses $-4\pi/5$ and all the terminators (switch-on) are at phase zero.

In **Figure 3** the pre-terminators (switch-off) and terminators (switch-on) are mapped back onto the SSN time-series. Panel (a) and (b) of **Figure 3** show that the terminators (red lines/circles) occur just before the 13 month smoothed monthly SSN up-crosses its slow trend. The pre-terminators (green lines/circles) occur after the corresponding down-crossing. This immediately suggests a straightforward method to roughly estimate these occurrence times direct from the SSN record, without first performing a Hilbert transform to obtain the analytic phase. In Panel (c) of **Figure 3**, the black crosses provide a rough estimate of the switch-on as occurring when the smoothed SSN up-crosses the slow trend, and the switch-off as occurring 12 months after the SSN down-crosses the slow trend. We can see that these rough estimates correspond quite closely to the actual terminator and pre-terminator occurrence times found from the analytic phase *via* Hilbert transform. For example, the terminator that ends cycle 24 and starts cycle 25 is found from the Hilbert transform to be at decimal year 2021.3, whereas the up-crossing is at 2021.5 We emphasise that the analytic phase determined by Hilbert transform is relative, to plot a phase value we have chosen a reference, here we set the phase to zero at the average phase of the terminators found by (McIntosh et al., 2019). The times at which the terminators and pre-terminators occur are independent of how the reference phase is chosen.

In identifying the pre-terminators (switch-off) and terminators (switch-on) times directly from the SSN time-series we exploited the fact that they occur close to the down-and up-crossings respectively of the slow trend by the smoothed SSN. We would expect a linear

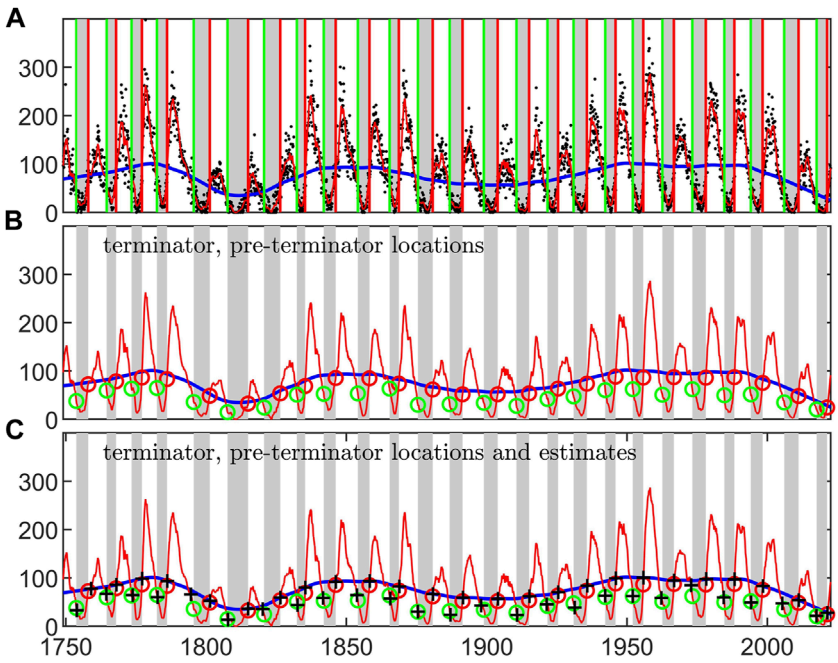

FIGURE 3
Switch-on and switch-off times overplotted on the monthly sunspot record. The 13 month running mean of the monthly sunspot number (red) and its 40 year (lowess) slow trend (blue) are overplotted on the quiet intervals (grey shading) between each pre-terminator and terminator. **(A)** also plots the monthly sunspot number (black dots) and vertical lines indicating the pre-terminators (green) and terminators (red) at the start and end of each quiet interval. **(B)** overplots circles on the 13 month running mean of the monthly SSN when the pre-terminators (green circles) and terminators (red circles) occur, that is, when the analytic phase is at $-4\pi/5$ and zero respectively. **(C)** is the same as **(B)** except that it also overplots (black crosses) estimates of the pre-terminators and terminators based solely on the monthly sunspot record; these are at the value of the 13 month smoothed SSN 12 month after the SSN down-crosses the slow trend (for the pre-terminators) and at the time when the SSN up-crosses the slow trend (for the terminators).

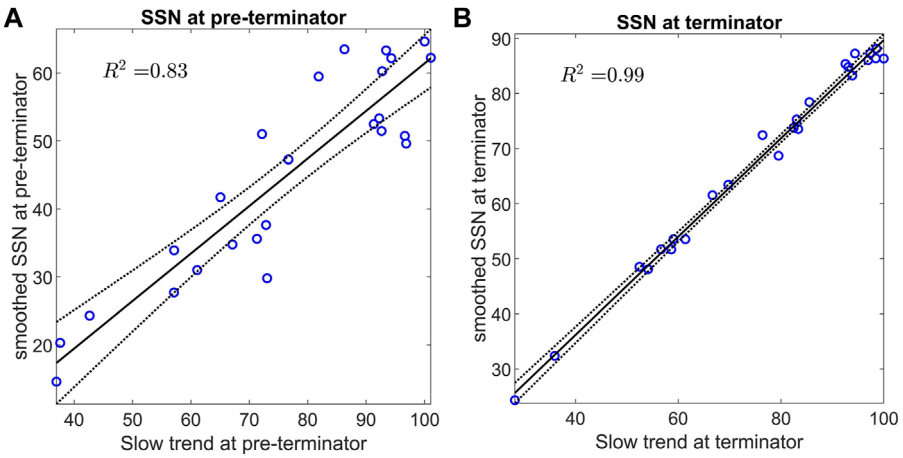

FIGURE 4
The slow trend predicts the smoothed sunspot number at the switch-off and switch-on of activity. Linear regression of 13 month smoothed sunspot number on its slow (40 year rlowess) trend (left) at the pre-terminators and (right) at the terminators. Best fit line (solid black line) and 95% confidence bounds (dashed black lines) are overplotted on the data (blue circles). The R^2 of each fit is indicated.

relationship between smoothed SSN and SSN slow trend to hold if we are sufficiently close to the times where they cross each other and share the same value. In Figure 4 we test to what extent the pre-terminators and terminators are within this linear regime. We performed a linear regression of the 13 month smoothed sunspot number on the slow trend for values determined at the pre-terminators (left panel) and terminators (right panel). The coefficients with 95% confidence bounds for the line $y = a\,(x - b)$ are for the terminators: $a = 0.89(0.85, 0.93)$; $b = -0.60(-3.75, 2.56)$ and the pre-terminators $a = 0.70(0.56, 0.84)$; $b = 12.13(-1.07, 25.34)$. The values of

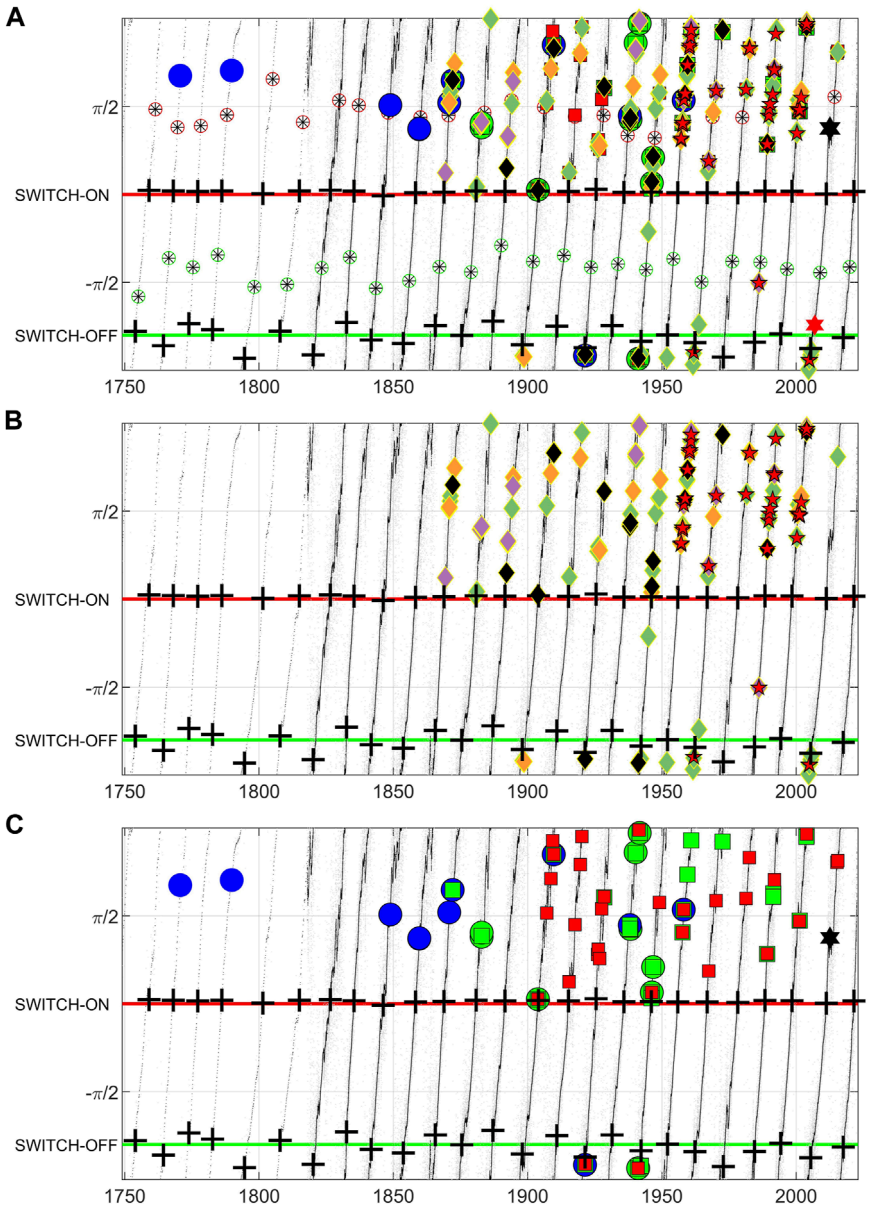

FIGURE 5
Charting solar cycle dependence of space weather impacts. The analytic phase of the monthly, and after 1818, daily SSN is plotted versus time. In all panels horizontal lines for phase $-4\pi/5$ (green) and zero (red) indicate the switch-off (pre-terminators) and switch-on (terminators) of activity. The black crosses are estimates of the switch-on/off times obtained directly from the monthly SSN as in **Figure 3**. **(A)**: Solar maxima and minima are plotted as red and green circled black asterisks respectively. Extreme space weather events are plotted on the chart. These are as follows. **(A, B)**: Red 5-pointed stars plot days when *Dst* <−250 *nT*. Diamonds plot days when the aa index has exceeded 300, 400, 500, and 600 nT (green, orange, cyan, and black). **(A, C)**: Blue and green circles from Table 1 and Table 2 of Knipp et al. (2021). Red 6-pointed star: a moderate December 2006 event discussed by Knipp et al. (2021). Green squares: Tables I, III, IV, and VII of Cliver and Svalgaard (2004). Red squares: Table 1 of Love (2021). Black 6-pointed star: July 2012 Carrington class event that missed the Earth Baker et al. (2013).

the coefficient of determination, R^2 of 0.83 and 0.99 for the pre-terminators and terminators respectively, suggest that they are indeed both within this linear regime. The linear relationship is stronger for the terminators as they are closer to the up-crossings than the pre-terminators are to the down-crossings. These linear relationships between smoothed and slow trend SSN then could form the basis of a method to translate forward predictions of the SSN into a prediction of when the next switch-off or switch-on of activity will occur. A forward prediction of the SSN would provide a prediction of both the slow trend and the 13 month smoothed SSN, when these two values satisfy the linear relationships in **Figure 4**, they predict the next switch-on or switch-off (where the 13 month smoothed SSN up-crosses or down-crosses the slow trend respectively). The uncertainties of this prediction are given by the 95% confidence bounds on the linear fit coefficients stated above, and can be read off the 95% confidence bounds plotted in **Figure 4**. These uncertainties would need to be combined with that of the underlying prediction of the SSN.

3.2 Charting

Both quantitative observations of geomagnetic activity, and qualitative indicators of space weather impacts, contain useful information in assessing risk, and relating it to hazard. Charting offers a method to combine this information on a cycle-by-cycle basis. **Figure 5** charts the last 24 Schwabe cycles. Each of the panels plots analytic phase versus time for the monthly, and overplotted, the daily SSN. Solar cycle maxima and minima are plotted in Panel (a) for reference. The analytic phases zero and $-4\pi/5$, that is, the switch-on and switch off obtained *via* Hilbert transform of the SSN as described above, are indicated with horizontal red and green lines respectively. Estimates of the switch-on and switch-off times, obtained directly from the SSN timeseries as detailed in **Figure 3**, are indicated by black crosses. These bracket the quiet interval of activity.

In Panel (b) we plot indicators of extreme space weather activity obtained directly from geomagnetic index time-series. Red 5-pointed stars plot days when $Dst < -250\ nT$. This may plot more than one star for an intense storm that lasts several days. Days when the *aa* index has exceeded $300, 400, 500, 600\ nT$ are plotted as diamonds, coloured green, orange, cyan, and black respectively. There is one extreme event during the quiet interval in 1986 [the event noted by Thomson et al. (2010)] and two more moderate events in 1944 and 1963.

We can instead plot notable storms that have been identified using a variety of different criteria. In Panel (c) we plot the following notable storms. The green squares plot events from Tables I, III, IV, and VII of Cliver and Svalgaard (2004). These range from storms seen in a single ground based magnetometer station that correlate with preceeding solar flares, to low latitude aurorae. The red squares plot the most intense storms in each solar cycle from cycle 14 on, identified from ground magnetograms and the Dst index in Table 1 of Love (2021). Blue and green circles are Table 1 (low latitude aurorae) and Table 2 (CSAGI list, storms which were associated with disruptive technology effects) respectively of Knipp et al. (2021). None of these events occur in the quiet interval.

We overplot all of the events in Panels (b) and (c) on Panel (a). These are heterogeneous data which could not be readily combined in a statistical study to quantify risk. Importantly, the effective "coverage" is not uniform in time, it depends on availability of observations, and in assessing impact, the nature and prevalence of technology which has evolved significantly over the last two centuries. Nevertheless, the chart provides a useful method to bring together and summarize these distinct classes of information. We can see that extreme events within the quiet interval are quite rare, but importantly, some of the most intense events can occur right at the boundaries of the quiet interval. For example, the "quiet time" 1903 event Hayakawa et al. (2020) which is an $aa > 600\ nT$ event (black diamond) and which features in multiple Tables of notable events is just at the switch-on. The black 6-pointed star plots the July 2012 Carrington class event that missed the earth Baker et al. (2013) in Panel (a) and although it is not at solar maximum, it is within the active interval.

The chart shown in **Figure 5** focuses on the most extreme events. These are more clearly organised by the Schwabe cycle than more moderate events (Tsurutani et al., 2006; Chapman et al., 2020b). The 27-days recurrence (solar rotation) seen in the *aa* index has a Hale cycle dependence (Sargent, 1985; 2021). This can be clearly resolved as a Hale cycle modulated declining phase in the approximately 22 year Hale cycle clock (Chapman et al., 2021). The occurrence of extreme events, as identified in geomagnetic index time-series, show the same solar cycle ordering as solar flare occurrence as can be seen in **Figure 3** [see also (Chapman et al., 2020b)], albeit over four cycles of X-ray flux observations. This is consistent with the idea that more moderate events are more likely to be associated with Hale cycle modulated high speed streams. Further work is needed to develop a chart appropriate for more moderate events; important since these can be disruptive to technology. An example is indicated in Panel (a) of **Figure 5** by the red 6-pointed star which is a December 2006 event discussed by Knipp et al. (2021) which, whilst having moderate Dst = - 147 nT had technological impact.

4 Summary and discussion

This paper is focused on how rare, extreme space weather storms are ordered by the Schwabe solar cycle. No two Schwabe cycles are of the same duration, but the Hilbert transform of the sunspot number (SSN) record can be used to map the non-uniform cycle duration onto a uniform 0 to 2π interval of analytic phase. The quiet interval of the solar cycle is located at a fixed phase interval of this solar cycle clock (Chapman et al., 2020b). In this paper the switch-off and switch-on of activity that bracket the quiet interval of the cycle are mapped from the clock (their analytic phases) back into the time-domain, to create a cycle-by-cycle chart of activity.

Once the chart is constructed from the SSN record, any event which has a known time of occurrence can be plotted on the chart. It thus provides a method to combine heterogeneous information. Space weather risk is routinely estimated from the statistics of events identified in long-term geomagnetic indices (Siscoe, 1976; Silbergleit, 1996; Silbergleit, 1999; Thomson et al., 2011; Riley, 2012; Riley and Love, 2016; Chapman et al., 2020a). Information on space weather hazard on the other hand is embodied in narratives around impacts on technological systems, economic, and societal impacts (Knipp et al., 2016; Knipp et al., 2021; Hapgood, 2019; Oughton et al., 2016; Oughton et al., 2017). It is well understood that the relationship between these is non-trivial, and solar cycle charting has the potential to yield new insights by combining this information.

When lists of the most notable storms are charted, none are found to occur in the quiet interval. Extreme events identified in geomagnetic indices only rarely occur in the quiet interval but the chance is not zero. There are examples of extreme events previously noted as occurring away from solar maximum, which when charted are found to be outside the quiet interval. One example is the Carrington class 2012 event that missed the Earth (Baker et al., 2013). Another is the 1903 event (Hayakawa et al., 2020) which occurred just at the switch-on. The fact that some of the most extreme events are found just at the boundary of the switch-off/on of activity underlines the need to quantify, and ideally predict, the switch-off and switch on times.

This paper shows how the switch-off and switch-on times can be extracted direct from the SSN time-series, without recourse to a Hilbert transform. They can be located with reference to the times at which the smoothed SSN crosses its (40 year smoothed, Gleissberg cycle tracking) slow trend. A rough approximation is that the switch-on is when the smoothed SSN up-crosses its slow trend, and that

the switch-off occurs 12 months after the down-crossing. There is no unique method for predicting the next activity switch-off/on from the SSN. The appropriate method will depend on the time horizon required for the prediction. If this time horizon is several years in advance of the times where the smoothed SSN up- or down-crosses its slow trend, then a full prediction of the non-linearly varying SSN is required. However, for a prediction horizon of perhaps less than a year, a simple linear extrapolation of the smoothed SSN and the slow trend may suffice. The linear relationships found here between smoothed SSN and slow trend at the switch-off/on would form part of this prediction. As extreme events have occurred close to the switch-off and switch-on times, these linear relationships could also be used to add a safety margin to any prediction based on forwards extrapolation. Determining the optimal methodology for such a prediction, and quantifying its accuracy and skilfulness is the topic of future work.

Finally, the locations of the switch-on and switch-off are estimated to be at particular fixed values of the analytic phase of the smoothed SSN, based on an 11 year Schwabe cycle (Chapman et al., 2020b). Whilst this orders the most extreme events, more moderate events have a Hale cycle dependence in their occurrence likelihood (Chapman et al., 2021). A variety of indicators of solar output are found to exhibit sharp changes at the switch-off (pre-terminator) and switch-on (terminator) of activity (Chapman et al., 2020b; Leamon et al., 2022), offering new insights into the physics of the solar cycle of activity. The estimated switch-on and switch-off times may change when our physical understanding is more complete.

Data availability statement

Publicly available datasets were analyzed in this study. This data can be found here: ISGI http://isgi.unistra.fr/. SILSO http://www.sidc.be/silso/datafiles F10.7 index https://www.spaceweather.gc.ca/solarflux/sx-en.php The GOES X-ray Flare dataset (NGDC) https://www.ngdc.noaa.gov/stp/space-weather/solar-data/solar-features/solar-flares/x-rays/.

Author contributions

The author confirms being the sole contributor of this work and has approved it for publication.

Funding

AFOSR grant FA8655-22-1-7056 and STFC grant ST/T000252/1.

Acknowledgments

The results presented in this paper rely in part on geomagnetic indices calculated and made available by ISGI Collaborating Institutes from data collected at magnetic observatories. We acknowledge the involved national institutes, the INTERMAGNET network (www.intermagnet.org) and ISGI (isgi.unistra.fr). We thank the World Data Center for Geomagnetism, Kyoto. We thank the World Data Center SILSO, Royal Observatory of Belgium, Brussels for provision of sunspot data. SC acknowledges AFOSR grant FA8655-22-1-7056 and STFC grant ST/T000252/1. SC thanks N. W. Watkins for useful discussions.

Conflict of interest

The author declares that the research was conducted in the absence of any commercial or financial relationships that could be construed as a potential conflict of interest.

Publisher's note

References

Baker, D. N., and Lanzerotti, L. J. (2016). Resource letter SW1: Space weather. *Am. J. Phys.* 84, 166–180. doi:10.1119/1.4938403

Baker, D. N., Li, X., Pulkkinen, A., Ngwira, C. M., Mays, M. L., Galvin, A. B., et al. (2013). A major solar eruptive event in July 2012: Defining extreme space weather scenarios. *Space weather.* 11, 585–591. doi:10.1002/swe.20097

Bergin, A., Chapman, S. C., Moloney, N., and Watkins, N. W. (2022). Variation of geomagnetic index empirical distribution and burst statistics across successive solar cycles. *J. Geophys. Res.* 127. doi:10.1029/2021JA029986

Boashash, B. (1992). Estimating and interpreting the instantaneous frequency of a signal. I. Fundamentals. *Proc. IEEE®*. 80 (4), 520–538. doi:10.1109/5.135376

Booth, R. J. (2021). Limitations in the Hilbert transform approach to locating solar cycle terminators. *Sol. Phys.* 296, 108. doi:10.1007/s11207-021-01833-1

Bubenik, D. M., and Fraser-Smith, A. C. (1977). Evidence for strong artificial components in the equivalent linear amplitude geomagnetic indices. *J. Geophys. Res.* 82, 2875–2878. doi:10.1029/ja082i019p02875

Chapman, S. C., Horne, R. B., and Watkins, N. W. (2020a). Using the *aa* index over the last 14 solar cycles to characterize extreme geomagnetic activity. *Geophys. Res. Lett.* 47. doi:10.1029/2019GL086524

Chapman, S. C., Lang, P. T., Dendy, R. O., Giannone, L., and Watkins, N. W. (2018a). Control system-plasma synchronization and naturally occurring edge localized modes in a tokamak. *Phys. Plasmas* 25, 062511. doi:10.1063/1.5025333

Chapman, S. C., McIntosh, S. W., Leamon, R. J., and Watkins, N. W. (2020b). Quantifying the solar cycle modulation of extreme space weather. *Geophys. Res. Lett.* 47. doi:10.1029/2020GL087795

Chapman, S. C., McIntosh, S. W., Leamon, R. J., and Watkins, N. W. (2021). The Sun's magnetic (Hale) cycle and 27 day recurrences in the aa geomagnetic index. *Ap. J.* 917, 54. doi:10.3847/1538-4357/ac069e

Chapman, S. C., Watkins, N. W., and Tindale, E. (2018b). Reproducible aspects of the climate of space weather over the last five solar cycles. *Space weather.* 16, 1128. doi:10.1029/2018SW001884

Cliver, E. W., and Svalgaard, L. (2004). The 1859 Solar-terrestrial disturbance and the current limits of extreme space weather activity. *Sol. Phys.* 224, 407–422. doi:10.1007/s11207-005-4980-z

Gabor, D. (1946). Theory of communication. Part 1: The analysis of information. *J. IEE Lond.* 93 (3), 429–441. doi:10.1049/ji-3-2.1946.0074

Gleissberg, W. (1967). Secularly smoothed data on the minima and maxima of sunspot frequency. *Sol. Phys.* 2, 231–233. doi:10.1007/bf00155925

Hapgood, M. (2019). The great storm of May 1921: An exemplar of a dangerous space weather event. *Space weather.* 17, 950–975. doi:10.1029/2019sw002195

Hathaway, D. H. (2015). The solar cycle. *Living Rev. Sol. Phys.* 12, 4. doi:10.1007/lrsp-2015-4

Hayakawa, H., Ribeiro, P., Vaquero, J. M., Gallego, M. C., Knipp, D. J., Mekhaldi, F., et al. (2020). The extreme space weather event in 1903 october/november:an outburst from the quiet sun. *Astrophysical J. Lett.* 897, L10. doi:10.3847/2041-8213/ab6a18

Knipp, D. J., Bernstein, V., Wahl, K., and Hayakawa, H. (2021). Timelines as a tool for learning about space weather storms. *J. Space Weather Space Clim.* 11, 29. doi:10.1051/swsc/2021011

Knipp, D. J., Ramsay, A. C., Beard, E. D., Boright, A. L., Cade, W. B., Hewins, I. M., et al. (2016). The May 1967 great storm and radio disruption event: Extreme space weather ande xtraordinary responses. *Space weather.* 14, 614–633. doi:10.1002/2016SW001423

Leamon, R. J., McIntosh, S. W., Chapman, S. C., and Watkins, N. W. (2021). Response to "limitations in the Hilbert transform approach to locating solar cycle terminators" by R. Booth. *Sol. Phys.* 296, 151. doi:10.1007/s11207-021-01897-z

Leamon, R. J., McIntosh, S. W., Chapman, S. C., and Watkins, N. W. (2020). Timing terminators: Forecasting sunspot cycle 25 onset. *Sol. Phys.* 295, 36. doi:10.1007/s11207-020-1595-3

Leamon, R. J., McIntosh, S. W., and Title, A. M. (2022). Deciphering solar magnetic activity, the solar cycle clock. *Front. Astron. Space Sci.* 9, 886670. doi:10.3389/fspas.2022.886670

Lockwood, M., Owens, M. J., Barnard, L. A., Scott, C. J., Watt, C. E., and Bentley, S. (2018). Space climate and space weather over the past 400years: 2. Proxy indicators of geomagnetic storm and substorm occurrence. *J. Space Weather Space Clim.* 8, A12. doi:10.1051/swsc/2017048

Love, J. J. (2021). Extreme-event magnetic storm probabilities derived from rank statistics of historical Dst intensities for solar cycles 14–24. *Space weather.* 19, e2020SW002579. doi:10.1029/2020SW002579

Marple, S. L. (1999). Computing the discrete-time analytic signal via FFT. *IEEE® Trans. Signal Process.* 47, 2600–2603. doi:10.1109/78.782222

Mayaud, P. N. (1980). "Derivation, meaning, and use of geomagnetic indices," in *Geophys. Monogr. Ser.* (Washington, D.C: AGU), Vol. 22. doi:10.1029/GM022

McIntosh, S. W., Leamon, R. J., Egeland, R., Dikpati, M., Fan, Y., and Rempel, M. (2019). What the sudden death of solar cycles can tell us about the nature of the solar interior. *Sol. Phys.* 294 (7), 88. doi:10.1007/s11207-019-1474-y

McIntosh, S. W., and Leamon, R. J. (2014). On magnetic activity band overlap, interaction, and the formation of complex solar active regions. *Astrophys. J. Lett.* 796, L19. doi:10.1088/2041-8205/796/1/l19

McIntosh, S. W., Wang, X., Leamon, R. J., and Scherrer, P. H. (2014). Identifying potential markers of the sun's giant convective scale. *Astrophys. J. Lett.* 784, L32. doi:10.1088/2041-8205/784/2/l32

Mitchell–Wallace, K., Jones, M., Hillier, J., and Foote, M. (2017). *Natural catastrophe risk management and modelling: A practitioner's guide*. New York, NY, USA: Wiley-Blackwell.

Oughton, E., Copic, J., Skelton, A., Kesaite, V., Yeo, Z. Y., Ruffle, S. J., et al. (2016). *Solar storm scenario, cambridge risk framework series, centre for risk studies*. Cambridge, England: University of Cambridge.

Oughton, E. J., Skelton, A., Horne, R. B., Thomson, A. W. P., and Gaunt, C. T. (2017). Quantifying the daily economic impact of extreme space weather due to failure in electricity transmission infrastructure. *Space weather.* 15, 65–83. doi:10.1002/2016SW001491

Owens, M. J., Lockwood, M., Barnard, L., and Davis, C. J. (2011). Solar cycle 24: Implications for energetic particles and long-term space climate change. *Geophys. Res. Lett.* 38, L19106. doi:10.1029/2011GL049328

Palŭs, M., and Notovná, D. (1999). Sunspot cycle: A driven nonlinear oscillator? *PRL* 83, 3406–3409. doi:10.1103/physrevlett.83.3406

Riley, P., and Love, J. J. (2016). Extreme geomagnetic storms: Probabilistic forecasts and their uncertainties. *Space weather.* 15, 53–64. doi:10.1002/2016SW001470

Riley, P. (2012). On the probability of occurrence of extreme space weather events. *Space weather.* 10, S02012. doi:10.1029/2011sw000734

Russell, C. T., Jian, L. K., and Luhmann, J. G. (2019). *The solar clock*. Rev. Geophys. 57, 1129–1145.

Sargent, H. H. (2021). *A revised 27 day recurrence index*. arXiv:2101.02155 [astro-ph.SR].

Sargent, H. H. (1985). Recurrent geomagnetic activity evidence for long-lived stability in solar wind structure. *J. Geophys. Res.* 90 (A2), 1425–1428. doi:10.1029/ja090ia02p01425

Silbergleit, V. M. (1999). Forecast of the most geomagnetically disturbed days. *Earth Planets Space* 51, 19–22. doi:10.1186/bf03352205

Silbergleit, V. M. (1996). On the occurrence of geomagnetic storms with sudden commencements. *J. Geomagn. Geoelectr.* 48, 1011–1016. doi:10.5636/jgg.48.1011

Siscoe, G. L. (1976). On the statistics of the largest geomagnetic storms per solar cycle. *J. Geophys. Res.* 81, 4782–4784. doi:10.1029/ja081i025p04782

Tapping, K. F. (2013). The 10.7 cm solar radio flux (F10.7). *Space weather.* 11, 394–406. doi:10.1002/swe.20064

Thomson, A. W. P., Dawson, E. B., and Reay, S. J. (2011). Quantifying extreme behavior in geomagnetic activity. *Space weather.* 9, S10001. doi:10.1029/2011SW000696

Thomson, A. W. P., Gaunt, C. T., Cilliers, P., Wild, J. A., Opperman, B., McKinnell, L.-A., et al. (2010). Present day challenges in understanding the geomagnetic hazard to national power grids. *Adv. Space Res.* 45, 1182–1190. doi:10.1016/j.asr.2009.11.023

Tsubouchi, K., and Omura, Y. (2007). Long-term occurrence probabilities of intense geomagnetic storm events. *Space weather.* 5, S12003. doi:10.1029/2007SW000329

Tsurutani, B. T., Gonzalez, W. D., Gonzalez, A. L. C., Guarnieri, F. L., Gopalswamy, N., Grande, M., et al. (2006). Corotating solar wind streams and recurrent geomagnetic activity: A review. *J. Geophys. Res.* 111, A07S01. doi:10.1029/2005JA011273

Vecchio, A. A., Lepreti, F., Laurenza, M., Alberti, T., and Carbone, V. (2017). Connection between solar activity cycles and grand minima generation. *Astron. Astrophys.* 599, A58. doi:10.1051/0004-6361/201629758

Yermolaev, Y. I., Lodkina, I. G., Nikolaeva, N. S., and Yermolaev, M. Y. (2013). Occurrence rate of extreme magnetic storms. *J. Geophys. Res. Space Phys.* 118, 4760–4765. doi:10.1002/jgra.50467

Frontiers in
Astronomy and Space Sciences

Explores planetary science and extragalactic astronomy in all wavelengths

Advances the understanding of our universe - from planetary science to extragalactic astronomy, to high-energy and astroparticle physics.

Discover the latest Research Topics

See more →

Frontiers

Avenue du Tribunal-Fédéral 34
1005 Lausanne, Switzerland
frontiersin.org

Contact us

+41 (0)21 510 17 00
frontiersin.org/about/contact